Synthesis of Interlocked [8+12] Organic Cages and Investigation of Catenation Mechanism

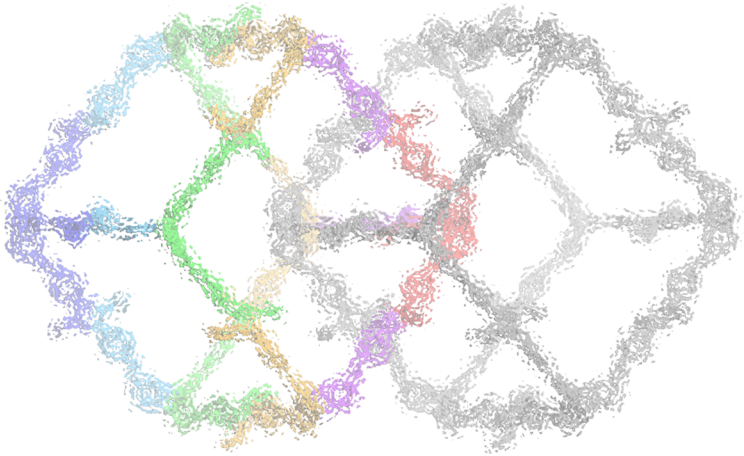

Gangxiang Zhou

周钢翔



Dissertation

Heidelberg

2022

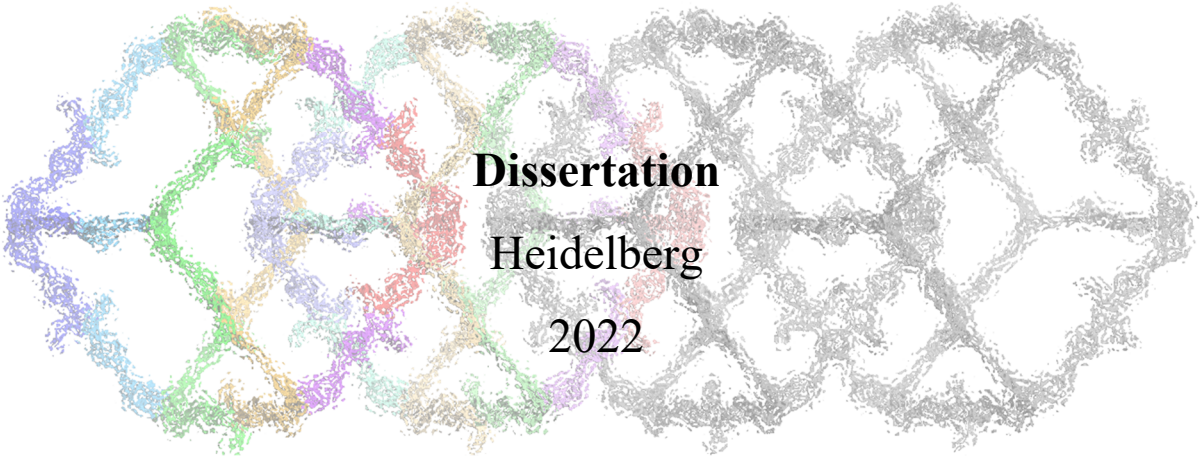

Inaugural-Dissertation

Zur Erlangung der Doktorwürde der

Naturwissenschaftlichen-Mathematischen Gesamtfakultät

der Ruprecht-Karls-Universität Heidelberg

vorgelegt von

Gangxiang Zhou, M. Sc.

aus Hubei, Volksrepublik China

Oktober 2022

Tag der mündlichen Prüfung: 02.12.2022

Synthesis of Interlocked [8+12] Organic Cages and Investigation of Catenation Mechanism

Gutacher: Prof. Dr. Michael Mastalerz

Prof. Dr. Milan Kivala

Abstract

This thesis describes the synthesis of interlocked giant [8+12] organic cages and the systematic investigations of the catenation mechanism. By tuning the substituents of the building blocks and the length of linkers, a series of monomeric cages with different volumes and structures were designed and synthesized. Based on these monomeric cages, four major factors in the catenation process were studied:

1. The effects of the size and cavity volume of the monomeric cage on catenation tendency (*Chapter 3.1*). Three types of triptycene triamine and two dialdehyde linkers were utilized to construct six catenanes and two organic cages. By investigating the relationship between the formation of catenanes and the size of monomeric cages, it was found, when the difference between the volume of the cage and its cavity is smaller, the monomeric cages tend to be interlocked more.

2. The structural effects on catenation (*Chapter 3.2*). To further figure out the driving force of catenation, several dialdehyde linkers with varied substituents were used to build monomeric cages. Experimental results showed that the structural changes of the monomeric cages significantly influenced the catenation results.

3. Solvent effects (*Chapter 3.3*). To explore the solvent effects on the catenation, a solvent screening was conducted for the synthesis of catenanes. Moreover, the solvent mixtures and several corresponding combinations were also investigated.

4. Synthesis of polycatenanes (*Chapter 3.4*). According to the studies of solvents and structural effects in previous chapters, the rational synthesis and isolation of dimer, trimer, and tetramer could be achieved by adjusting the ratio of solvent mixtures, type of building blocks, and the equivalents of linkers.

In addition, an ongoing project about obtaining single crystals of metal-assisted covalent organic frameworks (MSOFs) was shown in *Chapter 4*. The idea is to prepare the metal-organic frameworks (MOFs) single crystals first and then transform them into MSOFs single crystals by post-modification. Two approaches were designed and the corresponding MOFs were synthesized, unfortunately, only nanocrystals of MOFs were obtained currently.

Kurzfassung

Diese Dissertation beschreibt die Synthese von verschränkten, riesigen [8+12] organischen Käfigen, sowie die systemischen Untersuchungen des Caternierungsmechanismus. Durch Variation der Größe und des Einsatzes verschiedener Bausteine und Linker wurde eine Reihe von monomeren Käfigen mit unterschiedlichen Hohlraumvolumina und Geometriegrößen entworfen und synthetisiert. Basierend auf diesen monomeren Käfigen wurden vier Hauptfaktoren im Caternierungsmechanismus erforscht:

1. Der Einfluss der Käfig- und Hohlraumgröße auf die Verschränkungstendenz (Kapitel 3.1). Drei Varianten des Triptycentriamins und zwei Dialdehydlinker wurden verwendet, um sechs Käfig-Catenane und zwei organische Käfige zu konstruieren. Bei der Untersuchung der Beziehung zwischen der Bildung von Catenanen und der Größe der monomeren Käfige wurde festgestellt, dass die monomeren Käfige eher dazu neigen Catenane zu bilden, wenn die geometrische Größe deutlich kleiner als das Hohlraumvolumen ist.

2. Die strukturellen Auswirkungen auf die Verkettung (Kapitel 3.2). Um die treibende Kraft der Verkettung weiter zu untersuchen, wurden mehrere Dialdehyd-Linker mit unterschiedlichen aromatischen Eigenschaften und Substituenten zum Aufbau der monomeren Käfige verwendet. Experimentelle Ergebnisse zeigten, dass die Einführung von Substituenten oder das Wechseln der aromatischen Linker die Bildung der Catenane veränderte.

3. Lösungsmitteleinfluss (Kapitel 3.3). Um die Lösungsmitteleffekte auf die Catenation zu erforschen, wurde eine Versuchsreihe mit verschiedenen Lösungsmitteln sowie Lösungsmittelgemischen in unterschiedlichen Mischungsverhältnissen durchgeführt.

4. Synthese von Polycatenanen (Kapitel 3.4). Der Studien über Lösungsmittel- und Struktureffekten in den vorangegangenen Kapiteln zufolge, konnte die rationale Synthese und Isolierung von Di-, Tri- und Tetrameren durch geschickte Wahl der Verhältnisses der Lösungsmittelmischungen erreicht werden.

Darüber hinaus wurde in Kapitel 4 ein noch nicht abgeschlossenes Projekt zur Einkristallisation von metallunterstützten, kovalenten organischen Gerüsten (MSOFs) gezeigt. Die Idee ist, zunächst Einkristalle der metallorganischen Gerüste (MOFs) herzustellen und diese dann durch Postmodifikation in MSOFs-Einkristalle umzuwandeln. Zwei Ansätze wurden entworfen und die entsprechenden MOFs synthetisiert. Leider gelang es derzeit nur Nanokristalle von MOFs erhalten.

Table of Contents

1. Introduction 1
1.1 Mechanically Interlocked Cages 1
1.1.1 Interlocked Coordination Cages 2
1.1.2 Interlocked Organic Cages 5
1.2 Synthesis of Interlocked Cages 8
1.2.1 Coordination-Driven Synthesis of ICCs 8
1.2.2 Templates Mediated Synthesis of ICCs 10
1.2.3 Synthesis *via* Dynamic Covalent Chemistry 11
1.3 The Driving Force for the Catenation 14
1.3.1 Thermodynamically or Kinetically Controlled Synthesis 14
1.3.2 Supramolecular Interactions 16
1.4 Polycatenanes Based on Cages 20
2. Objectives 23
3. Results and Discussion 25
3.1 The Effects of Cage and Cavity Size on Catenation Tendency 25
3.1.1 Introduction 25
3.1.2 The Synthesis of Triptycenetriamine Building Blocks and Linkers 25
3.1.3 The Synthesis of HexBi-Cage, HexBi-Catenane 27
3.1.4 The Synthesis of HexTri-[2]Catenanes and HexTri-[3]Catenanes 35
3.1.5 The Synthesis of DecBi-Cage, DecBi-Catenane, and DecTri-Catenane 43
3.1.6 The Synthesis of ProBi-Catenane and ProTri-Catenane 47
3.1.7 Geometry Optimization and Size Calculation 50
3.1.8 Conclusion 52
3.2 The Investigation of Structural Effects on Catenation 53
3.2.1 Introduction 53
3.2.2 The Synthesis of HexPh-Cage and ProPh-Cage 53
3.2.3 The Synthesis of HexEth-Cage and HexPy-Cage 56
3.2.4 The Investigation of the Substituent's Influence on Catenation 60
3.2.5 Crystallization Experiments of Model Compounds 65
3.2.6 Theoretical Calculations of Rotational Barriers Energy 66
3.2.7 Conclusion 67
3.3 The Study of Solvent Effects on the Synthesis of IOCs 69

3.3.1 Introduction 69
3.3.2 The Synthesis of IOCs based on Linkers with Side Chains 69
3.3.3 The Investigation of Solvent Mixtures for IOCs Synthesis 72
3.3.4 The Study of Different Combinations of Mixture Solvents 75
3.3.5 Multiple Factors Simultaneously Influence the Synthesis of IOCs 77
3.3.6 Conclusion 79
3.4 The Controllable Synthesis and Isolation of Polycatenanes 81
3.4.1 Introduction 81
3.4.2 The Ratio of Solvent Mixture and the Amount of Building Blocks Influence on Catenation Degree 81
3.4.3 The Exploration of Different Building Blocks 84
3.4.4 ^{1}H NMR Assignment for ButDie-[4]Catenane 88
3.4.5 The Synthesis and Separation of Trimer and Dimer Catenane 90
3.4.6 Single Crystallization Experiments of ButDie-[4]Catenane 96
3.4.7 Conclusion 98
4. Crystallization of Metal-assisted Organic Frameworks 101
4.1 Introduction 101
4.2 Result and Discussion 103
4.2.1 Synthesis of Model Compounds 103
4.2.2 The Identification of Nano Crystals 104
4.2.3 Two-step Approach and Synthesis of Crystalline MOFs 108
4.2.4 Second Approach to the Single Crystalline MSOFs 113
4.3 Conclusion 116
5. Summary and Outlook 117
6. Experimental Section 121
6.1 General Remarks 121
6.1.1 Solvents 123
6.1.2 Chemicals and Reagents 124
6.1.3 General Procedures 126
6.2 Syntheses 128
6.2.1 Compounds of Chapter 3.1 128
6.2.2 Compounds of Chapter 3.2 143
6.2.3 Compounds of Chapter 3.4 156
6.2.4 Compounds of Chapter 4 158

7. Reference **167**
8. Appendix **173**
8.1 NMR spectra **173**
8.2 Mass Spectra **259**
8.3 X-ray Crystallographic Structure Determination **263**
9. Abbreviations **265**
10. Acknowledgments **267**

1. Introduction

1.1 Mechanically Interlocked Cages

Mechanically interlocked cages generally consist of two monomeric cages, which are linked together by interpenetrating their structures instead of forming chemical bonds.[1] Depending on the structure of the monomeric cage, the interlocked cages are divided into mainly two types i.e interlocked coordination cages (ICCs)[2] and interlocked organic cages (IOCs)[3]. Emerging as an interdisciplinary research field, the study of interlocked cages involves both two areas of mechanically interlocked molecules[4] and cage compounds[5].

In the past fifty years, substantial progress has been achieved in the study of mechanically interlocked molecules, which have been merged as an important topic in supramolecular chemistry.[6] The archetypal examples of mechanically interlocked molecules are rotaxanes, catenanes, and knots (Figure 1.1).[7] Interlocked cage is a type of catenane. Compared with [2]catenane based on two macrocycles, which are linked with monocycles, most interlocked cages are interlocked through multicycles (Figure 1.1 b, d).[3] This makes the structure of the interlocked cages more rigid and less flexible than [2]catenane or rotaxane molecules. Despite that, due to the dynamic nature of the mechanical bond—low energy barrier for relative movement of subcomponents (rotation of the rings, or the sliding of the rings along the polymeric thread),[8] interlocked cages are ideal candidates for being applied in numerous fields, for example, the design and synthesis of molecular machines, which was awarded the 2016 Nobel Prize in Chemistry.[9]

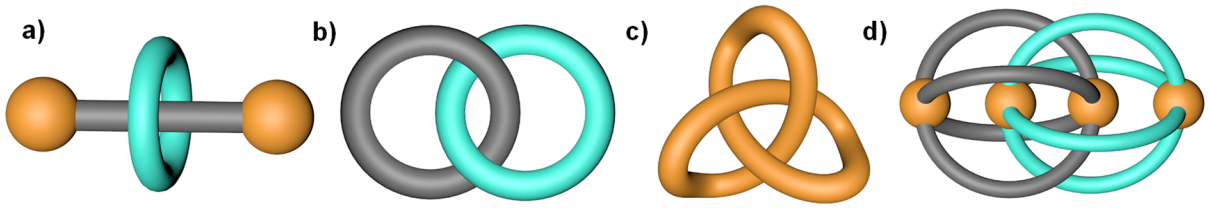

Figure 1.1: The illustration of rotaxane (a), catenane (b), knots (c), and interlocked cages (d).

As a novel kind of porous material, organic cages and coordination cages have diverse appealing artificial architectures and well-defined cavities.[5b-d] Interlocked cages retain the three-dimensional (3D) structures of monomeric cages and generate more complex topologies. However, the cavity and porosity of interlocked cages not only depend on the structures of monomeric cages but also on the way how they are interlocked.[3, 10] The cavity of monomeric cages is mostly occupied by other cages, therefore, only one interlocked cage that displays large porosity and high surface area has been reported up to date.[10a] Even though, it still spurred significant interest in the exploration of interlocked cages with novel topologies and properties.

Moreover, the interlocking of monomeric cages can generate multiple cavities for binding additional species, which also makes them a unique type of material for host-guest chemistry.[11] In addition, compared with the interpenetrated metal-organic frameworks (MOFs) or covalent organic frameworks (COFs), which are insoluble, most of the discrete and interlocked cages have good solubility.[12] Therefore, they could be applied as homogeneous catalysts,[13] drug delivers,[14] or processed into thin films,[15] membranes,[16] or even 3D-printing devices.[17]

Over the past decades, numerous coordination and organic cages with varied structures have been reported,[5b, 5c] in principle, lots of them could be interlocked to generate more complex structures in multiple ways. However, in comparison to monomeric cages, much fewer examples of interlocked cages were reported. Most interlocked cages were obtained as a result of serendipity, and they were found and isolated as the by-products during the syntheses of monomeric cages. Research work on systematic investigations of the catenation mechanism is even rare. Thus, rational design and synthesis of target interlocked cages remain a challenging task. There are a lot of scopes to explore interlocked cages in terms of their topologies, mechanism, and application.

Therefore, this introduction focuses on the development of ICCs, followed by a review of IOCs. Particular emphasis is placed on the design methodology, synthetic strategy, and topology of coordination and organic interlocked cages, especially the application of dynamic covalent chemistry and the study of catenation mechanism in IOCs − the main theme occurring recurrently through the work presented in this thesis.

1.1.1 Interlocked Coordination Cages

The monomeric coordination cages are constructed from coordinative assembly between metal nodes and organic ligands in the Platonic or Archimedean solids shape with an accessible cavity.[18] Due to the well-defined coordination geometries of metal ions and rigid ligands, it is possible to pre-design and synthesize coordination cages with the desired structures and topologies.[19]

The first ICCs (**4a, 4b**) were reported by Fujita's group in 1999 (Figure 1.2).[20] They employed triazine **1** and **2** as the ligands, and $[M(ethylenediamine)]^{2+}$ (M = Pd, Pt) units **3** as the connector to construct two triply interlocked coordination cages. Compounds **1**, **2**, and **3** (in a 3:1:1 ratio) were dissolved in water and heated at 100 °C for three days, the kinetically distributed mixture gradually turned into a thermodynamically stable interlocked structure (Figure 1.2 a). The inter-planar surface-to-surface distance between the two types of triazine ligand of monomeric [2+3] cage is 3.5 Å, which is the ideal distance for binding an aromatic

ring, The monomeric cages could interact with one another through the π-π interactions and form the thermodynamically favored interlocked structures (Figure 1.2 b).

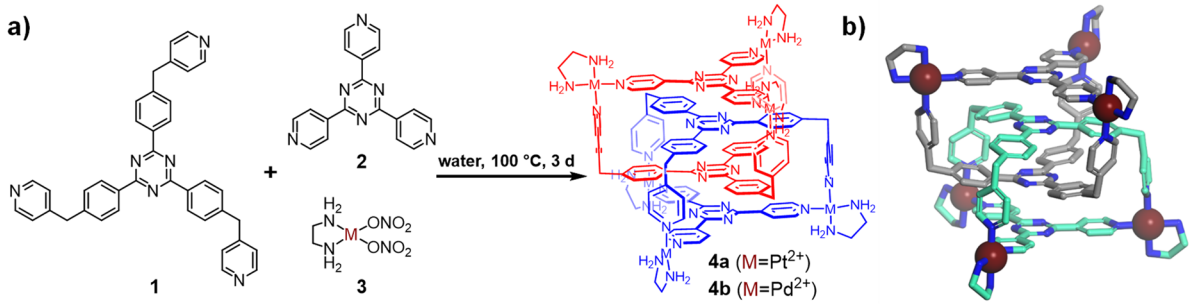

Figure 1.2: a) The synthesis of the ICCs **4a** and **4b** *via* self-assembly; b) side view of the sticks illustration of the X-ray crystal structure of **4a**, with one color for each monomer. CCDC: 1148701.[20]

The second example of ICCs was reported nearly a decade later by Hardie and co-workers. They used the cyclotriveratrylene-related ligand where three bipyridyl units act as coordinate sites, and Zn^{2+} or Co^{2+} ions to construct a triply interlocked chiral coordination cage **5** (Figure 1.3 a).[21] Interestingly, cyclotriveratrylene has a relatively rigid bowl shape, but there are no face-to-face π-π interactions between these molecular bowls. However, weak hydrogen bonding exists between the monomeric cages and was considered as the driving force for the catenation.

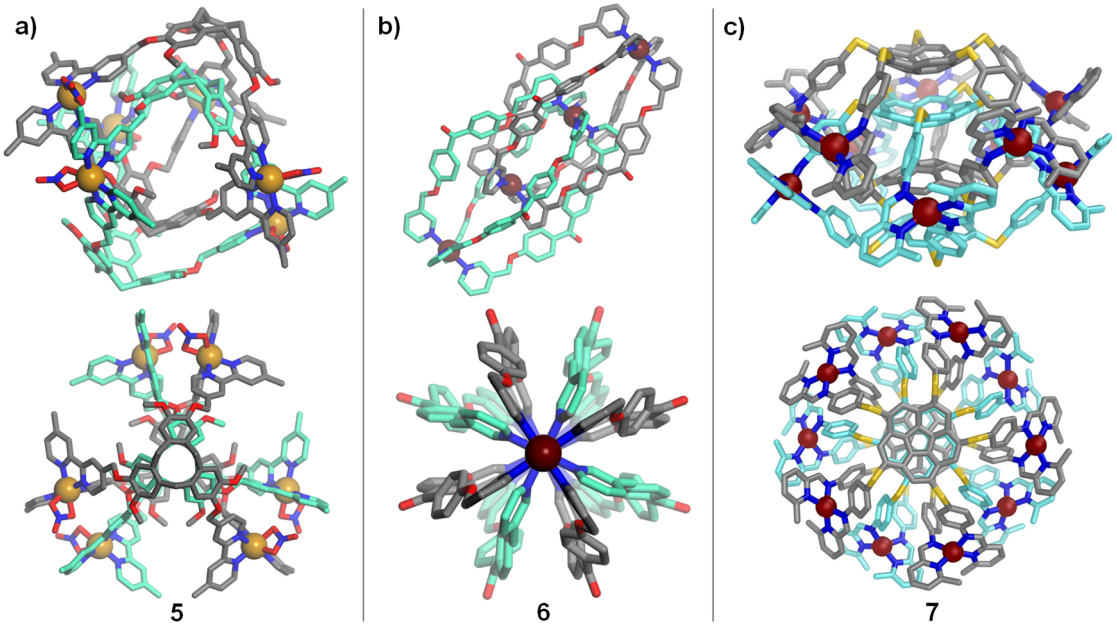

Figure 1.3: Side view (above) and the top view (below) of the sticks illustration of the X-ray crystal structure of ICCs: a) triply **5**, CCDC: 691575;[21] b) quadruply **6**, CCDC: 652007;[22] and c) quintuply **7**, CCDC: 1913638.[23] One color for each monomer.

The aforementioned examples of ICCs are all constructed from [2+3] monomeric cages and with triply interlocked topology. In 2008, Kuroda and co-workers designed and synthesized ICCs **6** with quadruply interlocked structures (Figure 1.3b).[22] They utilized the Pd^{2+} as the face of the polyhedron and pyridine as the bridging ligand to build the [2+4] monomeric cages. Since

Pd^{2+} prefers to adopt a well-defined square-planar geometry, such [2+4] coordination cages show high symmetry and predictable interlocking topology. Therefore, Pd^{2+} has become the one of most frequently used metal ions for the synthesis of ICCs.

In 2020, Nitschke and colleagues reported the first quintuply interlocked topology for interlocked cages.[23] They successfully synthesized a 5-fold interlocked $[Cu^{I}_{10}L_4]^{10+}$ [2]catenane **7** from CuI and corannulene-based subcomponent (Figure 1.3 c). The corannulene is a 5-fold-symmetric scaffold and a good candidate for functionalization with coordination motifs. The curved aromatic surface of corannulene can also enhance the guest binding properties of ICCs *via* aromatic stacking interactions. The distance between the mean planes of the central pentagons of the corannulenes is 6.93 Å, which creates a cavity that matches the form of the intercalated corannulene from the other cage. The resulting distance between corannulenes of monomeric cages is around 3.5 Å, a proper distance for the formation of π-π interactions. So far, three interlocking ways (triply, quadruply, and quintuply) of interlocked cages have been reported (Figure 1.3).

In addition, another special topology of ICCs was reported by Clever's group in 2018, where they prepared an unprecedented multi-cavity ICCs **9** featuring five consecutive pockets (Figure 1.4).[11b] The construction of ICCs has been considered a good way to generate multiple cavities by interlocking monomeric cages with a single cavity. Besides that, another strategy to obtain such architectures with distinguishable voids is the construction of multidentate ligands that assemble into hosts featuring two or more cavities linearly aligned in a peanut-type of fashion (Figure 1.4). Herein, they combined these two approaches and designed coordination cages with two cavities linearly aligned, then used them as precursors to construct a double quadruply interlocked coordination cage. The interpenetrated products were quantitatively produced by using the halide anions (Cl^-, Br^-) as the template.

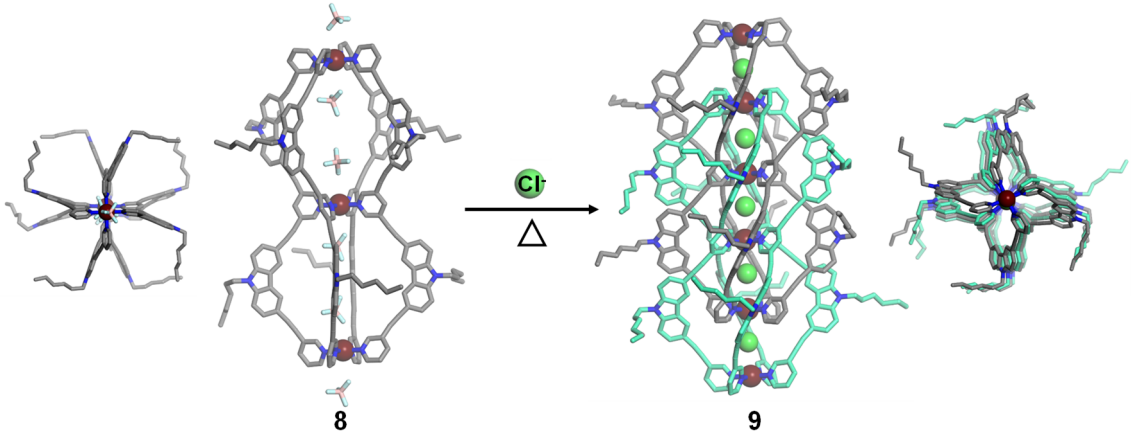

Figure 1.4: The illustration of the X-ray crystal structure of the monomer cage **8** (right, side view; left, top view) and ICCs **9** (left, side view; right, top view), CCDC: 1835888, 1835889.[11b]

1.1.2 Interlocked Organic Cages

Accordingly, IOCs consist of monomeric organic cages, which are typically constructed from organic building blocks *via* covalent bonding. In comparison to ICCs, IOCs appeared relatively later and are much less investigated.

In 2010, Cooper and co-workers reported the triply interlocked dimeric organic cages **11a, 12a,** and **13a** (Figure 1.5), based on [4+6] imine organic cages.[3] These IOCs were synthesized in a one-pot reaction by adding catalytic amounts of trifluoroacetic acid (Figure 1.5 a). The constructions of these IOCs were completely based on organic building units *via* imine bond formation, without any auxiliary templates. The single-crystal X-ray diffraction results revealed that π-π interaction between the faces of the monomeric cages is probably the driving force for the catenane formation (Figure 1.5 b). It was further supported by experimental results that the addition of competitive aromatic solvents to the synthetic reactions could suppress the formation of catenanes.

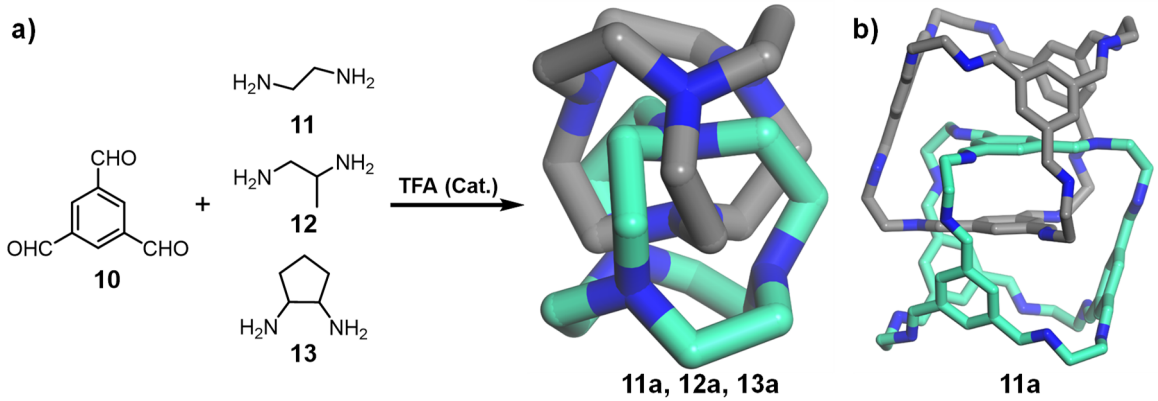

Figure 1.5: a) The synthesis of IOCs **11a**, **12a**, and **13a**, which were illustrated in the sticks model; b) The stick illustration of the X-ray crystal structure of the IOCs **11a**, CCDC: 68582.[3]

In 2014, Mastalerz's group described a quadruply interlocked dimer of giant [12+8] boronic ester cages **16**, which was synthesized in a one-pot 96-fold condensation reaction of 40 molecules (Figure 1.6 a).[10a] Unfortunately, because of the chemical lability of the 24 boronic ester groups, the interlocked structure can only exist in a solid state and it dissociates once dissolved in solvents. However, the crystalline material of **16** (Figure 1.6 b) displayed great porosity and the BET surface area is 1540 m^2g^{-1}. The pore-size distribution showed two distinct pores with narrow pore-size distributions with maxima at 1.4 nm and 2.0 nm (Figure 1.6 c), which correspond to two types of pores in the crystalline state. It is the biggest and first example of porous catenane reported up to date. In addition, some short contacts exist between the alkyl substituents of one monomeric cage and the aromatic planes of the triptycene units of the other cage. Such dispersion interactions are probably the driving force for catenane formation.

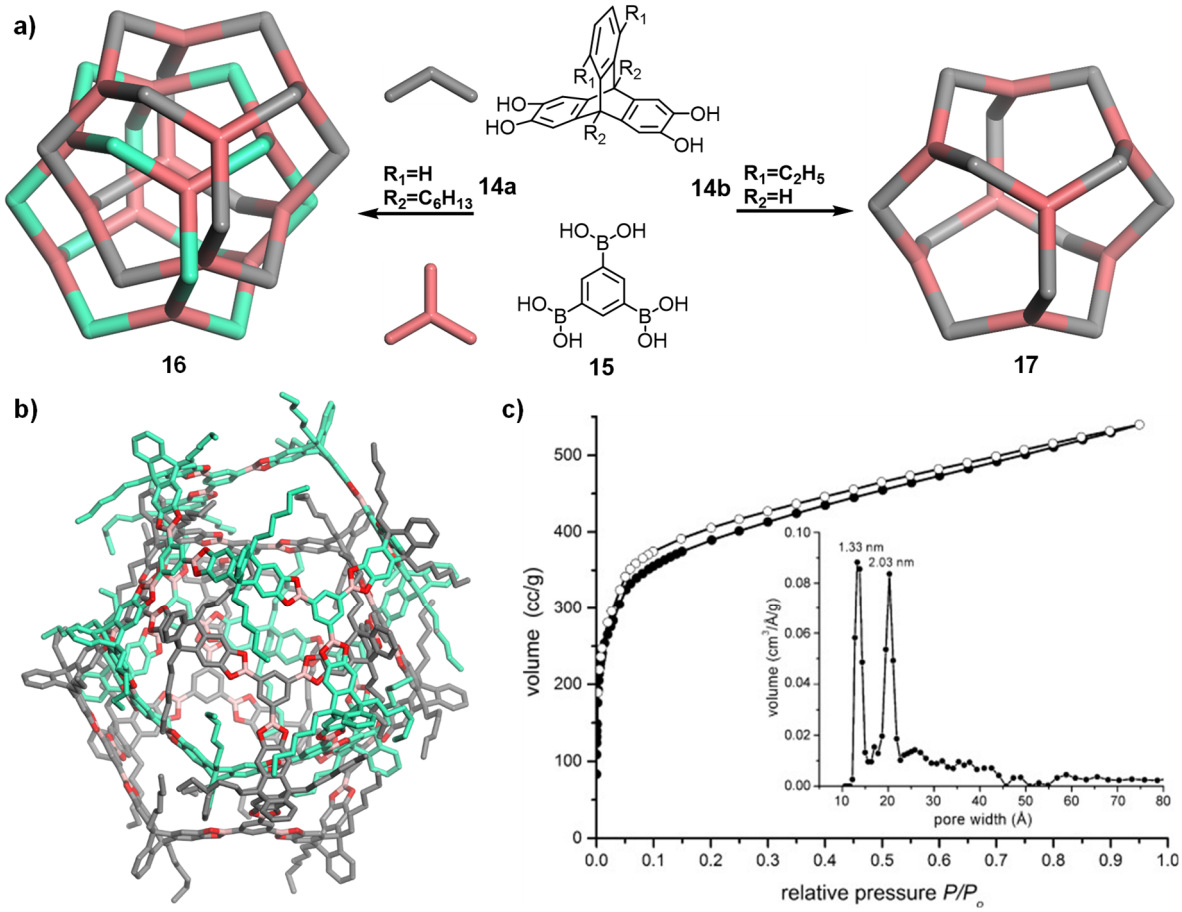

Figure 1.6: a) Synthesis of [12+8] boronic ester cages **17** and formation of the IOCs **16**; b) The sticks illustration of the X-ray crystal structure of the ICCs **16** with one color for each monomer, CCDC: 980837;[10a] c) Nitrogen sorption isotherm of crystalline materials **16**, the inset shows the pore-size distribution by NL-DFT. Copyright 2014, John Wiley and Sons.

The chemical stabilities of imine and boronic ester bonded organic cages are generally poor since they are quite sensitive to acidic and moisture environments. It is even worse for IOCs because there is not only decomposition but also dissociation of their cage units. In 2015, Zhang and colleagues reported permanently interlocked arylene-ethynylene organic cages **20** (Figure 1.7), which were constructed with benzoylbiphenyl-substituted alkynes building block **18** through a thermodynamic process involving alkyne metathesis.[10b]

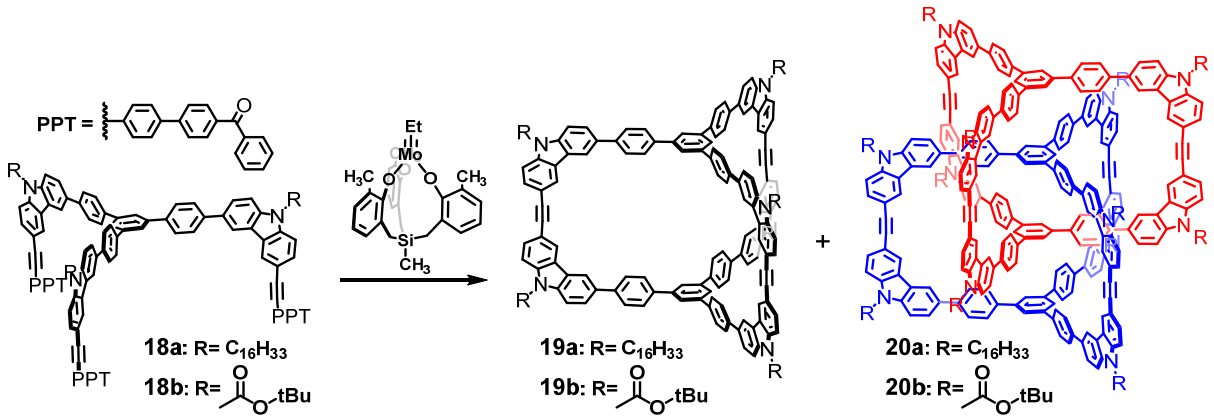

Figure 1.7: Synthesis of interlocked arylene-ethynylene cages **20a-b**.[10b]

Along with the formation of monomeric cage **19**, simultaneously, the thermodynamically favored products interlocked dimers were also obtained (**20a** and **20b**, Figure 1.7). The interlocked arylene-ethynylene cages are superiorly more stable due to the robust ethynylene linkages, whose disconnection and formation generally require the use of the catalyst.

Another approach to obtaining chemically stable IOCs is the post-modification of imine cages. In 2020, the group of Zhang reported dimeric IOCs constructed by [6+4] condensation of six diamine linkers and four trialdehyde panels (Figure 1.8).[24] Since the space volume is different between the outside surface and inner cavity, the voluminous reductant $NaBH(OAc)_3$ could not access the inner cavity of the IOCs. Therefore, the outer imine panels of IOCs **23** could be selectively reduced by $NaBH(OAc)_3$ to obtain IOCs **24** with dissymmetric cage units.

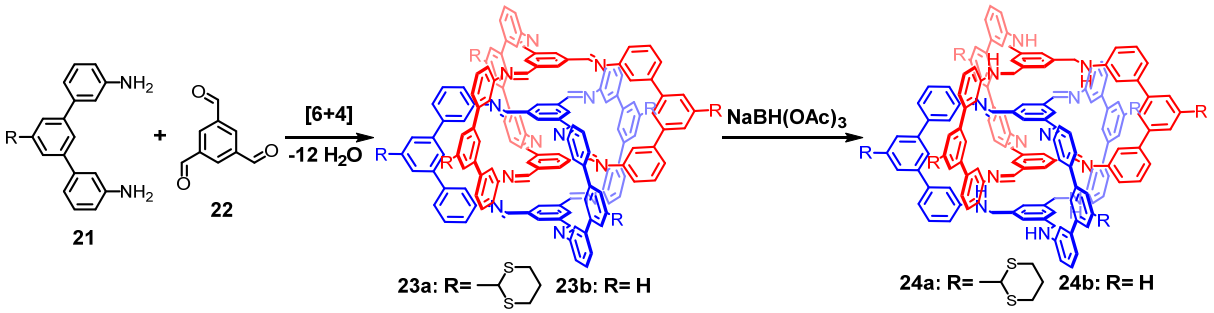

Figure 1.8: The [6+4] imine condensation of diamine linker **21** and trialdehyde **22** under TFA catalysis affords a catenane with symmetric cages **23**; subsequent selective reduction of the two exterior imine-based panels with large $NaBH(OAc)_3$ to obtain the dissymmetric cages **24**.[24]

Recently, Benke et al reported a series of triply interlocked [8+12] giant chiral imine cages.[25] By using different 1,4-substituted benzene dialdehydes as linkers, they successfully converted the monomeric cages into interlocked dimers and trimers (Figure 1.9). The weak local dipole-dipole interactions were proved to be the driving force for the catenane formation.

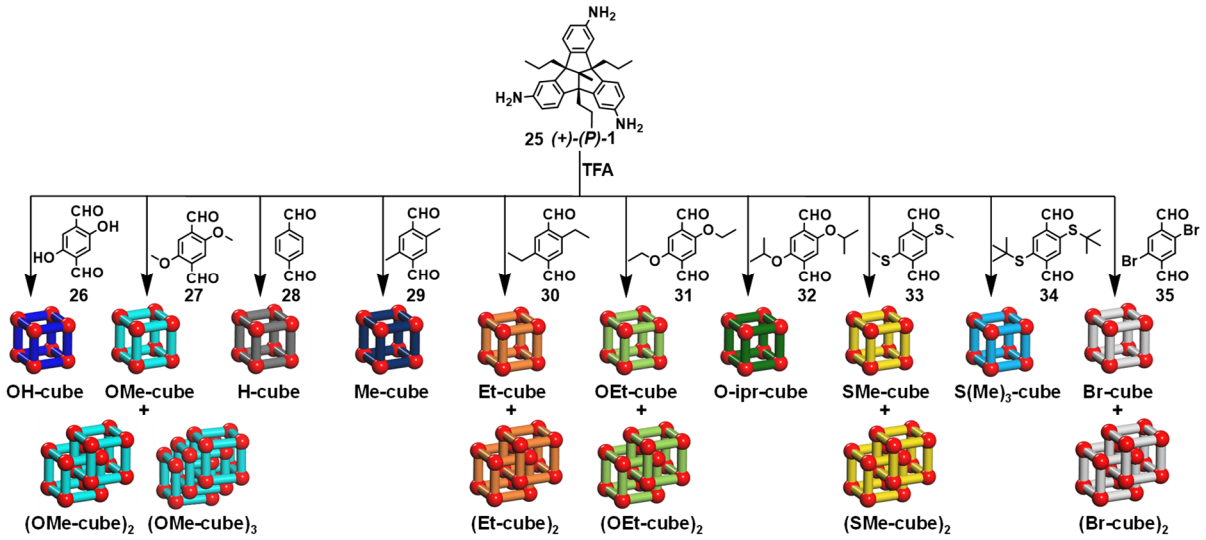

Figure 1.9: Reactions of various dialdehydes **26-35** with TBTQ triamine **25** giving cages or catenated cages (red balls represent the TBTQ units and colored struts the aldehyde or imine linker units).[25]

Overall, the research on interlocked cages is still in its infancy, and mainly focuses on the exploration of new structures. Most interlocked cages reported are based on relatively small monomeric cages, for example [2+3] or [4+6] cages.[3, 10b, 24, 26]. However, the first porous IOCs and trimeric catenane are all based on monomeric cages with big sizes and multiple opened windows.[10a, 25] It indicates that there is a great scope to explore interlocked cages constructed by bigger monomeric units, although the bigger size also brings more obstacles to the design, synthesis, and characterization of such interlocked cages. Therefore, more systematic research and investigation on such kinds of interlocked cages, especially the study of novel synthetic methods and catenation mechanisms are required.

1.2 Synthesis of Interlocked Cages

Although interlocked cages have attracted significant attention due to their diverse artificial interlocked structures and unique properties, rationally synthesizing such complex structures is inherently challenging. It has limited the exploration of interlocked cages with more complicated topologies and also their potential applications.[27] Currently, there is no widely applicable method for the synthesis of interlocked cages. Several often-used approaches for constructing interlocked cages are nearly the same as the methods for monomeric cages synthesis.[3, 5b, 5c, 10a] For ICCs, the effective method is coordination-driven self-assembly, with or without templates;[19, 28] for IOCs, it is the dynamic covalent chemistry (DCC).[29]

1.2.1 Coordination-Driven Synthesis of ICCs

The self-assembly process plays an important role in nature for living organisms.[30] Many common life mechanisms, for example, protein folding, nucleic acid assembly, and the formation of phospholipid membranes, ribosomes, and microtubules, are all based on the self-assembly phenomenon. These self-assembly processes are driven by weak, non-covalent interactions such as hydrogen bonding, donor-acceptor interaction, π-π stacking, van der Waals force, and hydrophilic or hydrophobic interactions. However, it is always challenging for scientists to control these interactions and produce similar artificial substances. The initial synthesis of big molecules is generally conducted in a stepwise or statistical threading approach, which is often laborious and generally ends in a low overall yield of the desired product.[31] However, the predictable metal−ligand bonding and well-defined coordination geometries overcome the main obstacle that these interactions mentioned above are not easily controlled for directional organizing subunits in certain positions. Therefore, it is possible to synthesize molecules with complex structures, and infinite frameworks in a one-step reaction.[19, 32]

The coordination-driven self-assembly was first applied for the synthesis of metal-complex,[33] for example, cyclam complexes (Figure 1.10, **36**).[34] The metal works as a template to arrange the ligands in order, then the bonding between these ligands can link them into the molecule with the desired topology. This approach not only significantly increased the efficiency of the synthesizing macrocyclic structures, but also dramatically changed the design and synthesis of mechanically interlocked structures (Figure 1.10, **37**).[35] However, during these syntheses of **36** and **37**, the metal ions only worked as templates and did not participate in the formation of their backbones, therefore these molecular structures could be retained even after the removal of metal ions. Since the 1990s, along with the explosive development of supramolecular chemistry and porous coordination polymers, for example, catenanes, MOFs, and coordination cages, the area of coordination-driven self-assembly chemistry has also experienced remarkable growth. Metal ions were not only working as templates but becoming a part of molecules to organize the ligands together to construct the higher-level structures (Figure 1.10, **38**, **4b**).[36]

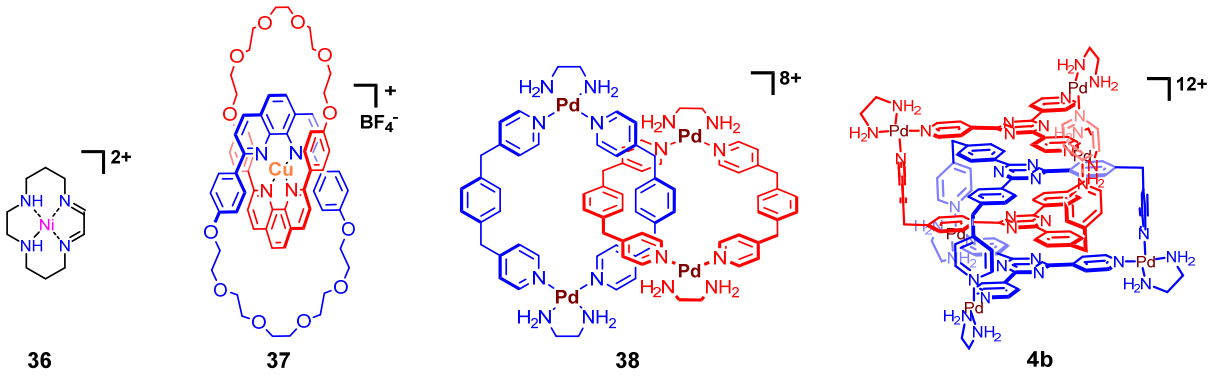

Figure 1.10: Metalloporphyrins **36**;[34] Coordination templated [2]catenane **37**;[35] Coordination linkage [2]catenane **38**;[36] Coordination linkage ICCs **4b**.[20]

Owing to the intermediate energies of metal−ligand bonds (15−50 kcal mol^{-1}), which are weaker than the energies of organic covalent bonds (60−120 kcal mol^{-1}) but stronger than dispersive interactions (0.5−10 kcal mol^{-1}), the metal-ligand bonding is reversible and relatively stable. Therefore, it became possible to produce coordination frameworks and polymers with long-range order structures and synthesize some highly ordered molecules such as the coordination cages and ICCs in a one-pot reaction by thermodynamic controlled synthesis (Figure 1.10, **4b**).[22] In comparison with the number of coordination cages or other coordination molecules, there are not many ICCs with novel topologies reported. Although more attention is paid to the exploration of catenation driving force and mechanism in recent years, coordination-driven self-assembly is always the initial and fundamental method of the ICCs synthesis.

1.2.2 Templates Mediated Synthesis of ICCs

Throughout the development of supramolecular chemistry, template-based synthesis undoubtedly is one of the most well-studied and prevalent synthetic methods.[9, 28, 37] The core of this method is using the template species to pre-organize the components in a controllable manner. As mentioned above, the template strategies have revolutionized the possibilities for the design and synthesis of mechanically interlocked structures, which could only be accomplished by using a statistical threading approach before. Because of well-defined coordination geometries and the proper reversibility of metal−ligand coordination bonding, metal ions become one of the most frequently used templates.

However, in the synthesis of ICCs, the metal ions often work as connectors and become part of the backbone of the monomeric cages, while the counter anions played the role of templates. A typical example was reported by Kuroda's group in 2012, they synthesized a quadruply interlocked coordination cage **40** and demonstrated the catenation was driven by the anion template effect.[38] Besides, the different template anions (PF_6^-, OTf^-, BF_4^-, NO_3^-) were also explored, and they found that the ICCs **40** only generated when using the BF_4^-, NO_3^- as templates. Moreover, the monomeric coordination cages were more tending to catenation with the NO_3^- as the templates and less with the BF_4^-. When synthesizing the ICCs with the mixture of PF_6^-, OTf^-, BF_4^-, and NO_3^-, the final product is **40**⊃$(NO_3|NO_3|NO_3)^{5+}$, which also proved that the NO_3^- is the more thermodynamically favored template.

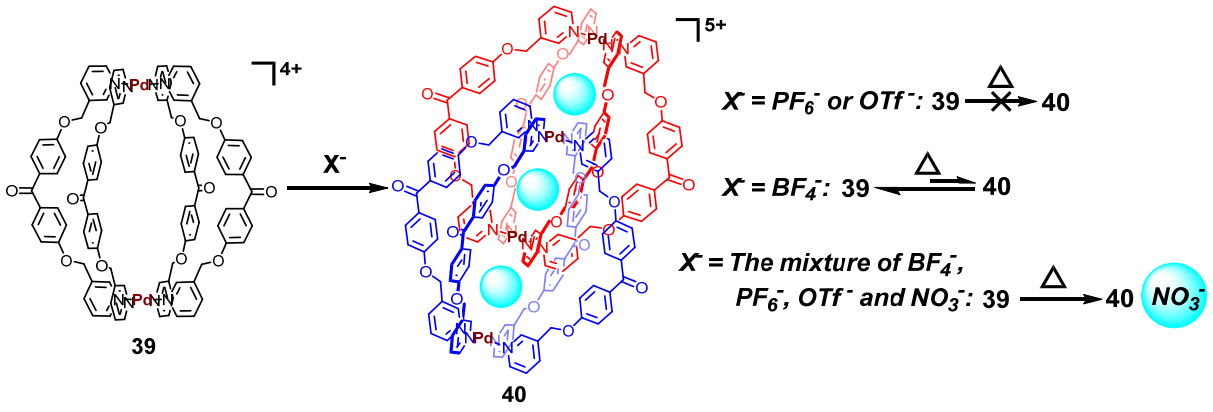

Figure 1.11: Dimerization of **39** into **40** in the presence of NO_3^-.[38]

Similarly, Clever and co-workers also demonstrated the mechanism of the anions template in the synthesis of ICCs. They used carbazole-based bis-pyridyl ligands and $Pd(BF_4)_2$ to construct a monomeric cage **41**, and there were no interlocked species formed in the presence of tetrafluoroborate anions (Figure 1.12 a).[39] However, when the addition of 1.5 equivalents of bromide or chloride to the solution of monomeric cages and heating for 5 hours, they observed the formation of a new species, which was determined to be the ICCs **42** (Figure 1.12

b). Unexpectedly, the further addition of halide anions did not lead to a complete cage-to-ICCs conversion, but instead, a second structural transition- triple catenane **43** (Figure 1.12 c). Excess amounts of halide anions compete with the pyridine ligands, and finally replaced two and four ligands of the monomeric and dimeric cages, respectively. The distance between the macrocycles of neutral catenane **43** is much closer in comparison with the monomeric cages of ICCs **42**, where anionic guests are enclosed between the square planar $[Pd(py)_4]^{2+}$ metal nodes. The six palladium centers are aligned in an almost linear fashion, whereas the bromide substituents occupy positions in a helical manner.

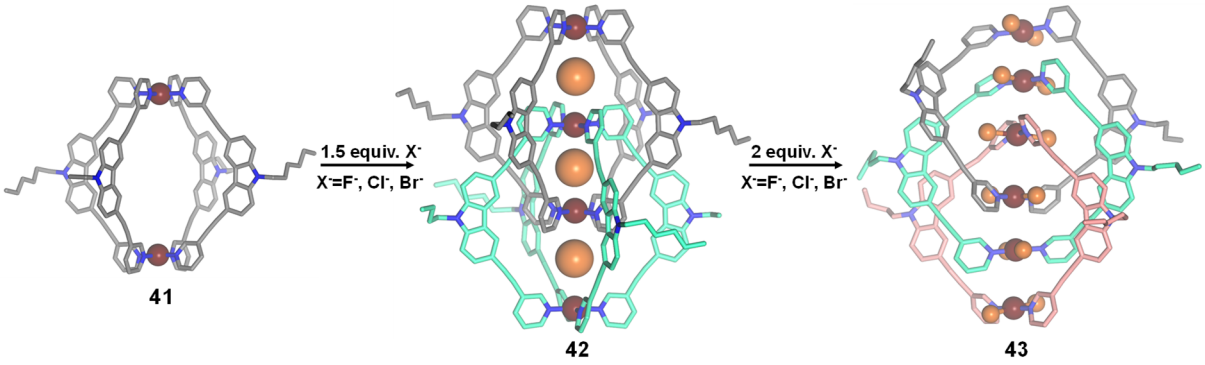

Figure 1.12: Stepwise assembly of the monomeric cage **41**, CCDC:1011498; the halide-templated double cage **42**, and the triple catenane **43** (model structure), CCDC: 1011499.[39]

With the continuous investigation and application of this methodology to the interlocked structure and supramolecular chemistry, the anion template synthesis has already been demonstrated as an effective approach for ICCs synthesis.[11b, 28, 40] Moreover, it was found that the type and amounts of the anion species can also influence the conformation of ICCs, which also shows the potential of the template methodology.[11a, 39] Unfortunately, the anion template method was not that effective and was rarely employed for the synthesis of IOCs. In 2009, Beer's Group reported the synthesis of a triply interlocked capsule by sulfate anion template.[41] However, the synthesis was conducted stepwise rather than in a one-pot reaction like most syntheses of IOCs. It also indicates that the exploration of novel template species is necessary for new synthesis requirements.

1.2.3 Synthesis *via* Dynamic Covalent Chemistry

The concept of dynamic covalent chemistry (DCC) refers to chemical reactions carried out reversibly under conditions of equilibrium control.[42] Emerging as an unprecedented approach to the synthesis of COFs, the core of DCC is the reversible formation and dissociation of covalent bonds. This reversibility introduces the "error checking" and "self-correcting" mechanism during the reaction, which allows these reaction intermediates can exchange rapidly

and generate the thermodynamically favored product (Figure 1.13).[43] Therefore, the amorphous covalent polymers or oligomers could gradually transform into covalent frameworks with long-range order structures.[44] Moreover, the covalent bonds are generally stronger than non-covalent interactions, thus most of COFs also have better stability in comparison with hydrogen-bonding organic frameworks (HOFs) and MOFs.[45]

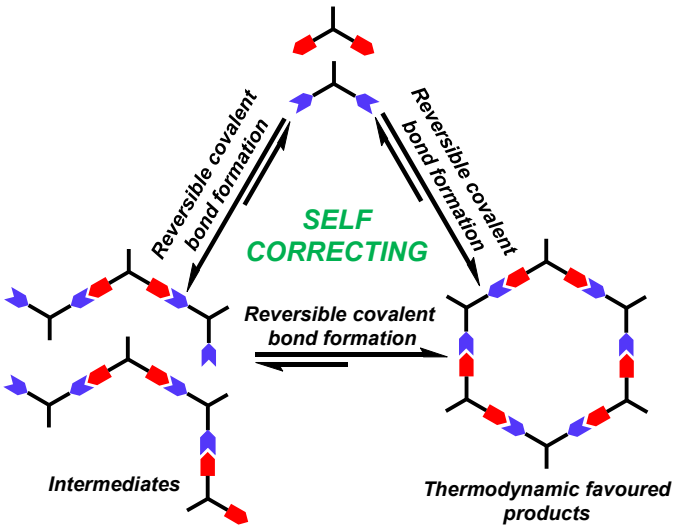

Figure 1.13: Illustration of dynamic covalent chemistry mechanism and the "self-correcting" process.

The underlying basis of DCC is the reversible organic reactions. In the past decades, over twenty kinds of dynamic covalent reactions have been reported, for example, the boronic ester condensation (Figure 1.14 a),[10a, 46] boroxine reaction (Figure 1.14 b),[47] imine formation (Figure 1.14 c),[42b, 48] and triazine condensation (Figure 1.14 d).[49] The type of dynamic covalent reactions is also one of the most important factors that influence the synthesis efficiency and properties of the materials.

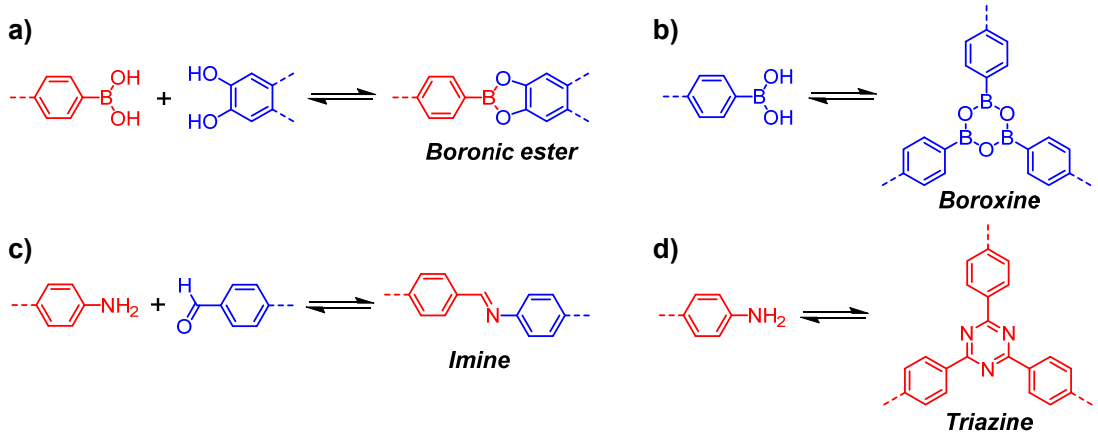

Figure 1.14: a) boronic ester condensation; b) boroxine reaction; c) imine formation; d) triazine condensation.

Another fundamental aspect of the DCC is the building blocks and linkers, which lead to the formation of frameworks and cages with different topologies and porosity. Most building blocks and linkers are symmetric and have more than one functional group such as the aldehyde or imine groups. By choosing the building blocks with different symmetries and geometries, it is possible to construct two-dimensional (2D) or three-dimensional (3D) frameworks with diverse cavities and channels.[50] For organic cages or IOCs, the type of building blocks is also crucial to obtaining the desired polyhedron structures.[51] Therefore, finding new dynamic

covalent reactions and novel building blocks is always challenging but beneficial to explore more novel porous organic materials with improved properties.

The appearance of DCC significantly changed the synthetic strategies of organic cages and IOCs,[29, 51a] and accelerated the development of this research area. The concept of organic cage compounds has been introduced for more than a half-century, which was much earlier than MOFs and COFs.[52] Most of the organic cages reported in the initial stage were constructed by irreversible covalent bonds (Figure 1.15).[53] These organic cages were generally synthesized stepwise to avoid undesired by-products. Therefore, these syntheses are always laborious and resulting overall low yields.[54]

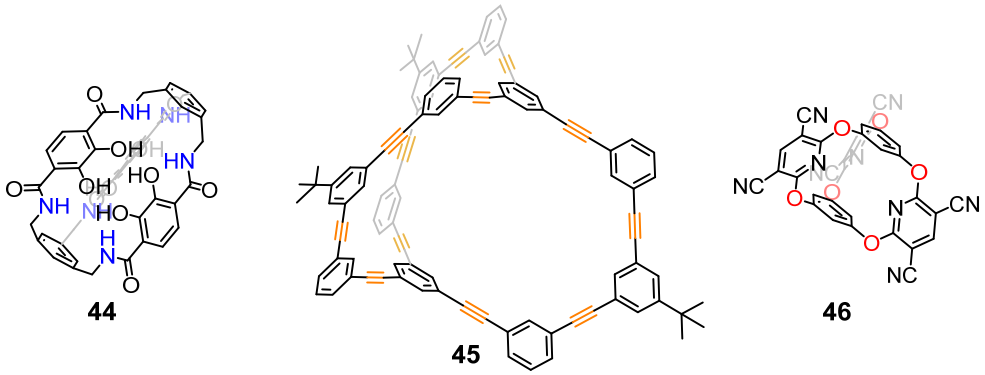

Figure 1.15: The organic cages (**44**[55], **45**[54a], **46**[56]) constructed by irrevesible bonds.

The DCC methodology makes it possible to synthesize organic cages in high or even quantitative yield in single-step and one-pot reactions. Therefore, the organic cages with diverse topologies could be explored, and their properties, for example, porosity, could be fully investigated.[29, 51] Cram and co-workers are the pioneers in applying DCC to cage synthesis. In 1991, they successfully synthesized a hemicarcerand through an imine condensation reaction in a relatively high yield.[57]

To date, more than hundreds of organic cages have been constructed *via* DCC reported,[58] and the imine condensation is one of the most frequently used reactions for organic cage and IOCs synthesis. But, if review the synthesis of monomeric organic cages and the corresponding IOCs *via* DCC, there is no big difference in the synthesis procedure, which were all constructed in one-pot reactions.[10, 59] However, only a small portion of single cages could interlock to the catenanes, especially since lots of cages even have similar structures. For example, the first IOCs **11a** reported by Cooper's group in 2010, was synthesized in acetonitrile with TFA as the catalyst. Interestingly, they also obtained its monomeric cage **47** in ethyl acetate without a catalyst one year ago (Figure 1.16). Therefore, it is necessary to figure out what the difference between them is, why monomeric cages could interlock and how to obtain the desired interlocked cages by controlling the reaction conditions.

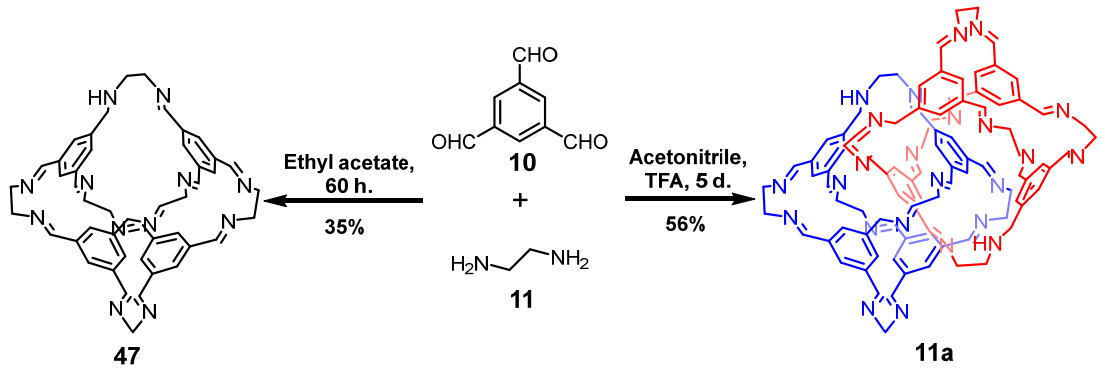

Figure 1.16: The same building blocks result in single cages and ICCs under different reaction conditions.[10, 59]

Overall, DCC is one of the foundations for organic materials research. It provides an effective method for the synthesis of organic cages and IOCs. Moreover, scientists have already found some methods, for example adding a modulator to better control the dynamic reaction process. However, it is challenging to pre-design and synthesize IOCs with desired structures and topologies, because the catenation mechanisms are still far from being fully understood. Therefore, more investigations of the catenation mechanism are urgently required for the development of IOCs.

1.3 The Driving Force for the Catenation

The study of the catenation mechanism, especially for IOCs, is still very much in its infancy, and as such, rational design and synthesis of interlocked cages are still difficult. The number of reported interlocked cages is also much rarer compared to infinite frameworks like MOFs and COFs. Over the past decades, there have been sporadic investigations on the catenation mechanism of interlocked cages,[20, 59] however, most of them were conducted with limited examples, which generally lack systematic discussion and persuasive conclusions. Even though, based on these investigation results, the identification of the driving force, which leads to the transformation from cages to ICCs, has been regarded as the basis of the catenation mechanistic studies. There are two mainstream opinions toward the driving force of interlocked cages: (1) the interlocked conformation is thermodynamically or kinetically favored; (2) the supramolecular interactions lead to the formation of interlocked cages.

1.3.1 Thermodynamically or Kinetically Controlled Synthesis

It is a widely accepted conclusion in supramolecular chemistry that catenated structures are thermodynamically more stable than their constituent monomeric components.[3, 20] As well known, thermodynamics provides the driving force of the reaction or systems to move from the initial state to the product state, whereas kinetics is concerned with the energy barriers of the

specific pathways in this process.[60] A typical schematic illustration (Figure 1.17) was shown here to explain the concept of thermodynamic versus kinetic control. Product II is thermodynamically more stable than the product I, however, its activation energy barrier (E_{aII}) is also higher. According to the Arrhenius equation (reaction rate = $Ae^{-Ea/RT}$), the most effective factor is the reaction temperature. Therefore, the general way to obtain thermodynamically favored products is to conduct the syntheses at relatively high temperatures.

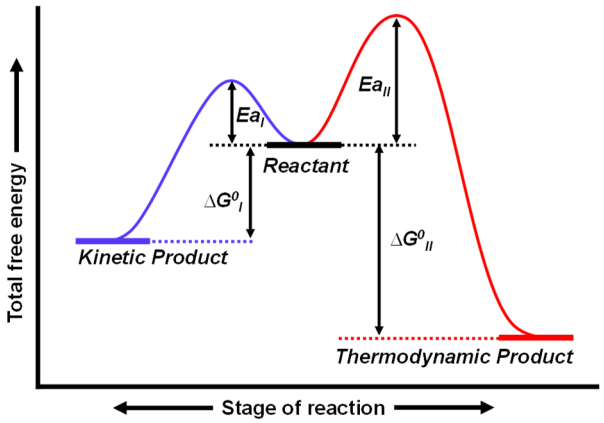

Figure 1.17: Schematic illustrations of thermodynamic control that involve two parallel reactions.

This catenation mechanism of interlocked coordination cages was systematically investigated by Fujita and co-workers.[20] To prove the interlocked cages are thermodynamically favored products, instead of using the building blocks **1** and **2** for the synthesis of **4b** in a one-pot reaction, they first prepared the monomeric coordination cages **48** and **49**, then mixed them in an aqueous solution (Figure 1.18). It was found that these two monomeric cages were reorganized into the ICCs **4b** in high yield. The NMR study showed that pure materials of cages **48** and **49** are stable in solution. However, after mixing them, the peaks of monomeric cages gradually disappeared; alternatively, another set of signals assignable to **4b** appeared. Finally, all components were completely transformed into ICCs **4b** after one day at room temperature. At elevated temperature (80 °C), the procedure was significantly accelerated and completed within 10 min. These results demonstrated that the formation of **4b** is due to their thermodynamically more stable conformation.

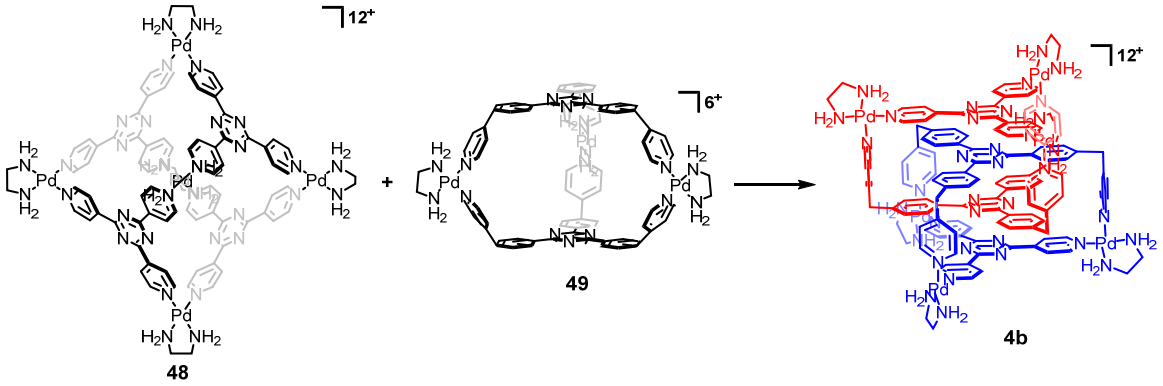

Figure 1.18: The reorganization from **48** and **49** to **4b**.[20]

However, in most cases, the synthesis always goes through a set of sequential reactions, the energy landscape of each reaction was briefly shown in Figure 1.19. Generally, the final

products are thermodynamically controlled with the global minimum in Gibbs free energy. Even though, during the reaction process, the product can also be isolated at the intermediate states corresponding to local minima by changing the reaction conditions suddenly, which was named the "kinetically interrupted thermodynamic" approach.[44, 60] For example, by adding anti-solvents or adjusting the ratio of mixture solvents to precipitate the intermediate products out. This approach is often used to synthesize organic cages. One typical example is the synthesis of IOCs mentioned before, which was reported by Mastalerz's group. They obtained giant boronic ester-linked IOCs **16** by crystallization of the monomeric cages in solution.[10a] The IOCs can exist in crystalline solid form and even be further activated for BET surface area measurement, which also displayed great porosity. However, the solid material decomposed into monomeric cages rapidly once being dissolved, which indicated that the monomeric cage conformation is thermodynamically more stable in solution, but the 'intermediate products'- IOCs still could be isolated by crystallization.

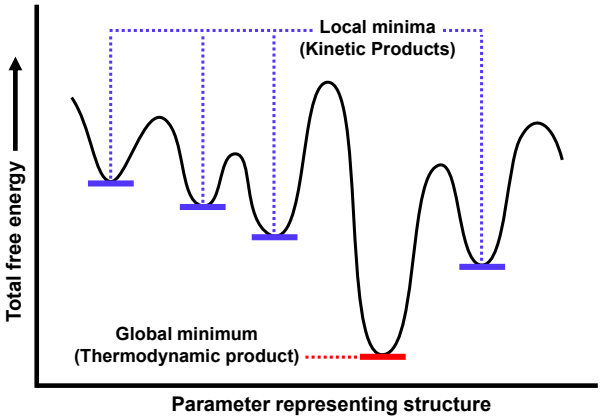

Figure 1.19: Schematic illustrations of kinetic control that involve a series of sequential reactions.

As such, it seems possible to switch the reaction process between thermodynamic control and kinetic control and thus obtain the target products. However, the kinetically controlled synthesis is highly relayed on the reaction conditions, such as temperature, solvents, concentration, catalyst, and even the property of the target products. When the properties of several products are quite similar, it will be difficult to find the right conditions for obtaining the aimed structure. Moreover, lots of IOCs are intermediate products in principle, because the interlocking procedure should be a constant continuous process once it starts. Except that there is the limitation of the structure, for example, the cavity of monomeric cages can only afford one another cage. Otherwise, the monomeric cages always tend to be interlocked into polymers. That's also why most reported IOCs are based on small monomeric cages with simple structures.[3, 20, 24] To obtain bigger interlocked cages with various topologies such as trimers or even bigger oligomers, the feasible method is still the kinetically controlled approach.

1.3.2 Supramolecular Interactions

Supramolecular interactions, as known as non-covalent interactions, are the general term for all other interaction forces except the covalent and ionic bonds. As mentioned before, non-covalent

interactions are generally much weaker than covalent bonds or ionic bonds. However, the cumulative effect of multiple associative non-covalent interactions can lead to the formation and control of the conformation of assembled compounds. Besides, the non-covalent interactions can influence the aggregation, tertiary and quaternary structure of large molecules, such as proteins and nucleic acids, as well as their stability and particular properties. Depending on the type of interacting force and where they exist, these non-covalent interactions can be classified into five categories: electrostatics interactions, H-Bonding, π-π interactions, van der Waals forces, and hydrophobic/solvophobic effects.

The non-covalent interactions widely exist during the interlocking process, not only between the monomeric cages but also between the reactants and solvents. Most investigations on the catenation mechanism demonstrated that these interactions between the monomeric cages are the driving force for interlocking behavior. As well as, the non-covalent interactions between the monomeric cages make the interlocked structure thermodynamically more stable, especially for interlocked cages synthesized without auxiliary template species. Of course, it doesn't mean that there are no interactions in the interlocked cages synthesized by the template method, which only indicates that the interactions are insufficient without the template species. Overall, according to their applications in the synthesis of interlocking cages, three interactions will be particularly discussed below:

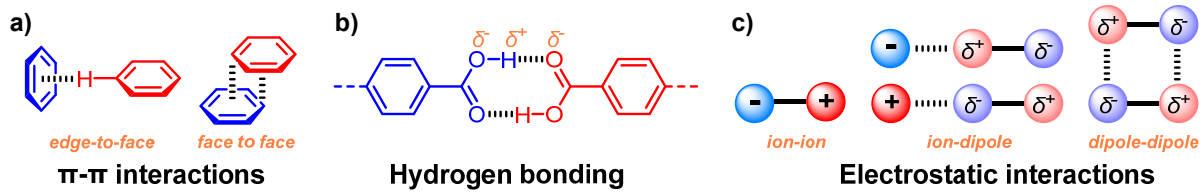

Figure 1.20: The illustration of a) π-π interactions, b) hydrogen bonding, and c) electrostatic interactions.

π-π interaction is one of the most frequently used supramolecular interactions in the synthesis of catenanes.[61] It generally exists between the aromatic rings arranged in an offset or parallel face-to-face manner, and face-to-edge stacked geometries are also observed (Figure 1.20a). For π-π interactions, the typical distance between two aromatic rings is around 3.5 Å. This kind of special conformation makes π-π interaction more controllable in comparison with other non-covalent interactions during the construction of interlocked species. The rational and efficient application of π-π interaction for the synthesis of interlocking structures dates back to the research of Stoddart.[62] In the late 1980s, they utilized the π-π interactions between the crown ethers **50** and the compound **51** to build a preorganized host-guest complex **52**, which was further reacted with 1,4-Bis(bromomethyl)benzene **43**, thus obtained [2]catenane **54** in an impressive 70% yield.[63]

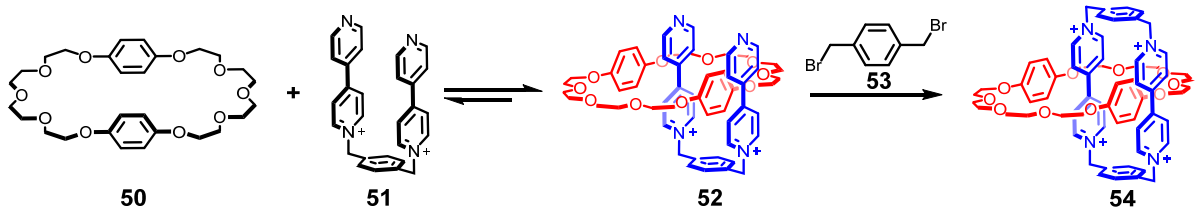

Figure 1.21: The scheme of the π-π interactions driving synthetic of [2]catenane **54**.[63]

Furthermore, for the synthesis of interlocked cages, especially IOCs, π-π interaction is almost the only driving force that could be intentionally introduced into the catenation process by pre-design the structure of the monomer cages. However, the occurrence of π-π interactions requires the proper distance, which is generally working for monomeric cages with smaller sizes and simple structures.

Hydrogen bonding can be considered a specific type of electrostatic interaction.[64] It is ubiquitous and plays a significant role in folding the secondary and tertiary structures of proteins and enzymes, as well as in DNA base-pair recognition. Moreover, hydrogen bonding has been employed to synthesize artificial chemicals and materials for a long time. A typical application is building infinite frameworks via hydrogen bonds, which are also known as hydrogen-bonding organic frameworks (HOFs). Hydrogen bonding is also one of the earliest non-covalent interactions applied in the synthesis of interlocked cages due to its better directional connectivity compared with other non-covalent interactions. As mentioned before, when Hardie and co-workers were investigating the single-crystal structures of the triply interlocked chiral coordination cage **5** (Figure 1.22), which was the second interlocked cage reported, the hydrogen bonding had been identified as the driving force of the catenation.[21] There were two types of hydrogen bonding interactions that occurred between the monomeric cages: The C-H···O hydrogen bonding between the unbound O of the nitrate ligand and the pendant methyl group on the bpy moieties (Figure 1.22 A); The second one is between a CH of the moiety of one monomer and the oxygen of OMe groups on the other monomer cages (Figure 1.22 B). The cumulative effect of two types of hydrogen bonding also makes the two cages of the catenane not interlock in a centered fashion. Compared with the π-π interaction, the formation of hydrogen bonding is more difficult to control since

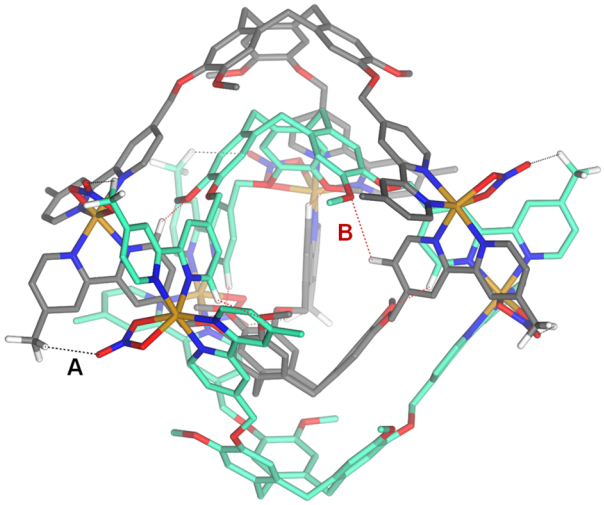

Figure 1.22: The view of two different hydrogen bonding from the crystal structure of ICCs **5**. Hydrogen atoms not involved are excluded for clarity. ICCs with one color for each monomer, CCDC: 691575.[24]

these functional groups are flexible without predictable direction. Therefore, it also challenging to employ hydrogen bonds as a driving force to build the interlocked cages.

Electrostatic interactions originate from the attractive electrostatic force between opposite charges, which are divided into ion-ion, ion-dipole, and dipole-dipole interactions. Electrostatic interactions have a vital significance in every corner of chemistry, and supramolecular chemistry is a research subject created to study electrostatic interactions. For example, self-assembly and host-guest chemistry are two main subtopics of supramolecular chemistry based on the application of electrostatic interactions. In addition, the constructions of all the interlocked cages mentioned in this introduction are more or less related to electrostatic interactions.

Recently Benke et. al reported the dimeric and trimeric catenation of monomeric cages driven by weak interactions (Section 1.1.2).[25] They screened a series of substituted terephthalaldehyde and TBTQ triamine to construct various [8+12] cube imine cages. By investigating the influence of the substitutes on the catenation behavior, it was found that the ICCs formed only when OMe, OEt, Et, SMe, and Br functional groups were present on the dialdehyde linkers, which can lead to such electrostatic interactions (Figure 1.23 a). Moreover, the DFT calculations of OMe-cube, as well as NOESY cross-peaks of imine C-H and the aromatic TBTQ protons, revealed a low barrier of rotation of the linker units at room temperature, which indicated that the triply interlocked cages tend to adopt conformations that have three such methoxy-methoxy interactions (Figure 1.23 b).

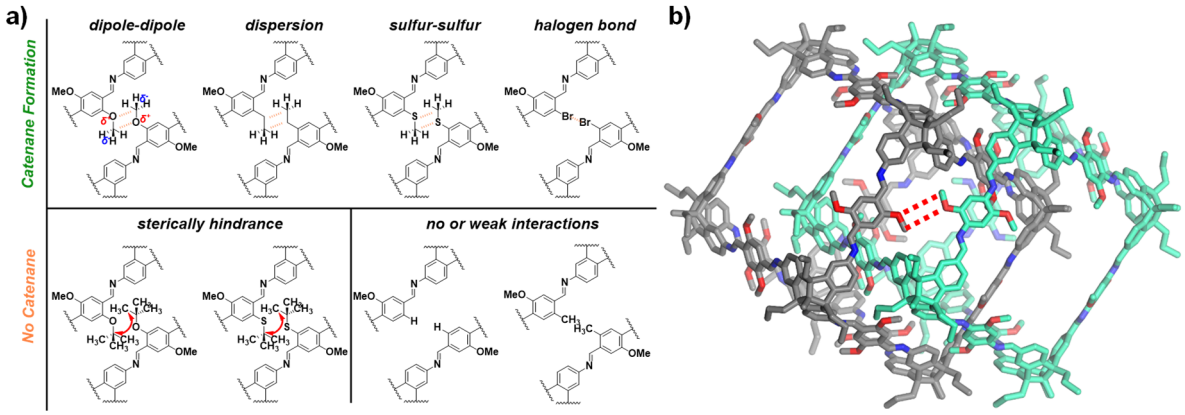

Figure 1.23: a) Summary of interactions resulting in catenane formation or their exclusion; b) Possible conformational arrangement of the two interlocked cages with the spatial arrangement of methoxy groups interacting via weak dipole-dipole forces (red dotted lines).[25]

Overall, although electrostatic interactions have been well-studied and investigated in the research of supramolecular chemistry for a long time, the exploration to apply them as a kind of driving force to build interlocked cages is still in its infancy. These reported examples displayed the great potential to employ such electrostatic interactions to rationally construct

interlocked cages. How to apply and control electrostatic interactions to build and construct the complex structure desired will be the core of the research field of interlocked cages.

1.4 Polycatenanes Based on Cages

The idea that cages could be self-interlocked into infinite polycatenanes has been proposed since the interlocked cages were discovered. The pioneering work of IOCs by Cooper group also concluded that:

"…such mechanically interlocked species could prove useful for the modular construction of complex porous materials from preformed 'porous' building blocks…for the self-assembly of supramolecular polymers."[3]

In principle, every vertex and edge of the cages with opened windows are a potential linkage for connecting to higher-level structures. Therefore, multiple catenations in each monomeric cage could lead to the formation of infinite polycatenanes. Furthermore, this strategy to construct the frameworks by interlocking the building blocks rather than bond formation would produce a revolution in the topology design, synthetic methodology, and even the application of organic porous materials.

Moreover, finding new linkage reactions and increasing the connectivity of building blocks are always challenging in the COFs research area. Scientists have already realized that organic cages could be a new kind of building block. In 2019, Wang and his co-workers first reported the synthesis of two-dimensional COFs based on cage building blocks, which have three aldehyde groups and are constructed by 6-fold Williamson-ether condensation.[65] One year later, Cooper and co-workers also used similar cages and terephthalaldehyde to build the first 3D COFs (Figure 1.24).[66] The cage building block **55** has six amine-reactive sites, whose connectivity has already exceeded most of the building blocks reported before. Besides, in 2019, Jiang's group also reported the HOFs based on cages.[67] However, all these cage units are still constructed by covalent bonding rather not catenation.

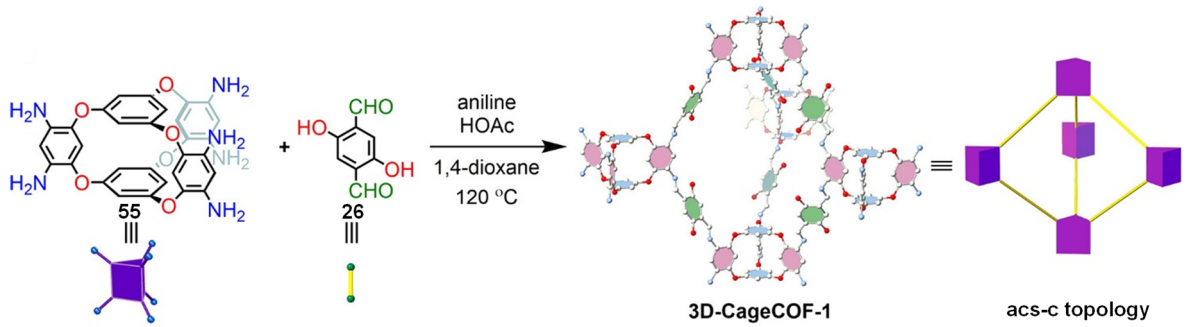

Figure 1.24: Scheme for the synthesis of 3D-CageCOF-1 from cages **55** and **26**, which can be topologically represented as a triangular prism and a linear strut, respectively. Atom colors: C, white; N, blue; O, red. H atoms are omitted for clarity.[66] Copyright 2020, American Chemical Society.

The first example of three-dimensional polycatenane based on cage compounds was reported in 2020 by Lu and co-workers, they used the Ag^+ nodes and 1,2,4-triazole as ligands to prepare the polycatenane **57** in water under hydrothermal reaction conditions.[68] Polycatenane **57** comprises polyhedral, three-dimensional, periodic extended architectures. The whole framework is composed of coordination cages, which are self-interlocked with six others through its vertices.

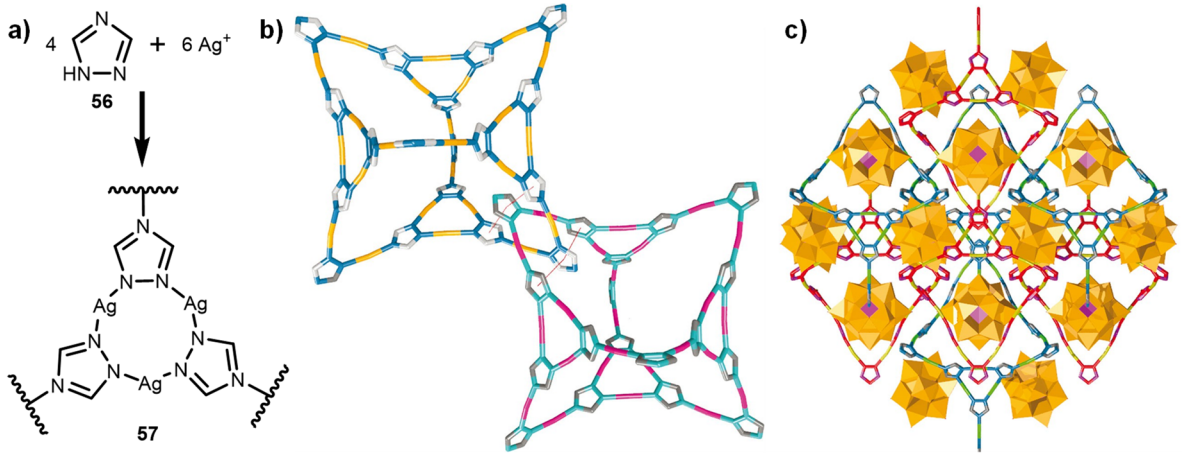

Figure 1.25: a) The synthesis of polycatenane **57**; b) X-ray crystallographic analysis shows that two identical nanocages have interlocked with one another through their vertices; each cage is shown in a different color; c) X-ray single-crystal structure of **57**, composed of two interpenetrating frameworks and polyoxometalate species. The two independent interpenetrating frameworks are distinguished by different colors, for clarity. Each framework is constructed from the polycatenation of a discrete adamantane-like cage, which is mechanically interlocked with six others through its six vertices.[68] Copyright 2020, Springer Nature.

Stefanie Dehnen's group also reported a one-dimensional polycatenane **60** consisting of a linear chain of interlocking coordination cages based on the trigonal ligand 2,4,6-tris(4-pyridyl)pyridine **58**, tris(4-pyridyl)-1,3,5-triazine ligand **59** and $ZnCl_2$ units.[69] These cage units are interlaced with a ligand-decorated plane of one coordination cage threaded through another, allowing for face-to-face π-π interactions of the ligand cores (Figure 1.23). Each cage is connected in this way to two adjacent ones, forming a straight, infinite strand of cages along the crystallographic c-axis.

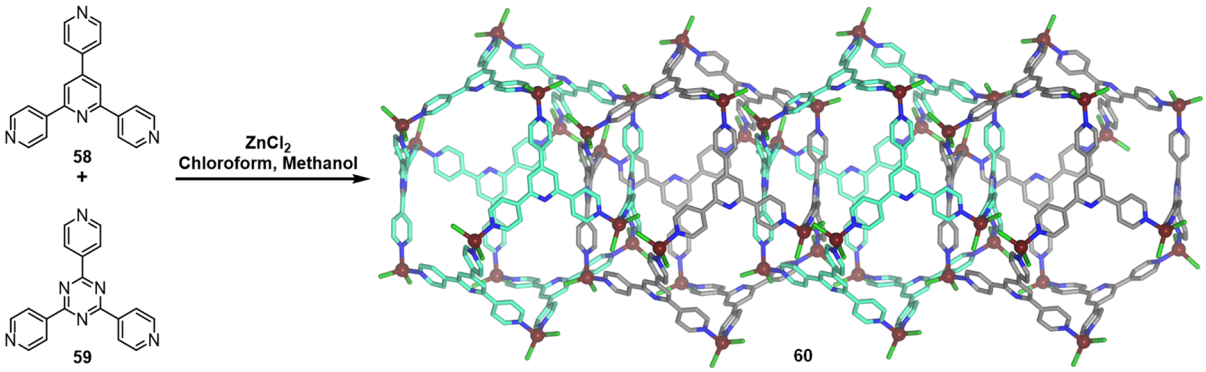

Figure 1.23: Structural fragment containing three interlaced icosahedral cages in ploycatenane **60**, CCDC: 809386.[69]

To date, the polycatenanes based on monomeric organic cages have not been reported yet. On the one hand, even the dimeric IOCs were rarely reported and it would be more challenging to synthesize polycatenane without systematic investigations and a full understanding of the catenation mechanism. On the other hand, the construction of the framework requires the bigger cavities and windows of monomeric cages, which can hold more than one other unit. But the monomeric cages with bigger sizes generally make it more challenging to isolate and characterize their interlocked species, even just dimers or trimers. Moreover, compared with MOFs or polycatenanes based on coordination cages, the single crystals of polycatenane based on organic cages are much more difficult to prepare. Without X-Ray data, the 2D-NMR experiments which were often employed to figure the conformation of IOCs will also be insufficient for ploycatenanes. Thus, finding effective methods to characterize and identify polycatenane is also the priority in this research topic.

Even though, it is still promising to prepare the polycatenane based on bigger monomeric cages, which requires more effort to investigate the catenation mechanism and the characterization methods. Moreover, the studies could start from the initial substructures such as trimers, tetramers, or oligomers which with lower catenation degrees. It will help us to understand more about the catenation mechanism, which will be the foundation for the development of polycatenane research in the future.

2. Objectives

Interlocked covalent organic cages have attracted considerable attention by the virtue of the artificial mechanically interlocked structure, as well as their fascinating porous properties which do not exist in most classic interlocked molecules. However, it is still a significant challenge to rationally design and synthesize interlocked organic cages. In contrast to a large number of monomeric organic cages with diverse structures, cages that could be self-interlocked are relatively rare. Although both of them are generally synthesized via dynamic covalent chemistry (DCC), the mechanism of the interlocking process from monomeric organic cage to catenane still needs to be further elucidated. This thesis aims to synthesize a series of catenanes based on [8+12] organic cages and systematically investigate the catenation mechanism of interlocked organic cages.

Chapter 3.1 focus on exploring how the size of monomeric cages influences the catenation results, which was often ignored during the discussion about the catenation mechanism. In this project, a series of giant [8+12] cube organic monomeric cages with different sizes and cavity volumes will be synthesized by using building blocks and linkers with different lengths to study the effects of size.

Chapter 3.2 investigates the structural effects of monomeric cages. Most catenanes reported were found of serendipity, and the study of driving force was also based on single examples. Herein, different linkers will be utilized to construct the monomeric cages, then investigate their influence on the catenation results.

Chapter 3.3 explores the influence of solvents on catenation. Solvents are always the first condition screened when the synthesis of a catenane, however, how it works during the interlocking process is still unknown. So, the investigation of solvent effects on catenation will be conducted.

Chapter 3.4 illustrates the attempts to synthesize the polycatenanes with lower polymerization degrees, for example, dimers, trimers, tetramers, or pentamers.

Chapter 4 tries to synthesize the crystalline MSOFs. The strategy is to first produce the crystalline MOFs and then transform them into crystalline MSOFs by post-modification.

3. Results and Discussion

3.1 The Effects of Cage and Cavity Size on Catenation Tendency

3.1.1 Introduction

In the research of IOCs, the size of monomeric cages (cage volume and cavity volume) (Figure 3.1.1) is an important factor in the catenation process but rarely investigated. Most of the reported IOCs and the corresponding studies of the catenation mechanism are based on small monomeric organic cages with simple topologies, for example [3+2] and [6+4] cages.[3, 10b, 24, 26, 70] Due to the small size of these cages, and therefore small cavity volume, all these IOCs are dimers. Although numerous organic cages with giant sizes and various topologies have been reported, IOCs consisting of big monomeric cages are still rare.[10a, 25] Therefore, more systematic research about the IOCs based on big monomeric cages are required. In this chapter, the relationship between the size of the monomeric cage and the catenation tendency has been investigated.

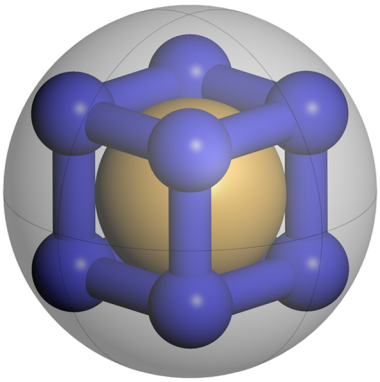

Scheme 3.1.1: Illustration of cage size (outer) and cavity volume (inner).

Herein, a series of triply interlocked [8+12] giant cube imine cages based on substituted triptycene triamine were designed and synthesized. Six corresponding monomeric cages have different cavity volumes and sizes, which were controlled by adjusting the size of building blocks and the length of linkers. Under similar conditions, it was found that when a monomeric cage has a bigger cavity or smaller size, it tends to be self-interlocked into IOCs more.

3.1.2 The Synthesis of Triptycenetriamine Building Blocks and Linkers

3,6,15-Triaminotriptycene is a distinctive building block with C_3 symmetry, and it was frequently used as the monomer for the syntheses of [2+3] and [4+6] cages.[71] However, the solubility of some cages based on 3,6,15-triaminotriptycene was insufficient for purification, characterization, or application processing.[71b, 71g] To increase the solubility of triptycene triamine, solubilizing alkyl chains were initially introduced to 1,8,13-trihydroxytriptycene **74** *via* Williamson ether reaction (Scheme 3.1.2), which could further increase the solubility of the corresponding cages. In addition, because of that the monomeric cages with longer outer chains also require more space in the cavity of the host cages when interlocking, the second function of these chains on triptycene triamine is to adjust the size of monomeric cages. Herein, three types of triptycene triamine substituted by different alkyl chains (propyl, hexyl, decyl)

respectively, were investigated. The syntheses of substituted triptycene triamine **81-83** are shown in Scheme 3.1.2.

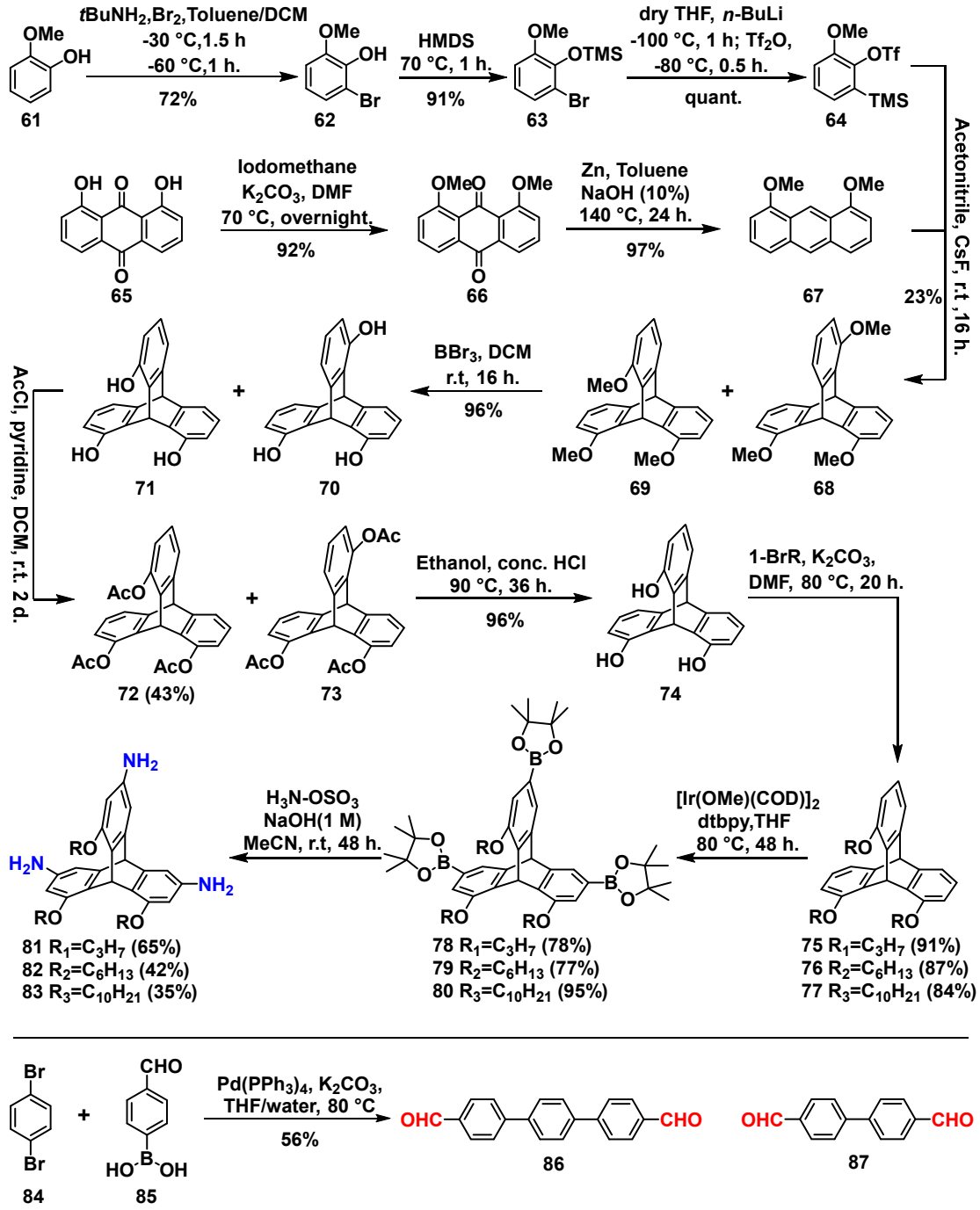

Scheme 3.1.2: Synthesis of triptycene triamine **81-83**[71g] and dialdehyde **86**[72]. Illustration of dialdehyde **87**.

Trihydroxytriptycene **74** was synthesized according to the literature,[71g] then reacted with the corresponding 1-bromoalkane to produce compounds **75-77** *via* Williamson ether reaction. Compounds **78-80** were synthesized through aromatic C–H borylation reaction and further treated with hydroxylamine-O-sulfonic acid under basic conditions to transform the boronic ester units into amine groups. The resulting crude products were further purified by column chromatography (ethyl acetate/petroleum ether, 5:1) to obtain **81-83**.[71k]

To tune the cavity volume of the monomeric cages, two linear dialdehydes **86-87** with different lengths, were utilized as the linkers to construct the monomeric cages. Terphenyl dialdehyde **86** was synthesized *via* the Suzuki-Coupling reaction,[72] and biphenyl dialdehyde **87** is commercially available (Scheme 3.1.2).

3.1.3 The Synthesis of HexBi-Cage, HexBi-Catenane[1]

The initial idea was to use triptycene triamine **82** with dialdehyde **87** to construct an [8+12] imine cage with great solubility for further investigation (Figure 3.1.3, HexBi-Cage). Depending on solvents and temperatures (Table 3.1.1), MALDI mass spectroscopy (MS) experiments showed the formation of [8+12] species (m/z = 6889.4), as well as an unexpected [16+24] product (m/z = 13781.2) (Figure 3.1.4). Moreover, monitoring by MS, the [8+12] species gradually disappeared and only [16+24] condensation products were left with increased reaction time at a higher temperature, which suggests that the [16+24] species are thermodynamically favored. It was also found that there were some precipitates formed in tetrahydrofuran (THF), especially at elevated temperatures, while homogeneous solutions were obtained with chloroform.

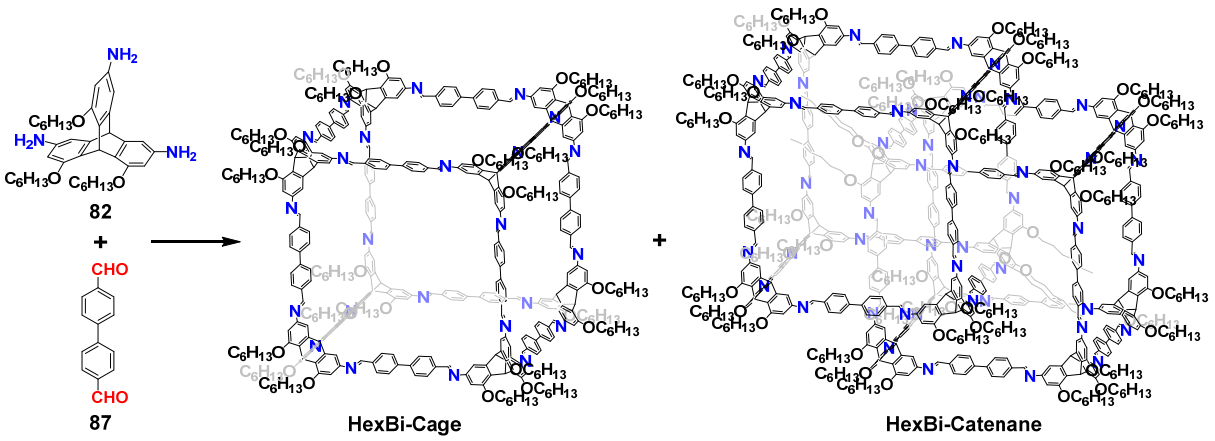

Scheme 3.1.3: The synthesis of [8+12] **HexBi**-Cage and [16+24] **HexBi**-Catenane.

Table 3.1.1 Screening conditions for the synthesis of **HexBi**-Cage and **HexBi**-Catenane.

Solvent	Temperature	TFA	Concentration[a]	Reaction time	Products detected by MS
Chloroform	r.t	4 mol%	5.3 mM	1 d	Figure 3.1.4 a
Chloroform	60 °C	4 mol%	5.3 mM	1 d	Figure 3.1.4 b
THF	r.t	4 mol%	5.3 mM	1 d	Figure 3.1.4 c
THF	70 °C	4 mol%	5.3 mM	1 d	Figure 3.1.4 b

a. Concentration of triptycene triamine **82**.

[1] Because of no standard guideline for naming new IOCs currently, the name of the IOCs and cages in this thesis is based on the type of building blocks and linkers used. For example, 1,8,13-tri**hexyloxy**-3,6,15-triaminotriptycene **82** and 4,4'-**biphenyl**dicarboxaldehyde **87** were employed here, the resulted monomeric cage and catenane was named **HexBi**-Cage and **HexBi**-Catenane respectively. Letter 'C' of **HexBi**-Cage and **HexBi**-Catenane is uppercase to show that it is special name belong to a specific product, rather not a common word.

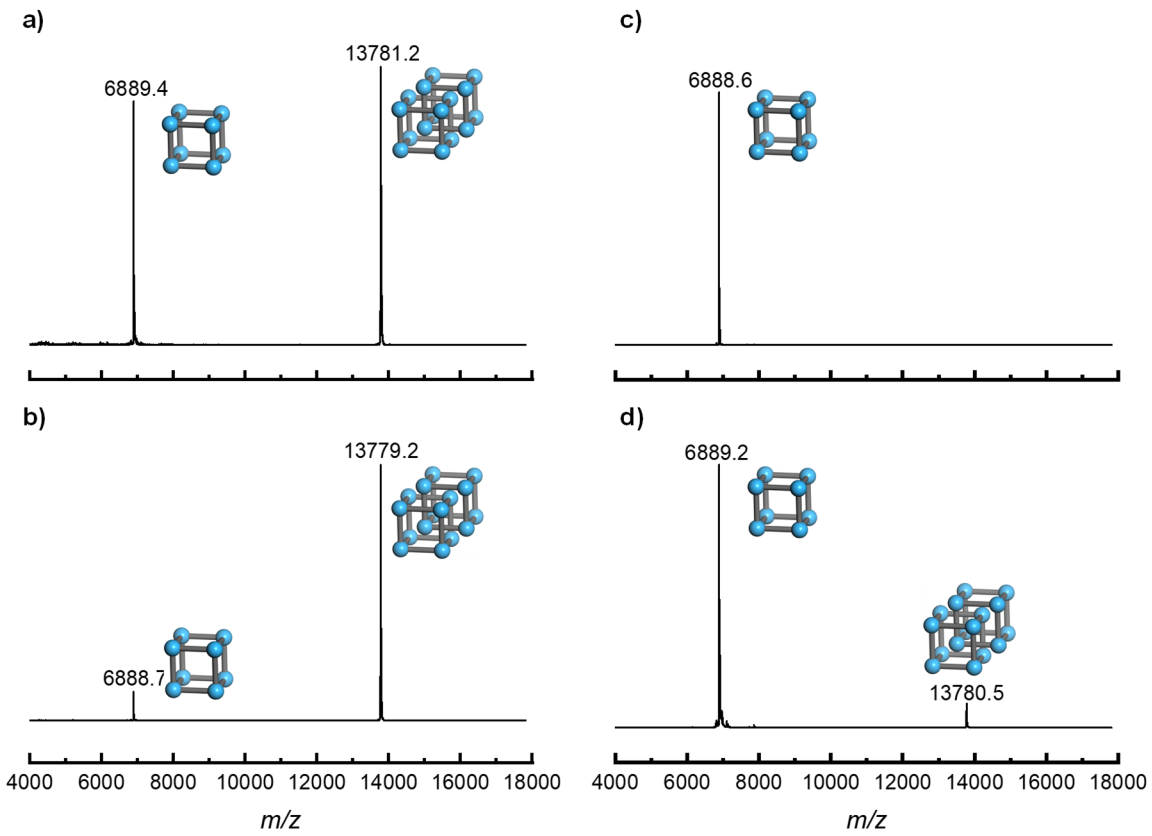

Figure 3.1.4: MALDI-MS of **HexBi**-Cage and **HexBi**-Catenane (the crude solution under different conditions in Table 3.1.1).

After the reaction, the crude solution was filtered through a Celite column, and the obtained solution was concentrated and precipitated with methanol. It is worth mentioning that filtration is necessary for all crude solutions, even if the crude solution already looks homogeneous. Because some oligomers would be insoluble after precipitation, they only could be removed through a short Celite column or syringe filter (0.45 μm). After precipitation, yellow precipitates were collected by centrifuging and purified by recycling gel permeation chromatography (r-GPC) with THF as the solvent. The r-GPC chromatograms showed that there were some bigger polymers formed, especially for the synthesis of HexBi-Cage (Figure 3.1.5 a&b, fractions colored in purple). Some smaller fragments were also found on GPC chromatograms (Figure 3.1.5 a&b, fractions colored in pink). These polymers and fragment fractions were analyzed by MS and NMR, but no peak was detected from 4000 to 40000 (m/z), and the NMR spectra also only showed several broad peaks, therefore it was not possible to identify them. In addition, the chromatogram showed a shorter retention time (third cycle, 73.3 minutes) for HexBi-Catenane compared with that of the HexBi-Cages (third cycle, 75.8 minutes), which is consistent with its larger size (Figure 3.1.5 a, b). Moreover, the MALDI-TOF MS and the isotope distribution pattern of the pure samples further confirmed the formation and isolation of HexBi-Cage and HexBi-Catenane (Figure 3.1.5 c, d).

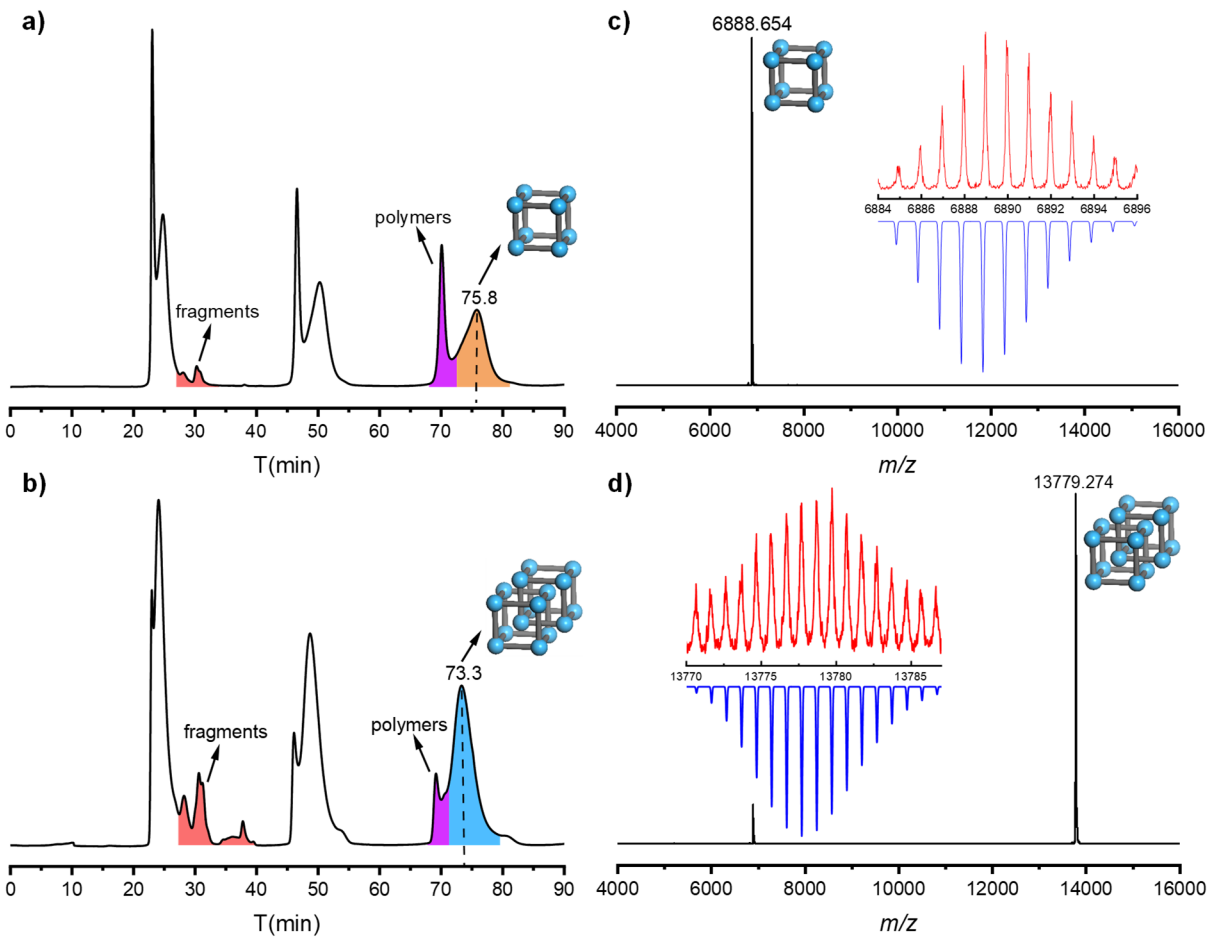

Figure 3.1.5: r-GPC chromatogram (THF, 5 mL/min, 40 °C, 3×100 Å columns) of the crude reaction mixture: a) **HexBi**-Cage (THF, TFA 4 mol%, r.t, 2 days), the retention time is 75.8 minutes (third cycles); b) **HexBi**-Catenane ($CHCl_3$, TFA 4 mol%, 60 °C, 7 days), the retention time is 73.3 minutes (third cycles). Corresponding MALDI-TOF mass spectra and the isotopic pattern (red, measured; blue, calculated): (c) **HexBi**-Cage, the calculated mass is 6883.832; (d) **HexBi**-Catenane, the calculated mass is 13767.666. Fragments and oligomers were not identified.

To figure out the conformations of HexBi-Cage and HexBi-Catenane, the pure cage and catenane compounds were employed to prepare the single crystals for collecting the single crystal diffraction data. However, the obtained crystals were hard to be handled and measured, because most of them cracked quickly once taken out of the solution. The collected single-crystal X-Ray diffraction data were all with low resolution (~1.7 Å), which is insufficient for resolving the structures. Such behavior was also observed for the following cages and catenanes. Two possible reasons lead to this problem: on the one hand, the structures of these two compounds are quite big and complex, especially with long flexible alkyl chains, which will increase the difficulty of measuring and solving single crystals; on the other hand, the cages and catenanes have big cavities and several opened windows, which make them easy to hold the solvents in the solution, but also easy to lose these solvents after being out of the solution. That's why they often cracked during the measurement. Therefore, the elucidation of the structures of these compounds was alternatively performed by 2D NMR spectroscopy. The ^{1}H-

NMR of HexBi-Cage was assigned and shown below (Figure 3.1.6), which corresponds to [8+12] cubic structure.

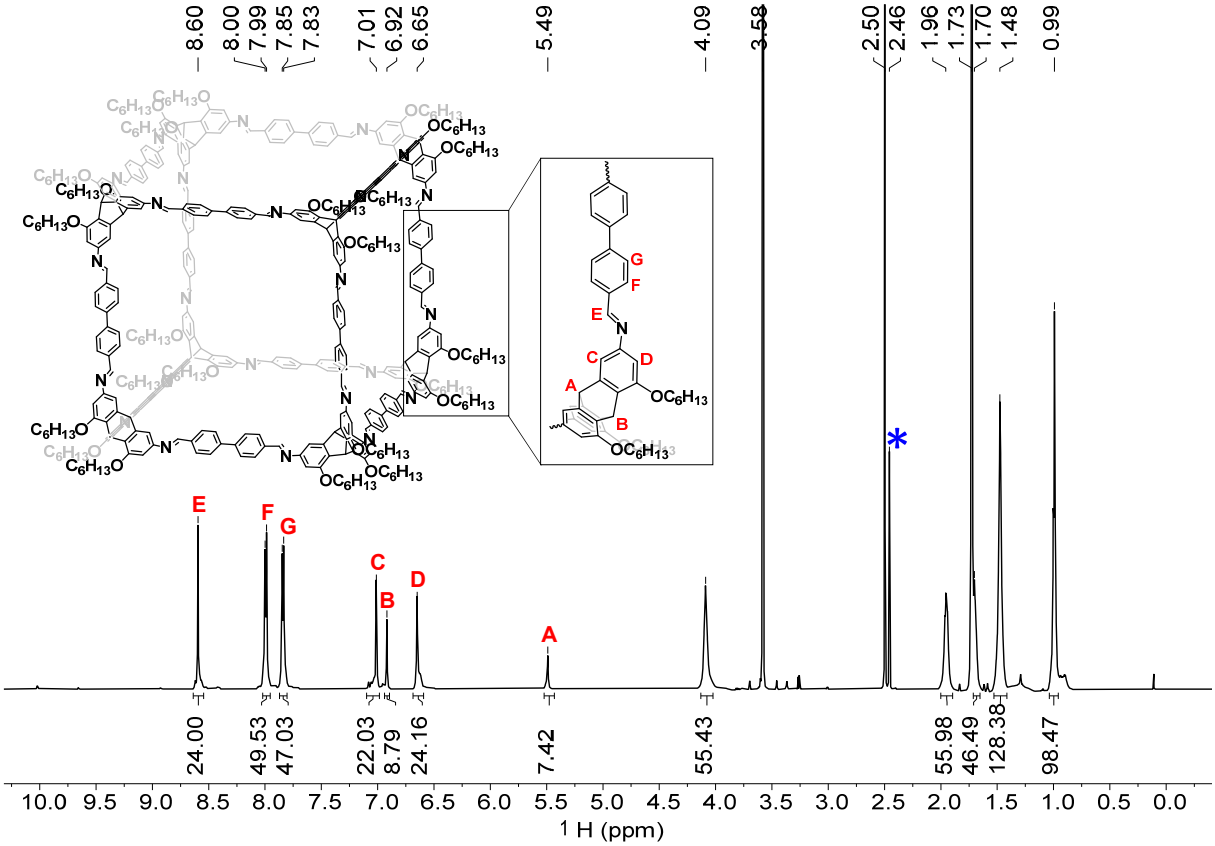

Figure 3.1.6: ^{1}H-NMR Spectrum (600 MHz) of **HexBi-Cage** in THF-d_8, Capital letters mark the position of protons, and * marks the water peak.

In contrast, the ^{1}H-NMR spectrum of HexBi-Catenane is more complicated (Figure 3.1.8). It is worth mentioning that the NMR spectra of HexBi-Catenane obtained in CD_2Cl_2 showed a better resolution, hence the following NMR measurements of catenane will be all prepared with CD_2Cl_2. Three possible conformations of HexBi-Catenane were shown in Figure 3.1.7, according to the symmetry, these conformations correspond to the different number of imine signals on the ^{1}H-NMR spectrum. The singly, triply, and quadruply conformer correspond to five, six, and four sets of imine peaks, respectively. According to the ^{1}H-^{1}H COSY and ^{1}H-^{13}C HSQC spectrum (Figure 3.1.8 c, d), six types of imine-

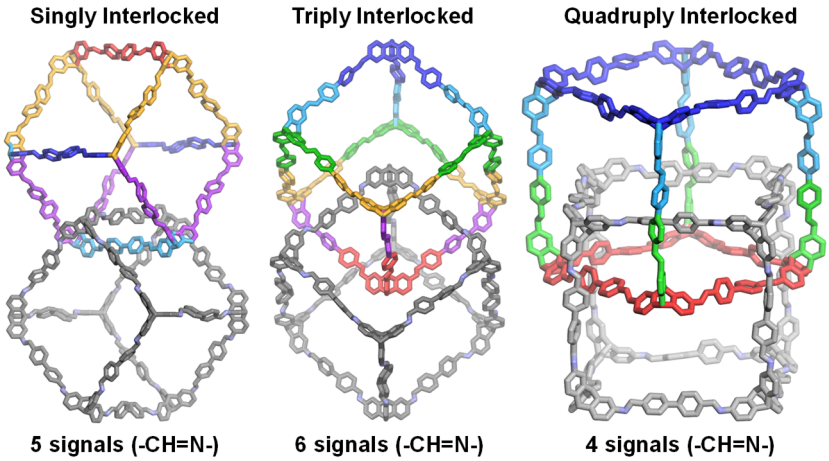

Figure 3.1.7: Illustration of three possible conformation for dimeric catenane, and the corresponding number of imines signals on ^{1}H NMR spectrum.

protons and six pairs of aromatic protons were identified, which corresponds to the triply interlocked conformation (Figure 3.1.8 f).

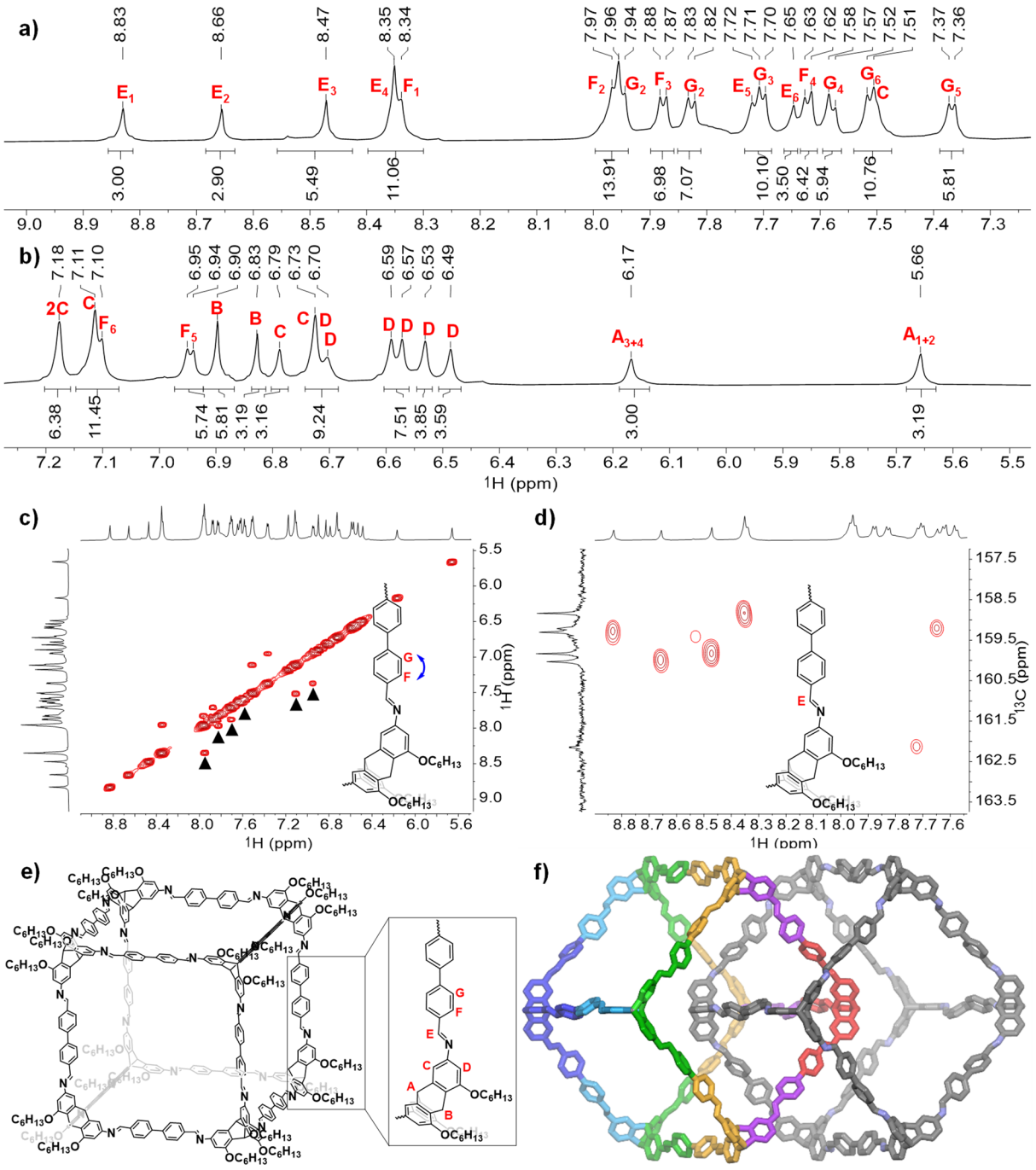

Figure 3.1.8: a), b) Assigned partial ^{1}H-NMR Spectrum (700 MHz) of **HexBi**-Catenane in CD_2Cl_2; c) Partial ^{1}H-^{1}H COSY spectrum showing the neighboring phenyl protons (*F, G*), black triangle marks the six signals; d) Partial ^{1}H-^{13}C HSQC spectrum showing the imine protons (*E*); e) Illustration of the monomeric cage of **HexBi**-Catenane and a repeated unit. f) The model of **HexBi**-Catenane based on NMR studies. Six colored parts indicate the positions of six different imine and neighboring aromatic protons; the outer chains were cleaved for clarity. Uppercase and lowercase letters mark the position of protons and carbons on the repeated unit, respectively. The number marks the different repeated units.

After identifying the signals of imine protons (*E*), the corresponding ^{13}C peaks (*e*) were also determined according to the ^{1}H-^{13}C HSQC spectrum (Figure 3.1.9 a). The pairs of doublet

neighboring aromatic signals (*F, G*) had been shown on ^{1}H-^{1}H COSY (Figure 3.1.8 c), however, the specific proton peaks of them haven't been distinguished yet. Due to the relation to the imine carbons (*e*), the neighboring aromatic protons *F* could be identified firstly based on the ^{1}H-^{13}C HMBC spectrum (Figure 3.1.9 b), and therefore, the left protons *G* were also assigned.

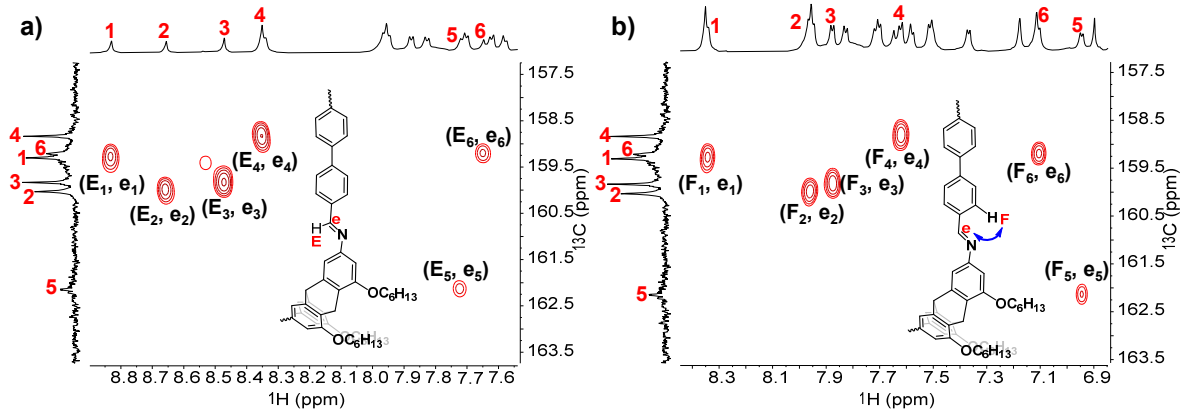

Figure 3.1.9: a) Partial ^{1}H-^{1}H HSQC (600 MHz, CD_2Cl_2) spectrum and b) Partial ^{1}H-^{13}C HMBC (600 MHz, CD_2Cl_2) spectrum of **HexBi**-Catenane. Uppercase and lowercase letters mark the position of the proton and carbon on the repeated unit, respectively. The number marks the different repeated units.

Accordingly, the ^{13}C peaks of aromatic carbons (*f*) were assigned based on the ^{1}H-^{13}C HSQC spectrum (Figure 3.1.10 a), but the resolution of ^{13}C peaks was not sufficient to determine the aromatic carbons *g*. In addition, because of the relation between aromatic carbons (*f*) and the neighboring imine protons (*E*), there were also six signals (*E, f*) on the ^{1}H-^{13}C HMBC spectrum (Figure 3.1.12 b), which once again proved the assignment above.

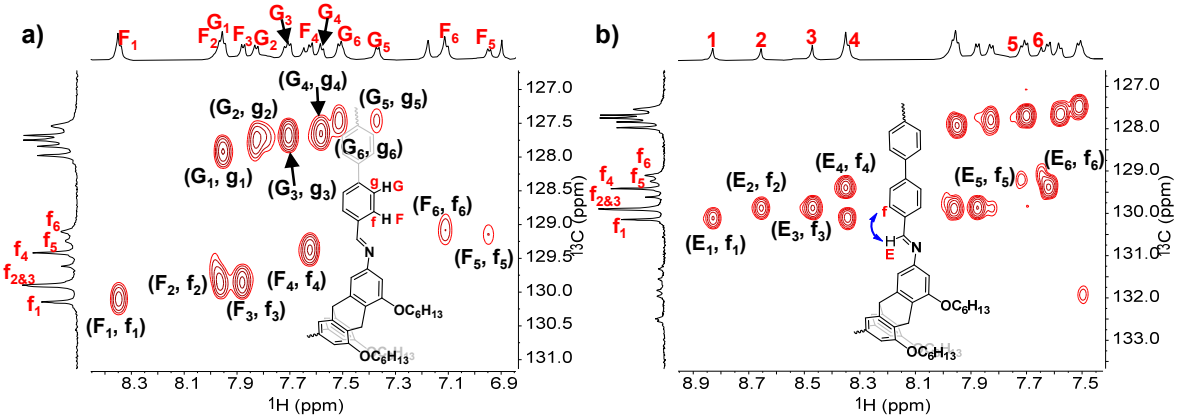

Figure 3.1.10: a) Partial ^{1}H-^{13}C HSQC (600 MHz, CD_2Cl_2) spectrum and b) Partial ^{1}H-^{13}C HMBC (600 MHz, CD_2Cl_2) spectrum of **HexBi**-Catenane. Uppercase and lowercase letters mark the position of protons and carbons on the repeated unit, respectively. The number marks the different repeated units.

Herein, all six imine peaks and twelve aromatic protons have been assigned, which identified the triply interlocked structure of HexBi-Catenane. It is worth mentioning the identification of the two triptycene bridgehead protons. They are quite special and able to provide crucial information for locating the different imine peaks or other peaks to the right positions (Figure 3.1.11). One triptycene bridgehead proton (*A*) has the neighboring aromatic

proton (*C*) while the other one (*B*) has none, therefore, it is easy to distinguish them by the ^{1}H-^{13}C HMBC spectrum. As shown in Figure 3.1.11 b, according to the symmetry of HexBi-Catenane, triptycene bridgehead carbon a_1 is correlated to one kind of neighboring proton (C_1), and carbon a_2 should be related to two types of the neighboring proton (C_1). Thus, if integrating the ^{1}H-^{13}C HMBC spectrum, there also should be two different ^{13}C peaks, one crosses one signal, and the other one crosses two signals. Therefore, the specific position of these signals could be figured out accordingly.

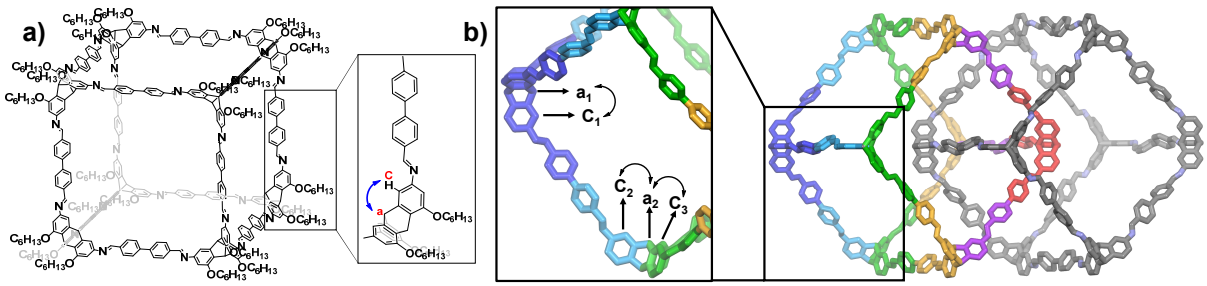

Figure 3.1.11: a) Illustration of the monomeric cage of **HexBi**-Catenane; b) 3D model of **HexBi**-Catenane, the cut picture shows two situations about triptycene bridgehead carbon (*a*) and the neighboring protons (*C*). Uppercase and lowercase letters mark the position of protons and carbons, respectively.

In principle, there should be eight ($4\times A+4\times B$) signals of triptycene bridgehead protons on the ^{1}H-^{13}C HSQC spectrum. Unfortunately, only four were observed (Figure 3.1.12 a), which means that the four pairs of peaks are somehow overlaid (2A+2A+2B+2B). Therefore, three signals (*C, a*) correspond to one ^{13}C peak (*a*) on the ^{1}H-^{13}C HMBC spectrum (Figure 3.1.12 b).

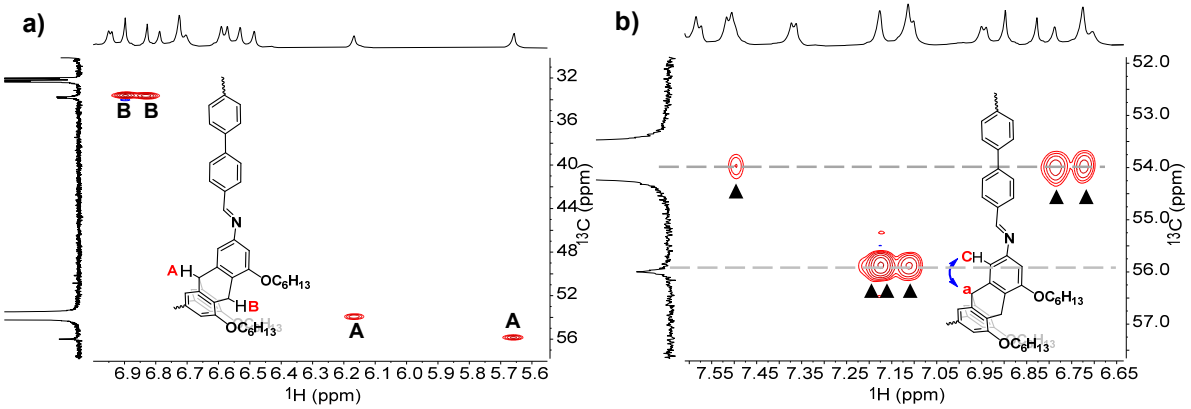

Figure 3.1.12: a) Partial ^{1}H-^{13}C HSQC (600 MHz, CD_2Cl_2) spectrum and b) Partial ^{1}H-^{13}C HMBC (600 MHz, CD_2Cl_2) spectrum of **HexBi**-Catenane. Uppercase and lowercase letters mark the position of protons and carbons on the repeated unit, respectively. Black triangles mark the six signals corresponding to two ^{13}C peaks, respectively.

The study of the ^{1}H-^{1}H NOSEY spectrum also proved such overlay. There are six signals which show the neighboring protons *A* and *E*, and one triptycene bridgehead proton peak at 5.66 ppm corresponds to the peak of E_1, E_2, and A_3, another peak at 6.17 ppm corresponds to the peaks of E_4, E_5, and E_6 (Figure 3.1.13a). Because the aromatic protons *C* on triptycene have already been identified before (Figure 3.1.12 b), the remaining protons *D* could be assigned according to the ^{1}H-^{13}C HSQC spectrum of the HexBi-Catenane (Figure 3.1.13a).

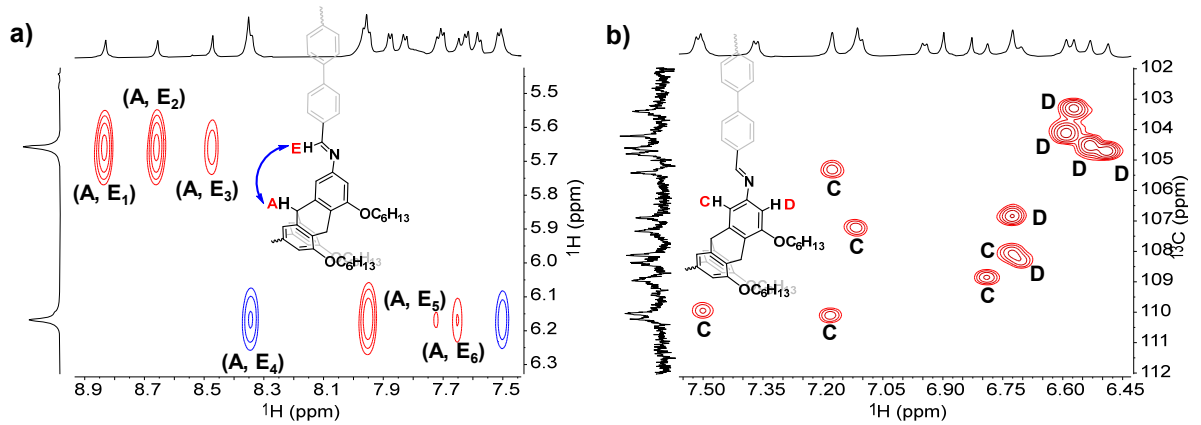

Figure 3.1.13: a) The ^{1}H-^{1}H NOSEY spectrum shows the correlation between imine protons and triptycene bridgehead protons (*A, E*); f) Partial ^{1}H-^{13}C HSQC spectrum showing the aromatic protons on triptycene (700 MHz, CD_2Cl_2). Capital and lowercase letters mark the position of protons and carbons respectively.

The diffusion-ordered NMR spectroscopy (^{1}H-DOSY) of the HexBi-Cage showed only one trace of signals with a diffusion coefficient of 2.13×10^{-10}m^2 s^{-1} corresponding to the solvodynamic radius of 2.1 nm (Figure 3.1.14a). And the diffusion coefficient of HexBi-Catenane is 2.34×10^{-10} m^{2}s^{-1} with a solvodynamic radius of 2.2 nm (Figure 3.1.15b). This is slightly larger than it is for HexBi-Cage, which is consistent with their calculated sizes based on optimized model structures (*Gaussian*, PM6).

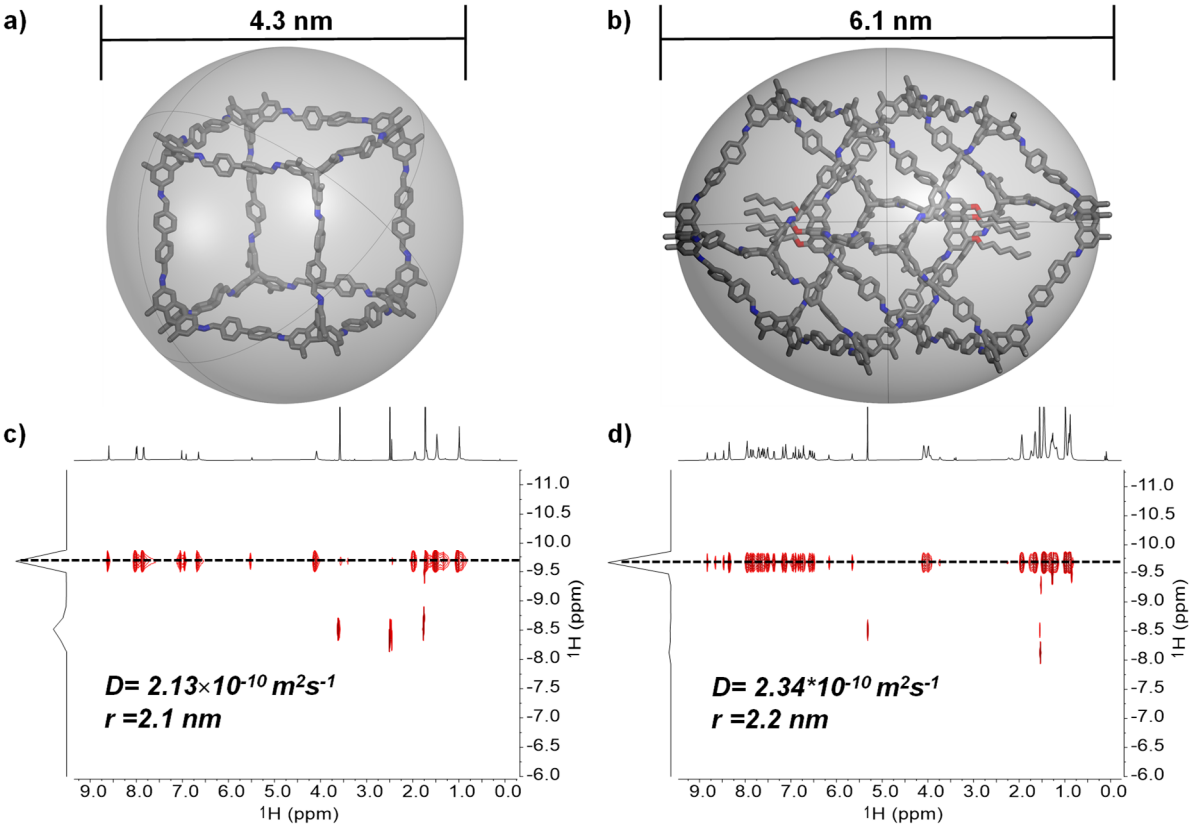

Figure 3.1.14: The optimized structure (*Gaussian*, PM6) and the diameter of a) **HexBi**-Cage and b) **HexBi**-Catenane, the outer chains were cleaved for the shorter calculation time. Their diameter was measured with *Materials Studio*. The ^{1}H-DOSY NMR of c) **HexBi**-Cage (400 MHz, THF-d_8) and d) **HexBi**-Catenane (400 MHz, CD_2Cl_2).

3.1.4 The Synthesis of HexTri-[2]Catenanes and HexTri-[3]Catenanes

After obtaining the HexBi-Catenane with the triptycene triamine **82** and biphenyl dialdehyde **87**, a longer linker − triphenyl dialdehyde **86** was used to construct a monomeric cage with bigger size, thus exploring its influence on the catenation process (Scheme 3.1.15). To make the results more comparable, the syntheses based on triphenyl dialdehyde **86** were conducted under the same conditions as that of HexBi-Catenane (Table 3.1.2). The formation of [16+24] species was also observed according to the mass spectra of the crude solutions. However, there were more precipitates in the reaction solution for the synthesis of HexTri-Catenane, which means more insoluble polymers or oligomers formed. Therefore, the concentrations of starting materials and the amount of trifluoroacetic acid (TFA) were varied for synthesis optimization (Table 3.1.2). It was found that fewer precipitates formed in the more dilute solution, and the amount of TFA made no big difference to the results.

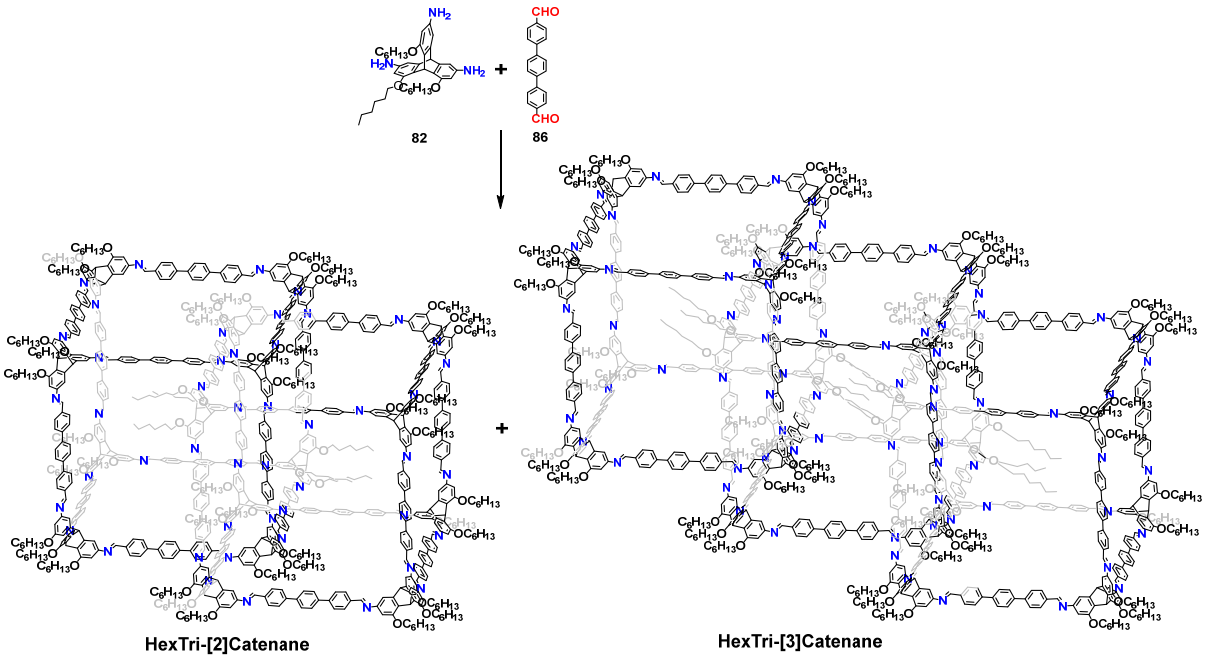

Scheme 3.1.15: Syntheses of **HexTri**-[2]Catenane and **HexTri**-[3]Catenane.

Table 3.1.2 Screening conditions for the synthesis of **HexTri**-Catenane.

Solvent	Temperature	TFA	Concentration[a]	Reaction time	Products detected by MS
$CHCl_3$	r.t	4 mol%	5.3 mM	5 d	Dimer
$CHCl_3$	60 °C	4 mol%	5.3 mM	5 d	Dimer
THF	r.t	4 mol%	5.3 mM	5 d	Dimer
THF	70 °C	4 mol%	5.3 mM	5 d	Dimer
$CHCl_3$	60 °C	8 mol%	5.3 mM	5 d	Dimer
$CHCl_3$	60 °C	4 mol%	2.6 mM	5 d	Dimer*

a. Concentration of triptycene triamine **82**; * fewer precipitates formed.

After the reaction, the mixture was filtered through a short Celite column to remove these insoluble solids, and the solution was concentrated and precipitated with methanol. The

solid was collected by centrifuge and dissolved in THF for further purification by r-GPC. The chromatogram showed three fractions, and the first two fractions (*1* and *2*) were not completely separated (Figure 3.1.16 a). Interestingly, the mass spectrum of fractions *1* and *2* showed the peaks of [8+12] (m/z=7823.3), [10+15] (m/z=11741.1), [16+24] (m/z=15655.0), [20+28] (m/z=19556.7), and [24+36] (m/z = 23467.5) species (Figure 3.1.16 c). A mixture of [16+24] dimer and [8+12] cage was detected in fraction *4* (Figure 3.1.16 e). Only fraction *3* was the pure [16+24] dimer according to the mass spectrum (Figure 3.1.16 d), although the yield was bad because most of the dimer was not separated.

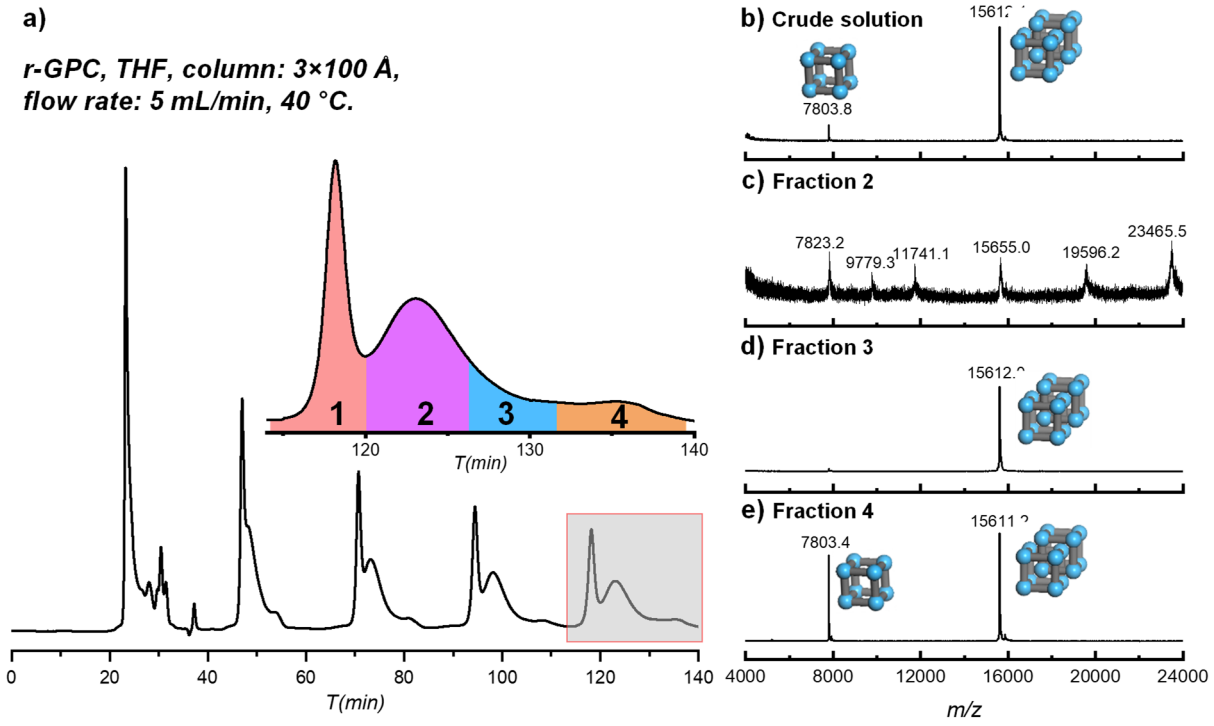

Figure 3.1.16: a) The r-GPC chromatogram of the crude products, the collected fractions were marked with different colors and numbers; The MALDI MS: b) crude solution; c) fraction *1* and *2*; d) fraction *3*; e) fraction *4*. The calculated mass of **HexTri**-Cage is 7796.208.

It seems when the size of compounds became bigger, the column system (3×100 Å columns) of r-GPC was not sufficient anymore for the separation. In principle, the bigger filler materials of columns and the combination of columns with different sizes are supposed to promote the separation of the compounds with bigger sizes.[73] Therefore, a new r-GPC column system (2×500 Å + 2×1000 Å columns) was set up and tested. As the GPC chromatograms showed (Figure 3.1.17), in comparison with the former system (3×100 Å columns), the new columns (2×500 Å + 2×1000 Å) indeed resulted in a much better separation performance to the mixture of bigger polymers (Figure 3.1.17, fraction colored in purple) and smaller catenanes (Figure 3.1.17, fraction colored in yellow). By comparison, the new columns even showed better separation of these polymers (the fraction (purple) with new columns consists of several

peaks while that of the previous columns only shows one peak)[1], the slow separation of trimer and dimer also could be achieved with the new columns.

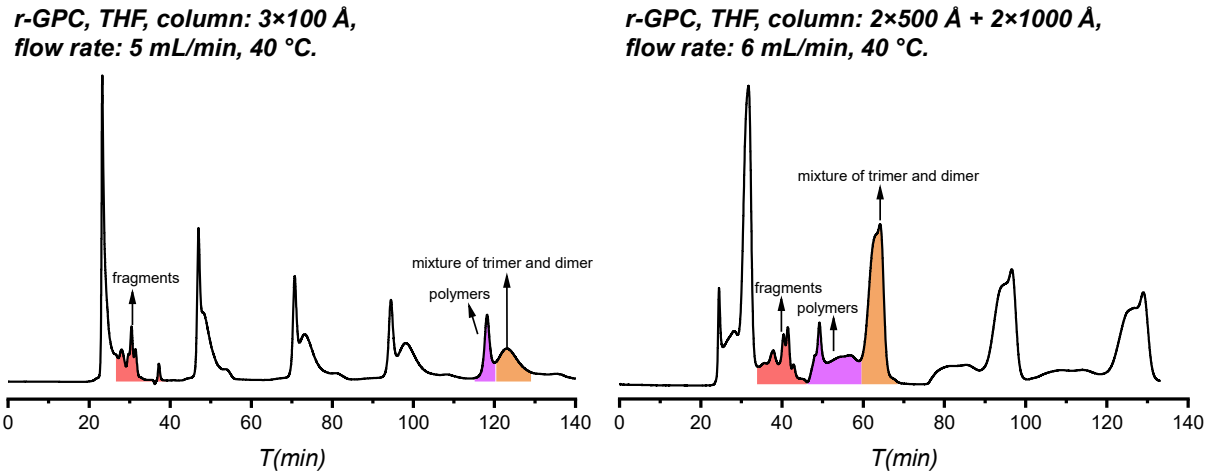

Figure 3.1.17: r-GPC chromatograms of the crude products of **HexTri**-Catenane with different columns.

However, the trimer and dimer are still difficult to be separated even running on r-GPC overnight (Figure 3.1.18 e). There were still quite a lot of bigger polymers mixed with the trimers fraction, which led to a broader peak on the r-GPC chromatogram (Figure 3.1.18 e). And these peaks will overlay with each other again before being completely separated. Therefore, the ratio of building blocks and linkers (triamine **82** and dialdehyde **86**) was explored to reduce the formation of oligomers (Table 3.1.3).

Table 3.1.3 Screening of ratios of building blocks for syntheses of **HexTri**-Catenane.

Solvent	**82**/**86**	Temperature	TFA	Concentration[a]	Reaction time	Products detected by MS
$CHCl_3$	8/12	60 °C	4 mol%	5.3 mM	5 d	Dimer
$CHCl_3$	8/10	60 °C	4 mol%	5.3 mM	5 d	Dimer
$CHCl_3$	8/14	60 °C	4 mol%	5.3 mM	5 d	Dimer

a. Concentration of triptycene triamine **82**.

Interestingly, comparing the r-GPC chromatograms of the crude products resulted in different ratios of building blocks, and much fewer polymers were generated (Figure 3.1.18, a to c, fractions colored in pink) with the ratio of 8/10 and 8/14. Moreover, after collecting the main fractions (Figure 3.1.18, a to c, fractions colored in green) and then injecting them for the second purification, the r-GPC chromatograms also showed better separation of the products at the ratio of 8/10 and 8/14 respectively (Figure 3.1.18, e to g, especially the separation of fractions colored in purple and blue). As the r-GPC chromatograms showed, the fraction *1* and *2* with the ratio of 8/12 were almost unseparated, but those with the ratio of 8/10 and 8/14 could be baseline separated (Figure 3.1.18 e, f, g). Moreover, by comparing the intensity of each

[1] These bigger polymers were collected and measured MS and NMR, but no peak was detected from 4000 to 40000 (m/z), and the NMR spectra also only showed several broad peaks. Therefore, these polymerss could be identified, which are the same for the fowllowing bigger polymers observed on r-GPC chromatogrms.

fraction on the r-GPC chromatograms, it was found that adjusting the ratio of building blocks also changed the relative yield of trimers and dimers. When using more triamine (8:10), the intensity of fraction *2* is bigger than fraction *3* (Figure 3.1.18 f). In contrast, the intensity of fraction *2* is smaller than fraction *3* (8:14) (Figure 3.1.18 g). This indicated that the higher amount of triamine promoted the formation of IOCs with higher catenation degrees, and similar results were also observed in *Chapter 3.3*.

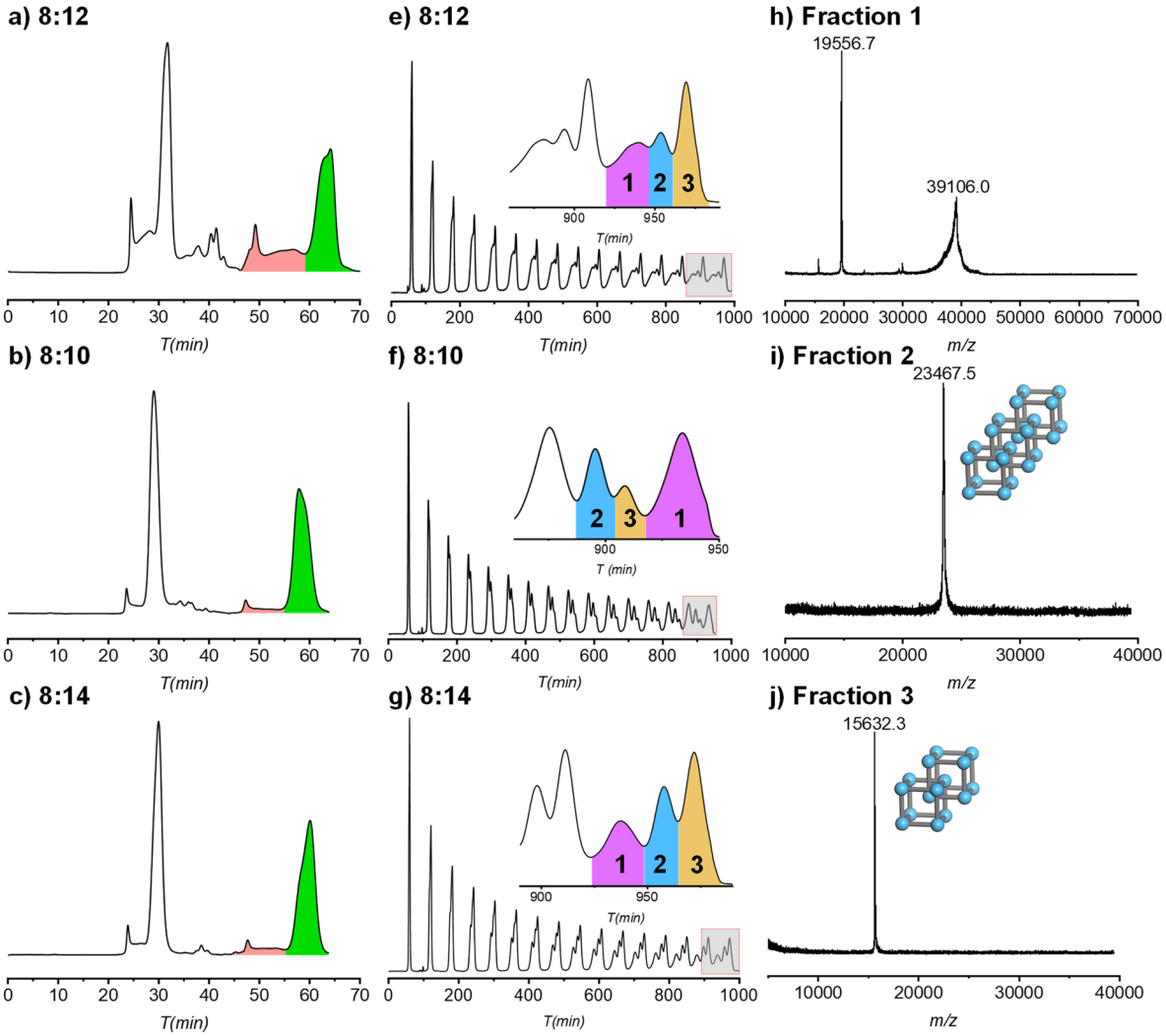

Figure 3.1.18: The r-GPC chromatograms of crude products[1] (THF, 6 mL/min, column: 2×500 Å + 2×1000 Å, 40 °C): a) 8/12; b) 8/10; c) 8/14, the green part was collect and concentrated for the second purification. The r-GPC chromatography of the second purification of green fractions (3 mL/min): e) 8/12; f) 8/10[2]; g) 8/14. MALDI-MS spectrum of each fraction: h) mixture of pentamer and the [20+28] species (m/z=19556.7), these two compounds were not separated[3], colored in purple; i) trimer, colored in blue; j) dimer, colored in yellow.

Overall, by adjusting the ratio of building blocks, the mass spectrum of the collected fraction (Figure 3.1.18 h, i, j) showed that the trimer (m/z = 23467.5) and dimer (m/z = 15632.3)

[1] The concentrations of injected solution were not identified, since the precipitated solid was dissolved in THF for purification without drying.
[2] The first fraction was accidently missed when collecting, so the order was not same as other two.
[3] There may be other unseparated oligomers which was bigger than pentamer (> 40000) and not detected by MS.

were completely separated, which corresponds to the HexTri-[3]Catenane and HexTri-[2]Catenane, respectively (Scheme 3.1.15). Accordingly, the 2D NMR experiments were performed with the purified products.

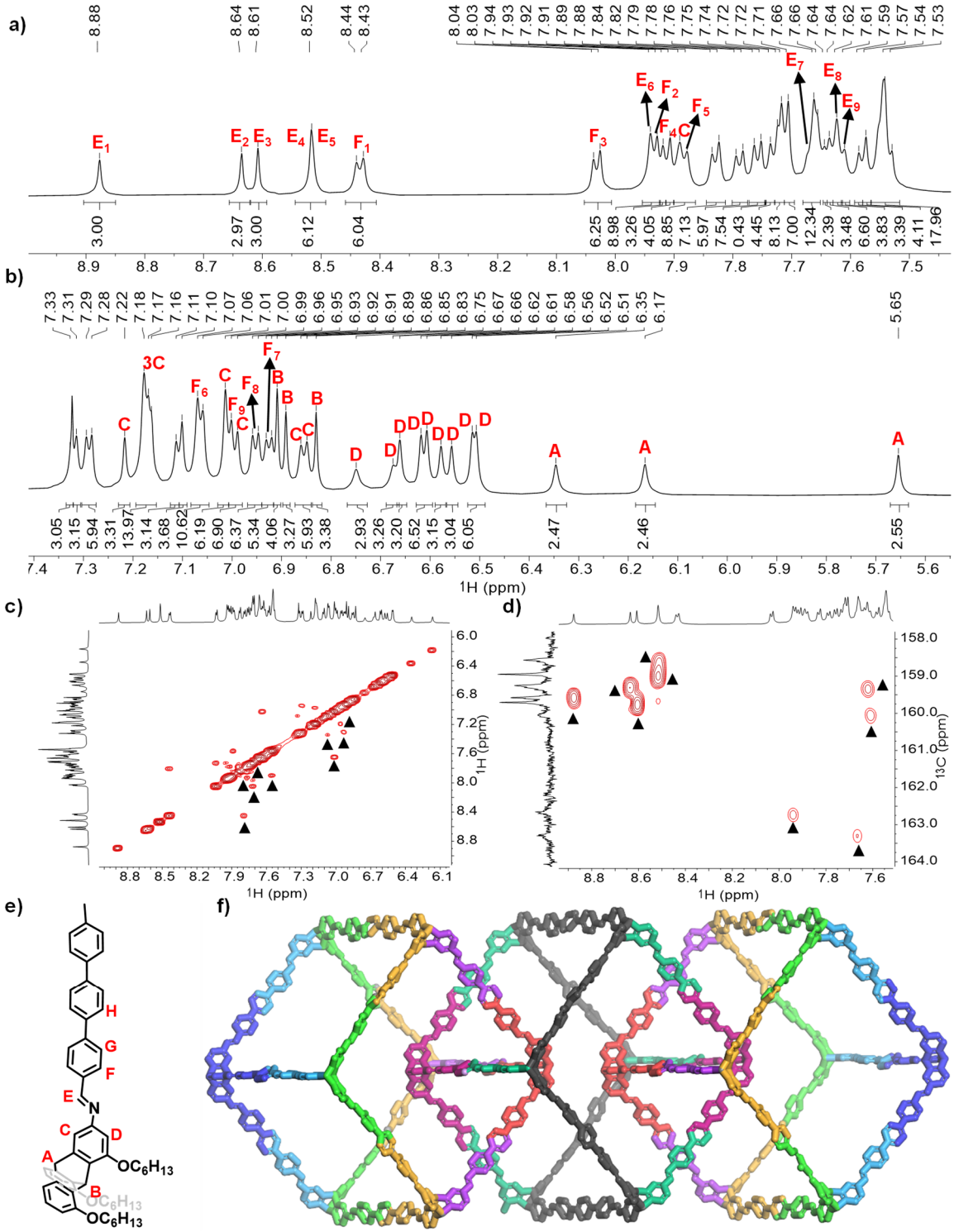

Figure 3.1.19: a), b) Assigned partial ^{1}H-NMR Spectrum (700 MHz) of **HexTri**-[3]Catenane in CD_2Cl_2; c) Partial ^{1}H-^{1}H COSY spectrum showing the neighboring phenyl protons (*F, G; H, I*); d) Partial ^{1}H-^{13}C HSQC spectrum showing the imine protons (*E*); e) Illustration of a repeated unit of **HexTri**-Catenane: f) The model of **HexTri**-[3]Catenane based on NMR studies. the outer chains were cleaved for clarity. Uppercase and lowercase letters mark the position of protons and carbons on the repeated unit, respectively. The number marks the different repeated units. Black triangles mark the nine signals.

The integration and assignment of the ^{1}H NMR spectrum of HexTri-[3]Catenane (Figure 3.1.19 a) were similar to that of HexBi-Catenane. However, the distribution of peaks at the aromatic region is denser due to the numerous aromatic protons (*F, G; H, I*) on the triphenyl dialdehyde **86**. The resolution of the ^{1}H-^{1}H COSY spectrum was not good enough to show all signals of neighboring aromatic protons (Figure 3.1.19 b, *F, G*; *H*). But according to the ^{1}H-^{13}C HSQC spectrum, nine different imine peaks still could be found (*E*), which indicates that the C_3 symmetry of HexTri-[3]Catenane (Figure 3.1.19 f) and its linear triply interlocked conformation.

Similarly, the peaks of bridgehead protons (*A, B*) of HexTri-[3]Catenane also overlap, there should be twelve but only six signals were observed on the ^{1}H-^{13}C HSQC spectrum (Figure 3.1.20 a). Even though, based on the relationship between the triptycene bridgehead carbons and the neighboring aromatic protons (*C, A*), the other two types of protons (*C, D*) on triptycene were assigned (Figure 3.1.21 b).

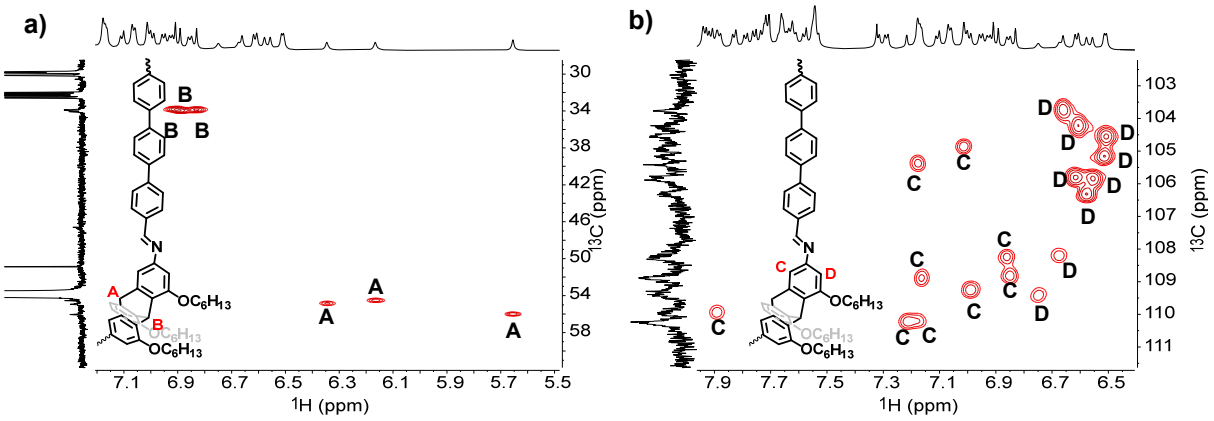

Figure 3.1.20: Partial ^{1}H-^{13}C HSQC (700 MHz, CD_2Cl_2) spectra show the a) bridgehead protons and b) aromatic protons on triptycene. Capital letters mark the position of protons.

In addition, it was found that the ^{1}H NMR spectrum of HexTri-[2]Catenane was not pure and the ^{13}C NMR spectrum also show low intensity (Figure 3.1.24). Therefore, the mass spectroscopy of the collected fraction of HexTri-[2]Catenane after GPC purification and the deuterated solution after NMR measurement was performed. And the mass spectra showed a new [32+48] species (m/z=31325.3) appeared in the deuterated solution (Figure 3.1.23), which means that further catenation or reaction happened during the preparation of the NMR sample. Interestingly, the same phenomenon also found that HexBi-Cage could still interlock into HexBi-Catenane in high concentration (around 2.9 mM) when preparing the sample for r-GPC separation. Such a procedure could happen slowly when storing the dilute THF solution of HexBi-Cage at room temperature for weeks. And the problem also occurred for other dimer catenane based on triphenyl triamine.

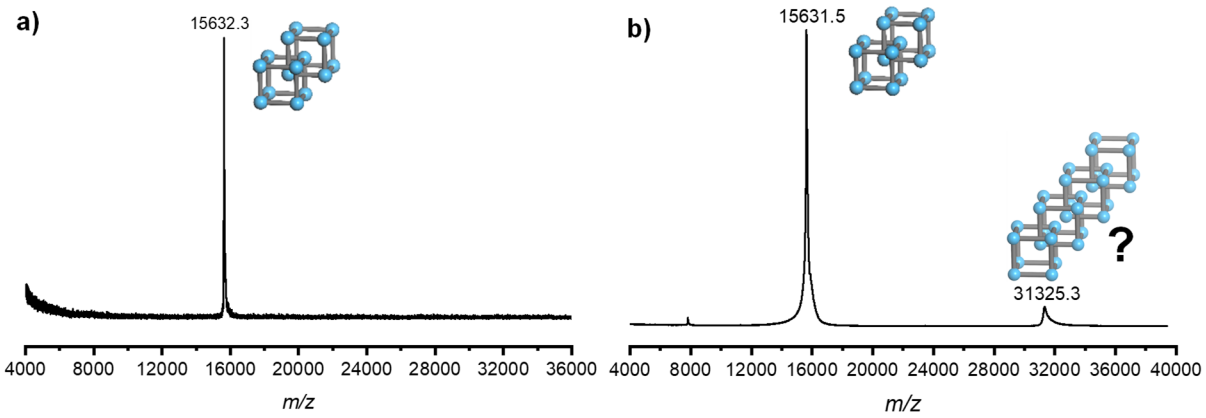

Figure 3.1.21: MALDI mass spectra of the HexTri-[2]Catenane: a) the collected fraction *3* after purification by r-GPC; b) the deuterated solution in CD_2Cl_2 after NMR measurement, tetramer was not identified.

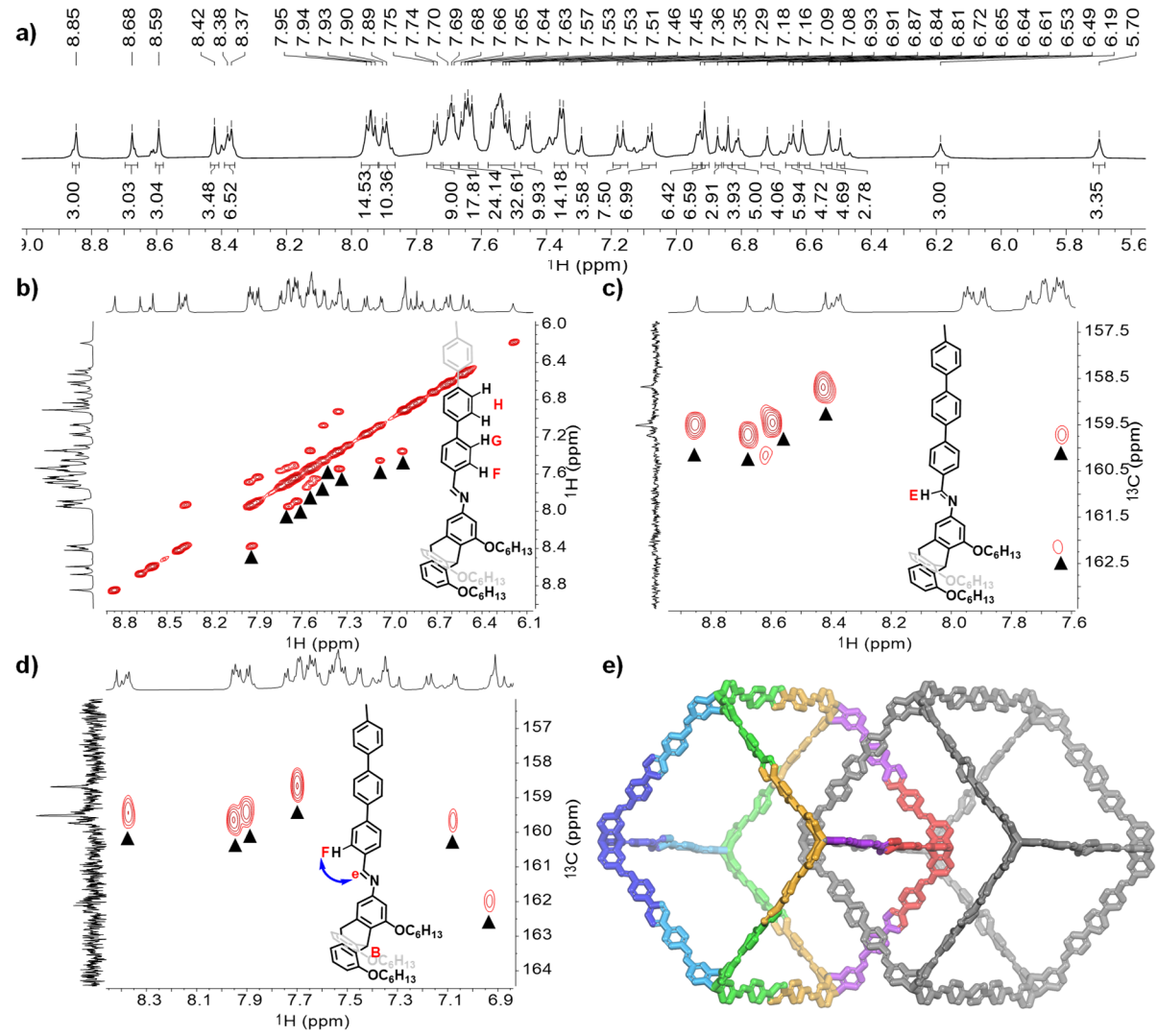

Figure 3.1.22: a) Partial ^{1}H-NMR Spectrum (700 MHz) of **HexTri**-[2]Catenane in CD_2Cl_2; b)Partial ^{1}H-^{1}H COSY spectrum showing the neighboring phenyl protons (*F, G; H*); c) Partial ^{1}H-^{13}C HSQC spectrum showing the imine protons(*E*); d) Partial ^{1}H-^{13}C HMBC spectrum shows the relation between imine carbons and neighboring aromatic protons (*F, e*); e) The model of **HexTri**-[2]Catenane based on NMR studies. the outer chains were cleaved for clarity. Uppercase and lowercase letters mark the position of protons and carbons on the repeated unit, respectively. Black triangles mark the number of signals.

Due to the further transformation, the ^{1}H NMR spectrum of HexTri-[2]Catenane was not pure and the resolution of the ^{13}C NMR spectrum was also low. Even though, nine pairs of neighboring phenyl protons and six different imine protons still could be identified according to the ^{1}H-^{1}H COSY spectrum (Figure 3.1.22 b) and the ^{1}H-^{13}C HSQC spectrum (Figure 3.1.22 c), which was further proved by ^{1}H-^{13}C HMBC spectrum (Figure 3.1.22 d). That all indicate that the HexTri-[2]Catenane also has a triply interlocked structure. Overall, the IOCs still could be formed when using the terphenyl dialdehyde **86**, and two IOCs — HexTri-[3]Catenane and HexTri-[2]Catenane were isolated. Both of them were proved to be triply interlocked according to the 2D NMR experiments, although the resolution of NMR spectra was not sufficient to assign every peak due to their complicated structures (of HexTri-[3]Catenane) or poor stabilities (of HexTri-[2]Catenane).

However, in comparison with the experimental results based on biphenyl dialdehyde **87**, there were still two interesting questions that need to figure out (Figure 3.1.23). First, why no HexTri-Cage or HexBi-[3]Catenane is obtained? As shown above, when using the biphenyl dialdehyde **87**, the products are HexBi-Cage and HexBi-Catenane, and no trimer was detected. In contrast, dimer and trimer were formed based on triphenyl dialdehyde **86**, but no monomeric cage was obtained. Second, why HexBi-Catenane could keep stable in high concentration while the HexTri-[2]Catenane could not? Under similar concentrations (~10 mg in 0.5 mL CD_2Cl_2: HexBi-Catenane, 1.45 mM; HexTri-[2]Catenane, 1.27 mM), HexBi-Catenane stayed pure after NMR measurement but HexTri-[2]Catenane could not.

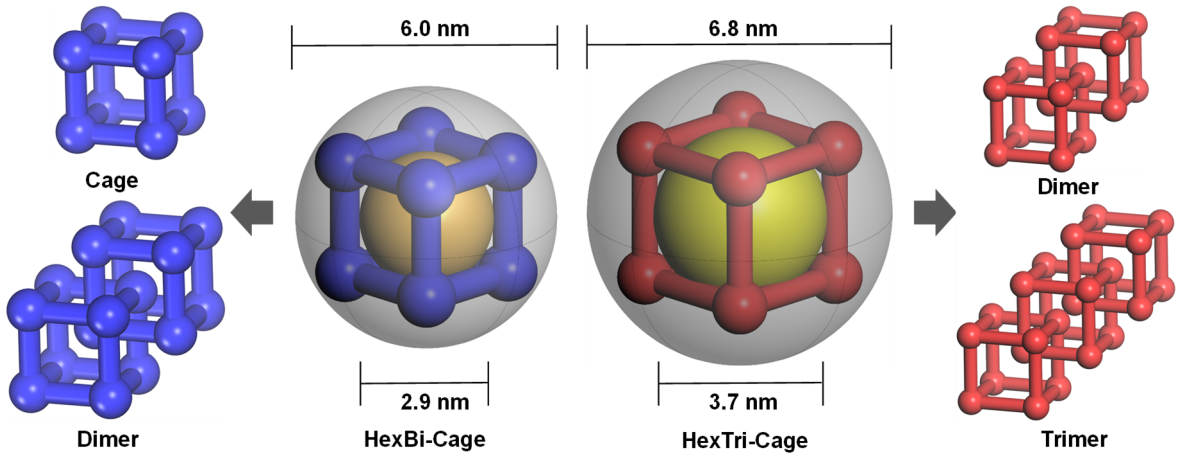

Scheme 3.1.23: Size comparison of the **HexBi**-Cage and **HexTri**-Catenane. Sizes were measured with Materials Studio based on optimized structures (PM6), which are shown in ball and stick models for clarity.

One possible reason is that the size difference between HexTri-Cage and HexBi-Cage leads to different catenation results. When changing the linker from biphenyl dialdehyde **87** to triphenyl dialdehyde **86**, the bigger cavity and windows of the corresponding monomeric cages probably make 'guest' cages or fragments easier to enter the cavity of 'host' cages, thus tend to

form IOCs more. Because no single crystal X-Ray diffraction data was collected, it is not possible to directly compare the conformation of these two catenanes. Therefore, to corroborate the hypothesis, the following experiments were conducted to investigate the influence of cage and cavity size on the catenation tendency.

3.1.5 The Synthesis of DecBi-Cage, DecBi-Catenane, and DecTri-Catenane

According to the triply interlocking conformation, the cavity of the 'host' cage was mainly occupied by the one vertex of the 'guest' cube cage. Because the volume of the cavity (decided by the length of linkers) and size of the cage (decided by the length of the linker and also the outer alkyl chains) both influence the catenation process, to investigate them dependently, the cavity volume was first made the control variable (still using biphenyl dialdehyde **87** as the linker). Then longer alkyl chains (decyl) were introduced to the triptycene triamine for increasing the size of monomeric cages. Therefore, it occupies more space and increases the steric hindrance during the interlocking process, which might suppress the catenation.

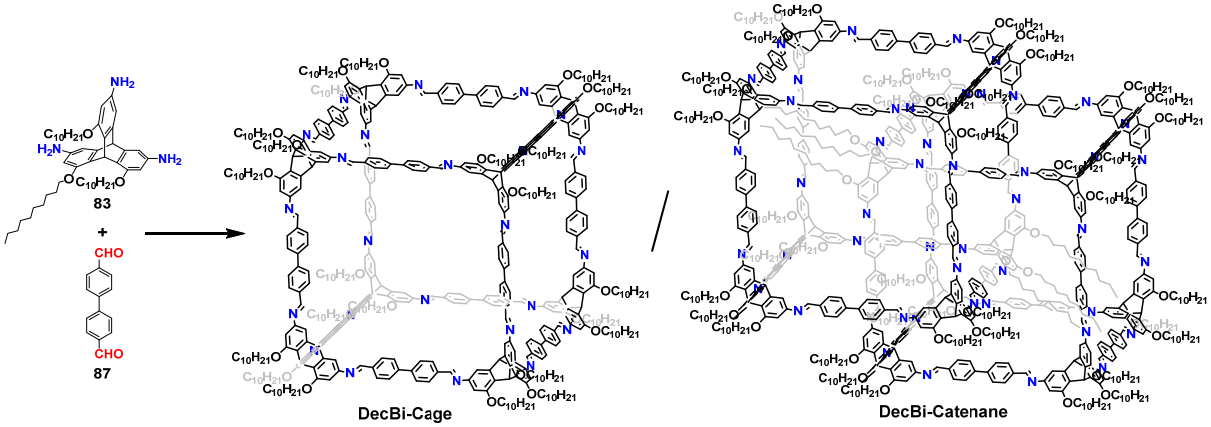

Scheme 3.1.24: Synthesis of **DecBi**-Cage and **DecBi**-Catenane.

Table 3.1.4 Screening conditions for the synthesis of **DecBi**-Cage and **DecBi**-Catenane.

Solvent	Temperature	TFA	Concentration[a]	Products detected by MS monitoring
Chloroform	r.t	4 mol%	5.3 mM	Figure 3.1.4 a (1 d), A (7 d)
Chloroform	60 °C	4 mol%	5.3 mM	Figure 3.1.4 b (1 d), B (7 d)
THF	r.t	4 mol%	5.3 mM	Figure 3.1.4 c (1 d), C (7 d)
THF	70 °C	4 mol%	5.3 mM	Figure 3.1.4 d (1 d), D (7 d)

a. Concentration of triptycene triamine **83**.

According to mass spectroscopy monitoring, it was found that the decyloxy chains indeed slow down the formation of catenane. For the synthesis of HexBi-Cage and HexBi-Catenane, the mass spectra showed intensive peaks of cage and catenane (Figure 3.1.4) with the reaction solution after one day. In contrast, only tiny peaks of [16+24] catenane and several broad peaks of smaller fragments were detected in the mass spectra of DecBi-Cage and Catenane (Figure 3.1.25 a-d). After seven days, the mass spectra showed that the formation of

DecBi-Catenane gradually reached the balance (Figure 3.1.25 A-D). This result supported the hypothesis before, although the triamine **83** with decyloxy chains still led to the formation of catenane. On the one hand, the increased size successfully suppressed the speed of the catenation process. On the other hand, the longer chains are also more flexible, and the steric hindrance between the cages might become stronger but still not enough to prevent the formation of catenane.

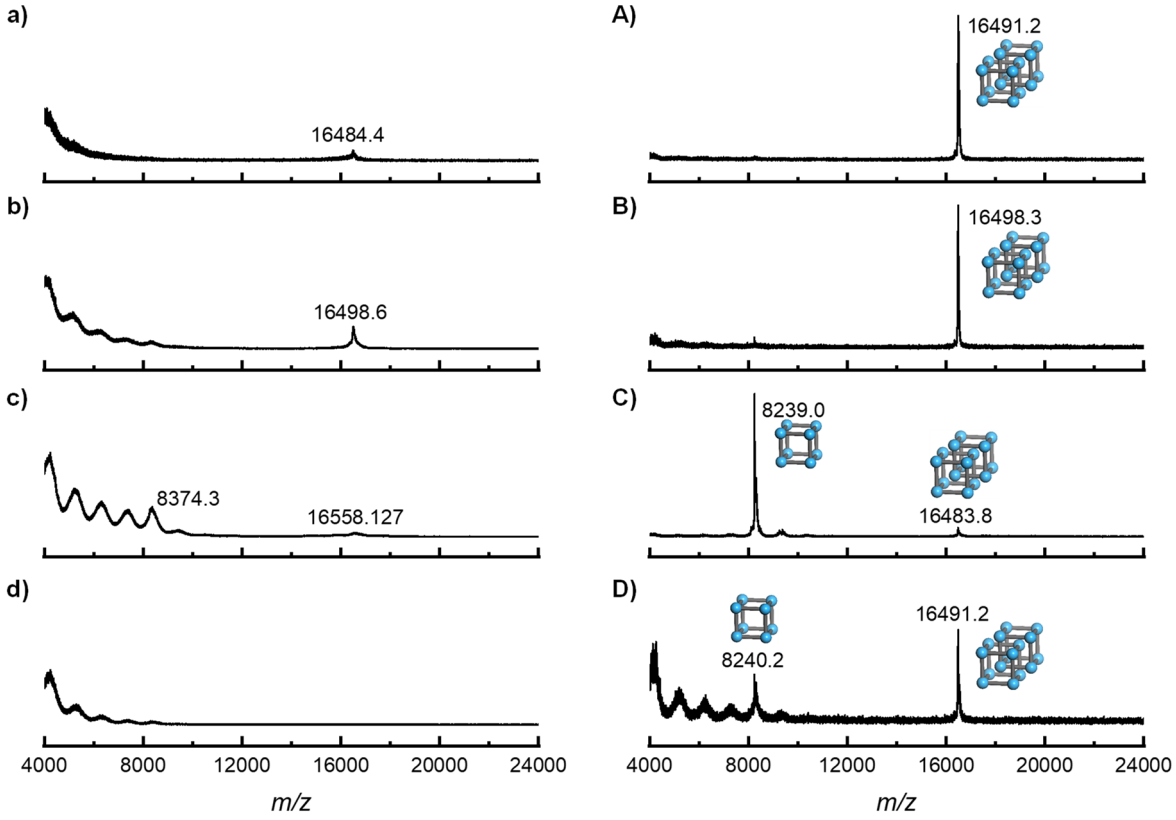

Figure 3.1.25: The MALDI mass spectra of the crude solution under different conditions. The calculated mass is 8229.335.

Similar to the workup procedure of HexBi-Catenane, DecBi-Cage and DecBi-Catenane were purified by r-GPC. As shown by the r-GPC chromatograms of the crude products (Figure 3.1.26 a, b), there were much more oligomers formed (purple fraction) in comparison with that of HexBi-Cage and Catenane. The possible reason is that the decyloxy chains have better solubility than hexyloxy ones, thus increasing the solubility of the corresponding oligomers and making them could not be removed by filtration. Another hypothesis is that the longer chains suppressed the formation of the catenane, and more random oligomers were thus generated.

The pure DecBi-Cage and DecBi-Catenane were obtained and identified by MALDI-TOF MS and the 2D NMR experiments (Appendix), which indicated their triply interlocked conformations.

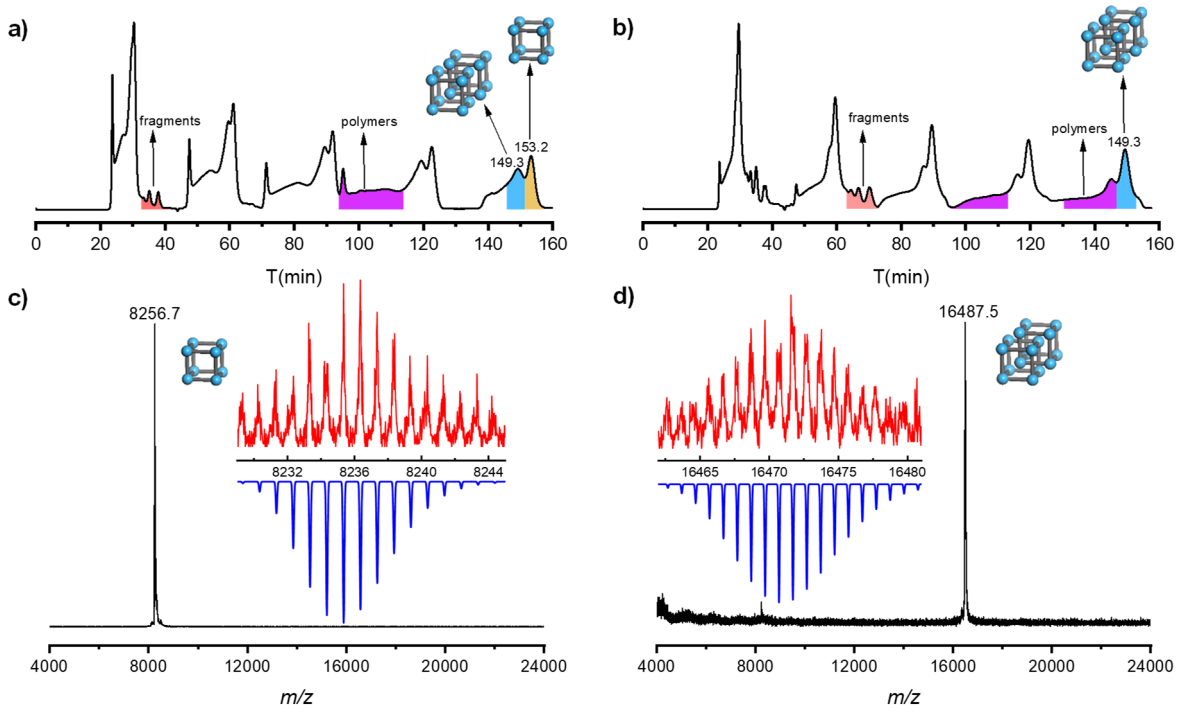

Figure 3.1.26: The r-GPC chromatograms (THF, 6 mL/min, column: 2×500 Å + 2×1000 Å, 40 °C) of the crude products and the corresponding retention time. a) DecBi-Cage (THF, TFA 4 mol%, r.t, 5 days); b) DecBi-Catenane ($CHCl_3$, TFA 4 mol%, 60 °C, 5 days); MALDI-TOF mass spectra and the isotopic patterns (red, measured; blue, calculated) of DecBi-Cage (c), and DecBi-Catenane (d).

In addition, triamine **83** was also used to construct a bigger monomeric cage with triphenyl dialdehyde **86** (Figure 3.1.30a). After the reaction (Table 3.1.5), only the formation of the dimer was detected by mass spectrum (Figure 3.1.20b).

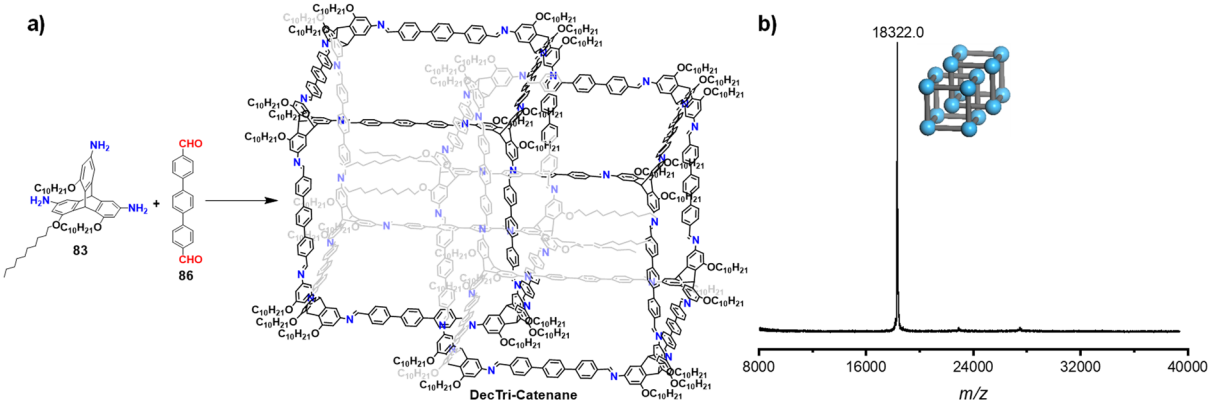

Figure 3.1.27: a) The synthesis of **DecTri**-Catenane; b) The mass spectrum of crude reaction solution ($CHCl_3$, TFA 4 mol%, 60 °C, 7 days). The calculated mass is 18283.422.

Table 3.1.5 Screening of ratios of building blocks for syntheses of **DecTri**-Catenane.

Solvent	**83**/**86**	Temperature	TFA	Concentration[a]	Reaction time	Products detected by MS
$CHCl_3$	8/12	r.t	4 mol%	5.3 mM	5 d	Dimer
$CHCl_3$	8/12	60 °C	4 mol%	5.3 mM	5 d	Dimer
THF	8/12	r.t	4 mol%	5.3 mM	5 d	Dimer
THF	8/12	70 °C	4 mol%	5.3 mM	5 d	Dimer
$CHCl_3$	8/12	60 °C	4 mol%	5.3 mM	5 d	Dimer
$CHCl_3$	8/10	60 °C	4 mol%	5.3 mM	5 d	Dimer

a. Concentration of triptycene triamine **83**.

The obtained crude products of DecTri-Catenane were also purified by r-GPC. Interestingly, in comparison with the GPC chromatograms of HexTri-Catenane (Figure 3.1.28 a, c), no fractions of trimer or pentamer were found in that of DecTri-Catenane. Only the fraction of oligomers (fraction colored in purple, Figure 3.1.20 b, d) and dimers (fraction colored in yellow, Figure 3.1.20 b, d) were collected by r-GPC purification. This is also a piece of evidence proving that the size of monomeric cages indeed influences the catenation results. Because when keeping the cavity volumes the same (all use biphenyl dialdehyde **87** as the linker) and increasing the size of cages (hexyloxy to decyloxy), no trimer and pentamer were observed anymore. Due to the bigger vertex taking more space in the cavity thus less free space is left for other guest cages. Moreover, the 8:10 ratio of building blocks also led to the formation of more oligomers, which was consistent with previous conclusions.

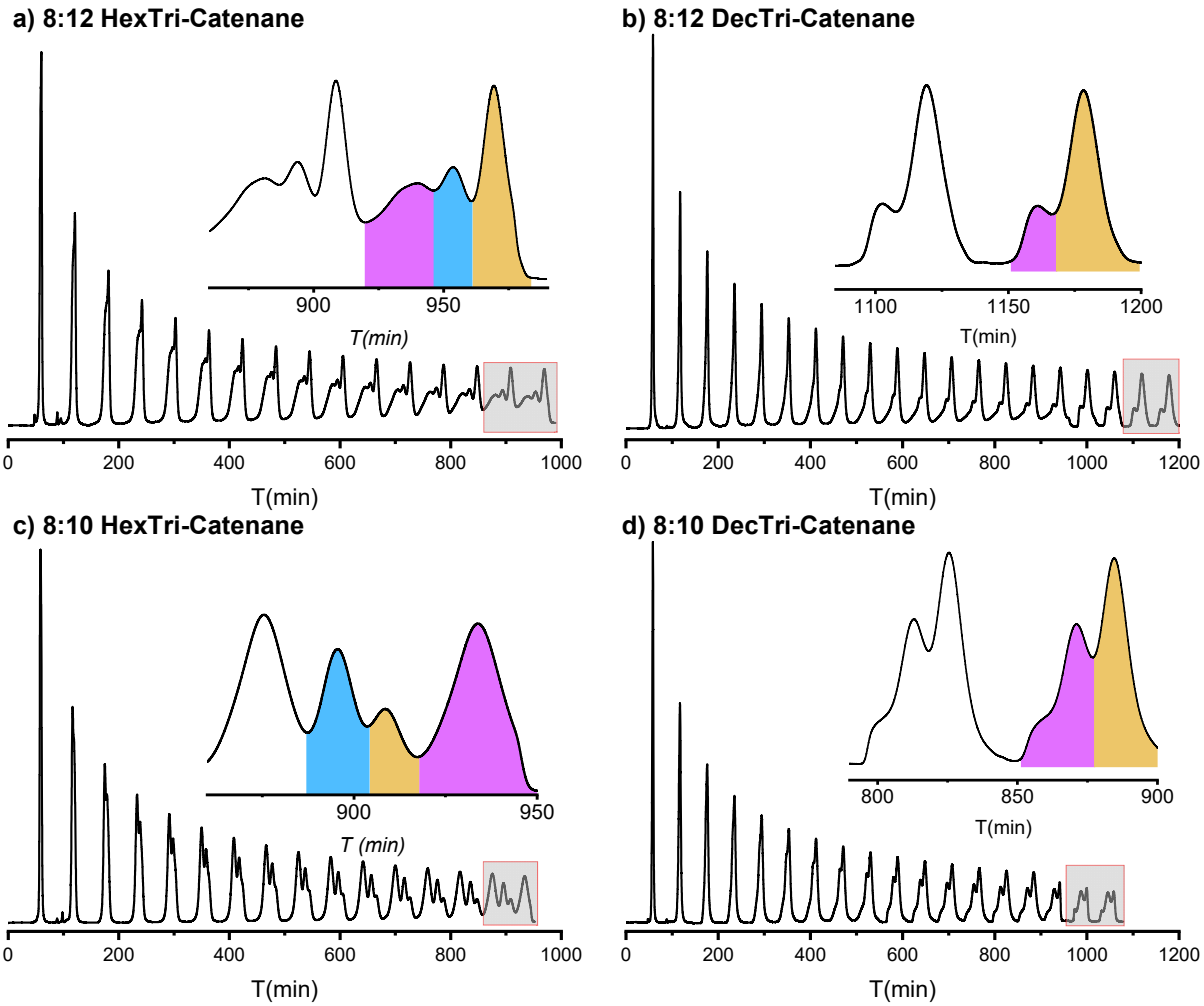

Figure 3.1.28: r-GPC chromatograms of products with different ratios of building blocks (THF, 3 mL/min, column: 2×500 Å + 2×1000 Å, 40 °C): a) 8/12, HexTri-Catenane; b) 8/12, DecTri-Catenane; c) 8/10, HexTri-Catenane; d) 8/10, DecTri-Catenane. Dimer (colored in yellow), oligomer (colored in purple), trimers (colored in blue).

The isolated pure DecTri-Catenane has also been characterized by 2D NMR spectroscopy. However, due to the same problems mentioned before, no intensive ^{13}C NMR

could be obtained, and the ^{1}H NMR is also not pure enough (Appendix). Even though, six different imine peaks could be identified, which showed its triply interlocked structure.

3.1.6 The Synthesis of ProBi-Catenane and ProTri-Catenane

Based on the experimental results above, it was found that the utilization of triamine with longer substituents did suppress the formation of the catenane, especially the trimers which need even more space inside the cage. In addition, there is also an opposite approach to further prove the influence of cage size. That is introducing the shorter chains to triptycene triamine and keeping the length of linkers the same, which will result in a monomeric cage with a smaller size. When the cavity volumes are the same, the smaller monomeric should be tending to interlock more. Therefore, a smaller building block with the propane chains — triptycene triamine **81**, was synthesized and used to construct a monomeric cage (Figure 3.1.29 a) with dialdehyde **87** and **86** under the same conditions as before (Table 3.1.6).

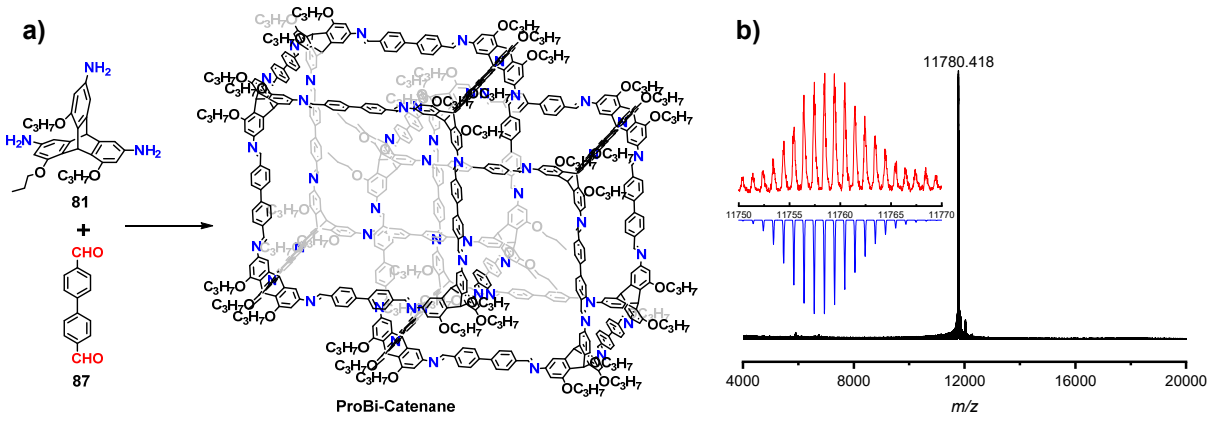

Scheme 3.1.29: a) Synthesis of **ProBi**-Catenane; b) The mass spectrum of crude reaction solution ($CHCl_3$, TFA 4 mol%, 60 °C, 7 days). The calculated mass of the dimer is 11749.412.

Table 3.1.6 Screening conditions for the synthesis of **ProBi**-Catenane.

Solvent	Temperature	TFA	Concentration[a]	Reaction time	Products detected by MS
Chloroform	r.t	4 mol%	5.3 mM	7 d	dimer
Chloroform	60 °C	4 mol%	5.3 mM	7 d	dimer
THF	r.t	4 mol%	5.3 mM	7 d	dimer
THF	70 °C	4 mol%	5.3 mM	7 d	dimer

a. Concentration of triptycene triamine **81**.

With biphenyl dialdehyde **87**, only dimeric catenane was observed after the reaction (Table 3.1.6). In comparison with the experimental results based on the same linker and triamine **82** (hexyloxy), the cavity volumes of the monomeric cages are the same. However, when changing the hexyloxy chains to propoxy chains to decrease the size of the monomeric cage, no single cage was observed by MS anymore. It once more proves that the size of monomeric cages and the volume of their cavity indeed influence the catenation tendency. After

purification by r-GPC, the pure compounds were also identified with MALDI-TOF MS (Figure 3.1.29 b) and 2D NMR experiments (Appendix), which showed that ProBi-Catenane also has a triply interlocked conformation.

Furthermore, triamine **81** was also used with triphenyl dialdehyde **86** to build a monomeric cage with an even bigger cavity (Figure 3.1.30 a). And after the reaction, no single cages were observed in the MS spectrum, however, dimer, trimer, and even pentamer were detected (Figure 3.1.31b).

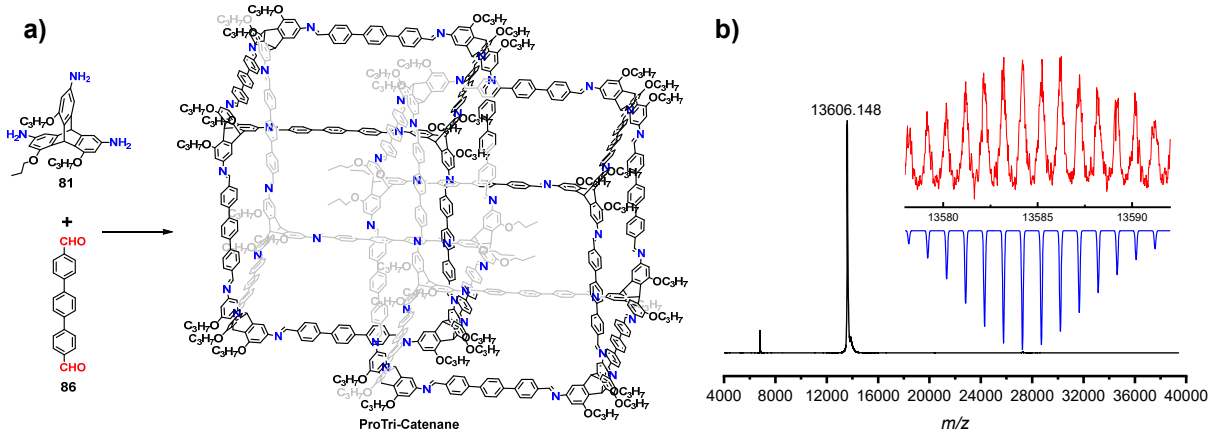

Scheme 3.1.30: a) Synthesis of **ProTri**-Catenane; b) The mass spectrum of crude reaction solution ($CHCl_3$, TFA 4 mol%, 60 °C, 7 days). The calculated mass of the dimer is 13585.072.

Table 3.1.6 Screening conditions for the synthesis of **ProTri**-Catenane.

Solvent	Temperature	TFA	Concentration[a]	Reaction time	Products detected by MS
Chloroform	r.t	4 mol%	5.3 mM	7 d	Figure 3.1.31 a
Chloroform	60 °C	4 mol%	5.3 mM	7 d	Figure 3.1.31 b
THF	r.t	4 mol%	5.3 mM	7 d	Figure 3.1.31 c
THF	70 °C	4 mol%	5.3 mM	7 d	Figure 3.1.31 d

a. Concentration of triptycene triamine **81**.

In addition, for the synthesis of ProTri-Catenane, more precipitates formed after the reaction in comparison with HexTri-Catenane and DecTri-Catenane. On the one hand, the solubility of propoxy chains is not good as hexyloxy or decyloxy chains, which also leads to poorer solubility of monomeric cages, catenane, and by-products; On the other hand, the super bigger cavity and small geometry size make the monomeric cage easily to interlocked and from bigger oligomers or even polymers. Anyway, after removing all the insoluble precipitates, the crude products were purified by r-GPC. Similar to HexTri-Catenanes, three fractions were found on the GPC chromatography, which corresponds to the mixture of pentamer and oligomer, trimer, and dimer, respectively (Figure 3.1.32 a). The fractions of ProTri-[2]Catenane and ProTri-[3]Catenane were collected and characterized by 2D NMR experiments. Similarly, no sufficient NMR data of ProTri-[2]Catenane and ProTri-[3]Catenane could be collected since further reaction happens during preparing the NMR samples. Unfortunately, ProTri-

[2]Catenane could form bigger stuff even in diluted solution for proton NMR measurement, which showed some impurity around the baseline (Figure 3.1.32 c).

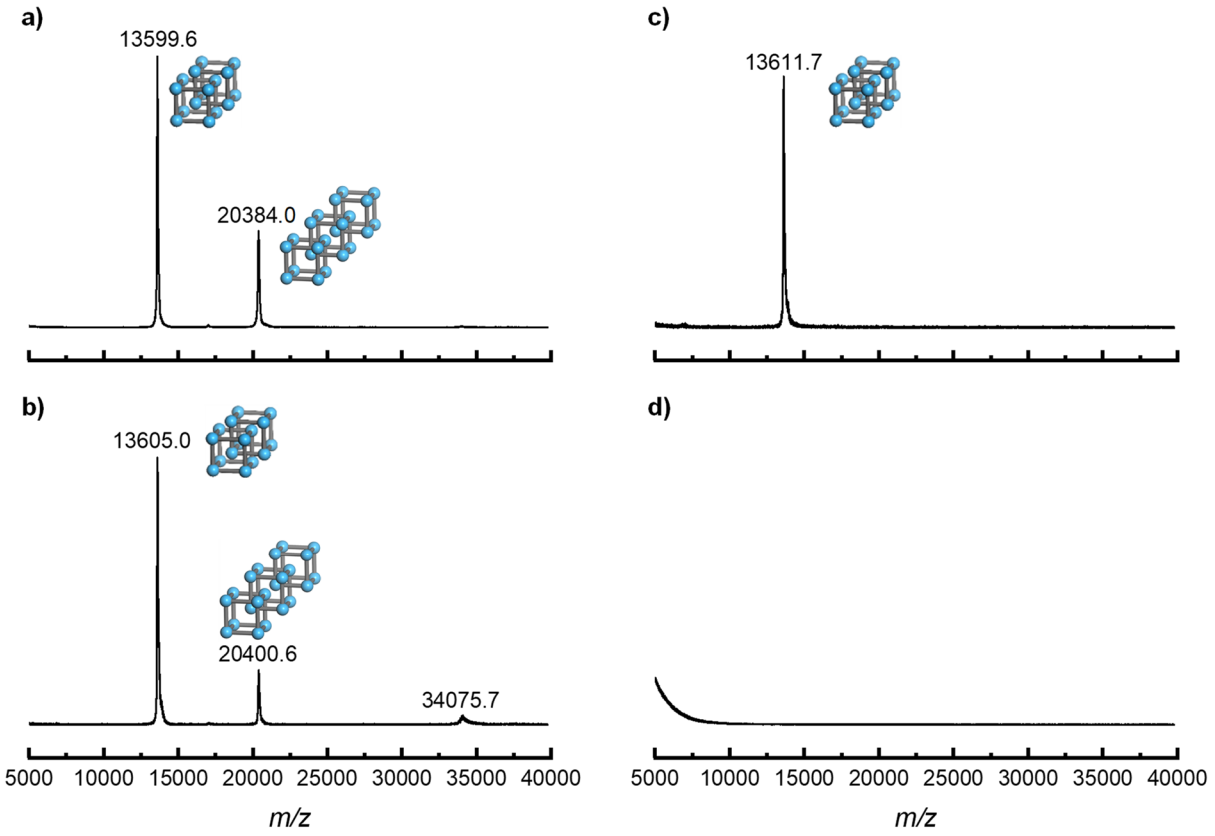

Figure 3.1.31: The MALDI mass spectra of **ProTri**-Catenane (the crude solution at different conditions): a) after 1 day; b) after 7 days. The calculated mass of the dimer is 13585.072.

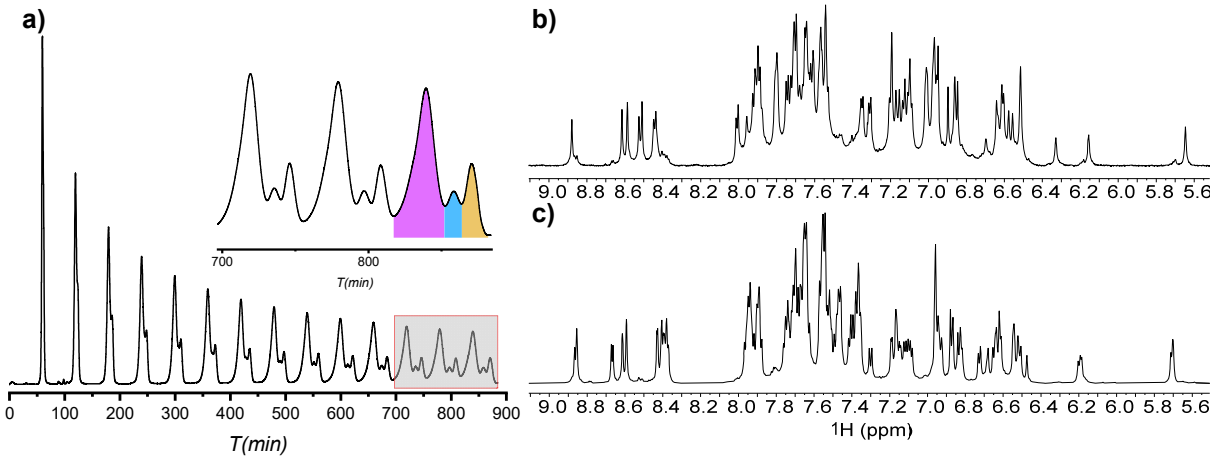

Figure 3.1.32: a) The r-GPC chromatogram (THF, 3 mL/min, column: 2×500 Å + 2×1000 Å, 40 °C) of the second injection of ProTri-Catenane ($CHCl_3$, TFA 4 mol%, 60 °C, 7 days); b) ^{1}H NMR of the trimer (fraction colored in blue); c) ^{1}H NMR of the dimer (fraction colored in yellow).

Overall, by designing and conducting the proof experiments in two opposite directions (keep cavity volume the same, change the size of the cage; keep the size the same, change the cavity volume), all the results showed that a monomeric cage with a bigger cavity volume or smaller size is more tending to catenation.

3.1.7 Geometry Optimization and Size Calculation

Besides conducting the experiments, the size of each monomeric cage was also calculated. Considering the triply interlocked way, the geometry radius and the cavity diameter were mainly discussed here, because these two parameters can represent the relative position of each monomeric cage when interlocking (Figure 3.1.37).

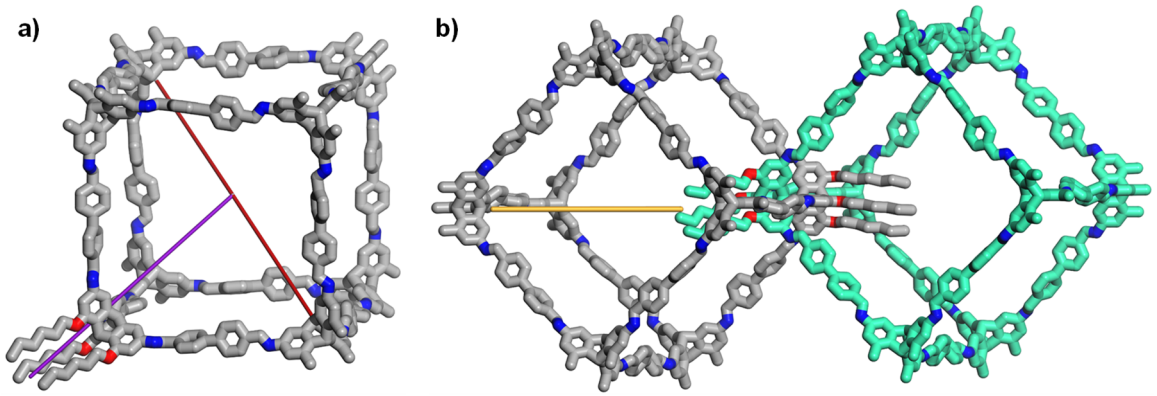

Figure 3.1.33: a) Illustration of the geometry radius (purple line) and the cavity diameter (red line), the cross point is the geometry center; b) The illustration of the free space diameter (yellow line), tightly interlocked conformation. All illustrations are based on **HexBi**-Cage.

$$\textit{Free Distance} = \frac{3}{2}\,\textit{Cavity Diameter} - \textit{Cage Radius}$$

Table 3.1.2 The calculated cavity diameter, geometric radius, and free distance of monomeric cages.

Monomeric cages	Cavity Diameter (Å)	Geometric Radius (Å)	Free Distance(Å)
HexBi-Cage	29.0	30.0	13.5
HexTri-Cage	37.0	34.0	21.5
DecBi-Cage	29.0	35.0	8.5
DecTri-Cage	37.0	39.0	16.5
ProBi-Cage	29.0	26.0	17.5
ProTri-Cage	37.0	30.0	25.5

Geometry radii were calculated with *Multiwfn*,[74] which is equal to the distances between the geometry center and the furthest hydrogen atom adding the radius of hydrogen atoms (1.2 Å). The cavity diameter was roughly measured by *Materials Studio 2020*, then subtracting the radius of two hydrogen atoms. All the monomeric cage structures were optimized by *Gaussian 16* (PM6) in advance. Considering their triply interlocked conformations and the steric hindrance, the free space could be defined as equal to the free distance between monomeric cages, which is the three-half of cavity diameter minus cage radius. The free distance is bigger, and there is more free space inside, which means the monomeric cages are easier to catenane. After arranging the free distance of the catenane structure in order (Figure 3.1.34), the relationship between the experiment results and the calculated free distance is exactly fitting to the hypothesis before: when the monomeric cage has a bigger cavity volume or relatively smaller size, it is more tending to be self-interlocked.

As shown above, when the free distance is 8.5 or 13.5 Å, single cages could be obtained. Since it increased to 16.5 Å, there was no monomeric left anymore after the reaction and all of them interlocked into catenane. And when the free distance came to 21.5 Å, the formation of trimers and pentamers could be observed, which means the free space has ready enough to hold more than one cage.

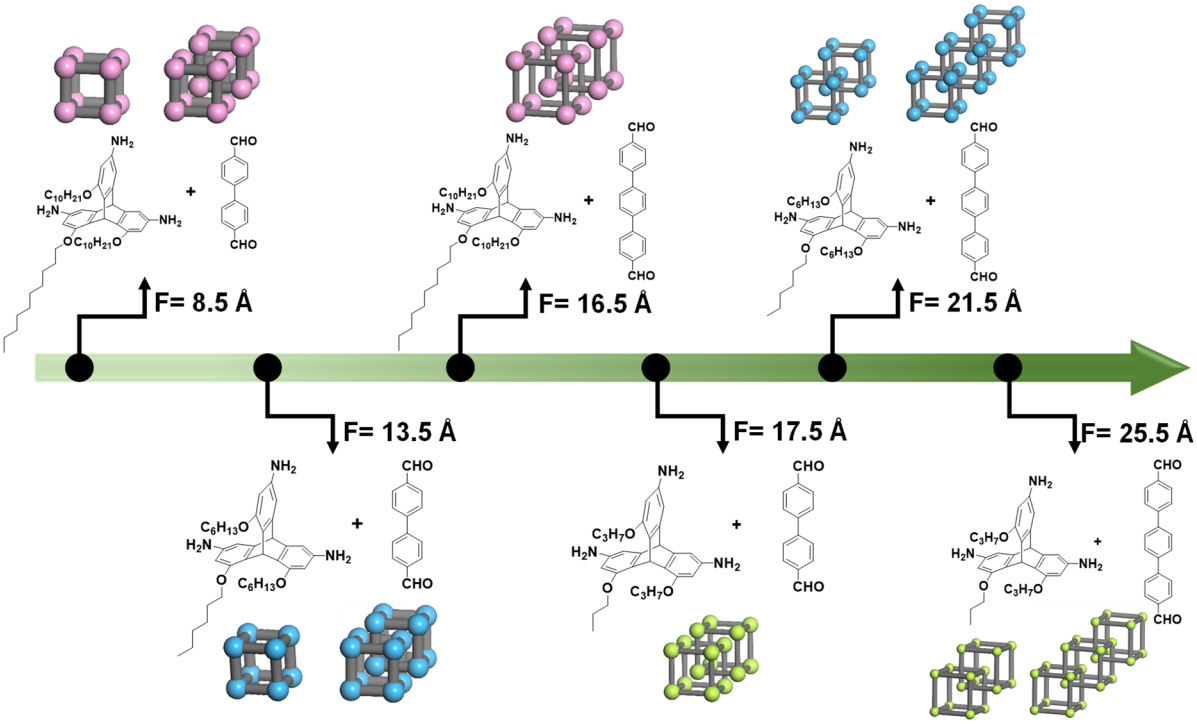

Figure 3.1.34: Sort by free distance from smallest to largest, followed by the building blocks and the corresponding products, which are illustrated by the stick-ball model: Hex-Catenane (blue); Dec-Catenane (purple); Pro-Catenane (green).

However, when it started to form the trimers, the reaction becomes a thermally controlled process, which means the catenation can happen continuously and generate the polycatenanes finally. These insoluble precipitates observed may be polycatenanes, but no sufficient method available to characterize and identify them yet. More investigation of polycatenane will be discussed in *Chapter 3.3*. Moreover, except for the influence of size, the formation of the interlocked cage is also influenced by other factors like the solvents, and interactions simultaneously. In this chapter, the investigations focus on the effects of the size of monomeric cages on the catenation tendency, and it is required to control the other conditions and keep them the same as possible. For example, when changing the length of alkyl chains, the solubility was also changed. But most experiments above were performed in chloroform and THF, in which all the monomers and products have good solubility. Then the solubility influence was limited to a narrow area. It is also the same for the interaction because the cube imine cages base on triptycene triamine, biphenyl, and triphenyl aldehyde could interlock into

catenane, and that is the prerequisite for this investigation. Of course, the studies of other effects, for example, solvents and structures influence, will be shown in *Chapter 3.2*.

3.1.8 Conclusion

To summarize, six monomeric cages with different cavity volumes and sizes were designed, and two [8+12] imine cube cages, six dimeric, and two trimeric IOCs were obtained eventually. All of them have good solubility and have been fully characterized except for the ^{13}C NMR spectra. To the best of our knowledge, the DecTri-Catenane is also the biggest ICCs reported. Moreover, the relationship between the size of the monomeric cage and the tendency to catenation was explored. It was found that when the monomeric cage has a bigger cavity volume and relatively smaller size, it is more tending to self-interlock into catenane. When the cavity is big enough, the formation of trimeric and pentameric interlocked cages was observed, which further indicates the importance of the size of monomeric cages on the catenation process. This is also the first systematic investigation into the influence of cavity and monomeric cage size on catenation tendency, which gives a new study perspective on the catenation mechanism.

3.2 The Investigation of Structural Effects on Catenation

3.2.1 Introduction

The identification of the driving force for catenation is significantly important during the investigation of the catenation mechanism. According to the reported studies,[3, 10, 25, 59] driving forces generally originate from the interactions between the structure of monomeric cages, especially for those syntheses without an auxiliary template species. In the investigations of IOCs, π-π interactions between the aromatic structures were frequently found to be the driving force for catenation.[3, 10b, 20] In previous work, a series of IOCs based on substituted triptycene triamines and linear dialdehydes were obtained, however, it is not clear what the driving force is and how it works in the construction of these IOCs. Since the backbone of the cubic monomeric cages only consists of aromatic rings, the first hypothesis was that the formation of these catenanes was driven by the π-π interaction between their aromatic edges. To prove this hypothesis, the following investigations were performed.

3.2.2 The Synthesis of HexPh-Cage and ProPh-Cage

Based on previous results, 1,4-phthalaldehyde **27** and triamine **82** were used to construct the monomeric cage (Figure 3.2.1a). Different solvents, concentrations of catalyst, and temperatures were also screened (Table 3.2.1). However, no catenane but [8+12] cage was observed on the mass spectra of the crude solutions.

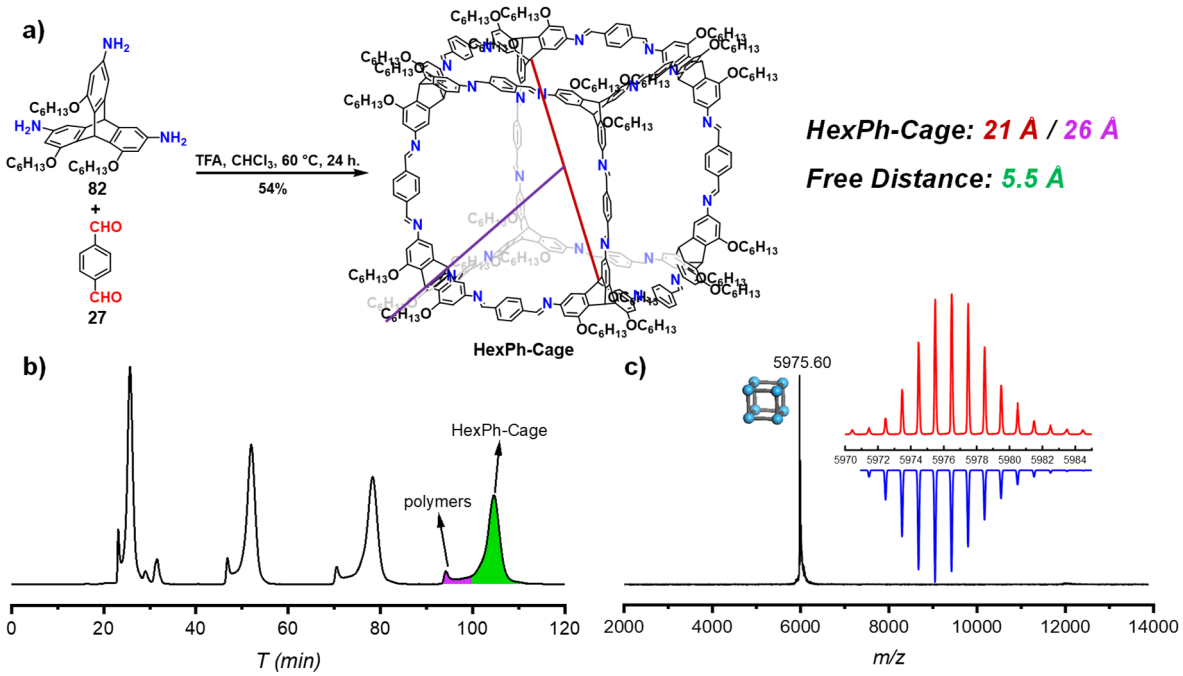

Figure 3.2.1: a) Synthesis of **HexPh**-Cage; b) r-GPC chromatogram (THF, 5 mL/min, 40 °C, 3×100 Å columns) of the crude product, unidentified polymers (colored in purple), the collected **HexPh**-Cage (colored in green); c) MALDI-TOF mass spectrum and the isotopic pattern (red, measured; blue, calculated) of **HexPh**-Cage.

Table 3.2.1 Screening conditions for the synthesis of **HexPh**-Cage.

Solvent	Temperature	TFA	Conc.[a]	Reaction time	Products detected by MS
$CHCl_3$	r.t	4 mol%	5.3 mM	7 d	Cage
$CHCl_3$	60 °C	4 mol%	5.3 mM	7 d	Cage
THF	r.t	4 mol%	5.3 mM	7 d	Cage
THF	70 °C	4 mol%	5.3 mM	7 d	Cage
$CHCl_3$	60 °C	8 mol%	5.3 mM	3 d	Cage
$CHCl_3$	60 °C	12 mol%	5.3 mM	3 d	Cage
THF	70 °C	8 mol%	5.3 mM	3 d	Cage
THF	70 °C	12 mol%	5.3 mM	3 d	Cage

a. Concentration of triptycene triamine **82**.

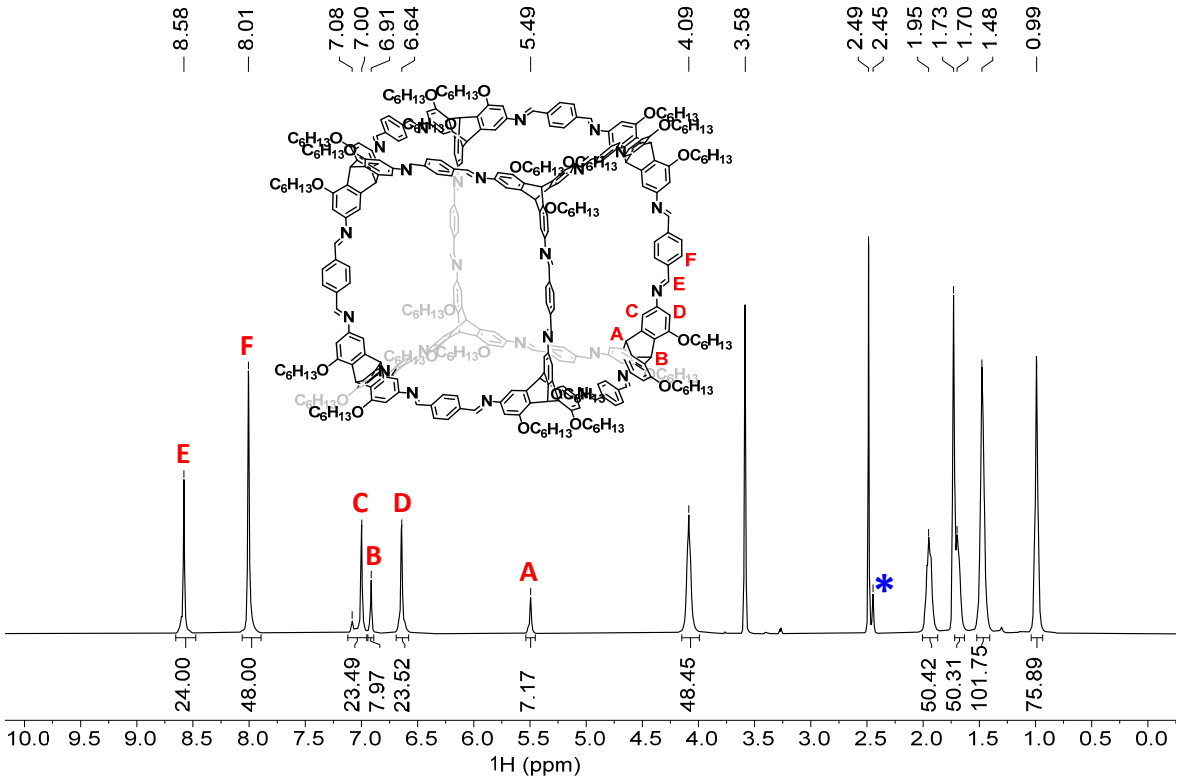

Figure 3.2.2: ^{1}H-NMR Spectrum (700 MHz) of **HexPh**-Catenane in THF-d_8, * marks the water peak.

HexPh-Cage was purified by r-GPC (Figure 3.2.1b), and further identified by MALDI-TOF MS (Figure 3.2.1c) as well as 2D NMR experiments (Figure 3.2.2). By comparing biphenyl dialdehyde **87**, terphenyl dialdehyde **86**, and 1,4-phthalaldehyde **27**, it was found that there are two main differences (Figure 3.2.3): the length of linkers, which leads to different cavity sizes; the number of aromatic rings, which may influence how the interaction happens. Therefore, the first possible reason why no interlocked species formed is that the cavity volume of HexPh-Cage is too small compared with its size. Based on the conclusion in *Chapter 3.1* the calculated cavity diameter, cage

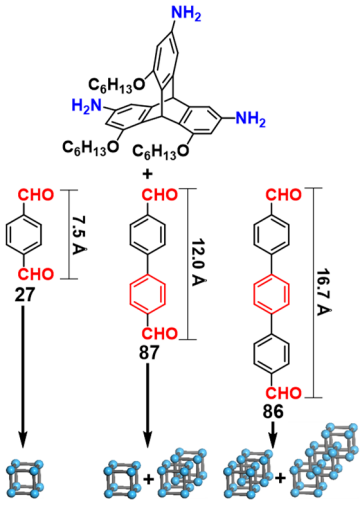

Figure 3.2.3: Summary of the results based on different linkers.

radius, and free distance of HexPh-Cage are 21 Å, 26 Å, and 5.5 Å, respectively. The free distance is smaller than 8.5 Å of DecBi-Cage, and it is the smallest among those explored before. Therefore it was also not clear if a free distance of 5.5 Å is enough for the catenation.

Since DecBi-Cage could interlock into the corresponding catenane, to further demonstrate if the influence of size prevails over the structural effects, triptycene triamine **81** and 1,4-Phthalaldehyde **27** were employed to construct the monomeric ProPh-Cage (Figure 3.2.4 a), whose free distance was calculated to be 9.5 Å (cavity diameter: 21 Å; cage radius: 22 Å). This value has already been bigger than DecBi-Cage's. Therefore, it should form interlocked cages when DecBi-Cage could. Otherwise, the reason why no catenane was formed with HexPh-Cage or ProPh-Cage is not the influence of size but the structural effects (the different number of aromatic rings).

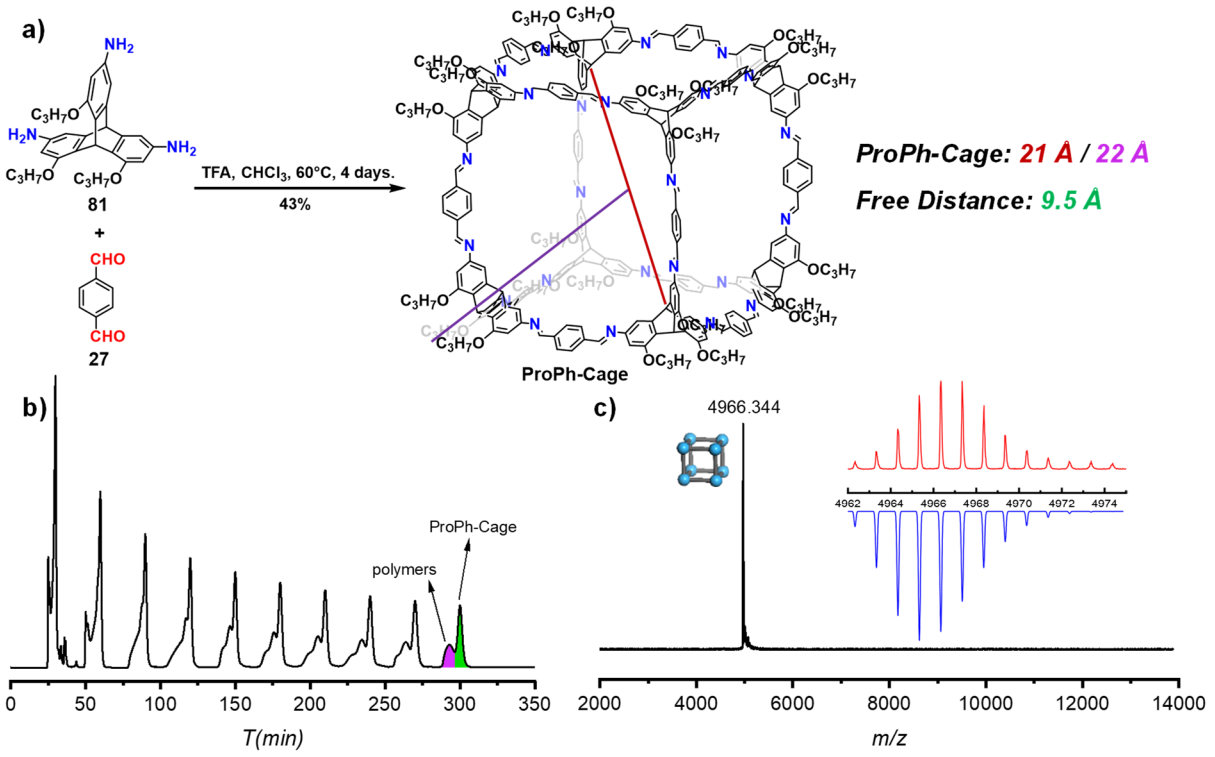

Figure 3.2.4: a) Synthesis of **ProPh**-Cage; b) r-GPC chromatogram (THF, 5 mL/min, 40 °C, 3×100 Å columns) of the crude products, unidentified polymers (purple), the collected fraction (green); c) MALDI-TOF mass spectra and the isotopic pattern (red, measured; blue, calculated) of **ProPh**-Cage.

However, under the same conditions (Table 3.2.1), only the formation of monomeric cages was observed after the reaction, which was separated by r-GPC (Figure 3.2.4 b). The ProPh-Cage was identified with MALDI-TOF MS (Figure 3.2.4 c) and 2D NMR experiments (Appendix). Interestingly, for the crude products under the same conditions, the r-GPC chromatogram showed that much more polymers were generated (Figure 3.2.4 b, fraction colored in purple) in comparison with that of HexPh-Cage (Figure 3.2.1 b, fraction colored in purple). However, no catenane was detected in these separated polymers. That means the

relatively smaller size of the building blocks probably provides more possibilities to generate the bigger polymers. It also proved that the factors influencing the formation of the interlocked cages are not the size but the difference of aromatic units between the 1,4-phthalaldehyde **27**, biphenyl dialdehyde **87**, and terphenyl dialdehyde **86**. Two and three phenyl rings could lead to the catenane but one phenyl ring could not, which indicates that the second aromatic ring is crucial to the formation of IOCs. Therefore, the following experiments were conducted to further explore the structure-depended catenation.

3.2.3 The Synthesis of HexEth-Cage and HexPy-Cage

1,2-bis(4-formylphenyl)ethyne **90** is a liner and rigid linker, which was often employed to construct cages and COFs. Compared with terphenyl dialdehyde **86**, ethyne dialdehyde **90** has a triple bond instead of a phenyl ring in the middle position, thus leading to different aromatic properties of the monomeric cages. Herein, ethyne dialdehyde **90** was synthesized according to the literature[75] and used to construct HexEth-Cage with triptycene triamine **82** (Scheme 3.2.5). The cage radius, cavity diameter, and free distance of HexEth-Cage are 33 Å, 35 Å, and 19.5 Å, respectively. In principle, there should be no size limitation to the catenation. The synthesis of HexEth-cage was conducted under the same conditions, for example in $CHCl_3$ and THF, which worked well for previous catenane synthesis (Table 3.2.2). However, no catenane and also no cage was observed.

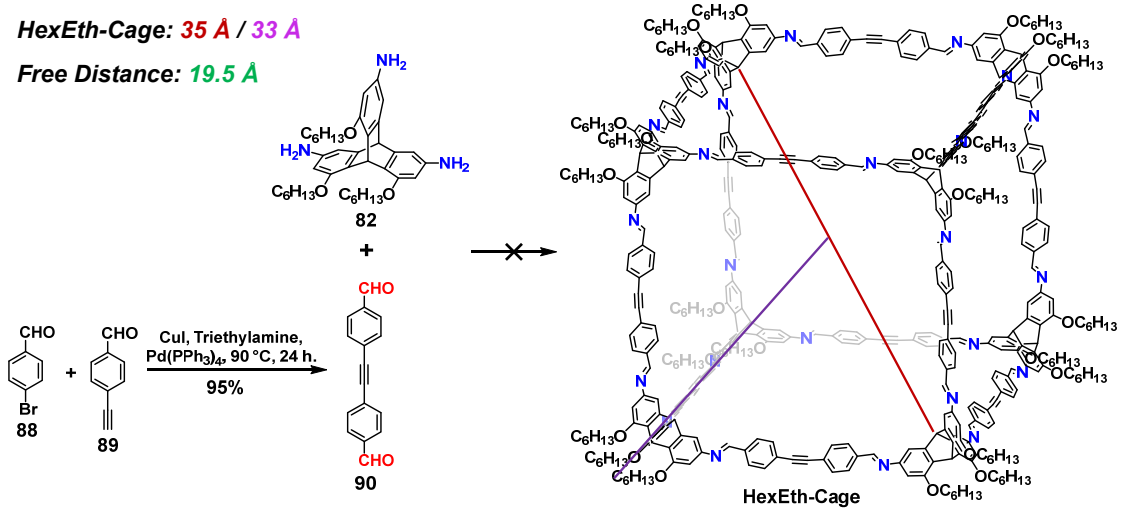

Scheme 3.2.5: The synthesis scheme of 1,2-bis(4-formylphenyl)ethyne **90** and **HexEth**-Cage.

It is worth mentioning that there was no precipitate observed in $CHCl_3$ and THF after the reaction, which indicated that not many polymers have been formed. However, there was also no formation of monomeric cages observed in the mass spectrum. Similar results have already been observed in the synthesis of HexBi-Catenane when using DMF as solvent (solvent effects will be further discussed in *Chapter 3.3*). More solvents such as ethanol, acetone,

toluene, DMF, and1,2-dichlorobenzene were further screened (Table 3.2.2), but no cage or catenane was observed in the reaction solution with any of them.

Table 3.2.2 Screening conditions for the synthesis of **HexEth**-Cage.

Solvent	Temperature	TFA	Concentration.[a]	Reaction time	Products detected by MS
$CHCl_3$	r.t	4 mol%	5.3 mM	7 d	no cage and no catenane
$CHCl_3$	60 °C	4 mol%	5.3 mM	7 d	no cage and no catenane
THF	r.t	4 mol%	5.3 mM	7 d	no cage and no catenane
THF	70 °C	4 mol%	5.3 mM	7 d	no cage and no catenane
ethanol	r.t	4 mol%	5.3 mM	7 d	no cage and no catenane
acetone	r.t	4 mol%	5.3 mM	7 d	no cage and no catenane
toluene	r.t	4 mol%	5.3 mM	7 d	no cage and no catenane
DMF	r.t	4 mol%	5.3 mM	7 d	no cage and no catenane
1,2-dichlorobenzene	r.t	8 mol%	5.3 mM	7 d	no cage and no catenane

a. Concentration of triptycene triamine **82**.

So, two possible factors influenced the formation of HexEth-Cage: the structure and solvent effects. Before finding a suitable solvent for HexEth-Cage synthesis, it is difficult to figure out which one is the dominant factor. Therefore, to make the results more comparable, 2,2'-bipyridine-5,5'-dicarbaldehyde **93** was synthesized (Figure 3.2.6) according to the literature.[76] In comparison with biphenyl dialdehyde **87**, dialdehyde **93** has the same length and similar solubility in $CHCl_3$ and THF. The difference between them is the aromatic properties and the torsion between the two aromatic rings, which could be seen from their electron density maps (Figure 3.2.7).

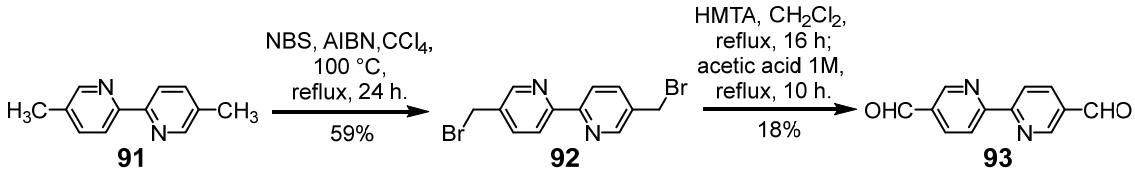

Figure 3.2.6: The synthesis scheme of 2,2'-Bipyridine-5,5'-dicarbaldehyde **93**.[76]

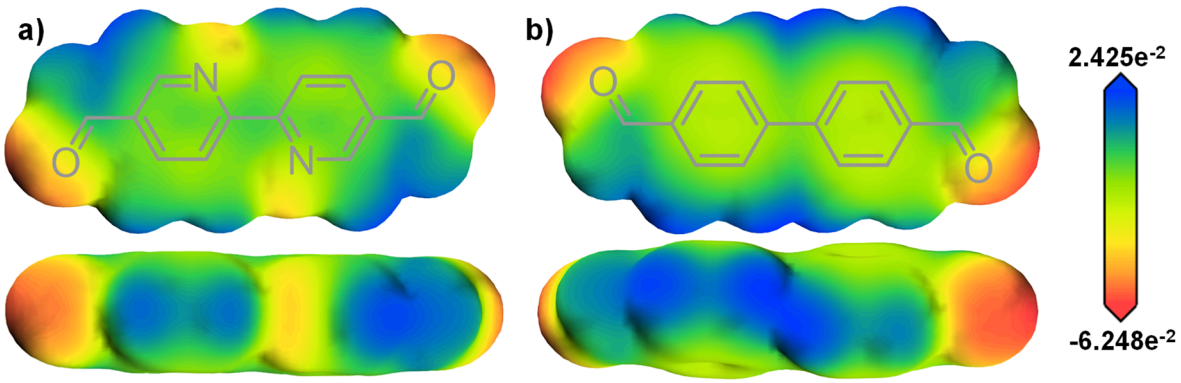

Figure 3.2.7: Electron density map top view (above) and side view (bottom) of a) 2,2'-Bipyridine-5,5'-dicarbaldehyde **93**; b) 4,4'-Biphenyldicarboxaldehyde **87**. Calculated by *Materials Studio 2020* (Dmol3).

Bipyridine dialdehyde **93** and triptycene triamine **82** were utilized to build the monomeric HexPy-Cage (Figure 3.2.8 a). HexPy-Cage has the same cavity volume and size as

HexBi-Cage. However, under the same reaction conditions, only the formation of HexPy-Cage was observed. In contrast, HexBi-Cage and HexBi-Catenane were both detected in previous experiments (*Chapter 3.1*).

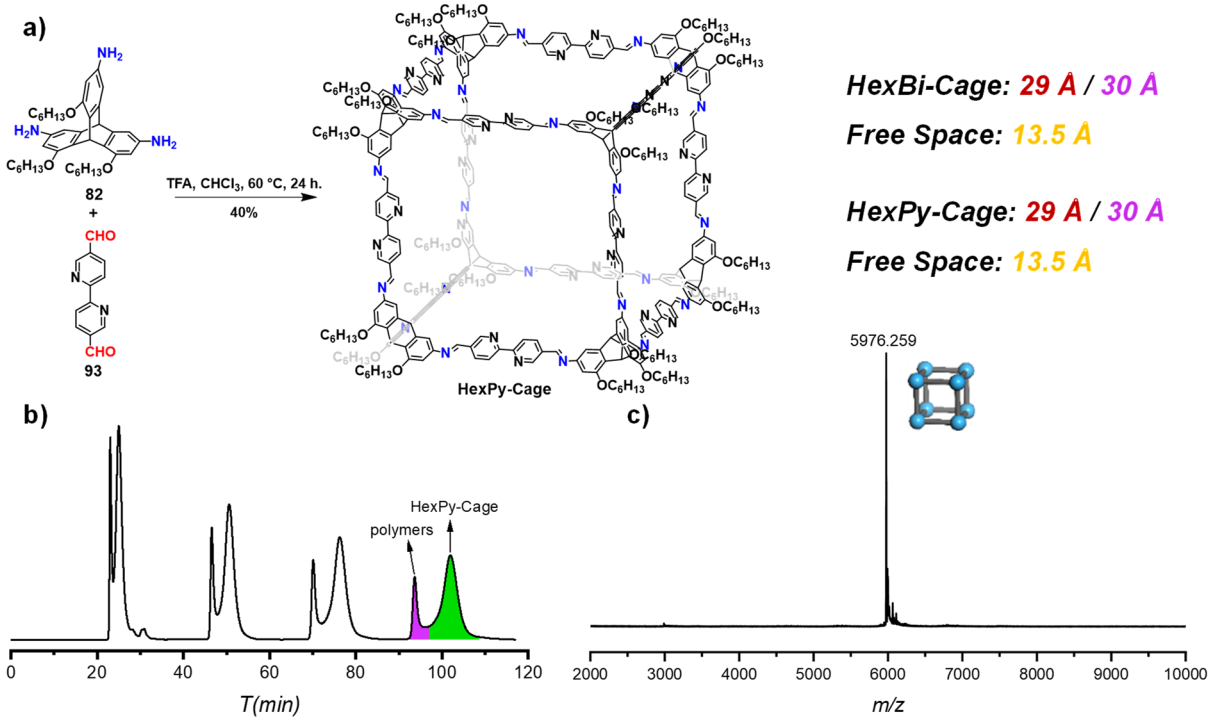

Figure 3.2.8: a) Synthesis scheme of **HexPy**-Cage; b) r-GPC chromatogram (THF, 5 mL/min, 40 °C, 3×100 Å columns) of the crude products, the fraction of unidentified polymers (colored in purple), the fraction collected (colored in green); c) MALDI mass spectra of **HexPy**-Cage.

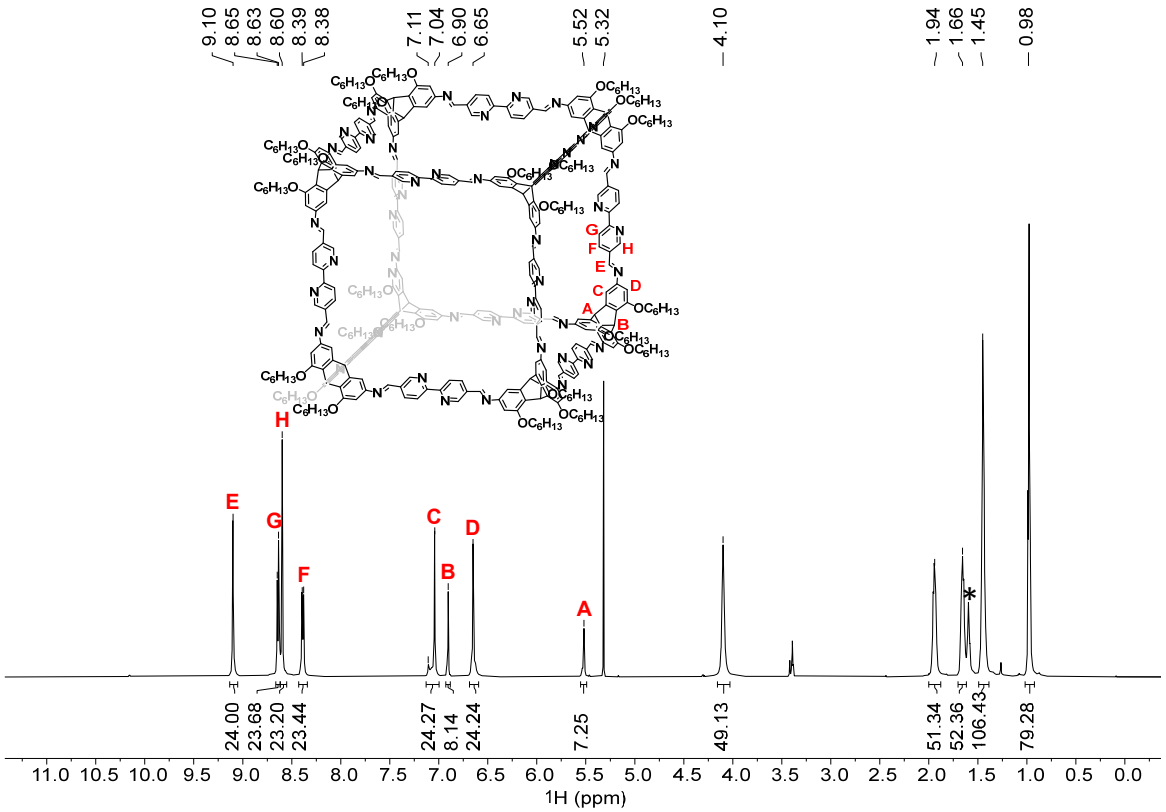

Figure 3.2.9: ^{1}H-NMR Spectrum (700 MHz) of **HexPy**-Cage in CD_2Cl_2, * marks the water peak.

In addition, some precipitates formed after the reaction, and it was also found that the amount of precipitate increased when the reaction was scaled up (it will be further discussed in *Chapter 3.4*). Similarly, HexPy-Cage was purified by r-GPC (Figure 3.2.8 b) and characterized by MALDI MS (Figure 3.2.8 c) as well as 2D NMR experiments (Figure 3.2.9).

Overall, it could conclude that the structure of the linkers, which are the edges of the cubic monomeric cage, significantly influences the formation of catenane. The experimental results indicated that the biphenyl ring is necessary for the catenation. However, it is not clear how the difference between the monomeric cages influenced the catenations. To explore what interactions may exist between the monomeric cages, the model structure of HexBi-Catenane and HexPy-Catenane were built and optimized by Gaussian (PM6) (Figure 3.2.10).

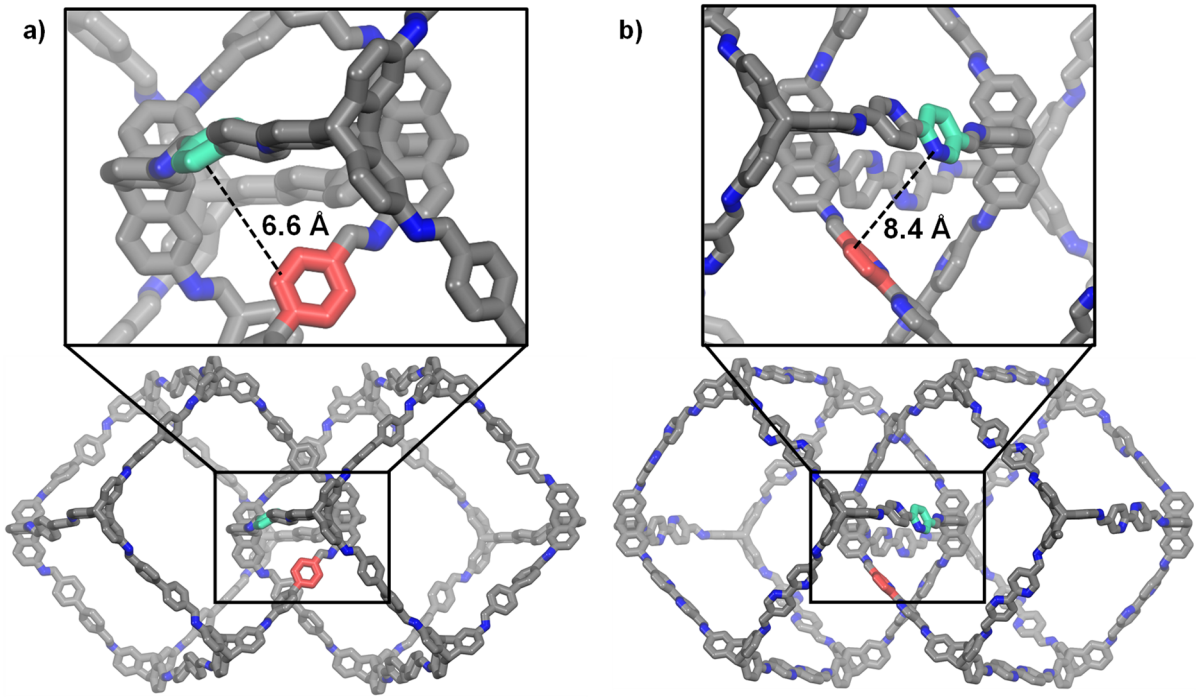

Figure 3.2.10: Optimized model structures (*Gaussian*, PM6), and the cutouts show the distance between the aromatic rings of the edge of monomeric cages: a) **HexBi**-Catenane, edge-to-face distance (~6.6 Å); b) **HexPy**-Catenane, face-to-face distance (~8.4 Å). All outer hexloxy chains were cleaved for clarity.

As shown in Figure 3.2.10, the structure of bipyridine is planar, and the biphenyl is slightly twisted (the dihedral angle of two neighboring phenyl rings is ~55°). Therefore the edge-to-face distance between the monomeric of HexBi-Catenane is 6.6 Å (Figure 3.2.10 a). In contrast, for optimized HexPy-Catenane, the face-to-face distance is 8.4 Å (Figure 3.2.10 b). Of course, these values could not represent the real situation since the interlocking conformation is flexible. Although the distance between the monomeric cages of HexBi-Catenane is shorter in comparison with that of HexPy-Catenane based on the optimized structures, such distance is still far to generate π-π interactions. This computed result still could not prove the existence of interactions between monomeric cages.

3.2.4 The Investigation of the Substituent's Influence on Catenation

To further explore the catenation driving force and find more experimental evidence of the structural effects, a series of triphenyl dialdehyde linkers substituted with alkyl chains were designed and synthesized to construct the cage and catenanes (Figure 3.2.11). The purpose of adding these side chains is to increase the steric hindrance of the edges of monomeric cages, thus blocking the interactions between them. If no catenane could be formed anymore, it means that the structural change does influence the formation of catenane.

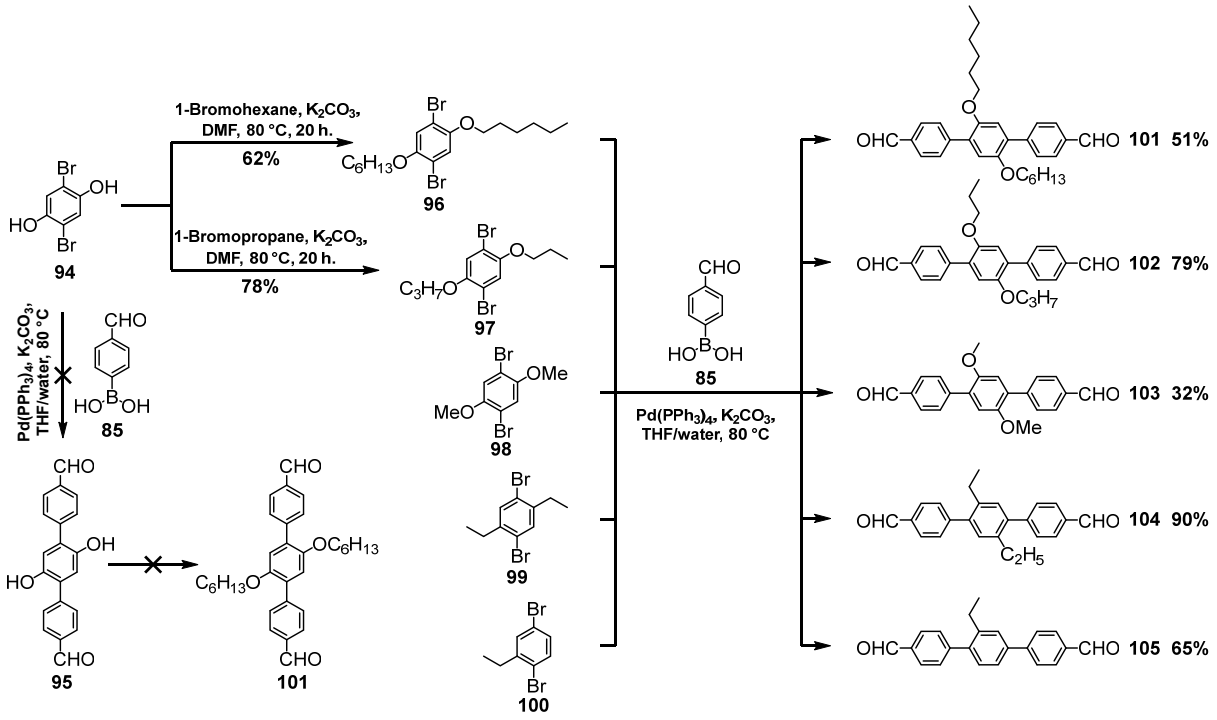

Scheme 3.2.11: Synthesis of different triphenyl dialdehydes substituted with side alkyl chains.

Compounds **96** and **97** were synthesized *via* Williamson ether reaction from **94**, and **97-100** are commercially available. These dibromo-compounds were further employed to synthesize the dialdehydes **101-105** *via* a Suzuki-Miyaura-Coupling reaction (Scheme 3.2.11). It is worth mentioning that the synthesis of compound **95** followed by the introduction of alkyl chains did not work, due to the poor solubility of compound **95**. The dialdehydes **101-105** were respectively utilized with triptycene triamine **82** to construct catenanes (Scheme 3.2.12) under the same conditions (Table 3.2.3).

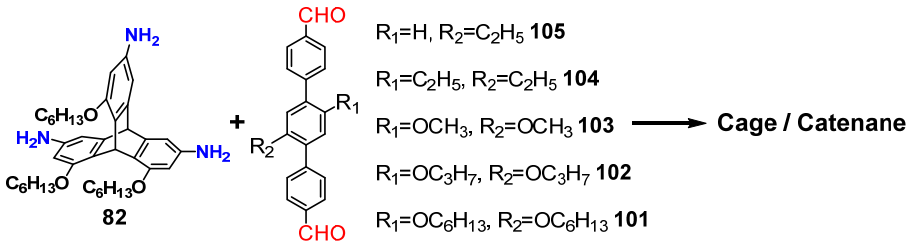

Scheme 3.2.12: Synthesis of cage or catenane based on triphenyl dialdehyde substituted with side alkyl chains.

Table 3.2.3 Screening conditions for the synthesis of cage or catenane based on different linkers.

Entry	Solvent	Temperature	TFA	Conc.[a]	Reaction time	Products detected by MS
82+105	$CHCl_3$	r.t	4 mol%	5.3 mM	7 d	Figure 3.2.13 a
82+105	$CHCl_3$	60 °C	4 mol%	5.3 mM	7 d	Figure 3.2.13 b
82+105	THF	r.t	4 mol%	5.3 mM	7 d	Figure 3.2.13 c
82+105	THF	70 °C	4 mol%	5.3 mM	7 d	Figure 3.2.13 d

a. Concentration of triptycene triamine **82**.

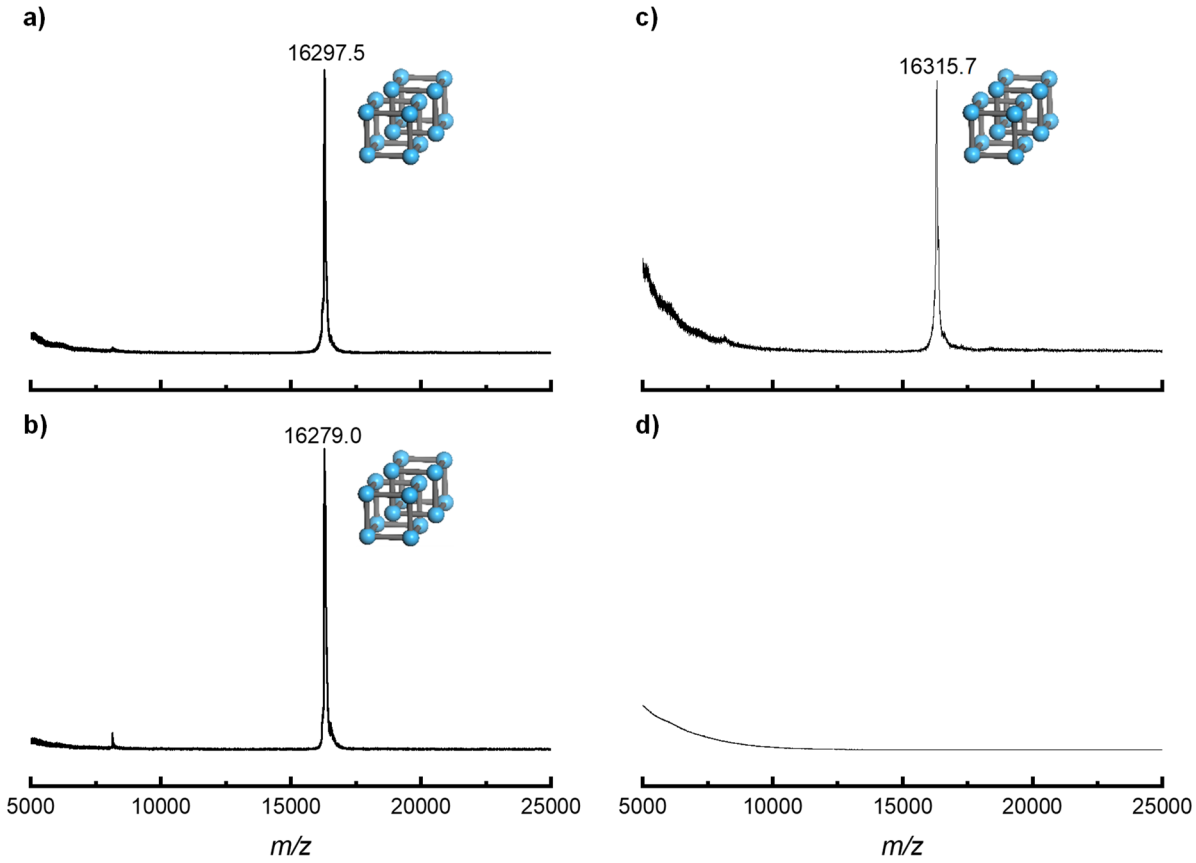

Figure 3.2.13: MALDI mass spectra of **HexTe**-Catenane (the crude solution under different conditions).

Interestingly, the formation of catenane was only observed when using the one-fold ethyl-substituted dialdehyde **105** as the linker (Figure 3.2.13). When both sides of the triphenyl dialdehyde are substituted by alkyl chains, no catenane is formed. These experiments indicate that there might exist interactions between the monomeric cages. Therefore the introduction of two alkyl chains makes the occurrence of interactions more difficult and prevents the formation of catenane. However, even the addition of the side chains prevented the formation of a catenane, but why was no cage formed either? In principle, although the steric hindrance suppressed the interlocking process, it should not influence the formation of monomeric cages. However, in the experiments above, except for compound **105**, for the remaining compounds, no cage and no catenane were detected by MALDI MS monitoring. Because there was also no monomeric cage obtained in the previous synthesis with terphenyl dialdehyde **86**, it was hard to attribute this problem to the influence of side chains.

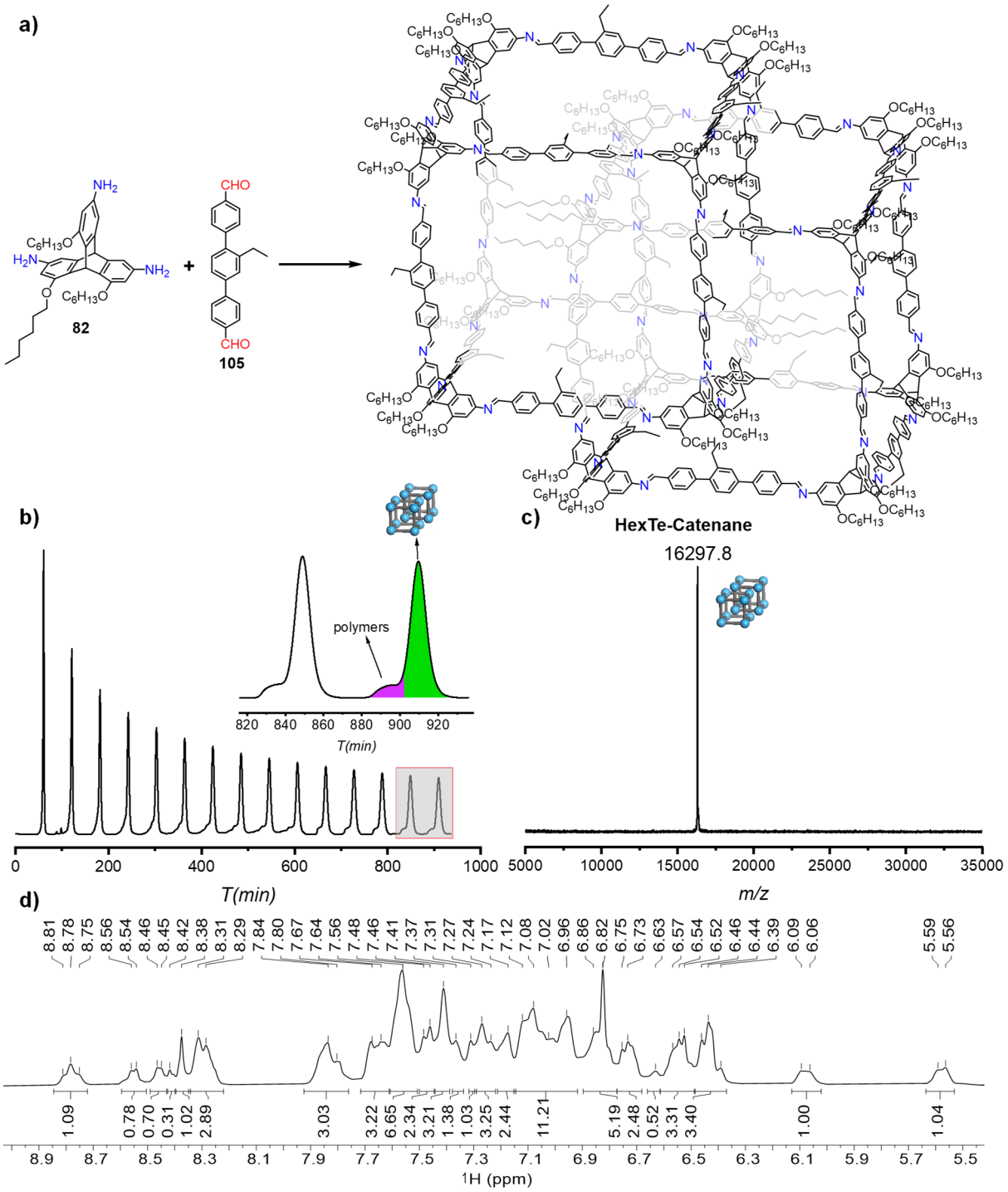

Figure 3.2.14: a) Synthesis of **HexTe**-Catenane; b) The r-GPC chromatogram (THF, 3 mL/min, 40 °C, 2×1000 Å + 2×500 Å columns) of the second purification, the fraction of unidentified polymers (pink), the fraction collected (green); c) MALDI MS of purified **HexTe**-Catenane; d) ^{1}H-NMR Spectrum (700 MHz) of **HexTe**-Catenane in CD_2Cl_2.

HexTe-Catenane was purified by r-GPC (Figure 3.2.14 a) and identified with MALDI MS (Figure 3.2.14 b), which all look pure already. Because the introduction of one-fold alkyl chains makes the topology of HexTe-Catenane not symmetric anymore, the ^{1}H NMR spectrum (Figure 3.2.14 c) resulted in multiple broad peaks and the ^{13}C NMR spectrum was also with low resolution. It also indicated that there is no self-sorting behavior during the reaction.

Since no cage was obtained based on terphenyl dialdehyde linkers before, therefore, the length of linkers was explored. Two substituted biphenyl dialdehyde **108** and **109** with shorter lengths were synthesized to repeat the similar experiments above (Scheme 3.2.15). To make them more comparable, these two linkers were also substituted with one side chain and two side chains respectively. Compounds **108** and **109** both have good solubility in common solvents like THF and $CHCl_3$. They were employed to construct the catenanes with triptycene triamine **82** under the same conditions. After the reactions, it was surprising to find that there was only the monomeric cage observed when using dimethyl biphenyl dialdehyde **108**. In contrast, the formation of both catenane and the monomeric cage was found in the MS spectra when methyl biphenyl dialdehyde **109** was used as the linker.

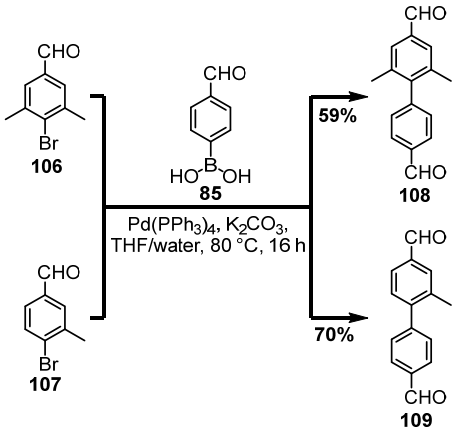

Scheme 3.2.15: The synthesis of triphenyl dialdehyde substituted with side alkyl chains.

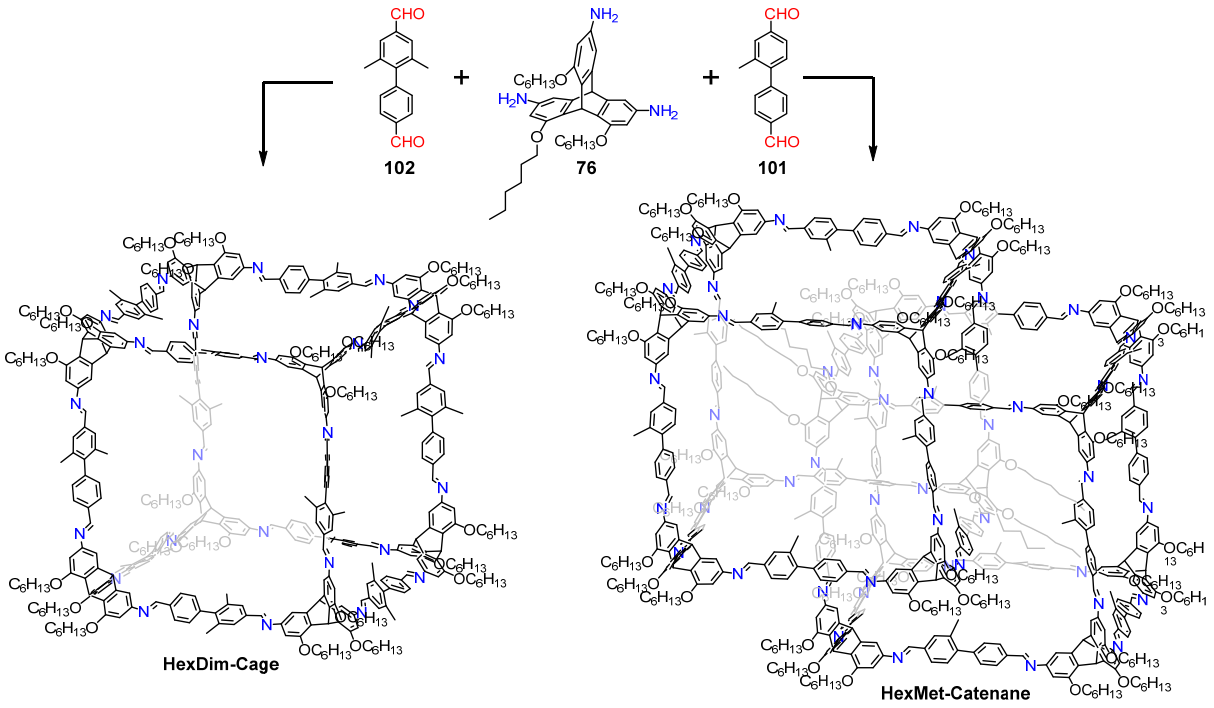

Scheme 3.2.16: Synthesis of **HexDim**-Cage and **HexMet**-Catenane.

Table 3.2.2 Screening conditions for the synthesis of **HexDim**-Cage and **HexMet**-Catenane.

Solvent	Temperature	TFA	Concentration[a]	Reaction time	Products detected by MS
$CHCl_3$	r.t	4 mol%	5.3 mM	7 d	Figure 3.2.17 a (HexDim), A (HexMet)
$CHCl_3$	60 °C	4 mol%	5.3 mM	7 d	Figure 3.2.17 b (HexDim), B (HexMet)
THF	r.t	4 mol%	5.3 mM	7 d	Figure 3.2.17 c (HexDim), C (HexMet)
THF	70 °C	4 mol%	5.3 mM	7 d	Figure 3.2.17 d (HexDim), D (HexMet)

a. Concentration of triptycene triamine **82**.

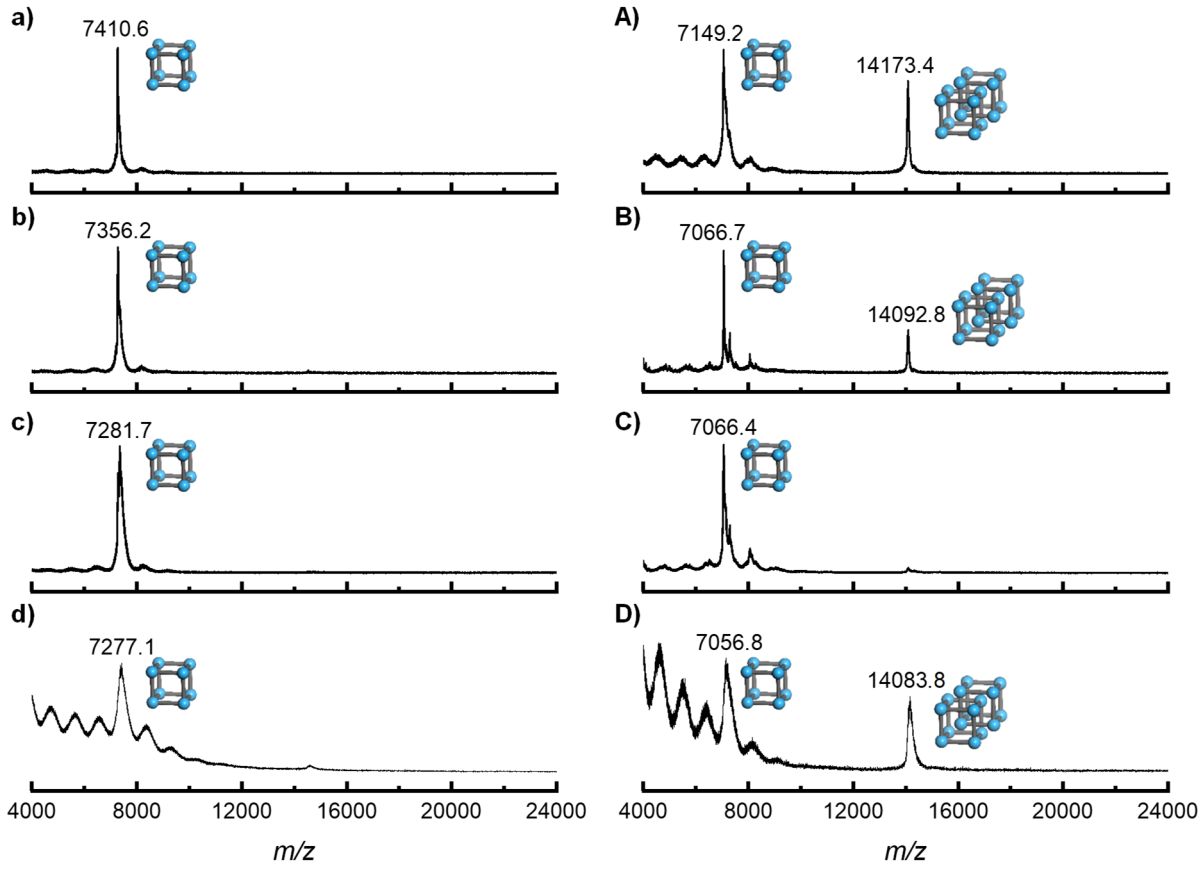

Scheme 3.2.17: MALDI mass spectra of the crude solution under different conditions: a-d) **HexTe**-Catenane; A-D) **HexMet**-Catenane. Calculated mass: **HexDim**-Cage, 7220.208; **HexMet**-Cage, 7052.020.

Although there was only a single peak of HexDim-Cage on the mass spectrum, it is difficult to obtain the pure cage compound. Once the products were precipitated with methanol, or the solvents evaporated in *vacuo*, the obtained residues couldn't be redissolved again. No precipitate or turbid solution was observed after the reaction. So, the insoluble solid was supposed to form during the work-up. Different anti-solvents such as pentane and acetonitrile were also tested but the results were the same. HexMet-Catenane was purified by r-GPC (Figure 3.2.18 a), and MS (3.2.18 b)and NMR were measured. However, due to its asymmetric conformation, it is not possible to identify its structure by 2D NMR experiments.

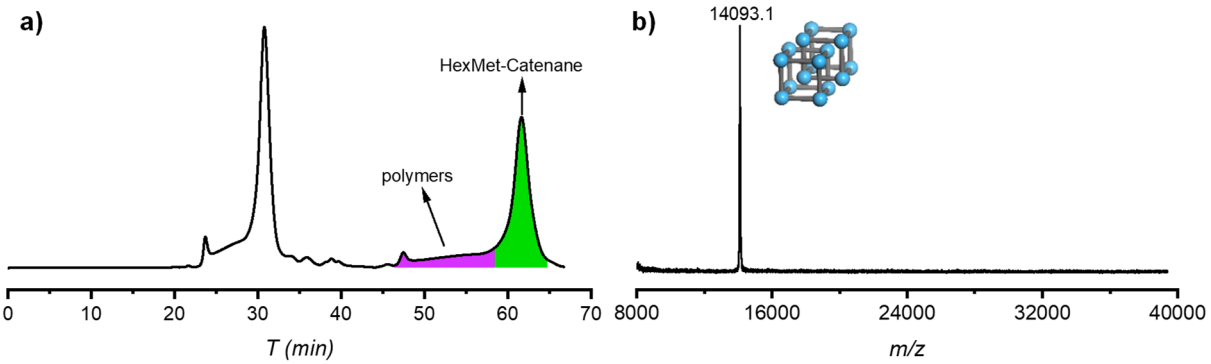

Scheme 3.2.18: a) r-GPC chromatogram (THF, 6 mL/min, 40 °C, 2×1000 Å + 2×500 Å columns) of **HexMet**-Catenane (crude products); b) MALDI MS of purified **HexMet**-Catenane.

Overall, these experimental results demonstrated that the length of linkers also influences the formation of monomeric cages. However, it is still not clear why the shorter linker can be used to build the monomeric cage but the longer one not. Although all the results indicated that the structure of the monomeric cage does influence the catenane, no direct results could elucidate how it works.

3.2.5 Crystallization Experiments of Model Compounds

In addition, two model compounds **109** and **110** with arms of different lengths were synthesized for preparing the single crystals (Figure 3.2.19), which may indicate some hint about the influence of different structures. triptycene triamine **106** was synthesized through the same approach as before (*Chapter 3.1*). This building block was intended to be employed as a linker to construct the monomeric cage with a relatively small size, however, it was found that the size of triptycene triamine **106** is quite close to the triptycene triamine **75** (propoxyl), which makes no difference to the results. Herein, it was used to synthesize the model compounds with biphenyl dialdehyde **107** and dialdehyde **108**. The single crystals were obtained by slowly diffusing methanol into chloroform solutions of the respective compounds at room temperature.

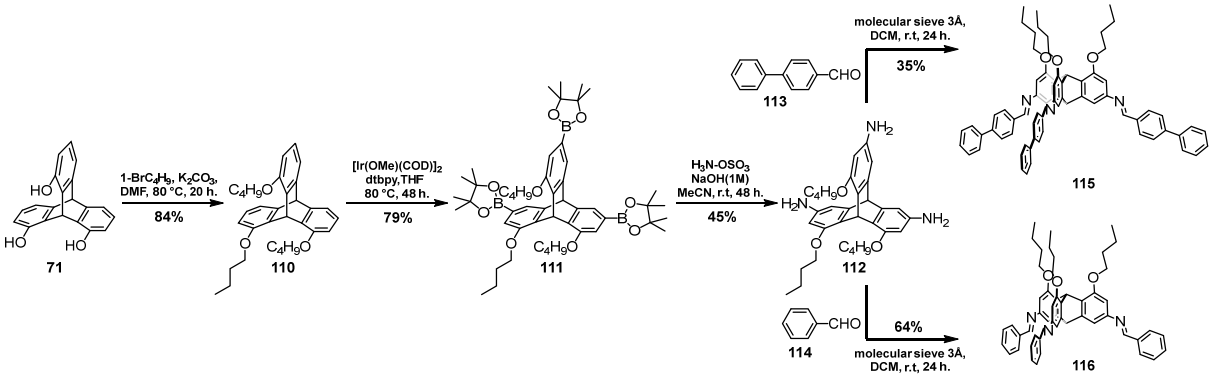

Scheme 3.2.19: Synthesis of the model compounds **115** and **116**.

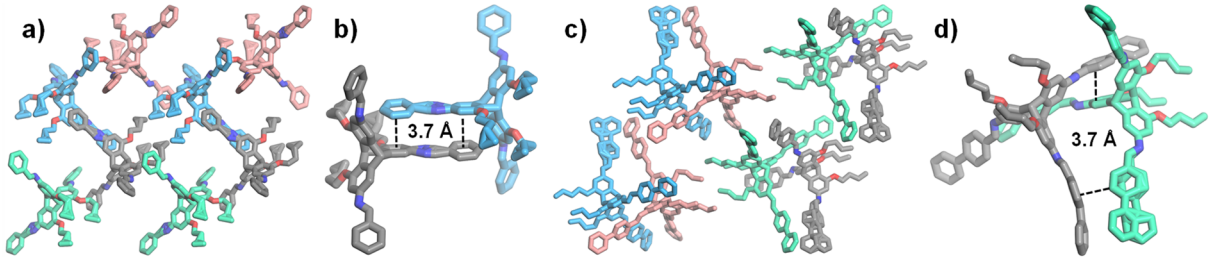

Scheme 3.2.20: a) The single crystal packing of model compound **116**; b) Pair of model compound **116** in single crystals; c) The single crystal packing of model compound **115**; d) Pair of model compound **115** in single crystals;

As the single crystal structures show (Figure 3.2.20), due to the flexibility of the arms and alkyl chains of the model compounds, these crystals do not show strong directional and regular packing. There indeed exist strong π-π interactions between the phenyl ring arms of the model compounds (Figure 3.2.20 d), or between the phenyl rings of arms and the aromatic rings

of the triptycene (Figure 3.2.20 a). However, the relative position of model compounds organized by the π-π interactions does not fit the structure of catenanes.

Another interesting result is that the model compound **115** with biphenyl ring is more flexible in comparison to **116** according to the single crystal structures, and there are strong π-π interactions between the biphenyl rings of model compound **115**. This is consistent with the hypothesis that the more flexible linker facilitates organizing monomeric cages to the position where the interactions can generate. According to the optimized catenane model, if assuming that the interaction exists, one of the most important factors is the rotation of the phenyl ring of the linkers. Therefore, the rotational barriers of each linker were calculated to see if there is some law to confirm the experimental result.

3.2.6 Theoretical Calculations of Rotational Barriers Energy

To investigate the steric effects in the different aldehyde linkers, the energy of every conformation with different dihedral angles was calculated (Scheme 3.2.21). The dihedral angle was changed in an interval of 2° in the range from 0° to 360°. A periodically changing curve was obtained, from which the maximum energy (E_{max}) and minimum energy (E_{min}) could be found. The rotational energy barriers (ΔE) were calculated following $\Delta E = E_{max} - E_{min}$. Figure 3.2.21 shows all the linkers and the corresponding torsion dihedral angle calculated.

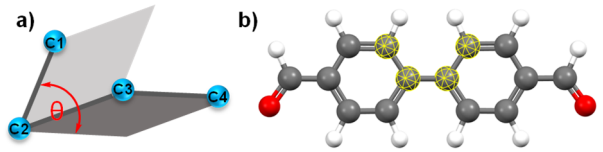

Scheme 3.2.21: a) The illustration of dihedral angle; b) the atoms chosen for calculation.

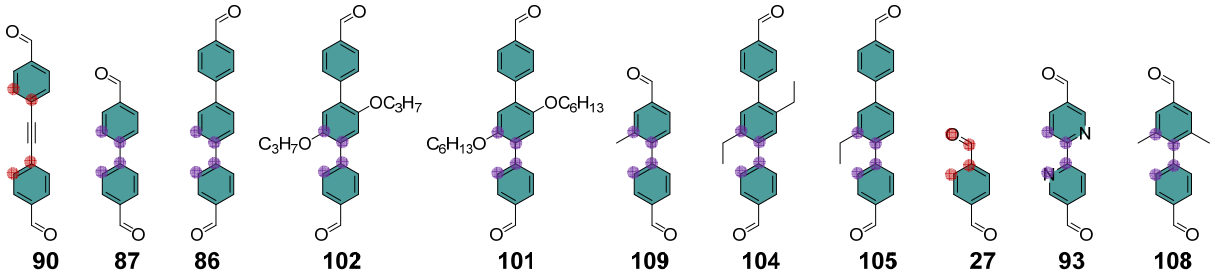

Scheme 3.2.22: The calculated linkers, the purple dots mark the dihedral angle calculated, and the red dots mark two special cases.

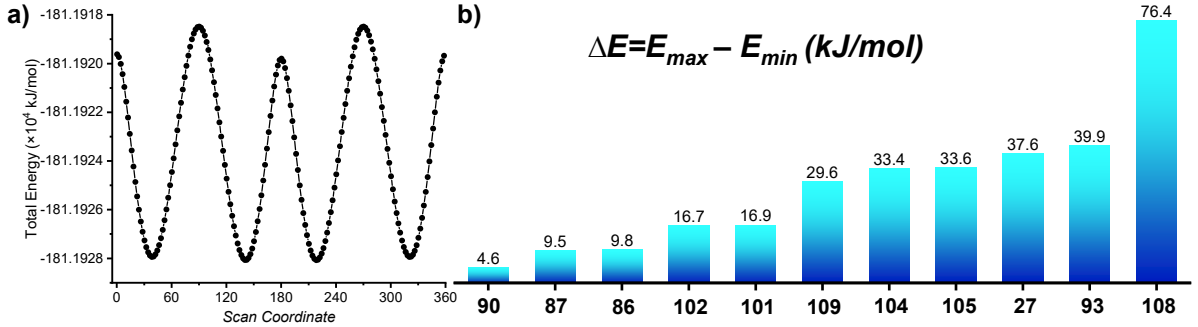

Scheme 3.2.23: a) calculated energy curve of **87**; b) The histogram of rotational energy barrier.

As the histogram shows, linker **108** has the highest rotation energy, and the following linkers are **93** and **27**. In the previous experiment, only monomeric cages were obtained after reactions with these three linkers. The rotational barrier of linker **90** is the smallest one, however, the same as linker **27**, it was a quite special linker that has no neighboring phenyl ring. Therefore, it could again be proved that the second phenyl is necessary for the catenation. Furthermore, the linker with the second smallest rotational barrier is **87**, followed by **86**, and these two linkers could easily form IOCs.

In addition, linkers **102** and **101** have similar rotation energy, and the next linkers are **109**, **104**, and **105**, which were at the same level. For linkers **109** and **105**, the formation of catenane has already been observed. So, in principle, the catenane with **104**, **102**, and **101** should also be obtained because their rotational barriers are all smaller than linker **105**. However, no catenane was obtained with them. That's because there is another important factor that influences the catenation, which will be discussed in *Chapter 3.3*.

Overall, the calculation results are highly consistent with the experiments, which demonstrated that the flexibilities and the rotation barriers indeed influenced the catenation. This also indicated that the driving force probably originates from the interaction between the linker of each monomeric cage, since there is the rotation of the phenyl ring.

3.2.7 Conclusion

In summary, the structural effect of the monomeric cage on the catenation was investigated in detail. It focused on the structural changes caused by different linkers. By designing and synthesizing HexPh-Cage and ProPh-Cage, the effect of size on the catenation was excluded. To further demonstrate the hypothesis that the interaction between the edges of monomeric cages leads to the formation of a catenane, the HexPy-Cage, which has the same topology as HexBi-Cage, was synthesized, and it proved that the type of linker does influence the catenation even though they have the same size and similar aromatic properties. Moreover, a series of linkers substituted with different side chains were synthesized. By studying their influence on the formation of a catenane, and according to the crystal structure analysis of model compound and theoretical calculations, it was found that the length and flexibility of linkers also make a difference in the catenation results. However, how the structural difference works during this process and if there are some kinds of interactions are still not demonstrated. Of course, it needs to be emphasized that the synthesis reaction of IOCs is a complex system controlled by several factors simultaneously, and the structural effect is just one of them. For example, when adjusting the substituents of linkers, the solubility of linkers and corresponding cages also

changed. It makes the whole investigation of structural effects more difficult. Overall, the structure of monomeric cages fundamentally influences the formation of IOCs. The solvent effects will be investigated and discussed in the next chapter.

3.3 The Study of Solvent Effects on the Synthesis of IOCs

3.3.1 Introduction

Interlocked cages have been considered thermodynamically more stable than their monomeric derivatives.[3, 20] Therefore, the synthesis of interlocked cages is a thermodynamic versus kinetic controlled process, which is significantly influenced by the reaction environments, for example, temperature, concentration, and solvents.[10a, 25, 59, 77] Most of the reported research on the interlocked cages mainly discussed the conditions of temperature and catalysts related to the thermodynamic process. However, the solvents were rarely investigated. Especially when finding that some monomeric cages couldn't interlock into catenane, most of them attributed this to the fact that their structure is not suitable for catenation, and the possible influence of solvent was ignored.[59]

In this chapter, systematic investigations were performed to explore the influence of solvents on the catenation of [8+12] imine monomeric cages. It was found that solvents play a much more crucial role during the catenation process. The function of solvents is not only dissolving the reactant and providing different reaction temperatures depending on their boiling points. The experimental results proved that the solvents could decide the formation of catenanes, and it is possible to control the catenation degree by adjusting the solvents.

3.3.2 The Synthesis of IOCs based on Linkers with Side Chains

In the previous works (*Chapter 3.2*), the structural effects have been studied by introducing different substitutes to the linkers of monomeric cages and comparing their influence on the catenation. Inspired by crystallization experiments of model compounds and electronic density calculations of the linkers, the rotation of phenyl rings of the linkers was also considered as a possible factor in the catenation. So, the theoretical calculations of the rotation barriers energy were further performed to see if there is any relationship between them. According to previous experimental results, the linker with a smaller rotation barrier is tending to catenation more.

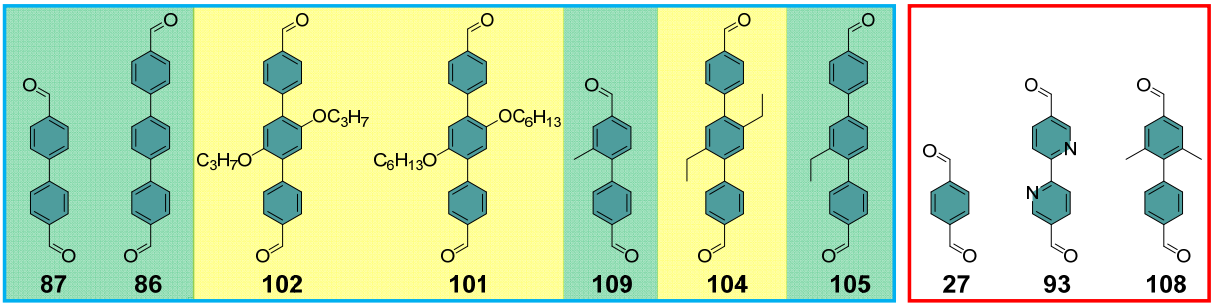

Figure 3.3.1: The linkers whose rotation barrier was calculated before, with an increasing barrier from left to right. Synthesis results: only cage (in red box); catenane (in green shadow); no cage and no catenane (in yellow shadow).

As it was shown in Figure 3.3.1, linkers **101**, **102**, and **105** are all supposed to form the IOCs since linker **105**, which has a higher rotation barrier, could generate the catenane. However, no catenane was observed based on these three linkers. Despite the two side chains increasing the steric hindrance, the monomeric cages are still possible to interlock due to their giant cavity.

The second reason is the solvent effects. After substituting these side chains, the solubility of linkers and the interactions between the linkers, cage fragments, and solvents also changed. As mentioned in previous chapters, to make all the experimental results more comparable, all experiments were conducted in tetrahydrofuran and chloroform. These two solvents have also been proven suitable for most of [8+12] imine cage and catenane syntheses based on different substituted triptycene triamines. However, regarding the change of linkers, it is necessary to explore the influence of solvents furthermore. Dialdehyde **104** and triptycene triamine **82** were first employed as an example to investigate the solvent effects on catenane synthesis (Scheme 3.3.2).

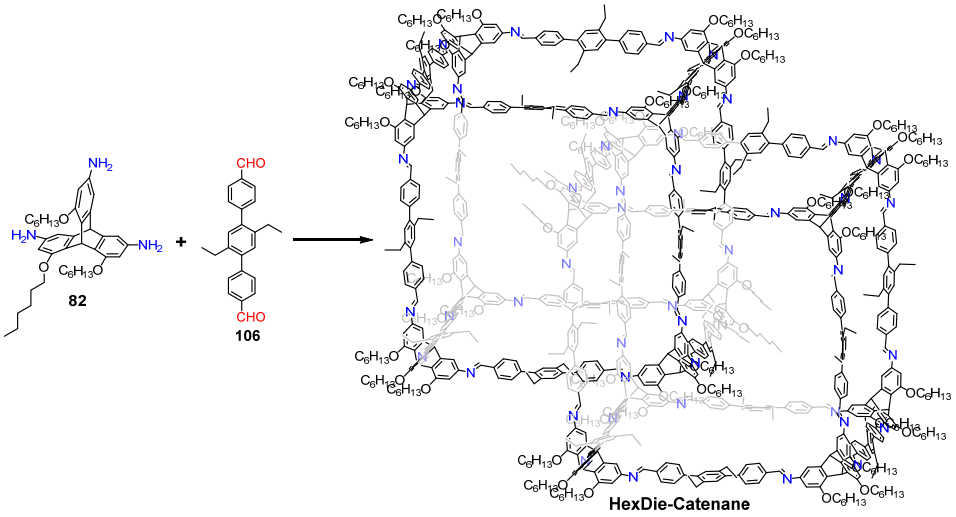

Scheme 3.3.2: Synthesis scheme of **HexDie**-Catenane.

Table 3.3.1 The solvents screening for the synthesis of **HexDie**-Catenane

Solvent	Temperature	TFA	Concentration[a]	Reaction time	Products detected by MS
$CHCl_3$	r.t	4 mol%	5.3 mM	7 d	no cage and no catenane
$CHCl_3$	60 °C	4 mol%	5.3 mM	7 d	no cage and no catenane
THF	r.t	4 mol%	5.3 mM	7 d	no cage and no catenane
THF	70 °C	4 mol%	5.3 mM	7 d	no cage and no catenane
CH_2Cl_2	r.t	4 mol%	5.3 mM	7 d	no cage and no catenane
acetone	r.t	4 mol%	5.3 mM	7 d	no cage and no catenane
toluene	r.t	4 mol%	5.3 mM	7 d	Figure 3.3.3 a
1,4-dioxne	r.t	4 mol%	5.3 mM	7 d	no cage and no catenane
1,2-dichlorobenzene	r.t	4 mol%	5.3 mM	7 d	Figure 3.3.3 b
benzene	r.t	4 mol%	5.3 mM	7 d	no cage and no catenane

a. Concentration of triptycene triamine **82**.

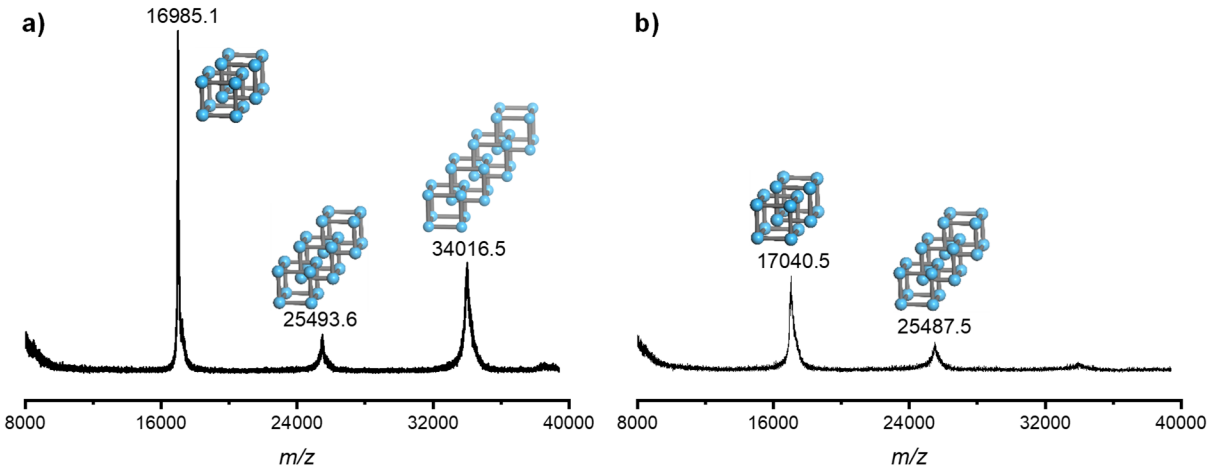

Figure 3.3.3: MALDI mass spectrum of crude solution: a) toluene; b) 1,2-dichlorobenzene.

Herein (Table 3.3.1), eight different solvents (polarity increasing): benzene, toluene, 1,2-dichlorobenzene, 1,2-dichloromethane, tetrahydrofuran, chloroform, 1,4-dioxane, and acetone, were screened for the synthesis of the HexDie-Catenane. After the reaction, the formation of [16+24], [24+36], and even [32+48] species could be observed in toluene and 1,2-dichlorobenzene according to MALDI MS (Figure 3.3.3). And no catenane had been detected in the other solvents. However, most of the products in toluene were precipitates after the reaction, and even more in 1,2-dichlorobenzene. These precipitates were also insoluble in other solvents such as THF, $CHCl_3$, and CH_2Cl_2. Therefore, the yield of catenane is not sufficient for further purification and characterization. Even though, it was worth to further testing if toluene also works for the other four substituted terphenyl dialdehydes below (Figure 3.3.4), which were conducted at room temperature and 100 °C, respectively (Table 3.3.2).

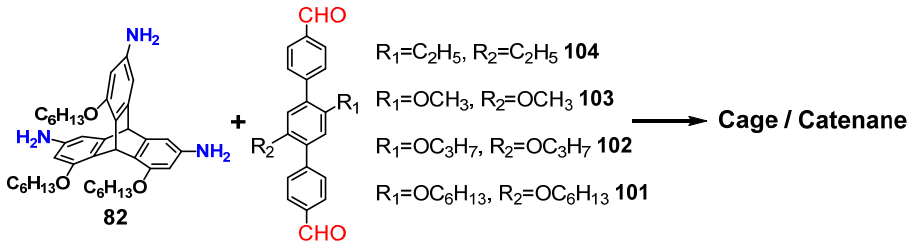

Figure 3.3.4: Screening linkers for the synthesis of cage or catenane in toluene.

Table 3.3.2 Screening of different linkers for the synthesis of cage or catenane in toluene

Entry	Solvent	Temperature	TFA	Concentration[a]	Reaction time	Products detected by MS
104	toluene	r.t	4 mol%	5.3 mM	5 d	catenane
	toluene	100 °C	4 mol%	5.3 mM	5 d	no catenane and cage
103	toluene	r.t	4 mol%	5.3 mM	5 d	no catenane and cage
	toluene	100 °C	4 mol%	5.3 mM	5 d	no catenane and cage
102	toluene	r.t	4 mol%	5.3 mM	5 d	catenane
	toluene	100 °C	4 mol%	5.3 mM	5 d	no catenane and cage
101	toluene	r.t	4 mol%	5.3 mM	5 d	catenane
	toluene	100 °C	4 mol%	5.3 mM	5 d	no catenane and cage

a. Concentration of triptycene triamine **82**.

Interestingly, it was found that there was a peak of [16+24] condensation product on the mass spectra of these crude solutions, except for the solution using dialdehyde **103** as the linker. This experimental result proved that toluene is a better solvent in comparison with $CHCl_3$ and THF. It somehow could provide the reaction environment for the catenation of these monomeric cages based on linkers with side chains, although, most products in toluene are insoluble precipitates.

3.3.3 The Investigation of Solvent Mixtures for IOCs Synthesis

While considering how to avoid the formation of precipitate and improve the yield of catenane in toluene, an interesting phenomenon was noticed: based on the same starting materials, there is no cage and catenane generated but a homogeneous solution obtained in THF or $CHCl_3$ after the reaction, although no catenane was observed. In contrast, the formation of catenane could be tracked in toluene, unfortunately, the yields were low due to the formation of insoluble precipitates. Therefore, it is natural to come to the idea of what will happens if using a mixture of toluene and $CHCl_3$ as the solvent to conduct these syntheses.

The first attempt is still the synthesis of HexDie-Catenane (Scheme 3.3.2), it was conducted in the mixture solvent of $CHCl_3$ and toluene, in a ratio of 1:2, 2:1, and 30:1 respectively (Table 3.3.3). Because the elevated temperature promotes the formation of precipitates in toluene according to the above experimental result (Table 3.3.2), the following syntheses were all conducted at room temperature.

Table 3.3.3 Screening of solvent mixtures for the synthesis of **HexDie**-Catenane

$CHCl_3$/toluene	Temperature	TFA	Concentration[a]	Reaction time	Products detected by MS
1:2	r.t	4 mol%	5.3 mM	7 d	Figure 3.3.5 a
2:1	r.t	4 mol%	5.3 mM	7 d	Figure 3.3.5 b
30:1	r.t	4 mol%	5.3 mM	7 d	no catenane and cage

a. Concentration of triptycene triamine **82**.

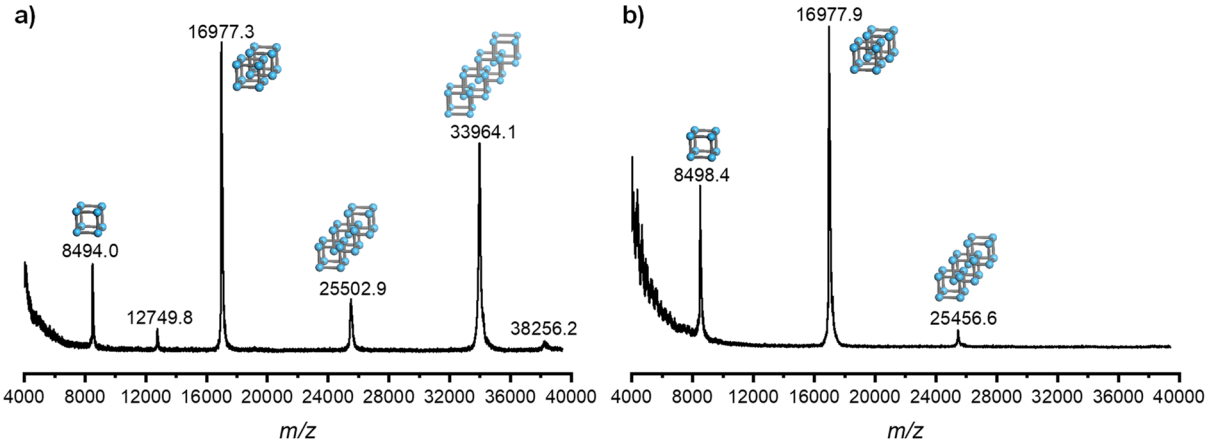

Figure 3.3.5: MALDI mass spectrum of crude solution: a) $CHCl_3$/toluene 1:2, TFA 4 mol%, r.t, 7 d; b) $CHCl_3$/toluene 2:1, TFA 4 mol%, r.t, 7 d.

By MALDI MS monitoring of the crude solution, it was found that there were [8+12], [16+24], and [24+36] species formed in the mixture solvent of $CHCl_3$ and toluene in the ratio of 1:2 and 2:1, respectively. Besides, [32+48] specie was first observed in a 1:2 ratio solvent mixture. The ratio of 30:1 was tried to test if the toluene just worked as a catalyst or template which generally requires only a tiny amount. However, no cage and no catenane were found, which means the toluene works not as a catalyst or template.

In addition, the most impressive result was that these solutions were all homogeneous after the reaction. To illustrate the state difference between the reaction solutions of tested solvents, a picture was taken to show four different representative situations (Figure 3.3.5). In comparison with the result in toluene (Figure 3.3.5d), only a little insoluble solid was formed and attached to the wall of the vials in the mixture solvent (Figure 3.3.5c). And the rest crude solution of $CHCl_3$ and toluene were homogeneous. Thus, it dramatically improved the yield of these soluble products. Moreover, the workup also became easier to remove all the insoluble solids completely before purification by r-GPC. For example, in comparison with the turbid THF solution (Figure 3.3.5b), there were nearly no small polymers formed in the solvent mixtures after the reaction. Because small polymers could only be removed by filtration through a Celite column or syringe filter (0.45 μm), which somehow cause the loss of product during this procedure. In addition, if these polymers haven't been removed completely, once the solvent evaporated, it will turn into a solid and couldn't be dissolved anymore.

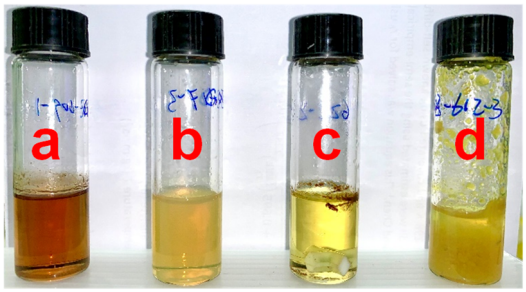

Figure 3.3.6: a) homogeneous solution in $CHCl_3$; b) turbid solution in THF; c) homogeneous solution in mixture solvent ($CHCl_3$/toluene 1:2); d) precipitates in toluene.

Another interesting result was that the mass spectra showed different intensity and diversity of peaks in the crude solution of $CHCl_3$/toluene in different ratios: the main peaks are [16+24], [32+48] species, and the rest weaker peaks were corresponding to [8+12], [12+18], [24+36], [36+54] species; In contrast, when the ratio of $CHCl_3$/toluene is 2:1, the [8+12], [16+24] was detected as the main peaks, besides, only a tiny peak of [24+36] species was found. That means the ratio of the mixture solvents could influence the catenation process. And it is possible to control the catenation degree by adjusting the ratio of solvents, thus isolating and obtaining each catenane effectively. That has never been reported before, and it will be further investigated and discussed in *Chapter 3.4*. To further test if this kind of mixture solvent also works well for other linkers with side chains, the same conditions (Table 3.3.3) were employed in the synthesis of catenane based on dialdehyde **99** (Scheme 3.3.7).

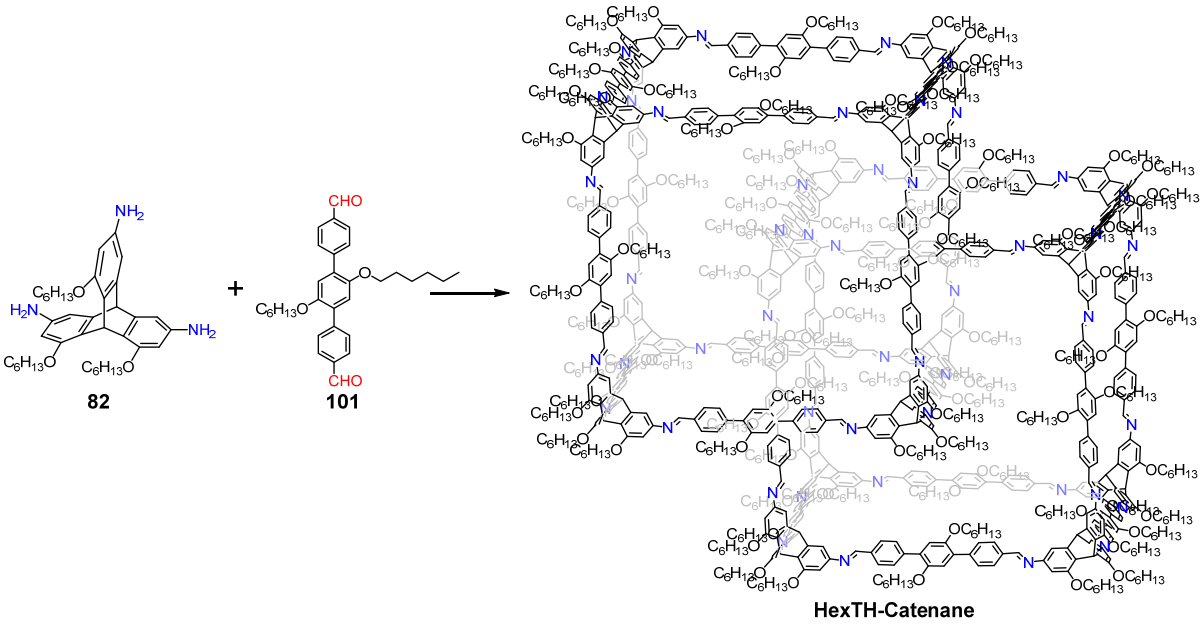

Scheme 3.3.7: Synthesis scheme of **HexTH**-Catenane.

Table 3.3.4 Screening of solvent mixtures for the synthesis of **HexTH**-Catenane

$CHCl_3$/toluene	Temperature	TFA	Concentration[a]	Reaction time	Products detected by MS
1:2	r.t	4 mol%	5.3 mM	7 d	Figure 3.3.8 a
2:1	r.t	4 mol%	5.3 mM	7 d	Figure 3.3.8 b
30:1	r.t	4 mol%	5.3 mM	7 d	Figure 3.3.8 c

a. Concentration of triptycene triamine **76**.

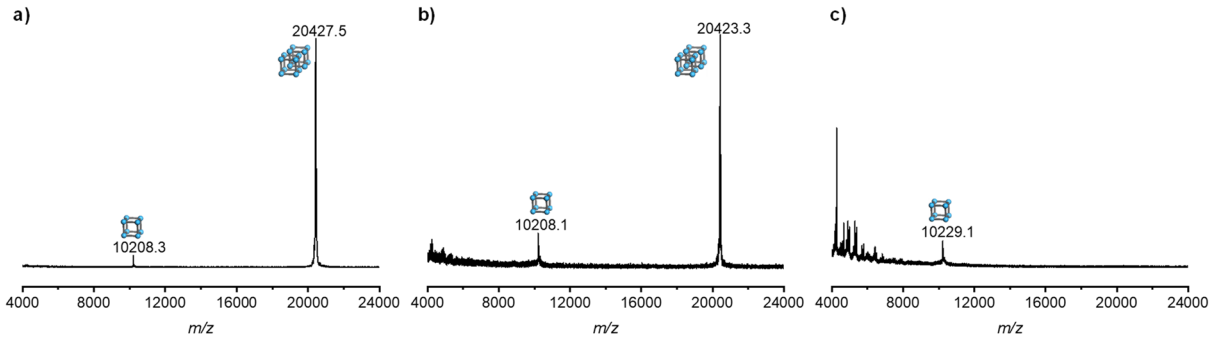

Figure 3.3.8: MALDI mass spectra of crude solution with the mixture of $CHCl_3$/toluene: a) 1:2; b) 2:1; c) 30:1.

As the mass spectra showed (Figure 3.3.8), the formation of [16+24] species was detected when the ratio of $CHCl_3$/toluene is 1:2 or 2:1, and there is also a small peak of [8+12] product found in the crude solution under all conditions. In addition, same to previous results, the tiny amount of toluene (100 µL in 3 mL $CHCl_3$) was not enough for the catenation. Moreover, these crude solutions are all homogeneous solutions with a little insoluble solid. The reaction solution mixture was precipitated with methanol and centrifuged to obtain the crude solid, which was further purified by r-GPC. As it was shown by the GPC chromatogram of the crude products, much fewer polymers and fragments were formed (Figure 3.3.9a, fraction colored in pink). After five cycles, the single fraction peak (Figure 3.3.9 a, colored in green) was collected for the second purification. The resulting chromatogram (after 15 cycles, Figure

3.3.9 b, fraction colored green) and the MS spectrum (Figure 3.3.7c) showed only one species. However, same to the problems mentioned in *Chapter 3.1*, it is also difficult to collect the clean NMR spectrum (Figure 3.3.7d), due to the further reaction during the preparation of NMR samples.

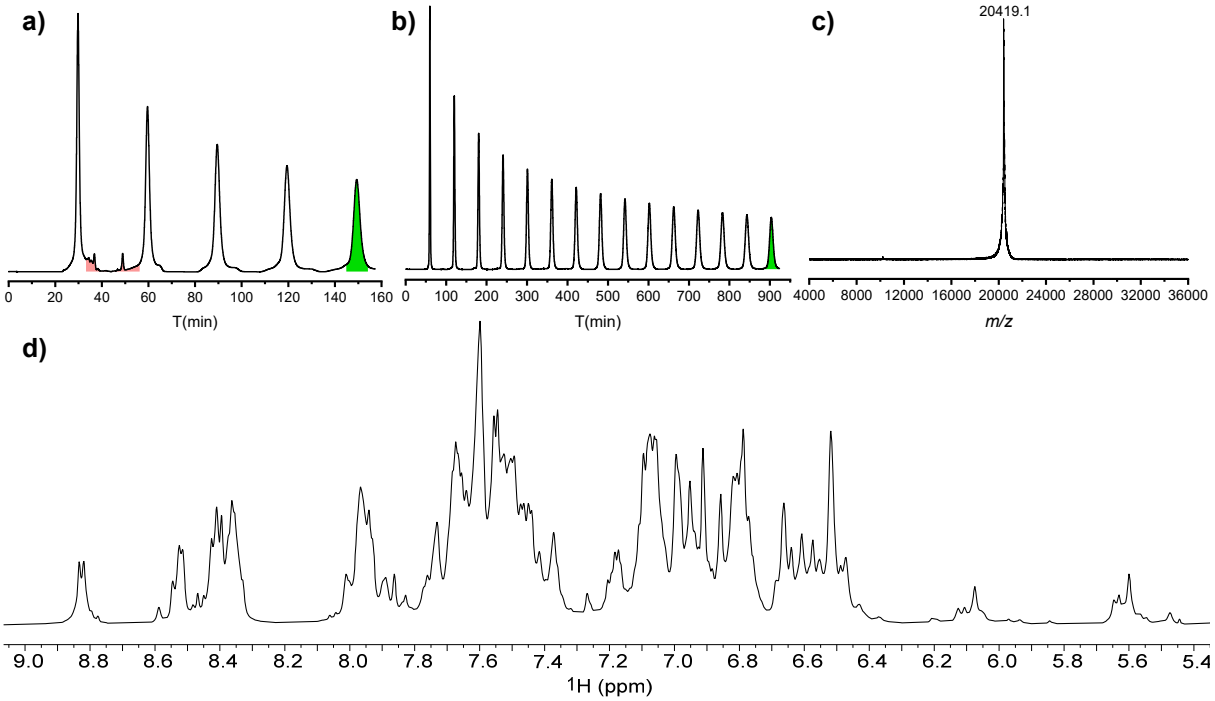

Figure 3.3.9: The r-GPC chromatograms (THF, 40 °C, 2×1000 Å + 2×500 Å columns): a) crude product, flow rate 6 mL/min, oligomers (pink), the collected fraction (green); b) reinjection of the green fraction of *a)*, flow rate 3 mL/min, the collected fraction (green). c) The MALDI-TOF MS spectrum of the green fraction of *b)*. d) The partial ^{1}H-NMR spectrum (700 MHz, 295 K, in CD_2Cl_2) of the purified **HexTH**-Catenane.

Overall, the investigations above demonstrated that the mixture solvents are indeed suitable for the synthesis of catenane based on the linkers with side chains. It not only provided the proper environment for catenation and also solved the yield problem caused by the formation of precipitates.

3.3.4 The Study of Different Combinations of Mixture Solvents

Based on all the studies in previous chapters, $CHCl_3$ and THF were regarded as the universal solvents for the synthesis of IOCs based on substituted triptycene triamine. Moreover, it was also found that $CHCl_3$ tends to promote the formation of catenane while THF suits the synthesis of monomeric cages (the syntheses of HexBi-Cage and DecBi-Cage in *Chapter 3.1*). Therefore, further investigation was performed on the mixture of THF and toluene. To be comparable, again the build blocks **76** and **99** were used to synthesize the target cages and catenanes (Figure 3.3.10 a), in the mixture of THF and toluene in four different ratios (Table 3.3.5). Interestingly, the MALDI MS spectrum of crude solution showed that only monomeric cages formed under

all these four conditions (Figure 3.3.10 b) as well as, except that the reaction solution of the mixture solvent in a 5:1 ratio was turbid, the rest solutions are all homogeneous.

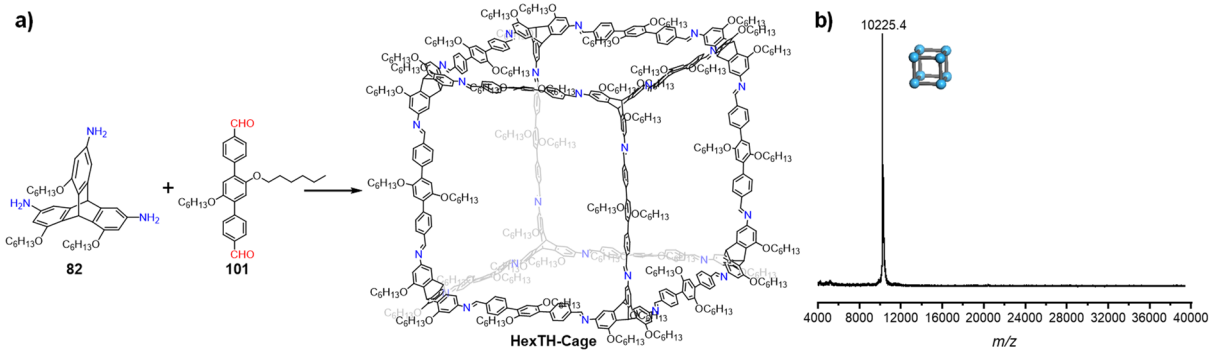

Figure 3.3.10: a) Synthesis scheme of **HexTH**-Cage; b) MALDI-MS spectrum of crude solution (THF/toluene = 1:2), the MS under the rest conditions are the same.

Table 3.3.5 Solvent mixture screening for the synthesis of **HexTH**-Catenane

THF/toluene	Temperature	TFA	Conc.[a]	Reaction time	Cage formation	Catenane formation
1:2	r.t	4mol%	5.3 mM	7d	yes	no
1:1	r.t	4mol%	5.3 mM	7d	yes	no
2:1	r.t	4mol%	5.3 mM	7d	yes	no
5:1	r.t	4mol%	5.3 mM	7d	yes	no

a. Concentration of triptycene triamine **76**.

However, similar to the HexDim-Cage in *Chapter 3.2*, while working up these reactions, it was found that once the products precipitated with methanol or just evaporate the solvents, the residues became insoluble. Anyway, in comparison with the results before, the addition of THF solved the precipitate problem, and the combination of THF and toluene also enable the formation of cages; on the other hand, in contrast to $CHCl_3$, the THF prevents the catenation and leads to the formation of monomeric cages. To make the whole story clear, a general overview of the synthesis of HexTH-Cage and HexTH-Catenane is necessary here (Figure 3.3.10).

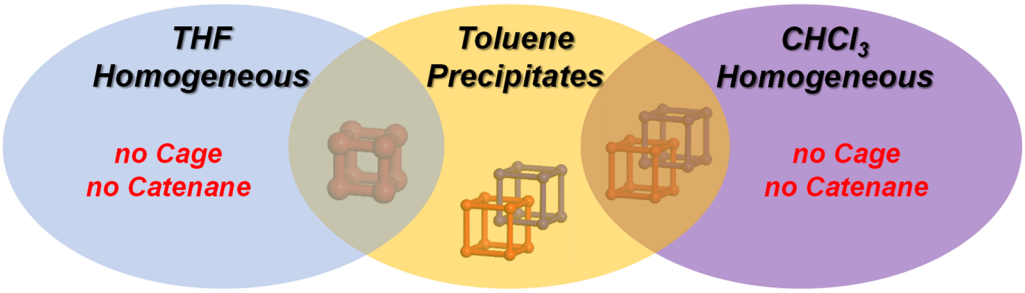

Figure 3.3.11: Illustration of the relationship between solvents and the formation of cage and catenane.

When using $CHCl_3$ and THF as solvents, no cage and no catenane were observed and the reaction solutions were homogeneous. After changing the solvents to toluene, catenane was generated but most of the products were insoluble precipitates, which led to low yield. Then the mixture of $CHCl_3$ and toluene was used to conduct the synthesis, and not only the catenane

was detected but the solution was also homogeneous. Finally, a different solvent combination – the mixture of THF and toluene was tested, and only the monomeric cage was found and the solutions were also homogeneous.

3.3.5 Multiple Factors Simultaneously Influence the Synthesis of IOCs

In *Chapter 3.2*, it was mentioned that the synthesis of IOCs is a complex system that was influenced by several factors simultaneously. Therefore, when investigating the structural effects, all experiments were performed in $CHCl_3$ and THF to limit the influence of other factors. These experimental results were also consistent with the theoretical calculation. The introduction of alkyl chains indeed increased the rotational energy barrier and suppressed the formation of IOCs. However, based on the investigation above, these linkers with two side chains also could form the catenane in toluene and the mixture solvents. To further test the influence of solvent, dialdehyde **108**, whose rotational energy barrier is the highest, was employed to construct the catenane in the solvent mixture of $CHCl_3$ and toluene at room temperature (Figure 3.3.12a).

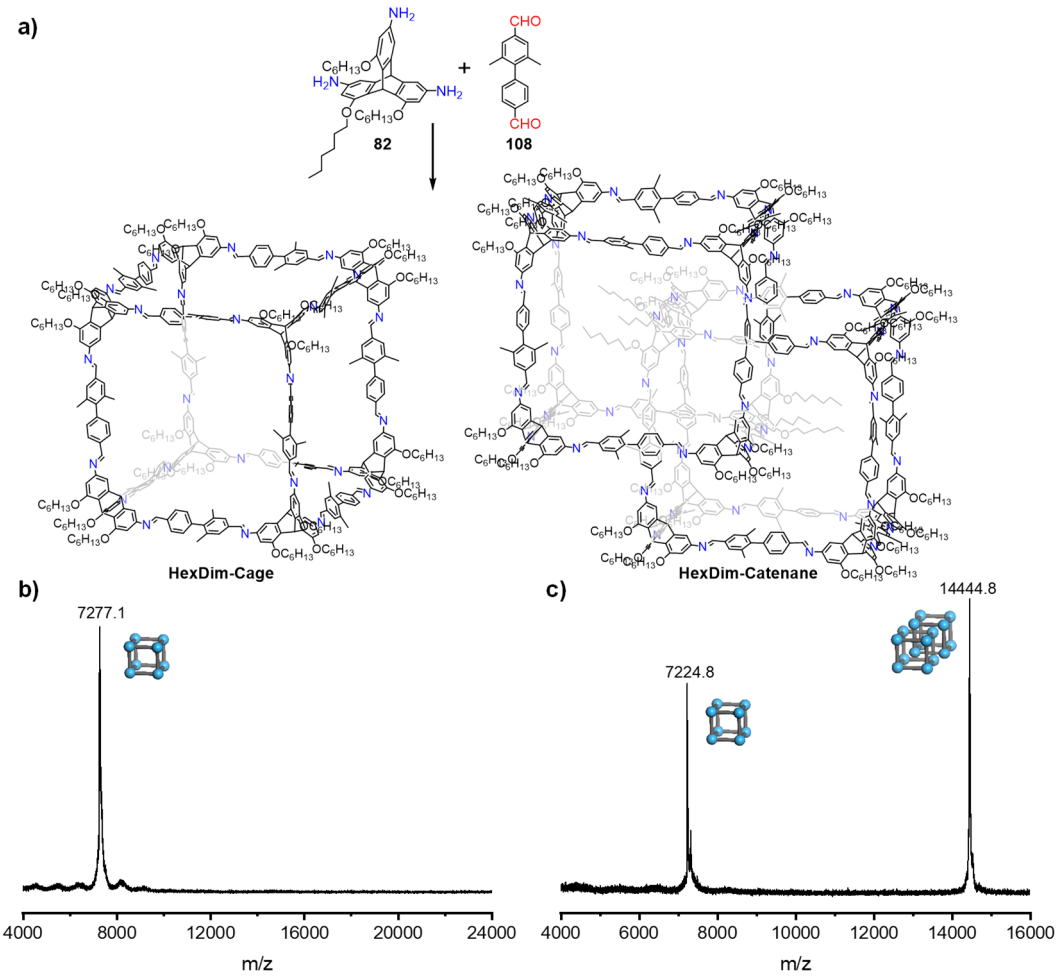

Figure 3.3.12: a) Synthesis scheme of **HexDim**-cage and **HexDim**-Catenane. MALDI MS of crude solution: a) $CHCl_3$, TFA 4 mol%, r.t, 7 days; b) $CHCl_3$/toluene = 1:1, TFA 4 mol%, r.t, 7 days.

As shown above, after changing the solvent from $CHCl_3$ to the mixture of $CHCl_3$ and toluene, the formation of catenane was observed (Figure 3.3.12 a, b). Unfortunately, the crude products of HexDim-Cage could not be dissolved anymore once precipitated, which made it difficult to work up and obtain pure products for characterization. Even though, the mass spectra showed the influence of solvent on the catenation. It indicated that the solvent factor and structural factor work simultaneously in the synthesis of IOCs. A summary of reaction results based on linkers **87**, **108**, **86**, and **104** in different solvents was shown below (Figure 3.3.13), two sets of linkers with the same length but different side chains were chosen to compare the influence of structure and solvent on catenane synthesis. First, $CHCl_3$ and THF are more suitable for the synthesis based on the linkers without side chains, while toluene and solvent mixtures worked better for the linkers with side chains. Also, when using the mixture of solvents, the different combinations decide the formation of cage or catenane. In addition, the use of a solvent mixture has a synergistic effect when synthesizing the catenane, it works much better than a single solvent.

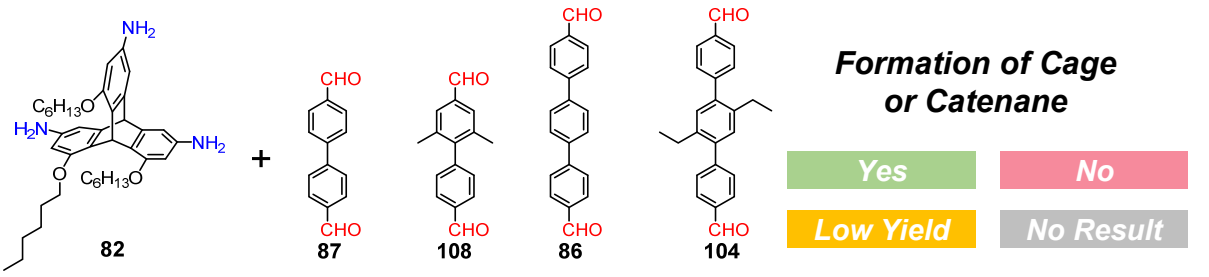

	$CHCl_3$	THF	Toluene	$CHCl_3$/Toluene	THF/Toluene
87	*Catenane*	*Cage*			*Catenane*
108	*Cage*	*Cage*		*Catenane*	
86	*Catenane*	*Catenane*			
104			*Catenane*	*Catenane*	*Cage*

Figure 3.3.13: The summary of reaction results with different linkers and solvents.

Overall, the syntheses of cages or catenanes are influenced by several factors, and these factors are not independent in most cases. For example, adding a side chain changes the structure and also the solubility of monomeric cages at the same time, the structural difference not only leads to the different interactions between the monomeric cages but also the different interactions between reactants, fragments, and solvents. That makes it more complicated to optimize the synthesis of IOCs and investigate the catenation mechanism. Therefore, it requires the researcher to control the number of possible factors when designing structures and planning the conditions for IOCs synthese.

3.3.6 Conclusion

In conclusion, solvents play a crucial role in the synthesis of IOCs, it not only provides the reaction environment but also influence the catenation procedure. Besides, the experimental results remind us that the formation of IOCs was influenced by several factors, the synthesis of catenane with different structures requires different solvents. Interestingly, adopting the mixture instead of single solvents was found to be an effective strategy to synthesize IOCs. The solvent mixtures were working synergistically. This finding also provides a new direction for adjusting the condition when having similar problems with the synthesis of IOCs. Even though, how these solvents work during the reaction procedure and why they could decide the catenation of the monomeric cage are still not clear. That requires more effort and a more detailed investigation of the mechanism. In addition, the influence of the ratio of the solvent mixture will be further discussed in *Chapter 3.4*.

3.4 The Controllable Synthesis and Isolation of Polycatenanes

3.4.1 Introduction

Mechanically interlocking has been regarded as an unprecedented method to construct infinite polymers or frameworks since first reported,[3, 78] However, the synthesis of such materials remains a significant challenge. Although some polycatenanes, ploythreads, polyknots, and the polycatenation of ICCs have been reported over the past decades,[78] the ploycatenane[1] based on organic cages has not been achieved yet. On the one hand, most organic polymers, are in a solid state after the reaction, which is the same for polycatenanes. Since it is always challenging to obtain single crystals of such organic polymers, there is no sufficient method to characterize the solid and prove it is a polycatenane rather than a random polymer. On the other hand, the construction of polycatenane requires an appropriate shape of a used cage as well as the presents of a cavity, to hold two other cages together.[25, 68-69] But the most reported IOCs consist of small monomeric cages, and the dimers are, generally, the favored products. For bigger monomeric cages, there are more possibilities to extend the structure and the situation is more complex. The formation of monomeric cages requires a homogeneous reaction environment,[51a, 79] Therefore, the synthesis of a polycatenane is hardly achievable, as the formation of the latest most likely leads to the formation of a precipitate. Overall, the synthesis of IOCs based on giant monomeric cages and a mechanism of their catenation requires deep investigations and tremendous afford.

In addition, since obtaining the polycatenane remains a challenge, it is more practical first to explore the simpler system, for example, the synthesis of oligomers with a lower catenation degree. In the previous experiments (*Chapters 3.1, 3.2,* and *3.3*), the trimer and tetramer have already been observed on the mass spectra. It was found that the structure of monomeric cages, the choice of solvents, and the ratio of building blocks all influenced the catenation degree. Likely, it is possible to perform a controllable target synthesis and isolate the oligomers with the desired degree of catenation degree by adjusting reaction conditions.

3.4.2 The Ratio of Solvent Mixture and the Amount of Building Blocks Influence on Catenation Degree

In *Chapter 3.3*, when investigating the solvent effects on the synthesis of catenane based on diethyl terphenyl dialdehyde **104** and triptycene triamine **82**, the formation of trimer and

[1] The following 'polycatenane' all refer to the polycatenane based on organic cages, moreover, the "polycatenane" in the title of this chapter is not exact polymer, it is more close to oligomer with low catenation degree.

tetramer species was observed on the mass spectrum. In addition, these syntheses were conducted in the mixture of $CHCl_3$ and toluene, and it was found that the formation of the products was also influenced by the ratio of the solvent mixture (Figure 3.4.1). Herein, the mixture of $CHCl_3$/toluene (1/1) was further tested for the synthesis HexDie-Catenane (Table 3.4.1).

Table 3.4.1 Screening the ratio of solvent mixtures for the synthesis of **HexDie**-Catenane

$CHCl_3$/toluene	Temperature	TFA	Concentration[a]	Reaction Time	Products Detected by MS
2:1	r.t	4 mol%	5.3 mM	7 d	Figure 3.4.1 b
1:1	r.t	4 mol%	5.3 mM	7 d	Figure 3.4.1 c
1:2	r.t	4 mol%	5.3 mM	7 d	Figure 3.4.1 d

a. Concentration of triptycene triamine **82**.

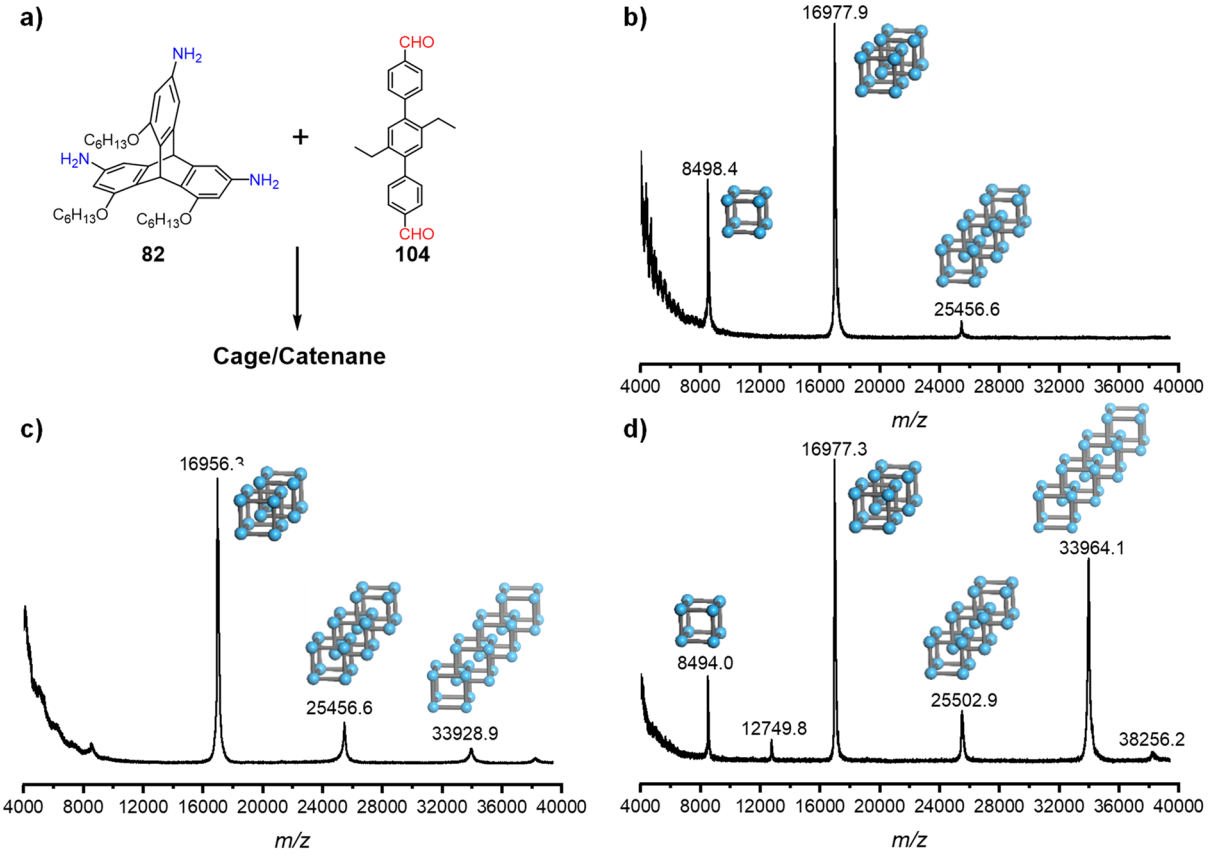

Figure 3.4.1: a) Synthesis of **HexDie**-Catenane; b-d) Mass spectra of the crude solutions under different conditions (Table 3.4.1). The calculated mass of the monomeric cage is 8468.959.

According to the mass spectra, the molecular weight of products became bigger as the amount of toluene increased. In the previous chapter, it was also found that when using pure toluene, only a small peak of the dimer was found on the mass spectrum and most of the products are insoluble solids, which is probably due to the high catenation degree leading to the formation of polymers. Unfortunately, there is not enough evidence to show that this is the case. In addition, by adjusting the proportion of the solvent mixture, it became possible to detect the intermediate oligomers (Figure 3.4.1d). However, under these conditions, several species were

detected in the crude solution, which cause problems for further isolation and purification. Thus, it is necessary to optimize conditions to selectively synthesize desired oligomers. Before performing a more elaborate investigation of the solvent mixtures, it is worth mentioning that according to the results in *Chapter 3.1*, using a relatively more amount of triamine promotes the formation of trimer catenane. Therefore, the amount of building block was further screened (Table 3.4.2), which was conducted in the mixture of $CHCl_3$ and toluene in a 1:1 ratio.

Table 3.4.2 Screening the amount of building blocks **82** in the synthesis of Catenane

76:**99**	Temperature	TFA	Concontration[a]	Reaction Time	Products Detected by MS
7:12	r.t	4 mol%	4.6 mM	7 d	Dimer
8:12	r.t	4 mol%	5.3 mM	7 d	Dimer
9:12	r.t	4 mol%	5.9 mM	7 d	Dimer
10:12	r.t	4 mol%	6.6 mM	7 d	Tetramer

a. Concentration of triptycene triamine **82**.

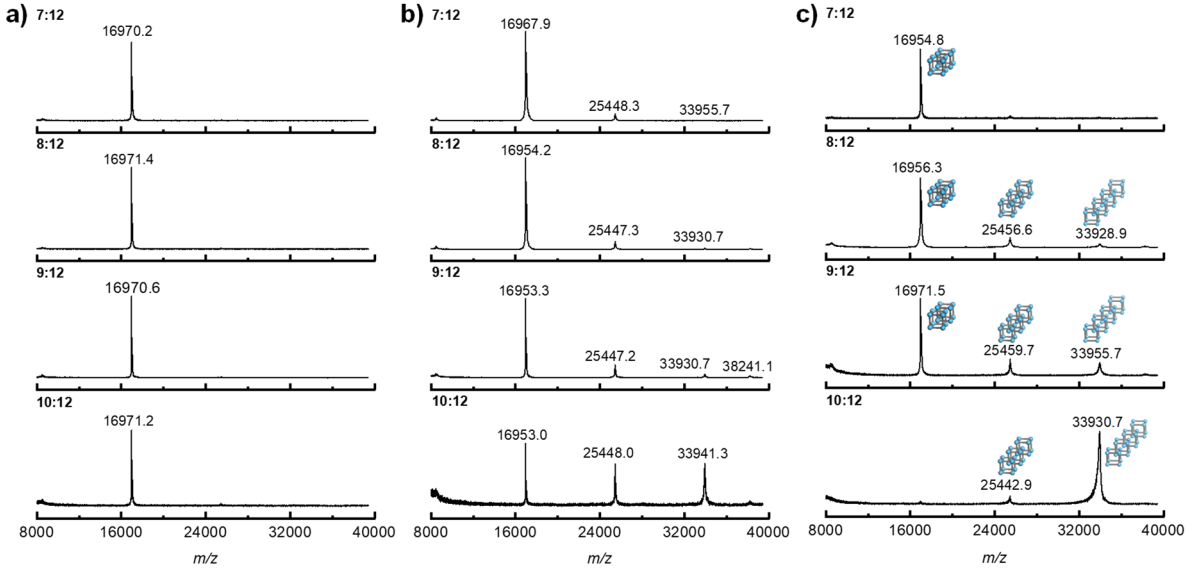

Figure 3.4.2: The MALDI MS monitoring of crude solution with different amounts of building blocks: a) after 1 day; b) after 3 days; c) after 7 days. The calculated exact mass of the monomeric cage is 8468.959.

The mass spectra above showed that the ratio of building blocks significantly influenced the catenation degree, only [16+24] dimer was detected when the ratio was 7:12, and the main product became the [32+48] tetramer species after increasing the amount of triamine **76** (10:12) (Figure 3.4.2 c). Moreover, under these two conditions, nearly only one product was detected on the mass spectrum, which means it is possible to synthesize selectively the specific oligomers by controlling the amount of starting materials. In addition, the main peaks are [16+24] species under all conditions after one day (Figure 3.4.2 a), and the main products, especially the product of 10:12 ratio, gradually transit into oligomers with a higher catenation degree three days later (Figure 3.4.2 b). The product of 7:12 is always the same while almost only tetramer is left with the 10:12 ratio after seven days (Figure 3.4.2 c). It indicated that the catenation procedure is also highly dependent on the reaction time.

Interestingly, the peak of the [40+60] specie, which refers to the pentamer, was also detected on the mass spectrum, but the peak was tiny and disappeared for a longer reaction time (Figure 3.4.2 b). One possible reason is that these species become bigger oligomers, which exceed the detection limits (40000), and need to be further investigated with MS monitoring. Another possibility is that the catenation process is a kinetically controlled reaction. Because these oligomers were the local minimum thermal favored products, their formation of them was controlled by the reaction conditions. For example, better solubility is beneficial to the formation of bigger oligomers. Therefore, the triptycene triamine substituted with decyloxy **77**, butyloxy **106**, and proxyloxy **75** were tested in the context of the solubility on the catenation degree, as long alkyl chains may significantly change the solubility of the monomeric cages and the corresponding oligomers.

3.4.3 The Exploration of Different Building Blocks

When using the 1,8,13-tridecyloxy-3,6,15-triaminotriptycene **77** as the building block, under the same conditions, there was no tetramer observed anymore, and the peaks of dimer and trimers were also quite weak (Figure 3.4.5).

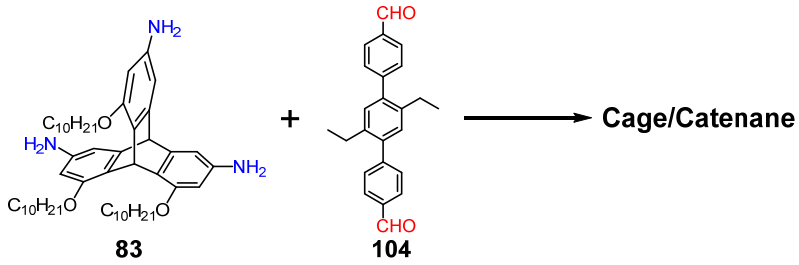

Scheme 3.4.3: The synthesis of Catenane with building blocks **83**.

Table 3.4.3 Screening the amount of building blocks **83** in the synthesis of Catenane

76:**99**	Temperature	TFA	Concontration[a]	Reaction Time	Products Detected by MS
7:12	r.t	4 mol%	4.6 mM	7 d	Figure 3.4.4
8:12	r.t	4 mol%	5.3 mM	7 d	
9:12	r.t	4 mol%	5.9 mM	7 d	
10:12	r.t	4 mol%	6.6 mM	7 d	

a. Concentration of triptycene triamine **83**.

Although there is also the factor that the length of decyloxy is longer than hexyloxy, which also may increase the steric hindrance and prevent the formation of oligomers. However, comparing the spectrum of crude solution at a 10:12 ratio, the intensive peak of the dimer decreased for a longer reaction time. and the formation of the trimer was also observed, which means it could form the bigger oligomers, otherwise, the main peak should be the dimer. Therefore, the reason tends to be that the longer alkyl chains increase the solubility of the monomeric cage and make it form bigger oligomers.

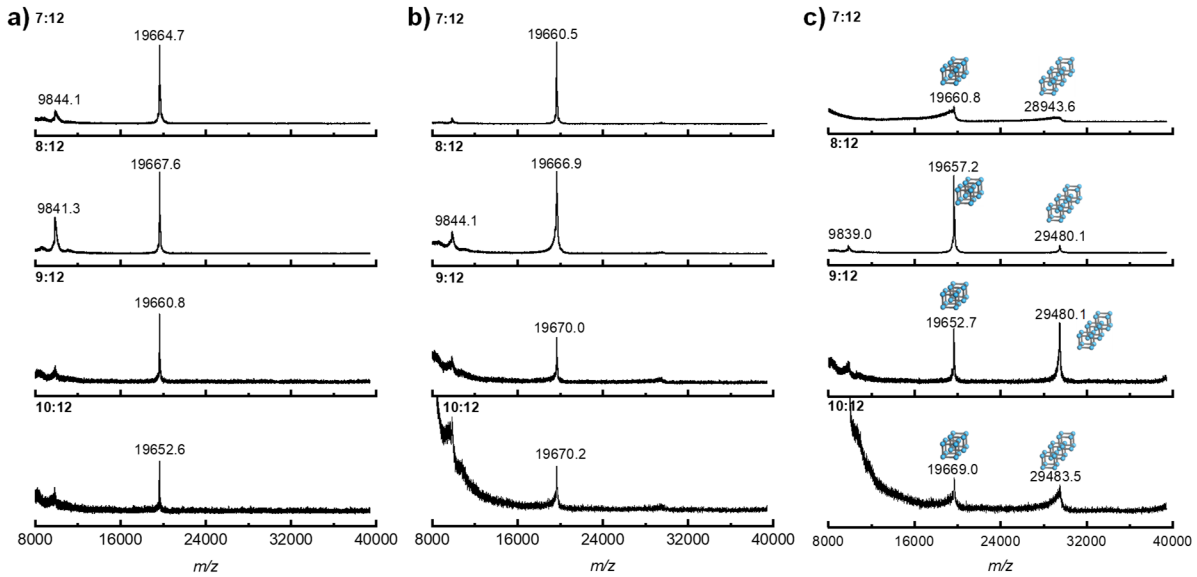

Figure 3.4.4: MALDI MS monitoring of crude solution with different amounts of building blocks: a) after 1 day; b) after 3 days; c) after 7 days. The calculated mass of the monomeric cage is 9814.462.

For building blocks **106** and **75** (the difference between butyloxy and propoxyl does not influence the reaction outcome), the mass spectrum showed a remarkably single and intensive peak of tetramer at a 10:12 ratio. Moreover, only one peak was observed at a 9:12 ratio (Figure 3.4.5b&c) in comparison with the result of the building blocks **76** (Figure 3.4.2c, 9:12). In addition, there is a dimer and a trimer observed under different conditions, but as increasing the amount of triamine, they all disappeared and only tetramer left.

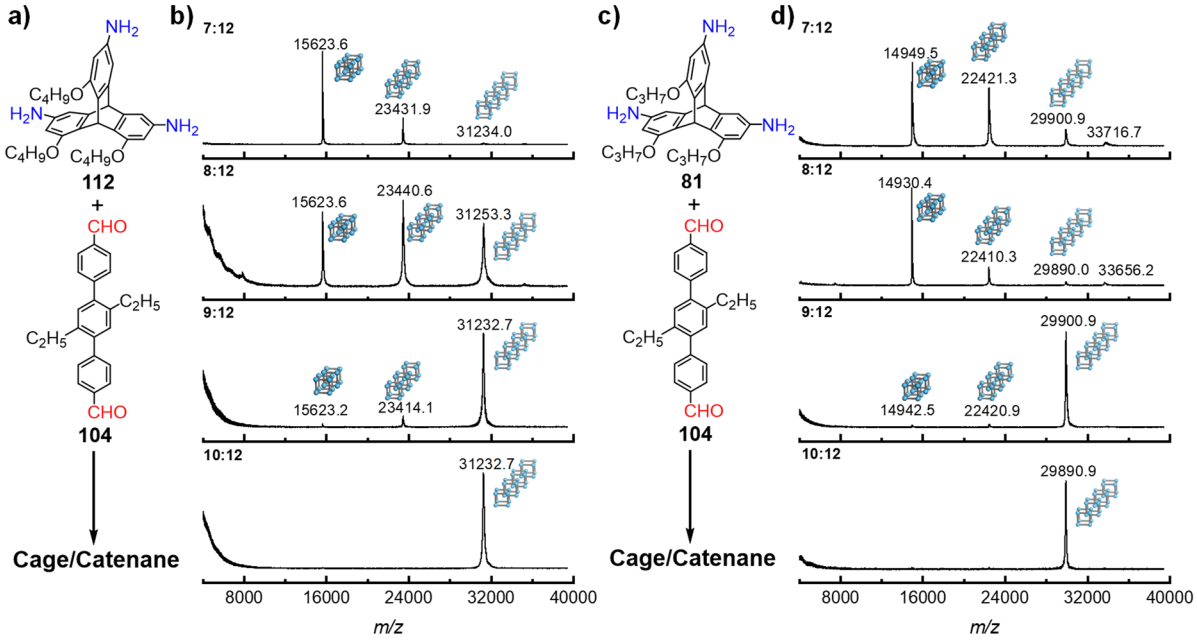

Figure 3.4.5: The synthesis of Catenane based on a) **112** and c) **104**, the reaction conditions are the same with Table 3.4.3. The MALDI MS monitoring of crude solution with different amounts of building blocks after 7 days: b) building block **112**; c) building block **81**. The calculated Exact Mass of monomeric cages is 7801.220 and 7464.850 respectively.

Besides the tetramer, the mass spectra of the reaction based on building blocks **106** (Figure 3.4.5b, 8:12) also show the formation of trimer and dimer, and the intensity of each peak is comparable. Moreover, by adjusting the ratio of building blocks from 7:12 to 10:12, the distribution of the products shows a clear low-to-high trend, which is better for further isolating the trimer and dimer by controlling the conditions (Figure 3.4.5b). As well as considering its slightly better solubility in comparison with building block **75**, the following investigations will be performed on building block **106**. Herein, the amount of catalyst was further investigated (Table 3.4.4).

Table 3.4.4 Screening the amount of TFA for the synthesis of **ButDie**-[4]Catenane

$CHCl_3$/toluene	**112**/**104**	Temperature	TFA	Concentration.[a]	Products Detected by MS
1:1	10:12	r.t	4 mol%	6.6 mM	Figure 3.4.6 a (1 d), A (7 d)
1:1	10:12	r.t	8 mol%	6.6 mM	Figure 3.4.6 b (1 d), B (7 d)
1:1	10:12	r.t	12 mol%	6.6 mM	Figure 3.4.6 c (1 d), C (7 d)

a. The concentration of 1,8,13-Tributyloxy-3,6,15-triaminotriptycene **112**.

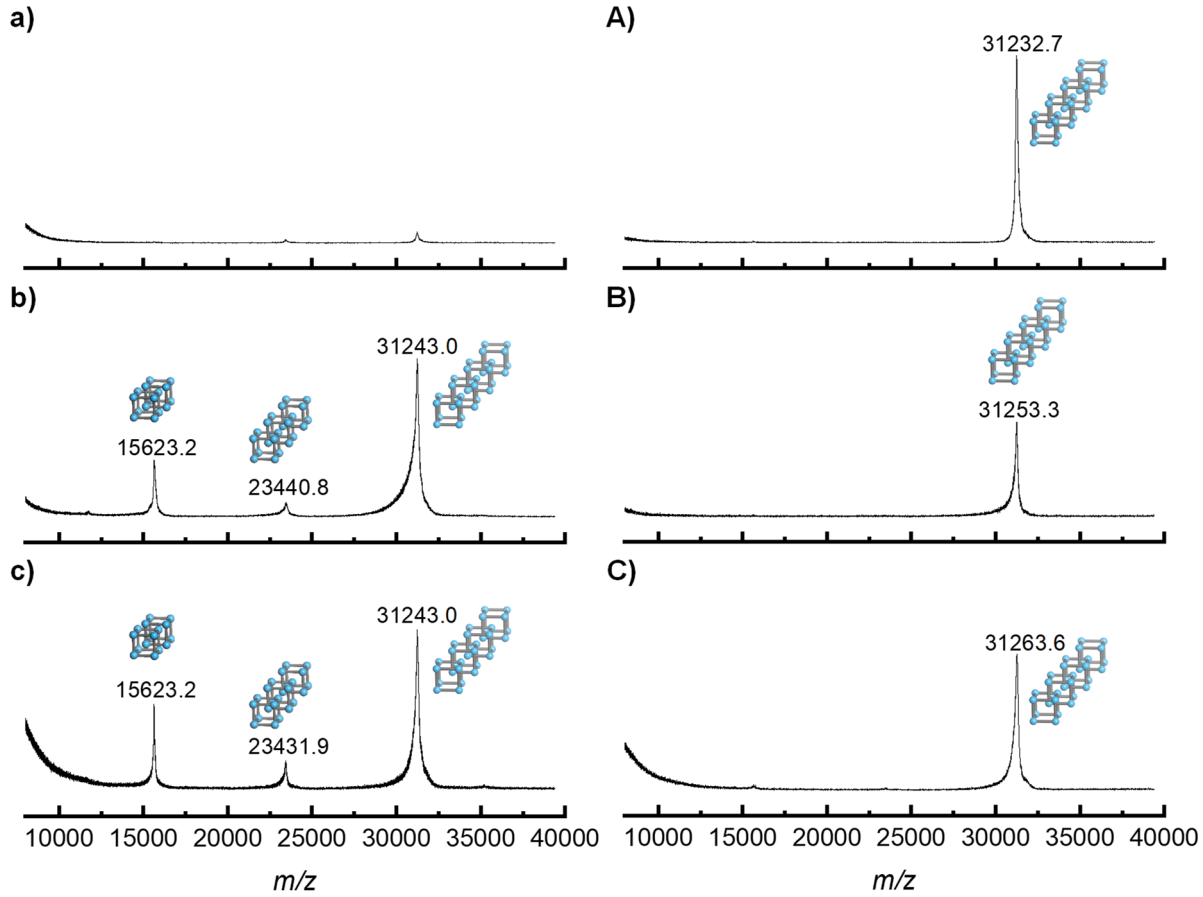

Figure 3.4.6: The MALDI MS monitoring of crude solution with different amounts of TFA: a-c) after 1 day; A-C) after 7 days. The calculated Exact Mass of monomeric cages is 7801.220.

As the MALDI mass spectra showed, the increase of TFA indeed accelerate the reaction rate (Figure 3.4.6a), but it made no difference to the final products which are all tetramer. However, it was observed that there were more precipitates formed by adding more TFA, which

significantly depress the yield of the tetramer. Therefore, 4 mol% TFA is more suitable for the synthesis of tetramer although it requires a longer reaction time.

Thence, the ButDie-[4]Catenane was synthesized with 4 mol% TFA in the mixture of $CHCl_3$ and toluene in a 1:1 ratio, the reaction was stirred at room temperature for 7 days (Figure 3.4.7a). After the reaction, there is a little brown insoluble solid formed and attached to the wall of the vials. The crude solution precipitated with methanol, and after centrifuging, the solid was collected and dissolved in THF for GPC purification.

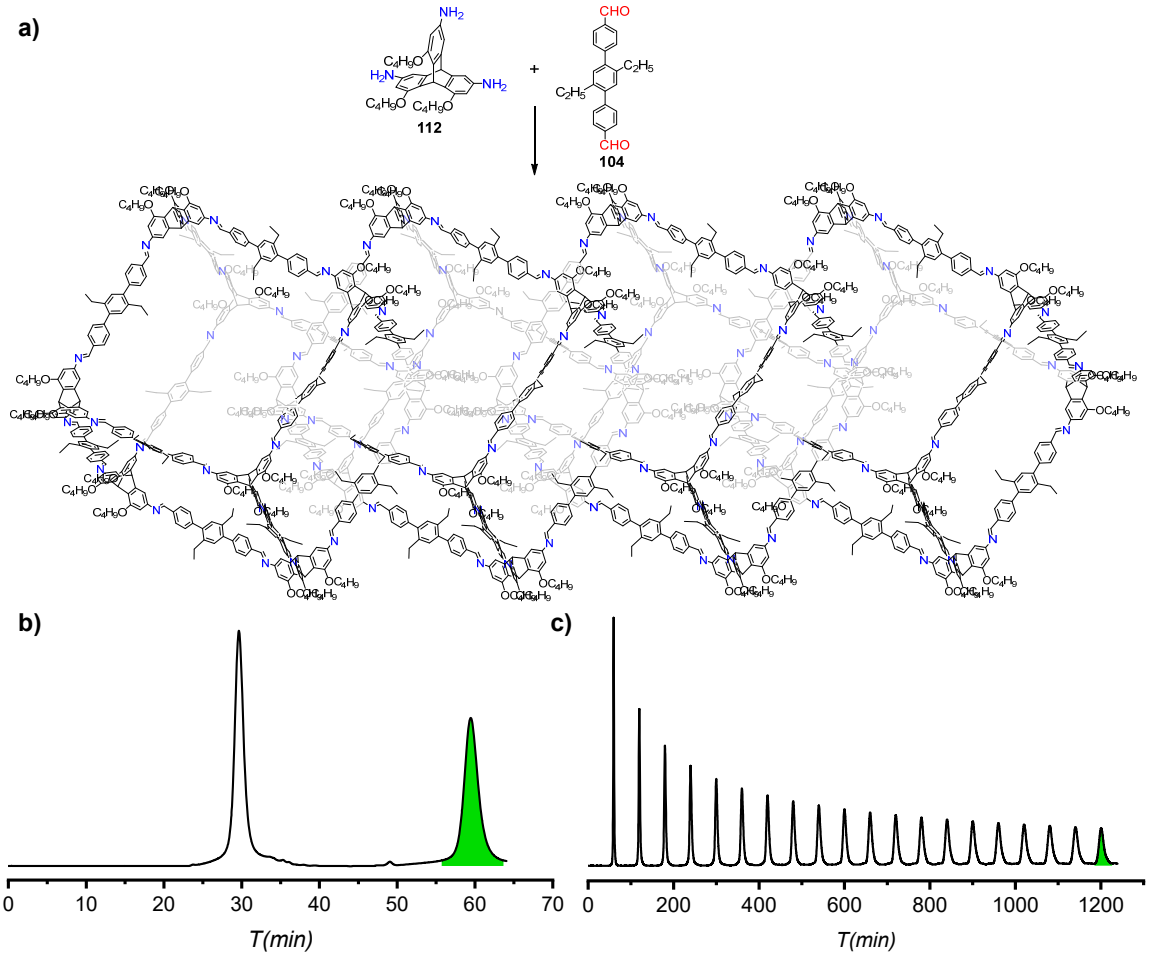

Figure 3.4.7: a) Synthesis of **ButDie**-[4]Catenane ($CHCl_3$/toluene = 1/1, **112**/**104** = 10/12, TFA 4 mol%, r.t, 7 days); b) The r-GPC chromatogram (THF, 6 mL/min, 40 °C, 2×1000 Å + 2×500 Å columns) of the crude products; c) Second purification of green fraction collected in b) (THF, 3 mL/min, 40 °C, 2×1000 Å + 2×500 Å columns).

Based on the GPC chromatogram of the crude product, there were not many fragments and oligomers formed after the reaction (Figure 3.4.7b), the main fraction was collected and concentrated for the second purification by r-GPC. After twenty cycles, the main product is still tetramer catenane (Figure 3.4.7c), which was obtained in 25% yield. It also indicated that the tetramer is the thermodynamically more stable product. The obtained ButDie-[4]Catenane was employed to prepare the single crystals, however, no sufficient data was collected yet. To figure out the conformation of the tetramer, the 2D NMR was measured.

3.4.4 ^{1}H NMR Assignment for ButDie-[4]Catenane

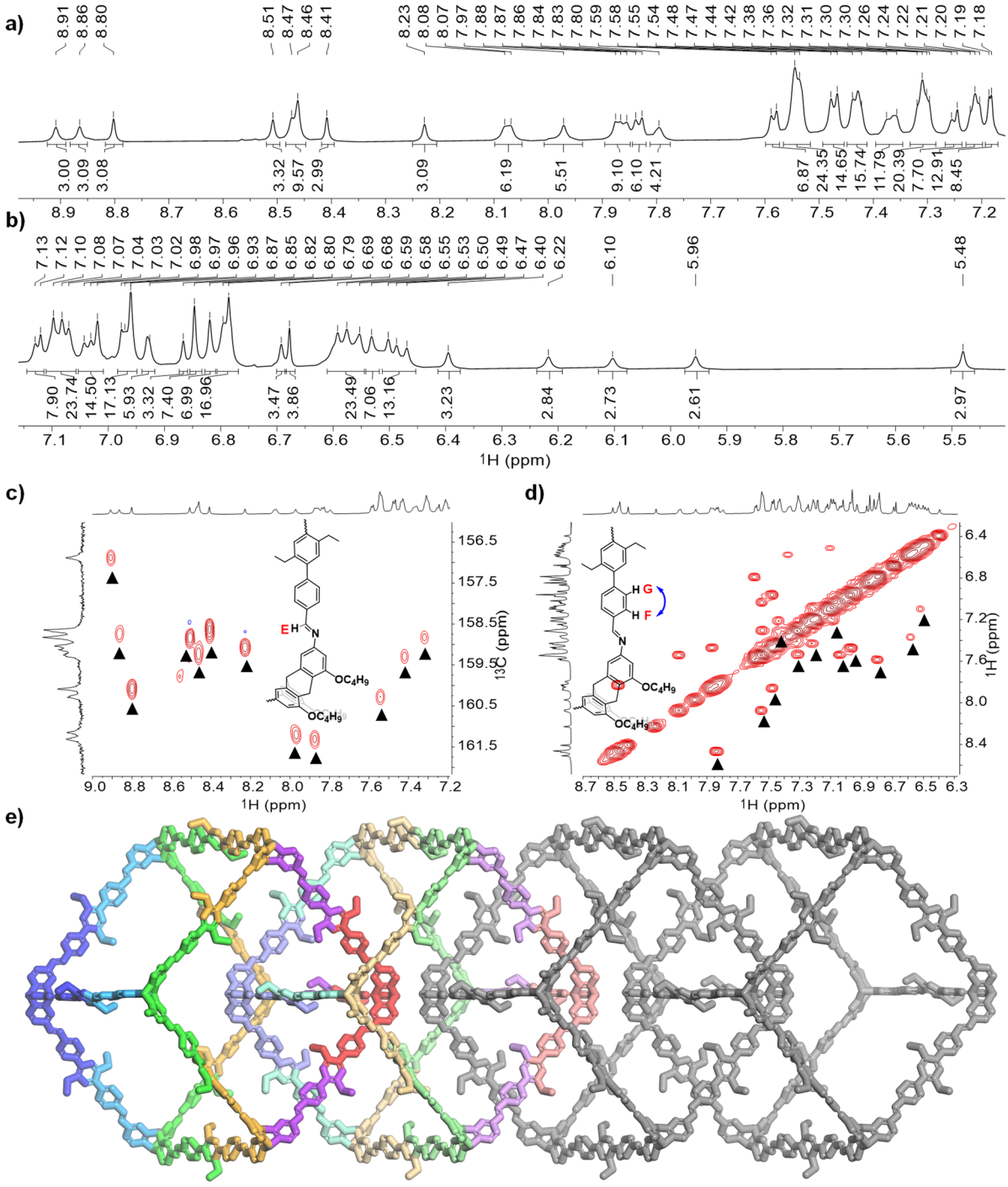

Figure 3.4.8: a, b) Partial ^{1}H NMR Spectrum (700 MHz, 303K) of **ButDie**-[4]Catenane in CD_2Cl_2; c) Partial ^{1}H-^{13}C HSQC spectrum showing the imine proton peaks; d) Partial ^{1}H-^{1}H COSY spectrum showing the neighboring phenyl protons; e) The model of triply interlocked cages, colored structure indicate the symmetry of **ButDie**-[4]Catenane, the outer chains were cleaved for clarity. Black triangles mark the signals.

The THF-*d*$_8$ and CD_2Cl_2 were employed to measure the 2D NMR at 333K and 303K respectively. The resolution of proton NMR with both deuterated solvents is quite similar while the 2D spectra with CD_2Cl_2 were better, therefore, the following discussions are all based on the results in CD_2Cl_2. Similar to the integration of the NMR spectrum of dimer and trimer in

Chapter 3.4, it was found that there are twelve different imine peaks exist according to the ^{1}H-^{13}C HSQC spectrum (Figure 3.4.8d), correspondingly, twelve pairs of neighboring aromatic protons were also indicated by the ^{1}H-^{1}H COSY spectrum (Figure 3.4.8e). This [12]-symmetry fits the linear triply interlocked conformation (Figure 3.4.8f). Another piece of evidence was inferred by the relationship of the protons on triptycene (position A and B in Figure 3.4.9 c). Interestingly, according to the symmetry of ButDie-[4]Catenane, there should be two situations on the ^{1}H-^{13}C HMBC spectrum: one proton peak corresponds to one bridge ^{13}C peak (Figure 3.4.9 b, C_1 to a_1); two proton peaks correspond to one bridge ^{13}C peak (Figure 3.4.9 b, C_1 and C_2 to a_2).

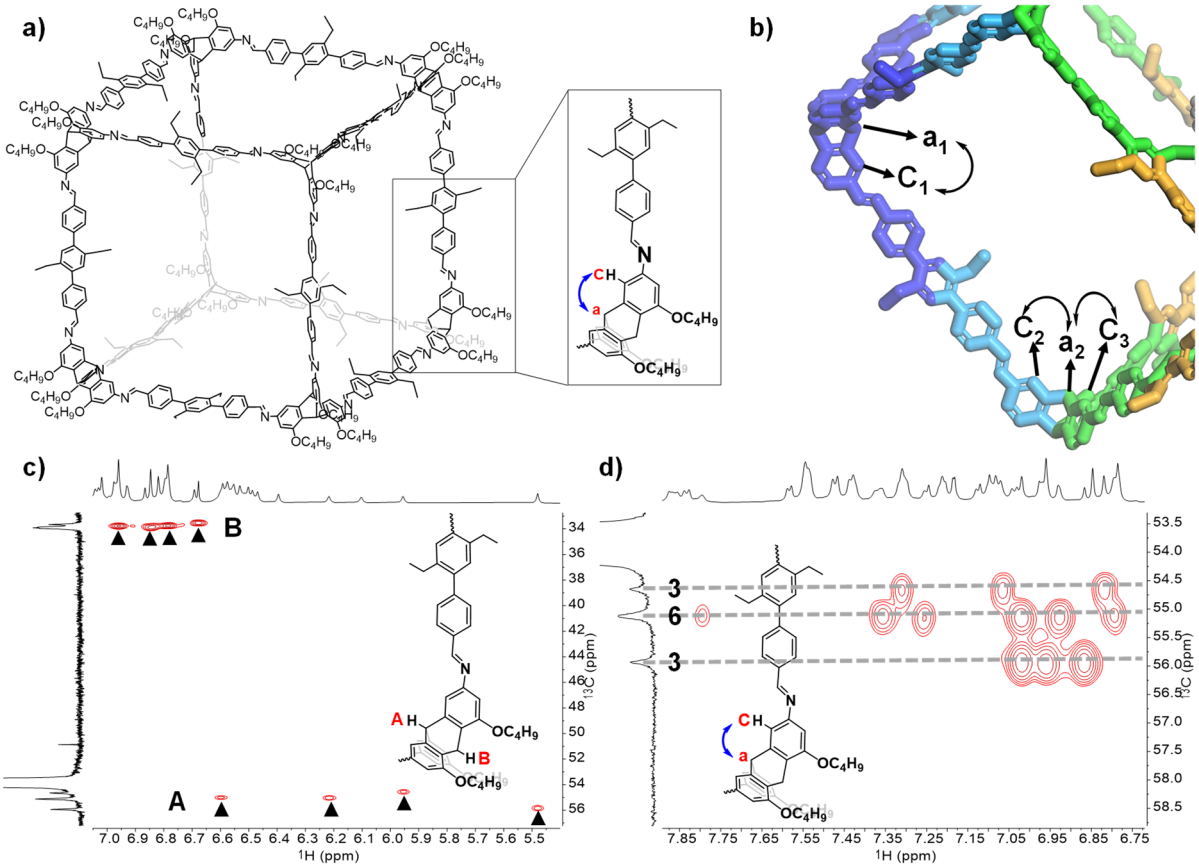

Figure 3.4.9: a) Partial ^{1}H-^{13}C HSQC spectrum showing peaks of protons on the bridge of triptycene, the position was marked by letters; b) Partial ^{1}H-^{13}C HMBC spectrum of the aromatic protons on the arm of triptycene which close to the protons on the bridge. Black triangles mark the signals.

In principle, there should be eight ^{13}C peaks and twelve signals on ^{1}H-^{13}C HMBC spectrum (four peaks correspond to one signal, and another four correspond to two signals). Unfortunately, due to the peaks overlapping, it is not possible to figure out the exact positions. The ^{1}H-^{13}C HSQC spectrum (Figure 3.4.9 c) showed that there were eight different peaks of protons on the bridge of triptycene, four of them correspond to the protons inside the monomeric cage, and the rest four are outside the cage. They are overlaid because there should be sixteen peaks (8/8) according to the symmetry. However, the ^{1}H-^{13}C HMBC spectrum

correctly showed twelve signals which refer to the correlation between the aromatic protons on the arm of triptycene and the carbons on the bridge (Figure 3.4.9 d). That also fits the symmetry of the tetramer catenane and proves the triply interlocked structure. Moreover, the signals were divided into four sets (4 × (1+2)), which also conforms to the inference above (Figure 3.4.9 d).

After figuring out the symmetry of ButDie-[4]Catenane, attempts were made to assign these peaks to the corresponding protons. According to the numbered imine protons, the neighboring aromatic protons on linkers should also be identified. However, due to the complex structure of ButDie-[4]Catenane, the resolution of the ^{13}C NMR spectrum is low, especially for the peaks of aromatic carbons, a lot of signals are indistinguishable, and the information is not sufficient to resolve the correlation between them (Figure 3.4.10 b). The neighboring aromatic protons also could not be assigned (Figure 3.4.10 a).

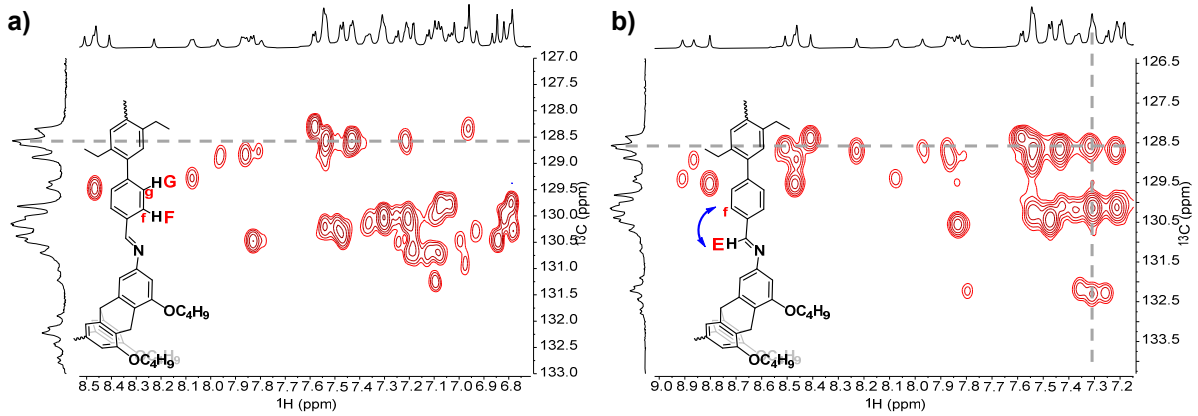

Figure 3.4.10: a) Partial ^{1}H-^{13}C HSQC spectrum showing the correlation between aromatic protons and the corresponding ^{13}C peaks; b) Partial ^{1}H-^{13}C HMBC spectrum showing the correlation between imine protons and neighboring aromatic carbons. The letters mark the position; Numbers show the relation between them; Dotted lines illustrate the indistinguishable signals.

Overall, the 12-symmetry of the ButDie-[4]Catenane was proven by 2D NMR experiments, which also revealed its linear triply interlocked conformation. However, due to the complexity of the formed catenane, it is not possible to assign every peak correctly.

3.4.5 The Synthesis and Separation of Trimer and Dimer Catenane

As mentioned before, when using triptycene triamine **106** as the building block and adjusting the ratio of starting materials, it was found that the products showed a gradual distribution from dimer, trimer to tetramer (Figure 3.4.5 b, 8:12), which indicated that it is possible to isolate these products by changing the conditions. Therefore, more ratios of solvent mixtures (Table 3.4.5) were explored using an 8:12 ratio of building blocks. As the mass spectra showed below, as adjusting the ratio of $CHCl_3$/toluene from 5:1 to 1:5, the distribution of products also gradually moved toward tetramer. Moreover, in comparison with the results when the solvents

mix ratio was 1:1 (Figure 3.4.5 b, 8:12), no peaks of tetramer were observed in the solvent mixture of 2:1 ratio, and the main products are the dimer and trimer (Figure 3.4.11 c).

Table 3.4.5 Screening the ratio of solvent mixture for the synthesis of **ButDie-[3]Catenane**

$CHCl_3$/toluene	Temperature	TFA	Concontration[a]	Reaction Time	Products Detected by MS
5:1	r.t	4 mol%	5.3 mM	7 d	Dimer & Trimer
2:1	r.t	4 mol%	5.3 mM	7 d	Dimer & Trimer
1:1	r.t	4 mol%	5.3 mM	7 d	Dimer,Trimer & Tetramer
1:2	r.t	4 mol%	5.3 mM	7 d	Tetramer
1:5	r.t	4 mol%	5.3 mM	7 d	Tetramer

a. Concentration of triptycene triamine **106**.

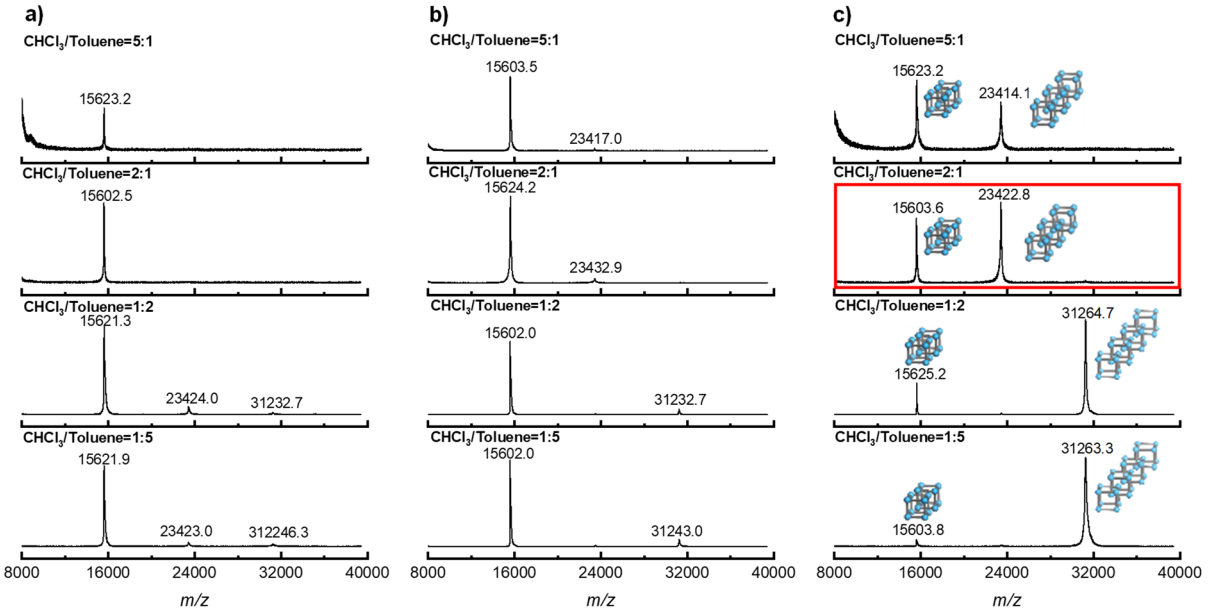

Figure 3.4.11: MALDI MS monitoring of crude solution with different solvent mix ratios: a) after 1 day; b) after 3 days; c) after 7 days. The ratio of building blocks is 8:12 (**106**:**96**). Calculated Exact Mass of the monomeric cage is 7801.220. The red box shows the ratio for further optimizations.

The reduction of the tetramer significantly facilitates subsequent purification and isolation of the trimer. Even though, this condition needs to be further optimized to improve the yield of the trimer since there were still lots of dimers formed simultaneously. According to the previous study, increasing the amount of triamine could promote the formation of catenane with a higher catenation degree. Thus, the ratio of building blocks was further explored in the mixture of $CHCl_3$/toluene in a 2:1 ratio (Table 3.4.6).

Table 3.4.6 Screening the amount of building blocks **106** in the synthesis of **ButDie-[3]Catenane**

106/96	Temperature	TFA	Conc.[a]	Reaction Time	Products Detected by MS
7:12	r.t	4 mol%	4.6 mM	7 d	Dimer
8:12	r.t	4 mol%	5.3 mM	7 d	Dimer & Trimer
9:12	r.t	4 mol%	5.9 mM	7 d	Dimer,Trimer & Tetramer
10:12	r.t	4 mol%	6.6 mM	7 d	Tetramer

a. Concentration of triptycene triamine **112**.

By MALDI MS monitoring, it was found that the relative intensity of the trimer indeed increased as adding more triamine **106**. When using a 10:12 of the building block **106** and **96**,

although there are small peaks of tetramer and dimer left, the main product is already trimer, which was also further proved by the GPC chromatogram (Figure 3.4.13 b). Besides, only the dimer peak was obtained on the mass spectrum when using the 7:12 of building blocks, and it should be the proper condition for dimer synthesis.

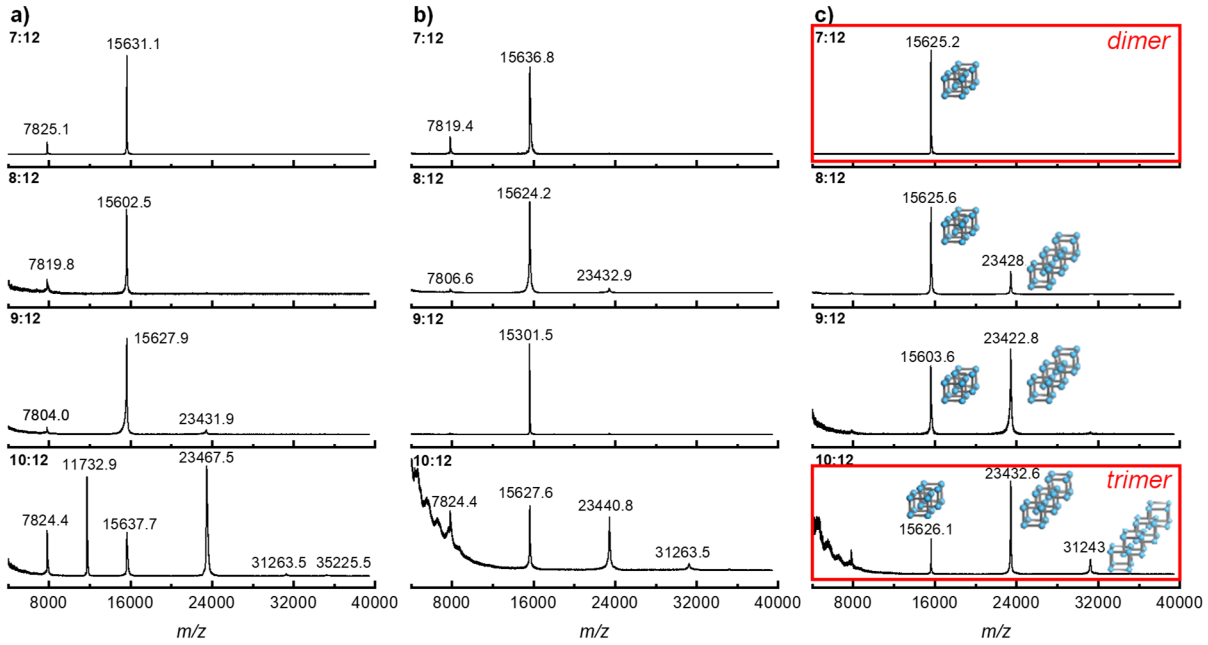

Figure 3.4.12: MALDI MS monitoring of crude solution with different solvent mix ratios: a) after 1 day; b) after 3 days; c) after 7 days. The solvent mix ratio is 8:12 ($CHCl_3$/toluene**)**. The calculated Exact Mass of the monomeric cage is 7801.220. Red boxes show the ratio for the synthesis of the dimer and trimer respectively.

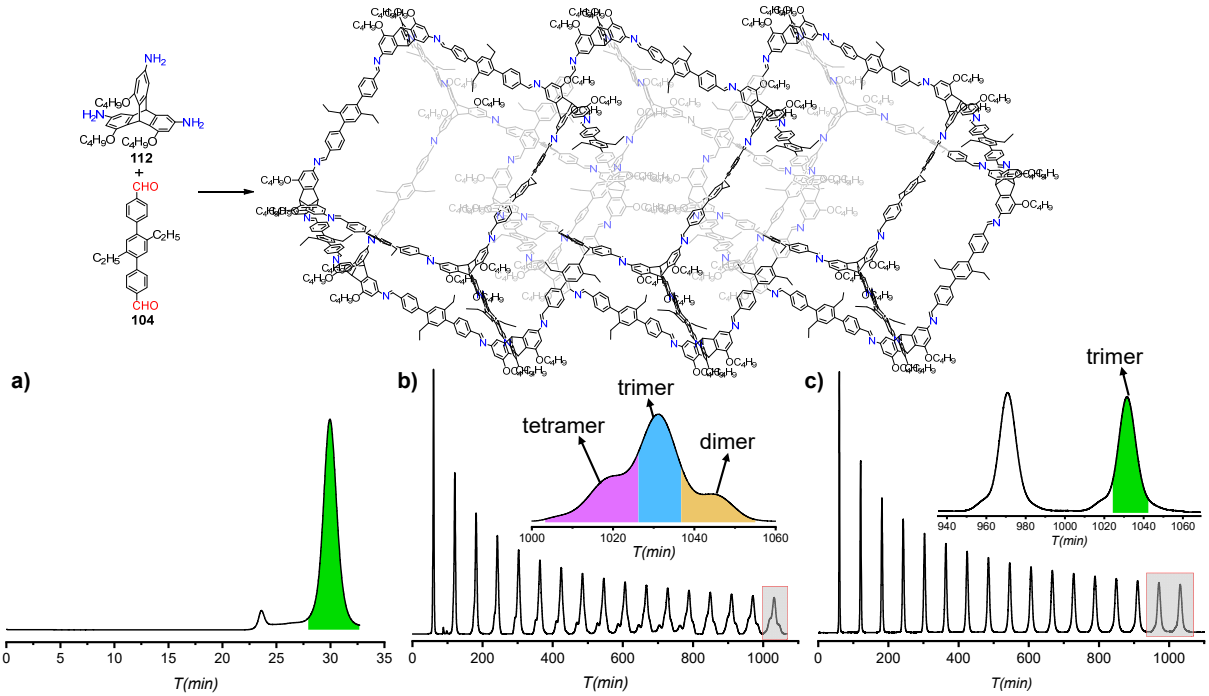

Figure 3.4.13: Synthesis of ButDie-[3]Catenane ($CHCl_3$/toluene = 2/1, **104**/**112** = 10/12, TFA 4 mol%, r.t, 7 days). a) The r-GPC chromatogram (THF, 6 mL/min, 40 °C, 2×1000 Å + 2×500 Å columns) of the crude products; b) The second purification of the fraction collected (colored in green) in a) (3 mL/min), the fraction of tetramer (colored in purple), trimer (colored in blue), dimer (colored in yellow); c) The third purification of fraction (colored in blue) collected in b), the fraction (colored in green) of the trimer.

Therefore, ButDie-[3]Catenane was synthesized in the mixture of $CHCl_3$/toluene (2:1) at room temperature, and the ratio of building blocks is 10:12. According to the GPC chromatogram, there are not many polymers that are bigger than the tetramer formed (Figure 3.4.13 a). The main fraction was collected and concentrated for the second purification, and it illustrated that the retention times of the dimer, trimer, and tetramer are quite close (Figure 3.4.13 b), which is not possible to be completely separated due to the overlay. Therefore, the fraction of trimer (colored in blue) was purified for the third time (Figure 3.4.13 c).

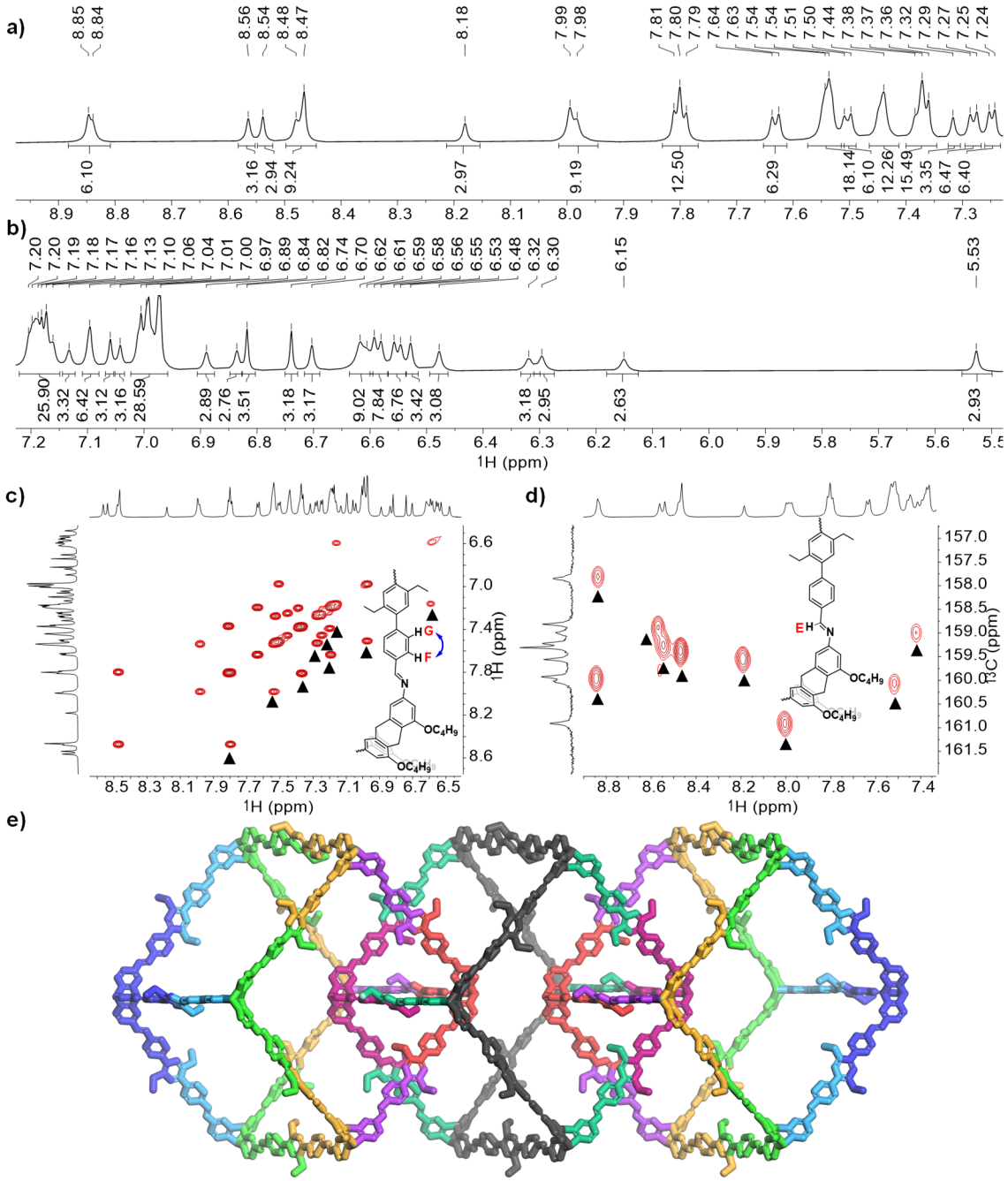

Figure 3.4.14: a, b) Partial ^{1}H-NMR Spectrum (700 MHz, 295 K) of **ButDie**-[3]Catenane in CD_2Cl_2; c) Partial ^{1}H-^{1}H COSY spectrum showing the neighboring phenyl protons; d) Partial ^{1}H-^{13}C HSQC spectrum showing the imine proton peaks; e) The model of triply interlocked cages, colored structure indicate the symmetry of **ButDie**-[3]Catenane, the outer chains were cleaved for clarity. Black triangles mark the signals.

According to the ^{1}H-^{13}C HSQC spectrum, it was found that there were nine different imine peaks (Figure 3.4.14 c), as well as nine signals at the aromatic region of the ^{1}H-^{1}H COSY spectrum, which correspond to the neighboring aromatic protons on the linkers (Figure 3.4.14 d). It indicates that the trimer is a linear triply interlocked structure (Figure 3.4.14 e). Similarly, the resolution of the NMR spectrum is also not sufficient for integrating these peaks correctly. therefore, it is difficult to assign them to the corresponding position.

The synthesis of ButDie-[2]Catenane was conducted in the mixture of $CHCl_3$ and toluene (2:1), the ratio of building block **106** and linker **96** is 7:12. The reaction was stirred at room temperature for 7 days, and the crude products were purified by GPC (Figure 3.4.15).

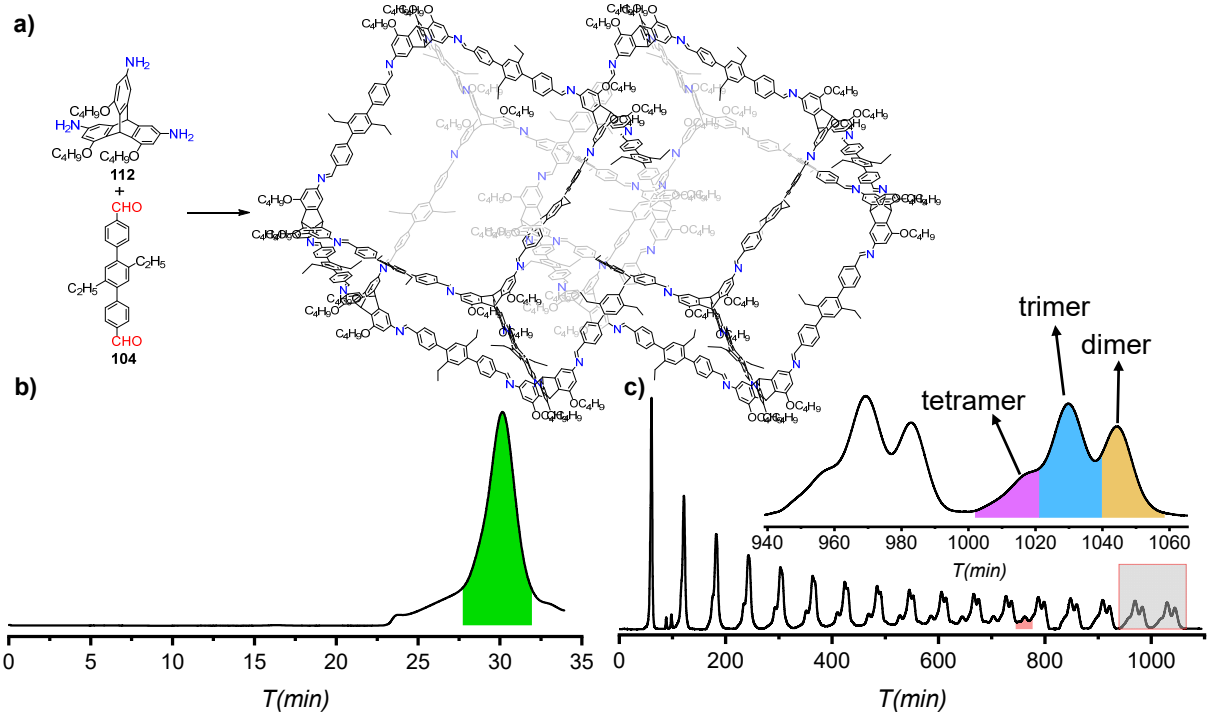

Figure 3.4.15: a) Synthesis of ButDie-[2]Catenane ($CHCl_3$/toluene = 2/1, **104**/**112** = 7/12, TFA 4 mol%, r.t, 7 days). b) The r-GPC chromatogram (THF, 6 mL/min, 40 °C, 2×1000 Å + 2×500 Å columns) of the crude products; c) Second purification of fraction (green) collected in a) (THF, 3 mL/min, 40 °C, 2×1000 Å + 2×500 Å columns). Tetramer (purple); trimer (blue); dimer (yellow); unidentified oligomers (pink).

However, the GPC chromatogram (Figure 3.4.15 c) still showed three fractions which indicate the formation of tetramer and trimer under the conditions for synthesizing dimer. The mass spectrum of the crude solution also only showed the main peak of the dimer and a tiny peak of the trimer (Figure 3.4.16 a). This result is quite similar to the dimers obtained in *Chapter 3.1*, which consist of triphenyl dialdehyde linkers. And those dimers tend to transit into bigger catenane during the preparation of the NMR samples, the same phenomenon was observed here again. After GPC separation, the mass spectrum of the dimer fraction showed a single peak of [16+24] specie (Figure 3.4.15 b). And after concentrating and measuring the NMR, the mass spectrum of the deuterated solution showed the peaks of the trimer, tetramer, and monomeric

cages (Figure 3.4.16 c). Interestingly, the tetramer had not been detected even in the crude solution. Therefore, the ^{1}H-NMR of the dimer is also not pure and could not be correctly assigned.

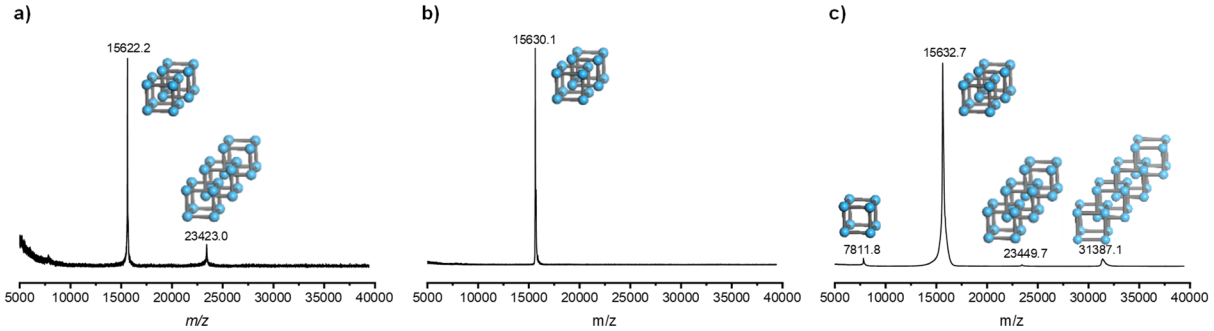

Figure 3.4.16: MALDI mass spectra: a) crude solution ($CHCl_3$/toluene = 2/1, **106**/**96** = 7/12, TFA 4 mol%, r.t, 7 days); b) dimer fraction of the GPC separation; c) deuterated solution after NMR measurement. The calculated exact mass of the monomeric cage is 7801.220.

In addition, when trying to scale up the reaction for the synthesis of ButDie-[2]Catenane and ButDie-[3]Catenane, it was found that the bigger reaction load results in the formation of larger catenanes despite concentrations of starting materials. As shown in Figure 3.4.17 a, when increasing the reaction volume from 3 mL to 15 mL, the main peaks transit from trimer to tetramer, and the yield of insoluble solids also increased. The same results were also obtained for the synthesis of the dimer, there is more trimer formed after scaling up the reaction (Figure 3.4.17 b).

Table 3.4.7 Screening the amount of building blocks **82** in the synthesis of Catenane

112:**104**	Temperature	TFA	Concontration[a]	Reaction Time	Volume	Products Detected by MS
10:12	r.t	4 mol%	6.6 mM	7 d	3 mL	Figure 3.4.17 a
10:12	r.t	4 mol%	6.6 mM	7 d	15 mL	Figure 3.4.17 b
7:12	r.t	4 mol%	4.6 mM	7 d	3 mL	Figure 3.4.17 c
7:12	r.t	4 mol%	4.6 mM	7 d	15 mL	Figure 3.4.17 d

a. The concentration of 1,8,13-Trihexyloxy-3,6,15-triaminotriptycene **82**.

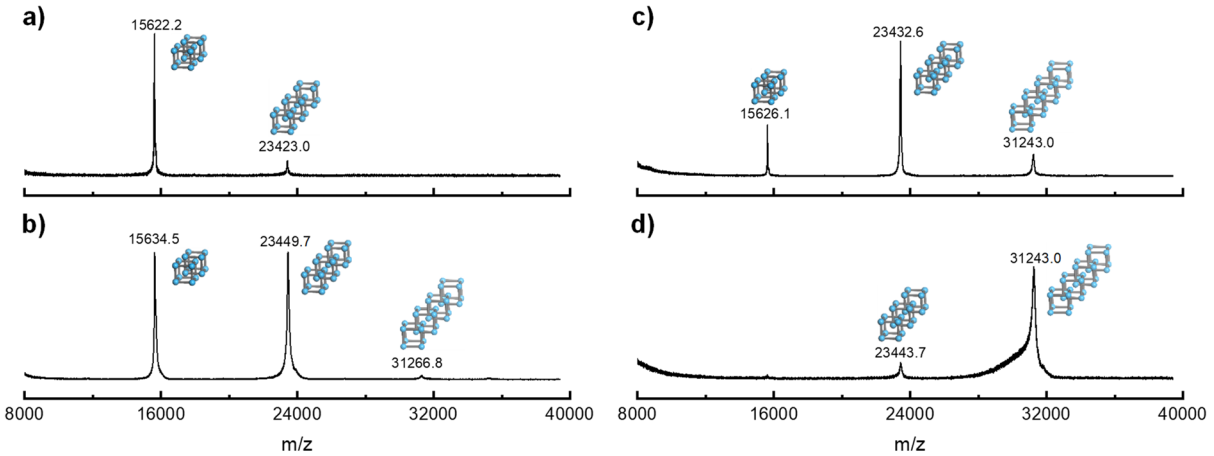

Figure 3.4.17: MALDI mass spectra: a) crude solution ($CHCl_3$/toluene = 2/1, **106**/**96** = 7/12, TFA 4 mol%, r.t, 7 days); b) dimer fraction after GPC separation; c) deuterated solution after NMR measurement; d)^{1}H NMR spectrum (in CD_2Cl_2, 700 MHz, 295 K). The calculated Exact Mass of the monomeric cage is 7801.220.

Overall, the DOSY NMR of each oligomer was also measured. The hydrodynamic radius of the dimer, trimer, and tetramer are 2.6, 2.8, and 2.9 nm respectively, which are also consistent with their successively larger structures (Figure 3.4.18).

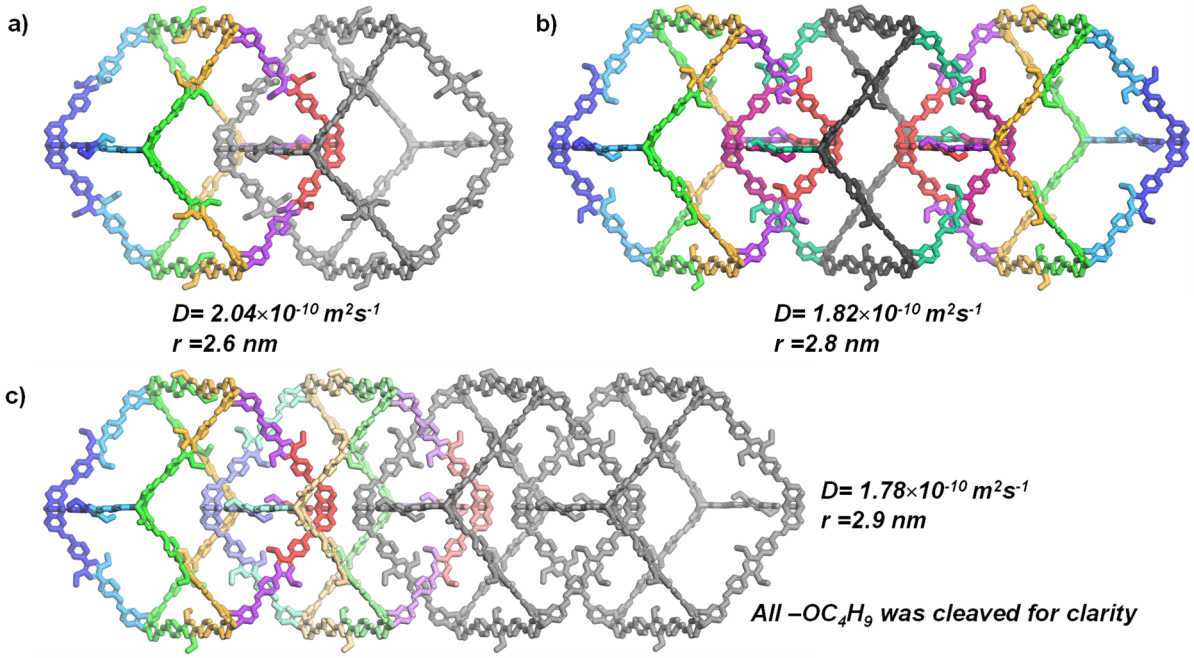

Figure 3.4.18: The illustration of a) ButDie-[2]Catenane, b) ButDie-[3]Catenane, and c) ButDie-[4]Catenane. *D*: Diffusion coefficients; *r*: hydrodynamic radii.

3.4.6 Single Crystallization Experiments of ButDie-[4]Catenane

As mentioned several times in this thesis, single-crystal X-Ray diffraction is always the most direct, effective, and accurate method to reveal the exact conformation of the polycatenanes. Single-crystal structures could illustrate the relative positions of monomeric cages, as well as the details of the architecture, for example, the distance between those aromatic rings. Therefore, it is possible to indicate the interaction between the cages and demonstrate what the driving force for catenation is. However, the single crystal of IOCs, especially those consisting of bigger monomeric cages, is still challenging to prepare, measure and resolve. Currently, no single crystal data have been collected for the cages and IOCs synthesized in this thesis, although lots of efforts have been paid to explore the preparation of single crystals. Herein, the main challenges and the explored solutions will be discussed and summarized below.

Due to the poor stability of imine monomeric cages, some classic single crystal preparation methods are not suitable for IOCs anymore, for example, slow evaporation of solvents, which will introduce moisture into the system and lead to the decomposition of IOCs (Figure 3.4.19 a). Moreover, even using the solvent diffusion method in a closed environment, because the time of crystallization is always quite long, and sometimes the solvents are not absolute anhydrous, the ICCs are also slowly decomposed (Figure 3.4.19 b). Therefore, those

IOCs could not be recycled anymore, which increases the trial-and-error costs since pure IOCs are also not easy to obtain. Moreover, the molecular sieve 3Å was found able to increase the stability of IOCs in the solution state due to the absorption of moisture, which was proved by NMR experiments. The aldehyde peak was detected after one day without molecular sieves, in contrast, the IOCs could keep stable for more than two weeks in the deuterated solution after adding the molecular sieves. Therefore, the molecular sieve 3Å was also added to the solution when preparing the single crystal to prevent the decomposition of IOCs. however, the crystals tend to grow on the surface of molecular sieves, and these crystals are twined and resulting in bad quality (Figure 3.4.19 c).

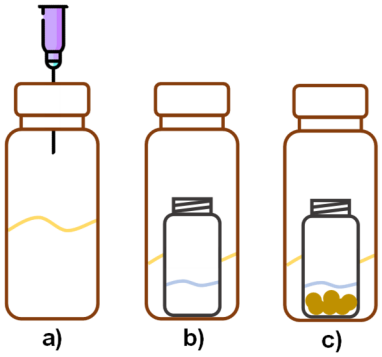

Figure 3.4.19: Illustrations of the devices for preparing single crystals: a) solvent evaporation; b) solvent diffusion; c) solvent diffusion with molecular sieves.

To solve this problem, another form of solvent diffusion method was utilized to prepare the single crystals of IOCs (Figure 3.4.20 b). In a long and relatively thin tube, there are three layers: the solution of IOCs was added to the bottom; The middle layer is the mixture of solvents and anti-solvents; The top layer is the pure anti-solvents. These three layers were separated because of the density difference, and also it requires adding each layer slowly and carefully when preparing the device. It still needs to add the molecular sieves to keep the IOCs stable, however, the molecular sieves are all at the bottom of the tube, and due to the concentration difference, the crystals will preferentially grow in the middle of the tube, thus avoiding the influence of molecular sieves. One advantage of this method is easy to control the crystallization speed by adjusting the ratio of the middle layer, for example, more anti-solvents will accelerate the speed. In addition, it is also convenient to recycle the IOCs if the crystallization failed, by shaking the tubes and collecting the precipitates. In comparison with the slow evaporation in NMR tubes (Figure 3.4.20 a), this method led to obtaining more crystals at once. Due to the bulkiness of obtained catenanes, a lot of solvent molecules crystallize to fill the space in the crystal structure. Therefore, very often it leads to crystal cracks when crystals are taken out from the mother liquid. Thus, the different solvent combinations were screened for the crystallization of ButDie-[4]Catenane and increased the stability of these crystals.

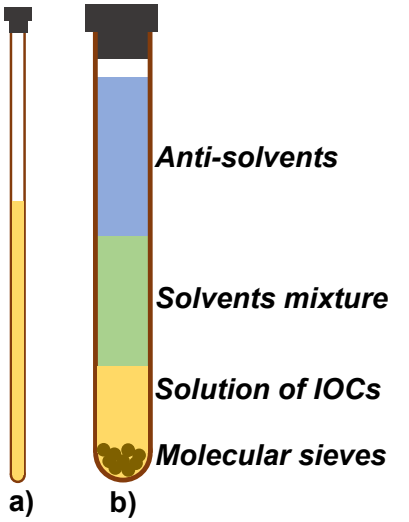

Figure 3.4.20: Illustrations of the devices for preparing single crystals: a) solvent evaporation in NMR tube; b) solvent diffusion between layers.

Table 3.4.7 Screening the solvents for crystallization of **ButDie**-[4]Catenane

Solvents	Anti-solvents	Crystallization	Measure results
chloroform	methanol	tiny crystals without regular shape*	cracked easily
chloroform	methanol	twined crystals	cracked easily
chloroform	hexane	precipitates	-
chloroform	pentane	precipitates	-
tetrahydrofuran	methanol	tiny needle-like crystals	-
dichloromethane	methanol	twined crystals*	cracked easily
1,4-dioxane	hexane	precipitates	-
1,2-dichlorobenzene	**methanol**	**rhombic crystals**	**resolution is poor**

*Prepared in NMR tubes by slow evaporation.

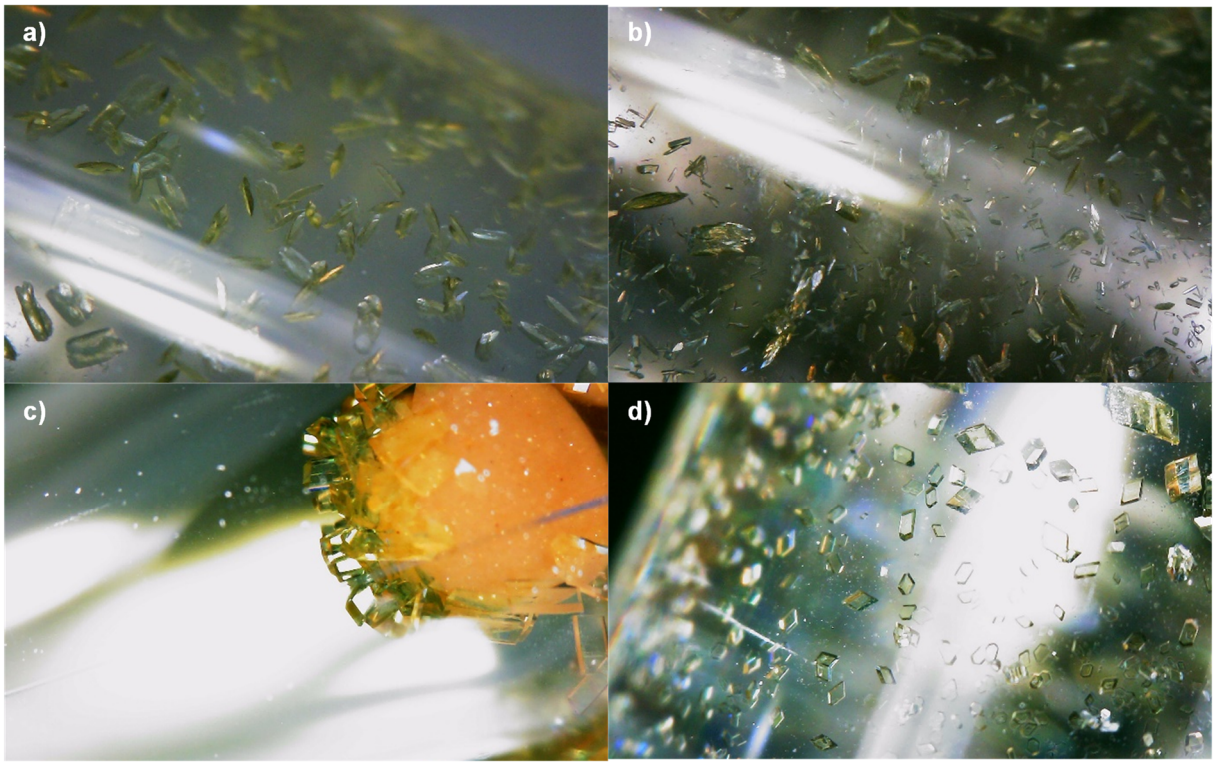

Figure 3.4.21: The optical photos of typical crystal morphologies: a) crystals of slow evaporation in NMR tube ($CHCl_3$ or CD_2Cl_2); b) crystals obtained by diffusion between solvent layers ($CHCl_3$ and methanol); c) crystals grow on the surface of molecular sieves; d: rhombic crystals obtained by diffusion between solvent layers (1,2-dichlorobenzene and methanol);

Results so far indicate that methanol is better than other anti-solvents like hexane, and pentane which were always precipitating the IOCs out. And 1,2-dichlorobenzene is better than $CHCl_3$ and THF, because of its higher boiling point which makes the crystals not that easy to crack. In addition, the morphologies of crystals obtained in 1,2-dichlorobenzene are much better than those in $CHCl_3$. However, the measured resolution is still not good enough for resolving the single crystal structure. And more attempts are underway.

3.4.7 Conclusion

In summary, the first tetrameric polycatenane based on organic cages was successfully synthesized and isolated. According to the studies in previous chapters, the ratio of solvents

mixture and the amount of building block were found to influence the catenation degree of IOCs, and they were further investigated in this chapter. It was found that using more toluene (for the mixture of $CHCl_3$ and toluene) and triamine building block promotes the formation of the polycatenane with a higher catenation degree. Therefore. the trimer and dimer could also be selectively synthesized by adjusting these two factors above. Although, the resolution of 2D NMR spectra was not enough for fully elaborating the structure of the polycatenane, and attempts to collect the single crystal structure data were also not successful, their conformations are still identified by 2D NMR spectra at least. Overall, these results again validate previous findings that it is possible to control the catenation procedure and selectively isolate the IOCs with desired catenation degree. It also provides a guideline for future synthesis of IOCs. In addition, the mechanism still needs to be further investigated and understood.

4. Crystallization of Metal-assisted Organic Frameworks

4.1 Introduction

The preparation of single-crystalline covalent organic frameworks (COFs) is still a significant challenge.[80] Due to the statistical nature of nuclei formation, amorphous solids are typically obtained first (kinetic product) and further transformed into a crystalline state (thermodynamic product).[43b] This procedure requires reversibility in bond formation that allows the network 'error-checking' process, which is also generally considered crucial in crystal growth. However, in comparison with metal-organic frameworks (MOFs)[81] and hydrogen-bonding organic frameworks (HOFs),[82] most covalent organic polymers are constructed by stronger covalent bonds which makes crystallization more difficult.

Currently, only a few examples that obtained the single crystals of organic polymers and successfully collected the single-crystal X-ray diffraction (SXRD) data, have been reported. In 2013, Wuest group constructed the diamondoid networks *via* trans-azodioxy linkages and first obtained covalent organic networks whose precise structure can be fully characterized by single-crystal X-ray diffraction.[83] However, this kind of covalent organic network exhibited poor porosity and stability properties. In 2014, A. Dieter Schlüter's group made a single-crystal two-dimensional polymer (2DP) by photochemical conversion.[84] But the structure is too special, and it is difficult to apply this method to the syntheses of other single-crystalline polymers. M. Yaghi and Wei Wang reported a general procedure to obtain large single crystals of three-dimensional imine-based COFs in 2018.[85] They introduce the imine-exchange strategy to increase the reversibility of imine bond formation and dissociation, which was achieved by adding a large excess of aniline to the reaction mixture, where aniline functions as a modulator. These COFs crystals were successfully characterized by single-crystal x-ray diffraction, and they also showed high Brunauer-Emmett-Teller (BET) surface area. At the same time, William R. Dichtel's group obtained the single crystal COF-5 by using a two-step procedure in which monomers are added slowly to preformed nanoparticle seeds.[86] However, the essence of construction by weak bonds makes most of them unstable even in some mild conditions. How to make the single crystalline COFs with high specific surface area, stability, as well as multiple functions, still needs to be investigated.

N, N'-Bis(salicylidene)ethylenediamine/phenylenediamine (Salen/Salphen) has been considered one of the most important ligands in the field of coordination chemistry.[87] Due to their ability to stabilize metal ions in various oxidation states, such complexes have been widely used as efficient catalysts for numerous organic transformations. It was first introduced to the

construction of COFs by the Wang group in 2017.[88] Liu and Cui reported a new metal-directed synthesis method through which two 2D chiral Salen-COFs were synthesized by using salicylaldehydes and 1,3,5-triphenylbenzene as the core structure in condensation reactions.[89] These Salen-COFs can serve as efficient and recyclable heterogeneous catalysts for several asymmetric transformations. They also have high stability in boiling water, and the alkylated materials even could retain good crystallinity under acidic (1M HCl) and alkaline conditions (9 M NaOH).

Interestingly, my former colleague Dr. Reinhard had synthesized a series of Salphen-based metal-assisted covalent organic frameworks (MSOFs) by using triptycene salicylaldehyde in a one-pot reaction, and these MSOFs also showed great porosity and stability.[90] And he was surprised to observe the formation of some nanocrystals (Figure 4.1.1) when trying to prepare them in step by step reaction.[91]

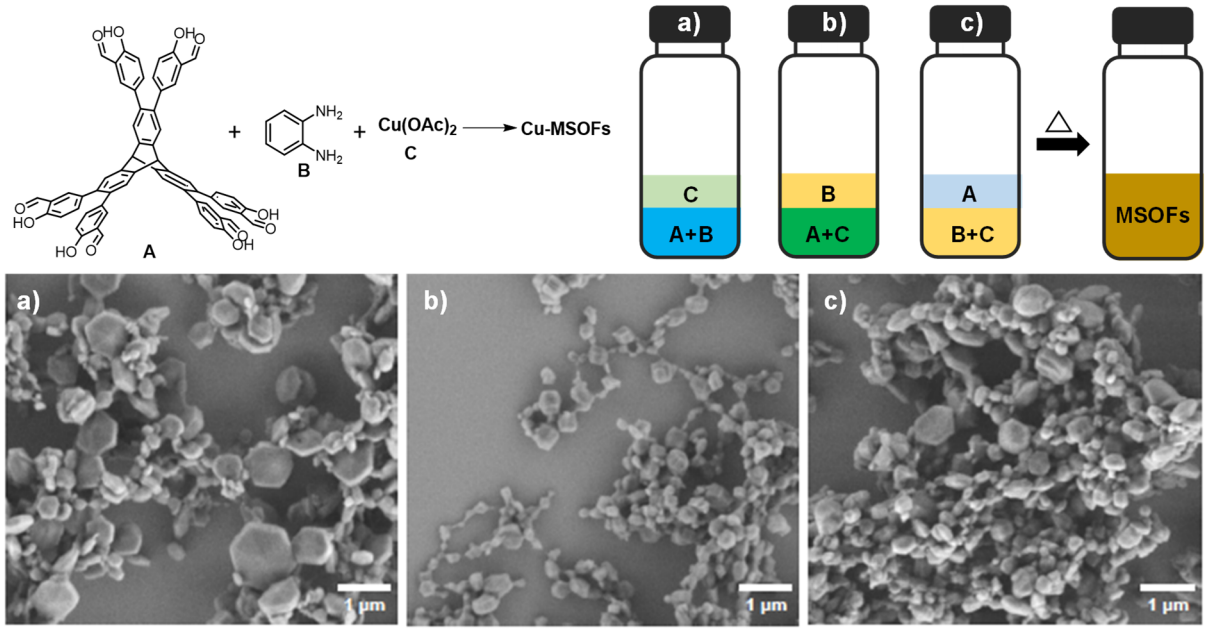

Figure 4.1.1: a) C (4.27 mM), 168 hours, DMF, 30 °C, (A+C) +B; b) C (4.27 mM), 17 hours, DMF, 70 °C, (A+C) +B; c) C (4.27 mM), 20 hours, DMF, 135 °C, (A+C) +B.[91]

As was illustrated in Figure 4.1.1, two substrates were mixed first and frozen in liquid nitrogen, then added the third reactant and frozen again. After reacting at a higher temperature for a longer time, some crystalline particles were observed by scanning electron microscope (SEM). Unfortunately, the results were not well repeatable and the sizes of these crystals mainly distribute at the nanoscale, it is still far from the size for SXRD measurement. However, it showed the hint that metal-assisted construction of COFs may be a way to prepare single crystalline COFs with high stability. Following these results, my topic is to further study the synthesis of the MSOFs, and figure out the influence of the order when mixing the substrates, as well as explore how to make them grow big enough for the SXRD measurement.

4.2 Result and Discussion

4.2.1 Synthesis of Model Compounds

To reveal the possible reaction path and the corresponding products in this one-pot reaction, a series of model compounds were synthesized. $Cu(OAc)_2$, *o*-Phenylenediamine **118**, and salicylaldehyde **117** were chosen to make the model compounds. As Scheme 2 shows, on the one hand, there are three approaches to synthesizing the Salphen complex **121**. Except for the one-pot reaction (B), it is also possible to obtain the imine ligand **120** and then coordinate with copper ions (C). However, the more attractive way is to synthesize the copper complex **119**, then react with *o*-Phenylenediamine **118** to produce the target product (A). Because it is generally much easier to obtain the single crystals of MOFs due to their ionic bonding, in comparison with directly preparing the single crystals of MSOFs or COFs in a one-pot reaction. It is a feasible method to prepare the single crystalline MOFs and then transform them into single crystalline MSOFs. On the other hand, these three paths could happen simultaneously in a one-pot reaction. Based on the experiment results of Dr. Reinhard, the morphologies of the nanocrystals under three conditions (Figure 4.1.1) were quite similar. It is quite difficult to figure out what these crystals exactly are and if they are pure or not, because they could be one of nano MOFs, COFs, MSOFs, or even a mixture of them.

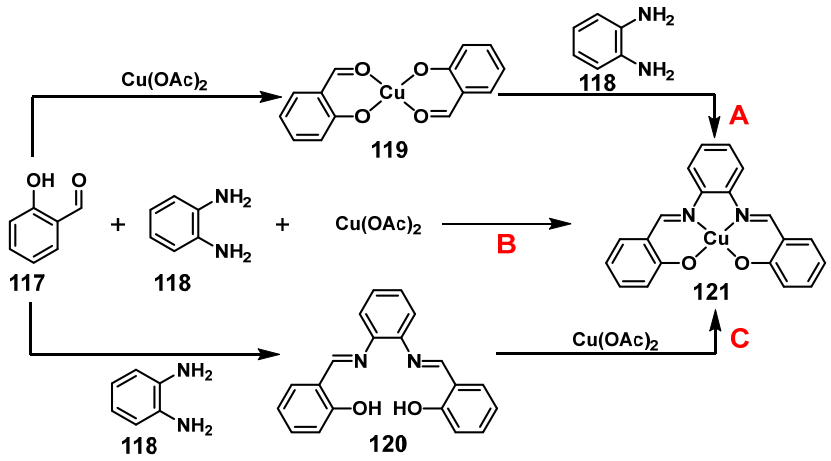

Scheme 4.2.1: Three synthetic routines of model compound **121**.

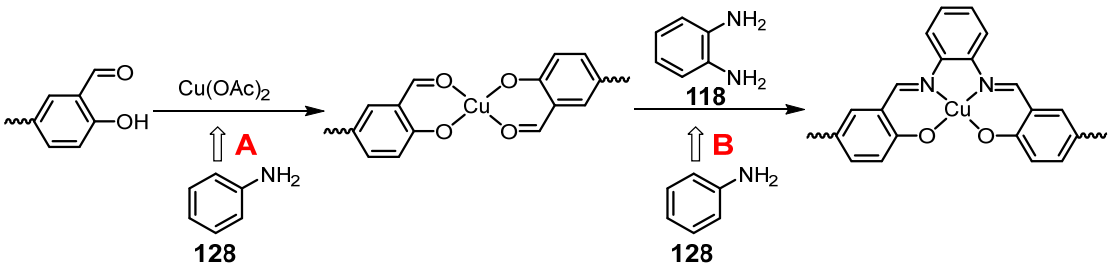

Scheme 4.2.3: Illustration of the two-step approach to the MSOFs, and the addition of the modulator: together with salicylaldehyde monomer (A); with o-Phenylenediamine (B).

Therefore, to figure out this problem, aniline was introduced into the system as a modulator and also an inhibitor, and the influence of aniline on each step was studied respectively. As was shown in Scheme 4, immediately adding the aniline to the mixture of salicylaldehyde monomer and $Cu(OAc)_2$, will inhibit the coordination due to the imine condensation between the aniline and salicylaldehyde monomer. Similarly, if adding the aniline together with *o*-Phenylenediamine, it will work as a modulator to slow down the reaction rate of *o*-Phenylenediamine and the coordinated salicylaldehyde monomer.

4.2.2 The Identification of Nano Crystals

Triptycene salicylaldehyde **127** was synthesized according to the literature. First, the experiment done by Dr. Reinhard was repeated without adding the aniline (Scheme 5). Compound **127** (150 µL, 4.27 mM) was mixed with $Cu(OAc)_2$ (150 µL, 39.7 mM) and frozen in liquid N_2, and *o*-Phenylendiamine **118** (150 µL, 38.4 mM) was added into the solid mixture and frozen. Then the mixture stood at an elevated temperature without stirring. The morphology of products was monitored by scanning electron microscopy (SEM). An appropriate amount of precipitate mixture was dispersed in isopropanol. After sonication and centrifugation, the solvents were removed then some new isopropanol was added. Repeat this procedure three times, and a drop of diluted isopropanol mixture was added to the silica wafer to prepare the sample for SEM measurement.

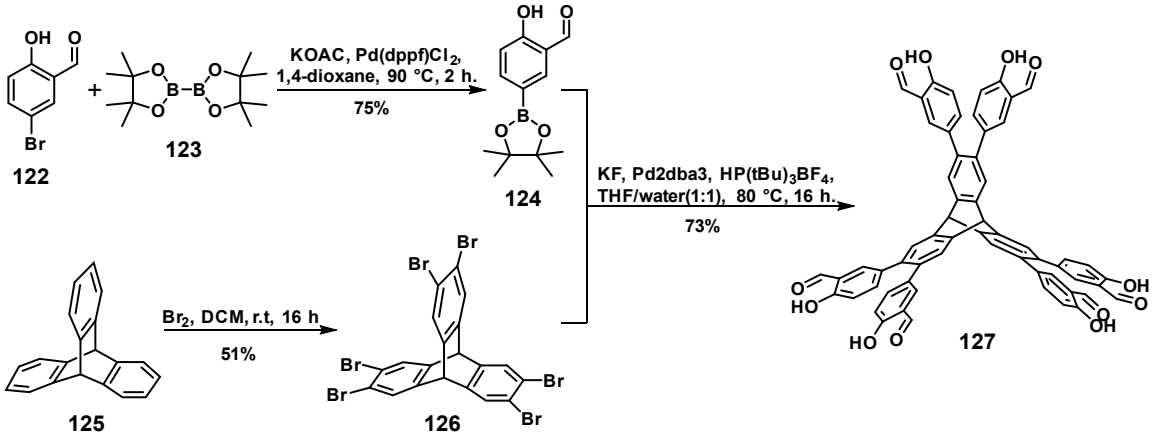

Scheme 4.2.2: Synthesis of monomer **127**.

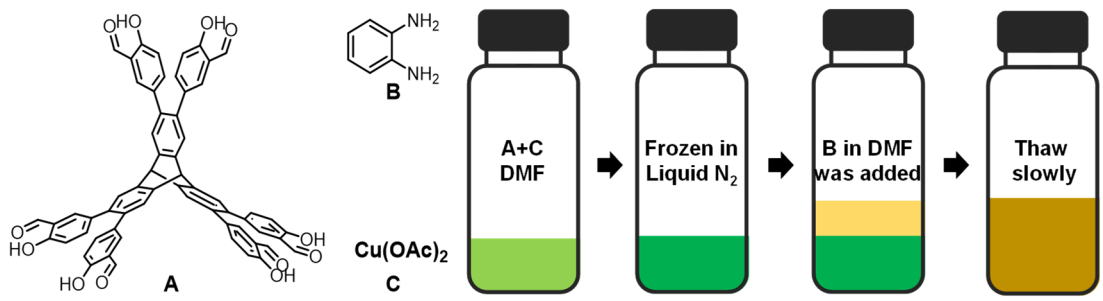

Scheme 4.2.4: Illustration of the experimental procedure.

Table 4.2.1 The synthetic conditions of **Cu-MOFs**

Order	C[a] [mM]	T[°C]	t [day]	SEM Images
(A+C)+B	4.27	30	1	Figure 4.2.5 a
(A+C)+B	4.27	30	7	Figure 4.2.5 b
(A+C)+B	4.27	50	1	Figure 4.2.5 c
(A+C)+B	4.27	50	7	Figure 4.2.5 d

a. Concentration of triptycene salicylaldehyde **127**.

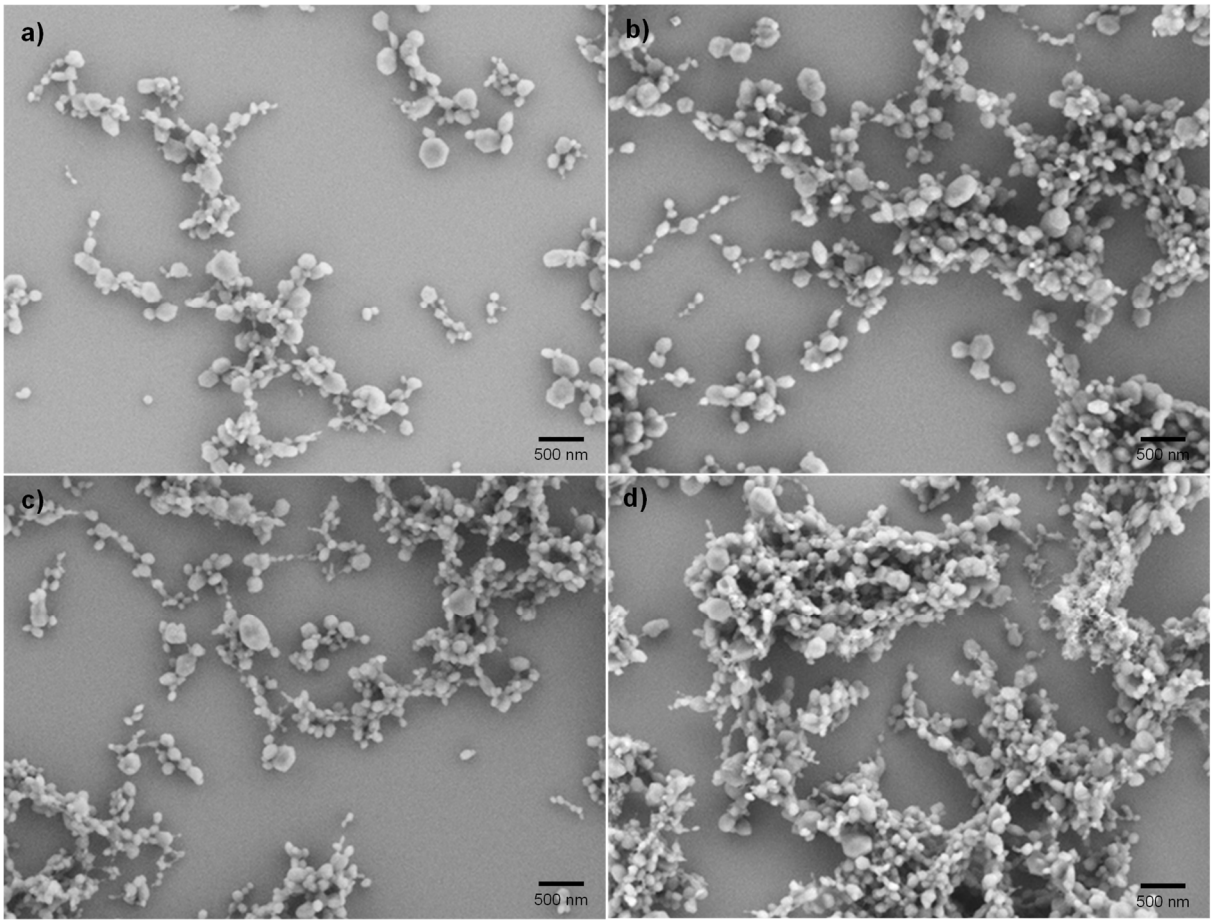

Scheme 4.2.5: SEM pictures of the products under the conditions in Table 4.2.1.

The obtained SEM pictures showed similar nano-crystals to the results of Dr. Reinhard. And morphologies of the products with different temperatures and reaction times are also the same. After proving these results are repeatable, then the aniline was introduced to the system. Same with the above experiment, after freezing the DMF solution of Compound **127** and $Cu(OAc)_2$, the aniline **128** was added together with *o*-Phenylendiamine **118** (Figure 4.1.6).

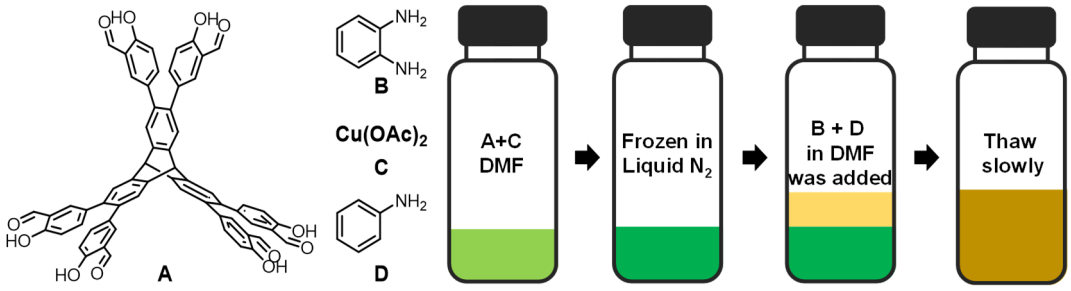

Scheme 4.2.6: Illustration of the experimental procedure.

Table 4.2.2 The synthetic conditions of **Cu-MOFs**

C[a] [mM]	C[b] [mM]	T[°C]	t [day]	SEM Images
4.27	42.7	30	2	Figure 4.2.7 a
4.27	85.4	30	2	Figure 4.2.7 b
4.27	128.1	30	2	Figure 4.2.7 c
4.27	170.8	30	2	Figure 4.2.7 d

[a] Concentration of triptycene salicylaldehyde **127**; [b] The concentration of aniline.

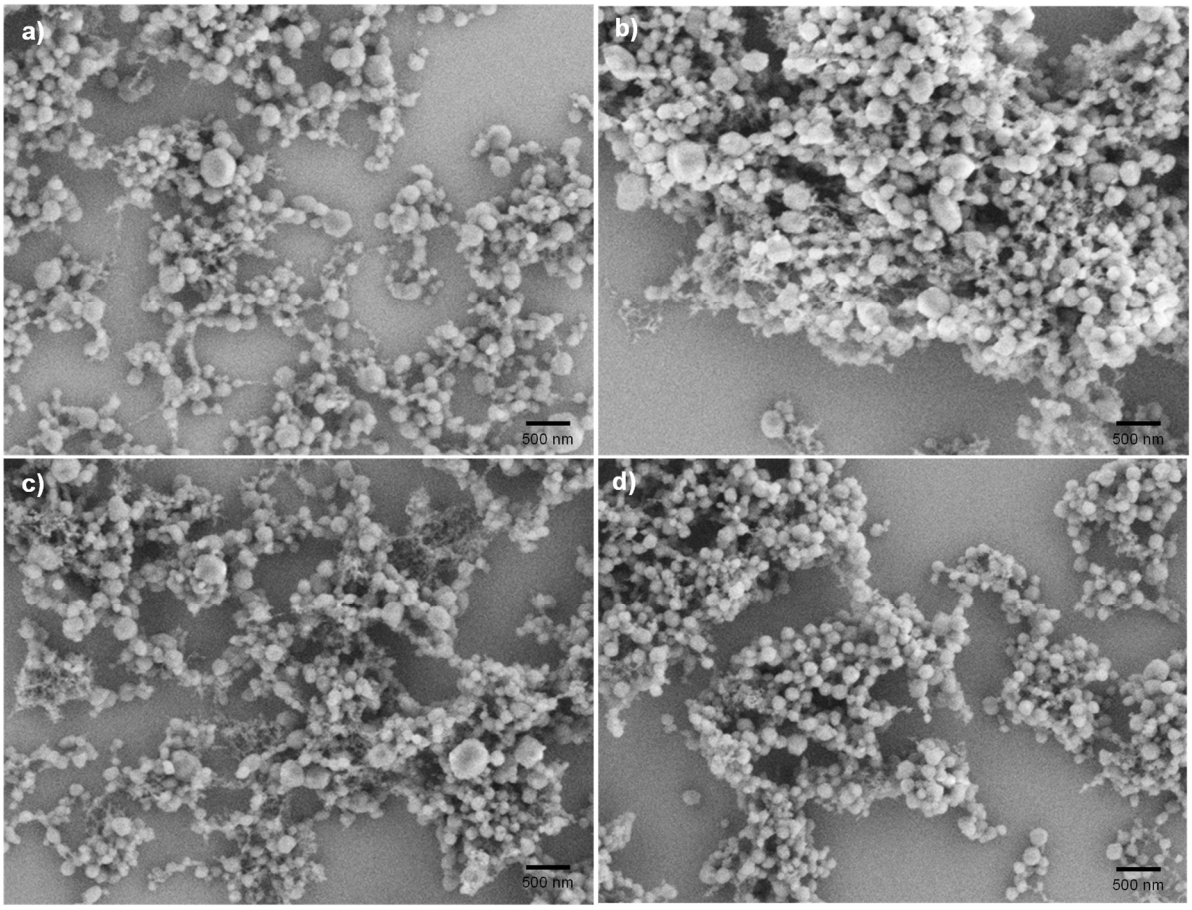

Scheme 4.2.7: SEM pictures of the products under the conditions in Table 4.2.2.

And after the reaction, the SEM picture (Figure 4.2.7) was obtained according to the similar method mentioned above. It was found that the addition of aniline, as well as increasing the amount made no difference to the formation of nanocrystals. Therefore, to further test the function of aniline, it was added to the solution of $Cu(OAc)_2$ at the same time as the salicylaldehyde monomer (Figure 4.2.8) (Table 4.2.2).

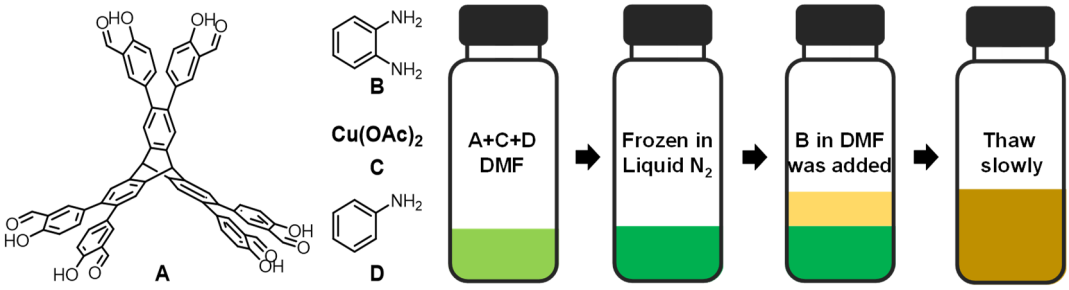

Scheme 4.2.8: Illustration of the experimental procedure.

However, after changing the order of adding the aniline, the SEM pictures showed that all the products are amorphous solids. It means that the aniline indeed inhibited the formation of nanocrystals. The nanocrystals could generate when adding aniline together with *o*-Phenylenediamine, rather not when adding together with salicylaldehyde monomer. It indicated that the formation of nanocrystals depends on the coordination procedure. To further prove it, the following experiment was performed. The rest conditions were the same as the above experiments (Table 4.2.2), but the mixture of salicylaldehyde monomer and $Cu(OAc)_2$ was firstly shaken for 30 minutes, then the aniline was added and the mixture was frozen in liquid N_2.

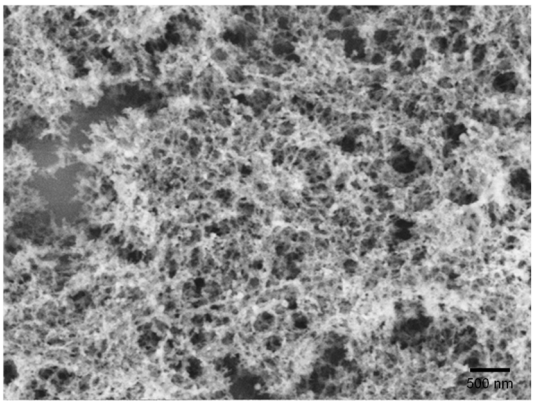

Scheme 4.2.9: One SEM picture of the products of Scheme 4.2.8. The rest omitted pictures are quite similar.

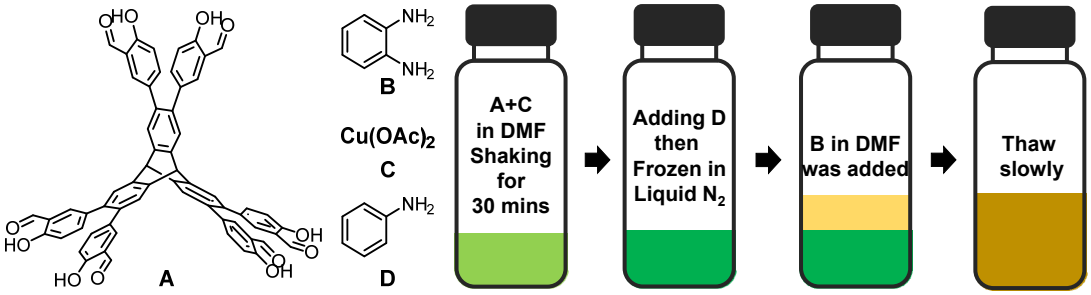

Scheme 4.2.10: Illustration of the experimental procedure.

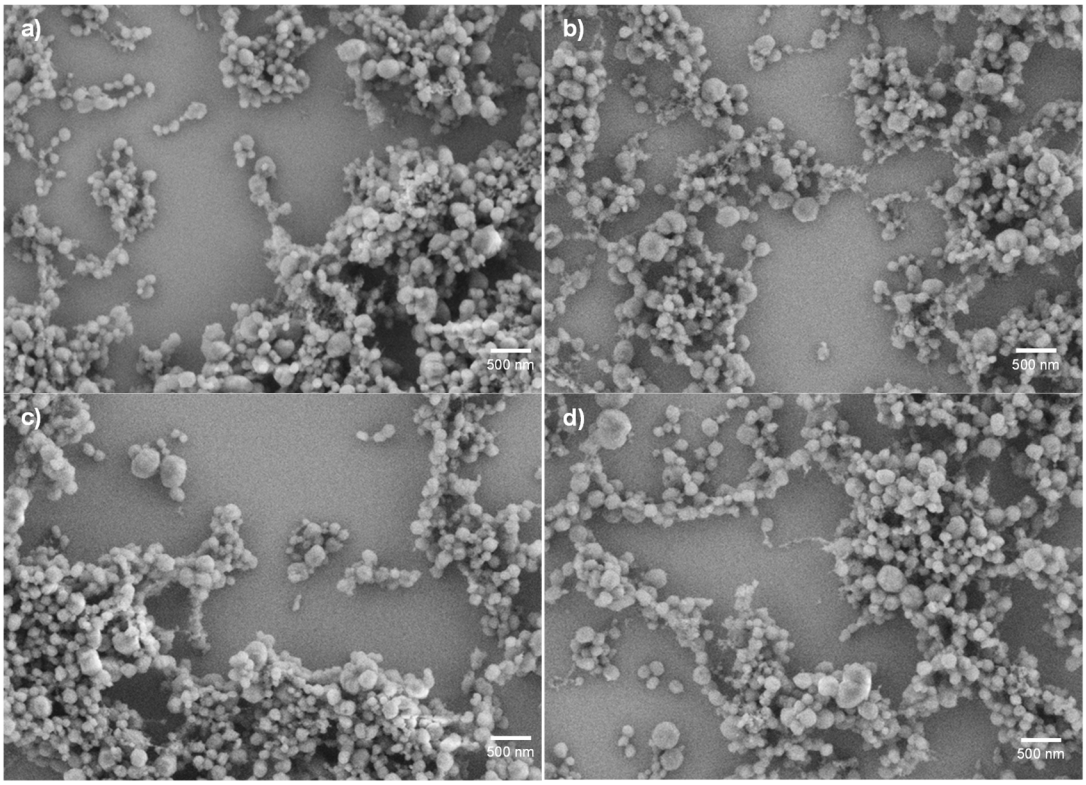

Scheme 4.2.11: SEM pictures of the products with the procedure in Scheme 4.2.10.

Interestingly, after shaking the mixture of salialdehyde monomer and $Cu(OAc)_2$ for 30 minutes and then adding aniline, the nanocrystals were observed again (Figure 4.2.11). Accordingly, it could conclude that the formation of these nanocrystals was controlled by the coordination process, although it is still unclear what these nanocrystals are. If the *o*-Phenylendiamine further reacted with the coordination product, these products should be MSOFs, if not, for example, if it just works as a modulator, the nanocrystals should be MOFs.

4.2.3 Two-step Approach and Synthesis of Crystalline MOFs

Based on the results above, it could be found that there are three substrates, two reaction types, and three possible different products in this system and these nanocrystals may be a mixture of several materials. Therefore, to avoid these problems, another approach is to obtain crystalline MOFs first, then reacted with the diamine to transform the crystalline MOFs into crystalline MSOFs. And some experiments were performed to explore the possibilities and try to get the single crystal MOFs. Because nucleation of the MOFs is quite fast, precipitates appeared immediately once mixing the solution of monomer and metal ions even in diluted conditions. Therefore, DMF was chosen as the solvent to increase the solubility of the intermediate products. And acetic acid was employed as the modulator to promote the reversibility of the reaction thus increasing the size and crystallinity of MOFs.

Triptycene salicylaldehyde **127** (2.5 mL, 2 mM) was mixed with acetic acid first. And then $Cu(OAc)_2$ (2.5 mL, 6 mM) was added, and the mixture stood at 100 °C without stirring for 7 days. After cooling slowly to room temperature, an appropriate amount of solid was prepared into samples for SEM measurement.

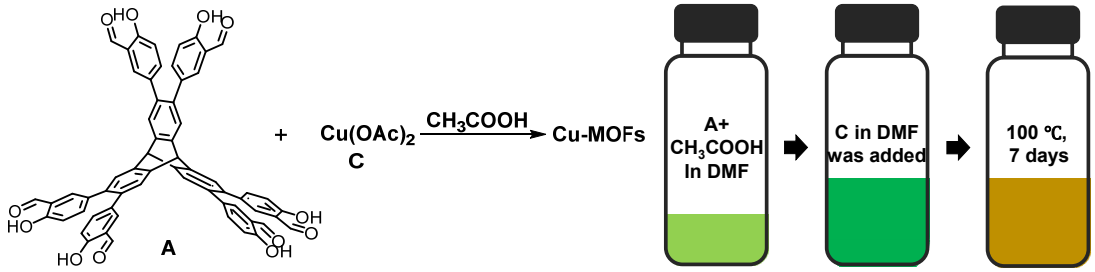

Figure 4.2.12: Illustration of the experimental procedure.

Table 4.2.3: The synthetic conditions of **Cu-MOFs**

$C^{[a]}$ [mM]	T[°C]	t [day]	$C^{[b]}$ [mM]	SEM Images
2	100	7	0	Figure 4.2.12 a
2	100	7	9	Figure 4.2.12 c
2	100	7	18	Figure 4.2.12 f
2	100	7	27	Figure 4.2.12 j

[a] Concentration of triptycene salicylaldehyde **127**; [b] The concentration of acetic acid.

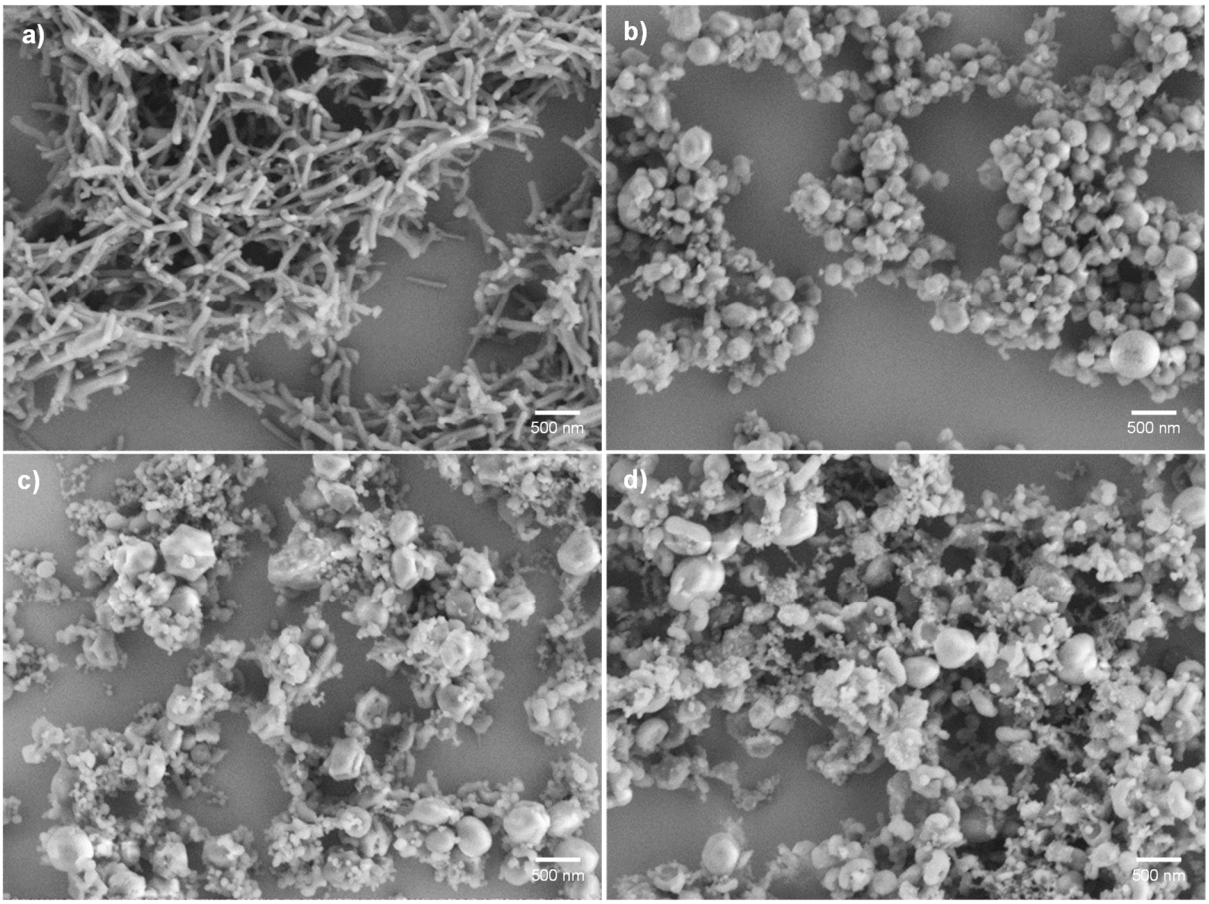

Figure 4.2.12: SEM pictures of the products under the conditions in Table 4.2.3.

According to the SEM pictures above, it is obvious that the addition of CH_3COOH indeed changed the morphology of the products. The crystals are stick shape with a uniform size of 500 nm without adding the acetic acid (Figure 4.2.12 a), while the crystal became ball shape there were also some hexagonal crystals with sizes of about 500 nm to 800 nm as increased the amount of acetic acid (Figure 4.2.12 c). However, when further increasing the concentration of acetic acid, the crystal size cannot get bigger, and they also start to lose the regular morphology. Moreover, besides the hexagonal nanocrystals, there were also some amorphous products formed, which are difficult to be removed. Therefore, another compound-salicylaldehyde was chosen to be the modulator, since it has the same coordination ability as the monomer **127**. And the corresponding complex **119** also has good solubility in DMF, which also promotes the exchanging process.

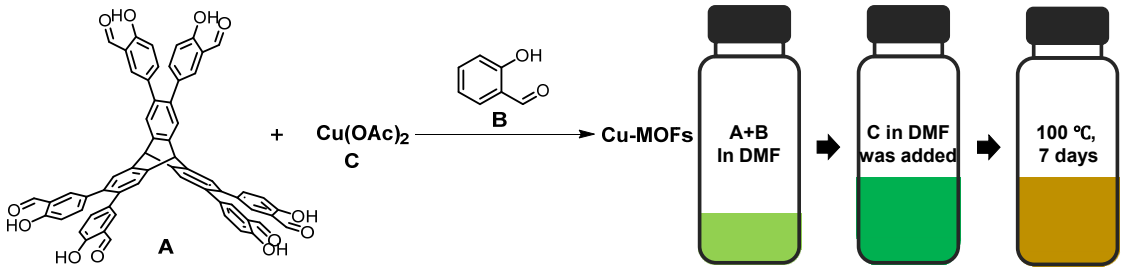

Figure 4.2.13: Illustration of the experimental procedure.

Table 4.2.4 The synthetic conditions of **Cu-MOFs**

$C^{[a]}$ [mM]	T[°C]	t [day]	$C^{[b]}$ [mM]	SEM Images
2	100	7	20	Figure 4.2.14 a
2	100	7	40	Figure 4.2.14 b
2	100	7	60	Figure 4.2.14 c/d
2	100	7	80	Figure 4.2.14 e
2	100	7	100	Figure 4.2.14 f
2	100	7	120	Figure 4.2.14 g
2	100	7	140	Figure 4.2.14 h
2	100	7	160	Figure 4.2.14 i/j
2	100	7	180	Figure 4.2.14 k
2	100	7	200	Figure 4.2.14 l

[a] Concentration of triptycene salicylaldehyde **127**; [b] The concentration of salicylaldehyde.

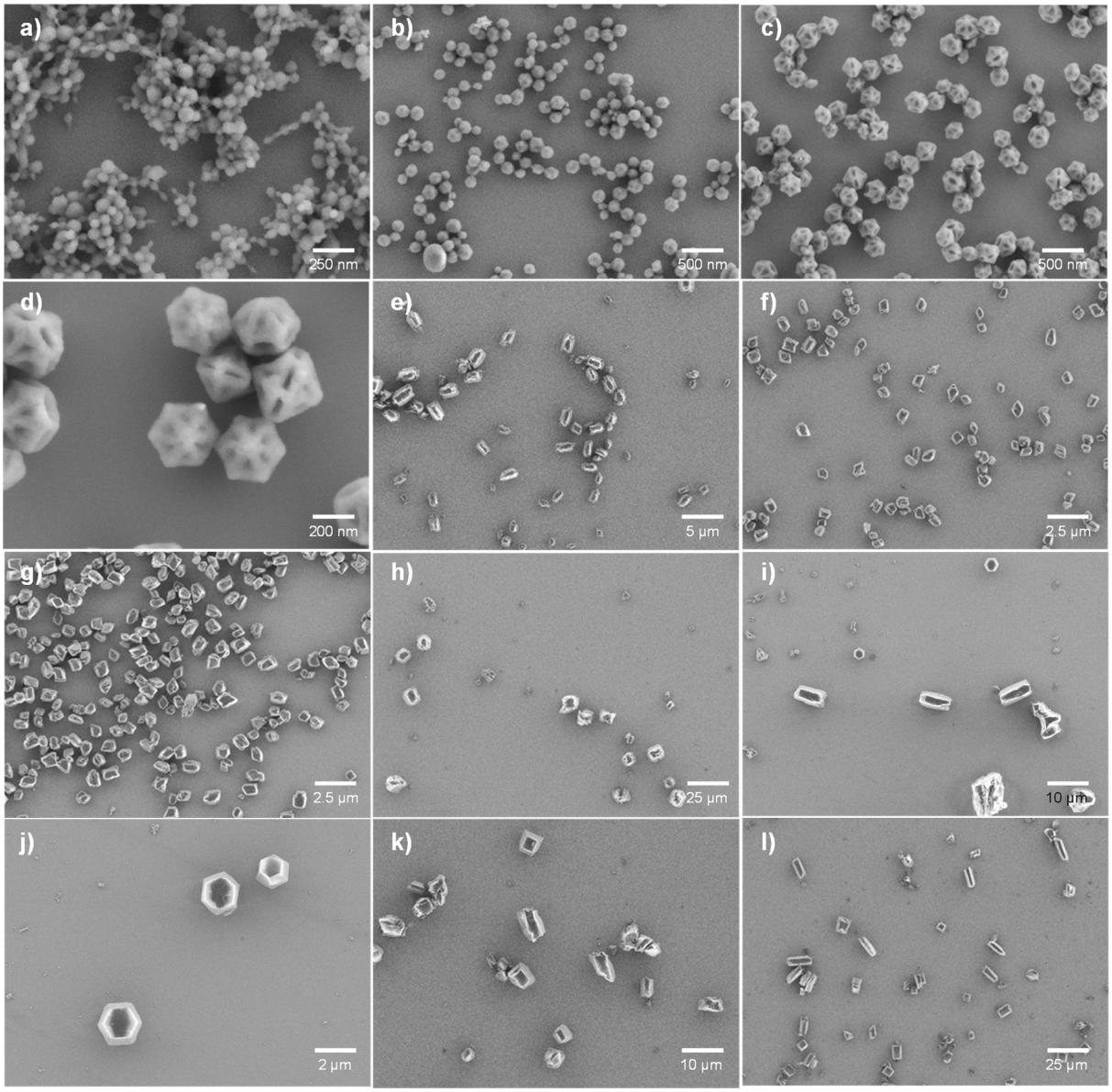

Figure 4.2.14: SEM pictures of Cu-MOFs under the conditions in Table 4.2.4.

As the SEM pictures above showed, the addition of salicylaldehyde significantly changed the morphology of the products. Especially when the concentration of the modulator was around 60 mM, the hexagonal nanocrystals with uniform regular shape and size were observed in SEM pictures (Figure 4.2.14 c). These nanocrystals are around 250 nm (Figure 4.2.14 d), and in hexagonal shape and with clear edges. The size of the crystals did get bigger as increased the concentration of salicylaldehyde, however, the morphology of the products changed from regular hexagonal shape to irregular particles after increasing the concentration of the modulator from 60 to 80 mM (Figure 4.2.14 c, e). The sizes of these irregular particles were around 1 to 10 μm, and sporadic hexagonal crystals (Figure 4.2.14 i, j) could be found in these particles. When the amount of salicylaldehyde is much more than the monomer **127**, as Figure 4.2.15 showed, the yield of the solid is much less, which means the main product became the smaller complex. More detailed concentrations were also screened from 20 mM to 80 mM, but no bigger nanocrystals were observed. By comparing the results of two different modulators, these nanocrystals have similar morphologies, while the yield of nanocrystals with salicylaldehyde is better, and fewer amorphous products were formed. It also indicates that these crystals should be the MOFs rather not complex **119**.

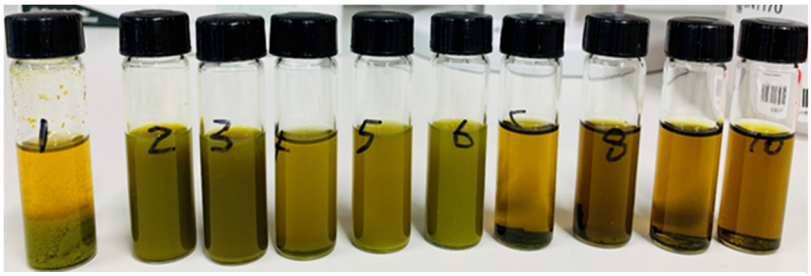

Figure 4.2.15: The picture of the reaction mixtures under the conditions in Table 4.2.14.

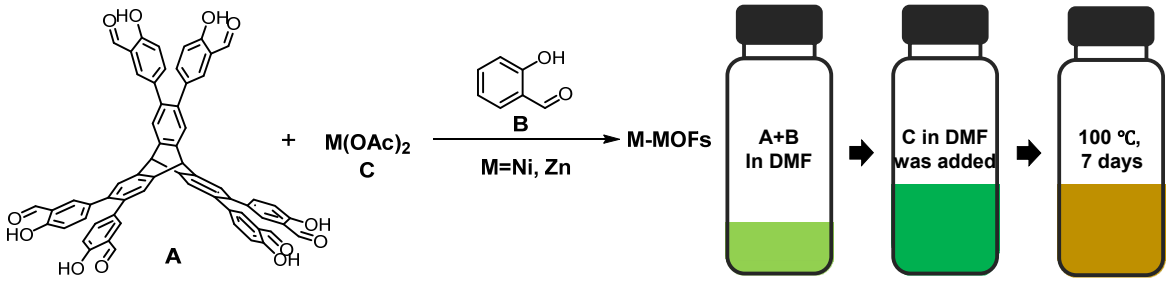

Figure 4.2.16: Illustration of the experimental procedure.

Table 4.2.5 The synthetic conditions of **Ni/Zn-MOFs**

C[a] [mM]	T[°C]	t [day]	C[b] [mM]	SEM Images
2	100	7	20	a
2	100	7	80	b
2	100	7	140	c
2	100	7	200	d

[a] Concentration of triptycene salicylaldehyde **127**; [b] Concentration of salicylaldehyde.

Furthermore, $Ni(OAc)_2$ and $Zn(OAc)_2$ were also employed to construct the MOFs, using salicylaldehyde as the modulator. After the reaction, needle-like Ni-MOFs, and rod-like

Zn-MOFs were obtained. Unfortunately, they are all nanoscale, it's unable to obtain bigger crystals with uniform size and good morphology.

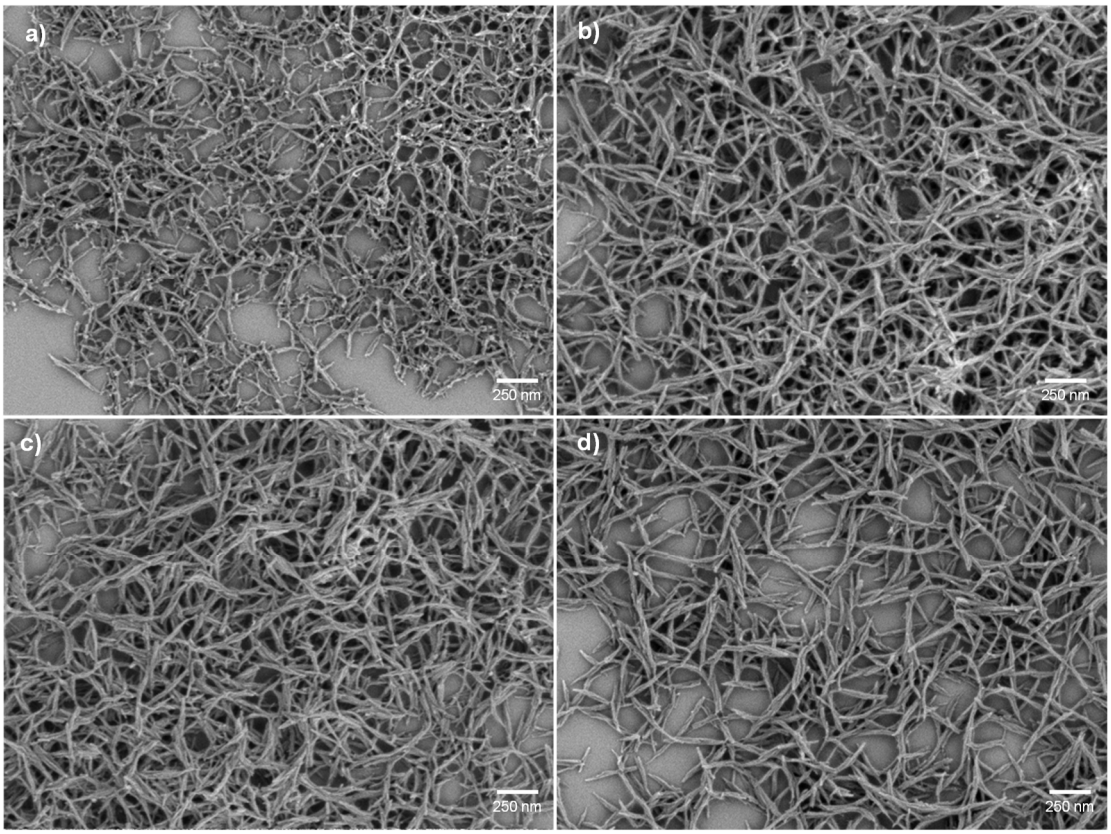

Figure 4.2.17: SEM pictures of the Ni-MOFs under the conditions in Table 4.2.5.

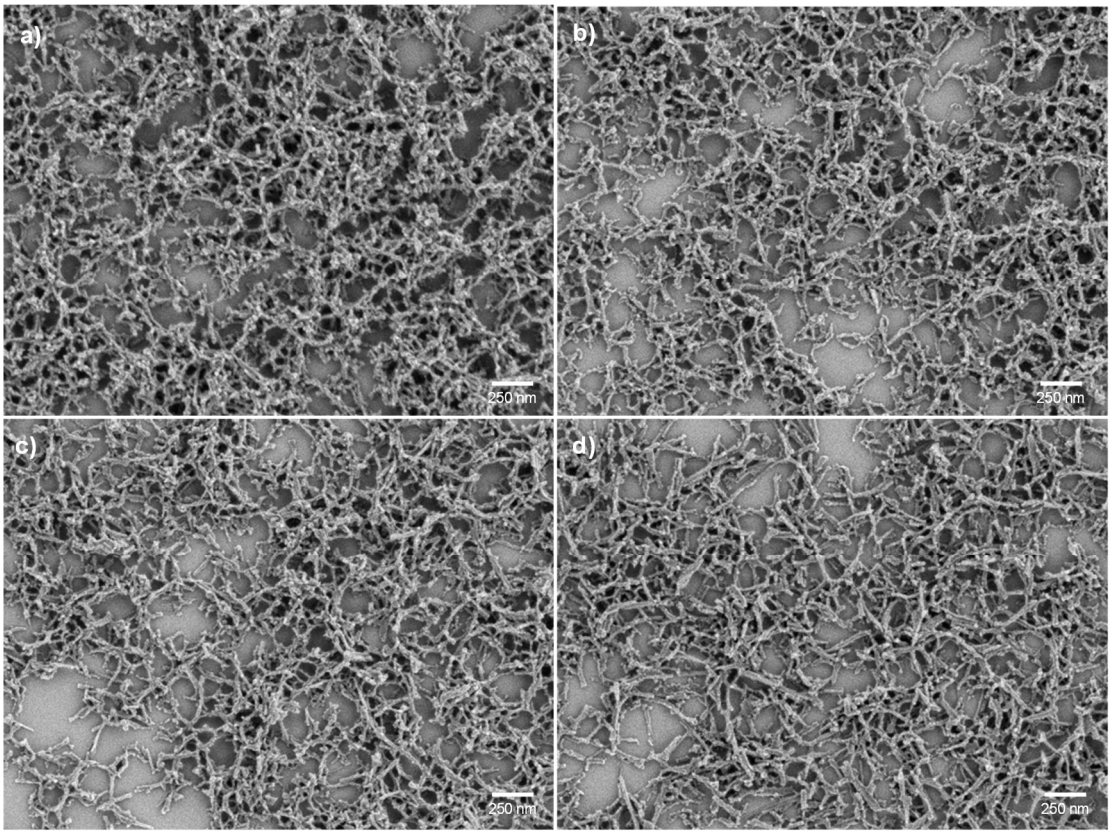

Figure 4.2.18: SEM pictures of the Zn-MOFs under the conditions in Table 4.2.5.

The powder X-Ray diffraction (PXRD) of these three MOFs nanocrystals was measured. The spectrum shows that both of the three nanocrystals have crystallites, especially the Cu-MOFs and Ni-MOFs. The PXRD patterns are not as good as some reported nanocrystal MOFs, considering the nanoscale size, PXRD patterns may show broad peaks. Another reason is that there are still some irregular or amorphous particles that can be found in SEM pictures, which indicate that the products were not pure enough.

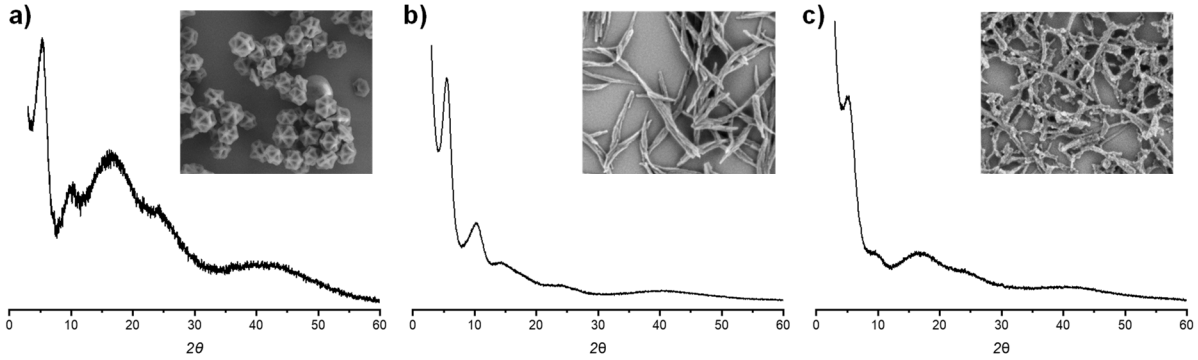

Figure 4.2.19: The PXRD of Cu-MOFs (a), Ni-COFs (b), Zn-COFs (c), and the corresponding SEM pictures.

Overall, by using salicylaldehyde as the modulator, nanocrystals with sizes of 200-300 nm could be obtained. The Cu-MOFs show a regular hexagonal shape and a special morphology. However, the size of these crystals is still far from the requirements for SXRD measurement.

4.2.4 Second Approach to the Single Crystalline MSOFs

As was mentioned above, a one-pot reaction is not a good method to prepare the crystalline MSOFs, because there are several substrates in one system, which make it more difficult to explore the conditions of crystal growth. Therefore, I tried to synthesize the single crystals of MOFs based on monomer **127**, then transform them into single crystals of MSOFs by reacting with *o*-Phenylendiamine **118**. Although no single crystals of MOFs were obtained, in principle, there is one problem during the post-modification procedure. In the coordination structure of monomer **127** and the metal ions, the aldehyde oxygen of two ligands was located at a diagonal position, but when reacting with the diamine, it requires them to rotate to the same side. This procedure could be easily achieved for the model compounds **121**, however, it may cause some problems, for example, the crack of crystals, for the MOFs structures.

Therefore, to simplify the reaction procedure and avoid such problems, a new building block was designed to construct the frameworks. As Scheme 4.2.20 showed below, following this synthesis routine, the single crystal of COFs could be synthesized in one-pot reactions. And there are only one bond formation possibility and one kind of product formed during the synthesis of MOFs, it is much easier to control the crystal growth. When transiting the crystal

MOFs into COFs through the Williamson ether reaction, except for adding a tiny amount of KI as the catalyst, no other reactants are needed. It also doesn't require the rotation of the coordination sites, which could avoid the collapse of the frameworks.

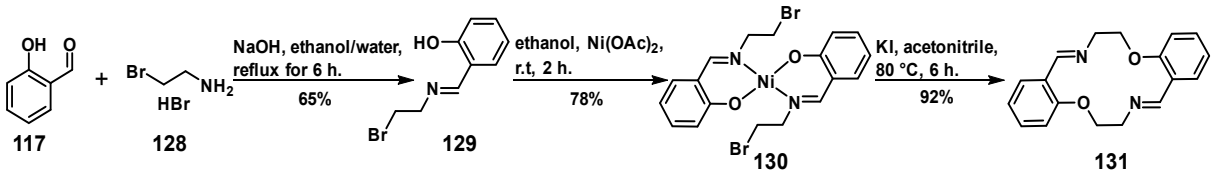

Scheme 4.2.20: Synthesis of model compound **131**.

Moreover, the transition from crystal MOFs to crystal COFs is through Williamson ether synthesis, at the same time, the metal ion will be cleaved. There are two react positions in these building blocks, as long as one side is reacted, it will be successfully connected to the covalent organic frameworks. It's worth noting that the yield of Williamson ether synthesis is 92% which is also good for such a transition. The corresponding monomer **132** was synthesized based on compound **127**. Herein, compound **129** was employed as the modulator, and the MOFs construction was performed as before.

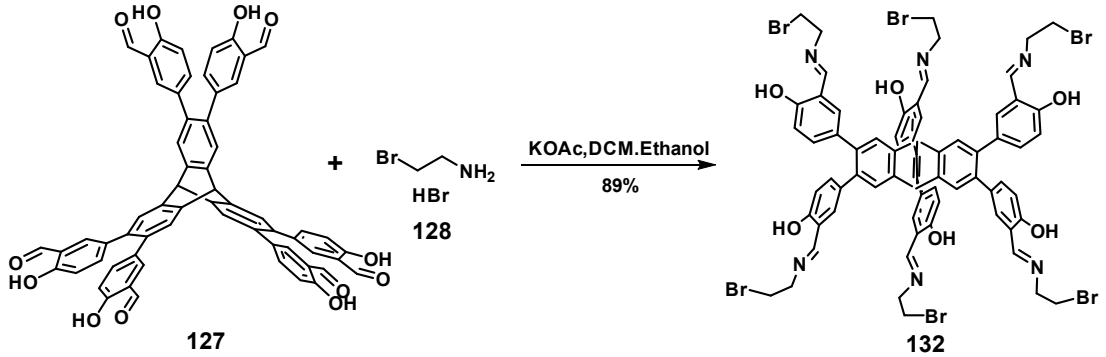

Scheme 4.2.21 Synthesis of monomer **132**.

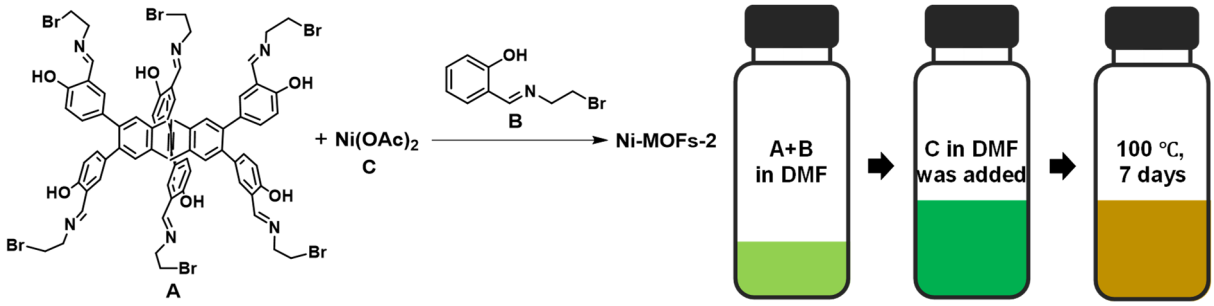

Figure 4.2.22: Illustration of the experimental procedure.

Table 4.2.6 The synthetic conditions of **Ni-MOFs-2**

C[a] [mM]	T[°C]	t [day]	C[b] [mM]	SEM Images
2	100	7	10	Figure 4.2.23 a
2	100	7	20	Figure 4.2.23 b
2	100	7	30	Figure 4.2.23 c
2	100	7	40	Figure 4.2.23 d

[a] Concentration of monomer **132**; [b] Concentration of compound **129**.

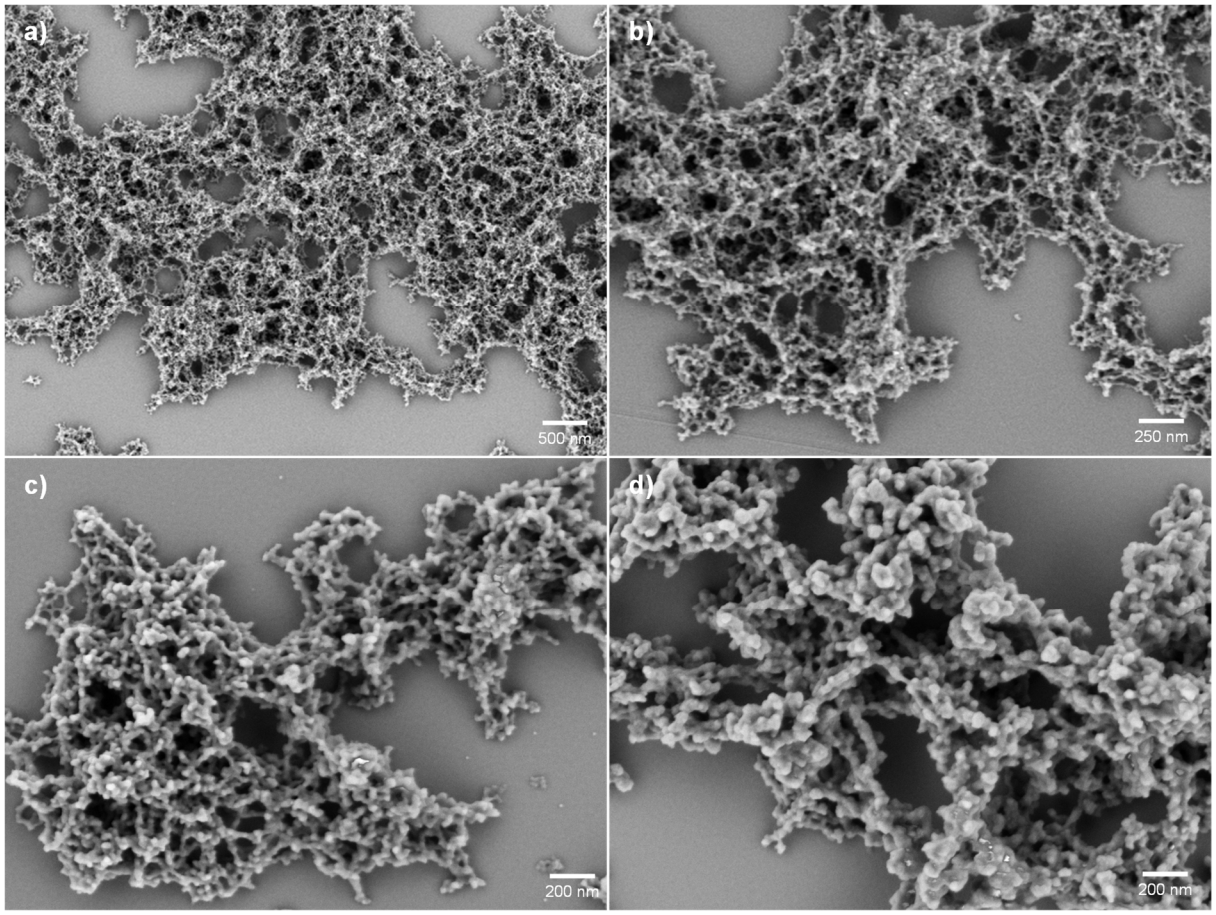

Figure 4.2.23: SEM pictures of the Ni-MOFs-2 modulated by compound **129**.

As the SEM picture shows, when the concentration of modulator **129** is lower than 20 mM, the products are amorphous solids (Figure 4.2.23 a, b). The products started to show crystallinity when the modulator concentration increased to 30 and 40 mM (Figure 4.2.23 c, d). But the size of these crystalline particles is much smaller than the Cu-MOF nanocrystals obtained before. It was also found that when the concentration of **129** increased to 50 mM, only a homogeneous solution was obtained after the reaction, which means the main product became the smaller soluble complexes. Acetic acid was also utilized as the modulator to tune the size of Ni-MOFs-2, and the concentration was also screened (5.6-11.9 mM), however, all the products are amorphous solid (Figure 4.2.24). Based on current experiment results, it was found that the coordination ability of monomer **132** was weak than monomer **127**. Because the reaction solution of monomer 132 turns to the homogenous solution at a

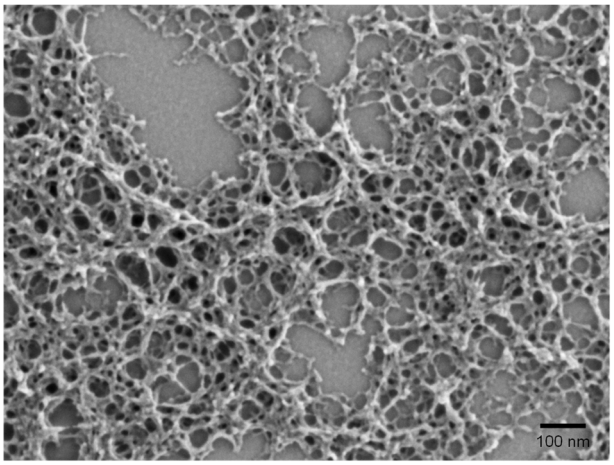

Figure 4.2.24: SEM pictures of the products modulated by acetic acid.

lower concentration of modulator. It is worth mentioning that the imine structure of the monomer may be not that stable in DMF solution at high temperatures, which also could change the coordination process and influence the formation of MOFs.

4.3 Conclusion

In summary, according to previous results of Dr. Reinhard, the synthesis of MSOFs in a one-pot reaction was first investigated. By introducing aniline to the synthesis as a modulator in a different order, it was found that the nanocrystals observed before may be just Cu-MOFs rather not Cu-MSOFs. Therefore, a two-step strategy was adopted to first prepare the single crystalline MOFs and then transform them into single crystalline MSOFs by post-modification. The acetic acid and salicylaldehyde were utilized as the modulator for the synthesis of crystalline MOFs, and the nanocrystals (~200 to 300 nm) of Cu-MOFs, Ni-MOFs, and Zn-MOFs based on salicylaldehyde triptycene **127** were obtained.

In addition, a sampler approach was designed, the 2-Bromoethylamine was first reacted with salicylaldehyde triptycene **127** to synthesize the monomer **132** *via* imine condensation. Therefore the post-modification could be conducted with Williamson ether reaction, which could avoid the rotation of the salicylaldehyde when transforming the MOFs to MSOFs. Unfortunately, no crystalline product was obtained currently, and it needs more investigation.

5. Summary and Outlook

This thesis presents the synthesis and characterization of a series of IOCs based on [8+12] cube cages. Accordingly, the factors that influence the formation of IOCs were investigated.

Chapter 3.1 explored and demonstrated the influence of cavity and monomeric cage size on catenation tendency. Six [16+24] dimeric catenanes, one [24+36] trimeric catenane, and two [8+12] monomeric cages were synthesized based on substituted triptycene triamine (Figure 5.1). By studying the relationship between the size of monomeric cages and the formation of IOCs, it was found that when the monomeric cages have a bigger cavity volume or a relatively smaller size, they are more tending to interlock into catenanes. When the cavity is big enough, the formation of pentameric and trimeric species could be found on the MS spectra. In addition, the trimeric catenane was obtained by changing the ratios of the building blocks and linkers, which could influence the yield of IOCs with different catenation degrees.

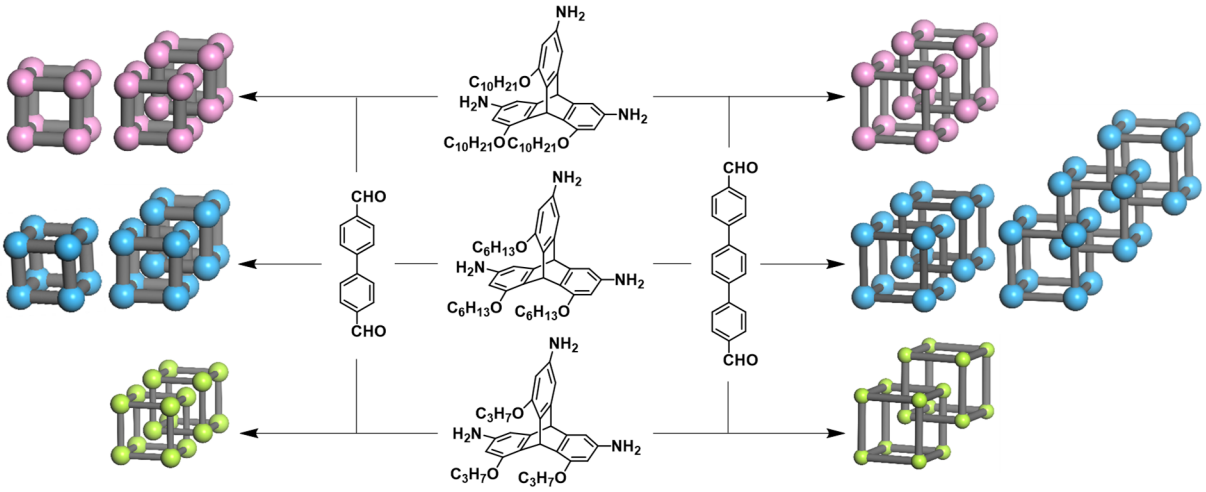

Figure 5.1 Illustration of the cages and catenanes (ball and stick model) obtained in *Chapter 3.1*.

The structural effect of the monomeric cage on the catenation was investigated in *Chapter 3.2*, which specifically focused on the structural changes caused by different linkers. A series of linkers were synthesized and utilized to construct the catenanes, and the results demonstrated that the structure of monomeric cages significantly influences the formation of IOCs (Figure 5.2). Because the synthesis of IOCs is controlled by several factors simultaneously, another related crucial factor—solvents were investigated and discussed in *Chapter 3.3*. Solvents were found to play a crucial role in the synthesis of IOCs, it not only provides the reaction environment but also influence the catenation procedure. Besides, adopting the mixture instead of single solvents is an effective strategy to synthesize IOCs, and the mixture solvents are working synergistically (Figure 5.2). In addition, the ratio of mixture solvent was also proven to influence the degree of the catenation.

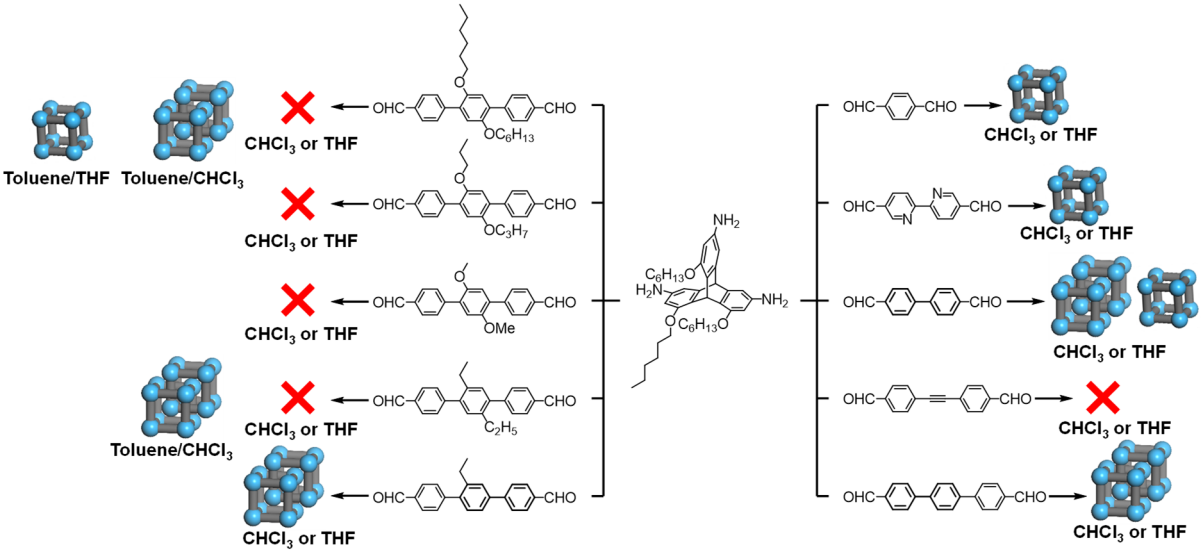

Figure 5.2 Illustration of the explored linkers and the solvents that influenced the formation of catenane (ball and stick model).

According to the results in previous chapters, the first tetramer polycatenane based on organic cages was successfully synthesized and isolated. Moreover, by adjusting the ratio of solvent mixtures and the amount of building block, it was possible to control the catenation degree of IOCs, thus isolating the corresponding trimer and dimer. It was found that using more toluene (for the mixture of $CHCl_3$ and toluene) and triamine building block promotes the formation of the polycatenane with a higher catenation degree.

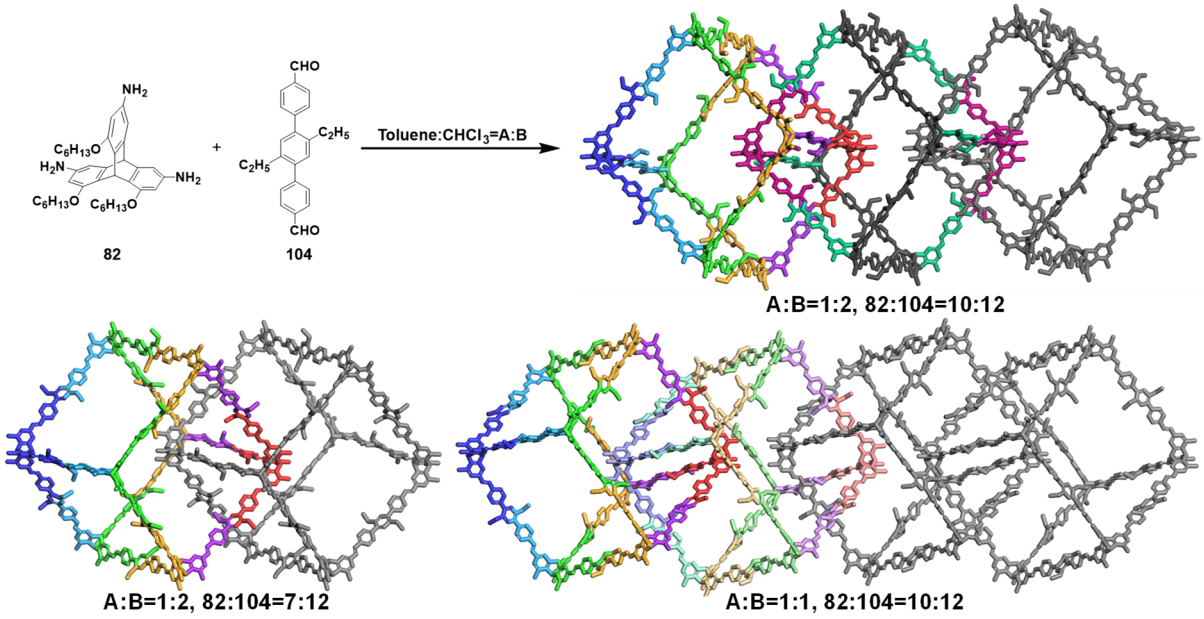

Figure 5.3 Synthesis of tetramer, trimer, and dimer (stick model) under different conditions, all butyl chains were cleaved for clarity.

Chapter 4 presented an ongoing project of preparing the crystalline MSOFs. A two-step strategy was adopted here, which is to first obtain the crystalline MOFs and then transform them into crystalline MSOFs by post-modification. Besides, the salicylaldehyde was utilized as

the modulator to promote the size of MOFs crystals. Unfortunately, only nanocrystals (~200-300 nm) of Cu-MOFs, Ni-MOFs, and Zn-MOFs were obtained currently (Figure 5.4).

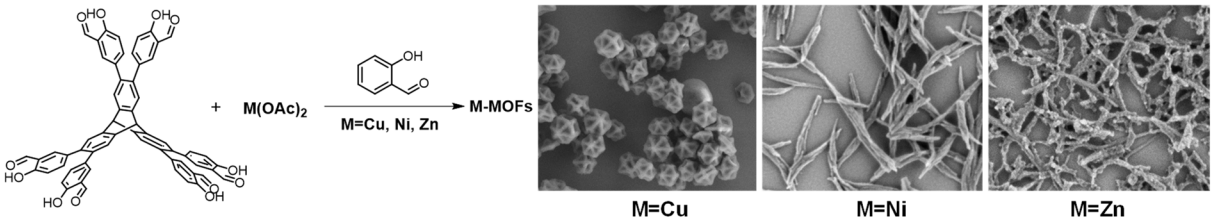

Figure 5.3 Preparation of Cu-MOFs, Ni-MOFs, and Zn-MOFs. The SEM pictures of obtained nanocrystals.

In summary, the research shown in this thesis provides a guideline for the synthesis of IOCs based on giant monomeric cages. The experimental results also demonstrate it is possible to control the catenation procedure and selectively synthesize and isolate the IOCs with the desired catenation degree. Although the resolution of 2D NMR spectra was not enough to fully elaborate some structures of them due to their complexity, it still showed the conformations of these IOCs. In addition, more investigations still need to be performed to explore the catenation mechanism of IOCs.

6. Experimental Section

6.1 General Remarks

Thin Layer Chromatography (TLC): For thin layer chromatography silica gel 60 F254 plates from Merck was used and examined under UV-light irradiation (254 nm and 365 nm).

Column Chromatography: Column chromatography[92] was performed using silica gel with particle sizes of 0.040 to 0.063 mm (Macherey-Nagel & Co. KG, Düren) using petroleum ether, ethyl acetate, dichloromethane, chloroform or their mixtures as eluents. For the elaboration of the right eluent, thin-layer chromatography was performed in a way that the fraction with the highest R_f value was $R_f < 0.4$, and this mixture was then used for the corresponding column chromatography.

Melting points (m.p.): Melting points (not corrected) were measured with a Büchi Melting Point B-545.

Elemental Analysis (EA): Elemental analysis was performed by the Microanalytical Laboratory of the University of Heidelberg using an Elementar Vario EL machine.

Infrared (IR) Spectroscopy: IR spectra were recorded neatly on a Fourier transform spectrophotometer (Bruker Lumos) equipped with a ZnSe ATR crystal. The signal intensity was described as s (strong), m (medium), and w (weak).

Nuclear Magnetic Resonance Spectroscopy (NMR): NMR spectra (^{1}H, ^{13}H, 2D coupling experiments) were recorded in $CDCl_3$, CD_2Cl_2, DMSO-*d*$_6$, or THF-*d*$_8$ using Bruker Avance 300 (300 MHz), Bruker Avance III 400 (400 MHz), Bruker Avance 500 (500 MHz), Bruker Avance III 600 (600 MHz) Bruker Avance III 700 (700 MHz) spectrometer at 298 K, unless otherwise mentioned. Chemical shifts (δ) are reported in parts per million (ppm) relative to traces of $CHCl_3$ (δ_H = 7.26 ppm, δ_C = 77.0 ppm), $CHDCl_2$ (δ_H = 5.32 ppm, δ_C = 54.0 ppm), THF-*d*$_8$ (δ_H = 1.72, 3.58 ppm, δ_C = 67.21, 25.31 ppm) or $(CD_3)_2SO$ (δ_H = 2.5 ppm, δ_C = 39.52 ppm) in the corresponding deuterated solvent. Signals were assigned by 2D NMR experiments (^{1}H,^{1}H-COSY, ^{1}H,^{1}H-NOESY, ^{1}H-DOSY, ^{1}H,^{13}C-HSQC, ^{1}H,^{13}C-HMBC).

Mass Spectrometry (MS): High-resolution mass spectrometry (HRMS) experiments were carried out on a Fourier Transform Ion Cyclotron Resonance (FT-ICR) mass spectrometer ApexQe hybrid 9.4 T (Bruker Daltonik GmbH, Bremen, Germany) equipped with a 9.4 T superconducting magnet and interfaced to an Apollo II MTP Dual ESI/MALDI source for

DART, ESI and MALDI experiments. MALDI-TOF MS experiments were carried out on a Bruker AutoFlex Speed time-of-flight with DCTB (*trans*-2-[3-(4-*tert*-butylphenyl)-2-methyl-2-propenylidene]malo-nonitrile) as matrix. Electron ionization (EI) mass spectra were recorded on a Varian 3800, on a JEOL JMS-700, or a JEOL AccuTOF GCx spectrometer. Molecule fragments were given as a mass-to-charge proportion (*m/z*).

X-ray crystal structure analysis: Crystal structure analysis was accomplished on Bruker APEX II Quazar diffractometer with a molybdenum source ($\lambda_{MoK\alpha}$ = 0.71073 Å) or an STOE Stadivari diffractometer with a copper source ($\lambda_{CuK\alpha}$ = 1.54178 Å). Intensities were corrected for Lorentz and polarization effects, an empirical absorption correction was applied using SADABS[93] based on the Laue symmetry of the reciprocal space. The structures were solved by intrinsic phasing or by direct methods with dual-space recycling and refined by full-matrix least squares methods based on F_2 against all unique reflections.[94] All non-hydrogen atoms were given anisotropic displacement parameters. Hydrogen atoms were input at calculated positions and refined with a riding model. When found necessary, disordered groups and/or solvent molecules were subjected to suitable geometry and restraints and/or constraints.

UV-VIS and Fluorescence Spectroscopy: Absorption spectra were recorded on Jasco UV-VIS V-730 spectrophotometer. Fluorescence spectra were recorded on a Jasco FP-8300 spectrofluorometer.

Recycling Gel Permeation Chromatography (*r*-GPC): Preparative GPC was performed on a Shimadzu LC-20AD recycling System using a PSS pre-column (size: 50×20 mm) and PSS SDV column (size: 300×20 mm, porosity: 3×100 Å; 2×500 Å + 2×1000 Å) with a flow-rate of 3~6 mL/min and a pressure maximum of 40 bar. The columns were temperature regulated (40 °C) by a CTO-20AC air circulation oven. Detection of the sample was realized by an SPD-M20A photodiode array with a wavelength range of 190 to 800 nm.

Theoretical Calculations: The geometry optimizations were performed based on Density Functional Theory (DFT)[95] calculations at PM6 for compounds in *Chapters 3.1* and *3.2*, or using Gaussian 09 package[96] for compounds in *Chapters 3.1* and *3.2*. The calculation of geometry radius was conducted by *Multiwfn*,[74a] which equals the distance from the geometry center to the furthest atom. The cavity diameters were measured by Materials Studio 2020. All the calculations are based on the optimized structure.

Software: Microsoft Word 2016 was used to write this thesis, chemical formulas were drawn using ChemDraw Professional 17.1.0.105 by Cambridgesoft, and graphs were processed with

OriginPro 8.5.0 by OriginLab Corp. IR and MS spectra were processed using ACD/Spectrus Processor (S40S41) by Advanced Chemistry Development, Inc. and plotted using OriginPro. NMR spectra were integrated and processed using MestReNova (v6.0.2-5475).

6.1.1 Solvents

The solvents were used from stock without further purification or drying unless otherwise noted. Dry solvents of THF (Honeywell ≥ 99.9%, inhibitor-free), DCM (Honeywell ≥ 99.8%, stab. with 0.2% amylene), diethyl ether (Honeywell ≥ 99.8%, stab. with 0.2% BHT) and toluene (Honeywell ≥ 99.7%) were obtained from MBraun Solvent Purification Systems (MB SPS-800).

Solvents	**Purities**	**Commercial source**
1,2-Dichlorobenzene-d_4	98%	Sigma-Aldrich
Acetone	≥ 99%	Honeywell
Chlorobenzene	99.8%	Sigma-Aldrich
Chloroform	> 99%	Sigma-Aldrich
Chloroform-*d*	99.8%	Sigma-Aldrich
Dichloromethane	n.d. (stab. with 0.2% ethanol)	VWR Chemicals
Dichloromethane-d_2	99.9%	Sigma-Aldrich
Diethyl ether	≥ 99.5%	Sigma-Aldrich
Ethanol	≥ 99.8%	Sigma-Aldrich
Ethyl acetate	≥ 99.5%	Honeywell
Methanol	≥ 99.8%	Honeywell
N, *N*-Dimethylformamide	≥ 99.8%	Sigma-Aldrich
n-Heptane	≥ 99%	Acros Organics
n-Hexane	98%	VWR Chemicals
n-Pentane	≥ 99%	Sigma-Aldrich
Petroleum ether (40-60 °C)		Honeywell
Tetrahydrofuran	≥ 99.9% (stab. with 250 ppm BHT)	Sigma-Aldrich
Toluene	≥ 99.7%	Sigma-Aldrich
Water	deionized	Uni-Heidelberg Institute

6.1.2 Chemicals and Reagents

All chemicals and reagents were used without further purification unless otherwise noted.

Chemicals	Purities	Commercial source
5-Bromosalicylaldehyde	≥ 98%	Sigma-Aldrich
[1,1′-Bis(diphenylphosphino)ferrocene]-dichloropalladium(II)	98%	Carbolution
bis(pinacolato)diboron	99%	Carbolution
Anthracene	99%	Acros Organics
Anthranilic acid	98%	Acros Organics
Bromine	≥ 99.99%	Sigma-Aldrich
1,8-Dihydroxyanthraquinone	96%	Sigma-Aldrich
2-Methoxyphenol	> 99%	Acros Organics
Hexamethylentetraamine	99%	Grüssing
Methyl iodide	≥ 99%	Sigma-Aldrich
n-Butyllithium solution 2.5 M in hexanes		Sigma-Aldrich
tert-Butylamine	≥ 98%	Sigma-Aldrich
Acetic acid	> 99%	Honeywell
Caesium fluoride	≥ 99.99%	Sigma-Aldrich
Potassium hydroxide		Institute Stock
Potassium carbonate	99%	Grüssing
Triethylamine	≥ 99.5%	Sigma-Aldrich
Trifluoromethanesulfonic anhydride	> 99%	Acros Organics
Zinc (powder)	95%	Grüssing GmbH
Boron tribromide	≥ 99%	Sigma-Aldrich
Celite 545		VWR Chemicals
N-Bromosuccinimid	≥ 99%	Sigma-Aldrich
5,5′-Dimethy-2,2′-bipyridine	99.8%	BLD pharm
4,4′-Di-*tert*-butyl-2,2′-dipyridyl	≥ 98%	Sigma-Aldrich
(1,5-Cyclooctadiene)(methoxy)iridium(I) dimer		Sigma-Aldrich
Hydrochloric acid	aq.36.5-38%	Sigma-Aldrich

1,4-Dibromo-2,5-diethylbenzene	≥ 98%	TCI
4-Formylphenylboronic acid	≥ 98%	BLD pharm
[1,1'-Biphenyl]-4,4'-dicarbaldehyde	95%	BLD pharm
N-Bromosuccinimide	99%	Sigma-Aldrich
n-Butyllithium solution (2.5 M in hexane)		Acros Organics
1,4-Dibromo-2,5-dimethoxybenzene	99.6%	BLD pharm
4-Bromo-3-methylbenzene	98%	abcr
1,4-Dibromo-2-ethylbenzene	96%	Alfa Aesar
Potassium carbonate	99%	Grüssing GMBH
Bis(triphenylphosphine)palladium(II) dichloride	98%	Carbolution
3-Bromobenzaldehyde	99%	BLD pharm
Sodium bicarbonate	100%	Grüssing GMBH
Sodium chloride	≥ 99.8%	Sigma-Aldrich
Sodium metabisulfite	97%	Honeywell
Sodium sulfate	≥ 99%	Bernd Kraft
Tetrakis(triphenylphosphine)palladium(0)	99%	Sigma-Aldrich
Nickel(II) acetate tetrahydrate	99%	Sigma-Aldrich
Copper(II) acetate monohydrate		Institute stock
Molecular sieve 3 Å		Carl Roth
Molecular sieve 4 Å		Carl Roth

6.1.3 General Procedures

General Procedure 1 (GP1) for Williamson ether reactions

1,8,13-Trihydroxytriptycene (2.80 g, 9.20 mmol) and potassium carbonate (7.60 g, 55.20 mmol) were suspended in DMF (80 mL) and stirred at 80 °C for 30 minutes. Then 1-Bromopropane (6.20 g, 50.60 mmol) was added and the mixture was stirred for another 20 hours at 80 °C. After cooling to room temperature, the brown suspension was poured into cold water (200 mL). The suspension was filtered and the solid was washed with water (2 × 100 mL) and methanol (2 × 100 mL), the product was dried in a vacuum to obtain 1,8,13-Tripropyloxytriptycene in 91% yield (3.60 g, 8.40 mmol) as a slightly brown powder.

General Procedure 2 (GP2) for aromatic C–H borylation reactions

A screw-capped vial was charged with (1,5-Cyclooctadiene) (methoxy) iridium(I)dimer (66.0 mg, 0.10 mmol, 5 mol%), 4,4'-di-tert-butyl-2,2'-dipyridyl (52.0 mg, 0.20 mmol, 10 mol%) and bis-(pinacolato) diborane (80.0 mg) under argon atmosphere (Glovebox). Dry THF (5 mL) was added and the mixture was sonication for 5 minutes at room temperature. The dark brown solution was transferred to another screw-capped vial charged with a suspension of 1,8,13-trihexyloxytripitycene (1.10 g, 2.00 mmol) and bis-(pinacolato) diborane (2.10 g, 9.00 mmol) in dry THF (10 mL) under argon atmosphere. The mixture was stirred at 80 °C for 48 hours. The solvent was evaporated under reduced pressure and the obtained brown oil liquid was suspended in methanol and treated with sonication for 10 minutes, the suspension was filtered and washed with methanol (3 × 20 mL). The obtained off-white solid was recrystallized from chloroform/ethanol to obtain 2,2'2"-(1,8,13-trihexyloxytriptycene-3,6,15-triyl)tris(4,4,5,5,-tetramethyl-1,3,2-diox)borolane in 77% yield (1.40 g, 1.53 mmol) as a light brown powder.

General Procedure 3 (GP3) for amination reaction via Hydroxylamine-O-sulfonic acid

1,8,13-Trihexyloxy-3,6,15-tris(pinacolato)borontriptycene (1.00 g, 1.00 mmol) was suspended in acetonitrile (15 mL) under argon atmosphere. An aqueous solution of sodium hydroxide (1 M, 15 mL) and Hydroxylamine-O-sulfonic acid (0.60 g, 5.00 mmol) was added and the mixture was stirred for 24 hours at room temperature. The obtained cloudy suspension was diluted with water (25 mL), extracted with ethyl acetate (3 × 50 mL) and the combined organic layer was dried over $MgSO_4$. The solution was evaporated to obtain orange solids and further purified by column chromatography (ethyl acetate/petroleum ether, 5:1) to obtain 1,8,13-Trihexyloxy-3,6,15-triaminotriptycene in 42% yield (250.0 mg, 0.40 mmol) as brown solid.

General Procedure 4 (GP4) for cage and catenane synthesis.[1]

1,8,13-Trihexyloxy-3,6,15-triaminotriptycene (9.6 mg, 16.0 μmol) and 1,4-Phthalaldehyde (3.2 mg, 24.0 μmol) were dissolved in 3 mL $CHCl_3$. Then TFA (in $CHCl_3$, 0.01 M, 4 mol%, 60 μL) was added and the light brown solution was stirred at 60 °C for 5 days. After cooling to room temperature, the solution was filtered through a small Celite® plug and then a syringe filter (0.45 μm)[2], the resulting solution was concentrated and precipitated by methanol, and the yellow precipitation was collected by centrifuge and washed with methanol for 3 times. The solid was directly dissolved in THF and purified by r-GPC, the desired fraction was collected and concentrated, then precipitated with methanol[3]. The precipitates were collected by centrifuge and dried under vacuum for 1 hour to obtain **HexTe-Cage** in 54% yield (6.4 mg, 1.1 μmol) as yellow solid.

1 The synthesis of all cages and catenanes mentioned in this thesis follows this procedure, otherwise, the specific conditions will be displayed accordingly.

[2] This step is necessary for all syntheses of cage and catenane in this thesis, even the reaction looks like homogeneous. There are always some invisible oligomers in the solution, which will be insoluble after precipitated and leading to the yield loss.

[3] This precipitation procedure will remove the Butylhydroxytoluol (BHT) in THF.

6.2 Syntheses

6.2.1 Compounds of Chapter 3.1

1,8,13-Trihydroxytriptycene **74**, and the corresponding substrates **62-73** were synthesized *via* previously reported synthetic routes.[71g]

1,8,13-Tripropyloxytriptycene (75)

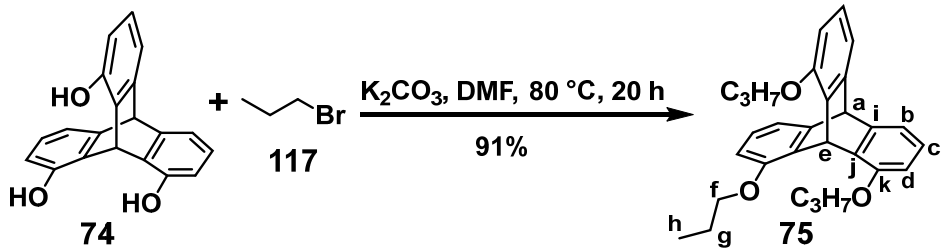

75 was synthesized according to **GP1** with 1,8,13-Trihydroxytriptycene (2.80 g, 9.20 mmol), Potassium carbonate (7.60 g, 55.20 mmol), 1-Bromopropane (6.20 g, 50.60 mmol), DMF (80 mL). The product was dried in a vacuum to obtain 1,8,13-Tripropyloxytriptycene in 91% yield (3.60 g, 8.40 mmol) as a slightly brown powder.

M.p. = 305 °C.

MS (ESI): *m/z* $[M]^+$ calcd. for $C_{29}H_{32}O_3Na^+$: 451.2244; found: 451.2244.

Elemental Analysis (%): calcd for $C_{29}H_{32}O_3$: C 81.27, H 7.53; found C 80.11, H 7.48.

^{1}H NMR (600 MHz, $CDCl_3$): δ (ppm)= 7.01-6.99 (d, 3H-*b*), 6.97 (s, 1H-*e*), 6.90-6.86 (t, 3H-*c*), 6.57-6.55 (d, 3H-*d*), 5.38 (s, 1H-*a*), 3.95-3.92 (t, 6H-*f*), 1.92-1.83 (m, 6H-*g*), 1.19-1.15 (t, 9H-*h*).

^{13}C-NMR (151 MHz, $CDCl_3$): δ (ppm) = 154.23 (C-*k*), 148.73 (C-*i*), 134.00 (C-*j*), 125.62 (C-*c*), 116.57 (C-*b*), 110.28 (C-*d*), 70.35 (C-*f*), 54.78 (C-*a*), 33.68 (C-*e*), 23.12 (C-*g*), 10.81 (C-*h*).

IR (ATR): $\tilde{\nu}$ (cm^{-1}) = 2960 (w), 2937 (w), 2875 (w), 1596 (m), 1573 (w), 1483 (m), 1465 (m), 1456 (m), 1442 (w), 1396 (m), 1267 (s), 1245 (m), 1109 (m), 1095 (s), 1070 (m), 1043 (w), 956 (w), 856 (m), 786 (w), 744 (w), 732 (s), 680 (m), 640 (w).

2,2'2"- (1,8,13-tripropyloxytriptycene-3,6,15-triyl) tris (4,4,5,5,-tetramethyl-1,3,2-diox) borolane (78)

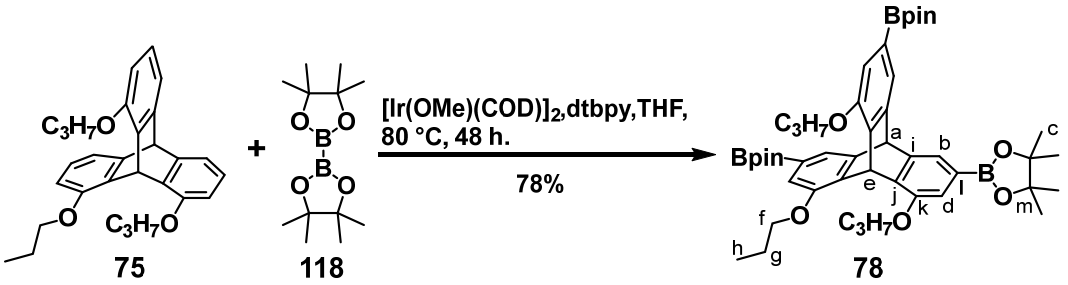

78 was synthesized according to **GP2** with (1,5-Cyclooctadiene)(methoxy)iridium(I)dimer (66.2 mg, 0.10 mmol, 5 mol%), 4,4'-di-tert-butyl-2,2'-dipyridyl (52.0 mg, 0.20 mmol, 10 mol%), bis-(pinacolato)diborane (2.10 g, 9.00 mmol), 1,8,13-1,8,13-Tripropyloxytriptycene (0.86 g, 2.00 mmol) and dry THF (15 mL). The obtained off-white solid was recrystallized from chloroform/ethanol to obtain 2,2'2"-(1,8,13-tripropyloxytriptycene-3,6,15-triyl)tris(4,4,5,5,-tetramethyl-1,3,2-diox)borolane in 78% yield (1.25 g, 1.55 mmol) as light brown powder.

M.p. = 346 °C.

MS (ESI): *m/z* $[M]^+$ calcd. for $C_{47}H_{65}B_3O_9^+$: 806.4908; found: 806.4937.

Elemental Analysis (%): calcd. for $C_{47}H_{65}B_3O_9$: C 70.00, H 8.12; found: C 69.81, H 7.88.

^{1}H NMR (600 MHz, $CDCl_3$): δ (ppm) = 7.42 (s, 3H-*b*), 7.00 (s, 1H-*e*), 6.98 (s, 3H-*d*), 5.45 (s, 1H-*a*), 3.98-3.96 (t, 6H-*f*), 1.89-1.83 (m, 6H-*g*), 1.20 (s, 36H-*c*), 1.16-1.13 (t, 9H-*h*).

^{13}C-NMR (151 MHz, $CDCl_3$): δ (ppm) = 154.00 (C-*k*), 147.96 (C-*i*), 136.68 (C-*j*), 126.67 (C-*l*), 122.81 (C-*b*), 116.35 (C-*d*), 83.63 (C-*m*), 70.39 (C-*f*), 54.41 (C-*a*), 34.37 (C-*e*), 24.88 (C-*g*), 23.11 (C-*c*), 10.83 (C-*h*).

IR (ATR): $\tilde{\nu}$ (cm^{-1}) = 2974 (w), 1587 (w), 1571 (w), 1479 (w), 1377 (s), 1355 (vs), 1288 (m),1261 (m), 1232 (m), 1139 (vs), 1107 (m), 1083 (m), 966 (m), 916 (w), 856 (m), 831 (w), 715 (w), 698 (s), 669 (m).

1,8,13-Tripropyloxy-3,6,15-triaminotriptycene (81)

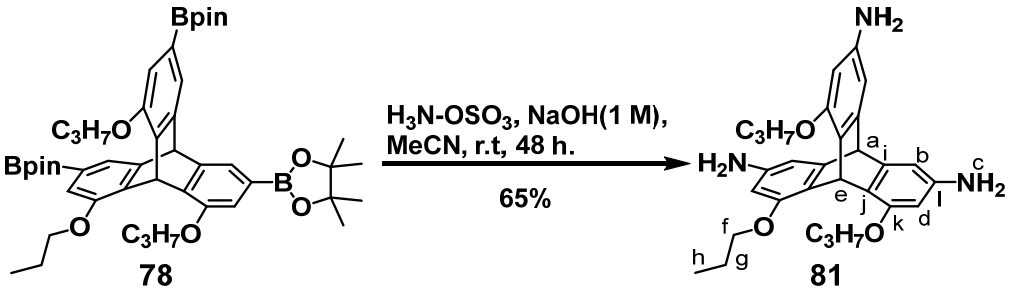

81 was synthesized according to **GP3** with 1,8,13-Tripropyloxy-3,6,15-tris(pinacolato)borontriptycene (0.80 g, 1.00 mmol), hydroxylamine-O-sulfonic acid (0.56 g, 5.00 mmol), acetonitrile (15 mL) and an aqueous solution of sodium hydroxide (1 M, 15 mL). The product was purified by column chromatography (ethyl acetate/petroleum ether, 5:1) to obtain 1,8,13-Tripropyloxy-3,6,15-triaminotriptycene in 65% yield (0.31 g, 0.65 mmol) as brown solid.

M.p. = 300 °C.

MS (ESI): *m/z* $[M]^+$ calcd. for $C_{29}H_{36}N_3O_3^+$: 474.2751; found: 474.2752.

Elemental Analysis (%): calcd. for $C_{29}H_{36}N_3O_3$: C 73.54, H 7.45, N 8.87; found: C 72.51, H 7.70, N 8.26.

^{1}H NMR (600 MHz, DMSO-d_6): δ (ppm) = 6.25 (s, 3H-*b*), 6.15 (s, 1H-*e*), 5.82 (s, 3H-*d*), 4.79 (s, 1H-*a*), 4.74 (s, 6H-*c*), 3.79-3.77 (m, 6H-*f*), 1.76-1.70 (m, 6H-*g*), 1.10-1.07 (m, 9H-*h*).

^{13}C-NMR (151 MHz, DMSO-d_6): δ (ppm) = 152.92 (C-*k*), 148.73 (C-*l*), 146.08 (C-*i*), 123.07 (C-*j*), 103.55 (C-*b*), 95.41 (C-*d*), 69.28 (C-*f*), 54.23 (C-*a*), 30.93 (C-*e*), 22.55 (C-*g*), 10.51 (C-*h*).

IR (ATR): $\tilde{\nu}$ (cm^{-1}) = 3336 (w), 2962 (m), 2935 (w), 2875 (w), 1598 (vs), 1494 (m), 1454 (m), 1323 (m), 1240 (m), 1195 (m), 1137 (vs), 1097 (s), 1070 (s), 973 (w), 838 (w), 817 (w), 757 (m), 678 (w).

1,8,13-Trihexyloxytriptycene (76)

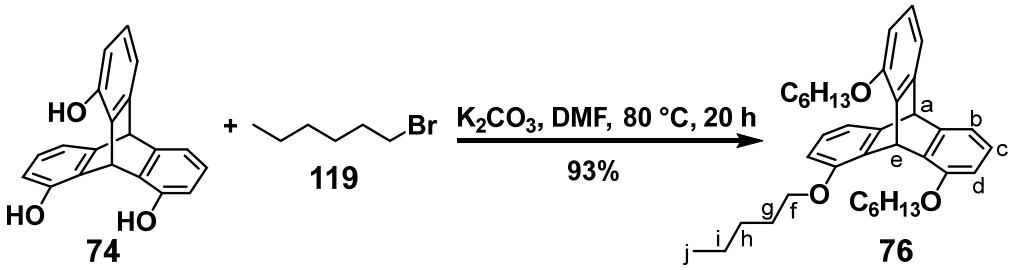

76 was synthesized according to **GP1** with 1,8,13-Trihydroxytriptycene (3.02 g, 10.00 mmol) and potassium carbonate (8.29 g, 60.00 mmol), 1-Bromohexane (9.10 g, 55.00 mmol) and DMF (100 mL). The product was dried in a vacuum to obtain 1,8,13-Trihexyloxytriptycene in 93% yield (5.17 g, 9.30 mmol) as a slightly brown powder.

M.p. = 225 °C.

^{1}H NMR (300 MHz, $CDCl_3$): δ (ppm) = 7.01-6.99 (d, 3H-*b*), 6.92-6.90 (d, 1H-*e*), 6.88-6.85 (d, 3H-*c*), 6.57-6.55 (d, 3H-*d*), 5.37 (s, 1H-*a*), 3.99-3.95 (t, 6H-*f*), 1.91-1.82 (m, 6H-*g*), 1.64-1.54 (m, 6H-*h*), 1.42-1.38 (m, 12H-*i*), 0.97-0.93 (t, 9H-*j*).

Analytical data are in accordance with those previously reported.[71k]

2,2'2"-(1,8,13-trihexyloxytriptycene-3,6,15-triyl)tris(4,4,5,5,-tetramethyl-1,3,2-diox)borolane (79)

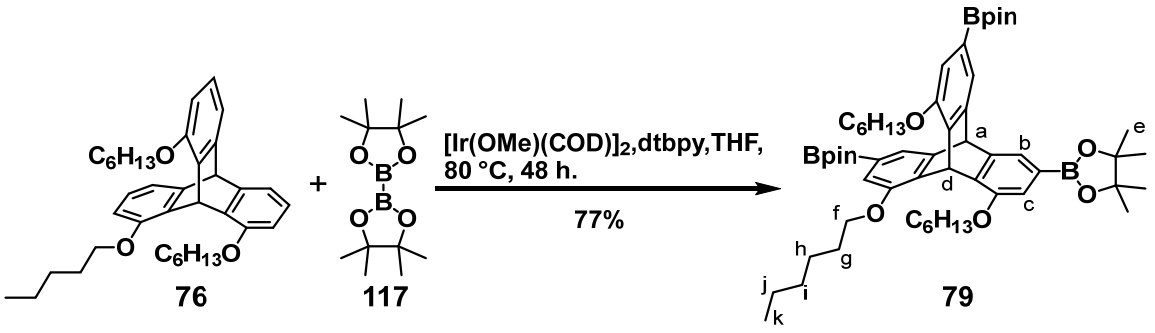

79 was synthesized according to **GP2** with (1,5-Cyclooctadiene)(methoxy)iridium(I)dimer (66.2 mg, 0.10 mmol, 5 mol%), 4,4'-di-tert-butyl-2,2'-dipyridyl (52.0 mg, 0.20 mmol, 10

mol%), bis-(pinacolato)diborane (2.12 g, 9.00 mmol), 1,8,13-trihexyloxytripitycene (1.12 g, 2.00 mmol) and dry THF (15 mL), The obtained off-white solid was recrystallized from chloroform/ethanol to obtain 2,2'2"-(1,8,13-trihexyloxytriptycene-3,6,15-triyl)tris(4,4,5,5,-tetramethyl-1,3,2-diox)borolane in 77% yield (1.40 g, 1.53 mmol) as the light brown powder.

M.p. = 305 °C.

^{1}H NMR (300 MHz, $CDCl_3$): δ (ppm) = 7.41 (s, 3H-*b*), 6.98 (s, 3H-*c*), 6.94 (s, 1H-*d*), 5.44 (s, 1H-*a*), 4.01-3.97 (t, 6H-*f*), 1.89-1.80 (m, 6H-*g*), 1.59-1.52 (m, 6H-*h*), 1.39-1.36 (m, 12H-*i, j*), 1.28 (s, 36H-*e*), 0.96-0.91 (t, 9H-*k*).

Analytical data are in accordance with those previously reported.[71k]

1,8,13-Trihexyloxy-3,6,15-triaminotriptycene (82)

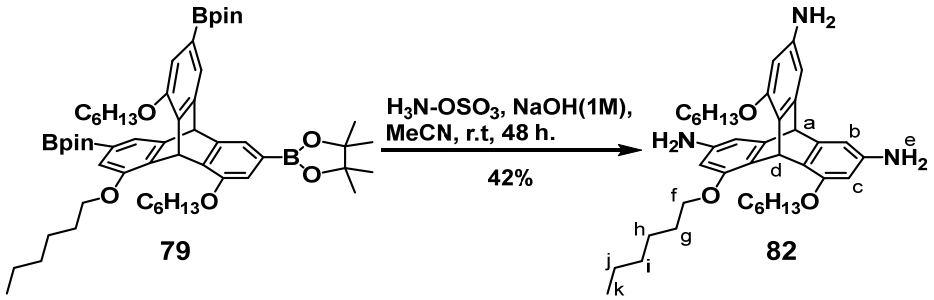

82 was synthesized according to **GP3** with 1,8,13-Trihexyloxy-3,6,15-tris(pinacolato)borontriptycene (1.00 g, 1.07 mmol), Hydroxylamine-O-sulfonic acid (0.56 g, 5.00 mmol), acetonitrile (15 mL) and an aqueous solution of sodium hydroxide (1M, 15 mL). The product was further purified by column chromatography (ethyl acetate/petroleum ether, 5:1) to 1,8,13-Trihexyloxy-3,6,15-triaminotriptycene in 42% yield (0.25 g, 0.42 mmol) as brown solid.

M.p. = 250 °C.

^{1}H NMR (300 MHz, DMSO-d_6): *δ* (ppm) = 7.41 (s, 3H-*b*), 6.98 (s, 3H-*c*), 6.94 (s, 1H-*d*), 5.44 (s, 1H-*a*), 4.01-3.97 (t, 6H-*f*), 3.23 (s, 6H-*e*), 1.89-1.80 (m, 6H-*g*), 1.59-1.52 (m, 6H-*h*), 1.39-1.36 (m, 12H-*i, j*), 0.96-0.91 (t, 9H-*k*).

Analytical data are in accordance with those previously reported.[71k]

1,8,13-Tridecayloxytriptycene (77)

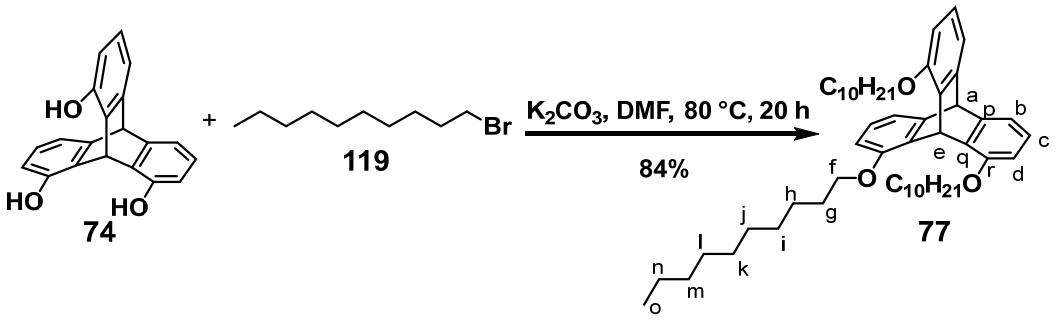

77 was synthesized according to **GP1** with 1,8,13-Trihydroxytriptycene (1.00 g, 3.30 mmol), Potassium carbonate (2.70 g, 19.80 mmol), 1-Bromodecane (3.80 g, 17.20 mmol) and DMF (30 mL). The product was dried in a vacuum to obtain 1,8,13-Tridecayloxytriptycene in 84% yield (2.00 g, 2.70 mmol) as a slightly brown powder.

M.p. = 224 °C.

MS (ESI): *m/z* $[M]^+$ calcd. for $C_{50}H_{74}O_3^+$: 722.563; found: 722.563.

Elemental Analysis (%): calcd. for $C_{50}H_{74}O_3$: C 83.05, H 10.32; found: C 82.78, H 9.99.

^{1}H NMR (600 MHz, $CDCl_3$): δ (ppm) = 7.00-6.99 (d, 3H-*b*), 6.91 (s, 1H-*e*), 6.89-6.85 (t, 3H-*c*), 6.56-6.55 (d, 3H-*d*), 5.37 (s, 1H-*a*), 3.98-3.95 (m, 6H-*f*), 1.90-1.83 (m, 6H-*g*), 1.62-1.55 (m, 6H-*h*), 1.90-1.83 (m, 36H-*i, j, k, l, m, n*), 0.92-0.88 (m, 9H-*o*).

^{13}C-NMR (151 MHz, $CDCl_3$): δ (ppm) = 154.25 (C-*r*), 148.71 (C-*q*, 134.04 (C-*p*), 125.60 (C-*c*), 116.58 (C-*b*), 110.44 (C-*d*), 69.05 (C-*f*), 54.78 (C-*a*), 33.73 (C-*e*), 32.14 (C- *alkyl*), 29.97 (C-*g*), 29.94 (C- *alkyl*), 29.90 (C- *alkyl*), 29.85 (C- *alkyl*), 29.61 (C- *alkyl*), 26.26 (C-*h*), 22.87 (C- *alkyl*), 14.27 (C-*o*).

IR (ATR): $\tilde{\nu}$ (cm^{-1}) = 2948 (w), 2920 (s), 2852 (m), 1596 (m), 1485 (m), 1467 (s), 1392 (w), 1280 (vs), 1249 (w), 1101 (s), 1066 (m), 786 (m), 738 (s), 640 (w).

2,2'2"- (1,8,13-tridecayloxytriptycene-3,6,15-triyl) tris (4,4,5,5, -tetramethyl-1,3,2-diox) borolane (80)

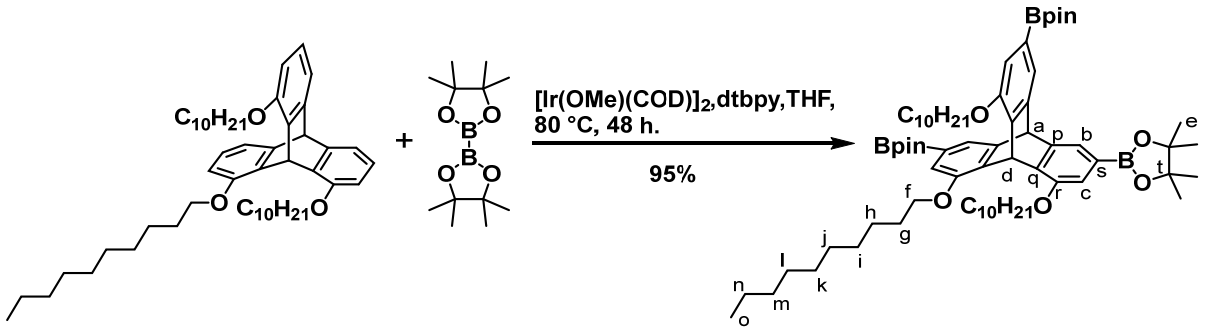

80 was synthesized according to **GP2** with (1,5-Cyclooctadiene)(methoxy)iridium(I)dimer (66.2 mg, 0.10 mmol, 5 mol%), 4,4'-di-tert-butyl-2,2'-dipyridyl (52.0 mg, 0.20 mmol 10 mol%), bis-(pinacolato)diborane (2.12 g, 9.00 mmol), 1,8,13-1,8,13-Tridecayloxytriptycene (1.50 g, 2.00 mmol) and bis-(pinacolato)diborane (2.12 g, 9.00 mmol) and THF (25 mL). The obtained off-white solid was recrystallized from chloroform/ethanol to obtain 2,2'2"-(1,8,13-trihexyloxytriptycene-3,6,15-triyl)tris(4,4,5,5,-tetramethyl-1,3,2-diox)borolane in 95% yield (2.10 g, 1.90 mmol) as the light brown powder.

M.p. = 85 °C.

MS (ESI): *m/z* $[M]^+$ calcd. for $C_{68}H_{107}B_3O_9^+$: 1100.8914; found: 1100.8242.

Elemental Analysis (%): calcd. for $C_{68}H_{107}B_3O_9$: C 74.18, H 9.8; found: C 74.20, H 10.12.

^{1}H NMR (600 MHz, $CDCl_3$): δ (ppm) = 7.41 (s, 3H-*b*), 6.97 (s, 1H-*c*), 6.94 (s, 1H-*d*), 5.44 (s, 1H-*a*), 4.00-3.97 (m, 6H-f), 1.86-1.82 (m, 6H-g), 1.59-1.54 (m, 6H-h), 1.40-1.28 (m, 72H-*i, j, k, l, m, n, e*), 0.92-0.88 (m, 9H-*o*).

^{13}C-NMR (151 MHz, $CDCl_3$): δ (ppm) = 154.03 (C-*r*), 147.97 (C-*p*), 136.72 (C-*q*), 122.83 (C-*b*), 116.46 (C-*c*), 83.63 (C-*s*), 69.02 (C-*f*), 54.00 (C-*a*), 34.40 (C- *alkyl*), 32.14 (C- *alkyl*), 29.98 (C- *alkyl*), 29.95 (C- *alkyl*), 29.90 (C- *alkyl*), 29.85 (C- *alkyl*), 29.62 (C- *alkyl*), 26.26 (C-*alkyl*), 24.89 (C- *alkyl*), 22.88 (C- *alkyl*), 14.29 (C-*o*).

IR (ATR): $\tilde{\nu}$ (cm^{-1}) = 2921 (m), 2852 (w), 1589 (w), 148 1(w), 1402 (m), 1355 (vs), 1328 (m), 1296 (m), 1251 (m), 1139 (s), 1107 (m), 1089 (m), 966 (m), 918 (w), 856 (m), 833 (w), 765 (w), 713 (w), 696 (m), 669 (w).

1,8,13-Tridecaxyloxy-3,6,15-triaminotriptycene (83)

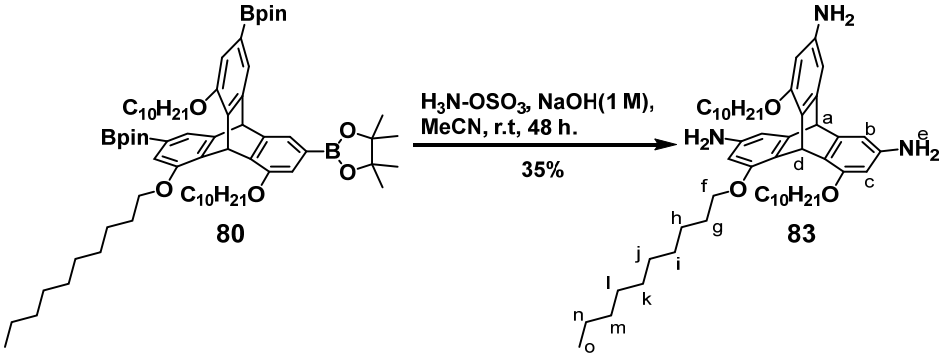

83 was synthesized according to **GP3** with 1,8,13-Tridecayloxy-3,6,15-tris(pinacolato)borontriptycene (1.10 g, 1.00 mmol), Hydroxylamine-O-sulfonic acid (0.56 g, 5.00 mmol), acetonitrile (15 mL) and an aqueous solution of sodium hydroxide (1 M, 15 mL). The product was further purified by column chromatography (ethyl acetate/petroleum ether, 5:1) to obtain 1,8,13-Trihexyloxy-3,6,15-triaminotriptycene in 35% yield (0.27 g, 0.35 mmol) as brown solid.

M.p. = 202 °C.

MS (ESI): *m/z* $[M]^+$ calcd. for $C_{50}H_{79}N_3O_3^+$: 769.6110; found: 769.4871.

Elemental Analysis (%): calcd. $C_{50}H_{77}N_3O_3$: C 78.18, H 10.10, N 5.47; found: C 77.29, H 10.99, N 5.32.

^{1}H NMR (600 MHz, DMSO-*d_6*): δ (ppm) = 6.24 (s, 3H-*b*), 6.10 (s, 1H-*d*), 5.81 (s, 3H-*c*), 4.78 (s, 1H-*a*), 4.70 (s, 1H-NH2), 3.80-3.77 (t, 6H-*f*), 1.76-1.69 (m, 6H-*g*), 1.55-1.49 (m, 6H-*h*), 1.34-1.28 (m, 36H-*i, j, k, l, m, n*), 0.89-0.86 (m, 9H-*o*).

^{13}C-NMR (151 MHz, DMSO-*d_6*): δ (ppm) = 152.95 (C-*r*), 148.66 (C-*p*), 146.00 (C-*q*), 123.06 (C-*b*), 103.56 (C-*b*), 95.50 (C-*c*), 67.99 (C-*f*), 54.19 (C-*a*), 31.40 (C-*d*), 29.46 (C- *alkyl*), 29.46

(C- *alkyl*), 29.31 (C- *alkyl*), 29.25 (C- *alkyl*), 28.86 (C- *alkyl*), 25.74 (C- *alkyl*), 22.12 (C- *alkyl*), 13.86 (C-*o*).

IR (ATR): $\tilde{\nu}$ (cm^{-1}) = 2956 (m), 2918 (s), 2850 (s), 1600 (vs), 1496 (m), 1456 (m), 1350 (m), 1325 (m), 1244 (m), 1197 (m), 1141 (vs), 1107 (m), 1078 (m), 975 (w), 817 (m), 763 (m), 719 (m), 680 (w).

[1,1':4',1''-Terphenyl]-4,4''-dicarbaldehyde (86)

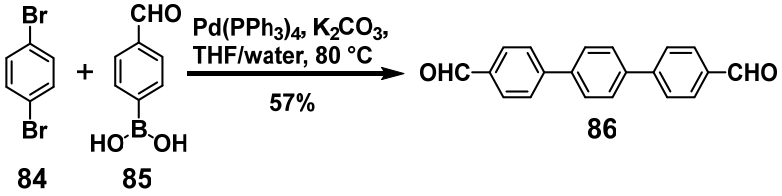

4-Formylphenylboronic acid (0.72 g, 4.80 mmol), 1,4-dibromobenzene (0.47 g, 2.00 mmol) was dissolved in 20 mL THF. 12 mL K_2CO_3 (2M) was added to the solution and bubbled with N_2 for 10 minutes. $Pd(PPh_3)_4$ (92.0 mg, 0.08 mmol) was added and the resulting mixture was stirred at 85 °C for 18 hours. The reaction mixture was extracted with DCM. The combined organic layer was washed with brine, dried over $MgSO_4$, and filtered. The solution was concentrated and precipitated with Et_2O to obtain [1,1':4',1''-Terphenyl]-4,4''-dicarbaldehyde in 57% yield (196.0 mg, 0.48 mmol) as the off-white solid.

M.p. = 220 °C.

^{1}H NMR (300 MHz, $CDCl_3$): δ (ppm) = 10.08 (s, 1H), 8.00-7.98 (d, 2H), 7.83-7.80 (d, 2H), 7.77 (s, 1H).

Analytical data are in accordance with those previously reported.[72]

HexBi-Cage

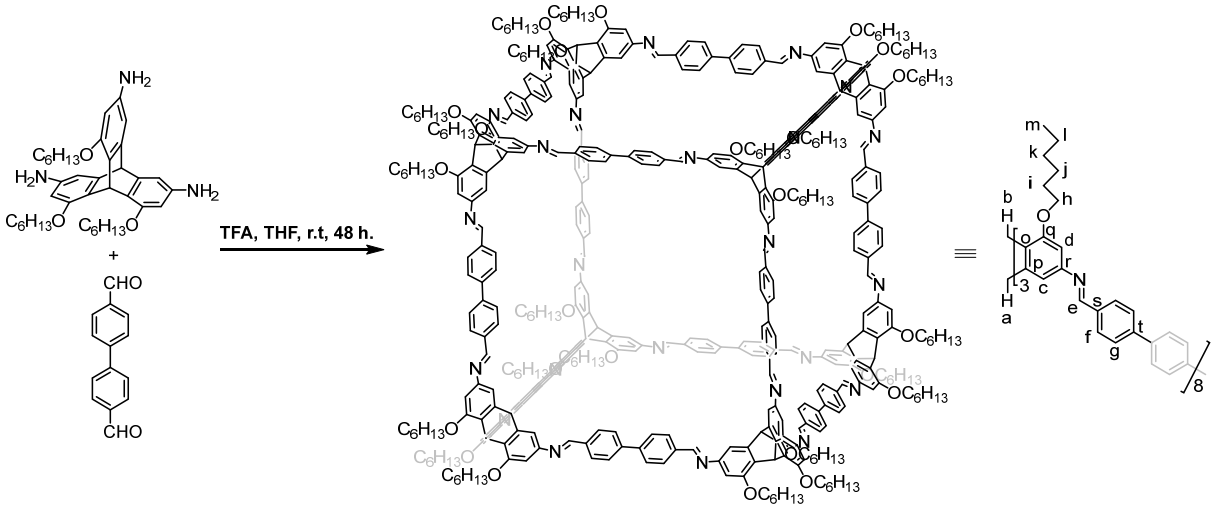

HexBi-Cage was synthesized according to **GP4** with 1,8,13-Trihexyloxy-3,6,15-triaminotriptycene (9.6 mg, 16.0 µmol), 4,4'-Biphenyldicarboxaldehyde (5.0 mg, 24.0 µmol),

THF (3 mL), and TFA (in THF, 0.01 M, 4 mol%, 60 µL). The light brown solution was stirred at r.t for 2 days. The crude product was purified by THF-GPC to obtain **HexBi-Cage** in 12% yield (1.6 mg, 0.23 µmol) as a yellow solid.

M.p. ≥ 355°C (decomposition).

MS (MALDI-TOF): *m/z* $[M]^+$ calcd. for $C_{472}H_{496}N_{24}O_{24}^+$: 6883.833; found: 6888.654.

Elemental Analysis (%): calcd. $C_{472}H_{496}N_{24}O_{24}$: C 82.29, H 7.26, N 4.88; found: C 78.76, H 7.26, N 4.68.

^{1}H NMR (600 MHz, THF-*d*$_8$): δ (ppm) = 8.60 (s, 24H-*e*), 8.00-7.99 (d, 48H-*f*), 7.85-7.83 (d, 48H-*g*), 7.01 (s, 24H-*c*), 6.92 (s, 8H-*b*), 6.65 (s, 24H-*d*), 5.49 (s, 8H-*a*), 4.09 (m, 48H-*h*), 1.95 (m, 48H-*i*), 1.70 (m, 48H-*j*), 1.47(m, 96H-*k, l*), 0.99 (s, 72H-*m*).

^{13}C-NMR (151 MHz, THF-*d*$_8$): δ (ppm) = 158.91 (C-*e*), 155.01 (C-*q*), 150.85 (C-*r*), 149.77 (C-*o*), 143.14 (C-*t*), 137.19 (C-*s*), 132.27 (C-*p*), 129.80 (C-*f*), 127.69 (C-*g*), 109.58 (C-*c*), 104.01 (C-*d*), 69.16 (C-*h*), 55.59 (C-*a*), 34.22 (C-*b*), 32.66 (C-*k*), 30.49 (C-*i*), 26.66 (C-*j*), 23.47 (C-*l*), 14.40 (C-*m*).

IR (ATR): $\tilde{\nu}$ (cm^{-1}) = 2950 (w), 2925 (m), 2856 (w), 1587 (vs), 1465 (m), 1429 (m), 1292 (m), 1118 (s), 1099 (s), 1066 (m),1002 (w), 972 (m), 835 (m), 815 (m), 723 (w).

HexBi-Catenane

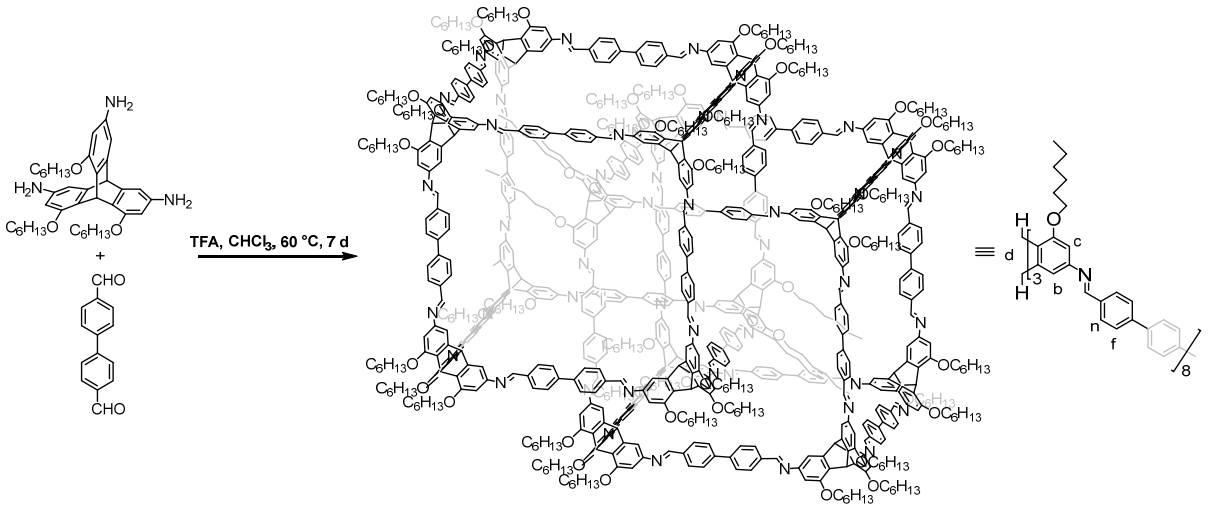

HexBi-Catenane was synthesized according to **GP4** with 1,8,13-Trihexyloxy-3,6,15-triaminotriptycene (9.6 mg, 16.0 µmol), 4,4'-Biphenyldicarboxaldehyde (5.0 mg, 24.0 µmol), $CHCl_3$ (3 mL), and TFA (in $CHCl_3$, 0.01 M, 4 mol%, 60 µL). The light brown solution was stirred at 60 °C for 7 days. The crude product was purified by THF-GPC to obtain **HexBi-Catenane** in 30 % yield (4.0 mg, 0.6 µmol) as a yellow solid.

M.p. ≥ 395°C (decomposition).

MS (MALDI-TOF): *m/z* $[M]^+$ calcd. for $C_{944}H_{992}N_{48}O_{48}^+$: 13767.666; found: 13779.274.

Elemental Analysis (%): calcd. for $C_{944}H_{992}N_{48}O_{48}$: C 82.29, H 7.26, N 4.88; found: C 81.50, H 7.46, N 4.61.

^{1}H NMR (700 MHz, CD_2Cl_2): δ (ppm) = 8.83 (s, 3H, HC=N), 8.66 (s, 3H, HC=N), 8.47 (s, 6H, HC=N), 8.35 (d, 6H, Ar-H_n), 8.34 (s, 6H, HC=N), 7.97-7.96 (d, 6H, Ar-H_f), 7.96-7.94 (d, 6H, Ar-H_n), 7.88-7.87 (d, 6H, Ar-H_n), 7.83-7.82 (d, 6H, Ar-H_f), 7.72 (s, 3H, HC=N), 7.71-7.70 (d, 6H, Ar-H_f) 7.65 (s, 3H, HC=N), 7.63-7.62 (d, 6H, Ar-H_n). 7.58-7.57 (d, 6H, Ar-H_f), 7.52-7.51 (d, 6H, Ar-H_f), 7.50 (s, 6H, Ar-H_b), 7.37-7.36 (d, 6H, Ar-H_f), 7.18 (s, 6H, Ar-H_b), 7.11 (s, 6H, Ar-H_b), 7.10 (d, 6H, Ar-H_f), 6.95-6.94 (d, 6H, Ar-H_f), 6.90 (s, 3H, H_d), 6.83 (s, 3H, H_d),6.79 (s, 3H, Ar-H_b), 6.73 (s, 6H, Ar-H_b),6.70 (s, 3H, Ar-H_c), 6.59(s, 3H, Ar-H_c), 6.57 (s, 3H, Ar-H_c), 6.53 (s, 3H, Ar-H_c),6.49 (s, 3H, Ar-H_c), 6.17 (s, 3H, H_d), 5.66 (s, 3H, H_d), 4.09-3.99 (m, 36H), 3.94 (s, 3H), 3.73 (s, 3H), 2.22 (s, 3H), 2.16 (s, 3H), 1.93 (m, 30H), 1.74 (m, 12H), 1.64 (m, 36H) 1.46 (m, 72H), 1.27-1.18 (m, 72H), 0.99 (m, 48H), 0.89 (m, 48H).

^{13}C-NMR (176 MHz, CD_2Cl_2): δ (ppm) = 161.80, 160.02, 159.82, 159.29, 159.20, 158.82, 154.84, 154.70, 154.55, 154.51, 154.31, 153.91, 151.67, 151.25, 150.61, 150.38, 150.28, 149.91, 149.64, 149.50, 149.50, 149.25, 149.07, 143.35, 143.15, 142.79, 142.70, 142.66, 136.49, 136.31, 136.15, 136.10, 136.00, 135.79, 132.54, 132.48, 131.95, 131.81, 131.54, 131.50, 130.13, 129.88, 129.61, 129.41, 129.23, 129.09, 127.97, 127.83, 127.74, 127.67, 127.53, 110.22, 109.94, 108.71, 108.37, 108.27, 107.33, 106.90, 105.41, 104.79, 104.360, 104.20, 103.39, 69.60, 69.52, 69.29, 69.05, 67.46, 55.99, 33.82, 33.73, 32.35, 32.32, 32.29, 32.25, 32.08, 31.99, 30.09, 30.05, 30.03, 30.00, 29.76, 29.72, 29.47, 26.23, 26.18, 26.00, 25.30, 23.12, 23.08, 23.00, 22.94.

IR (ATR): $\tilde{\nu}$ (cm^{-1}) = 2952 (w), 2927 (m), 2866 (w), 1589 (vs), 1465 (m), 1429 (m), 1294 (m), 1120 (s), 1099 (s), 1066 (w), 974 (m), 837 (m), 817 (s), 765 (w), 649 (w).

HexTri-[2]Catenane

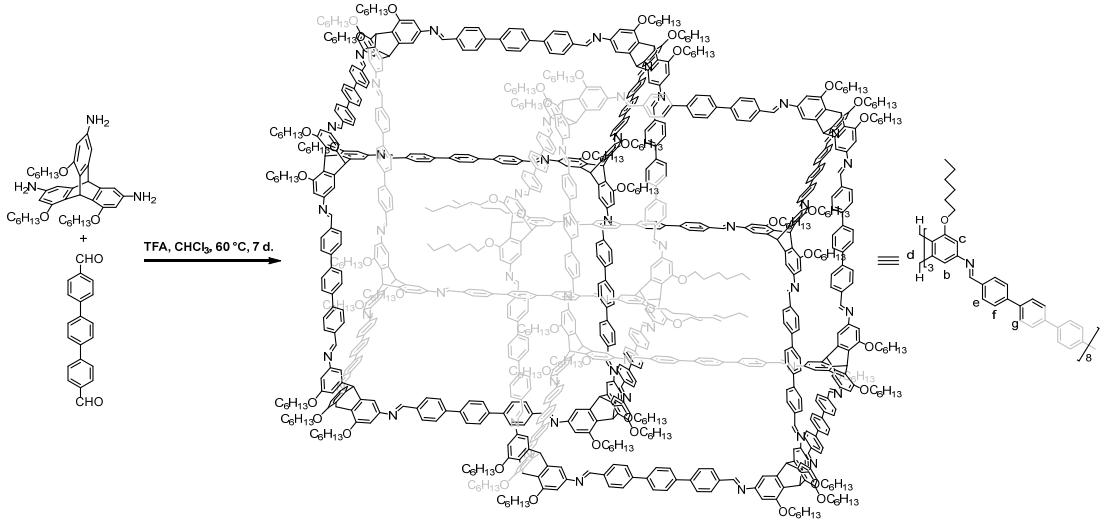

HexTri-Catenane was synthesized according to **GP4** with 1,8,13-Trihexyloxy-3,6,15-triaminotriptycene (9.6 mg, 16.0 µmol), [1,1':4',1''-Terphenyl]-4,4''-dicarbaldehyde (8.0 mg, 24.0 µmol), $CHCl_3$ (5 mL), and TFA (in $CHCl_3$, 0.01 M, 8 mol%, 120 µL). The light brown solution was stirred at 60 °C for 7 days. The crude product was purified by THF-GPC to obtain **HexTri-Catenane** in 13 % yield (2.0 mg, 0.13 µmol) as a yellow solid.

M.p. ≥ 355°C (decomposition).

MS (MALDI-TOF): *m/z* $[M]^+$ calcd. for $C_{1088}H_{1088}N_{48}O_{48}^+$: 15592.417, found: 15604.380.

^{1}H NMR (700 MHz, CD_2Cl_2, 303 K): δ (ppm) = 8.85 (s, 3H), 8.68 (s, 3H), 8.59 (s, 3H), 8.42 (s, 3H), 8.38-8.37 (d, 6H), 7.95-7.93 (m, 12H), 7.90-7.89 (d, 9H), 7.75-7.74 (d, 9H), 7.70-7.68 (m, 18H) 7.66-7.63 (m, 24H), 7.57-7.51 (m, 32H). 7.46-7.45 (m, 9H), 7.36-7.35 (d, 12H), 7.29 (s, 3H) 7.17-7.16 (d, 6H), 7.09-7.08 (d, 6H), 6.94-6.93 (d, 6H), 6.91 (s, 6H), 6.87 (s, 3H), 6.84 (s, 3H), 6.81 (s, 3H), 6.72 (s, 3H), 6.65 (s, 3H), 6.64 (s, 3H), 6.61 (s, 3H), 6.53 (s, 3H), 6.49 (s, 3H), 619 (s, 3H), 5.70 (s, 3H), 4.06-3.96 (m, 9H), 3.85-3.75 (m, 5H), 6.68-6.59 (t, 5H), 5.95 (s, 1H) 4.11-4.00 (m, *alkyl*), 2.00-1.94 (m, *alkyl*), 1.78 (s, *alkyl*), 1.68-1.64 (m, *alkyl*), 1.33-1.21 (m, *alkyl*), 0.99 (m, *alkyl*), 0.91 (m, *alkyl*).

^{13}C-NMR (176 MHz, CD_2Cl_2, 303 K): no sufficient spectrum was collected due to the complexity.

IR (ATR): $\tilde{\nu}$ (cm^{-1}) = 3026 (vw), 2950 (w), 2925 (m), 2856 (w), 1587 (vs), 1488 (m), 1465 (m), 1429 (m), 1290 (m), 1222 (w), 1174 (w), 1118 (w), 1099 (s), 1002 (m), 972 (m), 833 (m), 811 (vs), 727 (w), 649 (w).

HexTri-[3]Catenane

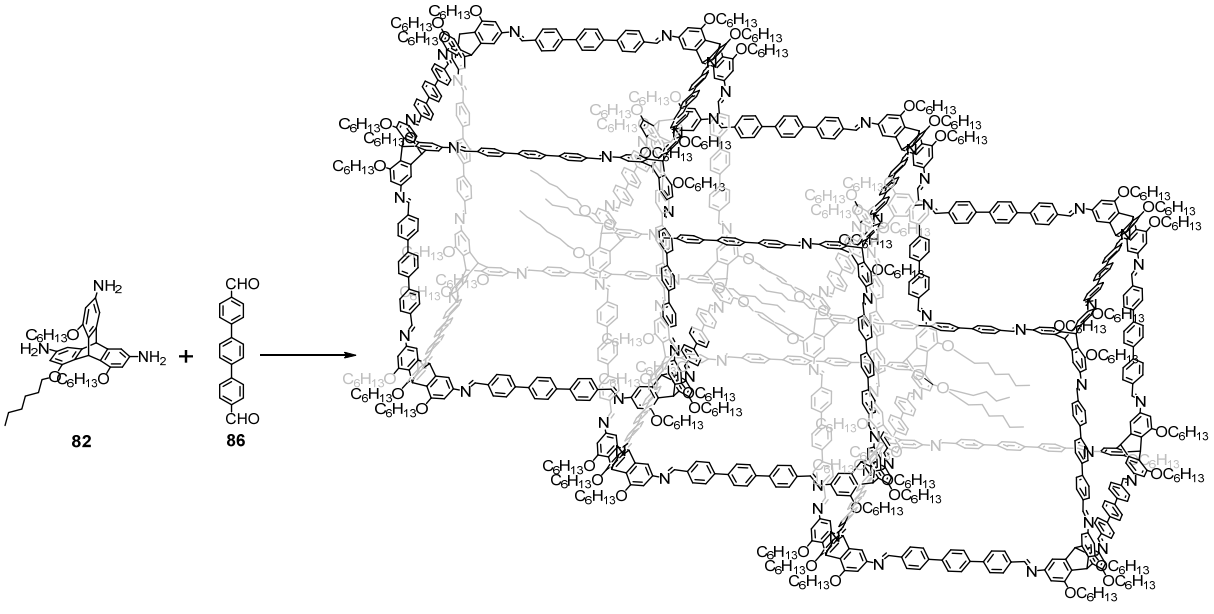

HexTri-[3]Catenane was synthesized according to **GP4** with 1,8,13-Trihexyloxy-3,6,15-triaminotriptycene (48.0 mg, 0.08 mmol), [1,1':4',1''-Terphenyl]-4,4''-dicarbaldehyde (27.0 mg, 0.10 mmol), $CHCl_3$ (15 mL), and TFA (in $CHCl_3$, 0.01 M, 4% mol, 300 µL). The light brown solution was stirred at 60 °C for 7 days. The crude product was purified by THF-GPC to obtain **HexTri-Catenane** in 10 % yield (6.0 mg, 0.12 µmol) as a yellow solid.

M.p. ≥ 330 °C (decomposition).

MS (MALDI): *m/z* $[M]^+$ calcd. for $C_{1630}H_{1630}N_{72}O_{72}^+$: 23362.610, found: 23467.529.

^{1}H NMR (700 MHz, CD_2Cl_2, 303K): δ (ppm) = 8.88 (s, 3H), 8.64 (s, 3H), 8.61 (s, 3H), 8.52 (s, 6H), 8.44-8.43 (d, 6H), 8.04-8.03 (d, 6H), 7.94-7.93 (d, 9H), 7.92 (s, 3H), 7.91 (s, 3H), 7.89-7.88 (d, 9H), 7.84 (s, 3H), 7.82 (s, 3H), 7.79-7.78 (d, 6H), 7.76-7.75 (d, 6H), 7.74 (s, 3H). 7.72-7.71 (m,15H), 7.66-7.61 (m, 27H), 7.59 (s, 3H), 7.57 (s, 3H), 7.54-7.53 (m, 15H), 7.33 (s, 3H), 7.31 (s, 3H), 7.29-7.28 (d, 6H), 7.22 (s, 3H), 7.18-7.16 (m, 12H), 7.11 (s, 3H), 7.10 (s, 3H), 7.07-7.06 (m, 9H), 7.01 (s, 6H), 7.00-6.99 (d, 6H), 6.96-6.95 (d, 6H), 6.93-6.92 (d, 6H), 6.91 (s, 3H), 6.89 (s, 3H), 6.86-6.85 (d, 6H), 6.83 (s, 3H), 6.75 (s, 3H), 6.67 (s, 3H), 6.66 (s, 3H), 6.62-6.61 (d, 6H), 6.58 (s, 3H), 6.56 (s, 3H), 6.52-6.51 (d, 6H), 6.35 (s, 3H), 6.17 (s, 3H), 5.65 (s, 3H), 4.06-3.96 (m, 9H), 3.85-3.75 (m, 5H), 6.68-6.59 (t, 5H), 5.95 (s, 1H), 4.13-4.09 (m, *alkyl*), 4.02-4.3.98 (m, *alkyl*), 3.93-3.89 (m, *alkyl*), 3.76-3.73 (m, *alkyl*), 2.00-1.94 (m, 9H), 1.78 (s, 5H), 1.68-1.64 (m, 15H), 4.06-3.96 (m, 9H), 1.97-1.95 (m, *alkyl*), 1.77-1.66 (m, *alkyl*), 1.49-1.46 (m, *alkyl*), 1.33-1.22 (m, *alkyl*), 1.01-0.87 (m, *alkyl*).

^{13}C-NMR (176 MHz, CD_2Cl_2, 303K): δ (ppm) = 163.28, 162.64, 159.71, 159.58, 159.28, 158.92, 158.57, 154.83, 154.63, 154.53, 154.05, 153.97, 152.51, 152.42, 151.11, 151.03, 150.50, 150.05, 149.68, 149.55, 149.49, 149.09, 144.12, 143.86, 143.53, 143.42, 143.31, 143.14, 142.74, 140.77, 140.03, 139.77, 139.47, 139.32, 139.17, 136.26, 136.01, 135.85, 135.57, 135.33, 133.35, 132.82, 132.69, 132.47, 132.25, 131.92, 131.49, 130.13, 130.01, 129.92, 129.86, 129.47, 129.34, 128.62, 128.20, 128.13, 128.05, 128.00, 127.93, 127.73, 127.65, 127.61, 127.54, 127.51, 127.07, 110.15, 109.54, 108.91, 108.41, 106.40, 105.89, 105.28, 105.21, 104.95, 104.58, 104.17, 103.79, 77.97, 69.77, 69.68, 69.58, 69.50, 69.42, 69.21, 68.21, 67.36, 56.18, 54.93, 54.55, 50.87, 34.07, 32.60, 32.55, 32.38, 32.36, 32.31, 32.22, 32.16, 32.11, 31.98, 30.15, 30.12, 29.89, 29.86, 29.79, 29.73, 26.30, 26.26, 26.14, 26.10, 26.07, 26.04, 25.95, 25.56, 25.53, 23.16, 23.10, 23.03, 22.99, 14.51, 14.18, 14.45, 14.39, 14.34.

IR (ATR): $\tilde{\nu}$ (cm^{-1}) = 2952 (w), 2927 (m), 2858 (w), 1589 (vs), 1488 (m), 1467 (m), 1429 (m), 1294 (m), 1224 (w), 1120 (w), 1101 (s), 1004 (m), 973 (m), 838 (m), 811 (vs), 727 (w), 649 (w).

DecBi-Cage

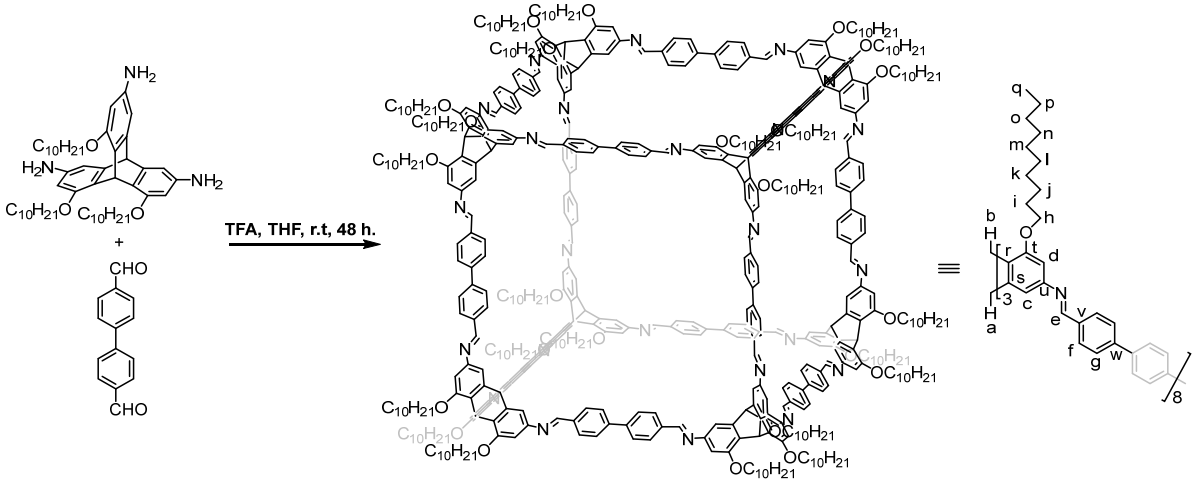

DecBi-Cage was synthesized according to **GP4** with 1,8,13-Tridecayloxy-3,6,15-triaminotriptycene (12.3 mg, 16.0 µmol), 4,4'-Biphenyldicarboxaldehyde (5.0 mg, 24.0 µmol), THF (5 mL), and TFA (in THF, 0.01 M, 4 mol%, 60 µL). The light brown solution was stirred at r.t for 2 days. The crude product was purified by THF-GPC to obtain **DecBi-Cage** in 18% yield (3.0 mg, 0.36 µmol) as a yellow solid.

M.p. ≥ 320°C (decomposition).

MS (MALDI-TOF): *m/z* $[M]^+$ calcd. for $C_{568}H_{688}N_{48}O_{48}^+$: 8229.353; found: 8229.323.

Elemental Analysis (%): calcd. for $C_{568}H_{688}N_{48}O_{48}$: C 82.84, H 8.42, N 4.08; found: C 80.03, H 8.65, N 3.95.

^{1}H NMR (700 MHz, CD_2Cl_2): δ (ppm) = 8.54 (s, 24H-*e*), 7.98-7.97 (d, 48H-*f*), 7.81-7.79 (d, 48H-*g*), 6.99 (s, 24H-*c*), 6.87 (s, 8H-*a*), 6.61 (s, 24H-*d*), 5.47 (s, 8H-*b*), 4.10-4.08 (m, 48H-*h*), 1.94-1.92 (m, 48H-*i*), 1.48-1.43 (m, 48H-*j*), 1.42-1.39 (m, 48H-*k*), 1.3.4-1.30 (m, 240H-*l, m, n, o, p*), 0.91-0.89 (m, 72H-*q*).

^{13}C-NMR (176 MHz, CD_2Cl_2): δ (ppm) = 159.37 (C-*e*), 154.67 (C-*t*), 150.54 (C-*u*), 149.25 (C-*r*), 143.06 (C-*w*), 136.37 (C-*v*), 131.69 (C-*s*), 129.62 (C-*f*), 127.72 (C-*g*), 109.19 (C-*c*), 104.45 (C-*d*), 68.85 (C-*h*), 55.51 (C-*a*), 33.74(C-*b*), 32.42 (C-*alkyl*), 30.48 (C- *alkyl*), 30.26 (C-*alkyl*), 30.12 (C- *alkyl*), 30.08 (C- *alkyl*), 29.90 (C- *alkyl*), 26.54 (C- *alkyl*), 23.14 (C- *alkyl*).

IR (ATR): $\tilde{\nu}$ (cm^{-1}) = 2922 (s), 2852 (m), 1589 (vs), 1465 (m), 1429 (m), 1294 (m), 1224 (w), 1118 (s), 1103 (s), 1068 (m), 974 (m), 873 (w), 835 (m), 815 (s), 721 (w).

DecBi-Catenane

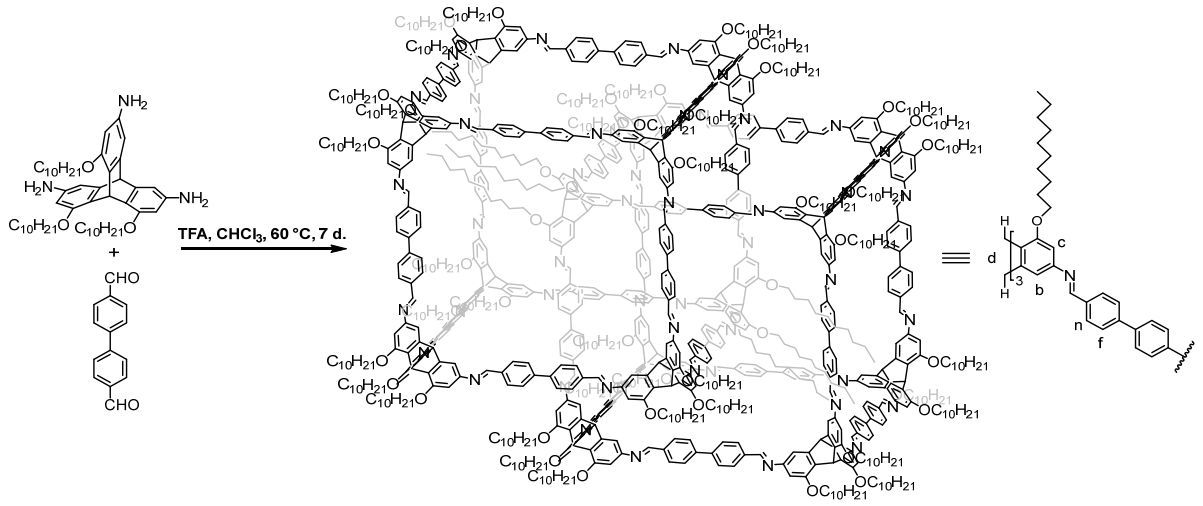

DecBi-Catenane was synthesized according to **GP4** with 1,8,13-Tridecayloxy-3,6,15-triaminotriptycene (12.3 mg, 16.0 µmol), 4,4'-Biphenyldicarboxaldehyde (5.0 mg, 24.0 µmol), $CHCl_3$ (5 mL), and TFA (in $CHCl_3$, 0.01 M, 8 mol%, 120 µL). The light brown solution was stirred at 60 °C for 7 days. The crude product was purified by THF-GPC to obtain DecBi-Catenane in 18 % yield (3.0 mg, 0.2 µmol) as a yellow solid.

M.p. ≥ 335°C (decomposition).

MS (MALDI-TOF): *m/z* $[M]^+$ calcd. for $C_{1136}H_{1376}N_{48}O_{48}^+$: 16458.670; found: 16470.690.

Elemental Analysis (%): calcd. for $C_{1136}H_{1376}N_{48}O_{48}$: C 84.01, H 7.12, N 3.67; found: C 82.30, H 8.16, N 3.88.

^{1}H NMR (700 MHz, CD_2Cl_2): δ (ppm) = 8.83 (s, 3H, HC=N), 8.65 (s, 3H, HC=N), 8.47 (s, 3H, HC=N), 8.36 (s, 6H, HC=N), 8.35-8.34 (d, 6H, Ar-H_n), 7.96-7.95 (d, 6H, Ar-H_f), 7.95-7.94 (d, 6H, Ar-H_n), 7.88-7.87 (d, 6H, Ar-H_n), 7.83-7.81 (d, 6H, Ar-H_f), 7.74 (s, 3H, HC=N), 7.71-7.7.70 (d, 6H, Ar-H_f), 7.66 (s, 3H, HC=N), 7.63-7.62 (d, 6H, Ar-H_n). 7.58-7.57 (d, 6H, Ar-H_f), 7.52-7.51 (d, 6H, Ar-H_f), 7.49 (s, 3H, Ar-H_b), 7.37-7.36 (d, 6H, Ar-H_f), 7.17-7.16 (d, 6H, Ar-H_b), 7.13 (s, 3H, Ar-H_b), 7.12-7.11 (d, 6H, Ar-H_n), 6.96-6.94 (d, 6H, Ar-H_n), 6.89 (s, 3H, H_d), 6.83 (s, 3H, H_d), 6.78 (s, 3H, Ar-H_b), 6.74 (s, 3H, Ar-H_b), 6.72 (s, 3H, Ar-H_c), 6.69 (s, 3H, Ar-H_c), 6.59 (s, 3H, Ar-H_c), 6.57 (s, 3H, Ar-H_c), 6.53 (s, 3H, Ar-H_c), 6.48 (s, 3H, Ar-H_c), 6.16 (s, 3H, H_d), 5.65 (s, 3H, H_d), 4.09-3.92 (m, 36H), 3.92 (s, 3H), 3.73 (s, 3H), 2.24(s, 3H), 2.15 (s, 3H), 1.94 (m, 30H), 1.75 (m, 12H), 1.64-1.63 (m, 36H) 1.47-1.46 (m, 72H), 1.41 (m, 36H), 1.35-1.27 (m,320H), 0.92-0.87 (m, 108H).

^{13}C-NMR (176 MHz, CD_2Cl_2): δ (ppm) = 162.14, 160.01, 159.84, 159.42, 159.25, 158.88, 155.02, 154.85, 154.45, 154.05, 151.82, 151.38, 150.74, 150.50, 150.03, 149.78, 149.62, 149.35, 149.19, 143.53, 143.29, 143.12, 142.94, 142.81, 136.61, 136.46, 136.29, 136.16,

135.96, 132.75, 132.18, 131.99, 131.79, 131.44, 130.21, 139.98, 129.68, 129.51, 129.34, 129.21, 128.07, 127.91, 127.83, 127.75, 127.61, 125.88, 110.28, 110.20, 109.14, 108.50, 108.28, 107.21, 105.29, 104.38, 103.88, 69.95, 69.89, 69.60, 69.52, 69.36, 67.52, 56.14, 54.00, 32.62, 32.54, 32.51, 32.49, 30.63, 30.58, 30.44, 30.37, 30.33, 30.30, 30.27, 30.25, 30.20, 30.15, 29.99, 29.95, 29.92, 29.88, 29.72, 26.73, 26.63, 26.42, 26.35, 25.95, 23.27, 23.22, 23.19, 14.39, 14.36.

IR (ATR): $\tilde{\nu}$ (cm^{-1}) = 2921 (s), 2852 (m), 1589 (vs), 1465 (m), 1431 (m), 1294 (m), 1118 (s), 1103 (s), 1066 (w), 973 (m), 837 (m), 817 (s), 721 (w), 649 (w).

DecTri-Catenane

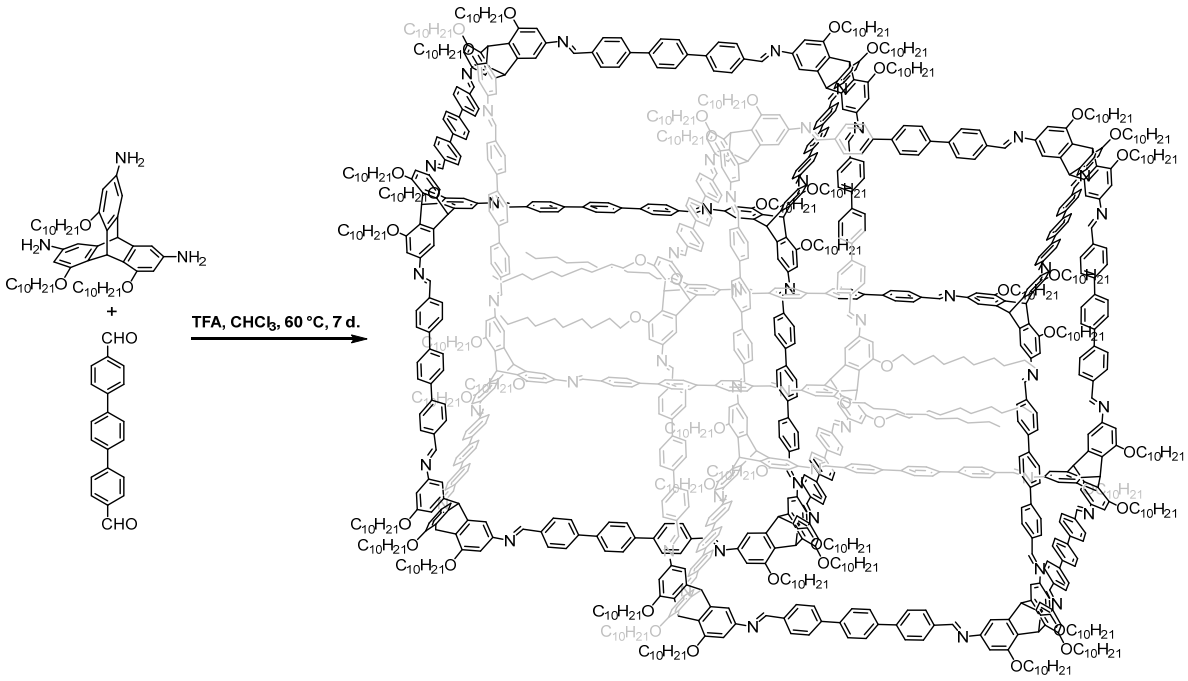

DecTri-Catenane was synthesized according to **GP4** with 1,8,13-Tridecayloxy-3,6,15-triaminotriptycene (12.3 mg, 16.0 µmol), [1,1':4',1''-Terphenyl]-4,4''-dicarbaldehyde (8.0 mg, 24.0 µmol), $CHCl_3$ (3 mL), and TFA (in $CHCl_3$, 0.01 M, 4 mol%, 60 µL). The light brown solution was stirred at 60 °C for 7 days. The crude product was purified by THF-GPC to obtain DecBi-Catenane in 10 % yield (1.5 mg, 0.07 µmol) as a yellow solid.

M.p. ≥ 350°C (decomposition).

MS (MALDI-TOF): *m/z* $[M]^+$ calcd. for $C_{1280}H_{1472}N_{48}O_{48}^+$: 18283.422; found: 18299.420.

Elemental Analysis (%): calcd. for $C_{1280}H_{1472}N_{48}O_{48}$: C 83.74, H 7.03, N 4.31; found: C 81.60, H 7.91, N 3.19.

^{1}H NMR (700 MHz, CD_2Cl_2, 303 K): δ (ppm) = 8.85 (s, 3H), 8.67 (s, 3H), 8.59 (s, 3H), 8.38-8.37 (m, 6H), 7.96-7.93 (m, 12H), 7.90-7.87 (m, 9H), 8.85 (s, 3H), 7.75-7.74 (d, 6H), 7.7.-7.69 (m, 12H), 7.66-7.63 (m, 21H), 7.57-7.52 (m, 27H), 7.46-7.45 (m, 6H), 7.36-7.36 (m, 18H), 7.29

(s, 3H), 7.18-7.17(d, 6H), 7.13 (s, 3H), 7.09-7.08 (d, 6H), 6.94-6.93 (d, 6H), 6.91 (s, 6H), 6.87 (s, 3H), 6.83 (s, 3H), 6.81 (s, 3H), 6.72 (s, 3H), 6.64 (s, 3H), 6.61 (s, 3H), 6.53 (s, 3H), 6.53 (s, 3H), 6.50 (s, 3H), 6.19 (s, 3H), 5.70 (s, 3H), 4.13-3.96 (m, *alkyl*), 1.98-1.94 (m, *alkyl*), 1.68-1.52(m, *alkyl*), 1.49-1.42 (m, *alkyl*), 1.36-1.29 (m, *alkyl*), 0.95-0.80 (m, *alkyl*).

^{13}C-NMR (176 MHz, CD_2Cl_2, 303 K): no sufficient spectrum was collected due to the complexity.

IR (ATR): $\tilde{\nu}$ (cm^{-1}) = 2948 (w), 2921 (m), 2850 (m), 1589 (vs), 1488 (m), 1465 (m), 1429 (m), 1294 (m), 1118 (s), 1103 (s), 1068 (m), 1002 (m), 943 (m), 817 (vs), 723 (w).

ProBi-Catenane

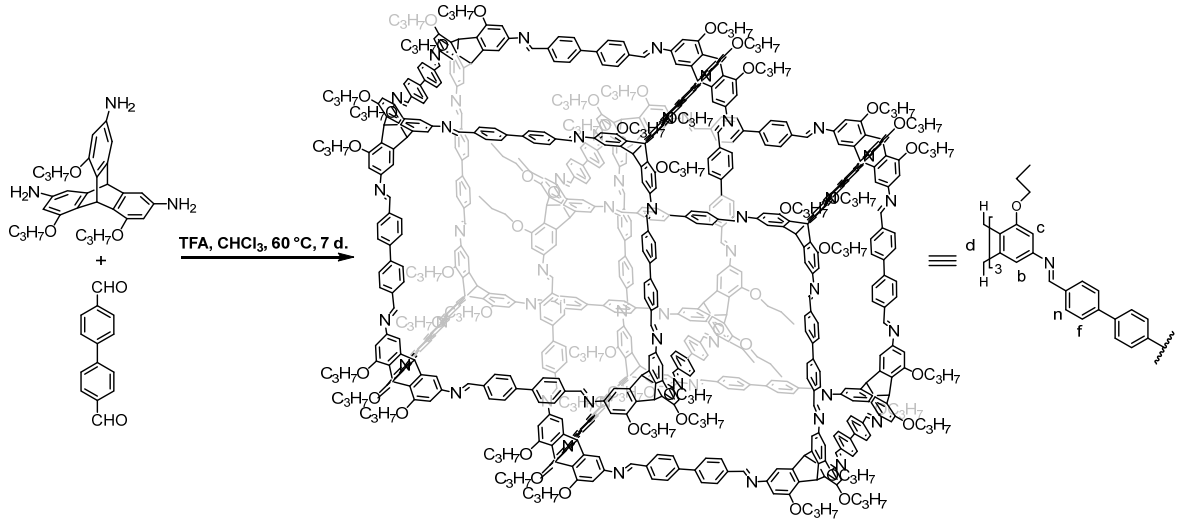

ProBi-Catenane: was synthesized according to **GP4** with 1,8,13-Tripropyloxy-3,6,15-triaminotriptycene (7.6 mg, 16.0 µmol), 4,4'-Biphenyldicarboxaldehyde (5.0 mg, 24.0 µmol), $CHCl_3$ (5 mL), and TFA (in $CHCl_3$, 0.01 M, 8 mol%, 120 µL). The light brown solution was stirred at 60 °C for 7 days. The crude product was purified by THF-GPC to obtain **ProBi-Catenane** in 15 % yield (1.8 mg, 0.15 µmol) as a yellow solid.

M.p. ≥ 370°C (decomposition).

MS (MALDI-TOF): *m/z* $[M]^+$ calcd. for $C_{800}H_{704}N_{48}O_{48}^+$: 11749.412; found: 11759.418.

Elemental Analysis (%): calcd. for $C_{800}H_{704}N_{48}O_{48}$: C 81.72, H 6.03, N 5.72; found: C 76.47, H 5.79, N 5.33.

^{1}H NMR (700 MHz, CD_2Cl_2): δ (ppm) = 8.83 (s, 3H, HC=N), 8.65 (s, 3H, HC=N), 8.47 (s, 6H, HC=N), 8.36 (s, 6H, HC=N), 8.35 (d, 6H, Ar-H_n), 7.96 (d, 6H, Ar-H_n), 7.95 (d, 6H, Ar-H_f), 7.87-7.88 (d, 6H, Ar-H_n), 7.83-7.82 (d, 6H, Ar-H_f), 7.74 (s, 3H, HC=N), 7.71-7.70 (d, 6H, Ar-H_f), 7.67 (s, 3H, HC=N), 7.63-7.62 (d, 6H, Ar-H_n), 7.59-7.58 (d, 6H, Ar-H_f), 7.52-7.51 (d, 6H, Ar-H_f), 7.51 (s, 3H, Ar-H_b), 7.40-7.39 (d, 6H, Ar-H_f), 7.17 (s, 6H, Ar-H_b), 7.13-7.12 (d, 6H,

Ar-H_n), 7.11 (s, 3H, Ar-H_b), 6.99-6.98 (d, 6H, Ar-H_n), 6.94 (s, 3H, H_d), 6.85 (s, 3H, H_d), 6.79 (s, 3H, Ar-H_b), 6.74 (s, 3H, Ar-H_b), 6.72 (s, 3H Ar-H_c), 6.66 (s, 3H, Ar-H_c), 6.60 (s, 3H, Ar-H_c), 6.57 (s, 3H, Ar-H_c), 6.54 (s, 3H, Ar-H_c), 6.50 (s, 3H, Ar-H_c), 6.16 (s, 3H, H_d), 5.65 (s, 3H, H_d), 4.06 (m, 24H), 3.96 (m, 24H), 3.70 (m, 6H), 1.95 (m, 36H), 1.23 (m, 64H), 1.03 (t, 12H), 0.96 (t, 12H), 0.54 (t, 12H).

^{13}C-NMR (176 MHz, CD_2Cl_2): δ (ppm) = 161.87, 160.02, 159.81, 159.33, 159.19, 158.83, 154.80, 154.67, 154.49, 154.27, 153.89, 151.57, 151.22, 150.58, 150.41, 150.29, 149.88, 149.72, 149.50, 149.07, 143.38, 143.13, 142.99, 142.81, 136.49, 136.62, 136.09, 135.79, 132.55, 131.99, 131.85, 131.59, 131.42, 130.14, 129.86, 129.61, 129.42, 129.24, 129.06, 127.98, 127.83, 127.73,127.68, 127.55, 110.23, 108.60, 107.96, 107.74, 106.87, 105.35, 104.64, 103.67, 71.06, 70.67, 70.51, 70.27, 68.82, 67.14, 55.96, 54.00, 33.73, 30.41, 30.09, 23.29, 23.05, 22.58, 11.54, 10.67, 9.80.

IR (ATR): $\tilde{\nu}$ (cm^{-1}) = 2962 (w), 2935 (w), 2875 (w), 1589 (vs), 1469 (m), 1429 (m), 1292 (m), 1224 (w), 1118 (s), 1099 (s), 1068 (m), 973 (m), 875 (w), 815 (m), 765 (w), 649 (w).

6.2.2 Compounds of Chapter 3.2

HexTe-Cage

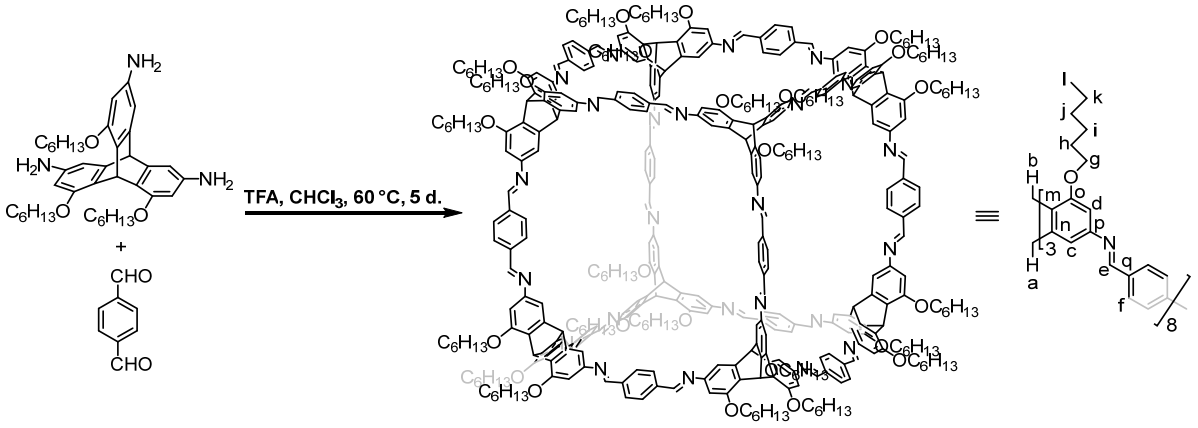

HexBi-Cage was synthesized according to **GP4** with 1,8,13-Trihexyloxy-3,6,15-triaminotriptycene (9.6 mg, 16.0 µmol), 1,4-Phthalaldehyde (3.2 mg, 24.0 µmol), $CHCl_3$ (3 mL), and TFA (in THF, 0.01 M, 4 mol%, 60 µL). The light brown solution was stirred at r.t for 5 days. The crude product was purified by THF-GPC to obtain **HexBi-Cage** in 54% yield (6.4 mg, 1.1 µmol) as a yellow solid.

M.p. ≥ 390 °C (decomposition).

MS (ESI): *m/z* $[M]^+$ calcd. for $C_{400}H_{448}N_{24}O_{24}^+$: 5971.457, found: 5975.259.

Elemental Analysis (%): ($C_{472}H_{496}N_{24}O_{24}$) Calcd. C 82.29, H 7.26, N 4.88 found: C 78.76, H 7.26, N 4.68.

^{1}H NMR (600 MHz, THF-d_8): δ (ppm) = 8.58 (s, 24H-*e*), 8.01 (s, 48H-*f*), 7.00 (s, 24H-*c*), 6.91 (s, 8H-*b*), 6.64 (s, 24H-*d*), 5.49 (s, 8H-*a*), 4.09 (s, 48H-*g*), 1.95 (s, 48H-*h*), 1.70 (s, 48H-*i*), 1.48 (s, 96H-*j, k*), 0.99 (s, 72H-*l*).

^{13}C-NMR (151 MHz, THF-d_8): δ (ppm) = 159.10 (C-*e*), 155.04 (C-*o*), 150.89 (C-*p*), 149.76 (C-*m*), 139.80 (C-*q*), 132.36 (C-*n*), 129.48 (C-*f*), 109.48 (C-*c*), 104.10 (C-*d*), 69.12 (C-*g*), 56.00 (C-*a*), 34.26 (C-*b*), 32.65 (C-*k*), 30.45 (C-*h*), 25.67 (C-*i*), 23.46 (C-*j*), 14.39 (C-*l*).

IR (ATR): $\tilde{\nu}$ (cm^{-1}) = 2952 (m), 2927 (m), 2868 (w), 2858 (w), 1623 (w), 1591 (vs), 1467 (m), 1431 (m), 1377 (w), 1298 (s), 1224 (w), 1118 (s), 1099 (s), 1066 (w), 972 (m), 869 (w), 829 (m), 767 (w), 727 (w), 864 (w).

ProTe-Cage

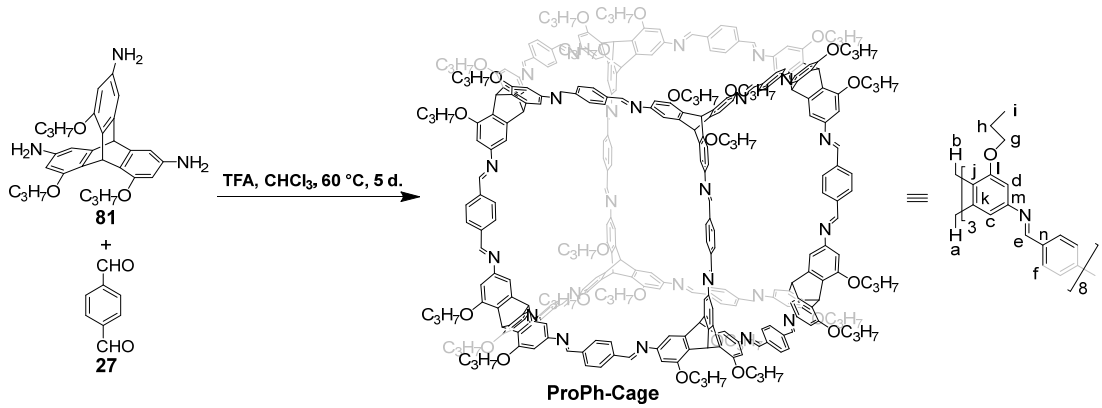

ProTe-Cage was synthesized according to **GP4** with 1,8,13-Tripropyloxy-3,6,15-triaminotriptycene (7.5 mg, 16.0 µmol), 1,4-Phthalaldehyde (3.2 mg, 24.0 µmol), DCM (3 mL), and TFA (in THF, 0.01 M, 4 mol%, 60 µL). The light brown solution was stirred at r.t for 5 days. The crude product was purified by THF-GPC to obtain **ProTe-Cage** in 65% yield (6.5 mg, 1.3 µmol) as a yellow solid.

M.p. = > 325°C (decomposition).

MALDI-TOF: *m/z* $[M+4H]^+$ calcd. for $C_{328}H_{304}N_{24}O_{24}$: 4962.33, found: 4966.34.

Elemental Analysis (%): calcd. for ($C_{328}H_{304}N_{24}O_{24}$) C 79.33, H 6.17, N 6.77; found: C 77.09, H 6.31, N 6.80.

^{1}H NMR (600 MHz, CD_2Cl_2): δ (ppm) = 8.52 (s, 24H-*e*), 7.98 (s, 48H-*f*), 6.99 (s, 24H-*c*), 6.91 (s, 8H-*a*), 6.61 (s, 24H-*d*), 5.48 (s, 8H-*b*), 4.04 (s, 48H-*g*), 1.93 (s, 48H-*h*) 1.21 (s, 72H-*i*).

^{13}C NMR (151 MHz, CD_2Cl_2): δ (ppm) = 159.38 (C-*e*), 154.67 (C-*l*), 150.49 (C-*m*), 149.22 (C-*j*), 139.08 (C-*n*), 131.79 (C-*k*), 129.41 (C-*f*), 109.14 (C-*c*), 104.01 (C-*d*), 70.60 (C-*e*), 55.46 (C-*a*), 33.73 (C-*g*), 23.28 (C-*h*), 10.87 (C-*i*).

IR (ATR): $\tilde{\nu}$ (cm^{-1}) = 2960 (w), 2933 (m), 2873 (w), 1699 (w), 1589 (vs), 1463 (m), 1429 (m), 1296 (s), 1118 (s), 1095 (s), 1068 (m), 972 (m), 825 (m), 756 (w).

4,4'-(Ethyne-1,2-diyl)dibenzaldehyde (90)

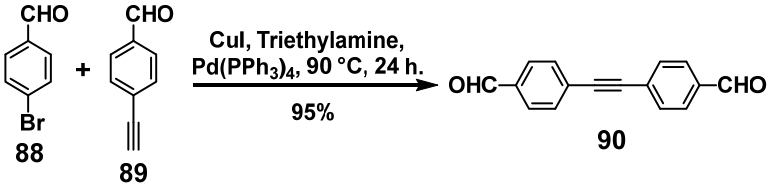

In an oven, a dried round-bottomed flask equipped with a stirrer bar was added 4-bromobenzaldehyde (0.20 g, 1.10 mmol), 4-ethynylbenzaldehyde (0.20 g, 1.50 mmol) and copper iodide (21.0 mg, 0.11 mmol) before the flask was evacuated and refilled with N_2 (×3). Triethylamine (8 mL) was added and the mixture was degassed (N_2 bubbling, 15 mins) before the addition of $Pd(PPh_3)_4$ (64.0 mg, 0.05 mmol). The resulting suspension was heated at reflux for 24 h before being allowed to cool to room temperature. The reaction was diluted with water (200 mL) and the product was extracted with DCM (2 × 200 mL) before the combined organic layers were dried ($MgSO_4$) and passed through a small Celite® plug. Hexane (200 mL) was added and the DCM was carefully removed in a vacuum to afford a dark yellow precipitate. The precipitate was collected by filtration and dried in a vacuum to afford the desired product **90** which was used without further purification (0.25 g, 1.00 mmol, 97%).

M.p. = 205 °C.

^{1}H NMR (300 MHz, $CDCl_3$): δ (ppm) = 10.04 (s, 1H), 7.91-7.88 (d, 2H), 7.72-7.69 (d, 2H).

Analytical data are in accordance with those previously reported.[75]

2,2'-Bipyridine-5,5'-dicarbaldehyde (93)

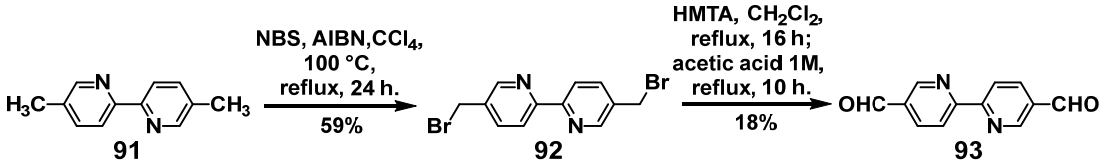

5,5'-dimethyl-2,2'-bipyridine (5.50 g, 30.00 mmol) was heated at reflux in tetrachloromethane (150 mL) for 30 min. Then N-bromosuccinimide (NBS) (11.70 g, 66.00 mmol) and 2,2'-azobis(2-methylpropionitrile) (AIBN) (0.30 g, 1.80 mmol) were added into the solution. The reaction mixture was heated at reflux overnight. Upon completion, the solvent was evaporated in vacuo and the crude product was recrystallized from tetrahydrofuran to yield **92** as a white powder (6.00 g, 59%).

M.p. = 193 °C.

^{1}H NMR (300 MHz, $CDCl_3$): δ (ppm) = 8.71 (s, 1H), 8.48-8.45 (d, 1H), 7.92-7.89 (dd, 1H), 4.54 (s, 2H).

Dry glassware was charged with 5,5'-bis(bromomethyl)-2,2'-bipyridine (3.42 g, 10.00 mmol) and hexamethylenetetraamine (6.30 g, 45.00 mmol). The solids were dissolved in 150 mL of

dry dichloromethane, and the solution was brought to reflux in the air. After approximately 30 minutes, a precipitate began forming. The reaction mixture was continued to reflux for 12 hours, then allowed to cool to room temperature. The solution was filtered and the white solid was taken up in 100 mL of 1 M acetic acid. The solution was brought to reflux for 10 hours, cooled, and briefly placed in the freezer to precipitate the organic product. The white solid was collected by filtration (0.35 g, 18% yield). The product was crystallized by slow evaporation of an acetone solution.

M.p. = 225 °C.

^{1}H NMR (300 MHz, $CDCl_3$): δ (ppm) = 8.71 (s, 1H), 8.48-8.45 (d, 1H), 7.92-7.89 (dd, 1H), 4.54 (s, 2H).

Analytical data are in accordance with those previously reported.[76, 97]

HexPy-Cage

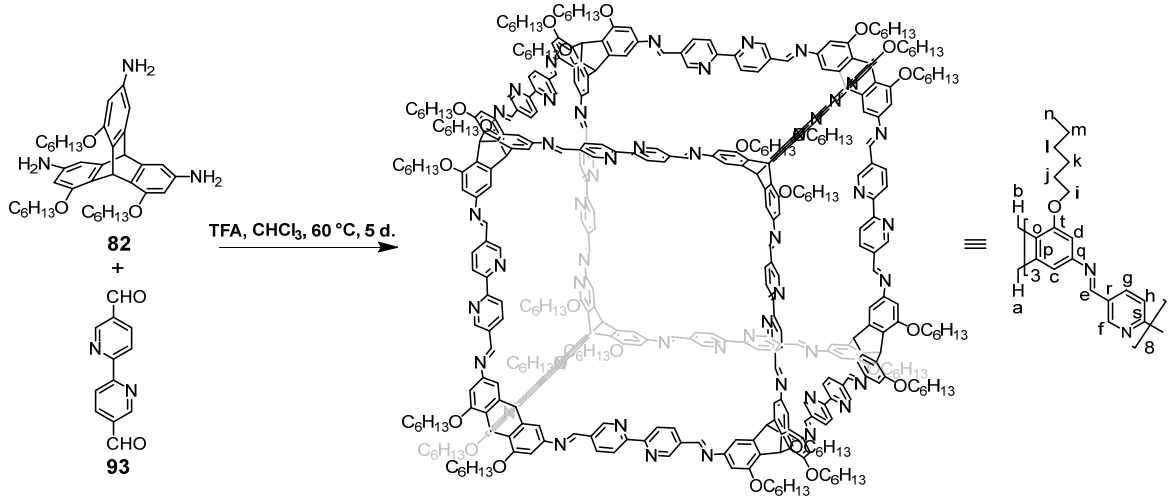

HexPy-Cage was synthesized according to **GP4** with 1,8,13-Trihexyloxy-3,6,15-triaminotriptycene (9.6 mg, 16.0 µmol), 2,2'-Bipyridine-5,5'-dicarbaldehyde (5.1 mg, 24.0 µmol), $CHCl_3$ (3 mL), and TFA (in THF, 0.01 M, 4 mol%, 60 µL). The light brown solution was stirred at r.t for 5 days. The crude product was purified by r-GPC to obtain **HexPy-Cage** in 40% yield (5.5 mg, 0.8 µmol) as a yellow solid.

M.p. ≥ 365 °C (decomposition).

MS (MALDI-TOF): *m/z* $[M]^+$ calcd. for $C_{448}H_{472}N_{48}O_{24}^+$: 6907.719, found: 6913.014.

Elemental Analysis (%): ($C_{448}H_{472}N_{48}O_{24}$) Calcd. C 77.84, H 6.88, N 9.73 found: C 75.79, H 7.16, N 9.08.

^{1}H NMR (600 MHz, CD_2Cl_2): δ (ppm) = 9.10 (s, 24H-*e*), 8.65-8.63 (d, 24H-*h*), 8.60 (s, 24H-*f*), 8.39-8.38 (d, 24H-*g*), 7.04 (s, 24H-*c*), 6.90 (s, 8H-*b*), 6.65 (s, 24H-*d*), 5.52 (s, 8H-*a*), 4.10 (s, 48H-*i*), 1.94 (s, 48H-*j*), 1.65 (s, 48H-*k*), 1.45 (s, 96H-*l, m*), 0.98 (s, 72H-*n*).

^{13}C-NMR (151 MHz, CD_2Cl_2): δ (ppm) = 157.47 (C-*r*), 156.82 (C-*f*), 154.63 (C-*o*), 150.61 (C-*e*), 150.04 (C-*s*), 149.11 (C-*o*), 136.22 (C-*g*), 132.44 (C-*p*), 131.92 (C-*t*), 121.65 (C-*h*), 109.32 (C-*c*), 103.73 (C-*d*), 69.18 (C-*i*), 55.52 (C-*a*), 34.27 (C-*b*), 32.10 (C-*k*), 29.85 (C-*j*), 26.05 (C-*k*), 23.28 (C-*n*), 22.99 (C-*l*), 14.25 (C-*n*).

IR (ATR): $\tilde{\nu}$ (cm^{-1}) = 2952 (w), 2925 (m), 2860 (w), 1699 (m), 1587 (vs), 1558(s), 1541 (s), 1471 (s), 1458 (s),1431 (m), 1294 (m), 1112 (m), 1097 (s), 1053 (m), 968 (m), 837 (s), 740 (m), 646 (m).

1,4-Dibromo-2,5-dihexyloxybenzene (96)

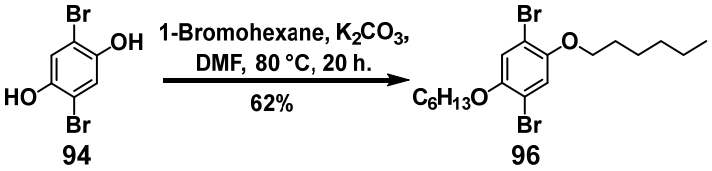

2,5-Dibromohydroquinone (1.34 g, 5.00 mmol), 1-bromohexane (2.10 g, 12.50 mmol), and anhydrous K_2CO_3 (3.50 g, 25.00 mmol) were added to dry DMF (20 mL) and the mixture was heated at 100 °C for ∼15 hours. The reaction mixture was cooled to room temperature, then transferred to a beaker containing 100 mL of ice water and stirred for 30 min. The precipitate was filtered, washed with water (3 × 30 mL), and dried in a vacuum. The product was recrystallized from a mixture of EtOH and $CHCl_3$ and isolated as white crystals (1.34 g, 3.00 mmol, 62%).

M.p. = 55 °C.

^{1}H NMR (300 MHz, $CDCl_3$): *δ* (ppm) = 7.07 (s, 1H), 3.97-3.92 (m, 2H), 1.85-1.75 (m, 2H), 1.50-1.46 (m, 2H), 1.36-1.34 (m, 4H), 0.93-0.88 (m, 3H).

Analytical data are in accordance with those previously reported.[98]

1,4-dibromo-2,5-bis(decoxy)benzene (97)

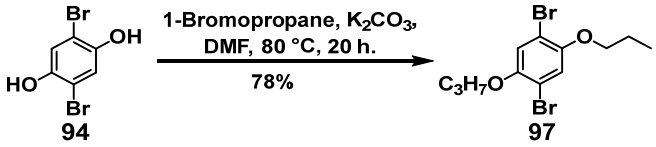

2,5-Dibromohydroquinone (1.34 g, 5.00 mmol), 1-Bromopropane (3.00 g, 12.50 mmol), and anhydrous K_2CO_3 (3.50 g, 25.00 mmol) were added to dry DMF (20 mL) and the mixture was heated at 100 °C for ∼15 hours. The reaction mixture was cooled to room temperature, then transferred to a beaker containing 100 mL of ice water and stirred for 30 min. The precipitate was filtered, washed with water (3 × 30 mL), and dried in a vacuum. The product was recrystallized from a mixture of EtOH and $CHCl_3$ and isolated as white crystals (1.38 g, 3.90 mmol, 78%).

M.p. = 70 °C.

^{1}H NMR (300 MHz, $CDCl_3$): δ (ppm) = 7.09 (s, 1H), 3.94-3.90 (m, 2H), 1.89-1.77 (m, 2H), 1.08-1.03 (m, 3H).

Analytical data are in accordance with those previously reported.[98]

2',5'-Dihexyloxy-p-terphenyl-4,4''-dialdehyde (101)

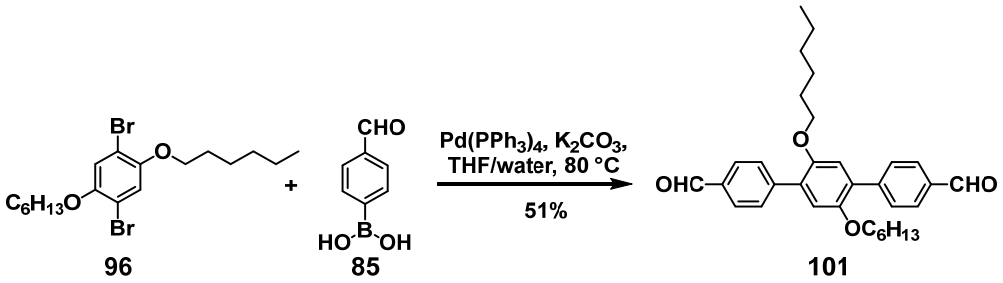

96 85 101

1,4-Dibromo-2,5-dihexyloxybenzene (0.44 g, 1.00 mmol), 4-Formylphenylboronic acid (0.37 g, 2.50 mmol), and $Pd(PPh_3)_4$ (46.0 mg, 0.04 mmol) were mixed in a flask that was deaerated and filled with nitrogen. THF (20 mL) and 2 M sodium carbonate (6 mL) were added. The mixture was refluxed under nitrogen overnight. After cooling, the separated organic layer was dried with $MgSO_4$. Recrystallization from ethanol yielded 0.25 g (51%) of bright yellow-green crystals.

M.p. = 252 °C.

^{1}H NMR (300 MHz, $CDCl_3$): δ (ppm) = 10.07 (s, 1H), 7.95-7.93 (d, 2H), 7.79-7.76 (d, 2H), 7.01 (s, 1H), 3.97-3.9 (m, 2H), 1.72-1.64 (m, 2H), 1.38-1.24 (m, 6H), 0.86-0.83 (m, 3H).

Analytical data are in accordance with those previously reported.[99]

2',5'-Dipropyloxy-p-terphenyl-4,4''-dialdehyde (102)

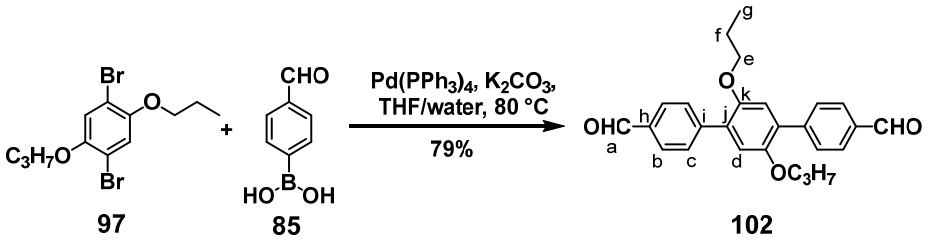

97 85 102

1,4-Dibromo-2,5-dipropyloxybenzene (0.20 g, 1.00 mmol), 4-Formylphenylboronic acid (0.22 g, 1.50 mmol), K_2CO_3 (0.60 g, 4.50 mmol) and $Pd(dppf)Cl_2$ (35.0 mg, 0.05 mmol) were mixed in a flask that was deaerated and filled with nitrogen. 1,4-Dioxane and water (3:1, 20 mL) and 2 M sodium carbonate (6 mL) were added. The mixture was refluxed under nitrogen overnight. After cooling, the mixture was extracted with THF, and the combined organic layer was dried with $MgSO_4$. Precipitation from methanol yielded 0.19 g (80%) of yellow solid.

M.p. = 140 °C.

MS (MALDI-TOF): *m/z* $[M]^+$ calcd. for $C_{26}H_{26}O_4^+$: 402.183; found: 6888.654.

Elemental Analysis (%): calcd. $C_{26}H_{26}O_4$: C 77.59, H 6.51; found: C 76.70, H 6.44.

^{1}H NMR (600 MHz, $CDCl_3$): δ (ppm) = 10.07 (s, 1H-*a*), 7.95-7.93 (d, 2H-*b*), 7.79-7.77 (d, 2H-*c*), 7.01 (s, 1H-*d*), 3.94-3.90 (t, 2H-*e*), 1.77-1.68 (m, 2H-*f*), 0.96-0.93 (t, 3H-*g*).

^{13}C-NMR (151 MHz, THF-d_8): δ (ppm) = 192.16 (C-*a*), 150.52(C-*k*), 144.73(C-*i*), 135.20 (C-*h*), 130.30 (C-*c*), 129.57(C-*b*), 116.05 (C-*d*), 71.35 (C-*e*), 22.83 (C-*f*), 10.82 (C-*g*).

IR (ATR): $\tilde{\nu}$ (cm^{-1}) = 2962 (w), 2941 (vm), 2879 (vw), 2819 (vw), 2727 (vw), 1697 (m), 1600 (m), 1568 (w), 1523 (w), 1494 (w), 1481 (w), 1392 (m), 1307 (w), 1269 (w), 1211(s), 1172 (m), 1055 (s), 1024(m), 825 (m), 808 (vs), 763 (w).

2',5'-Dimethoxy-p-terphenyl-4,4''-dialdehyde (103)

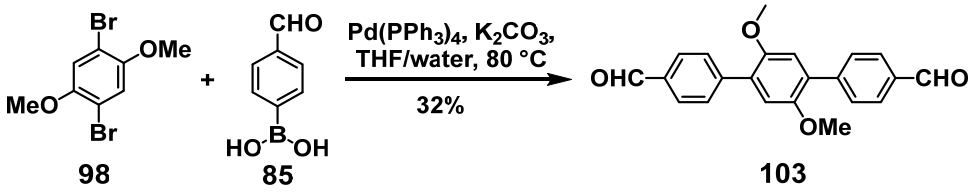

98 85 103

1,4-Dibromo-2,5-dimethoxybenzene (0.30 g, 1.00 mmol), 4-Formylphenylboronic acid (0.45 g, 1.50 mmol), and $Pd(PPh_3)_4$ (46.0 mg, 0.04 mmol) were mixed in a flask that was deaerated and filled with nitrogen. THF (20 mL) and 2 M sodium carbonate (6 mL) were added. The mixture was refluxed under nitrogen overnight. After cooling, the separated organic layer was dried with $MgSO_4$. Recrystallization from ethanol yielded 0.11 g (32%) of bright yellow solid.

M.p. = 107 °C.

^{1}H NMR (300 MHz, $CDCl_3$): δ (ppm) = 10.07 (s, 1H), 7.98-7.95 (d, 2H), 7.78-7.75 (d, 2H), 7.01 (s, 1H), 3.83 (s, 3H).

Analytical data are in accordance with those previously reported.[100]

2',5'-diethyl-p-terphenyl-4,4''-dialdehyde (104)

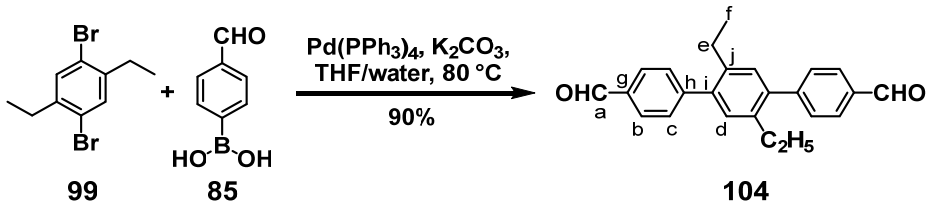

99 85 104

1,4-Dibromo-2,5-diethylbenzene (0.58 g, 2.00 mmol), 4-Formylphenylboronic acid (0.90 g, 6.00 mmol), and $Pd(PPh_3)_4$ (92.0 mg, 0.08 mmol) were mixed in a flask that was deaerated and filled with nitrogen. THF (12 mL) and 2 M sodium carbonate (12 mL) were added. The mixture was refluxed under nitrogen overnight. After cooling, the separated organic layer was dried with $MgSO_4$. Recrystallization from ethanol yielded 0.62 g (90%) of bright yellow solid.

M.p. = 140 °C.

MS (MALDI-TOF): *m/z* $[M]^+$ calcd. for $C_{24}H_{22}O_2^+$: 342.162; found: 6888.654.

Elemental Analysis (%): calcd. $C_{24}H_{22}O_2$: C 84.18, H 6.48; found: C 83.40, H 6.50.

^{1}H NMR (600 MHz, $CDCl_3$): δ (ppm) = 10.09 (s, 1H-*a*), 7.98-7.95 (d, 2H-*b*), 7.56-7.54 (d, 2H-*c*), 7.17 (s, 1H-*d*), 2.64-2.59 (m, 2H-*e*), 1.13-1.09 (t, 3H-*f*).

^{13}C-NMR (151 MHz, $CDCl_3$): δ (ppm) = 192.07 (C-*a*), 148.30(C-*h*), 140.41(C-*i*), 139.02 (C-*j*), 135.26 (C-*g*), 130.27(C-*d*), 130.11 (C-*c*), 129.77 (C-*b*), 25.85 (C-*e*), 15.74 (C-*f*).

IR (ATR): $\tilde{\nu}$ (cm^{-1}) = 2966 (w), 1704 (s), 1693 (m), 1600 (m), 1568 (w), 1487 (w), 1461 (w), 1382 (m), 1375 (w), 1301 (w), 1294 (w), 1207(m), 1170 (m), 1105 (w), 1055 w), 1012(w), 902 (w), 833 (vs), 756 (m).

2'-ethyl-p-terphenyl-4,4''-dialdehyde (104)

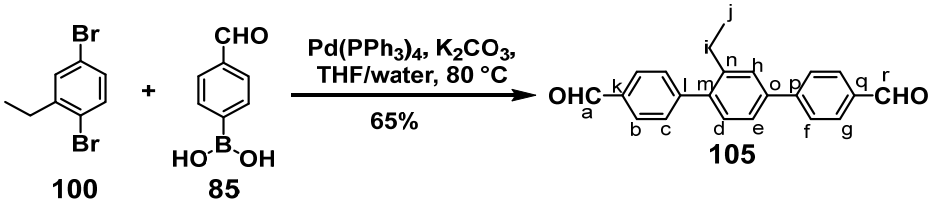

1,4-Dibromo-2-ethylbenzene (0.53 g, 2.00 mmol), 4-Formylphenylboronic acid (0.90 g, 6.00 mmol), and $Pd(PPh_3)_4$ (92.0 mg, 0.08 mmol) were mixed in a flask that was deaerated and filled with nitrogen. THF (12 mL) and 2 M sodium carbonate (12 mL) were added. The mixture was refluxed under nitrogen overnight. After cooling, the separated organic layer was dried with $MgSO_4$. Recrystallization from ethanol yielded 0.62 g (90%) of bright yellow solid.

M.p. = 128 °C.

MS (MALDI-TOF): *m/z* $[M]^+$ calcd. for $C_{22}H_{18}O_2^+$: 314.130; found: 6888.654.

Elemental Analysis (%): calcd. $C_{24}H_{22}O_2$: C 84.05, H 5.77; found: C 82.66, H 5.80.

^{1}H NMR (600 MHz, $CDCl_3$): δ (ppm) = 10.09(s, 1H-*a*), 10.08 (s, 1H-*r*), 8.00-7.96 (t, 4H-*b, g*), 7.82-7.80 (d, 2H-*f*), 7.61 (s, 1H-*h*), 7.56-7.52 (m, 3H-*c, e*), 7.33-7.31 (d, 1H-*d*), 2.72-2.66 (m, 2H-*i*), 1.18-1.15 (t, 3H-*j*).

^{13}C-NMR (151 MHz, $CDCl_3$): δ (ppm) = 192.03 (C-*a*), 191.99 (C-*r*), 147.91 (C-*l*), 146.93 (C-*p*), 142.41 (C-*n*), 140.70 (C-*m*), 139.83 (C-*o*), 135.53 (C-*q*), 135.37 (C-*k*), 130.57 (C-*d*), 130.47 (C-*g*), 130.06 (C-*c*), 129.81 (C-*b*), 128.08 (C-*h*), 127.84 (C-*f*), 124.96 (C-*e*), 26.46 (C-*i*), 15.81 (C-*j*).

IR (ATR): $\tilde{\nu}$ (cm^{-1}) = 2966 (w), 2927 (vw), 1691 (s), 1600 (s), 1564 (m), 1384 (m), 1303 (w), 1207 (m), 1163 (m), 1002 (m), 831 (m), 813 (vs), 692 (m).

4'-Formyl-2,6-dimethyl[1,1'-biphenyl]-4-dicarboxaldehyde (108)

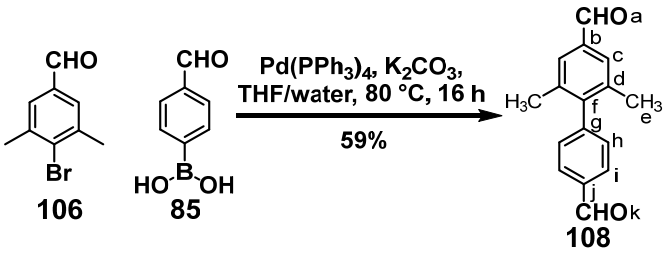

4-Bromo-3,5-dimethylbenzaldehyde (0.20 g, 1.00 mmol), 4-Formylphenylboronic acid (0.45 g, 3.00 mmol), and $Pd(PPh_3)_4$ (46.0 mg, 0.04 mmol) were mixed in a flask that was deaerated and filled with nitrogen. THF (10 mL) and 2 M sodium carbonate (6 mL) were added. The mixture was refluxed under nitrogen overnight. After cooling, the separated organic layer was dried with $MgSO_4$. Recrystallization from ethanol yielded 0.14 g (59%) of colorless solid.

M.p. = 89 °C.

MS (MALDI-TOF): *m/z* $[M+Na]^+$ calcd. for $C_{16}H_{14}O_2Na^+$: 261.099; found: 262.845.

Elemental Analysis (%): calcd. $C_{16}H_{14}O_2$: C 80.65, H 5.92; found: C 80.46, H 5.88.

^{1}H NMR (600 MHz, $CDCl_3$): δ (ppm) = 10.11 (s, 1H-*k*), 10.02 (s, 1H-*a*), 8.03-8.01 (d, 2H-*i, g*), 7.66 (s, 2H-*c*), 7.35-7.33 (d, 2H-*h*), 2.11 (s, 6H-*e*).

^{13}C-NMR (151 MHz, $CDCl_3$): δ (ppm) = 192.43 (C-*a*), 191.93 (C-*k*), 146.92 (C-*f*), 146.76(C-*g*), 136.93 (C-*o*), 135.85 (C-*j*), 135.67 (C-*b*), 131.87 (C-*d*), 130.34 (C-*i*), 129.36 (C-*h*), 128.99 (C-*c*), 20.85 (C-*e*).

IR (ATR): $\tilde{\nu}$ (cm^{-1}) = 2833 (w), 2738 (w), 1703 (s), 1683 (s), 1596 (s), 1566 (m), 1384 (m), 1298 (m), 1166 (w), 1143 (m), 999 (m), 869 (w), 833 (vs), 742 (m), 684 (m).

4'-Formyl-2-methyl[1,1'-biphenyl]-4-dicarboxaldehyde (109)

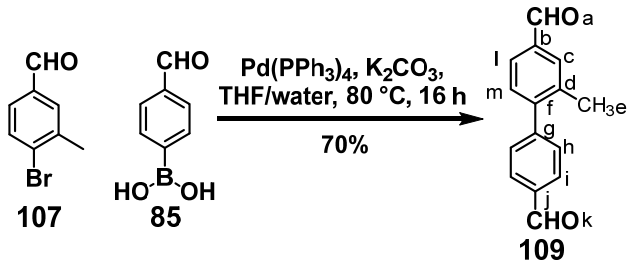

4-Bromo-3-methylbenzaldehyde (0.40 g, 2.00 mmol), 4-Formylphenylboronic acid (0.90 g, 6.00 mmol), and $Pd(PPh_3)_4$ (92.0 mg, 0.08 mmol) were mixed in a flask that was deaerated and filled with nitrogen. THF (20 mL) and 2 M sodium carbonate (12 mL) were added. The mixture was refluxed under nitrogen overnight. After cooling, the separated organic layer was dried with $MgSO_4$. Recrystallization from ethanol yielded 0.16 g (70%) of bright yellow solid.

M.p. = 128 °C.

MS (MALDI-TOF): *m/z* $[M+H_2O]^+$ calcd. for $C_{15}H_{14}O_3^+$: 242.094; found: 242.850.

Elemental Analysis (%): calcd. $C_{15}H_{12}O_2$: C 80.34, H 5.59; found: C 80.08, H 5.39.

^{1}H NMR (600 MHz, $CDCl_3$): δ (ppm) = 10.09 (s, 1H-*k*), 10.04 (s, 1H-*a*), 8.01-7.96 (d, 2H-*i*), 7.81(s, 1H-*c*), 7.79-7.77 (d, 2H-*l*), 7.51-7.49 (d, 2H-*h*), 7.41-7.39 (d, 2H-*m*), 2.34 (m, 2H-*e*).

^{13}C-NMR (151 MHz, $CDCl_3$): δ (ppm) = 192.14 (C-*a*), 191.90 (C-*k*), 147.05(C-*l*), 146.81(C-*f*), 136.49 (C-*d*), 136.10 (C-*b*), 135.70 (C-*j*), 131.87 (C-*c*), 130.40(C-*m*), 129.88 (C-*i*), 129.72 (C-*h*), 127.55 (C-*l*), 20.47 (C-*e*).

IR (ATR): $\tilde{\nu}$ (cm^{-1}) = 2833 (w), 2738 (w), 1703 (s), 1683 (s), 1596 (s), 1566 (m), 1384 (m), 1298 (m), 1166 (w), 1143 (m), 999 (m), 869 (w), 833 (vs), 742 (m), 684 (m).

IR (ATR): $\tilde{\nu}$ (cm^{-1}) = 2815 (w), 2725 (w), 1697 (s), 1598 (s), 1560 (m), 1382 (m), 1299 (w), 1207 (s), 1161 (m), 1004 (m), 952 (w), 835 (m), 833 (m), 779 (m), 736 (m), 655 (m).

1,8,13-Tributyloxytriptycene (110)

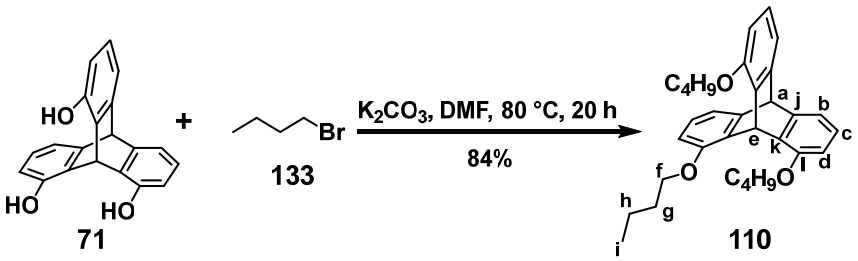

110 was synthesized according to **GP1** with 1,8,13-Trihydroxytriptycene (1.80 g, 6.00 mmol), Potassium carbonate (5.00 g, 36.00 mmol), 1-Bromobutane (4.50 g, 33.00 mmol), DMF (50 mL). The product was dried in a vacuum to obtain 1,8,13-Tributyloxytriptycene in 84% yield (2.40 g, 6.10 mmol) as a slightly brown powder.

M.p. = 272 °C.

MS (ESI): *m/z* $[M+Na]^+$ calcd. for $C_{32}H_{38}O_3Na^+$: 493.271; found: 493.271.

Elemental Analysis (%): calcd for $C_{32}H_{38}O_3$: C 81.66, H 8.14; found C 81.44, H 8.02.

^{1}H NMR (600 MHz, $CDCl_3$): δ (ppm)= 7.00-6.98 (d, 3H-*b*), 6.94 (s, 1H-*e*), 6.89-6.86 (t, 3H-*c*), 6.57-6.54 (d, 3H-*d*), 5.37 (s, 1H-*a*), 3.99-3.96 (t, 6H-*f*), 1.88-1.81 (m, 6H-*g*), 1.72-1.62 (m, 6H-*h*), 1.07-1.03 (t, 9H-*i*).

^{13}C-NMR (151 MHz, $CDCl_3$): δ (ppm) = 154.24 (C-*l*), 148.73 (C-*k*), 133.93 (C-*j*), 125.61 (C-*c*), 116.50 (C-*b*), 110.05 (C-*d*), 68.45 (C-*f*), 54.78 (C-*a*), 33.68 (C-*e*), 32.00 (C-*g*), 19.54 (C-*h*), 14.23 (C-*i*).

IR (ATR): $\tilde{\nu}$ (cm^{-1}) = 2952 (m), 2929 (m), 2869 (m), 1596 (s), 1483 (m), 1467 (s), 1394 (m), 1274 (vs), 1255 (s), 1097 (s), 1080 (s), 1031 (m), 954 (m), 786 (s), 771 (m), 742 (s), 727 (vs), 638 (m).

2,2'2"- (1,8,13-tributyloxytriptycene-3,6,15-triyl) tris (4,4,5,5, -tetramethyl-1,3,2-diox) borolane (111)

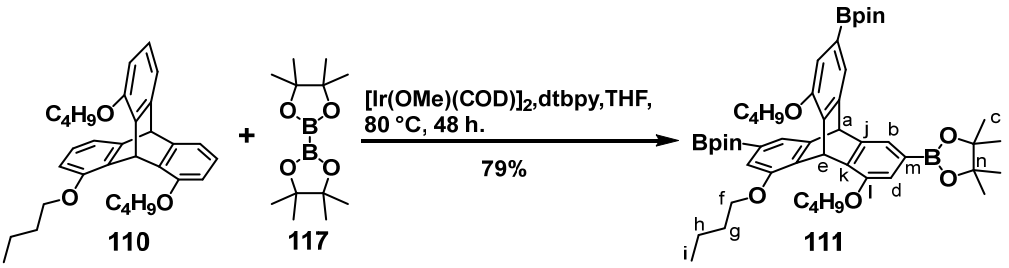

111 was synthesized according to **GP2** with (1,5-Cyclooctadiene)(methoxy)iridium(I)dimer (66.2 mg, 0.10 mmol, 5 mol%), 4, 4'-di-tert-butyl-2, 2'-dipyridyl (52.0 mg, 0.20 mmol 10 mol%), bis-(pinacolato)diborane (2.12 g, 9.00 mmol), 1,8,13-tributyloxytriptycene (0.94 g, 2.00 mmol) and dry THF (15 mL). The obtained off-white solid was recrystallized from chloroform/ethanol to obtain 2, 2', 2"-(1, 8, 13-tripropyloxytriptycene-3,6,15-triyl)tris(4, 4, 5, 5,-tetramethyl-1, 3, 2-diox)borolane **111** in 79% yield (1.34 g, 1.57 mmol) as the light brown powder.

M.p. = 347 °C.

MS (ESI): *m/z* $[M+Na]^+$ calcd. for $C_{50}H_{71}B_3O_9Na^+$: 871.527; found: 871.528.

Elemental Analysis (%): calcd. for $C_{50}H_{71}B_3O_9$: C 70.77, H 8.43; found: C 70.49, H 8.32.

^{1}H NMR (600 MHz, $CDCl_3$): δ (ppm) = 7.42 (s, 3H-*b*), 6.98 (s, 3H-*d*), 6.97 (s, 1H-*e*), 5.45 (s, 1H-*a*), 4.02-4.00 (t, 6H-*f*), 1.85-1.81 (m, 6H-*g*), 1.68-1.64 (m, 6H-*h*), 1.28 (s, 36H-*c*), 1.05-1.02 (t, 9H-*i*).

^{13}C-NMR (151 MHz, $CDCl_3$): δ (ppm) = 154.01 (C-*l*), 147.96 (C-*j*), 136.61 (C-*k*), 122.76 (C-*b*), 116.09 (C-*d*), 83.63 (C-*n*), 68.46 (C-*f*), 54.41 (C-*a*), 34.35 (C-*e*), 31.98 (C-*g*), 24.88 (C-*c*), 19.50 (C-*h*), 14.24 (C-*i*).

IR (ATR): $\tilde{\nu}$ (cm^{-1}) = 2976 (w), 2956 (w), 2931 (w), 2869 (w), 1589 (w), 1479 (w), 1353 (vs), 1296 (m), 1249 (s), 1139(s), 1103 (m), 1083 (m), 966 (s), 919 (m), 856 (m), 765 (w), 713 (w), 696 (s), 669 (m).

1,8,13-Tributyloxy-3,6,15-triaminotriptycene (112)

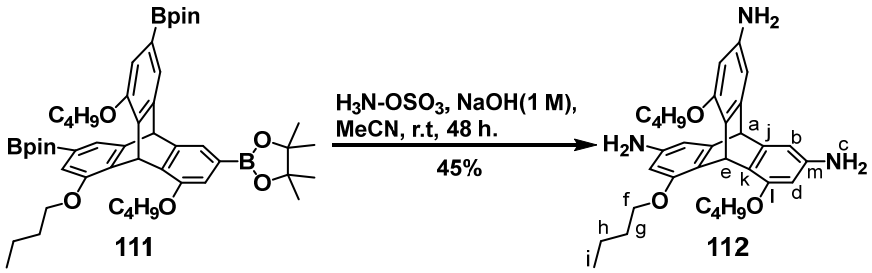

112 was synthesized according to **GP3** with 1,8,13-tributyloxy-3,6,15-tris(pinacolato)borontriptycene (0.85 g, 1.00 mmol), hydroxylamine-O-sulfonic acid (0.56 g, 5.00 mmol), acetonitrile (15 mL) and an aqueous solution of sodium hydroxide (1 M, 15 mL). The product was purified by column chromatography (ethyl acetate/petroleum ether, 5:1) to

obtain 1,8,13-Tripropyloxy-3,6,15-triaminotriptycene in 45% yield (0.23 g, 0.45 mmol) as the brown solid.

M.p. > 292 °C (decomposed).

MS (ESI): *m/z* $[M+Na]^+$ calcd. for $C_{32}H_{41}N_3O_3Na^+$: 538.304; found: 538.304.

Elemental Analysis (%): calcd. for $C_{32}H_{41}N_3O_3$: C 74.53, H 8.01, N 8.15; found: C 73.22, H 7.86, N 7.61.

^{1}H NMR (600 MHz, DMSO-d_6): δ (ppm) = 6.24 (s, 3H-*b*), 6.12 (s, 1H-*e*), 5.81 (s, 3H-*d*), 4.78 (s, 1H-*a*), 4.73 (s, 6H-*c*), 3.81-3.79 (t, 6H-*f*), 1.73-1.69 (m, 6H-*g*), 1.62-1.56 (m, 6H-*h*), 1.01-0.99 (m, 9H-*i*).

^{13}C-NMR (151 MHz, DMSO-d_6): δ (ppm) = 152.95 (C-*l*), 148.72 (C-*j*), 146.07 (C-*k*), 122.99 (C-*m*), 103.46 (C-*b*), 95.17 (C-*d*), 67.41 (C-*f*, 54.22 (C-*a*), 31.49 (C-*g*), 30.89 (C-*e*), 18.97(C-*h*), 14.00 (C-*i*).

IR (ATR): $\tilde{\nu}$ (cm^{-1}) = 3597 (vw), 3340 (w), 2954 (m), 2931 (m), 2869 (m), 1596 (vs), 1494 (s), 1456 (s), 1346 (m), 1321 (s), 1240 (m), 1195 (m), 1139 (vs), 1101 (s), 1076 (s), 1039 (m), 833 (m), 808 (m), 767 (m), 678(w).

Model Compound (115)

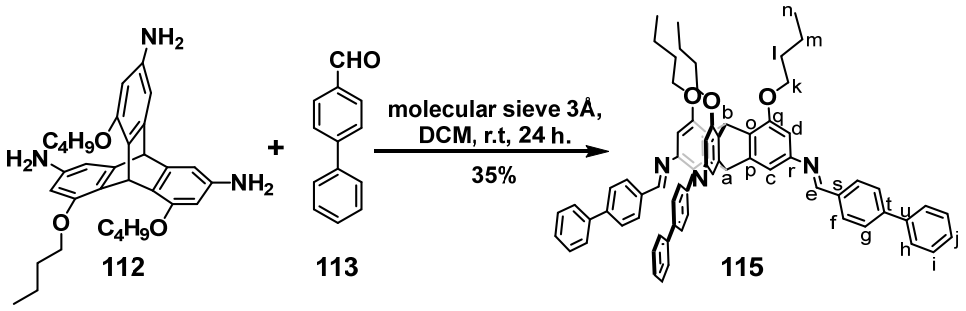

1,8,13-tributyloxy-3,6,15-triaminotriptycene **112** (83.0 mg, 0.16 mmol), and 4-Biphenylaldehyde **113** (92.0 mg, 0.50 mmol) were mixed in a flask. $CHCl_3$ (10 mL) and molecular sieve 3 Å were added. The mixture was refluxed overnight. After cooling, the solution was filtered to remove the molecular sieves, and the solution was concentrated and precipitated with methanol. The collected solid was dried under vacuum to obtain the 115 in 35% yield (56.0 mg, 0.05 mmol) as brown solid.

M.p. = 136 °C.

MS (MALDI-TOF): *m/z* $[M]^+$ calcd. for $C_{71}H_{65}N_3O_3^+$: 1007.502; found: 6888.654.

Elemental Analysis (%): calcd. $C_{71}H_{65}N_3O_3$: C 84.57, H 6.50, N, 4.17; found: C 84.56, H 6.41, N 4.17.

^{1}H NMR (600 MHz, $CDCl_3$): δ (ppm) = 8.48 (s, 3H-*e*), 7.94-7.92 (d, 6H-*f*), 7.70-7.68 (d, 6H-*g*), 7.65-7.64 (d, 6H-*h*), 7.48-7.45 (t, 6H-*l*), 7.40-7.36 (t, 3H-*j*), 6.98 (s, 3H-*c*), 6.92 (s, 1H-*b*),

6.56 (s, 3H-*d*), 5.45 (s, 1H-*a*), 4.08-4.05 (t, 6H-*k*), 1.93-1.86 (m, 6H-*l*), 1.76-1.66 (m, 6H-*m*), 1.10-1.07 (t, 9H-*n*).

^{13}C-NMR (151 MHz, $CDCl_3$): δ (ppm) = 159.21 (C-*e*), 154.39 (C-*o*), 150.23 (C-*r*), 148.99 (C-*p*), 143.99 (C-*t*), 140.49 (C-*u*), 135.47 (C-*s*), 131.65 (C-*q*), 129.33 (C-*f*), 129.03 (C-*l*), 127.98 (C-*j*), 127.55 (C-*g*), 127.32 (C-*h*), 108.57 (C-*c*), 104.09 (C-*d*), 68.40 (C-*k*), 55.38 (C-*a*), 33.43 (C-*b*), 31.93 (C-*l*), 20.27 (C-*m*), 14.26 (C-n).

IR (ATR): $\tilde{\nu}$ (cm^{-1}) = 2966 (w), 2927 (vw), 1691 (s), 1600 (s), 1564 (m), 1384 (m), 1303 (w), 1207(m), 1163 (m), 1002 (m), 831 (m), 813 (vs), 692 (m).

Model Compound (116)

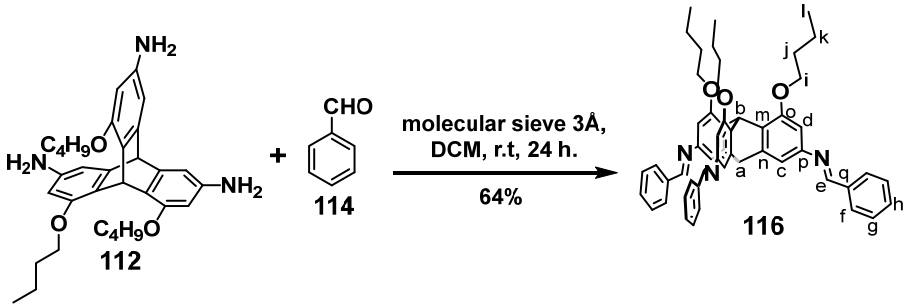

1,8,13-tributyloxy-3,6,15-triaminotriptycene **112** (83.0 mg, 0.16 mmol), and Benzaldehyde **114** (53.0 mg, 0.50 mmol) were mixed in a flask. $CHCl_3$ (10 mL) and molecular sieve 3 Å were added. The mixture was refluxed overnight. After cooling, the solution was filtered to remove the molecular sieves, and the solution was concentrated and precipitated with methanol. The collected solid was dried under vacuum to obtain the **115** in 64% yield (80.0 mg, 0.10 mmol) as a brown solid.

M.p. = 110 °C.

MS (MALDI-TOF): *m/z* $[M]^+$ calcd. for $C_{71}H_{65}N_3O_3^+$: 779.408; found: 6888.654.

Elemental Analysis (%): calcd. $C_{71}H_{65}N_3O_3$: C 81.61, H 6.85, N 5.39; found: C 81.22, H 6.54, N 5.72.

^{1}H NMR (600 MHz, $CDCl_3$): δ (ppm) = 8.43 (s, 3H-*e*), 7.87-7.84 (m, 6H-*f*), 7.45-7.44 (m, 9H-*h*, *g*), 6.94 (d, 3H-*c*), 6.89 (s, 1H-*b*), 6.53-6.52 (d, 3H-*d*), 5.41 (s, 1H-*a*), 4.06-4.03 (t, 6H-*i*), 1.91-1.85 (m, 6H-*j*), 1.74-1.65 (m, 6H-*k*), 1.09-1.05 (t, 3H-*l*).

^{13}C-NMR (151 MHz, $CDCl_3$): δ (ppm) = 159.69 (C-*e*), 154.35 (C-*o*), 150.18 (C-*d*), 148.96 (C-*n*), 136.49 (C-*q*), 131.60 (C-*m*), 131.29 (C-*h*), 128.84 (C-*f*, *g*), 108.52 (C-*c*), 104.00 (C-*d*), 68.37 (C-*i*), 55.34 (C-*a*), 33.38 (C-*b*), 31.92 (C-*j*), 19.56 (C-*k*), 14.25 (C-*l*).

IR (ATR): $\tilde{\nu}$ (cm^{-1}) = 2956 (w), 2933 (w), 2871 (w), 1627 (m), 1589 (vs), 1577 (m), 1465 (m), 1450 (m), 1431 (m), 1367 (w), 1299 (s), 1232 (w), 1218 (w), 1120 (vs), 1099 (s), 1072(m), 970 (m), 875 (w), 837 (m), 757 (s), 692 (s), 646 (w).

6.2.3 Compounds of Chapter 3.4

ButDie-[4]Catenane

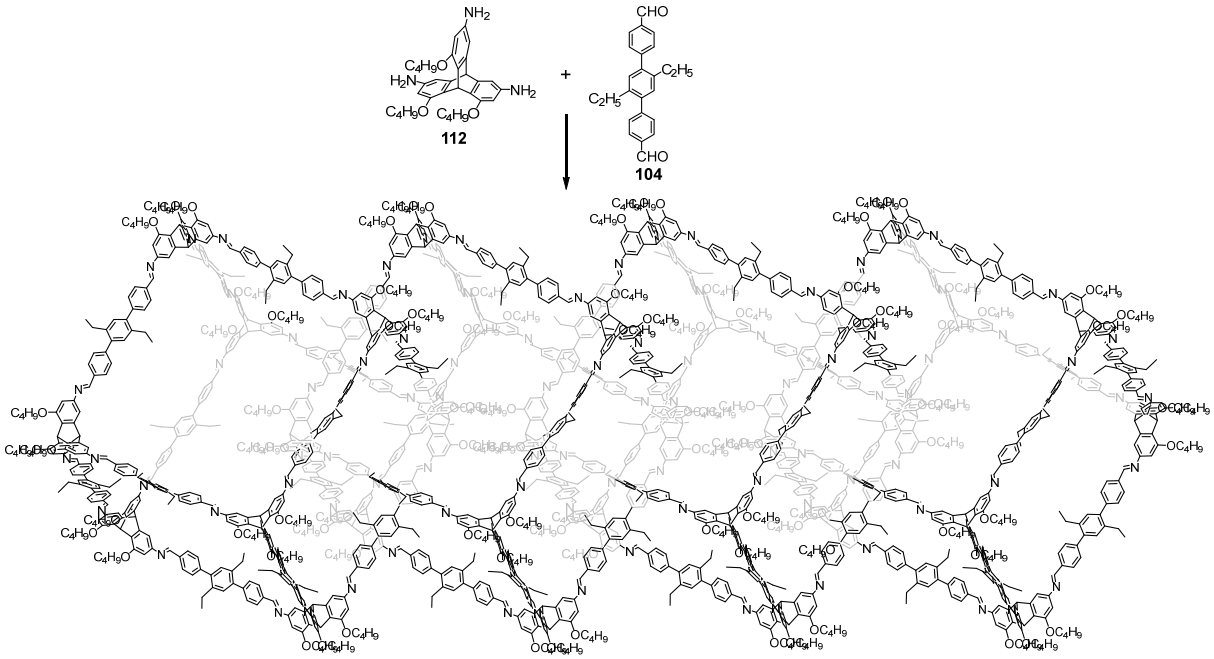

ButDie-[4]Catenane was synthesized according to **GP4** with 1,8,13-tributyloxy-3,6,15-triaminotriptycene (9.6 mg, 16.0 µmol), 2',5''-diethyl-p-terphenyl-4,4''-dialdehyde (8.2 mg, 24.0 µmol), $CHCl_3$ (1.5 mL) + toluene (1.5 mL), and TFA (in $CHCl_3$, 0.01 M, 4% mol, 60 µL). The light brown solution was stirred at r.t for 7 days. The crude product was purified by THF-GPC to obtain **ButDie-[4]Catenane** in 25 % yield (3.8 mg, 0.11 µmol) as a yellow solid.

M.p. ≥ 365 °C (decomposition).

MS (MALDI): *m/z* $[M]^+$ calcd. for $C_{2176}H_{2176}N_{96}O_{96}^+$: 31184.834; found: 31232.762.

Elemental Analysis (%): calcd. for $C_{2176}H_{2176}N_{96}O_{96}$: C 83.89, H 7.61, N 3.97; found: C 83.45, H 6.95, N 4.03.

^{1}H NMR (700 MHz, CD_2Cl_2, 303 K): δ (ppm) = 8.91 (s, 3H), 8.86 (s, 3H), 8.80 (s, 3H), 8.51 (s, 3H), 8.47 (s, 3H), 8.46 (d, 6H), 8.41 (s, 3H), 8.23 (s, 3H), 8.08-8.07 (d, 6H), 7.97 (s, 3H), 7.88 (s, 3H), 7.87-7.86 (d, 6H), 7.84-7.83 (d, 6H), 7.80 (s, 3H), 7.59-7.58 (d, 6H), 7.55-754 (m, 24H), 7.48-7.47 (d, 12H), 7.44-7.42 (m, 12H), 7.38-7.36 (m, 12H), 7.32-7.30 (m, 18H), 7.26 (s, 3H), 7.26 (s, 3H), 7.22-7.19 (m, 12H), 7.19-7.18 (d, 6H), 7.13-7.12 (d, 6H), 7.10-7.07 (m, 24H), 8.85 (s, 6H), 6.82 (s, 6H), 6.80 (s, 6H), 6.79 (s, 6H), 6.69 (d, 6H), 7.02 (s, 3H), 6.58 (s, 3H), 6.59-6.55 (m, 24H), 6.53 (s, 6H), 6.49 (s, 6H), 6.47 (s, 6H), 6.40 (s, 3H), 6.20 (s, 3H), 6.10 (s, 3H), 5.96 (s, 3H), 5.48 (s, 3H). (massive alkyl peaks were omitted)

^{13}C-NMR (176 MHz, CD_2Cl_2, 303 K): δ (ppm) = 161.31, 161.15, 160.28, 160.09, 159.26, 159.13, 159.04, 158.83, 158.66, 156.88, 154.82, 154.62, 154.50, 154.35, 154.24, 153.90,

151.25, 150.98, 150.72, 150.41, 149.94, 149.67, 149.54, 149.40, 149.06, 148.81, 148.64, 147.44, 145.98, 145.53, 145.45, 145.21 ,145.08, 144.81, 144.45, 141.49, 141.34, 140.97, 140.82, 140.60, 140.48, 140.33, 139.99, 139.80, 139.62, 139.50, 139.37, 139.33, 139.19, 139.16, 139.02, 138.94, 136.29, 136.02, 135.51, 135.49, 135.33, 135.24, 135.18, 132.78, 132.69, 132.47, 132.45, 132.22, 132.12, 131.90, 131.22, 131.02, 130.70, 130.48, 130.38, 130.18, 130.14, 130.02, 129.81, 129.47, 129.35, 128.89, 128.64, 128.60, 128.39, 128.36, 111.34, 110.19, 109.67, 108.89, 108.56, 107.76, 106.57, 105.92, 105.52, 105.14, 104.91, 104.71, 104.23, 103.98, 103.18, 69.32, 69.06, 68.97, 68.79, 68.65, 68.54, 66.89, 66.83, 55.93, 55.12, 54.65, 33.91, 33.66, 32.34, 32.28, 32.21, 32.13, 32.10, 31.91, 31.79, 31.61, 26.75, 26.50, 26.42, 26.37, 26.26, 26.22, 26.10, 25.74, 20.03, 19.99, 19.94, 19.92, 19.79, 19.67, 19.58, .19.52, 19.48, 19.44, 19.26, 19.17, 16.19, 16.17, 16.04, 16.00, 15.96, 15.82, 15.78, 15.71, 15.64, 15.56, 15.44, 15.37, 15.26, 14.63, 14.59, 14.54, 14.40, 14.37, 14.35, 14.26, 14.14, 14.06, 13.97.

IR (ATR): $\tilde{\nu}$ (cm^{-1}) = 2960 (m), 2933 (w), 2871 (w), 1591 (vs), 1487 (m), 1463 (m), 1431 (m), 1301 (m), 1222 (w), 1120 (s), 1101 (s), 1072 (m), 973 (m), 879 (w), 835 (m), 759 (w), 734 (w).

ButDie-[3]Catenane

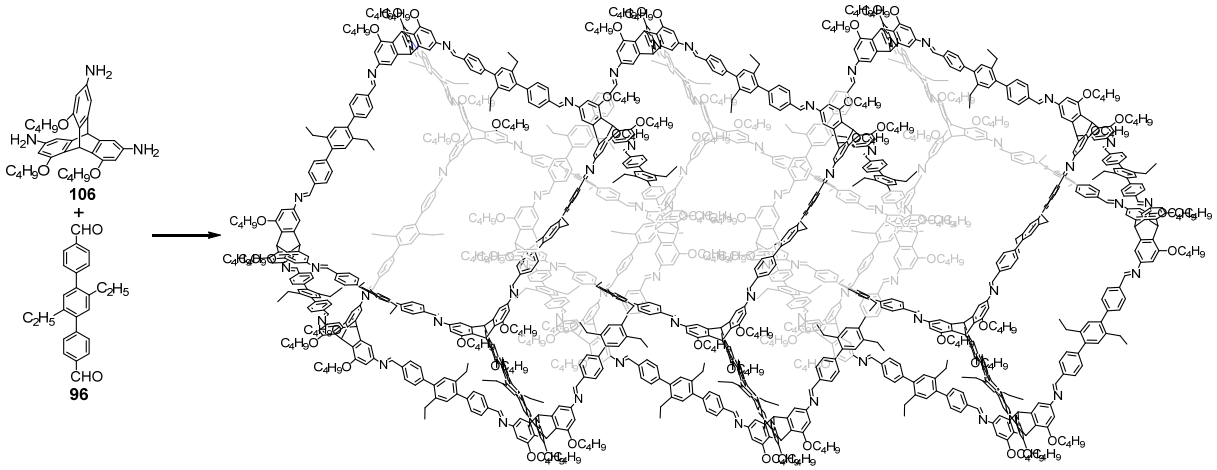

ButDie-[3]Catenane was synthesized according to **GP4** with 1,8,13-tributyloxy-3,6,15-triaminotriptycene (7.0 mg, 14.0 µmol), [1,1':4',1''-Terphenyl]-4,4''-dicarbaldehyde (8.2 mg, 24.0 µmol), $CHCl_3$ (2.0 mL) + toluene (1.0 mL), and TFA (in $CHCl_3$, 0.01 M, 4 mol%, 60 µL). The light brown solution was stirred at r.t for 4 days. The crude product was purified by THF-GPC to obtain **ButDie-[3]Catenane** in 5 % yield (1.0 mg, 0.05 µmol) as a yellow solid.

M.p. ≥ 365 °C (decomposition).

MS (MALDI-TOF): *m/z* $[M]^+$ calcd. for $C_{1632}H_{1632}N_{72}O_{72}^+$: 23388.625; found: 23424.048.

^{1}H NMR (700 MHz, CD_2Cl_2): δ (ppm) = 8.84-8.83 (d, 6H), 8.56 (s, 3H), 8.54 (s, 3H), 8.48-8.46 (m, 9H), 8.19 (s, 3H), 9.00-7.97 (m, 9H), 7.82-7.79 (m, 12H), 7.64-7.63 (d, 6H), 7.54-7.50

(m, 24H), 7.46-7.45 (m, 9H), 7.41 (s, 3H), 7.39-7.36 (m, 15H), 7.32 (s, 3H), 7.28-7.27 (d, 6H), 7.25-7.24 (d, 6H), 7.20-7.15 (m, 24H), 7.12 (s, 3H), 7.10 (s, 6H), 7.06 (s, 3H), 7.04 (s, 3H), 7.01-7.00 (d, 6H), 6.99-6.96 (m, 18H), 6.87 (s, 3H), 6.82 (s, 3H), 6.81 (s, 3H), 6.73 (s, 3H), 6.70 (s, 3H), 6.59-6.57 (m, 12H), 6.55-6.54 (d, 6H), 6.52 (s, 3H), 6.30 (s, 3H), 6.14 (s, 3H), 5.53 (s, 3H). (massive alkyl peaks were omitted)

^{13}C-NMR (176 MHz, CD_2Cl_2): δ (ppm) =160.82, 160.00, 159.46, 159.29, 159.17, 158.91, 158.79, 157.72, 154.68, 154.58, 154.53, 154.39, 154.12, 153.82, 151.09, 150.57, 150.40, 150.26, 150.18, 149.78, 149.70, 149.58, 149.32, 149.13, 148.76, 148.69, 148.31, 145.78, 145.21, 145.10, 145.02, 144.87, 144.58, 141.34, 141.25, 140.80, 140.69, 140.49, 140.38, 140.14, 139.63, 139.53, 139.47, 139.34, 139.15, 139.09, 138.95, 135.84, 135.74, 135.29, 135.26, 135.15, 135.07, 132.36, 132.21, 132.08, 131.86, 131.54, 131.10, 130.65, 130.48, 130.42, 130.34, 130.01, 129.92, 129.81, 129.35, 129.04, 128.75, 128.51, 128.38, 110.56, 109.75, 109.21, 109.03, 108.42, 107.49, 10684, 106.56, 106.22, 106.18, 105.41, 104.72, 104.38, 103.88, 103.82, 69.17, 69.96, 68.81, 68.57, 68.38, 66.76, 55.78, 54.93, 33.73, 33.55, 32.24, 32.18, 32.03, 31.82, 31.78, 31.59, 30.46, 30.09, 26.55, 26.39, 26.25, 26.15, 26.00, 25.93, 19.98, 19.96, 19.92, 19.87, 19.61, 19.44, 19.32, 19.07, 16.02, 15.93, 15.84, 15.77, 15.75, 15.68, 15.58, 15.43, 15.32, 14.57, 14.37, 14.34, 14.26, 14.11, 14.0.

IR (ATR): $\tilde{\nu}$ (cm^{-1}) = 2958 (m), 2931 (w), 2871 (w), 1589 (vs), 1485 (m), 1463 (m), 1431 (m), 1301 (m), 1222 (w), 1120 (s), 1101 (s), 1072 (s), 972 (m), 877 (m), 835 (s), 759 (w), 734 (w), 648 (w).

6.2.4 Compounds of Chapter 4

2,3,6,7,12,13-Hexa-(3'-carbonyl-4'-hydroxyphenyl)triptycene (127)

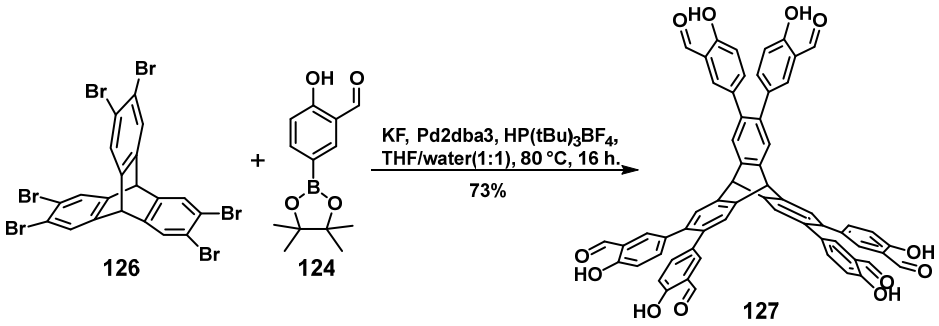

Hexabromotriptycene **126** (271.0 mg, 0.37 mmol), 3-Carbonyl-4-hydroxyphenylboronic acid pinacol ester **124** (646.0 mg, 2.60 mmol) and KF (389.0 mg, 6.70 mmol) were mixed in 12.4 mL 1:1 (v/v) THF/H_2O. Pd_2dba_3 (40.9 mg, 0.05 mmol, 0.12 equiv.) and $HP(tBu)_3BF_4$ (32.4 mg, 0.11 mmol) were added to the mixture, then stirred for 16 h at 80 °C. After cooling to r.t. The organic phase was separated and washed with sat. NH_4Cl solution, H_2O, and brine. After drying

over $MgSO_4$, filtration, and evaporation of the solvent the crude product was purified via precipitation from hot $CHCl_3$ with CH_3OH, and **127** was obtained in 73% yield (264mg, 0.27mmol) as an off-white solid.

M.p. = > 250 °C (decomposition).

^{1}H NMR (300 MHz, $CDCl_3$): δ (ppm) =10.93 (s, 6H), 9.74 (s, 6H), 7.57 (s, 6H), 7.32-7.32 (d, 6H), 7.22-7.21 (d, 3H), 7.19-7.18 (d, 3H), 6.85-6.82 (d, 6H), 5.70 (s, 2H).

Analytical data are in accordance with those previously reported.[90]

N-salicylidin-2-bromoethylimine (139)

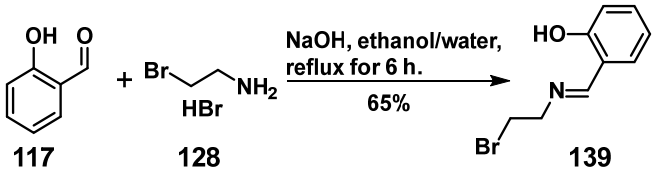

A solution of sodium hydroxide (0.80 g, 20.00 mmol) in 10 mL water was slowly added to the mixture of salicylaldehyde **117** (2.44 g, 20.00 mmol) and 2-bromoethyl ammonium hyrobromide **128** (4.1g, 20.00 mmol) in 150 mL ethanol. Refluxed for 6 hours, evaporated part of solvent to 50 mL. Poured the solution into 200 cold water. Lots of precipitation appeared. Put them in the fridge for 2 hours, filtered them, and dried in a vacuum to give **139** in 65% yield (2.98 g, 13.00 mmol) as a yellow solid.

M.p. = 70 °C.

^{1}H NMR (300 MHz, DMSO-d_6): δ (ppm) = 12.97 (s, 1H), 8.38 (s, 1H), 7.37-7.27 (m, 2H), 6.99-6.87 (m, 2H), 4.03-3.99 (m, 2H), 4.67-3.63 (m, 2H).

Analytical data are in accordance with those previously reported.[101]

Complex 140

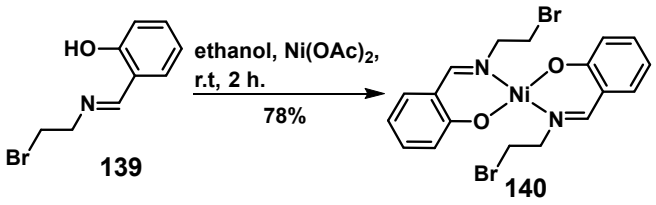

N-salicylidin-2-bromoethylimine **139** (456.0 mg, 2.00 mmol) dissolved in 40 mL ethanol was added to the solution of $Ni(OAc)_2$ (274.0 mg, 1.10 mmol) in 40 mL ethanol. Stirred at r.t. for 2 hours. Filtered and washed with ethanol to give **140** in 78% yield (0.40 g, 0.78 mmol) as green solid.

M.p. = 212 °C.

MS (MALDI-TOF): *m/z* $[M]^+$ calcd. for $C_{18}H_{18}N_2O_2Br_2Ni^+$: 509.9, found: 511.0 (M+2H).

Analytical data are in accordance with those previously reported.[101]

Compound 141

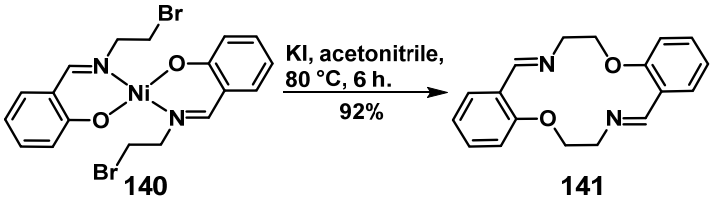

Complex **140** (25.0 mg, 0.05 mmol) was dissolved in 6ml acetonitrile, and KI (5.0 mg, 0.03 mmol) was added to the solution. Stirred at 80 °C for 6 hours. After cooling to r.t. Remove the solvent and washed it with water, and dried with a vacuum to obtain **141** in 92% yield (13.5 mg, 0.045mmol) as orange solid.

M.p. = 203 °C.

^{1}H NMR (300 MHz, DMSO-*d*$_6$): δ (ppm) = 8.76 (s, 1H), 7.60-7.57 (d, 1H), 7.40-7.35 (m, 1H), 7.01-6.90 (m, 2H), 4.17-4.14 (m, 2H), 3.93-3.92 (m, 2H).

Analytical data are in accordance with those previously reported.[101]

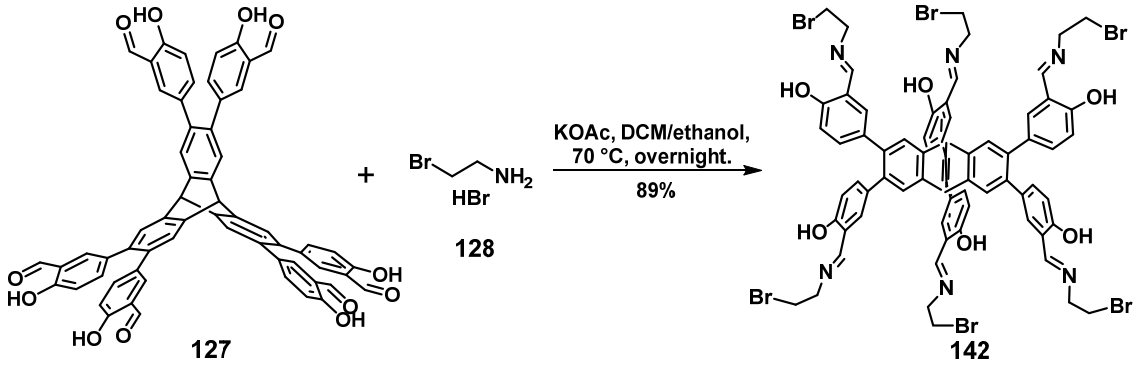

Compound 142: 2,3,6,7,12,13-Hexa-(3'-carbonyl-4'-hydroxyphenyl)triptycene **127** (98.0 mg, 0.10 mmol) and 2-bromoethyl ammonium hyrobromide **128** (133mg, 0.65 mmol) were dissolved in 20 mL DCM, KOAc (63.0 mg, 0.65 mmol) and 5 mL ethanol were added to the solution. The mixture was refluxed at 70 °C overnight. After cooling to r.t. there were some insoluble solids. Filtered and evaporated the solvents to obtain **142** in 89% yield (145.0 mg, 0.89 mmol) as yellow solid.

M.p. = > 190°C (decomposition).

MS (ESI): m/z $[M]^+$ calcd. for $C_{74}H_{62}N_6O_6Br_6^+$: 1603.983, found: 1632.9649.

Elemental Analysis (%): ($C_{74}H_{62}N_6O_6Br_6$) Calcd. C 55.18, H 3.88, N 5.22 found: C 55.57, H 4.08, N 5.25.

^{1}H NMR (300 MHz, $CDCl_3$): δ (ppm) = 8.17 (s, 6H), 7.51 (s, 6H), 7.26 (s, 6H), 7.07-7.05 (m, 6H), 7.00 (d, 6H), 6.83-6.81 (d, 6H), 5.62 (s, 2H), 3.97-3.95 (m, 12H), 3.64-3.61 (m, 12H).

IR (ATR): $\tilde{\nu}$ = 1628 cm^{-1} (vs), 1582 (m), 1489 (w), 1472 (w), 1456 (w), 1435 (w), 1406 (w), 1373 (w), 1335 (w), 1259 (m), 1238 (w), 1215 (m), 1167 (w), 1084 (w), 1074 (w), 1049 (w), 878 (w).

7. Reference

[1] R. M. Zhu, J. W. Ding, L. Jin, H. Pang, *Coordination Chemistry Reviews.* **2019**, *389*, 119-140.

[2] M. Fujita, N. Fujita, K. Ogura, K. Yamaguchi, *Nature.* **1999**, *400*, 52-55.

[3] T. Hasell, X. Wu, J. T. Jones, J. Bacsa, A. Steiner, T. Mitra, A. Trewin, D. J. Adams, A. I. Cooper, *Nature Chemistry.* **2010**, *2*, 750-755.

[4] R. S. Forgan, J. P. Sauvage, J. F. Stoddart, *Chemical Reviews.* **2011**, *111*, 5434-5464.

[5] (a) G. Zhang, M. Mastalerz, *Chemical Society Reviews.* **2014**, *43*, 1934-1947; (b) T. Hasell, A. I. Cooper, *Nature Reviews Materials.* **2016**, *1*; (c) M. Mastalerz, *Angewandte Chemie-International Edition.* **2010**, *49*, 5042-5053; (d) S. R. Seidel, P. J. Stang, *Accounts of Chemical Research.* **2002**, *35*, 972-983; (e) L. Chen, Q. H. Chen, M. Y. Wu, F. L. Jiang, M. C. Hong, *Accounts of Chemical Research.* **2015**, *48*, 201-210.

[6] (a) G. Gil-Ramirez, D. A. Leigh, A. J. Stephens, *Angewandte Chemie-International Edition.* **2015**, *54*, 6110-6150; (b) N. H. Evans, P. D. Beer, *Chem Soc Rev.* **2014**, *43*, 4658-4683.

[7] R. S. Forgan, J. P. Sauvage, J. F. Stoddart, *Chemical Reviews.* **2011**, *111*, 5434-5464.

[8] E. M. G. Jamieson, F. Modicom, S. M. Goldup, *Chemical Society Reviews.* **2018**, *47*, 5266-5311.

[9] J. H. van Maarseveen, M. D. Cornelissen, S. Pilon, *Synthesis.* **2021**, *53*, 4527-4548.

[10] (a) G. Zhang, O. Presly, F. White, I. M. Oppel, M. Mastalerz, *Angewandte Chemie-International Edition.* **2014**, *53*, 5126-5130; (b) Q. Wang, C. Yu, H. Long, Y. Du, Y. Jin, W. Zhang, *Angewandte Chemie-International Edition.* **2015**, *54*, 7550-7554.

[11] (a) S. Freye, J. Hey, A. Torras-Galan, D. Stalke, R. Herbst-Irmer, M. John, G. H. Clever, *Angewandte Chemie-International Edition.* **2012**, *51*, 2191-2194; (b) R. Zhu, I. Regeni, J. J. Holstein, B. Dittrich, M. Simon, S. Prevost, M. Gradzielski, G. H. Clever, *Angewandte Chemie-International Edition.* **2018**, *57*, 13652-13656.

[12] (a) T. R. Cook, Y. R. Zheng, P. J. Stang, *Chemical Reviews.* **2013**, *113*, 734-777; (b) S. Pullen, G. H. Clever, *Accounts of Chemical Research.* **2018**, *51*, 3052-3064.

[13] Y. Fang, J. A. Powell, E. R. Li, Q. Wang, Z. Perry, A. Kirchon, X. Y. Yang, Z. F. Xiao, C. F. Zhu, L. L. Zhang, F. H. Huang, H. C. Zhou, *Chemical Society Reviews.* **2019**, *48*, 4707-4730.

[14] N. Ahmad, H. A. Younus, A. H. Chughtai, F. Verpoort, *Chemical Society Reviews.* **2015**, *44*, 9-25.

[15] Q. L. Song, S. Jiang, T. Hasell, M. Liu, S. J. Sun, A. K. Cheetham, E. Sivaniah, A. I. Cooper, *Advanced Materials.* **2016**, *28*, 2629.

[16] A. He, Z. W. Jiang, Y. Wu, H. Hussain, J. Rawle, M. E. Briggs, M. A. Little, A. G. Livingston, A. I. Cooper, *Nature Materials.* **2022**, *21*, 463.

[17] M. S. Zhang, L. Y. Li, Q. M. Lin, M. Tang, Y. Y. Wu, C. F. Ke, *Journal of the American Chemical Society.* **2019**, *141*, 5154-5158.

[18] (a) S. R. Seidel, P. J. Stang, *Accounts of Chemical Research.* **2002**, *35*, 972-983; (b) T. R. Cook, P. J. Stang, *Chemical Reviews.* **2015**, *115*, 7001-7045.

[19] R. Chakrabarty, P. S. Mukherjee, P. J. Stang, *Chemical Reviews.* **2011**, *111*, 6810-6918.

[20] N. F. Makoto Fujita, Katsuyuki Ogura & Kentaro Yamaguchi, *Nature.* **1999**.

[21] J. F. Aleema Westcott, † Lindsay P. Harding,‡ Pierre Rizkallah,§ and Michaele J. Hardie, *Journal of the American Chemical Society.* **2008**.

[22] M. Fukuda, R. Sekiya, R. Kuroda, *Angewandte Chemie-International Edition.* **2008**, *47*, 706-710.

[23] T. K. Ronson, Y. Wang, K. Baldridge, J. S. Siegel, J. R. Nitschke, *Journal of the American Chemical Society.* **2020**, *142*, 10267-10272.

[24] P. Li, S. Xu, C. Yu, Z. Y. Li, J. Xu, Z. M. Li, L. Zou, X. Leng, S. Gao, Z. Liu, X. Liu, S. Zhang, *Angewandte Chemie-International Edition.* **2020**, *59*, 7113-7121.

[25] K. T. Benke BP, Graf J, Mastalerz M, *ChemRxiv. .* **2021**, *Cambridge: Cambridge Open Engage*.

[26] Z. Sun, P. Li, S. Xu, Z. Y. Li, Y. Nomura, Z. Li, X. Liu, S. Zhang, *Journal of the American Chemical Society.* **2020**, *142*, 10833-10840.

[27] (a) S. La Cognata, A. Miljkovic, R. Mobili, G. Bergamaschi, V. Amendola, *Chempluschem.* **2020**, *85*, 1145-1155; (b) M. Frank, M. D. Johnstone, G. H. Clever, *Chemistry.* **2016**, *22*, 14104-14125.

[28] S. Freye, R. Michel, D. Stalke, M. Pawliczek, H. Frauendorf, G. H. Clever, *Journal of the American Chemical Society.* **2013**, *135*, 8476-8479.

[29] Y. Jin, Q. Wang, P. Taynton, W. Zhang, *Accounts of Chemical Research.* **2014**, *47*, 1575-1586.

[30] (a) A. C. Mendes, E. T. Baran, R. L. Reis, H. S. Azevedo, *Wiley Interdisciplinary Reviews-Nanomedicine and Nanobiotechnology.* **2013**, *5*, 582-612; (b) P. R. Sundararajan, *Pure and Applied Chemistry.* **2004**, *76*, X-X; (c) M. Hruby, *Chemicke Listy.* **2018**, *112*, 294-300.

[31] (a) E. Wasserman, *Journal of the American Chemical Society.* **1960**, *82*, 4433-4434; (b) I. T. Harrison, S. Harrison, *Journal of the American Chemical Society.* **1967**, *89*, 5723-&.

[32] T. R. Cook, Y. R. Zheng, P. J. Stang, *Chemical Reviews.* **2013**, *113*, 734-777.

[33] L. Fabbrizzi, M. Licchelli, L. Mosca, A. Poggi, *Coordination Chemistry Reviews.* **2010**, *254*, 1628-1636.

[34] B. E. K., *Inorganic Chemistry.* **1972**, *11*, 2273-2274.

[35] J.-P. S. a. J. P. K. C. O. Dietrich-Buchecker, *Tetrahedron Letters.* **1983**, *24*, 5095-5098.

[36] M. Fujita, F. Ibukuro, H. Hagihara, K. Ogura, *Nature.* **1994**, *367*, 720-723.

[37] (a) M. S. Vickers, P. D. Beer, *Chemical Society Reviews.* **2007**, *36*, 211-225; (b) J. E. M. Lewis, P. D. Beer, S. J. Loeb, S. M. Goldup, *Chemical Society Reviews.* **2017**, *46*, 2577-2591.

[38] R. Sekiya, M. Fukuda, R. Kuroda, *Journal of the American Chemical Society.* **2012**, *134*, 10987-10997.

[39] R. Zhu, J. Lubben, B. Dittrich, G. H. Clever, *Angewandte Chemie-International Edition.* **2015**, *54*, 2796-2800.

[40] (a) M. Frank, J. Hey, I. Balcioglu, Y. S. Chen, D. Stalke, T. Suenobu, S. Fukuzumi, H. Frauendorf, G. H. Clever, *Angewandte Chemie-International Edition l.* **2013**, *52*, 10102-10106; (b) S. Loffler, A. Wuttke, B. Zhang, J. J. Holstein, R. A. Mata, G. H. Clever, *Chemical Communications.* **2017**, *53*, 11933-11936.

[41] Y. T. Li, K. M. Mullen, T. D. W. Claridge, P. J. Costa, V. Felix, P. D. Beer, *Chemical Communications.* **2009**, 7134-7136.

[42] (a) S. J. Rowan, Stuart J. Cantrill, Graham RL Cousins, Jeremy KM Sanders, and J. Fraser Stoddart, *Angewandte Chemie International Edition.* **2002**, *41*, 898-952; (b) M. E. Belowich, J. F. Stoddart, *Chemical Society Reviews.* **2012**, *41*, 2003-2024.

[43] (a) Y. Jin, C. Yu, R. J. Denman, W. Zhang, *Chemical Society Reviews.* **2013**, *42*, 6634-6654; (b) Y. Wang, J. He, C. Liu, W. H. Chong, H. Chen, *Angewandte Chemie International Edition.* **2015**, *54*, 2022-2051.

[44] A. J. Greenlee, C. I. Wendell, M. M. Cencer, S. D. Laffoon, J. S. Moore, *Trends in Chemistry.* **2020**, *2*, 1043-1051.

[45] J. Hu, S. K. Gupta, J. Ozdemir, M. H. Beyzavi, *ACS Applied Nano Materials.* **2020**, *3*, 6239-6269.

[46] G. Zhang, O. Presly, F. White, I. M. Oppel, M. Mastalerz, *Angewandte Chemie-International Edition.* **2014**, *53*, 1516-1520.

[47] A. P. Cote, A. I. Benin, N. W. Ockwig, M. O'Keeffe, A. J. Matzger, O. M. Yaghi, *Science.* **2005**, *310*, 1166-1170.

[48] J. L. Segura, M. J. Mancheno, F. Zamora, *Chemical Society Reviews.* **2016**, *45*, 5635-5671.

[49] (a) M. J. Bojdys, J. Jeromenok, A. Thomas, M. Antonietti, *Advanced Materials.* **2010**, *22*, 2202; (b) P. Katekomol, J. Roeser, M. Bojdys, J. Weber, A. Thomas, *Chemistry of Materials.* **2013**, *25*, 1542-1548.

[50] S. J. Lyle, P. J. Waller, O. M. Yaghi, *Trends in Chemistry.* **2019**, *1*, 172-184.

[51] (a) G. Zhang, M. Mastalerz, *Chemical Society Reviews.* **2014**, *43*, 1934-1947; (b) M. Mastalerz, *Accounts of Chemical Research.* **2018**, *51*, 2411-2422.

[52] P. E. Eaton, and Thomas W. Cole, *Journal of the American Chemical Society.* **1964**, *86*, 3157-3158.

[53] (a) L. A. Paquette, Robert J. Ternansky, Douglas W. Balogh, and Gary Kentgen, *Journal of the American Chemical Society.* **1983**, *105*, 5446-5450; (b) W. D. Fessner, Bulusu ARC Murty, Jürgen Wörth, Dieter Hunkler, Hans Fritz, Horst Prinzbach, Wolfgang D. Roth, Paul von Ragué Schleyer, Alan B. McEwen, and Wilhelm F. Maier, *Angewandte Chemie International Edition.* **1987**, *26*, 452-454.

[54] (a) Z. Wu, Stephen Lee, and Jeffrey S. Moore, *Journal of the American Chemical Society.* **1992**, *114*, 8730-8732; (b) A. Avellaneda, P. Valente, A. Burgun, J. D. Evans, A. W. Markwell-Heys, D. Rankine, D. J. Nielsen, M. R. Hill, C. J. Sumby, C. J. Doonan, *Angewandte Chemie-International Edition.* **2013**, *52*, 3746-3749; (c) M. M. Naseer, D. X. Wang, L. A. Zhao, Z. T. Huang, M. X. Wang, *Journal of Organic Chemistry.* **2011**, *76*, 1804-1813.

[55] W. Kiggen, F. Vogtle, *Angewandte Chemie-International Edition in English.* **1984**, *23*, 714-715.

[56] J. L. Katz, K. J. Selby, R. R. Conry, *Organic Letters.* **2005**, *7*, 3505-3507.

[57] M. L. C. Quan, D. J. Cram, *Journal of the American Chemical Society.* **1991**, *113*, 2754-2755.

[58] (a) T. Kunde, T. Pausch, B. M. Schmidt, *European Journal of Organic Chemistry.* **2021**, *2021*, 5844-5856; (b) R. L. Greenaway, K. E. Jelfs, *Chempluschem.* **2020**, *85*, 1813-

1823; (c) D. Chakraborty, P. S. Mukherjee, *Chemical Communications.* **2022**, *58*, 5558-5573.

[59] S. Xu, P. Li, Z.-Y. Li, C. Yu, X. Liu, Z. Liu, S. Zhang, *CCS Chemistry.* **2021**, *3*, 1838-1850.

[60] Y. Xia, X. Xia, H. C. Peng, *J Am Chem Soc.* **2015**, *137*, 7947-7966.

[61] J. L. A. Jonathan W. Steed, *Supramolecular Chemistry*, 3rd ed., Wiley, **2022**.

[62] (a) B. L. Allwood, N. Spencer, H. Shahriarizavareh, J. F. Stoddart, D. J. Williams, *Journal of the Chemical Society-Chemical Communications.* **1987**, 1064-1066; (b) B. Odell, M. V. Reddington, A. M. Z. Slawin, N. Spencer, J. F. Stoddart, D. J. Williams, *Angewandte Chemie-International Edition in English.* **1988**, *27*, 1547-1550.

[63] P. R. Ashton, T. T. Goodnow, A. E. Kaifer, M. V. Reddington, A. M. Z. Slawin, N. Spencer, J. F. Stoddart, C. Vicent, D. J. Williams, *Angewandte Chemie-International Edition in English.* **1989**, *28*, 1396-1399.

[64] T. Steiner, *Angewandte Chemie-International Edition.* **2002**, *41*, 48-76.

[65] J. X. Ma, J. Li, Y. F. Chen, R. Ning, Y. F. Ao, J. M. Liu, J. L. Sun, D. X. Wang, Q. Q. Wang, *Journal of the American Chemical Society.* **2019**, *141*, 3843-3848.

[66] Q. Zhu, X. Wang, R. Clowes, P. Cui, L. J. Chen, M. A. Little, A. I. Cooper, *Journal of the American Chemical Society.* **2020**, *142*, 16842-16848.

[67] B. Han, H. L. Wang, C. M. Wang, H. Wu, W. Zhou, B. L. Chen, J. Z. Jiang, *Journal of the American Chemical Society.* **2019**, *141*, 8737-8740.

[68] X. Kuang, X. Wu, R. Yu, J. P. Donahue, J. Huang, C. Z. Lu, *Nature Chemistry.* **2010**, *2*, 461-465.

[69] J. Heine, J. Schmedt auf der Gunne, S. Dehnen, *Journal of the American Chemical Society.* **2011**, *133*, 10018-10021.

[70] H. Li, H. Zhang, A. D. Lammer, M. Wang, X. Li, V. M. Lynch, J. L. Sessler, *Nature Chemistry.* **2015**, *7*, 1003-1008.

[71] (a) M. Mastalerz, M. W. Schneider, I. M. Oppel, O. Presly, *Angewandte Chemie-International Edition.* **2011**, *50*, 1046-1051; (b) M. W. Schneider, H. J. S. Hauswald, R. Stoll, M. Mastalerz, *Chemical Communications.* **2012**, *48*, 9861-9863; (c) M. W. Schneider, L. G. Lechner, M. Mastalerz, *Journal of Materials Chemistry.* **2012**, *22*, 7113-7116; (d) M. W. Schneider, I. M. Oppel, M. Mastalerz, *Chemistry-a European Journal.* **2012**, *18*, 4156-4160; (e) M. W. Schneider, I. M. Oppel, H. Ott, L. G. Lechner, H. J. S. Hauswald, R. Stoll, M. Mastalerz, *Chemistry-a European Journal.* **2012**, *18*, 836-847; (f) M. Mastalerz, *Synlett.* **2013**, *24*, 781-786; (g) S. M. Elbert, F. Rominger, M. Mastalerz, *Chemistry-a European Journal.* **2014**, *20*, 16707-16720; (h) X. Y. Hu, W. S. Zhang, F. Rominger, I. Wacker, R. R. Schroder, M. Mastalerz, *Chemical Communications.* **2017**, *53*, 8616-8619; (i) A. S. Bhat, S. M. Elbert, W. S. Zhang, F. Rominger, M. Dieckmann, R. R. Schroder, M. Mastalerz, *Angewandte Chemie-International Edition.* **2019**, *58*, 8819-8823; (j) P. E. Alexandre, W. S. Zhang, F. Rominger, S. M. Elbert, R. R. Schroder, M. Mastalerz, *Angewandte Chemie-International Edition.* **2020**, *59*, 19675-19679; (k) M. Holsten, S. Feierabend, S. M. Elbert, F. Rominger, T. Oeser, M. Mastalerz, *Chemistry-a European Journal.* **2021**, *27*, 9383-9390.

[72] M. Kwit, P. Skowronek, H. Kolbon, J. Gawronski, *Chirality.* **2005**, *17*, S93-S100.

[73] D. H. Thorsten Hofe, Friedhelm Gores, https://www.scharlab.com/docs/ebooks/descargarpdf.php?id=953, **2007**.

[74] (a) T. Lu, F. W. Chen, *Journal of Computational Chemistry.* **2012**, *33*, 580-592; (b) http://sobereva.com/multiwfn/.

[75] R. Greenaway, V. Santolini, M. J. Bennison, B. M. Alston, C. J. Pugh, M. A. Little, M. Miklitz, E. G. B. Eden-Rumps, R. Clowes, A. Shakil, H. J. Cuthbertson, H. Armstrong, M. E. Briggs, K. E. Jelfs, A. I. Cooper, *Nature Communications.* **2018**, *9*.

[76] E. M. Johnson, R. Haiges, S. C. Marinescu, *Acs Applied Materials & Interfaces.* **2018**, *10*, 37919-37927.

[77] P. Li, Z. Sun, J. Chen, Y. Zuo, C. Yu, X. Liu, Z. Yang, L. Chen, E. Fu, W. Wang, J. Zhang, Z. Liu, J. Hu, S. Zhang, *Journal of the American Chemical Society.* **2022**, *144*, 1342-1350.

[78] (a) L. Carlucci, G. Ciani, D. M. Proserpio, *Coordination Chemistry Reviews.* **2003**, *246*, 247-289; (b) Z. Niu, H. W. Gibson, *Chem Rev.* **2009**, *109*, 6024-6046.

[79] (a) M. Mastalerz, *Accounts of Chemical Research.* **2018**, *51*, 2411-2422; (b) M. E. Briggs, A. I. Cooper, *Chemistry of Materials.* **2017**, *29*, 149-157; (c) H. L. Wang, Y. H. Jin, N. N. Sun, W. Zhang, J. Z. Jiang, *Chemical Society Reviews.* **2021**, *50*, 8874-8886.

[80] (a) Y. B. Zhang, J. Su, H. Furukawa, Y. F. Yun, F. Gandara, A. Duong, X. D. Zou, O. M. Yaghi, *Journal of the American Chemical Society.* **2013**, *135*, 16336-16339; (b) Y. Z. Liu, Y. H. Ma, Y. B. Zhao, X. X. Sun, F. Gandara, H. Furukawa, Z. Liu, H. Y. Zhu, C. H. Zhu, K. Suenaga, P. Oleynikov, A. S. Alshammari, X. Zhang, O. Terasaki, O. M. Yaghi, *Science.* **2016**, *351*, 365-369; (c) C. S. Diercks, O. M. Yaghi, *Science.* **2017**, *355*.

[81] (a) A. Fuchs, P. Mannhardt, P. Hirschle, H. Z. Wang, I. Zaytseva, Z. Ji, O. Yaghi, S. Wuttke, E. Ploetz, *Advanced Materials.* **2022**, *34*; (b) H. Furukawa, K. E. Cordova, M. O'Keeffe, O. M. Yaghi, *Science.* **2013**, *341*, 974.

[82] (a) I. Hisaki, C. Xin, K. Takahashi, T. Nakamura, *Angewandte Chemie-International Edition.* **2019**, *58*, 11160-11170; (b) Y. F. Han, Y. X. Yuan, H. B. Wang, *Molecules.* **2017**, *22*.

[83] D. Beaudoin, T. Maris, J. D. Wuest, *Nature Chemistry.* **2013**, *5*, 830-834.

[84] M. J. Kory, M. Worle, T. Weber, P. Payamyar, S. W. van de Poll, J. Dshemuchadse, N. Trapp, A. D. Schluter, *Nature Chemistry.* **2014**, *6*, 779-784.

[85] T. Q. Ma, E. A. Kapustin, S. X. Yin, L. Liang, Z. Y. Zhou, J. Niu, L. H. Li, Y. Y. Wang, J. Su, J. Li, X. G. Wang, W. D. Wang, W. Wang, J. L. Sun, O. M. Yaghi, *Science.* **2018**, *361*, 48-52.

[86] A. M. Evans, L. R. Parent, N. C. Flanders, R. P. Bisbey, E. Vitaku, M. S. Kirschner, R. D. Schaller, L. X. Chen, N. C. Gianneschi, W. R. Dichtel, *Science.* **2018**, *361*, 53.

[87] P. G. Cozzi, *Chemical Society Reviews.* **2004**, *33*, 410-421.

[88] L. H. Li, X. L. Feng, X. H. Cui, Y. X. Ma, S. Y. Ding, W. Wang, *Journal of the American Chemical Society.* **2017**, *139*, 6042-6045.

[89] X. Han, Q. C. Xia, J. J. Huang, Y. Liu, C. X. Tan, Y. Cui, *Journal of the American Chemical Society.* **2017**, *139*, 8693-8697.

[90] D. Reinhard, W. S. Zhang, Y. Vaynzof, F. Rominger, R. R. Schroder, M. Mastalerz, *Chemistry of Materials.* **2018**, *30*, 2781-2790.

[91] D. Reinhard. PhD thesis **2020**, Ruprecht-Karls-Universität Heidelberg.

[92] W. C. Still, M. Kahn, A. Mitra, *The Journal of Organic Chemistry.* **1978**, *43*, 2923-2925.

[93] G. M. Sheldrick, *SADABS 2012/1: Program for Absorption Correction; Bruker Analytical X-ray Division*, Madison (USA), **2012**.

[94] G. M. Sheldrick, *Acta Crystallogr A.* **2008**, *64*, 112-122.

[95] (a) P. Hohenberg, W. Kohn, *Phys Rev.* **1964**, *136*, B864-B871; (b) W. Kohn, L. J. Sham, *Phys Rev.* **1965**, *140*, A1133-A1138; (c) R. G. Parr, W. Yang, *Density-functional theory of atoms and molecules, 1. ed.*, Oxford Univ. Press, New York, NY, **1994**; (d) W. Koch, *Chemist's Guide to Density Functional Theory, 2. ed.*, Wiley-VCH, Weinheim, **2001**.

[96] M. J. Frisch, G. W. Trucks, H. B. Schlegel, G. E. Scuseria, M. A. Robb, J. R. Cheeseman, G. Scalmani, V. Barone, B. Mennucci, G. A. Petersson, H. Nakatsuji, M. Caricato, X. Li, H. P. Hratchian, A. F. Izmaylov, J. Bloino, G. Zheng, J. L. Sonnenberg, M. Hada, M. Ehara, K. Toyota, R. Fukuda, J. Hasegawa, M. Ishida, T. Nakajima, Y. Honda, O. Kitao, H. Nakai, T. Vreven, J. A. Montgomery Jr., J. E. Peralta, F. Ogliaro, M. Bearpark, J. J. Heyd, E. Brothers, K. N. Kudin, V. N. Staroverov, K. T., R. Kobayashi, J. Normand, K. Raghavachari, A. Rendell, J. C. Burant, S. S. Iyengar, J. Tomasi, M. Cossi, N. Rega, J. M. Millam, M. Klene, J. E. Knox, J. B. Cross, V. Bakken, C. Adamo, J. Jaramillo, R. Gomperts, R. E. Stratmann, O. Yazyev, A. J. Austin, R. Cammi, C. Pomelli, J. W. Ochterski, R. L. Martin, K. Morokuma, V. G. Zakrzewski, G. A. Voth, P. Salvador, J. J. Dannenberg, S. Dapprich, A. D. Daniels, Ö. Farkas, J. B. Foresman, J. V. Ortiz, J. Cioslowski, D. J. Fox, *Gaussian 09, Revision D.01*, Gaussian, Inc., Wallingford CT, **2016**.

[97] L. L. Tian, C. Wang, S. Dawn, M. D. Smith, J. A. Krause, L. S. Shimizu, *Journal of the American Chemical Society.* **2009**, *131*, 17620-17629.

[98] C. L. Moy, R. Kaliappan, A. J. McNeil, *Journal of Organic Chemistry.* **2011**, *76*, 8501-8507.

[99] M. Zheng, L. M. Ding, Z. Q. Lin, F. E. Karasz, *Macromolecules.* **2002**, *35*, 9939-9946.

[100] Y. B. Borozdina, E. Mostovich, V. Enkelmann, B. Wolf, P. T. Cong, U. Tutsch, M. Lang, M. Baumgarten, *Journal of Materials Chemistry C.* **2014**, *2*, 6618-6629.

[101] G. S. R.W.Kluiber, *Inorganica Chimica Acta.* **1970**, *4*, 226-230.

8. Appendix

8.1 NMR spectra

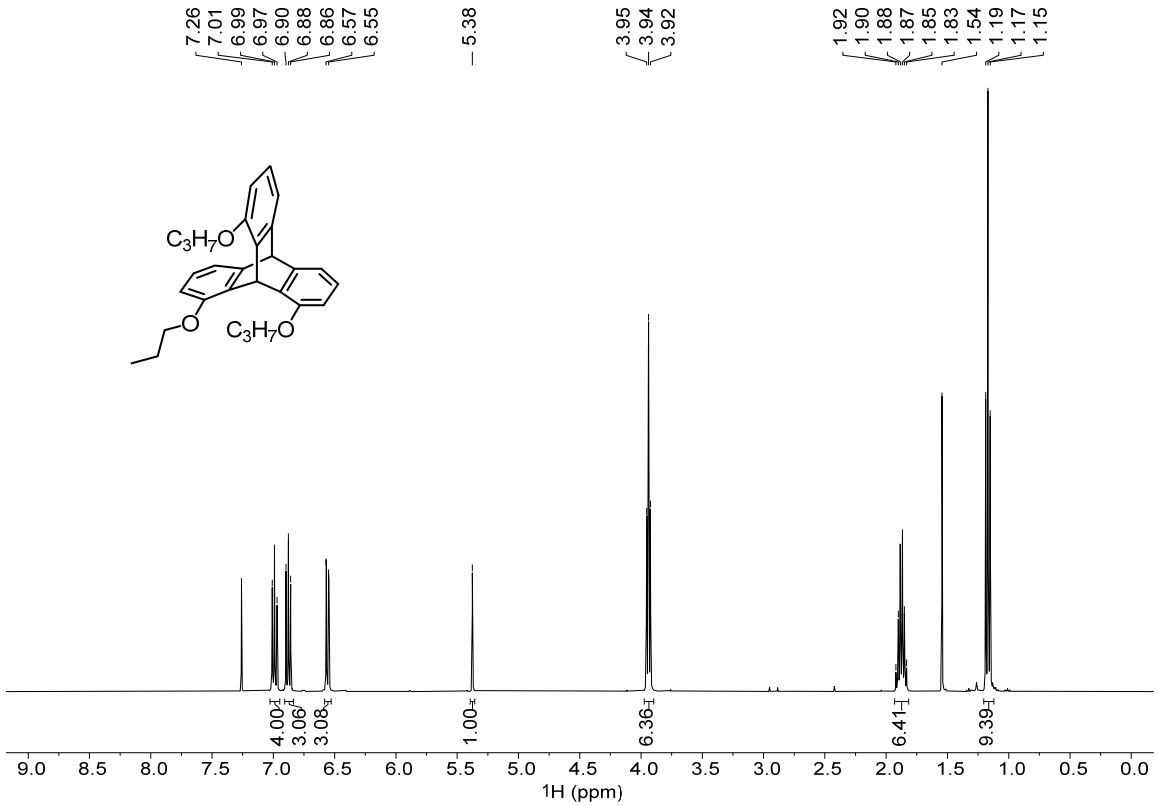

Figure 8.1.1: ^{1}H NMR spectrum (600 MHz, $CDCl_3$) of **75**.

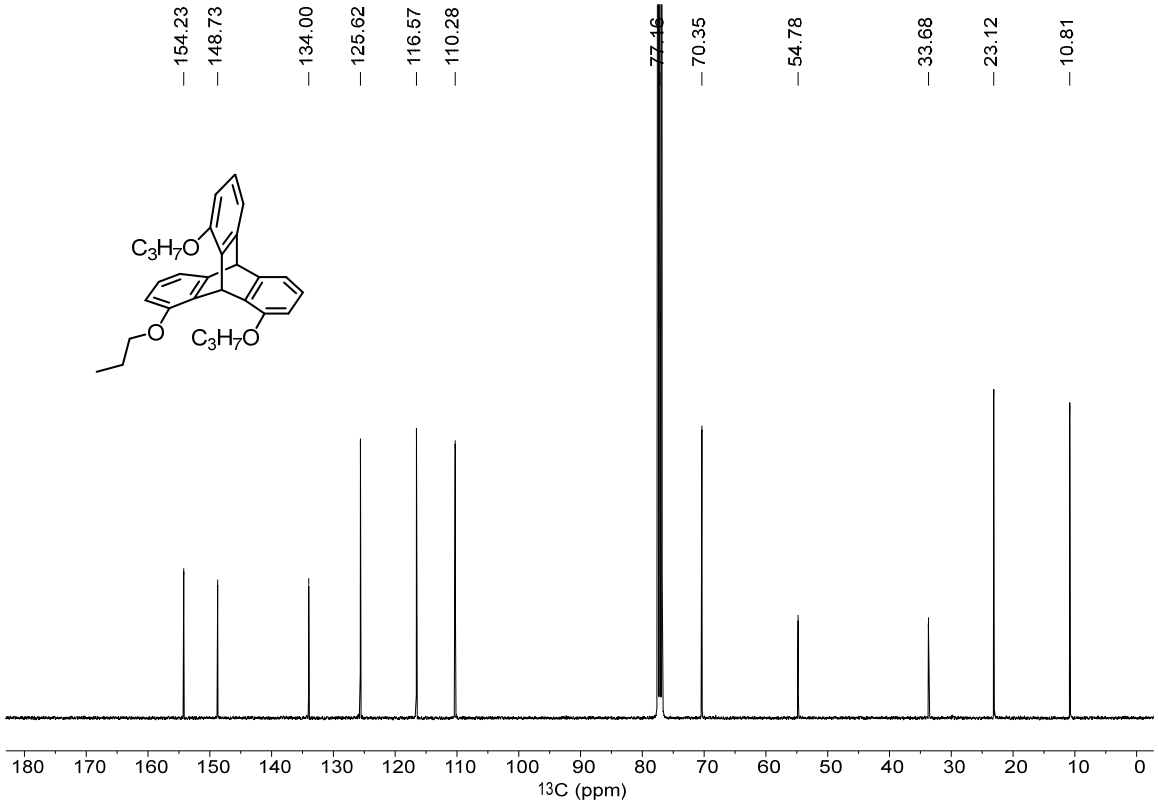

Figure 8.1.2: ^{13}C NMR spectrum (151 MHz, $CDCl_3$) of **75**.

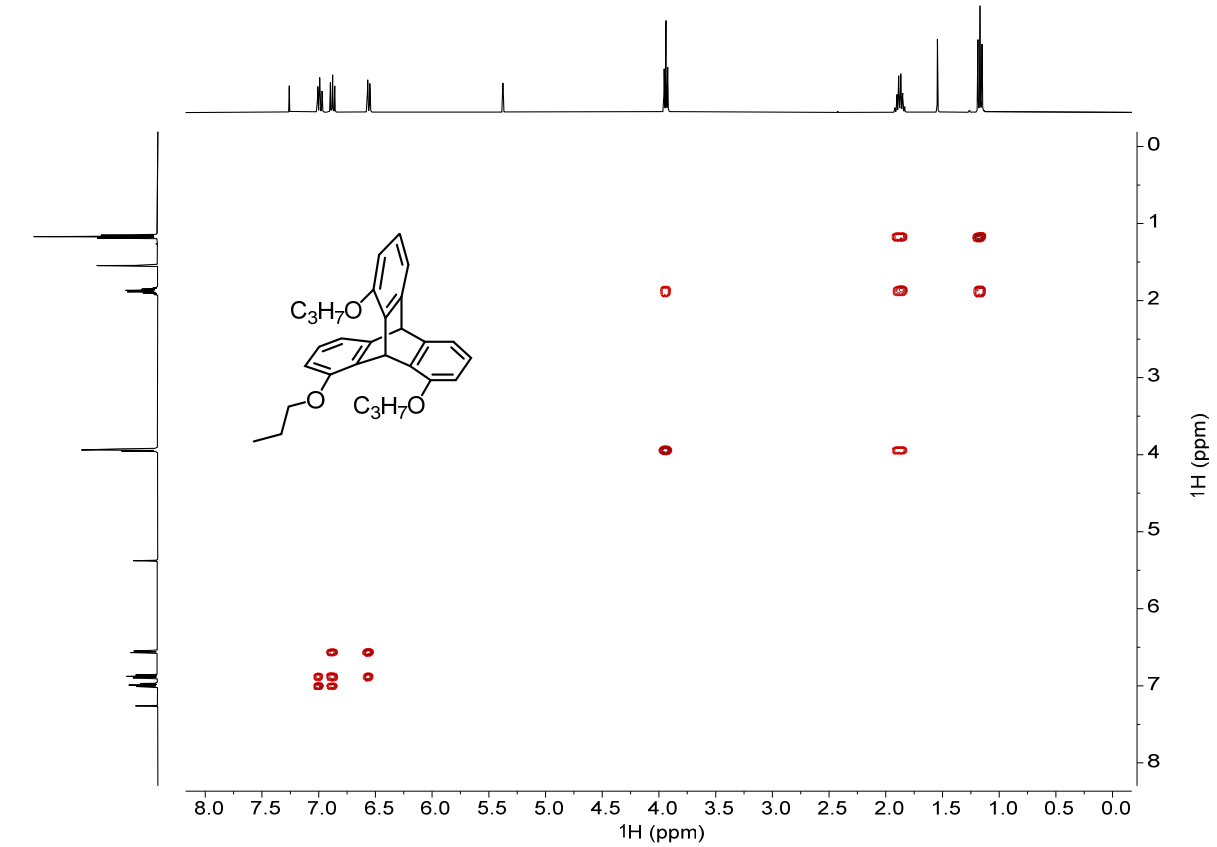

Figure 8.1.3: ^{1}H-^{1}H COSY NMR spectrum (600/600 MHz, $CDCl_3$) of **75**.

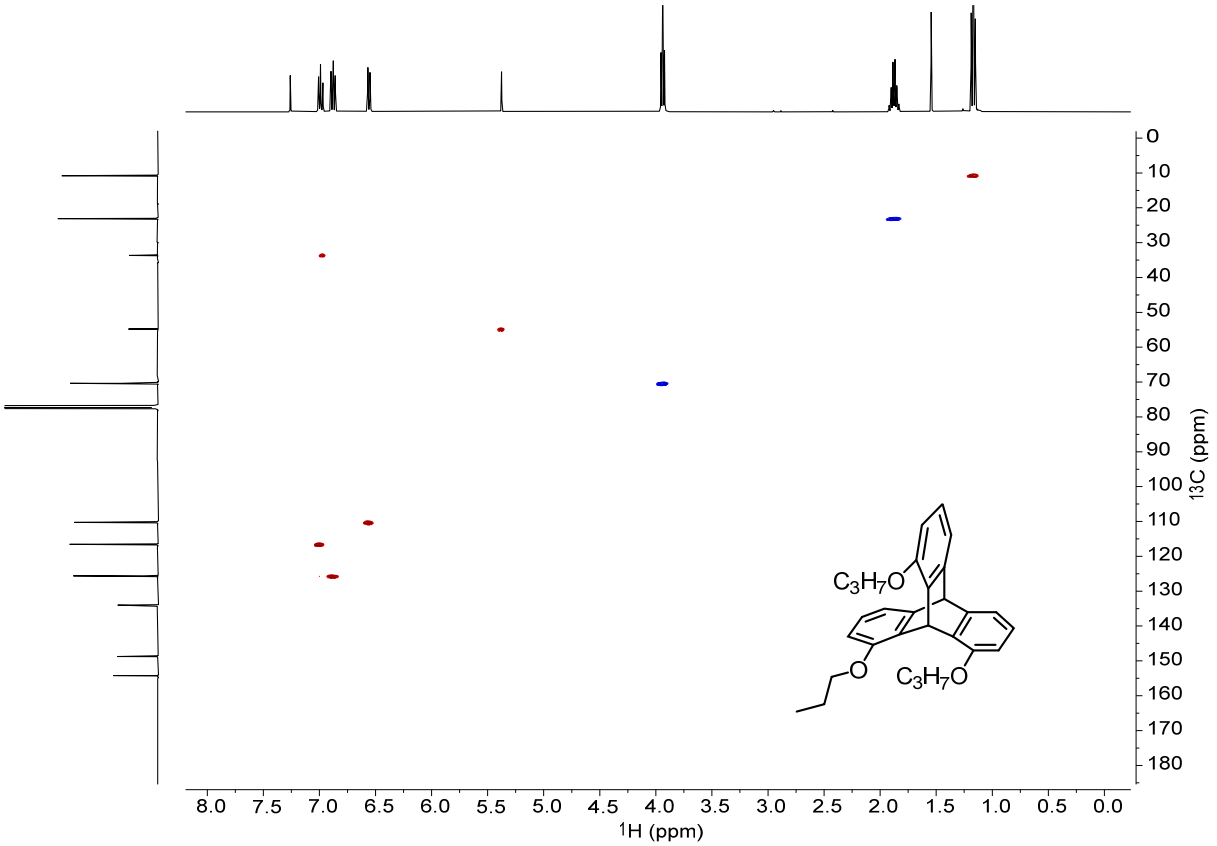

Figure 8.1.4: ^{1}H-^{13}C HSQC NMR spectrum (600/151 MHz, $CDCl_3$) of **75**.

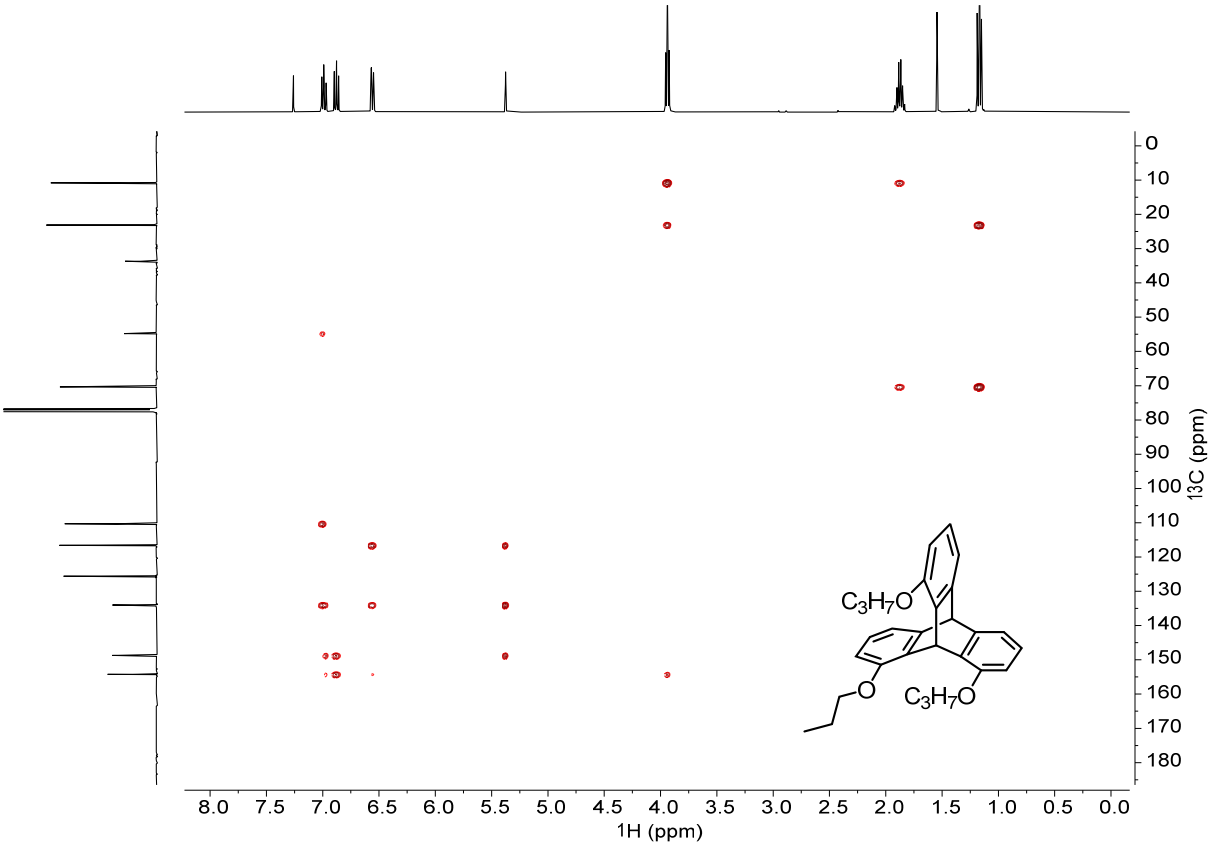

Figure 8.1.5: ^{1}H-^{13}C HMBC NMR spectrum (600/151 MHz, $CDCl_3$) of **75**.

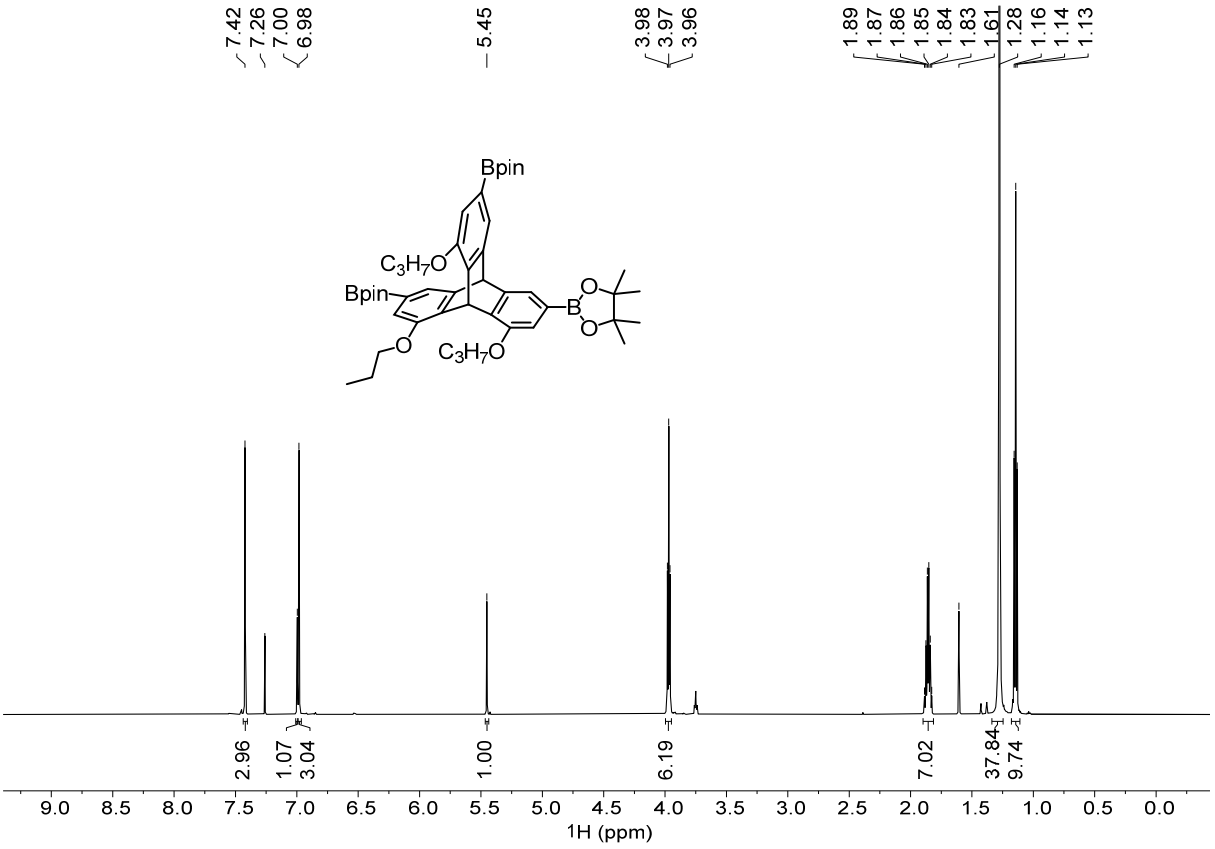

Figure 8.1.6: ^{1}H NMR spectrum (600 MHz, $CDCl_3$) of **78**.

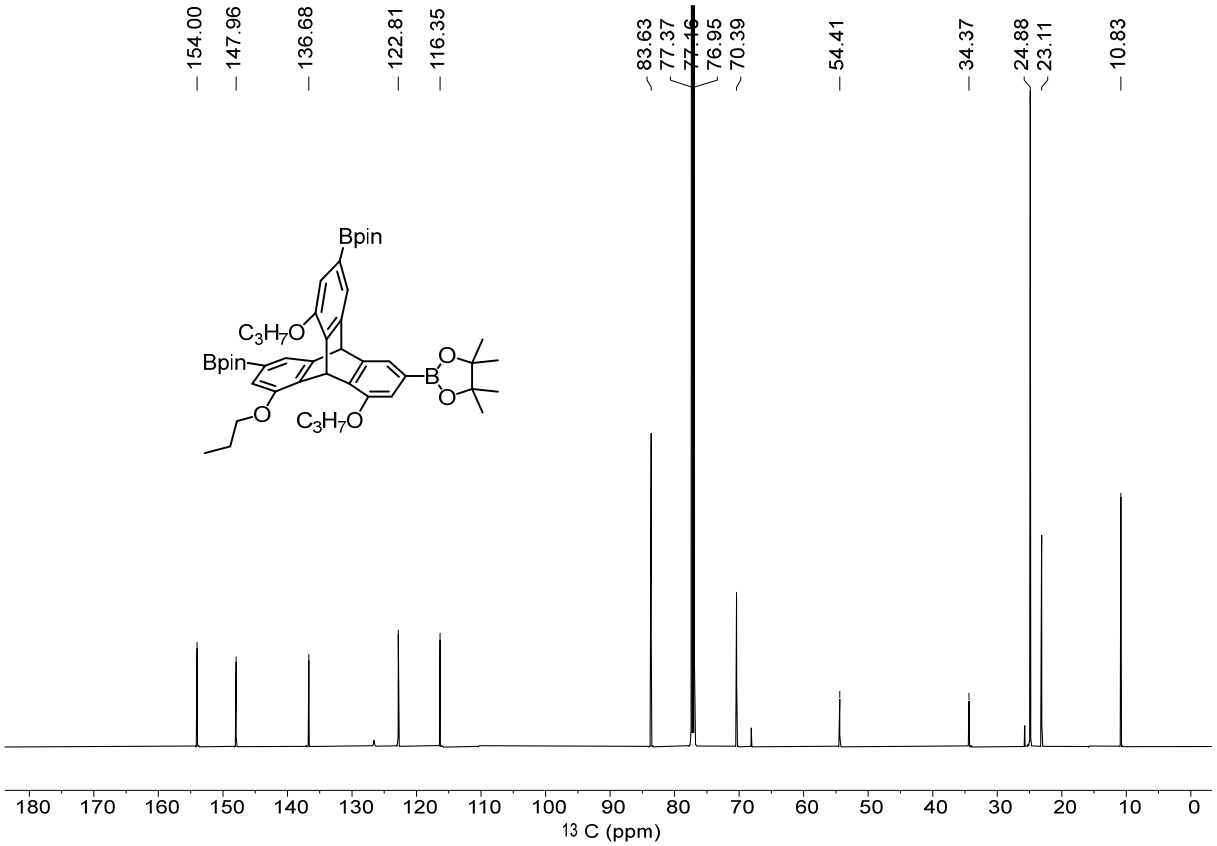

Figure 8.1.7: ^{13}C NMR spectrum (151 MHz, $CDCl_3$) of **78**.

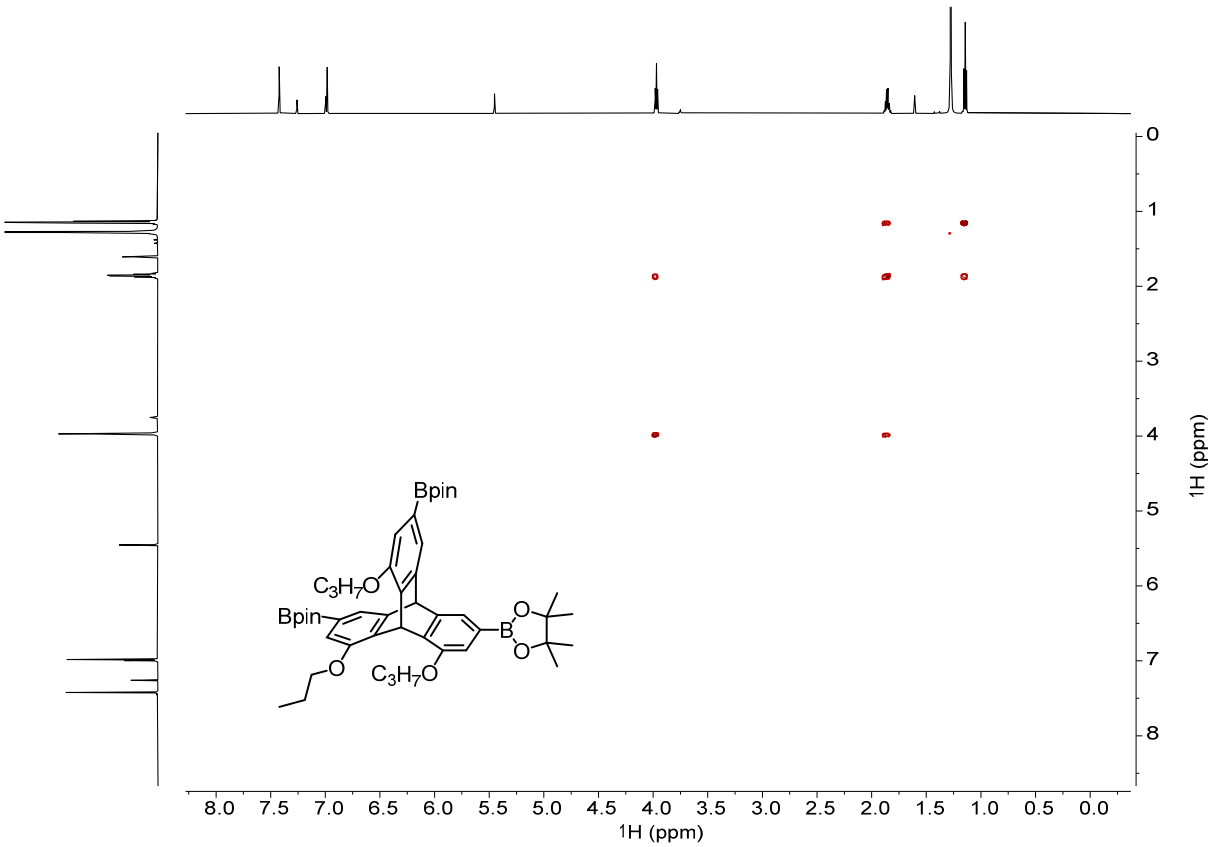

Figure 8.1.8: ^{1}H-^{1}H COSY NMR spectrum (600/600 MHz, $CDCl_3$) of **78**.

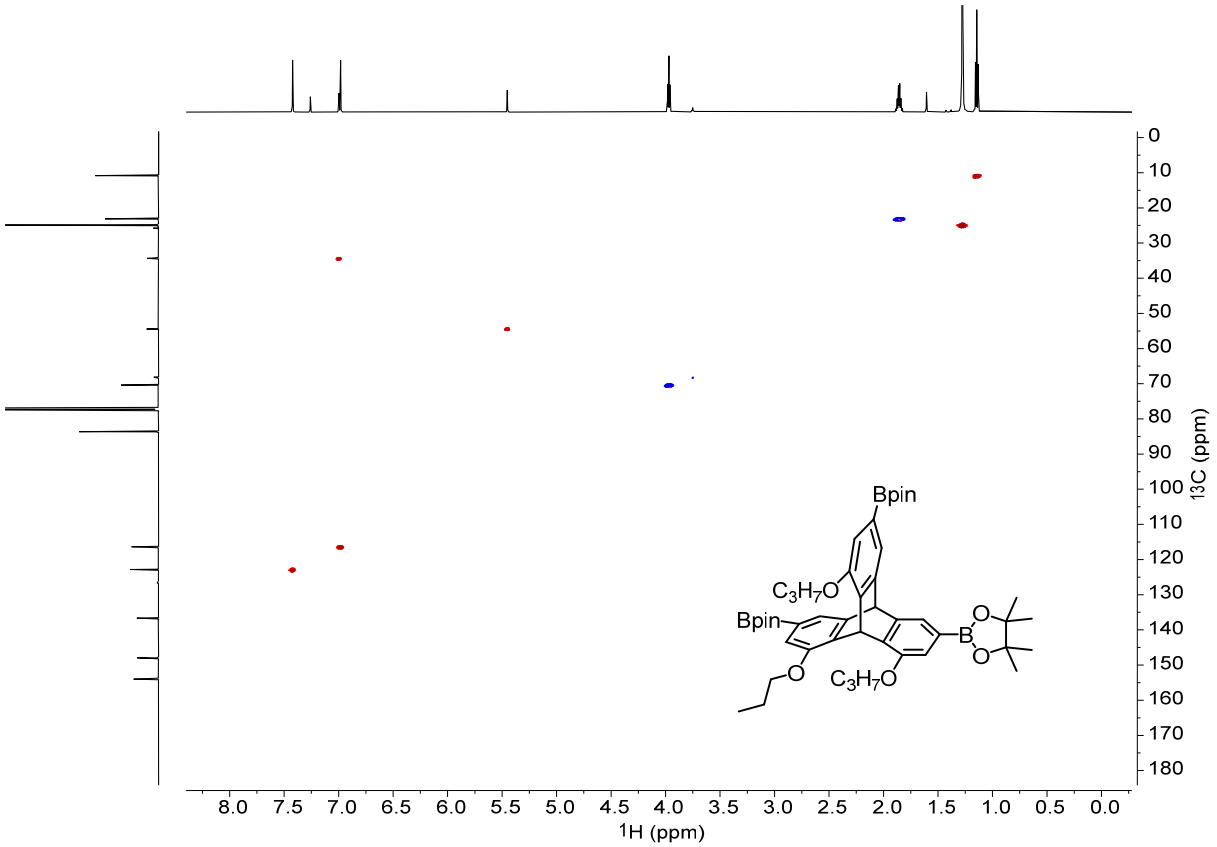

Figure 8.1.9: ^{1}H-^{13}C HSQC NMR spectrum (600/151 MHz, $CDCl_3$) of **78**.

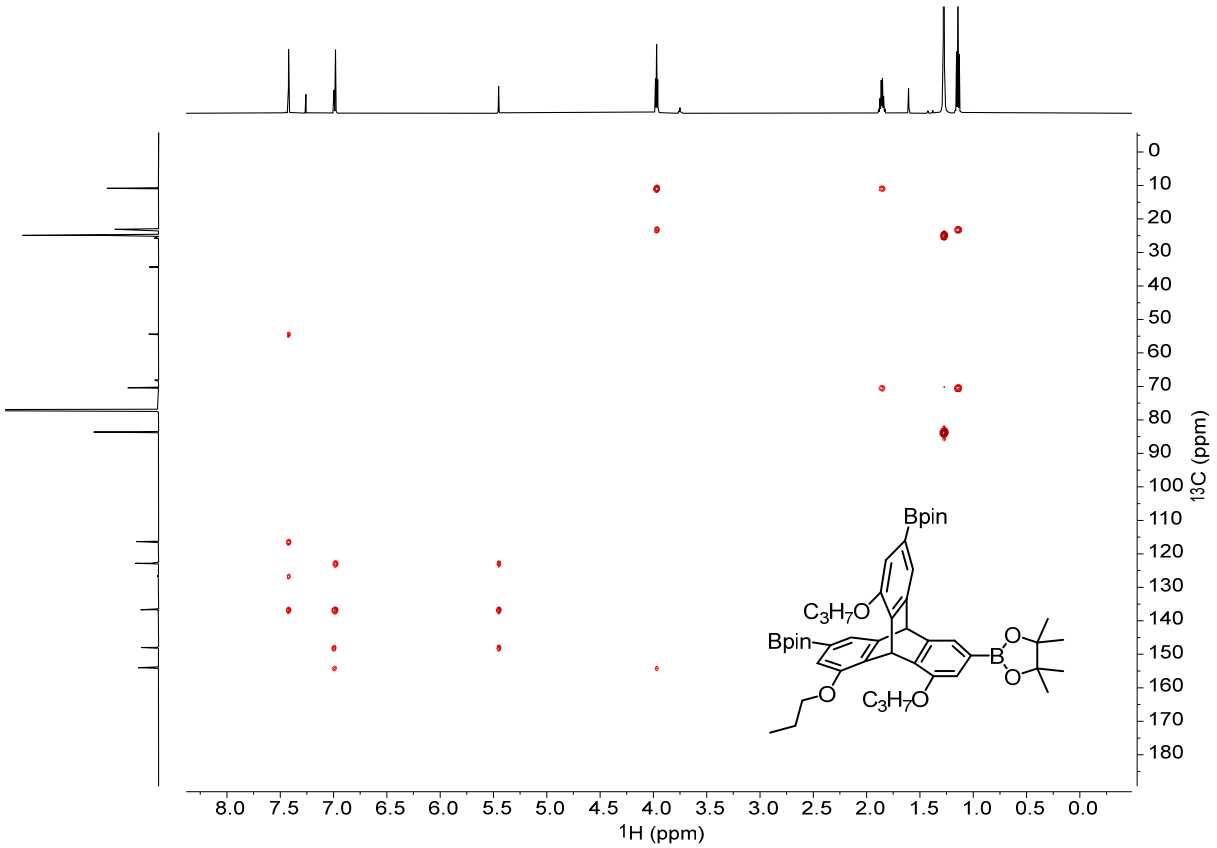

Figure 8.1.10: ^{1}H-^{13}C HMBC NMR spectrum (600/151 MHz, $CDCl_3$) of **78**.

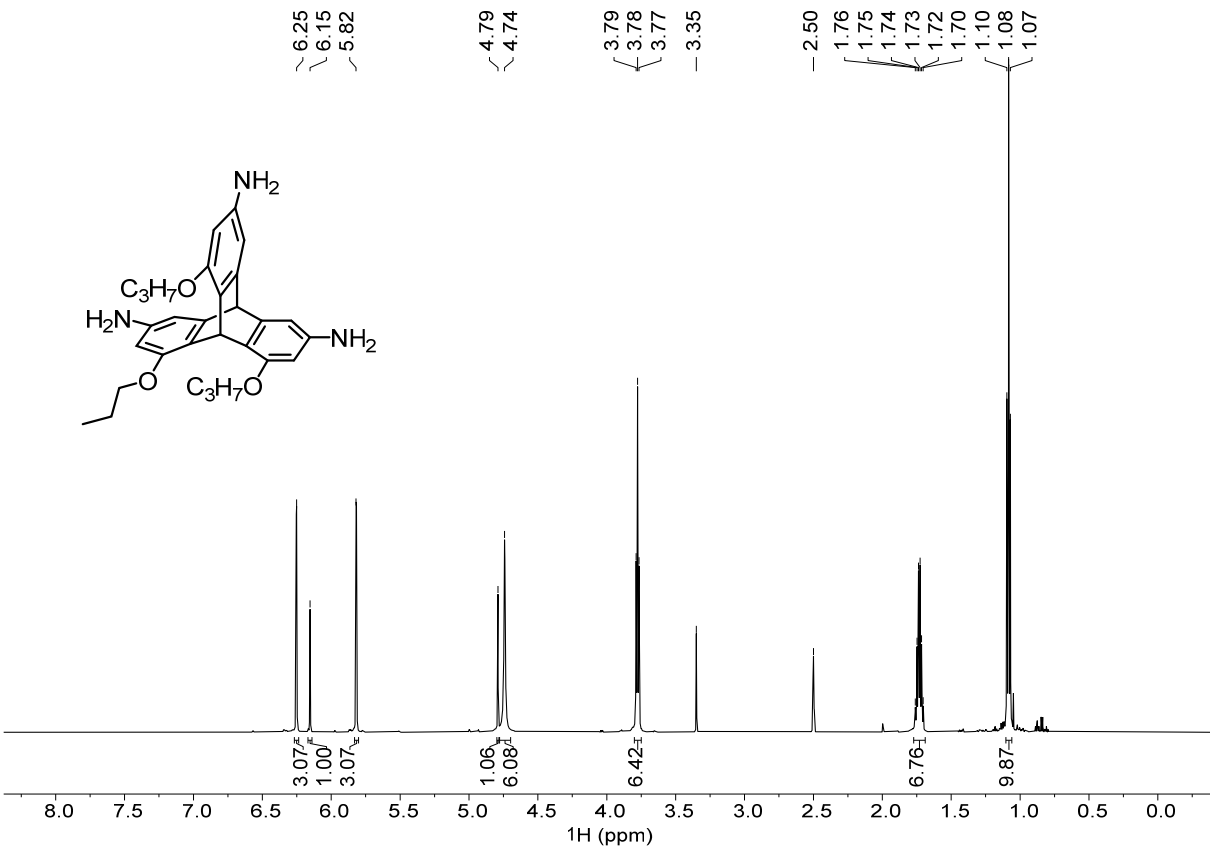

Figure 8.1.11: ^{1}H NMR spectrum (600 MHz, DMSO-d_6) of **81**.

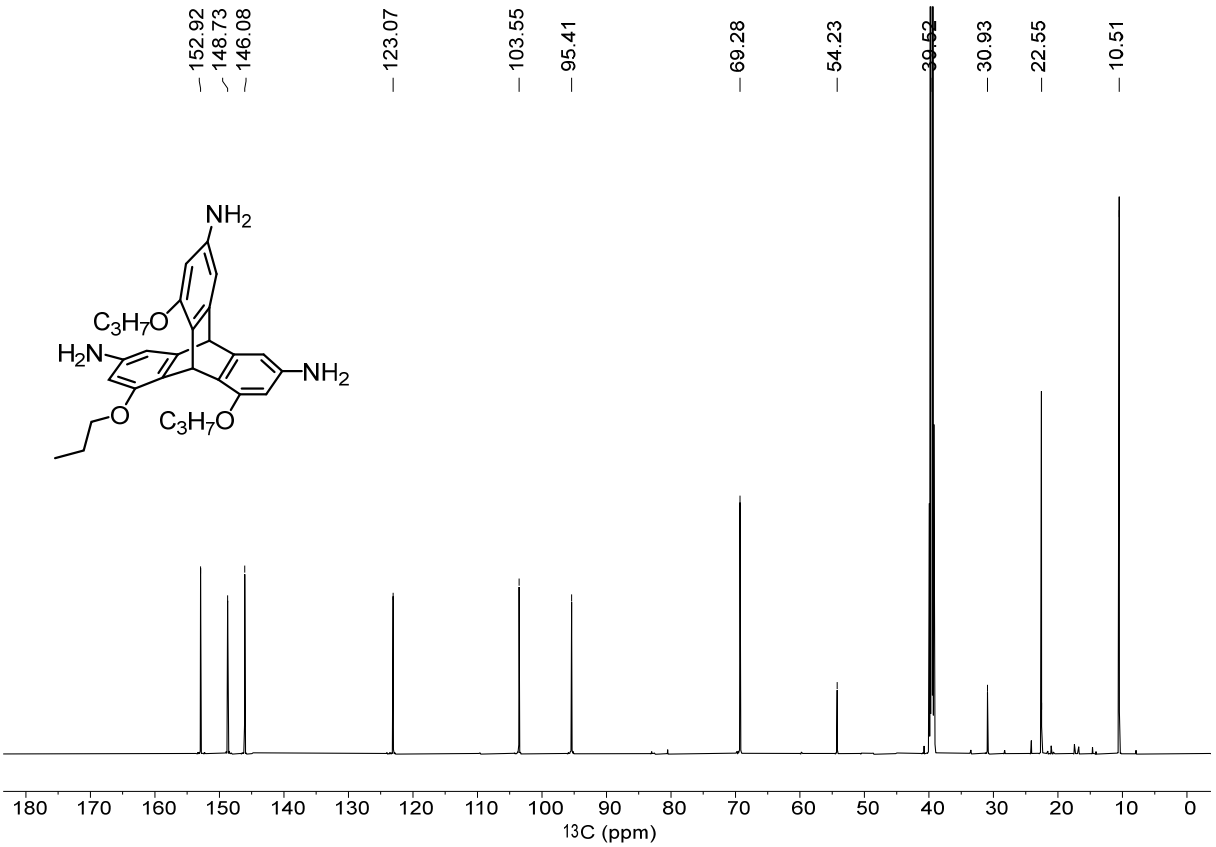

Figure 8.1.12: ^{13}C NMR spectrum (151 MHz, DMSO-d_6) of **81**.

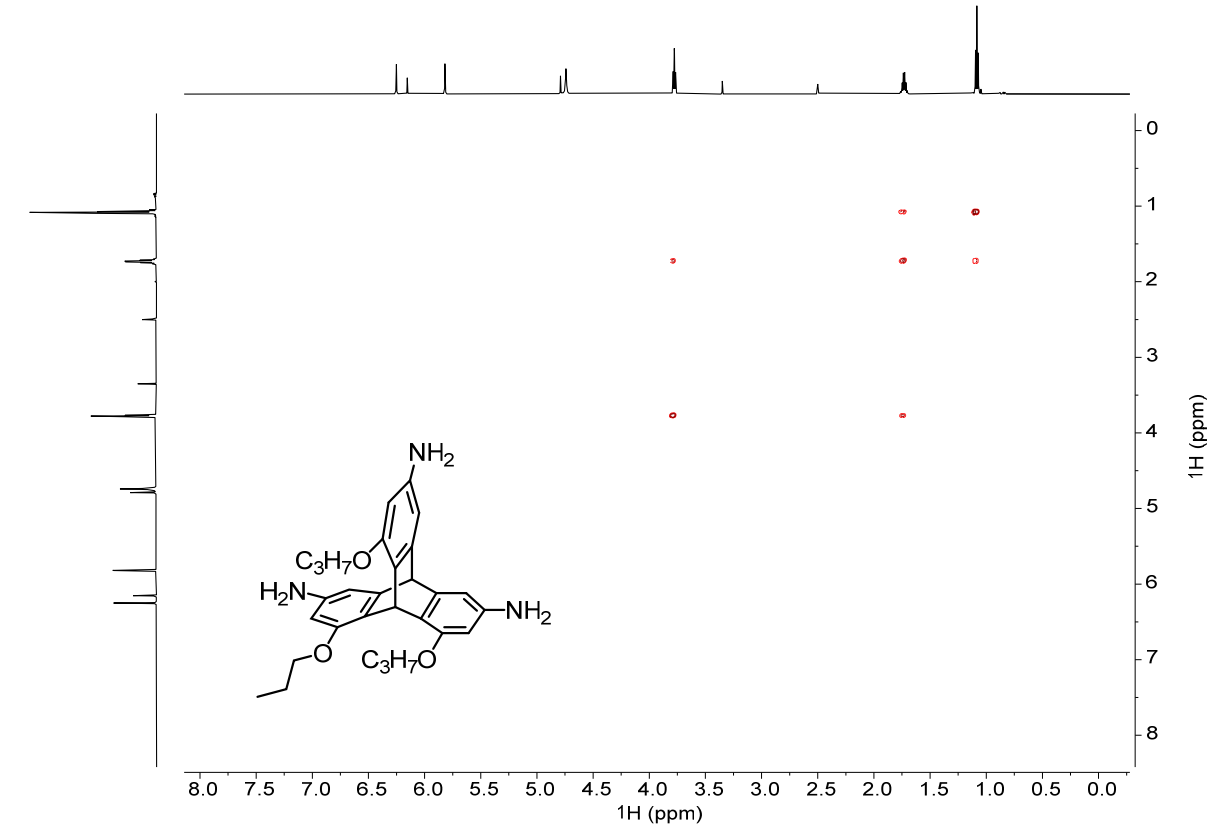

Figure 8.1.13: ^{1}H-^{1}H COSY NMR spectrum (600/600 MHz, DMSO-d_6) of **81**.

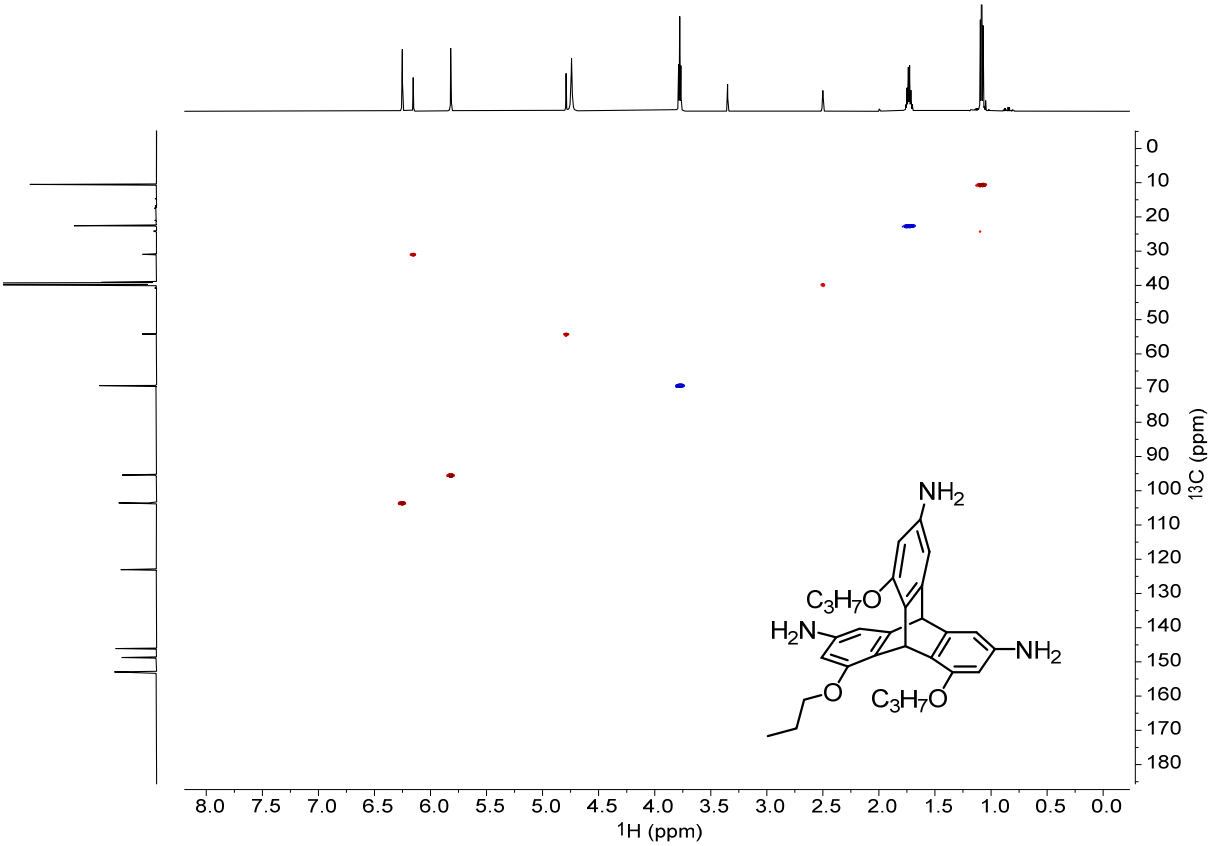

Figure 8.1.14: ^{1}H-^{13}C HSQC NMR spectrum (600/151 MHz, DMSO-d_6) of **81**.

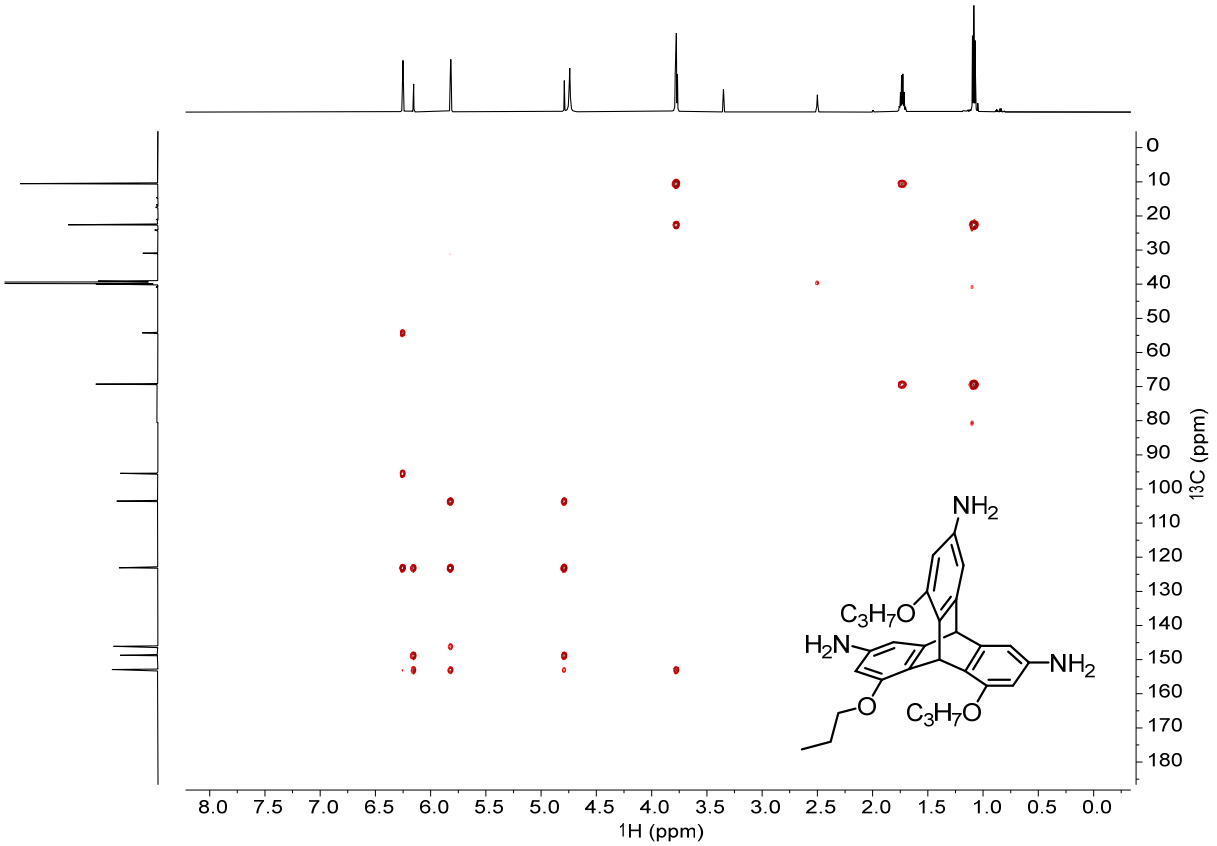

Figure 8.1.15: ^{1}H-^{13}C HMBC NMR spectrum (600/151 MHz, DMSO-d_6) of **81**.

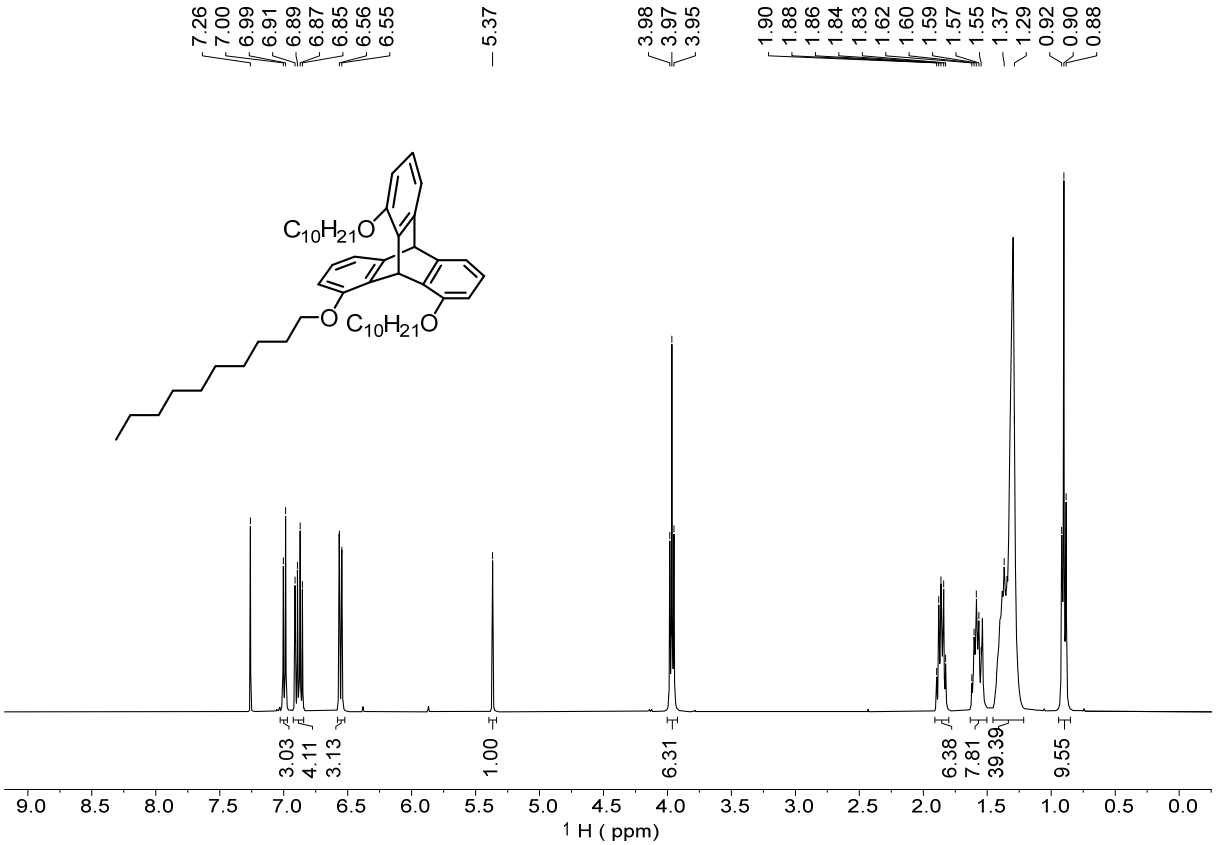

Figure 8.1.16: ^{1}H NMR spectrum (600 MHz, $CDCl_3$) of **77**.

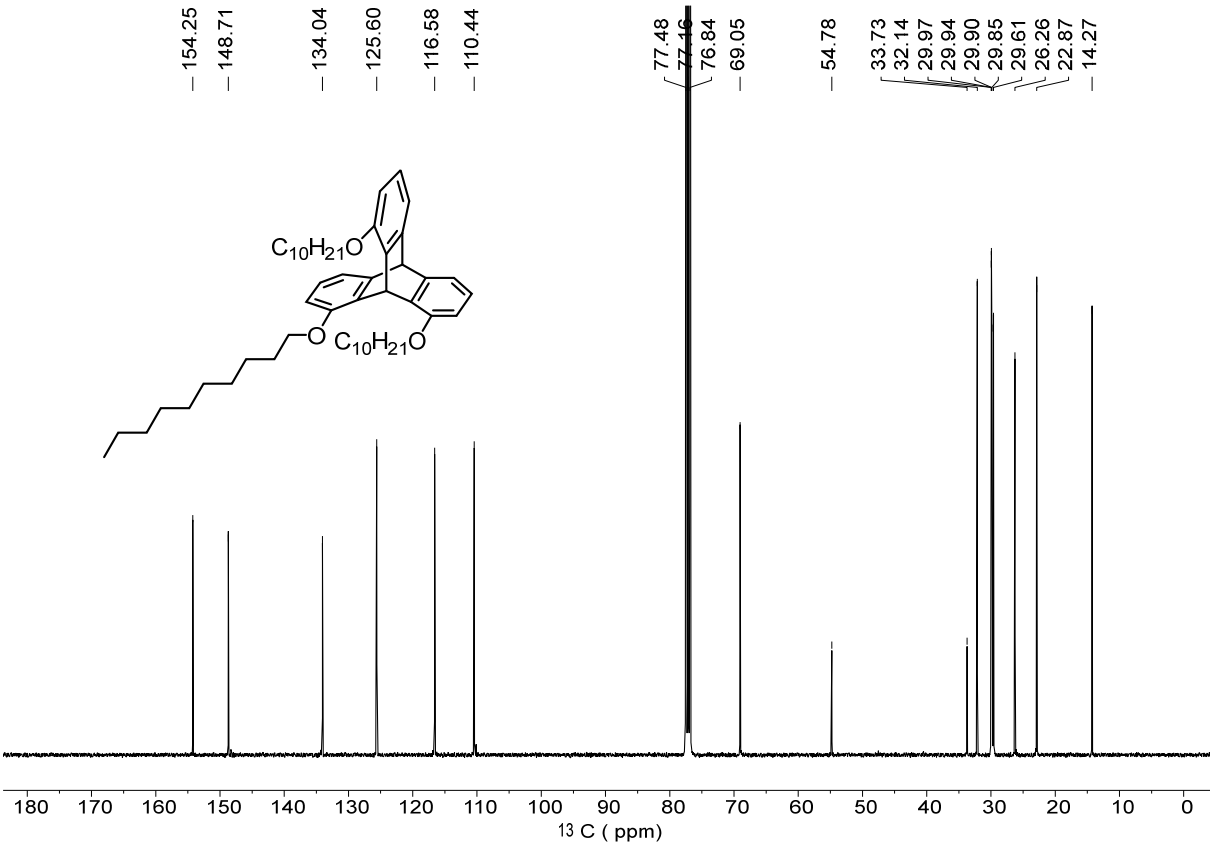

Figure 8.1.17: ^{13}C NMR spectrum (151 MHz, $CDCl_3$) of **77**.

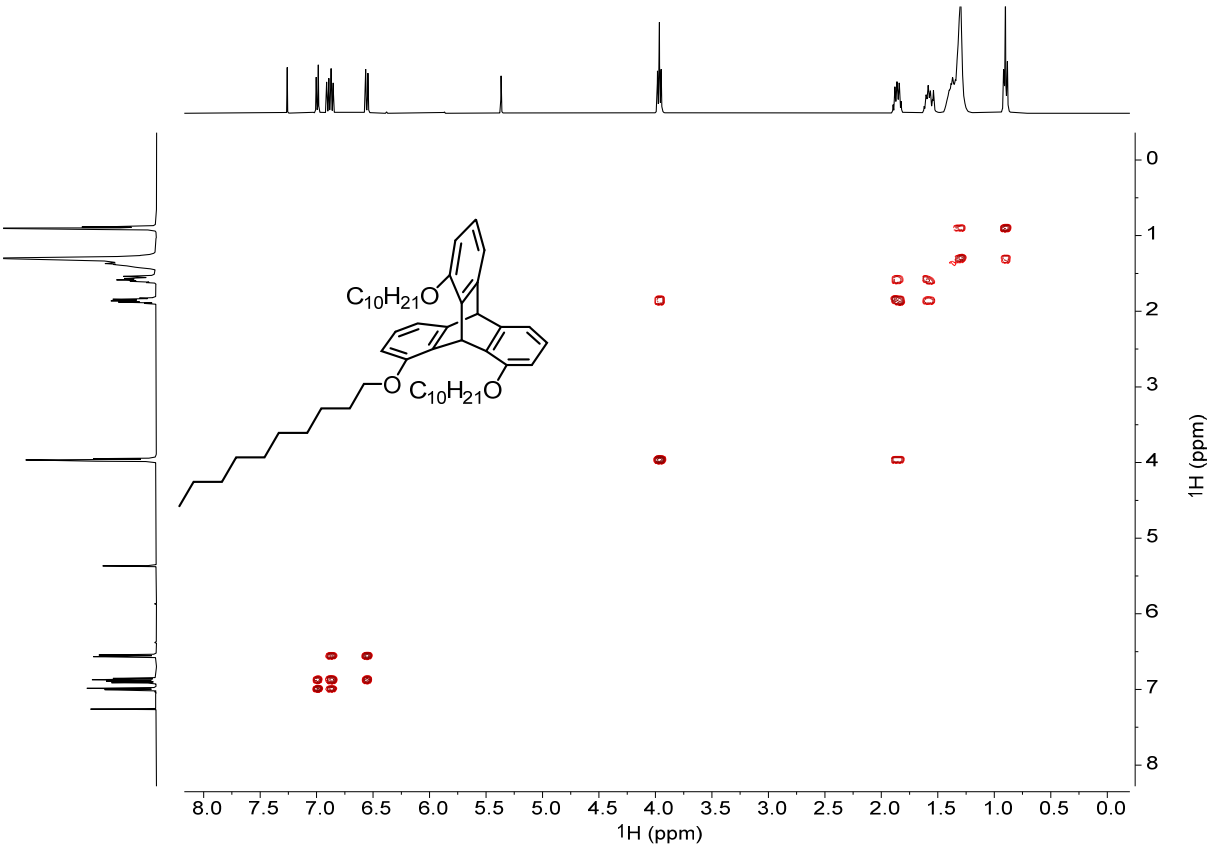

Figure 8.1.18: ^{1}H-^{1}H COSY NMR spectrum (600/600 MHz, $CDCl_3$) of **77**.

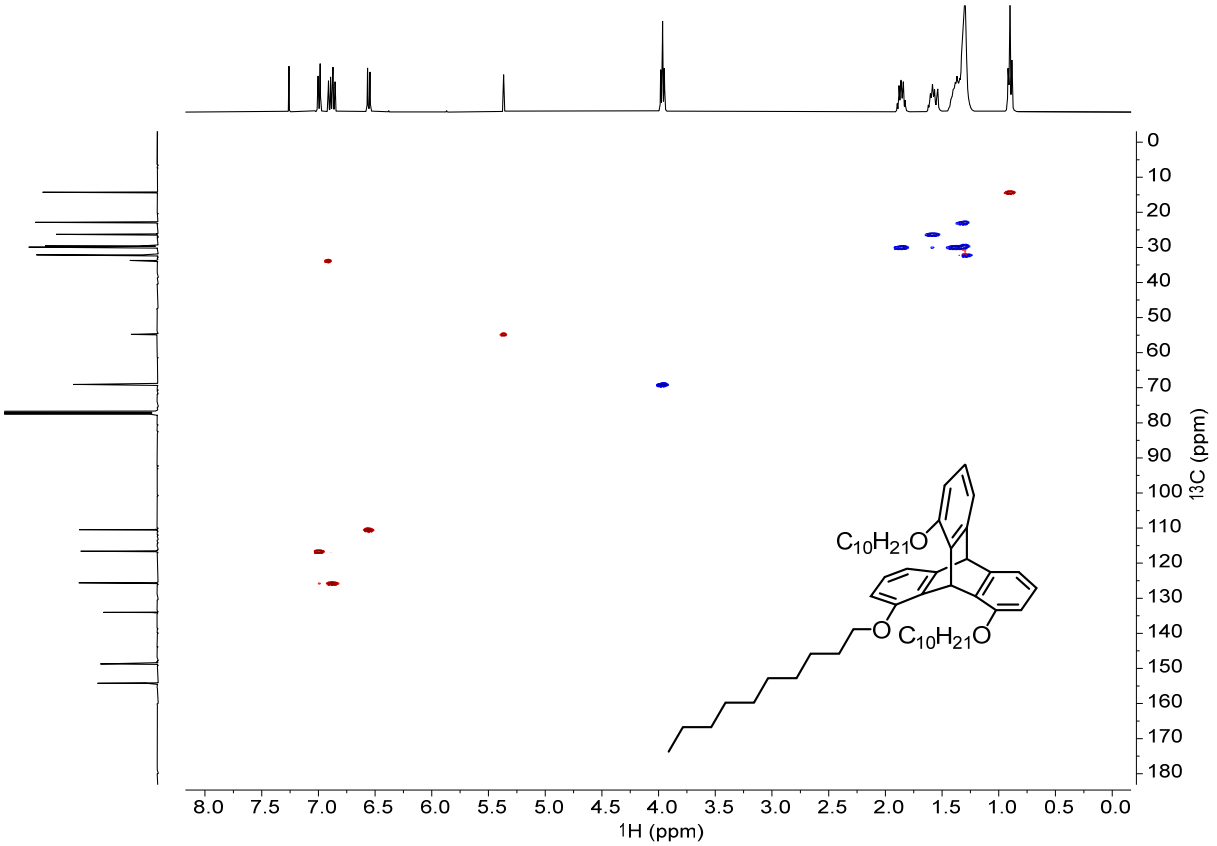

Figure 8.1.19: ^{1}H-^{13}C HSQC NMR spectrum (600/151 MHz, $CDCl_3$) of **77**.

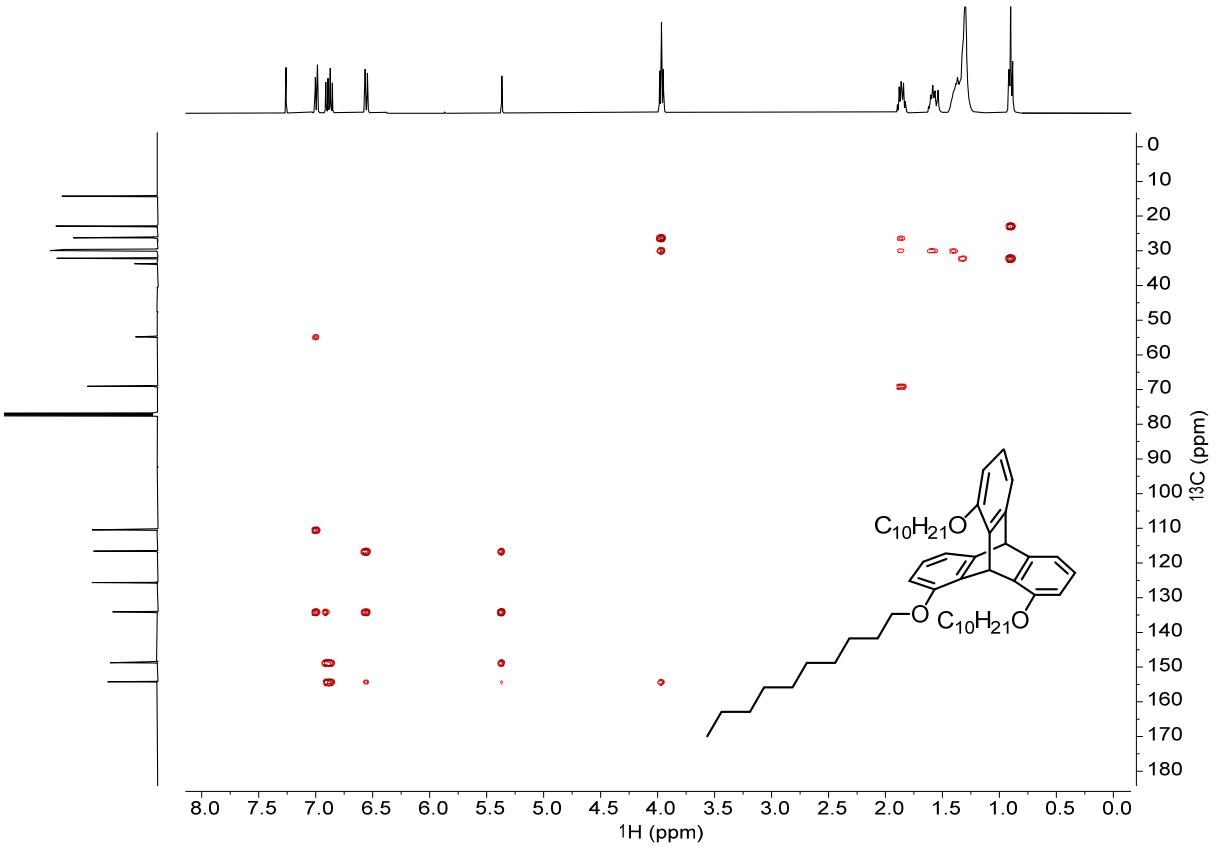

Figure 8.1.20: ^{1}H-^{13}C HMBC NMR spectrum (600/151 MHz, $CDCl_3$) of **77**.

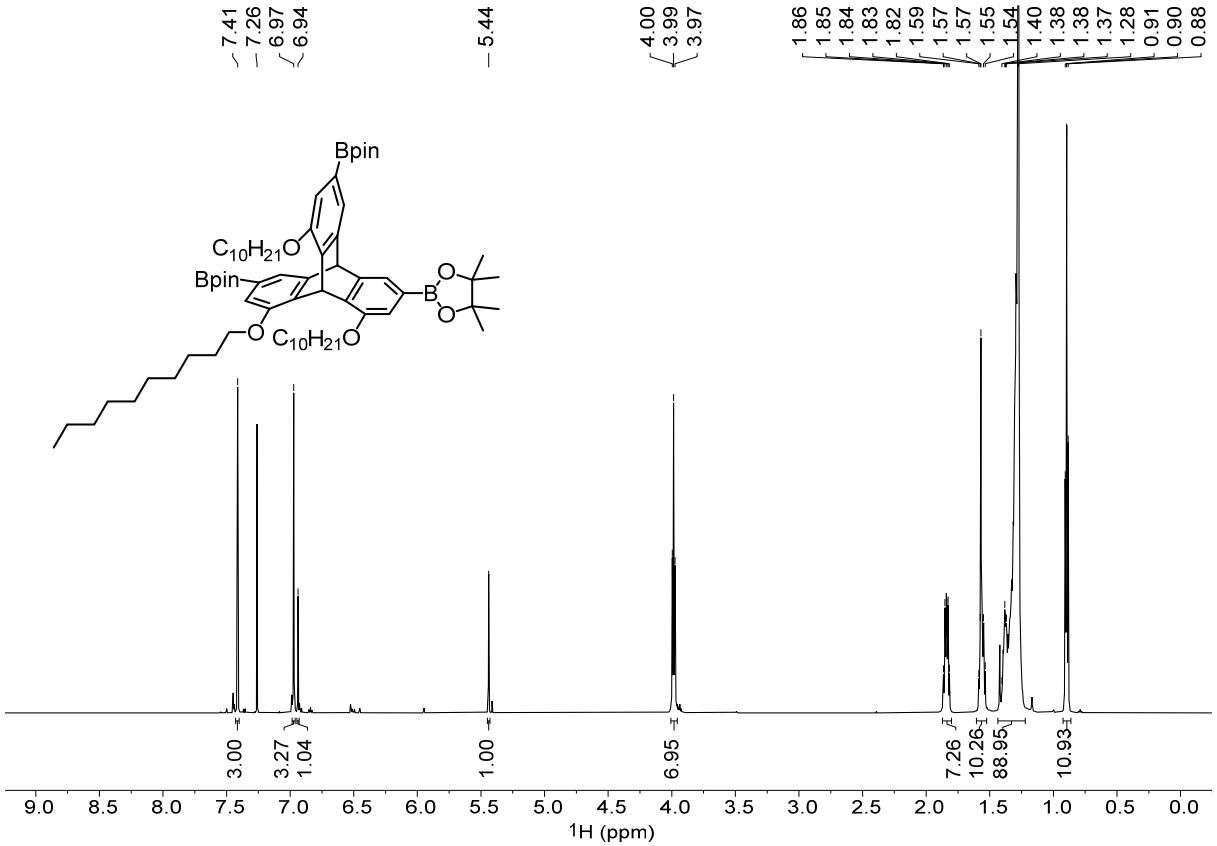

Figure 8.1.21: ^{1}H NMR spectrum (600 MHz, $CDCl_3$) of **80**.

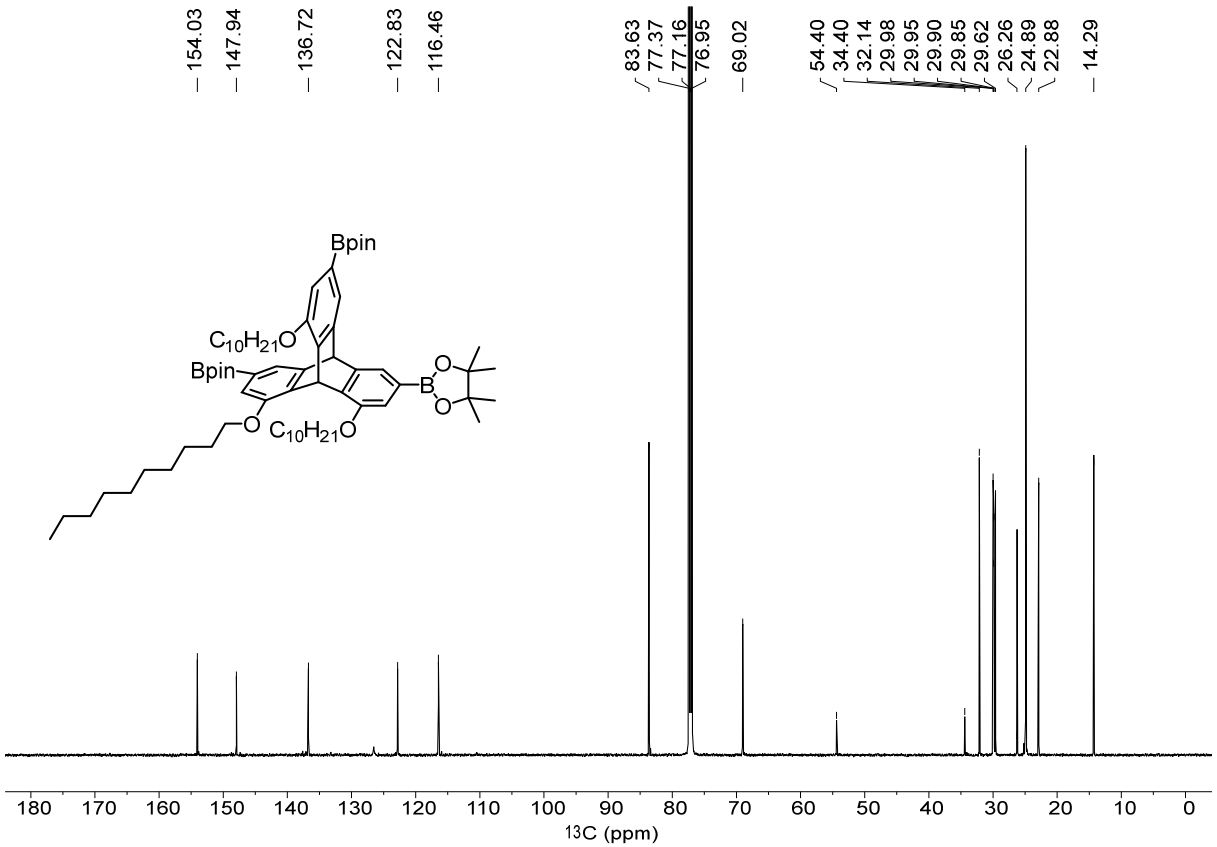

Figure 8.1.22: ^{13}C NMR spectrum (151 MHz, $CDCl_3$) of **80**.

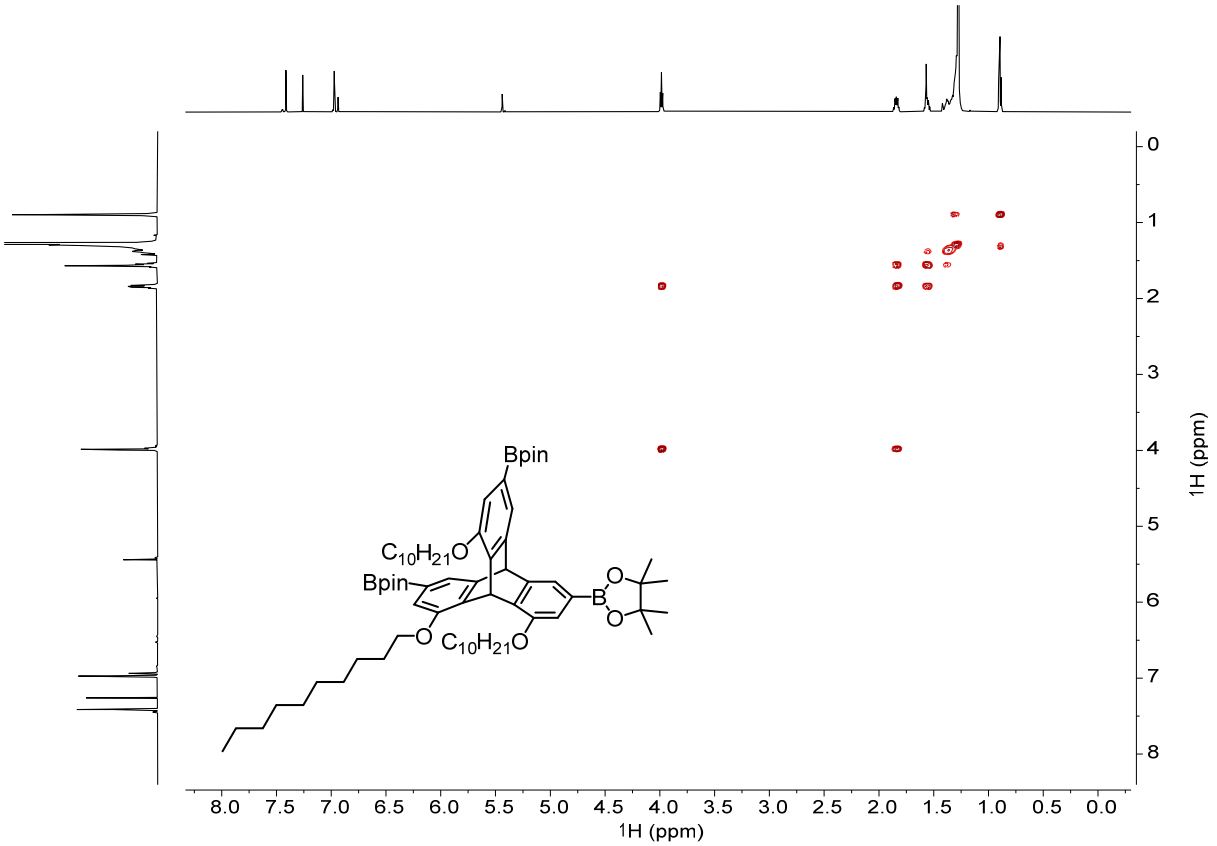

Figure 8.1.23: ^{1}H-^{1}H COSY NMR spectrum (600/600 MHz, $CDCl_3$) of **80**.

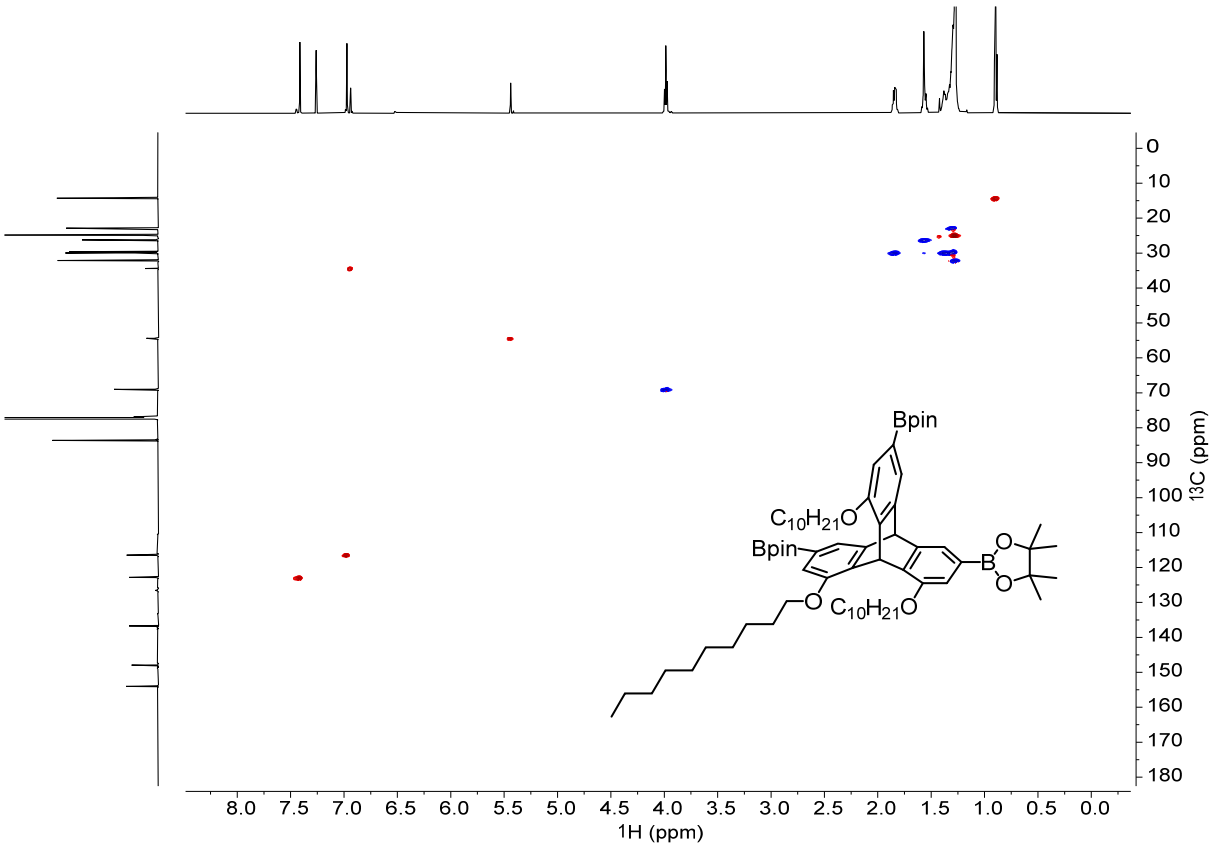

Figure 8.1.24: ^{1}H-^{13}C HSQC NMR spectrum (600/151 MHz, $CDCl_3$) of **80**.

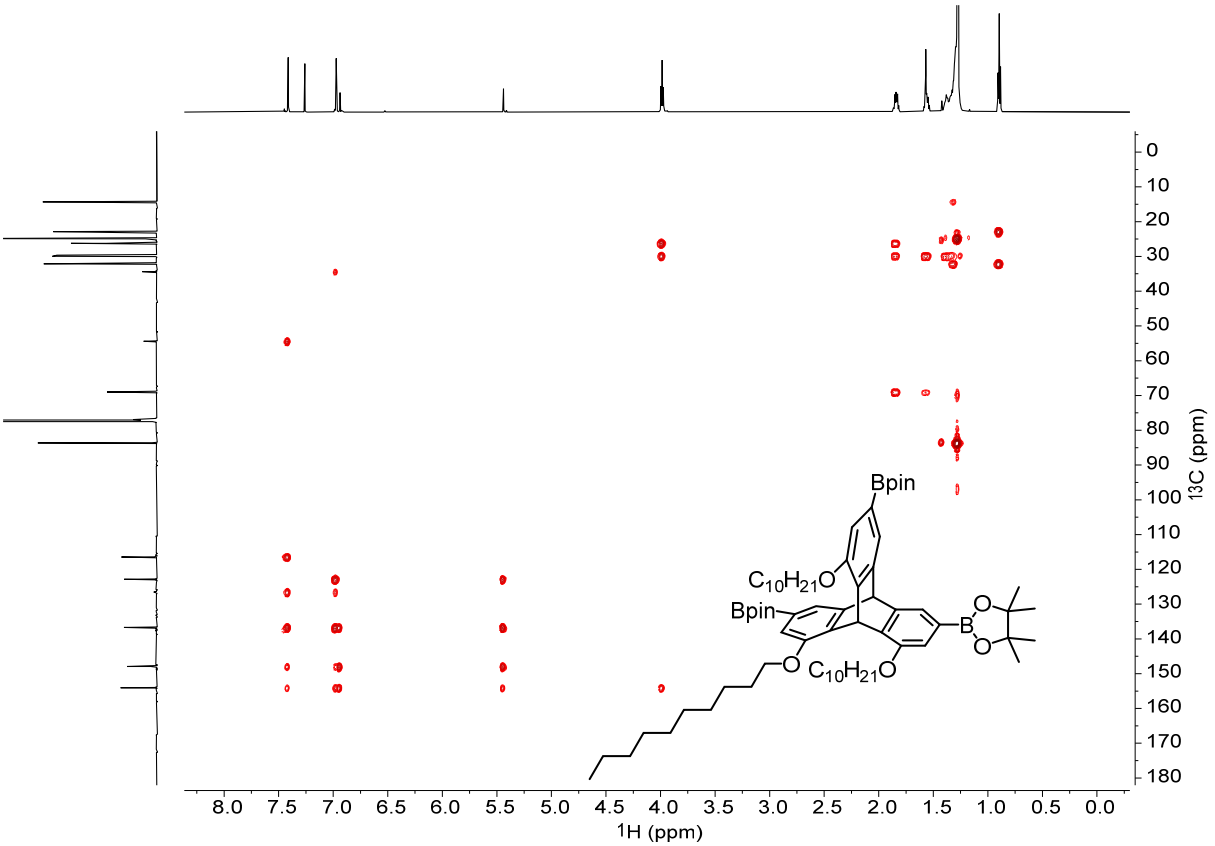

Figure 8.1.25: ^{1}H-^{13}C HMBC NMR spectrum (600/151 MHz, $CDCl_3$) of **80**.

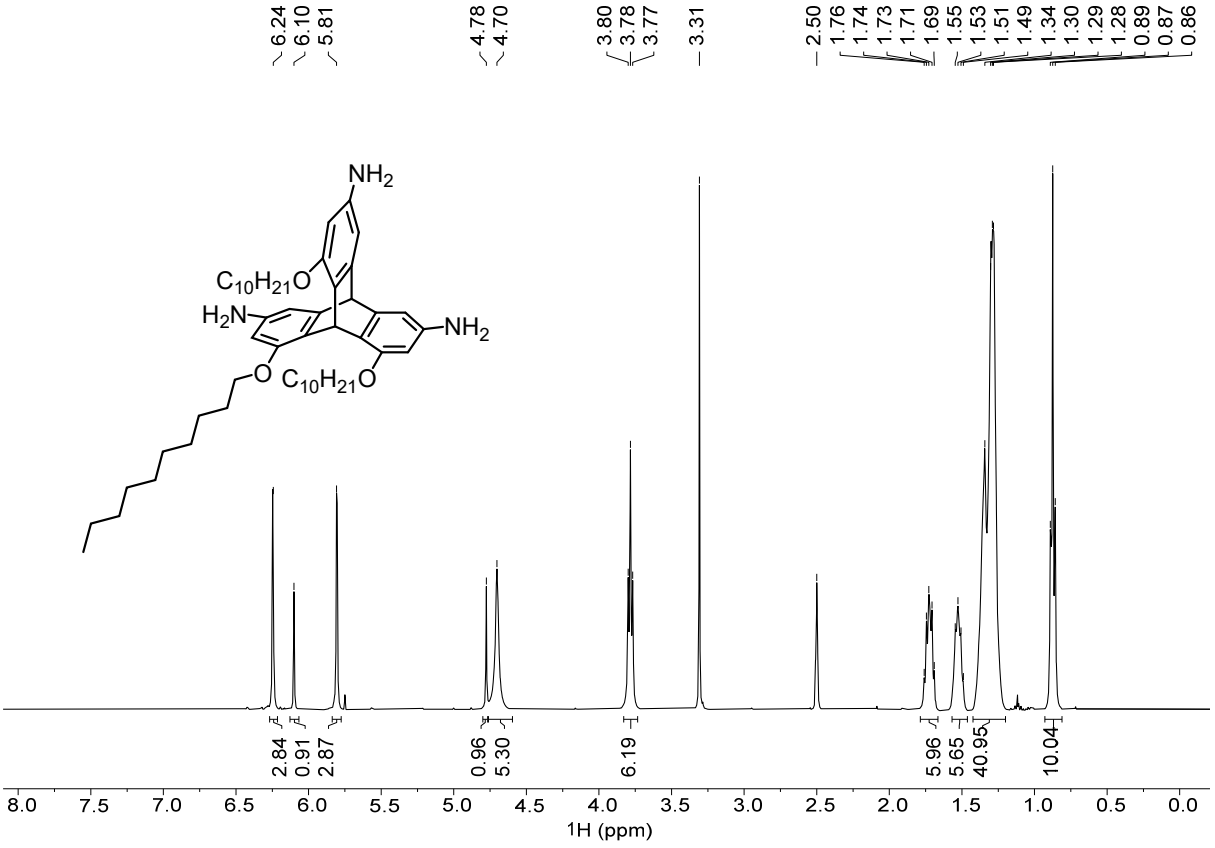

Figure 8.1.26: ^{1}H NMR spectrum (600 MHz, DMSO-d_6) of **83**.

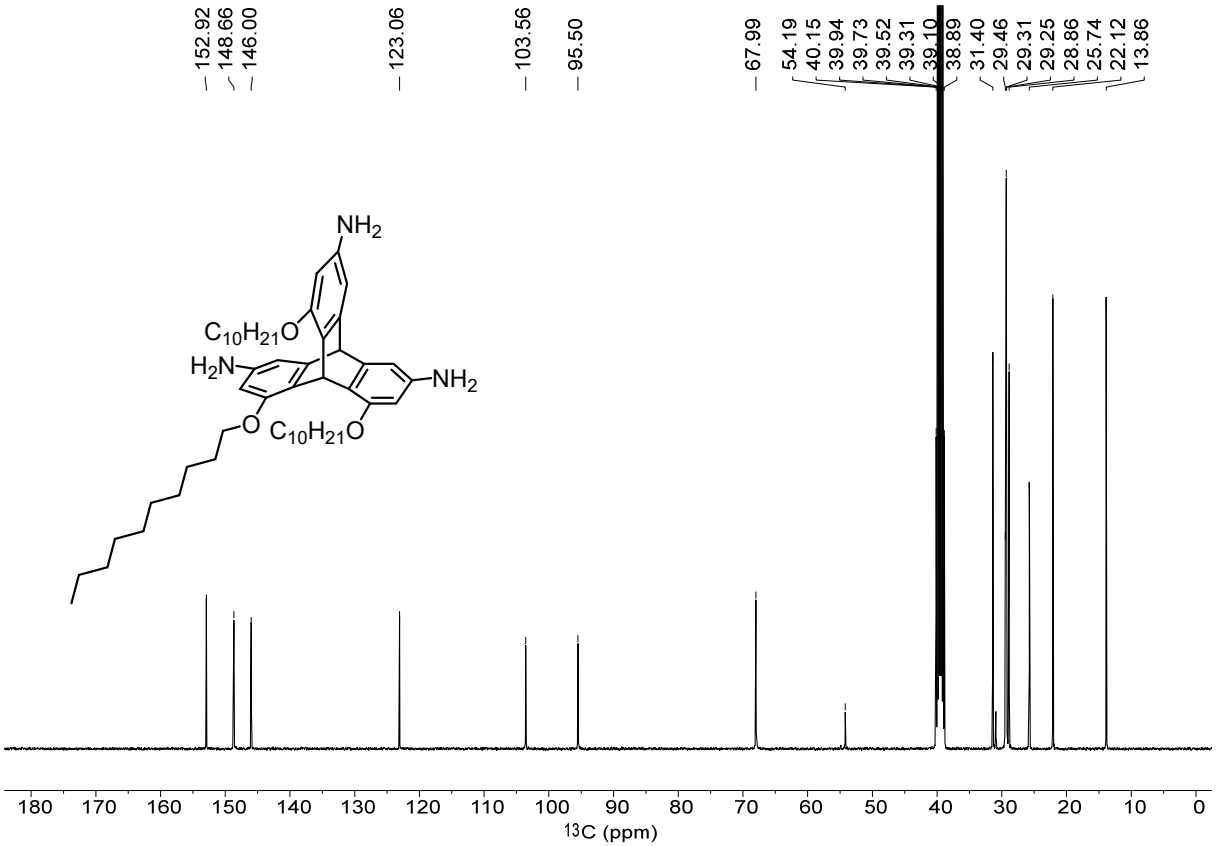

Figure 8.1.27: ^{13}C NMR spectrum (151 MHz, DMSO-d_6) of **83**.

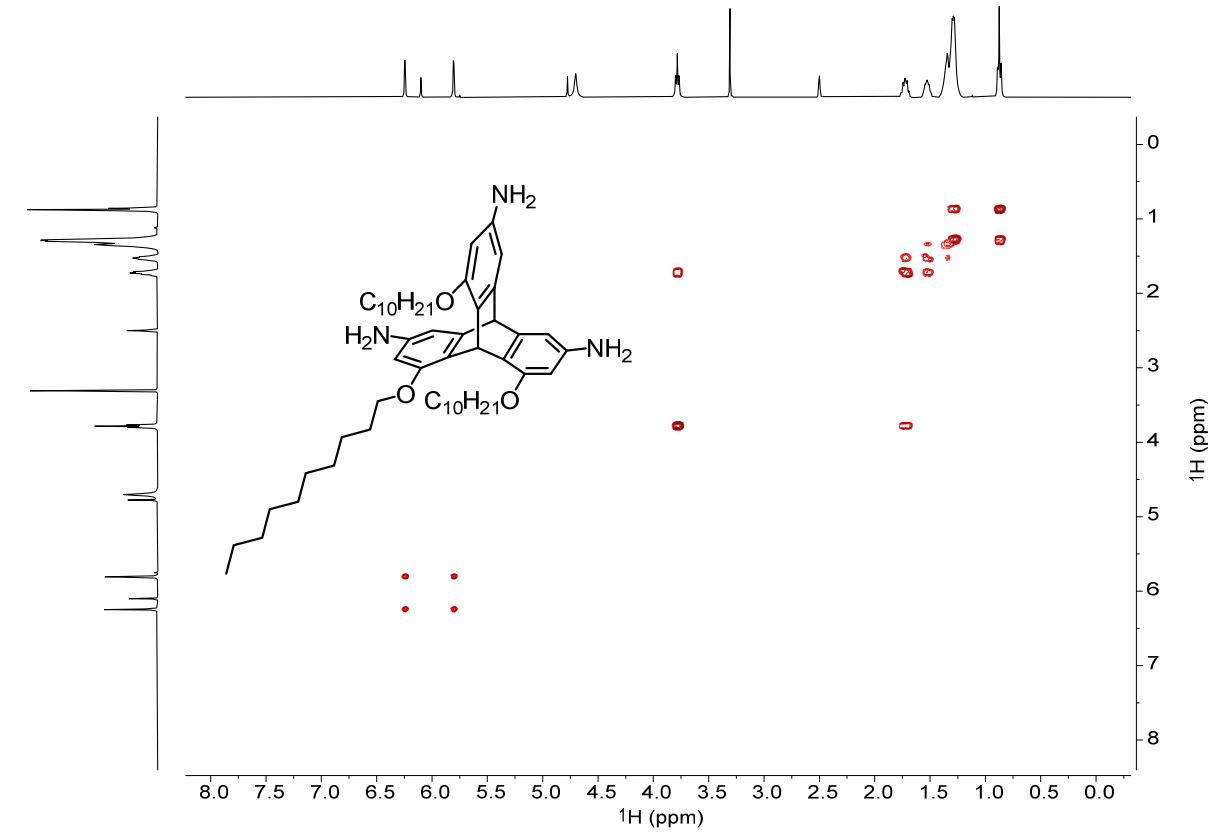

Figure 8.1.28: ^{1}H-^{1}H COSY NMR spectrum (600/600 MHz, DMSO-d_6) of **83**.

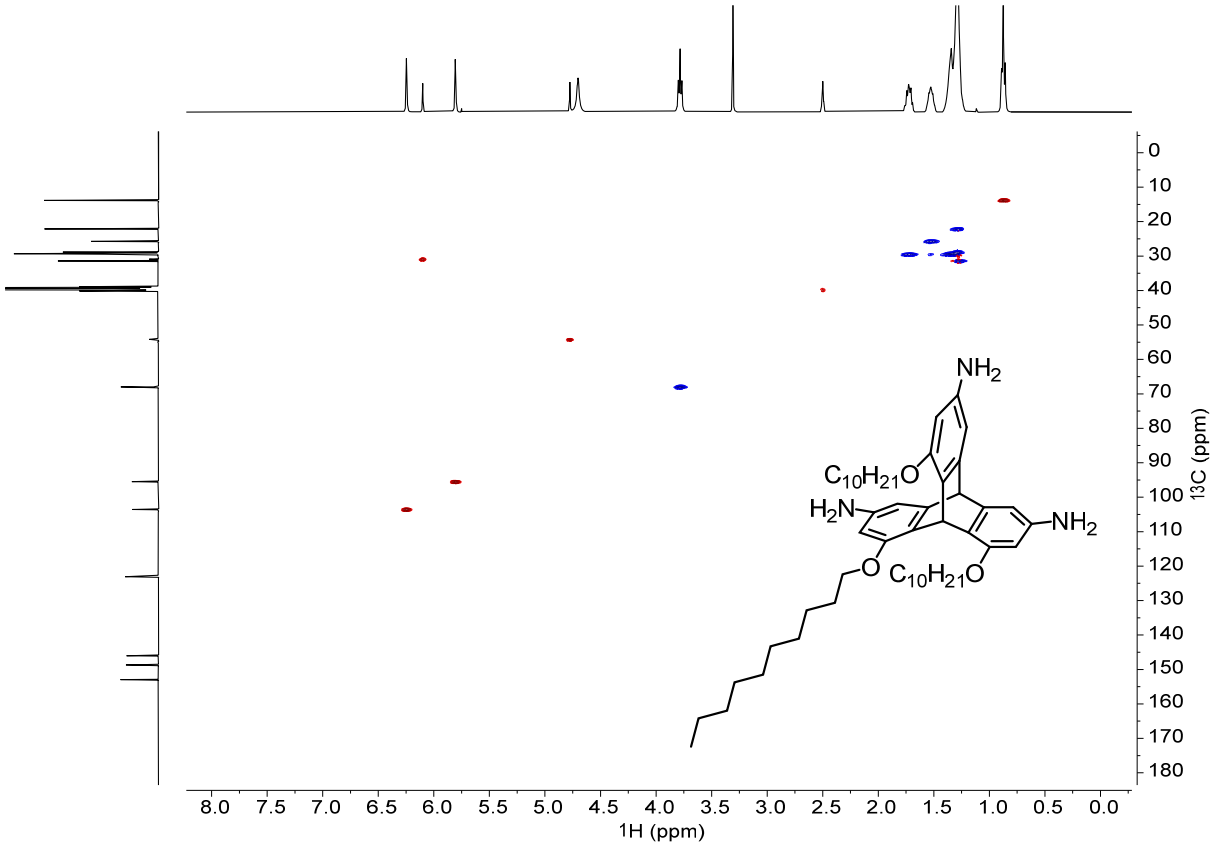

Figure 8.1.29: ^{1}H-^{13}C HSQC NMR spectrum (600/151 MHz, DMSO-d_6) of **83**.

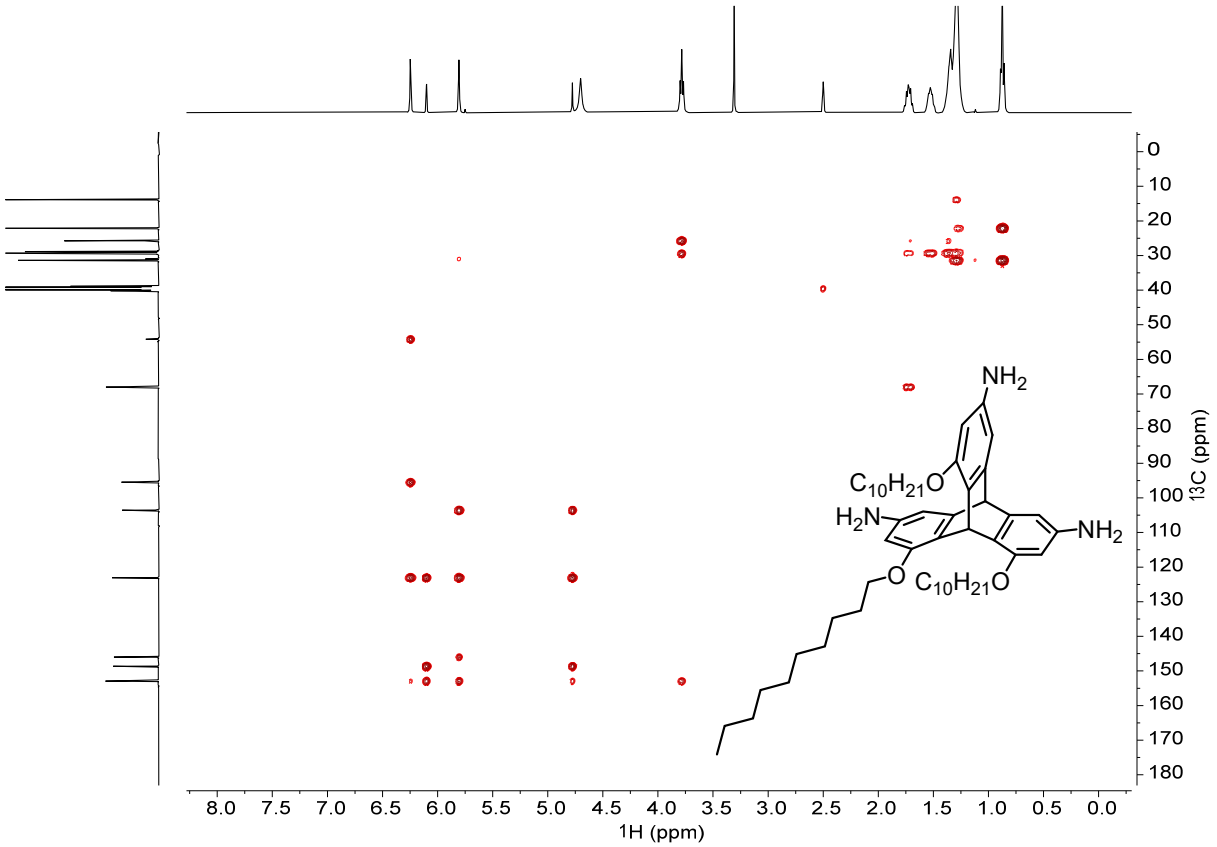

Figure 8.1.30: ^{1}H-^{13}C HMBC NMR spectrum (600/151 MHz, DMSO-d_6) of **83**.

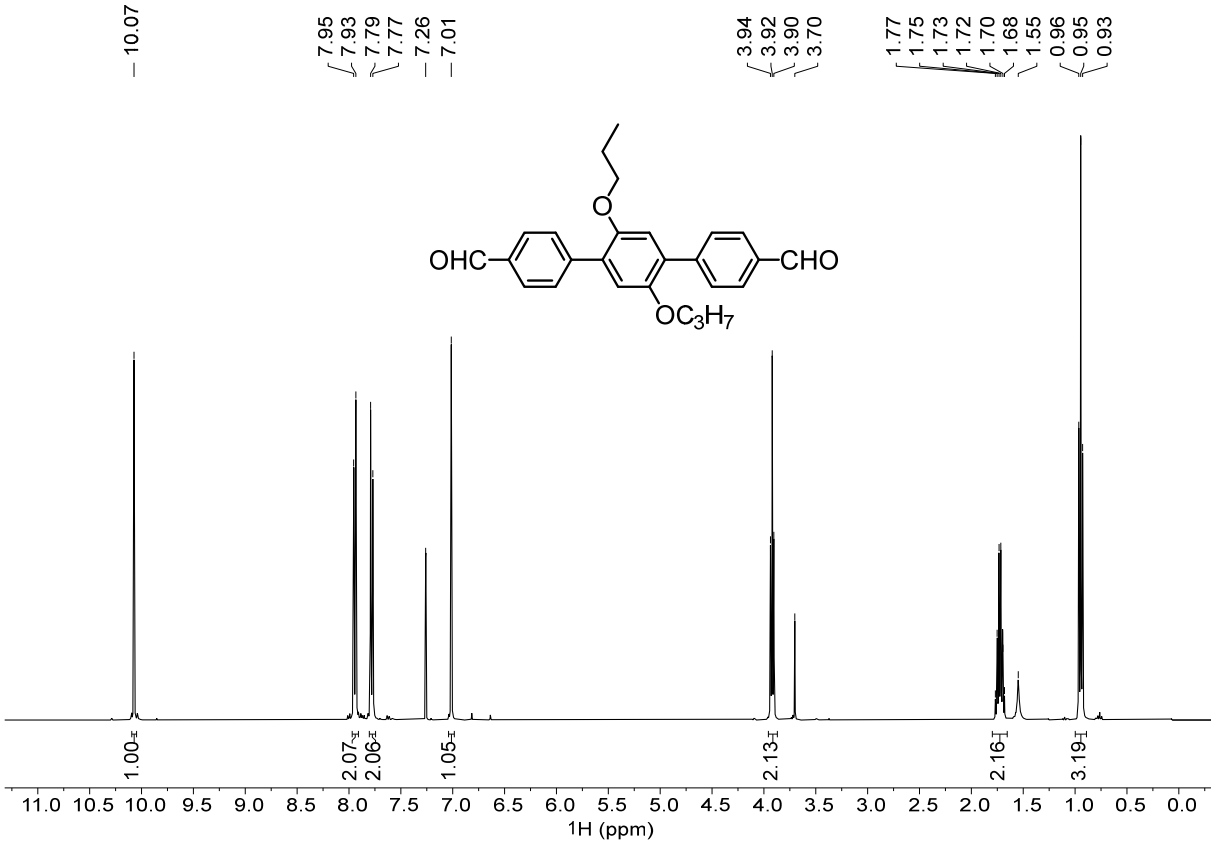

Figure 8.1.31: ^{1}H NMR spectrum (600 MHz, $CDCl_3$) of **102**.

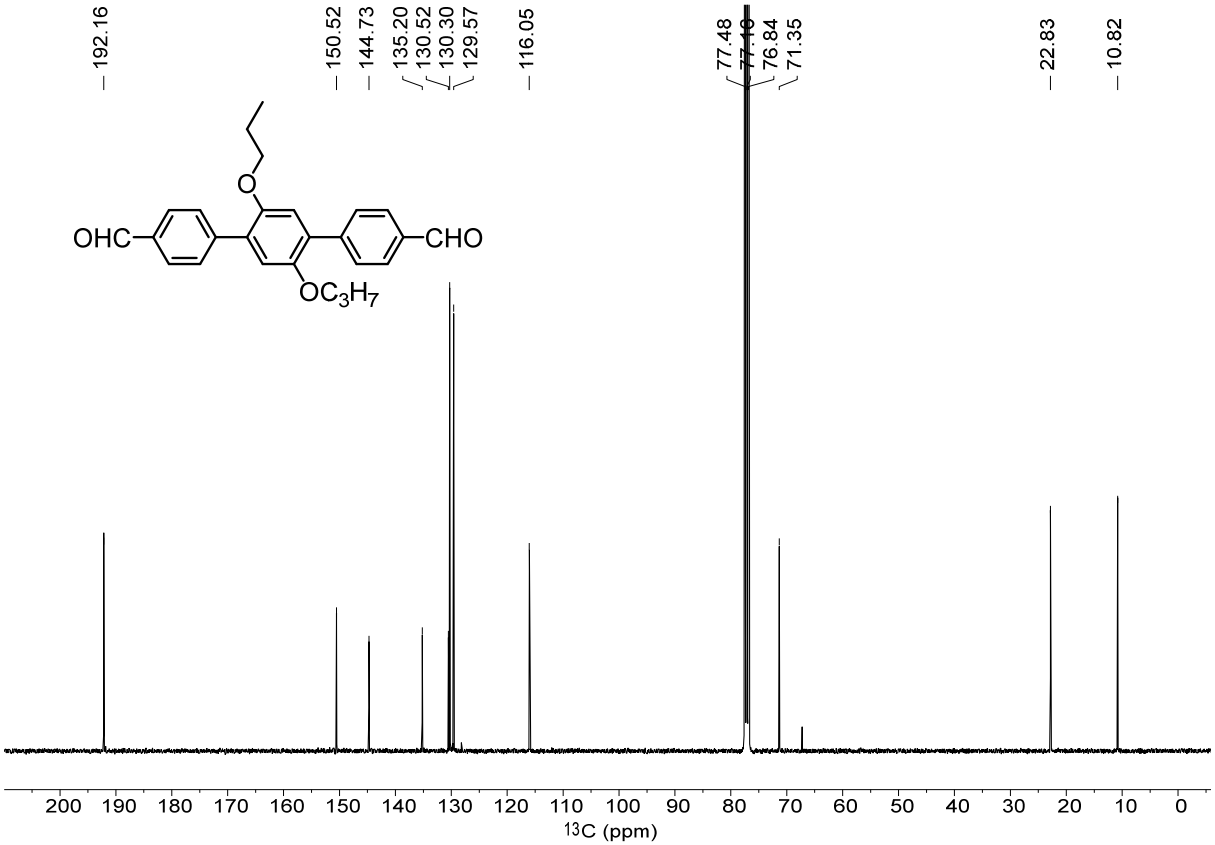

Figure 8.1.32: ^{13}C NMR spectrum (151 MHz, $CDCl_3$) of **102**.

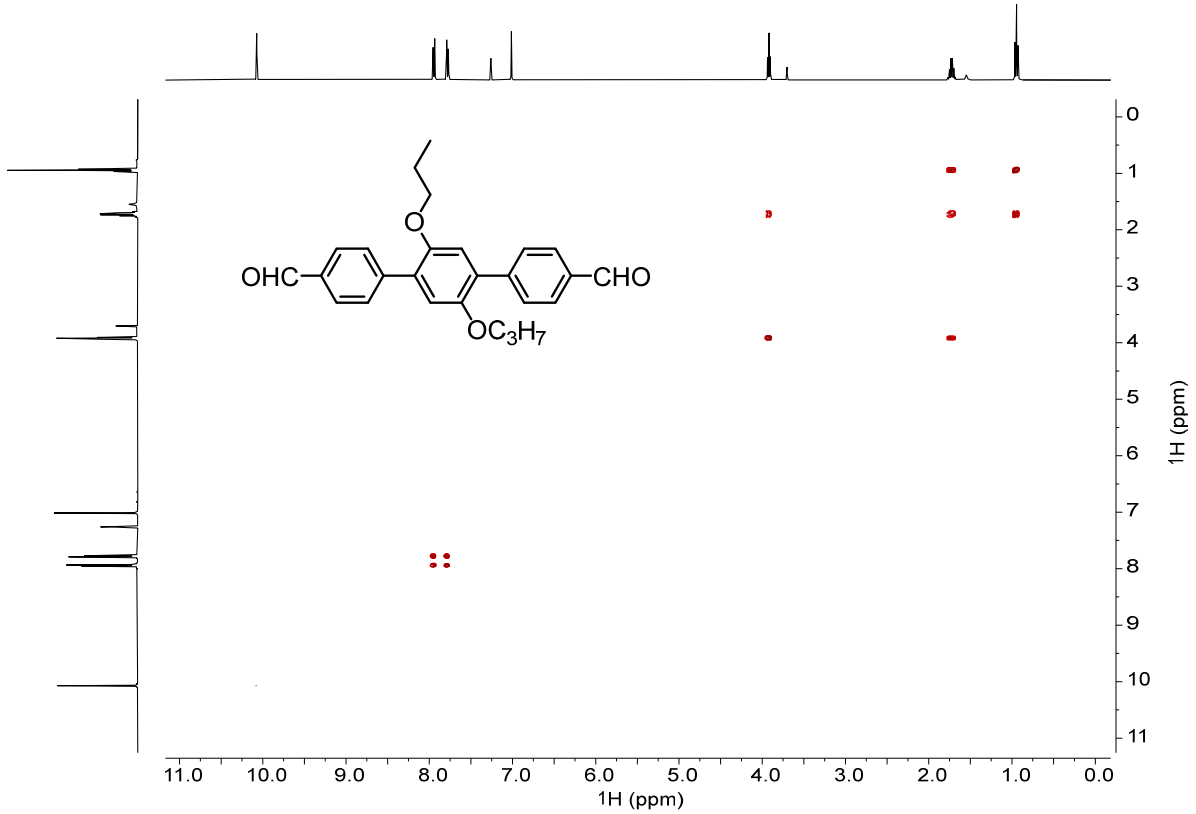

Figure 8.1.33: ^{1}H-^{1}H COSY NMR spectrum (600/600 MHz, $CDCl_3$) of **102**.

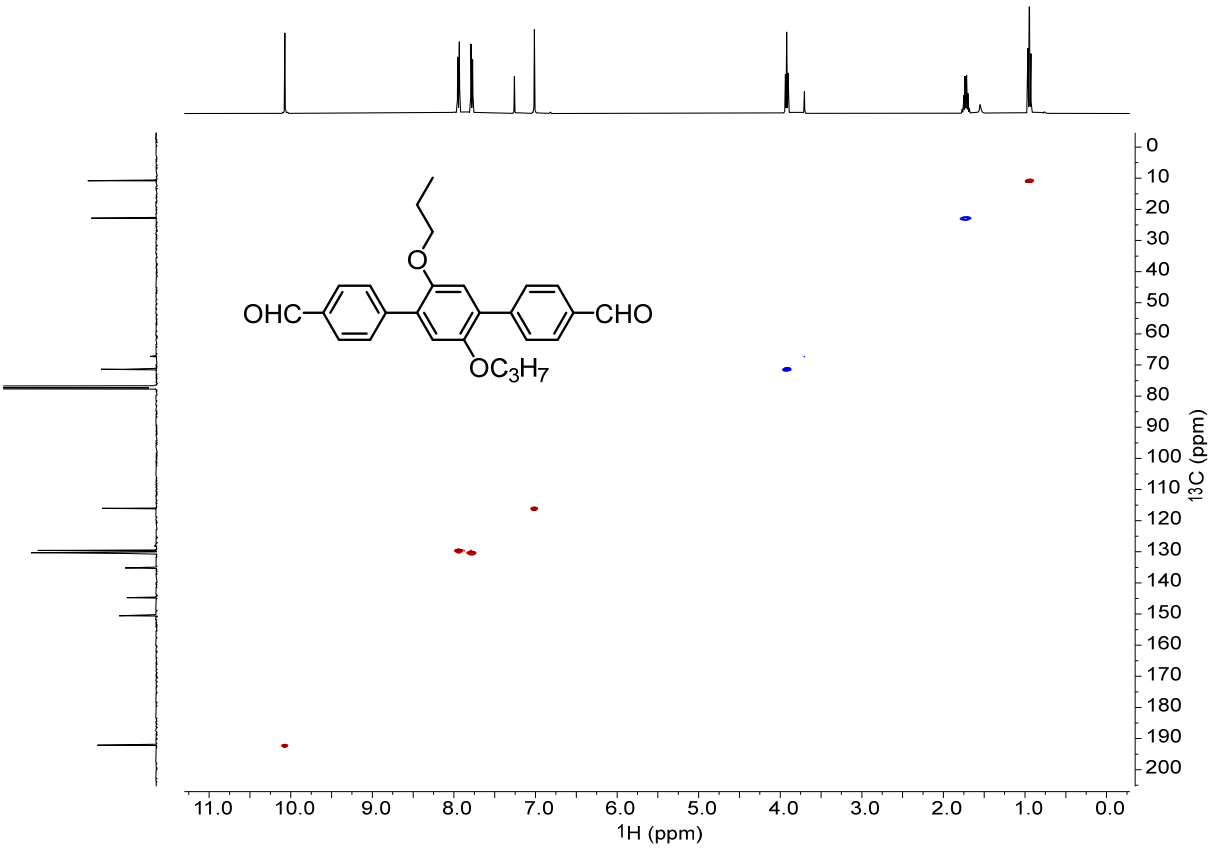

Figure 8.1.34: ^{1}H-^{13}C HSQC NMR spectrum (600/151 MHz, $CDCl_3$) of **102**.

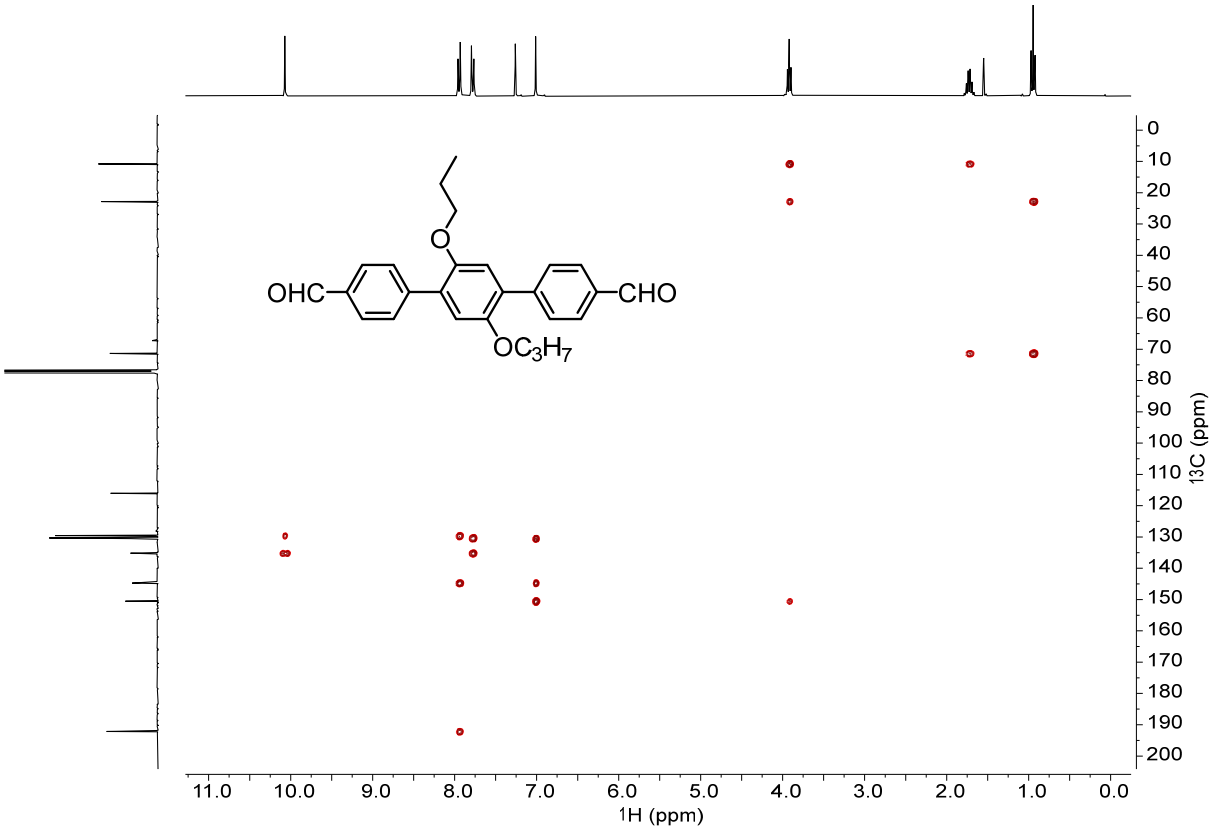

Figure 8.1.35: ^{1}H-^{13}C HMBC NMR spectrum (600/151 MHz, $CDCl_3$) of **102**.

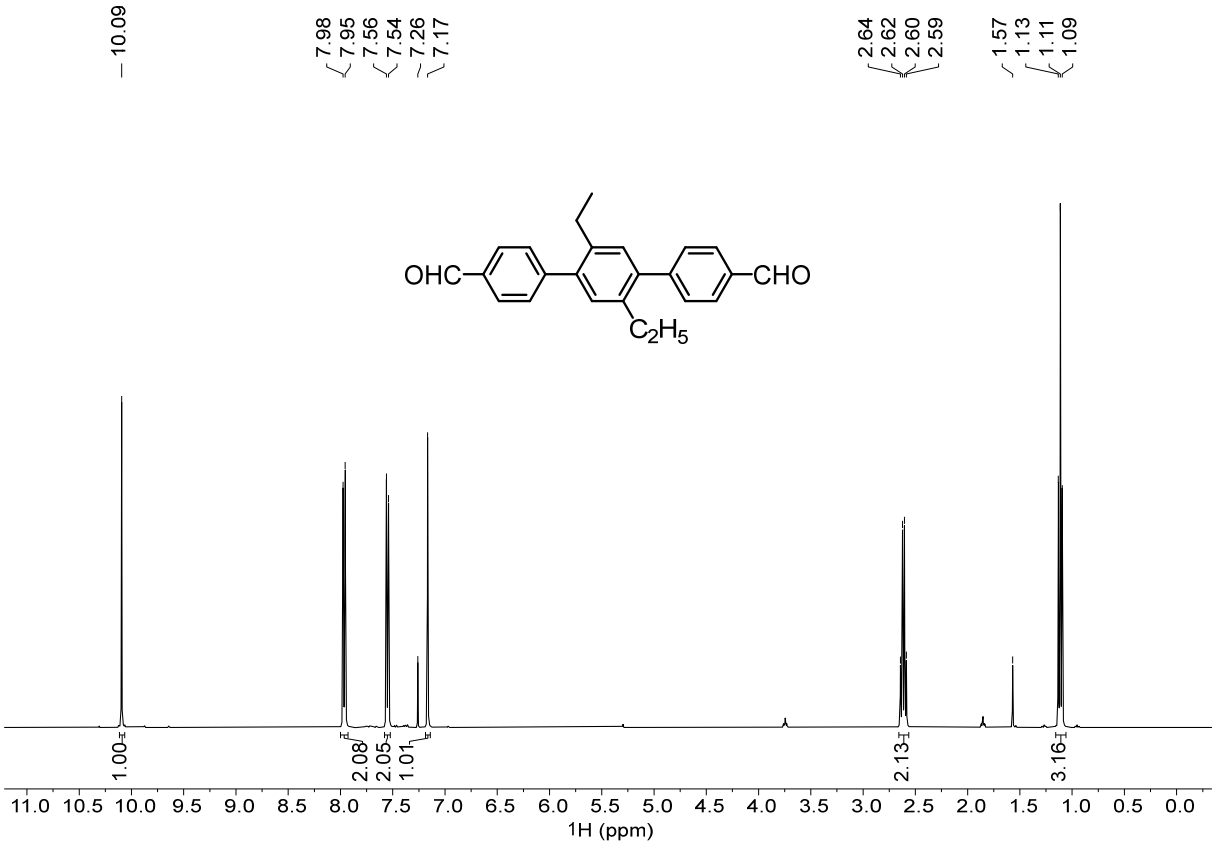

Figure 8.1.36: ^{1}H NMR spectrum (600 MHz, $CDCl_3$) of **104**

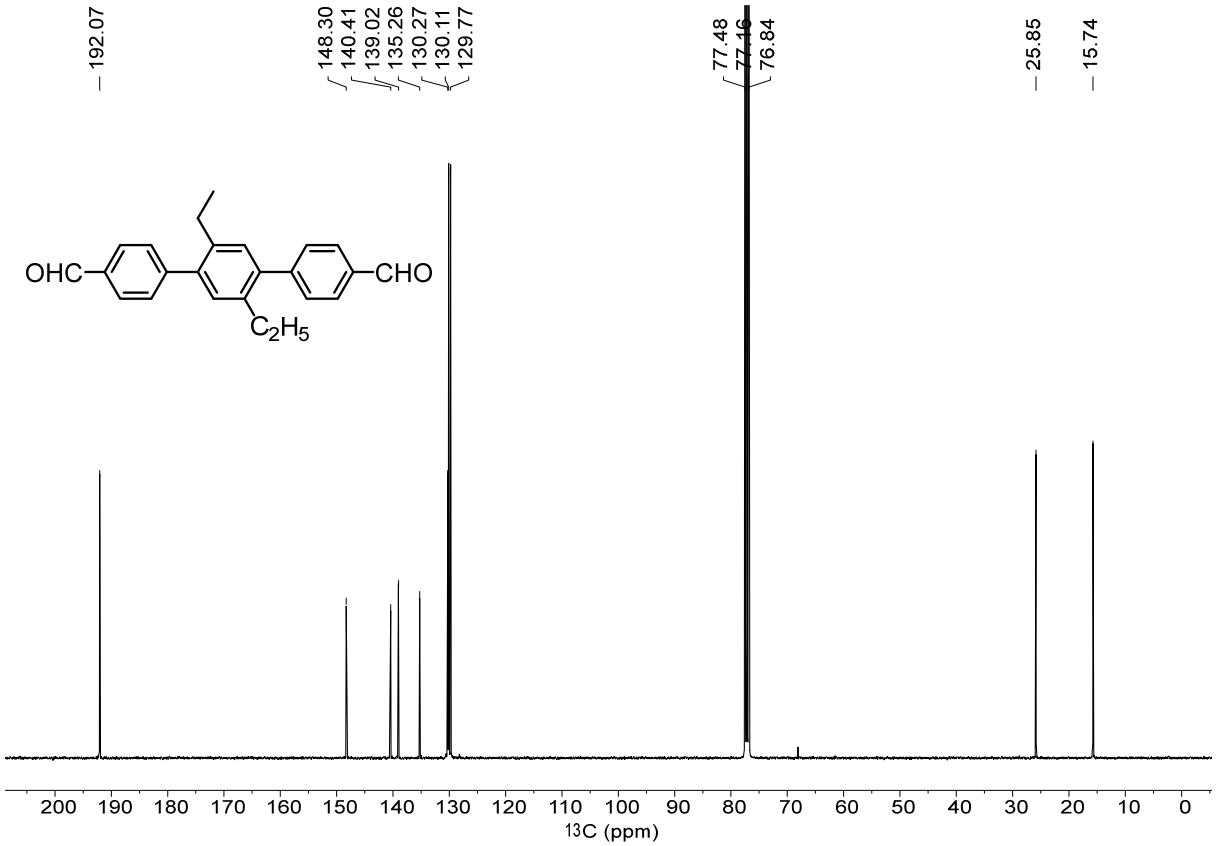

Figure 8.1.37: ^{13}C NMR spectrum (151 MHz, $CDCl_3$) of **104**.

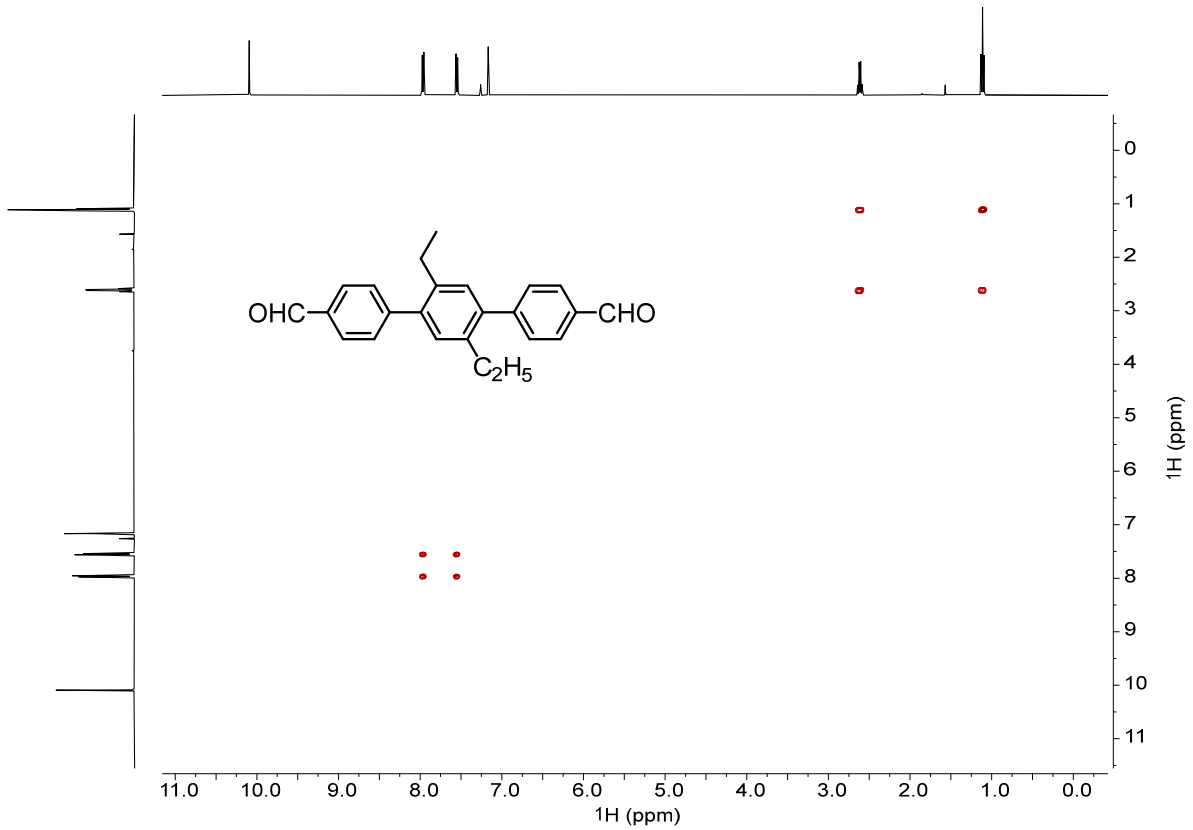

Figure 8.1.38: ^{1}H-^{1}H COSY NMR spectrum (600/600 MHz, $CDCl_3$) of **104**.

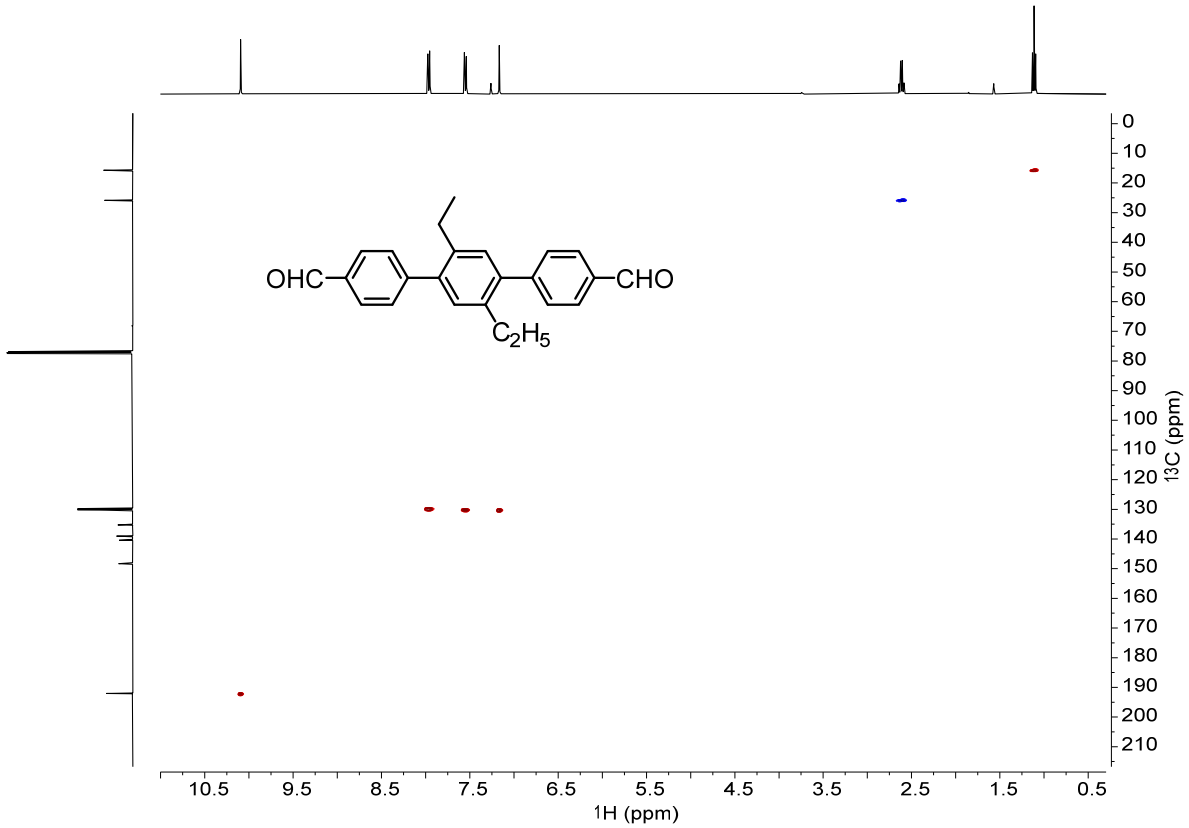

Figure 8.1.39: ^{1}H-^{13}C HSQC NMR spectrum (600/151 MHz, $CDCl_3$) of **104**.

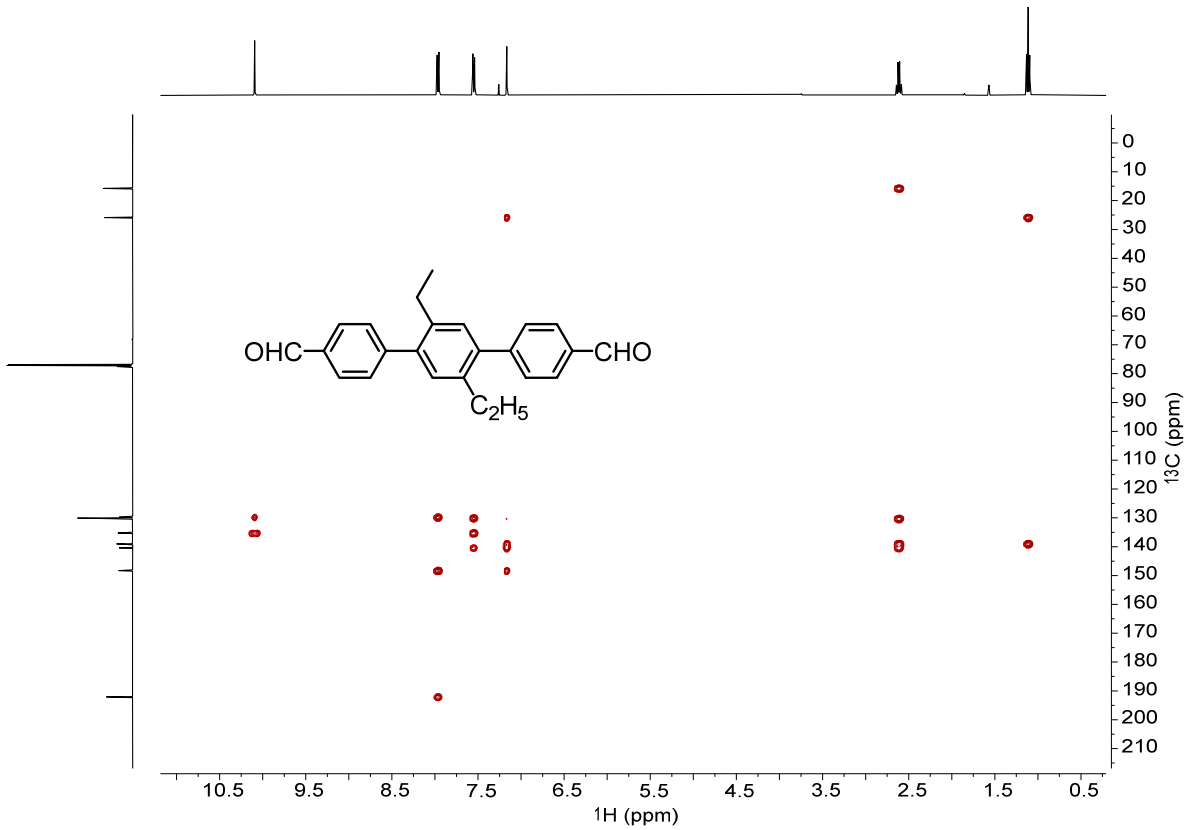

Figure 8.1.40: ^{1}H-^{13}C HMBC NMR spectrum (600/151 MHz, $CDCl_3$) of **104**.

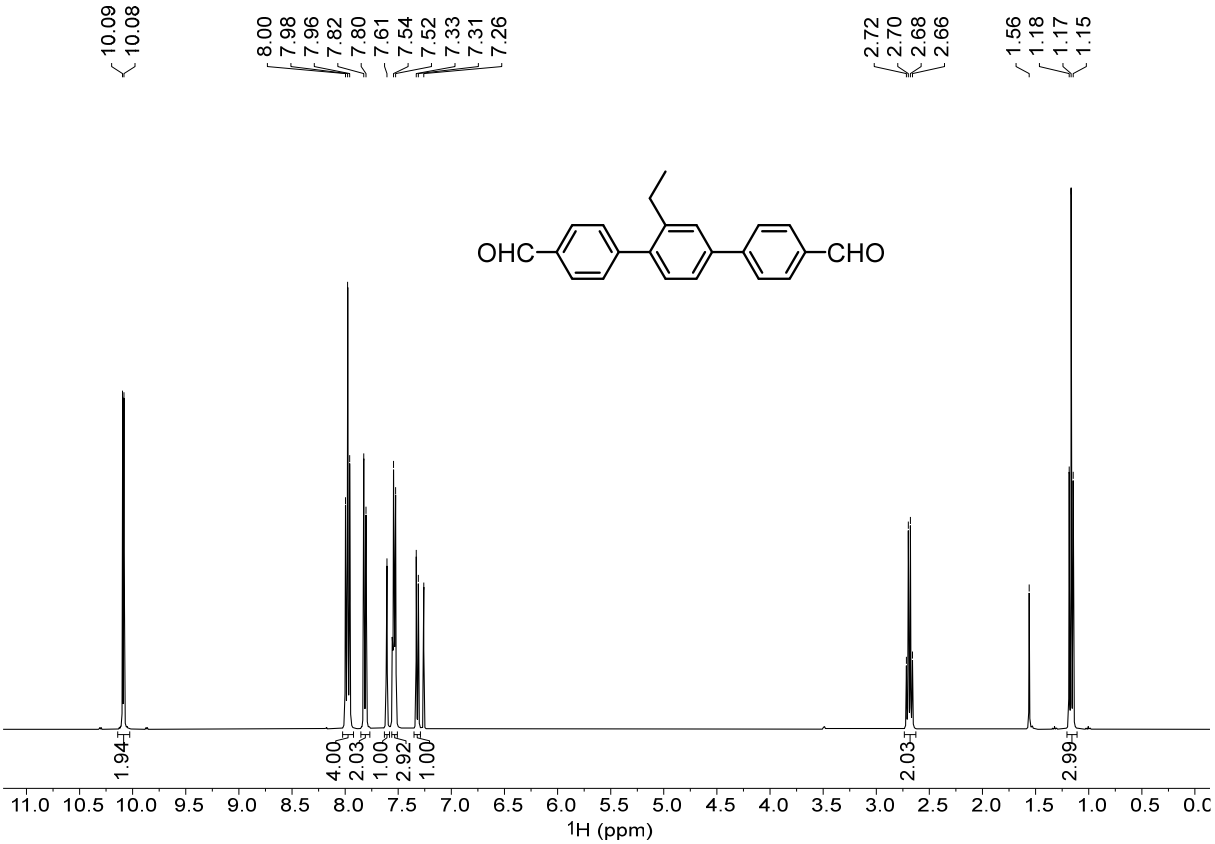

Figure 8.1.41: ^{1}H NMR spectrum (600 MHz, $CDCl_3$) of **105**.

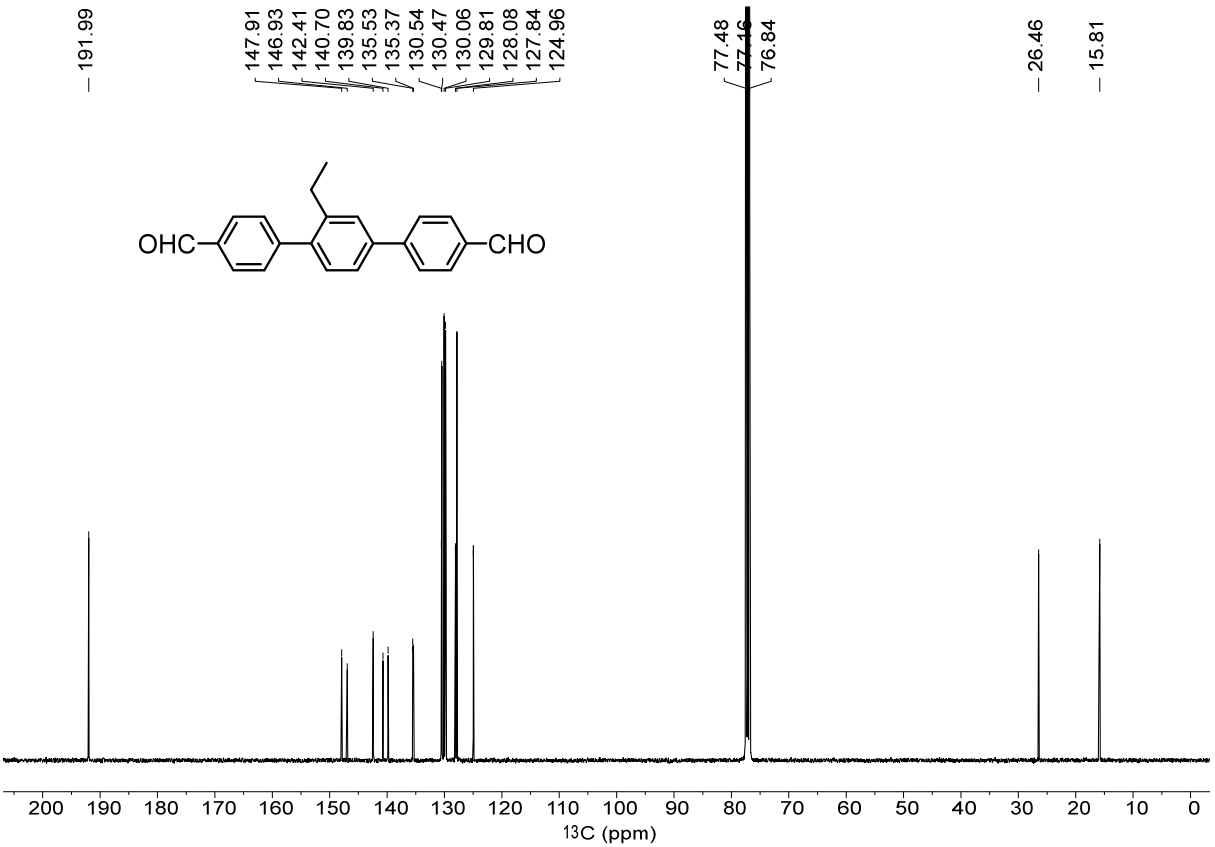

Figure 8.1.42: ^{13}C NMR spectrum (151 MHz, $CDCl_3$) of **105**.

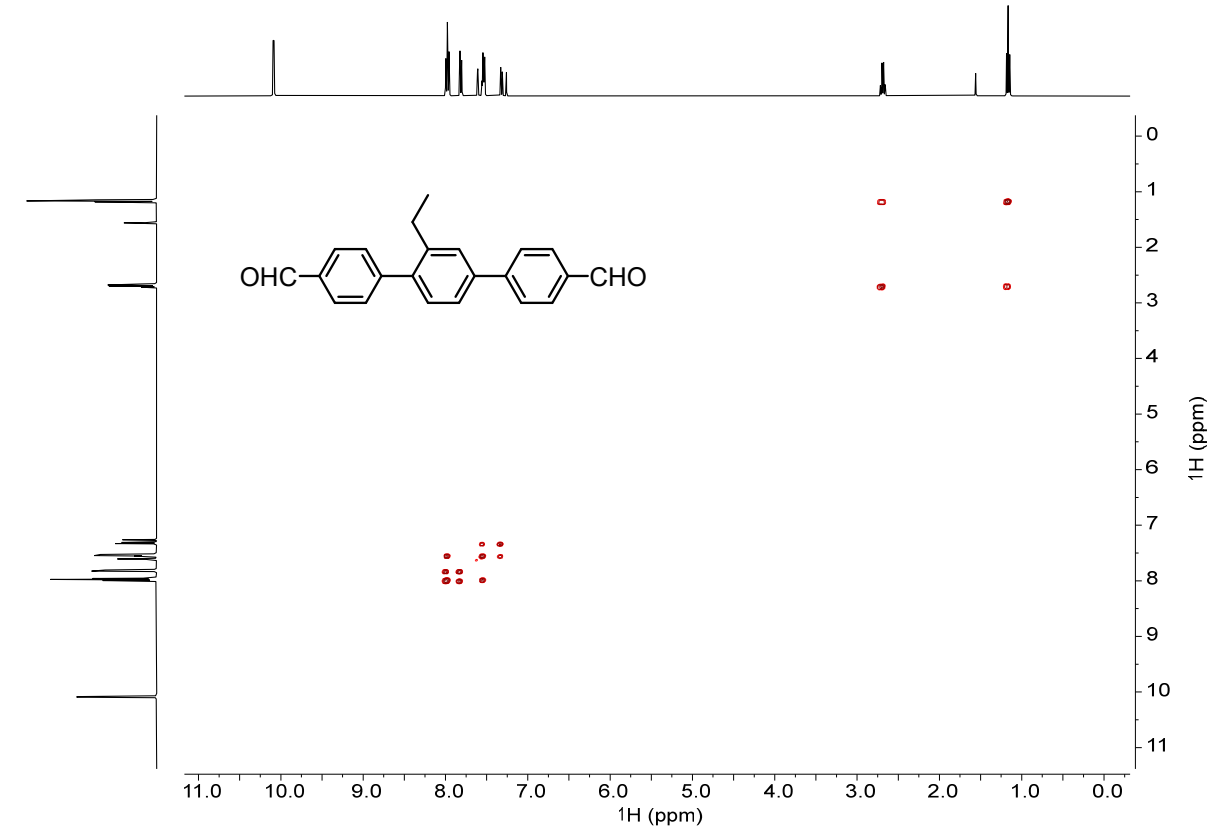

Figure 8.1.43: ^{1}H-^{1}H COSY NMR spectrum (600/600 MHz, $CDCl_3$) of **105**.

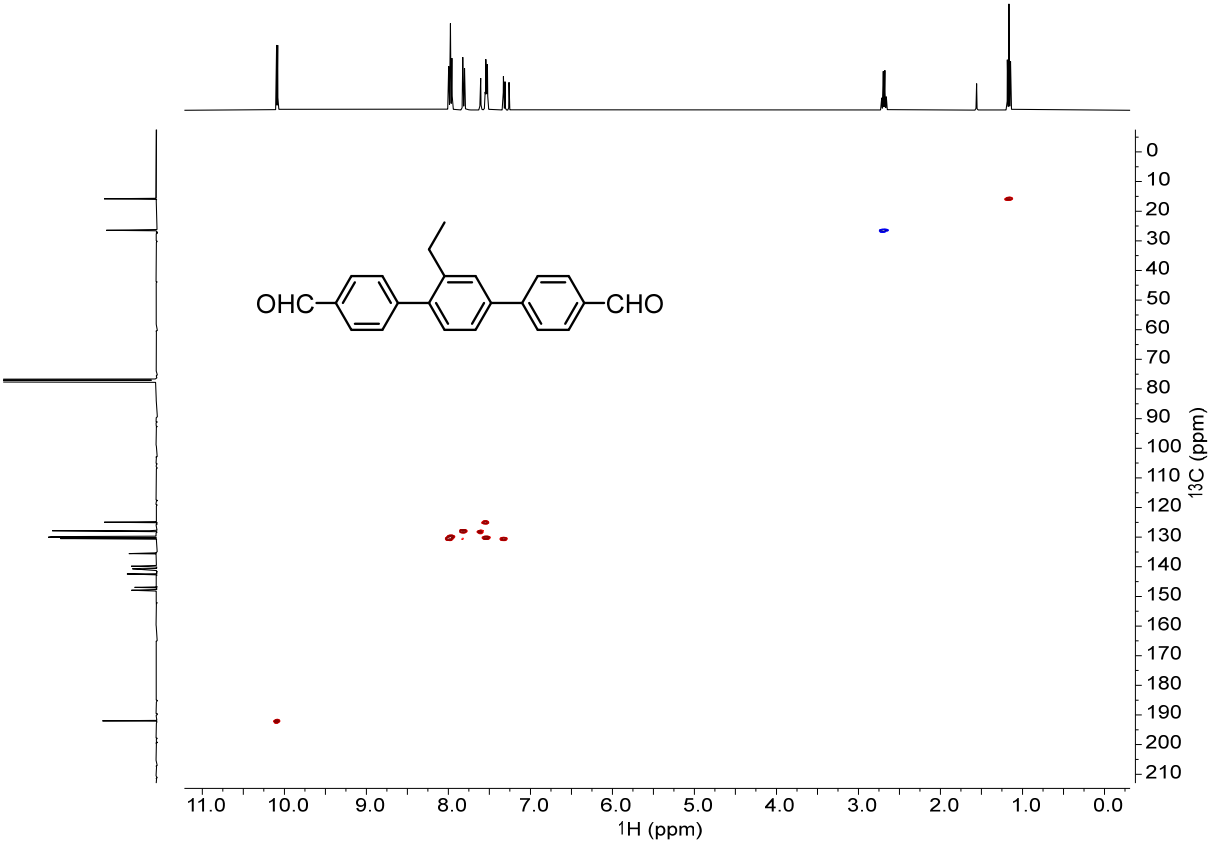

Figure 8.1.44: ^{1}H-^{13}C HSQC NMR spectrum (600/151 MHz, $CDCl_3$) of **105**.

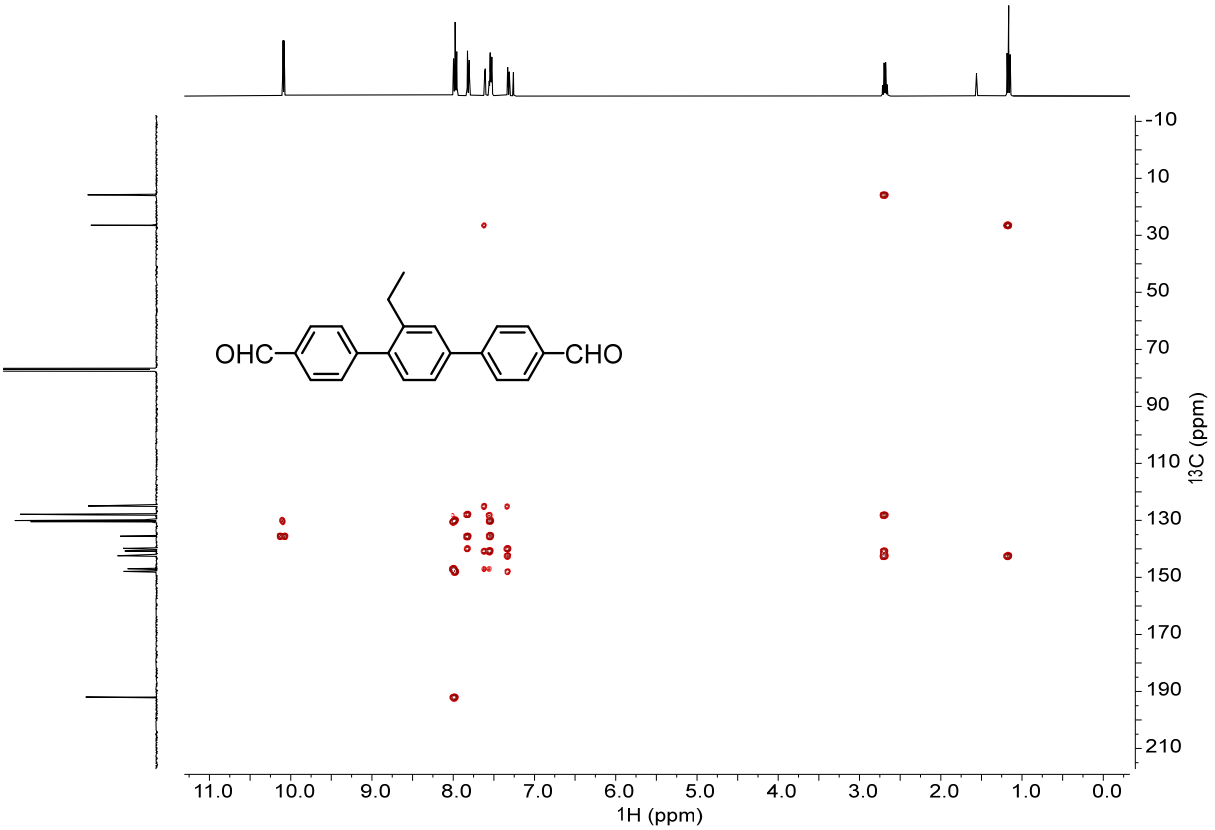

Figure 8.1.45: ^{1}H-^{13}C HMBC NMR spectrum (600/151 MHz, $CDCl_3$) of **105**.

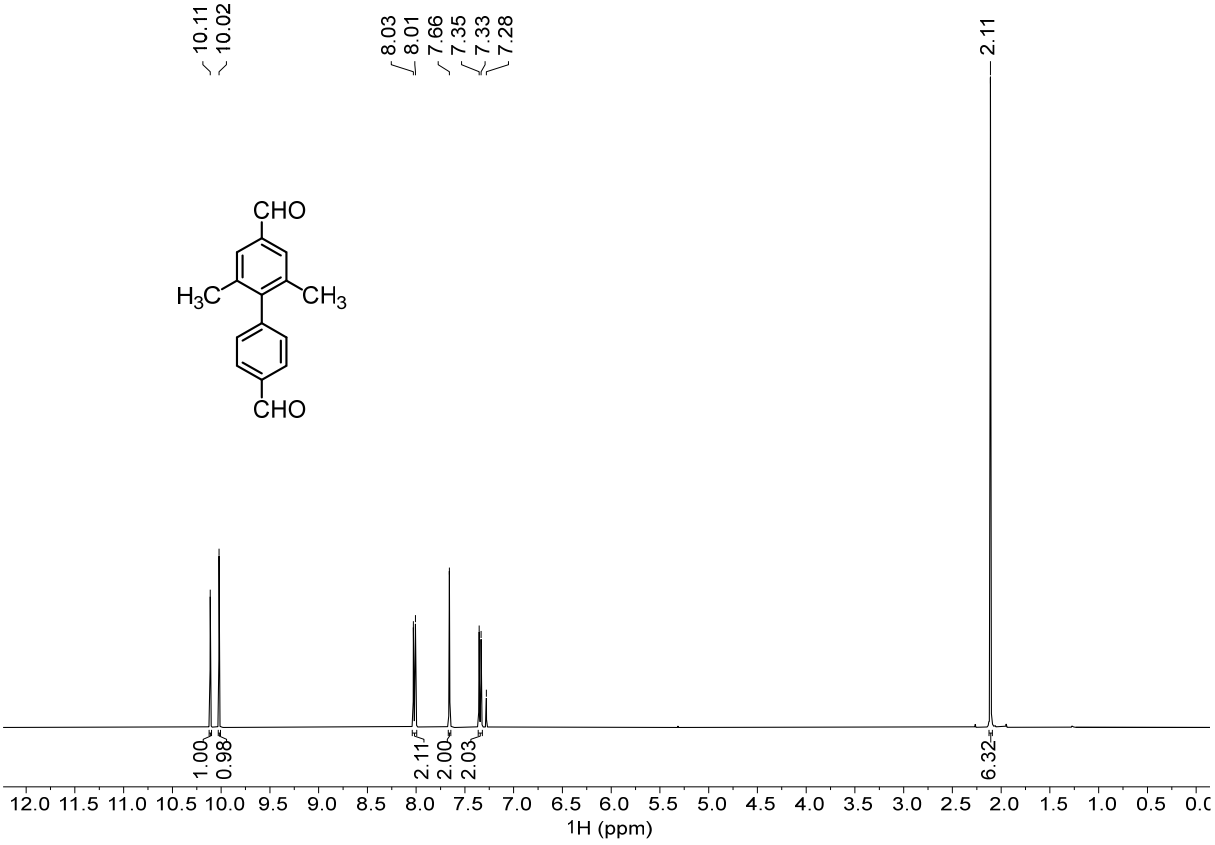

Figure 8.1.46: ^{1}H NMR spectrum (600 MHz, $CDCl_3$) of **108**.

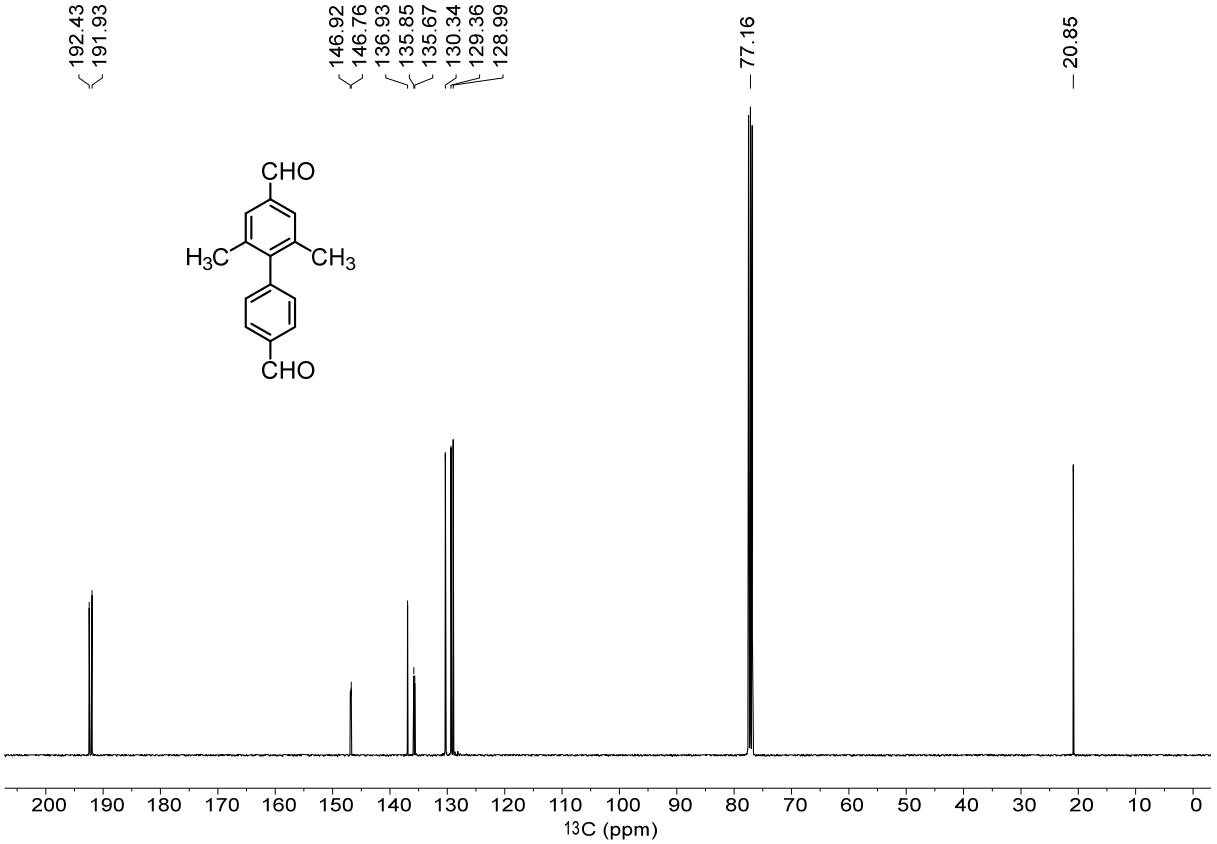

Figure 8.1.47: ^{13}C NMR spectrum (151 MHz, $CDCl_3$) of **108**.

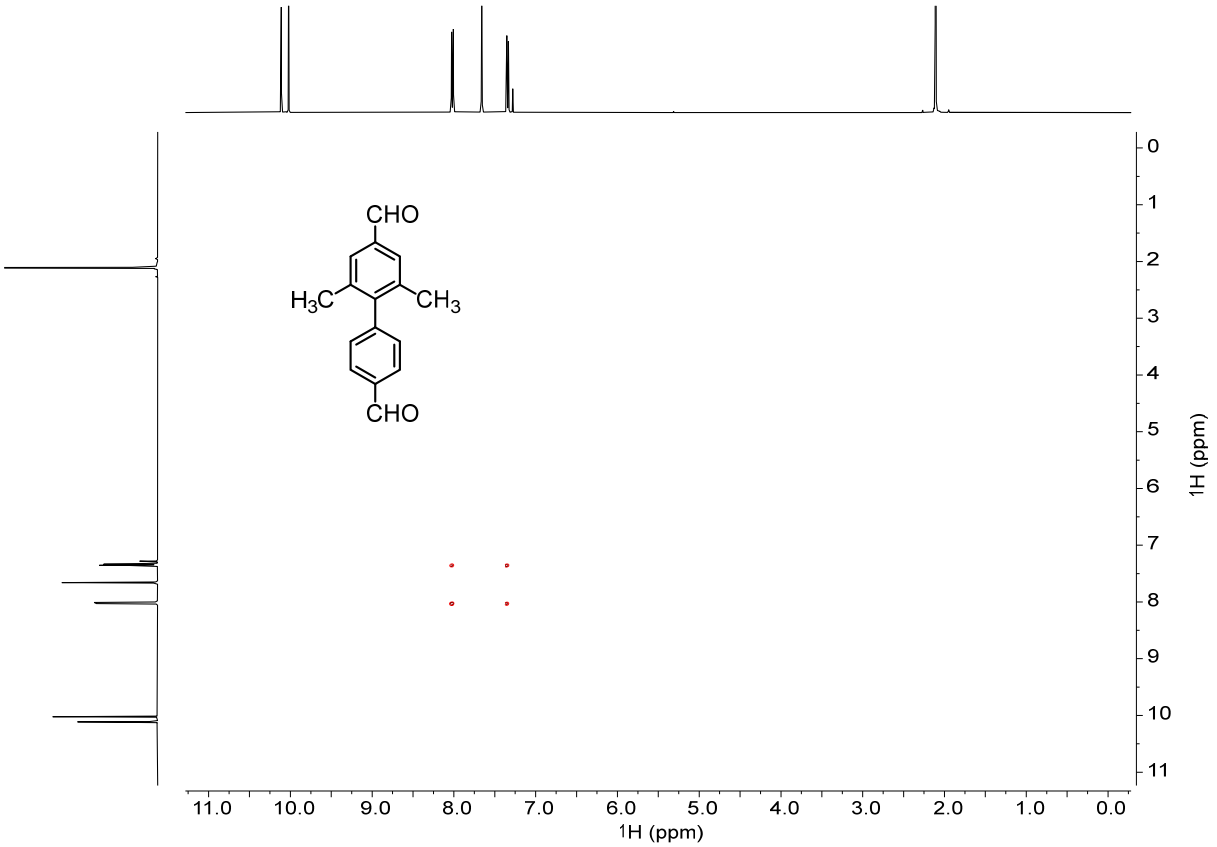

Figure 8.1.48: ^{1}H-^{1}H COSY NMR spectrum (600/600 MHz, $CDCl_3$) of **108**.

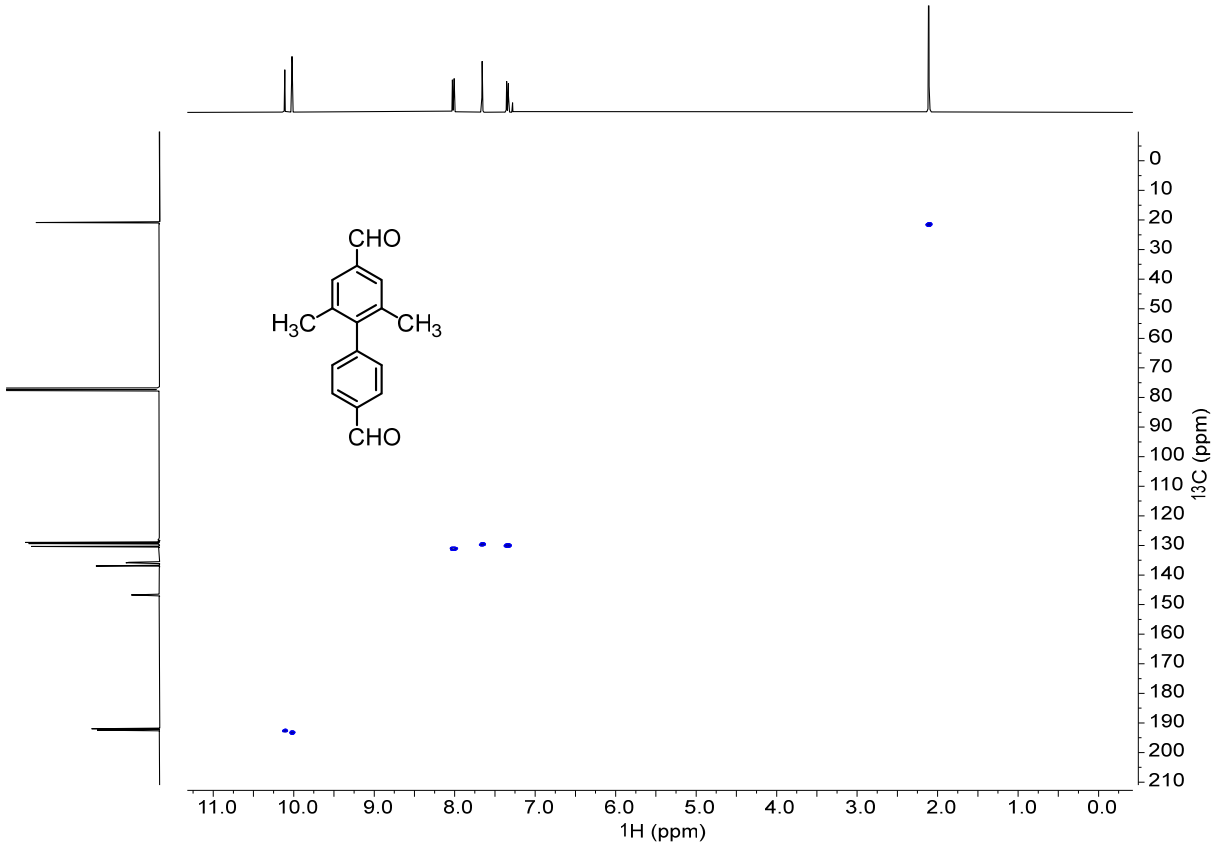

Figure 8.1.49: ^{1}H-^{13}C HSQC NMR spectrum (600/151 MHz, $CDCl_3$) of **108**.

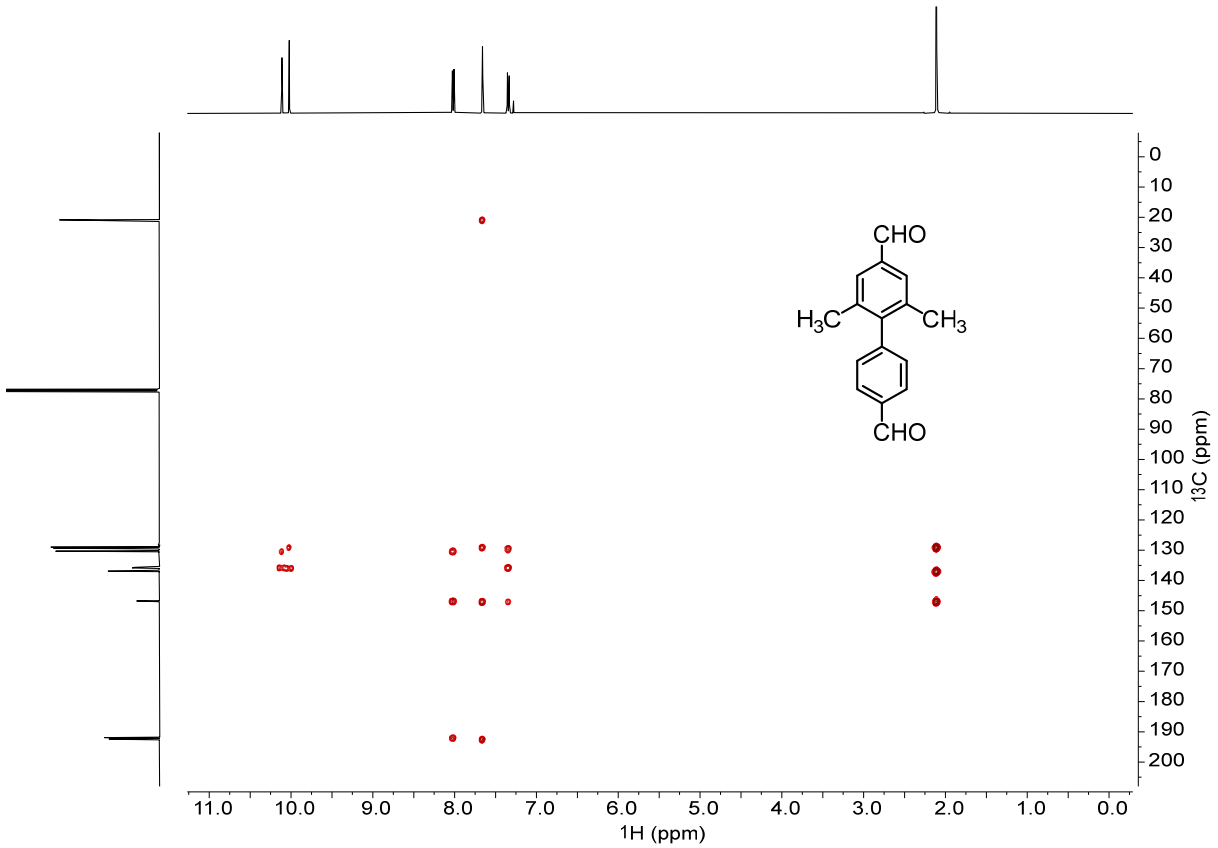

Figure 8.1.50: ^{1}H-^{13}C HMBC NMR spectrum (600/151 MHz, $CDCl_3$) of **108**.

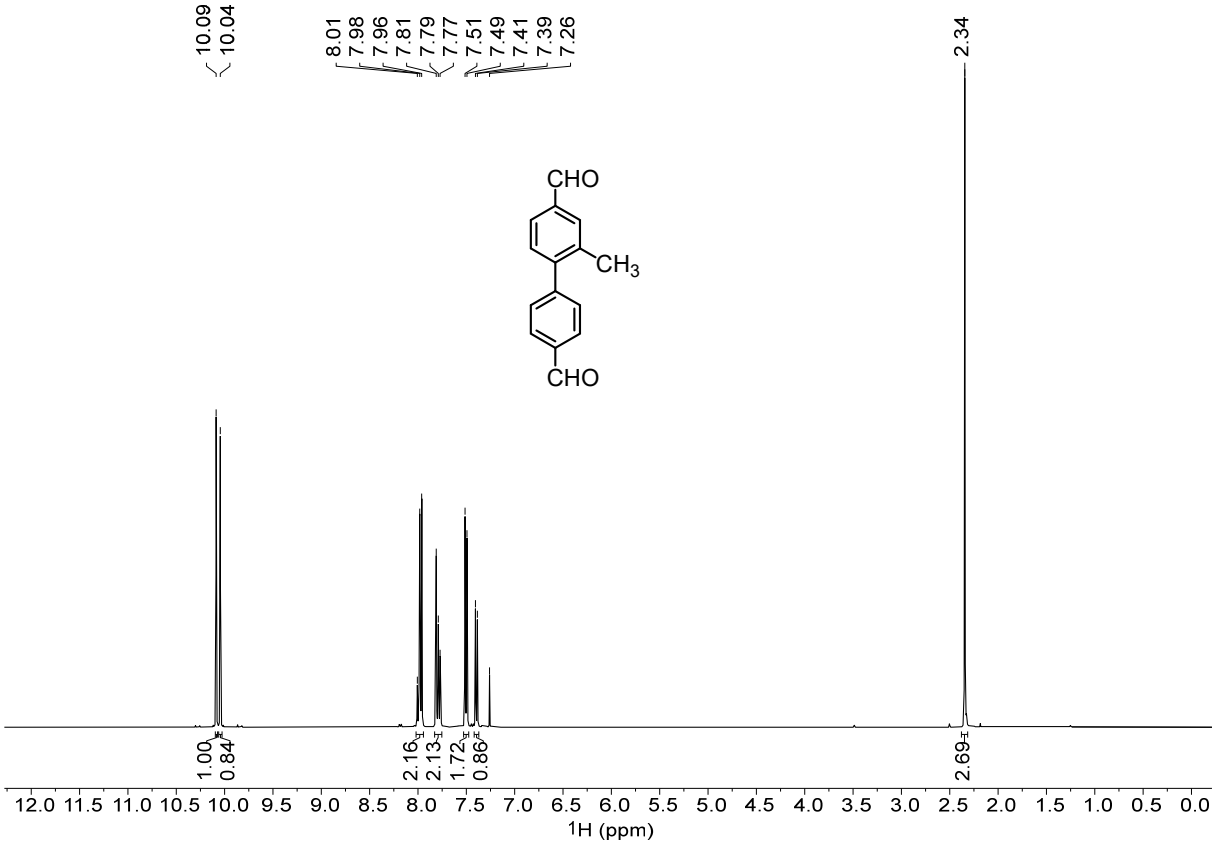

Figure 8.1.51: ^{1}H NMR spectrum (600 MHz, $CDCl_3$) of **109**.

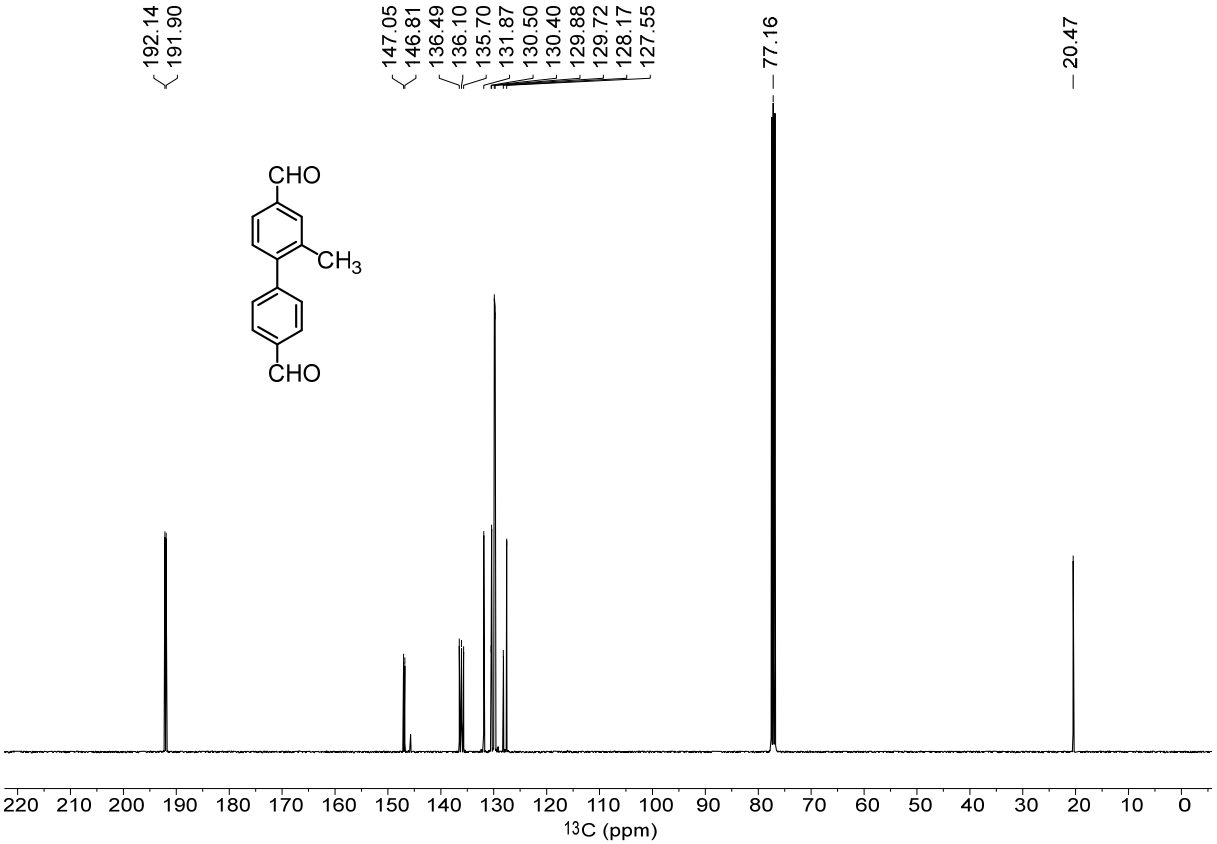

Figure 8.1.52: ^{13}C NMR spectrum (151 MHz, $CDCl_3$) of **109**.

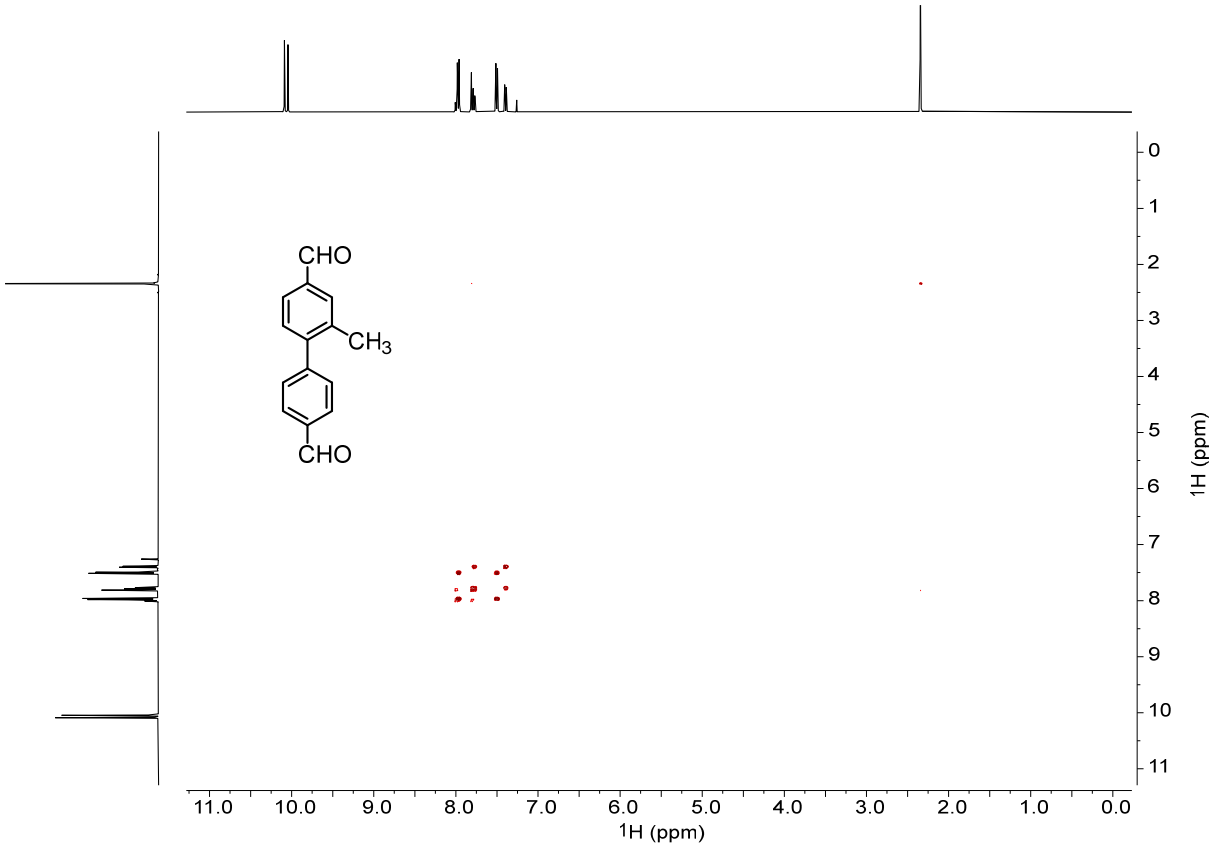

Figure 8.1.53: ^{1}H-^{1}H COSY NMR spectrum (600/600 MHz, $CDCl_3$) of **109**.

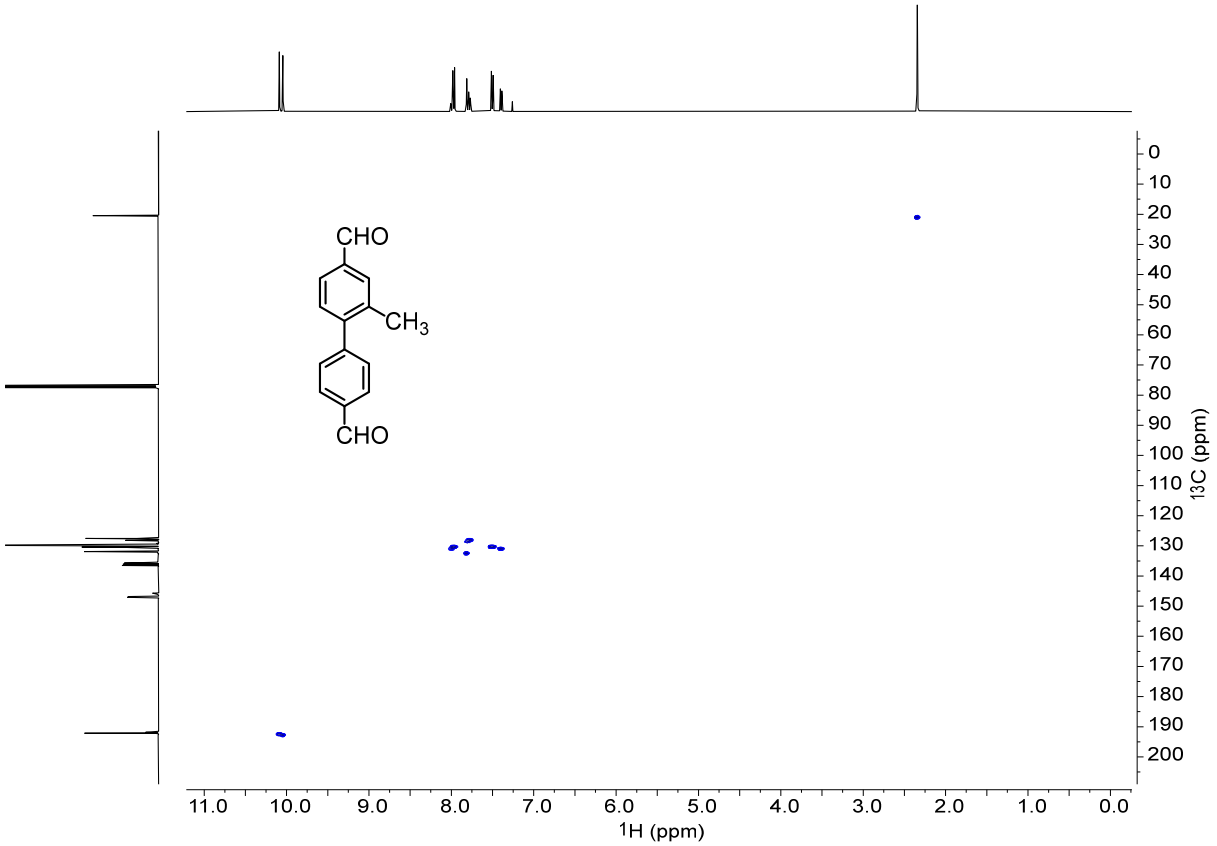

Figure 8.1.54: ^{1}H-^{13}C HSQC NMR spectrum (600/151 MHz, $CDCl_3$) of **109**.

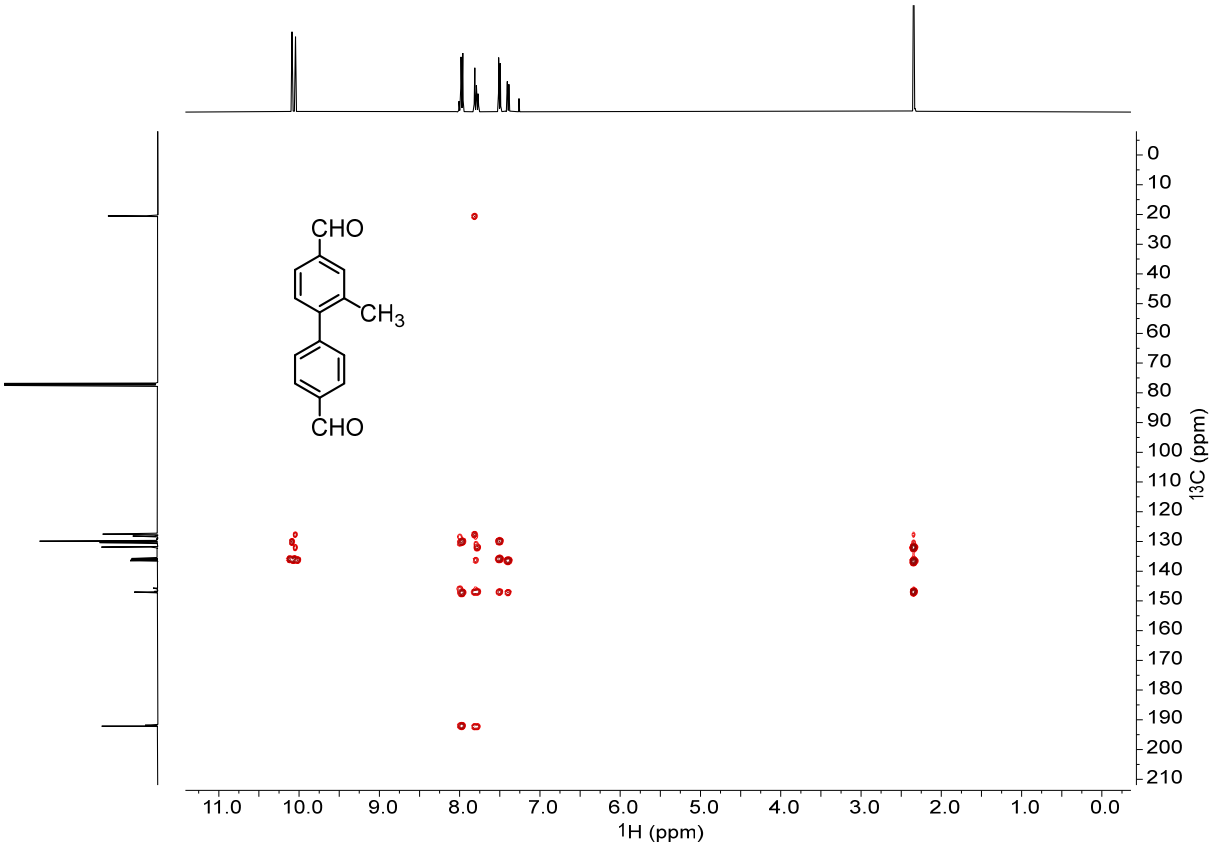

Figure 8.1.55: ^{1}H-^{13}C HMBC NMR spectrum (600/151 MHz, $CDCl_3$) of **109**.

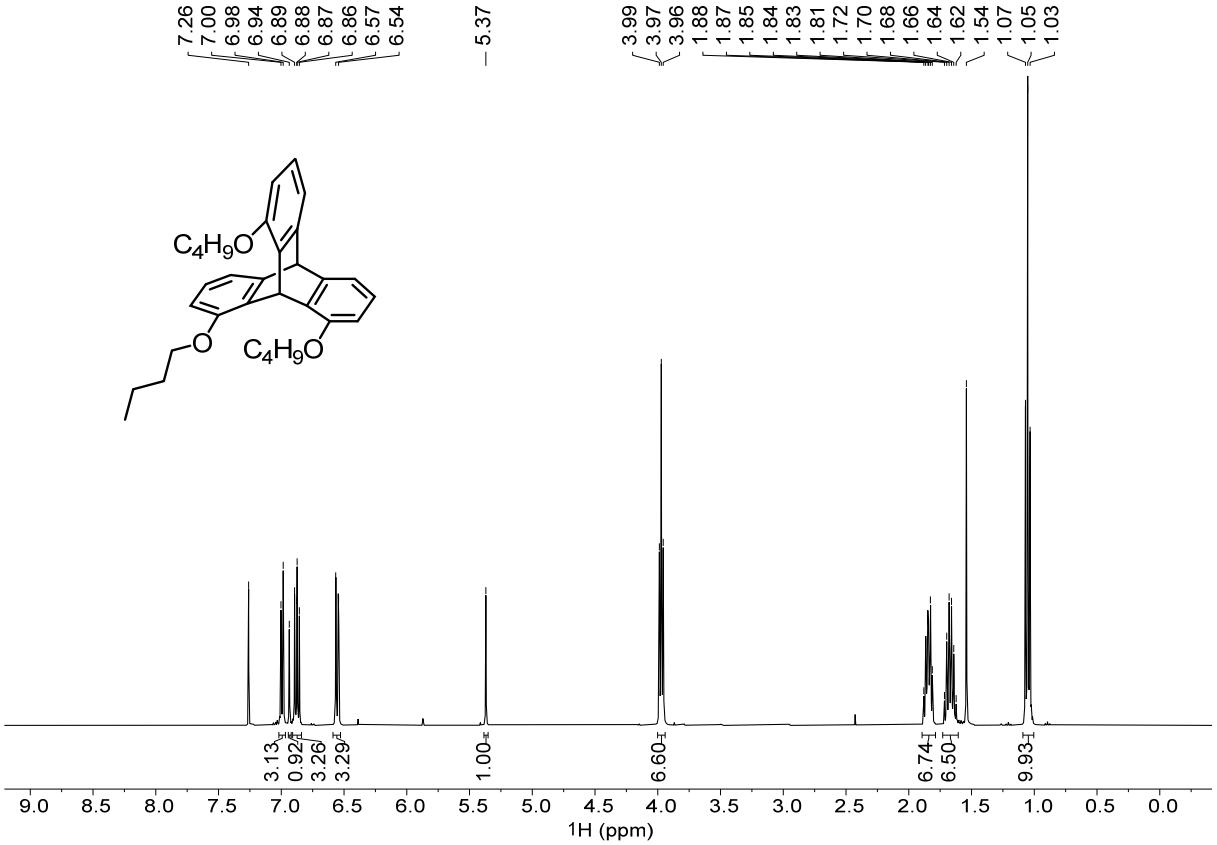

Figure 8.1.56: ^{1}H NMR spectrum (600 MHz, $CDCl_3$) of **110**.

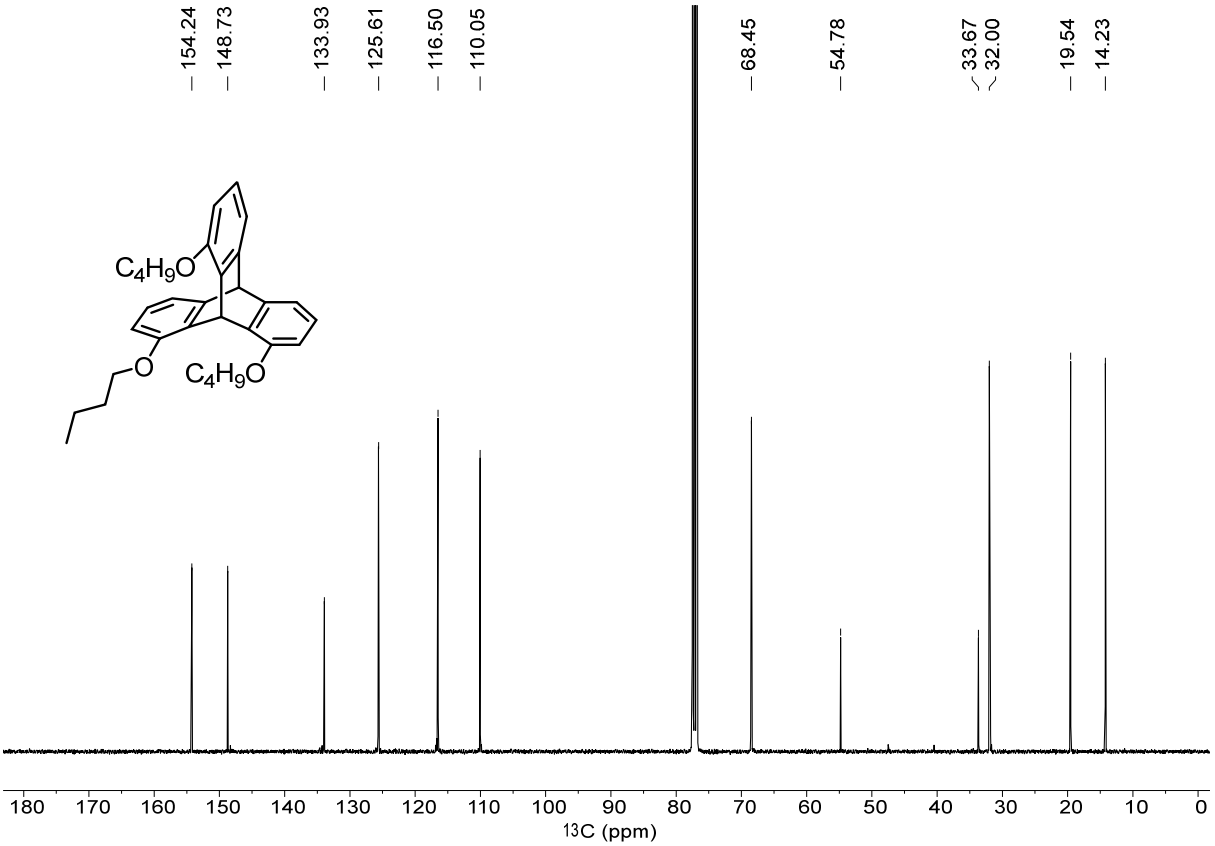

Figure 8.1.57: ^{13}C NMR spectrum (151 MHz, $CDCl_3$) of **110**.

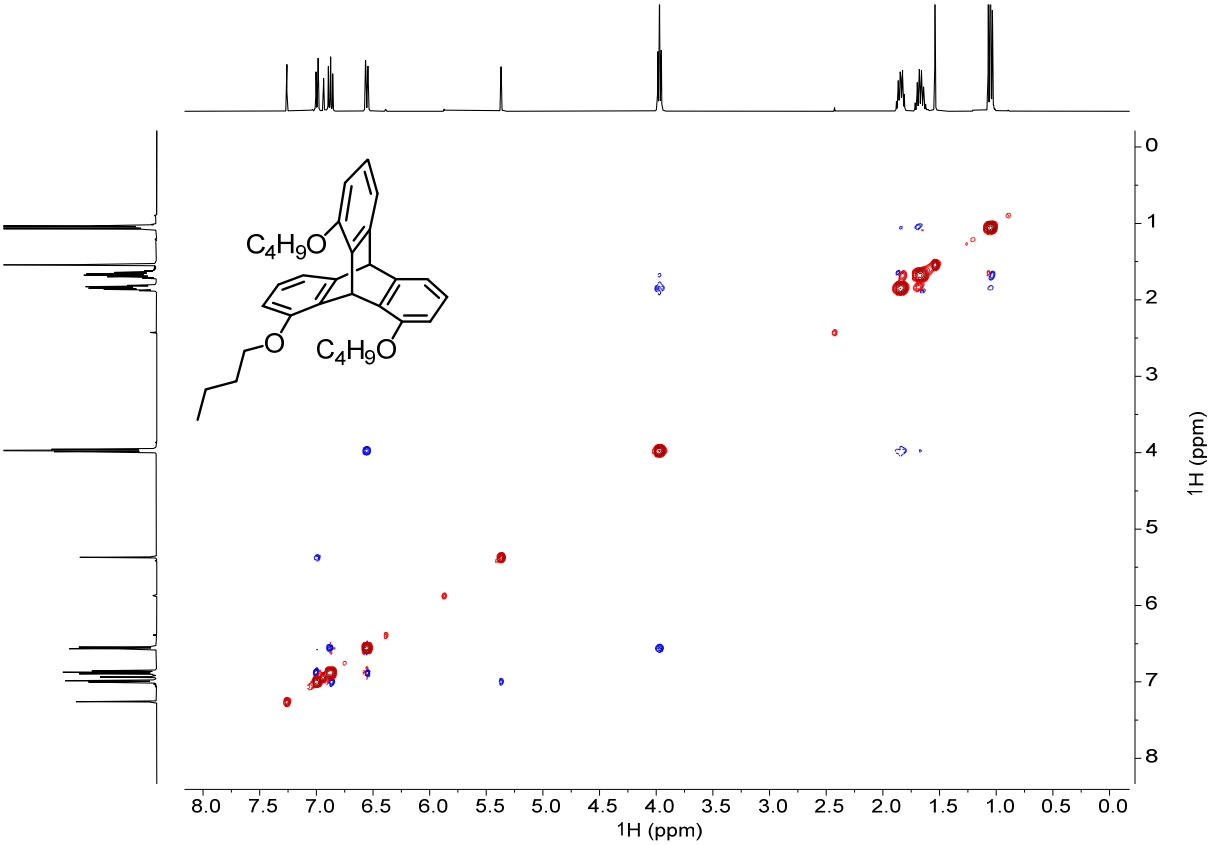

Figure 8.1.58: ^{1}H-^{1}H COSY NMR spectrum (600/600 MHz, $CDCl_3$) of **110**.

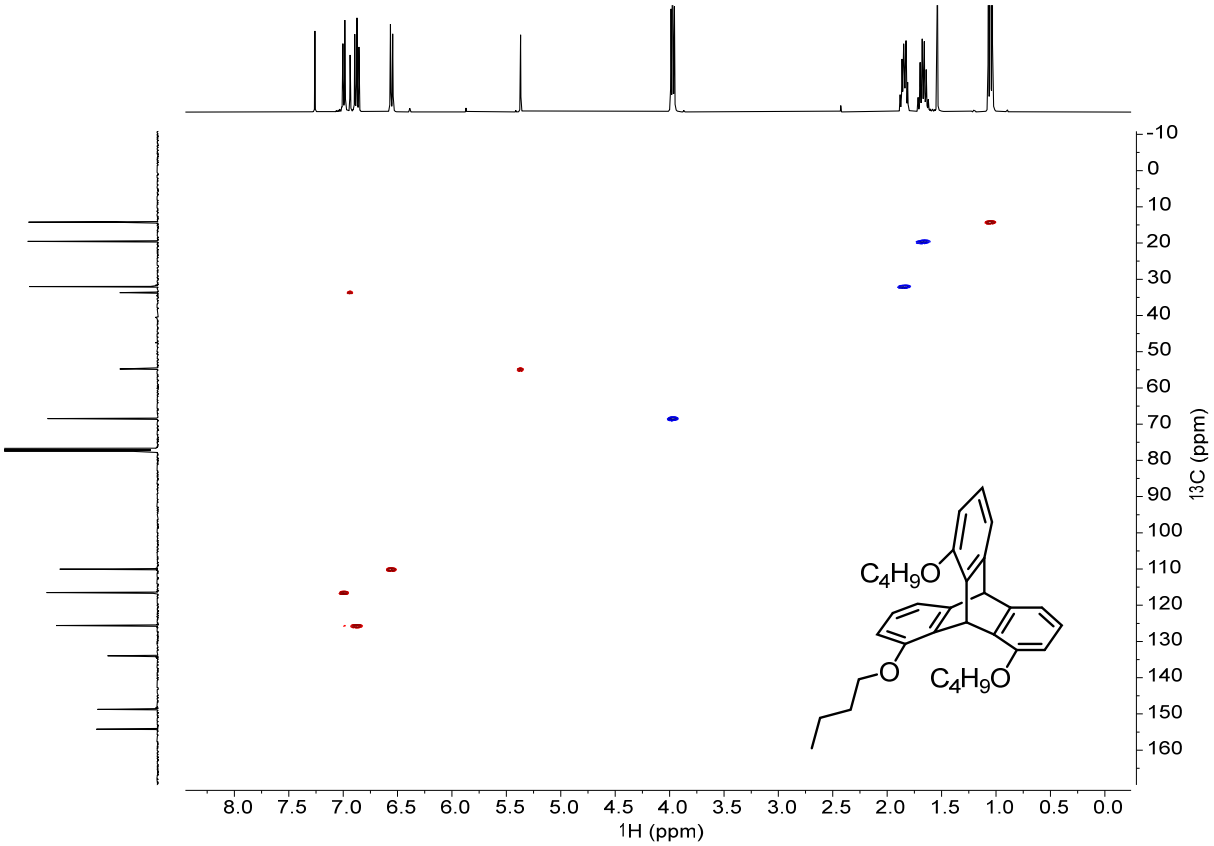

Figure 8.1.59: ^{1}H-^{13}C HSQC NMR spectrum (600/151 MHz, $CDCl_3$) of **110**.

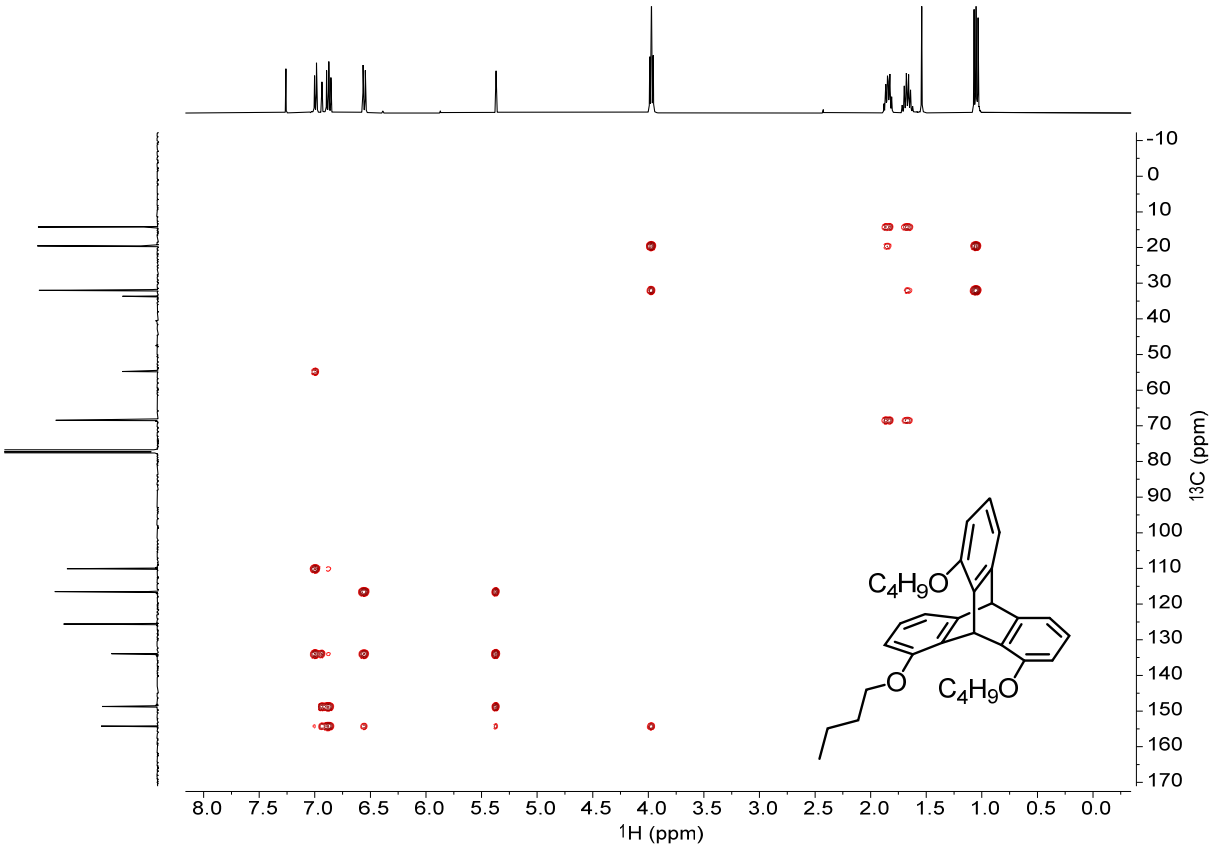

Figure 8.1.60: ^{1}H-^{13}C HMBC NMR spectrum (600/151 MHz, $CDCl_3$) of **110**.

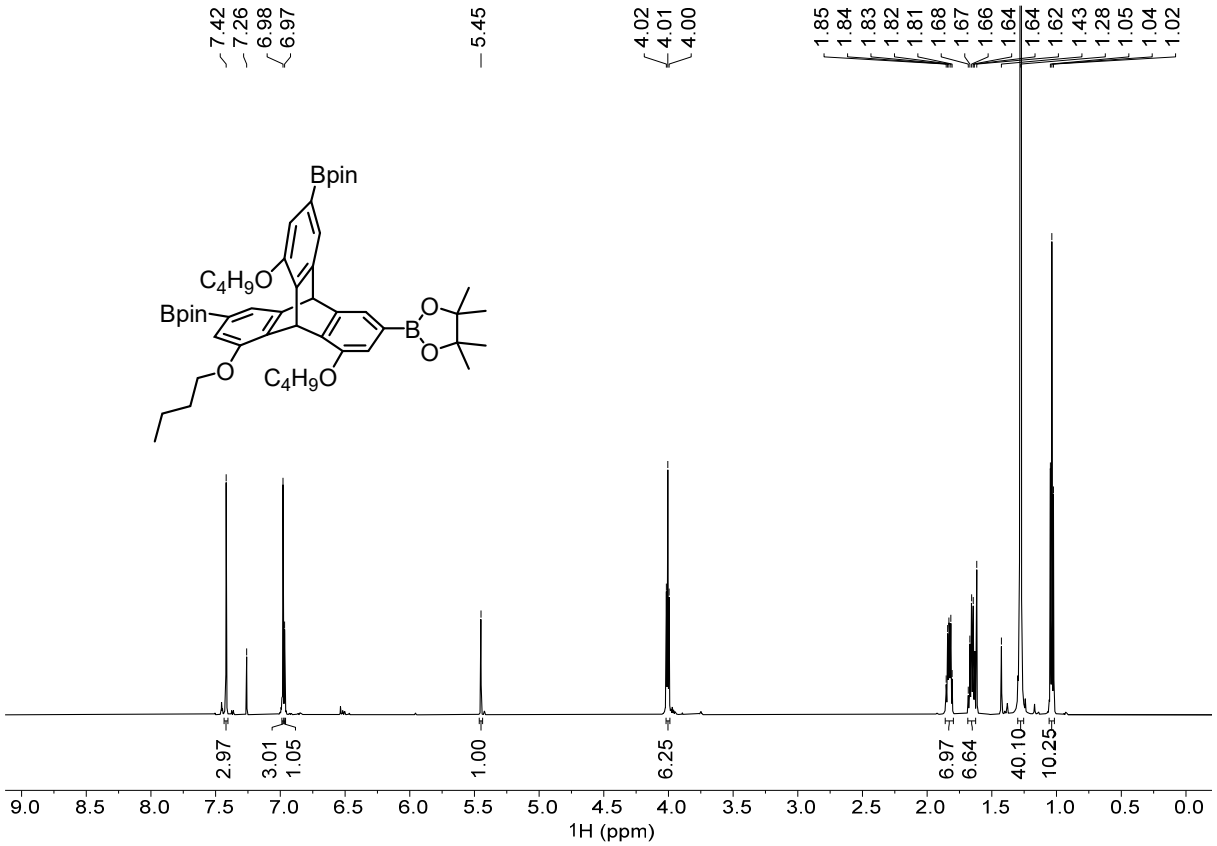

Figure 8.1.61: ^{1}H NMR spectrum (600 MHz, $CDCl_3$) of **111**.

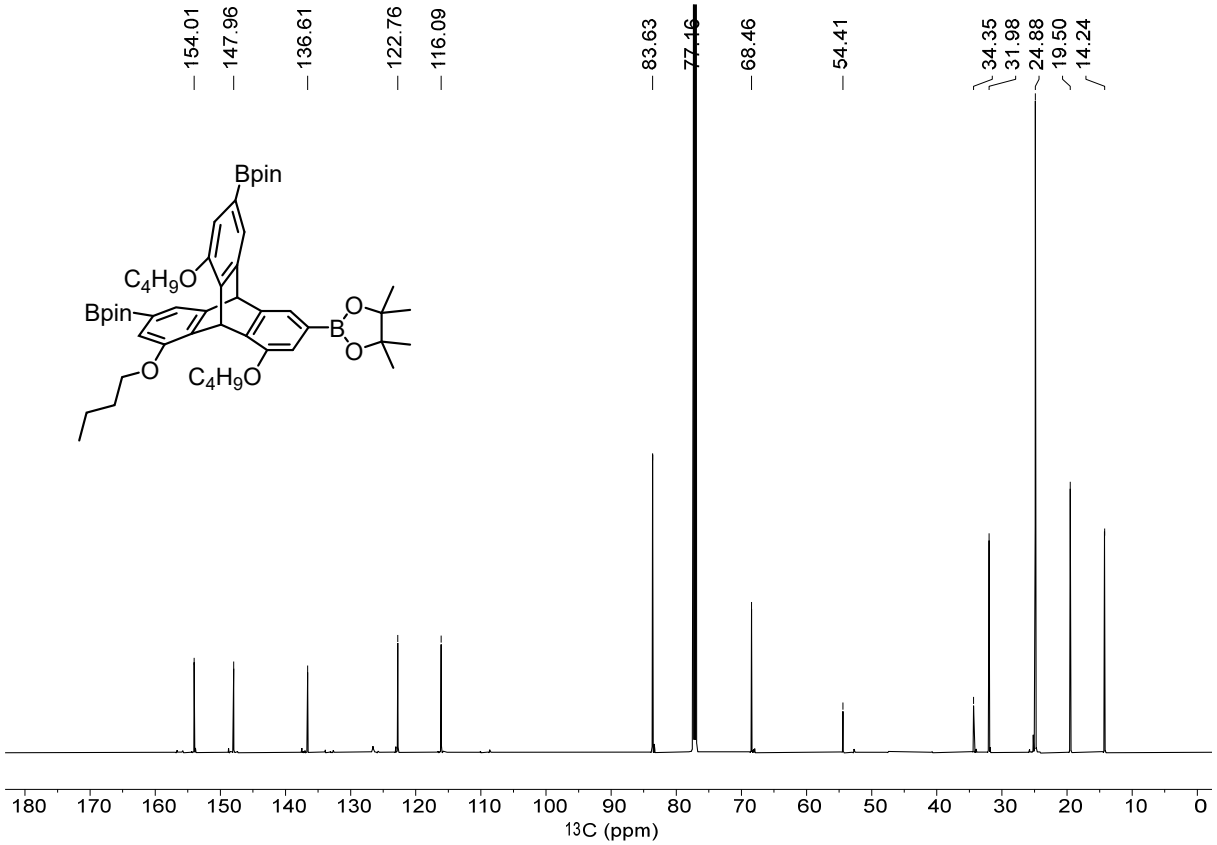

Figure 8.1.62: ^{13}C NMR spectrum (151 MHz, $CDCl_3$) of **111**.

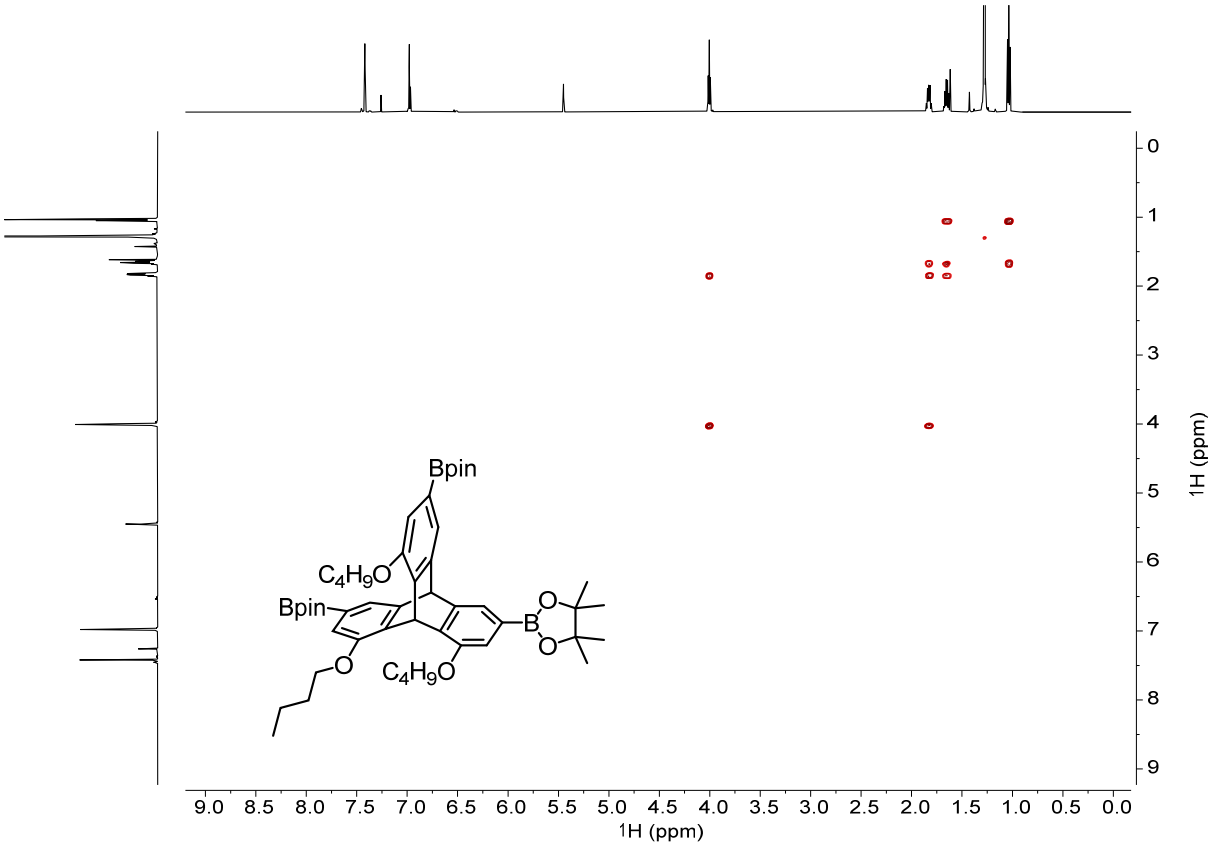

Figure 8.1.63: ^{1}H-^{1}H COSY NMR spectrum (600/600 MHz, $CDCl_3$) of **111**.

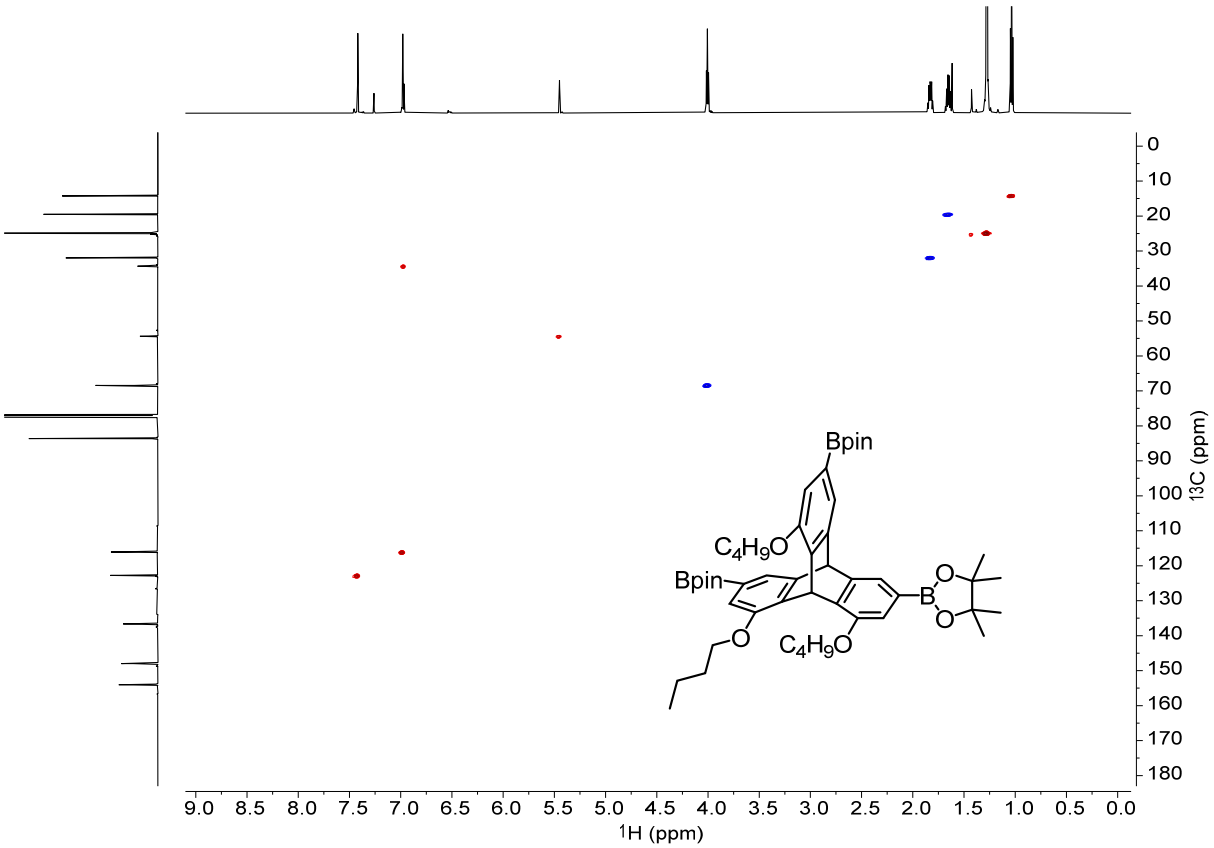

Figure 8.1.64: ^{1}H-^{13}C HSQC NMR spectrum (600/151 MHz, $CDCl_3$) of **111**.

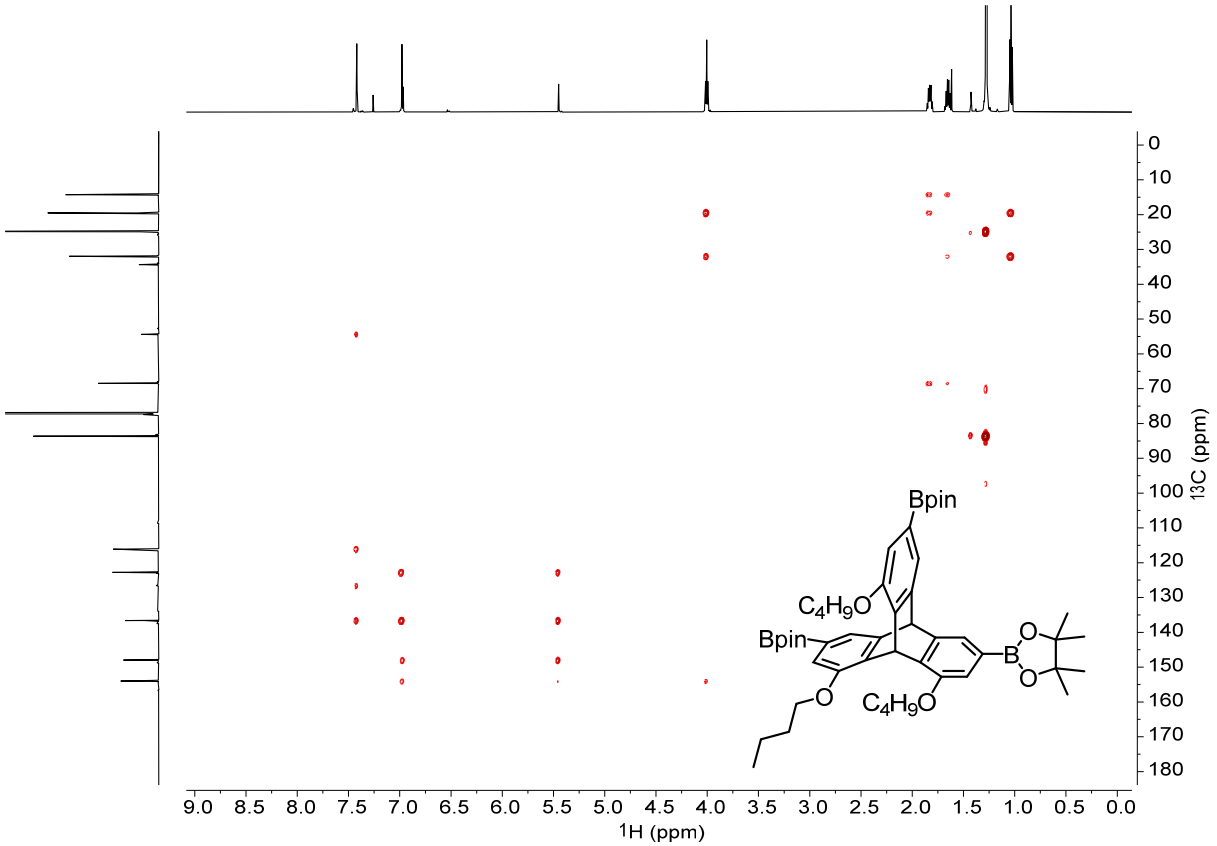

Figure 8.1.65: ^{1}H-^{13}C HMBC NMR spectrum (600/151 MHz, $CDCl_3$) of **111**.

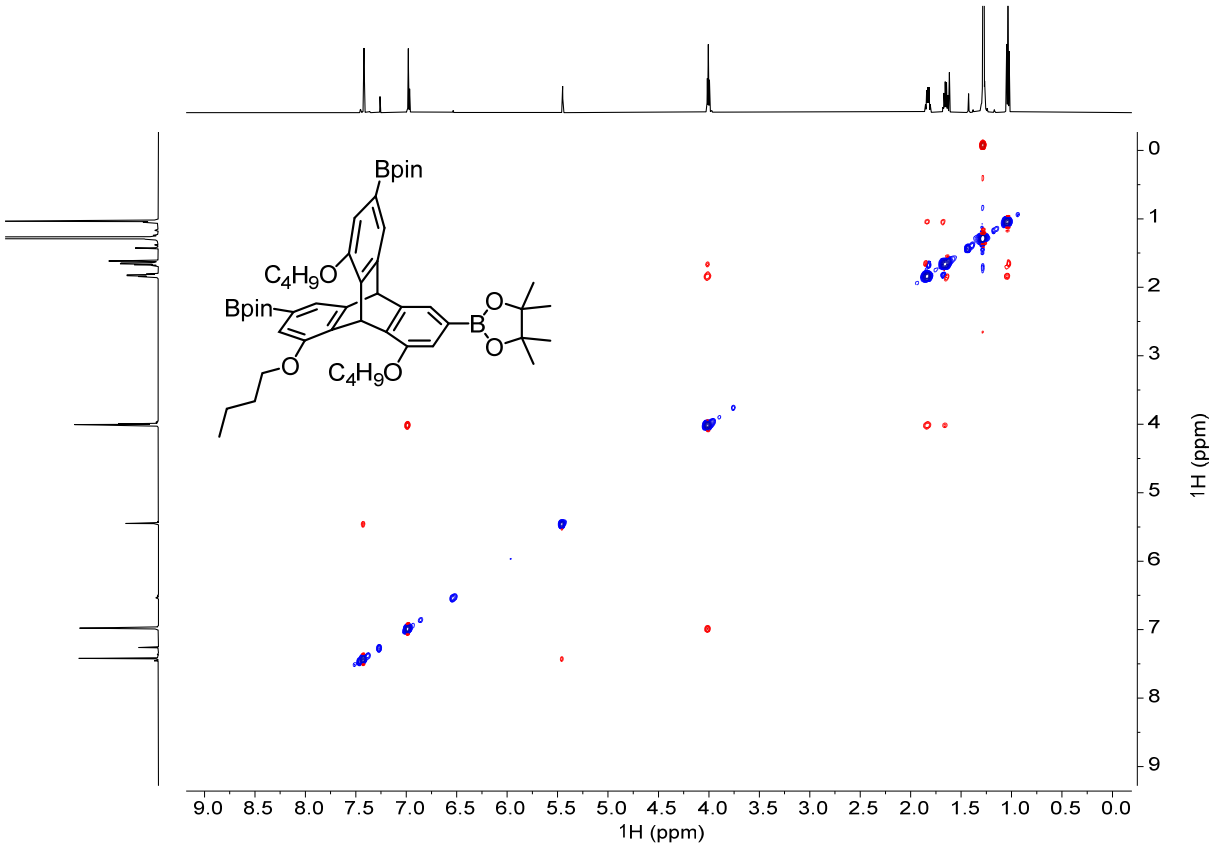

Figure 8.1.66: ^{1}H-^{1}H NOESY NMR spectrum (600/600 MHz, $CDCl_3$) of **111**.

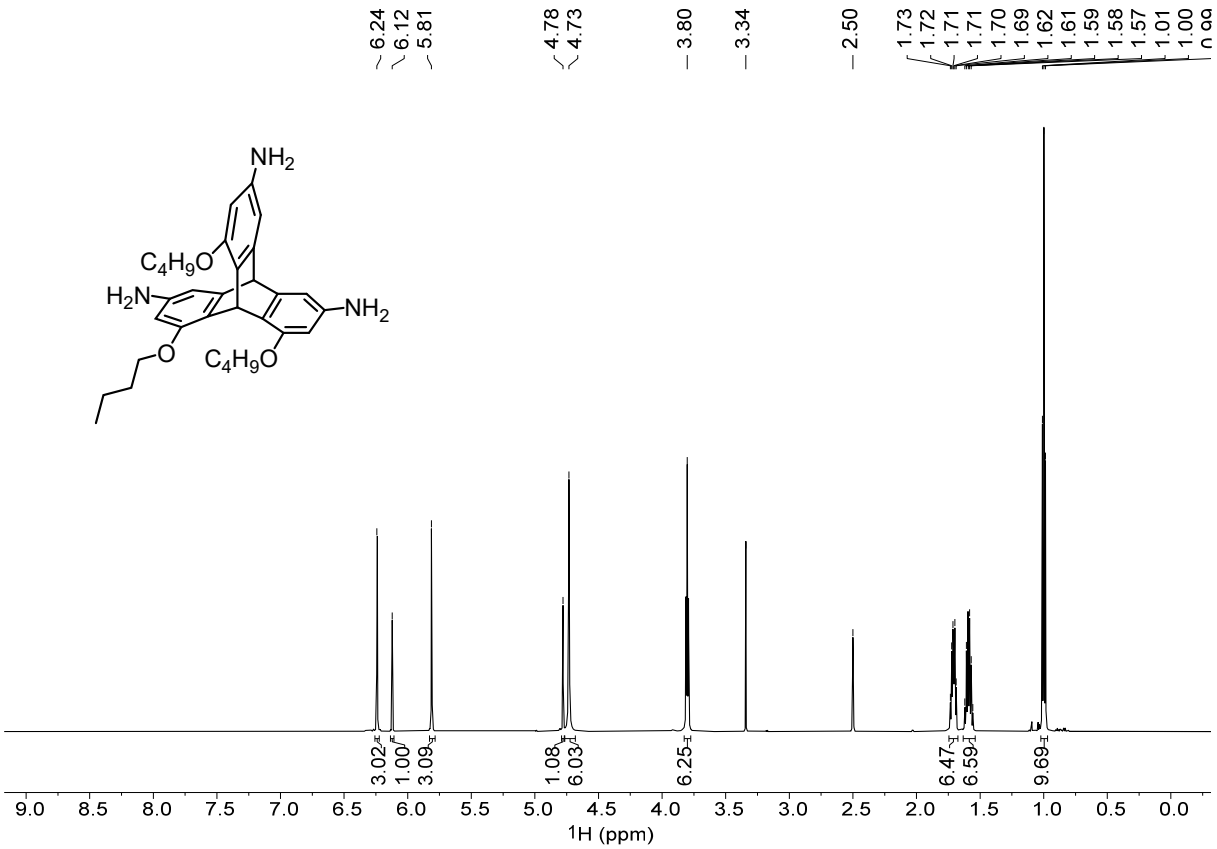

Figure 8.1.67: ^{1}H NMR spectrum (600 MHz, DMSO-*d*$_6$) of **112**.

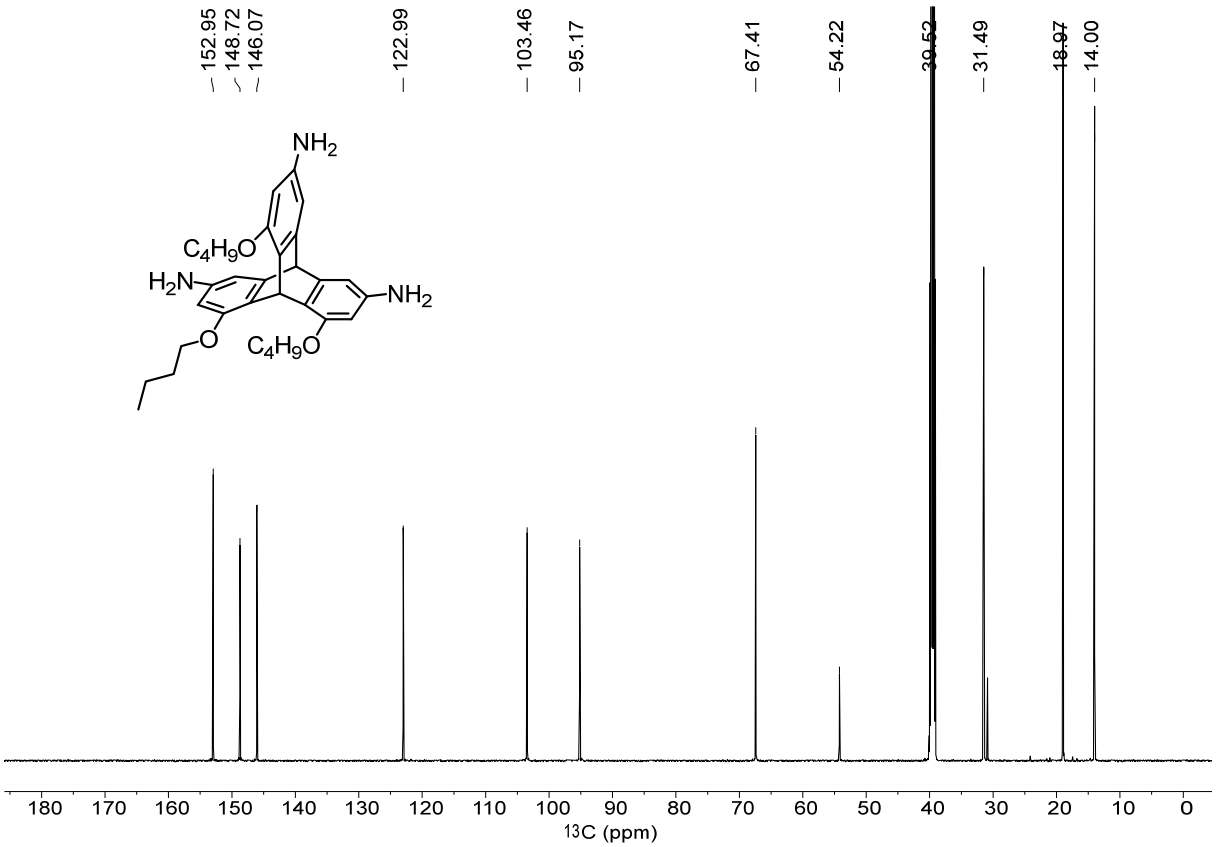

Figure 8.1.68: ^{13}C NMR spectrum (151 MHz, DMSO-*d*$_6$) of **112**.

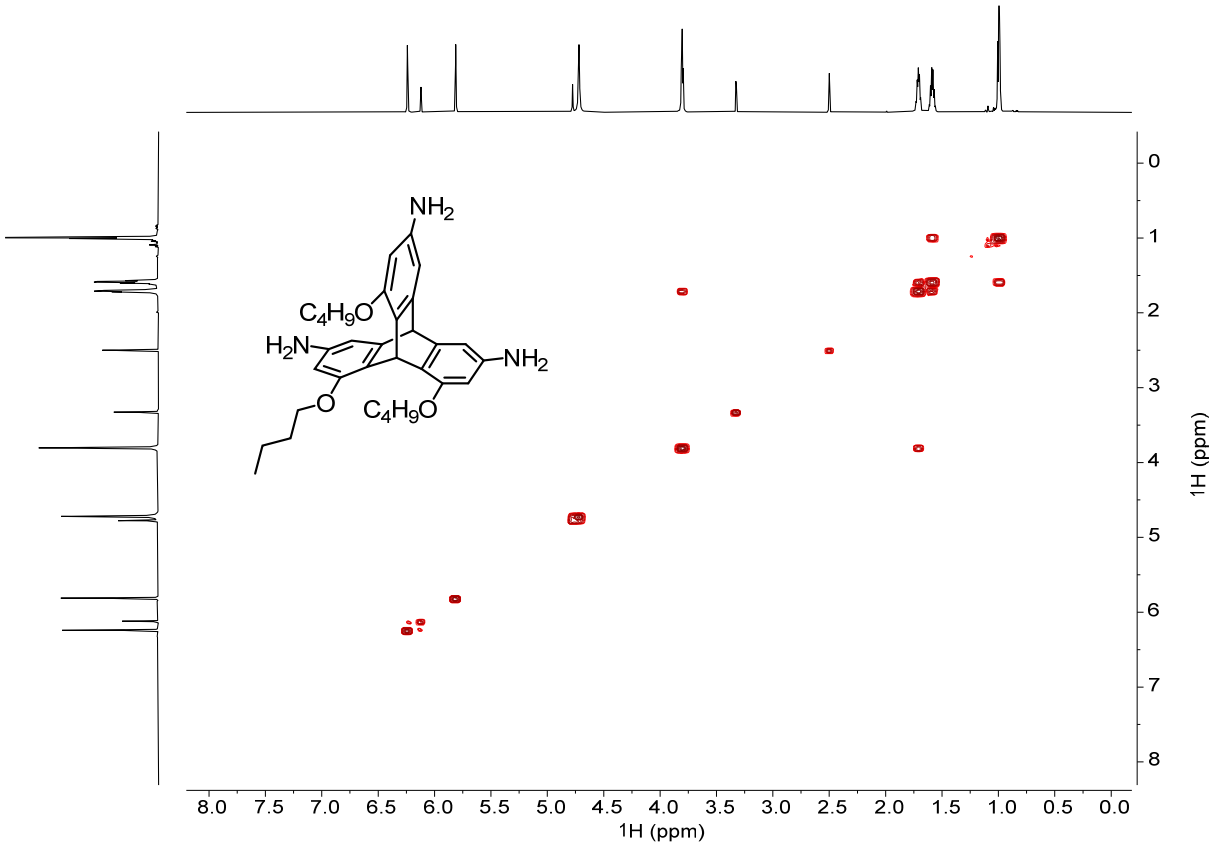

Figure 8.1.69: ^{1}H-^{1}H COSY NMR spectrum (600/600 MHz, DMSO-d_6) of **112**.

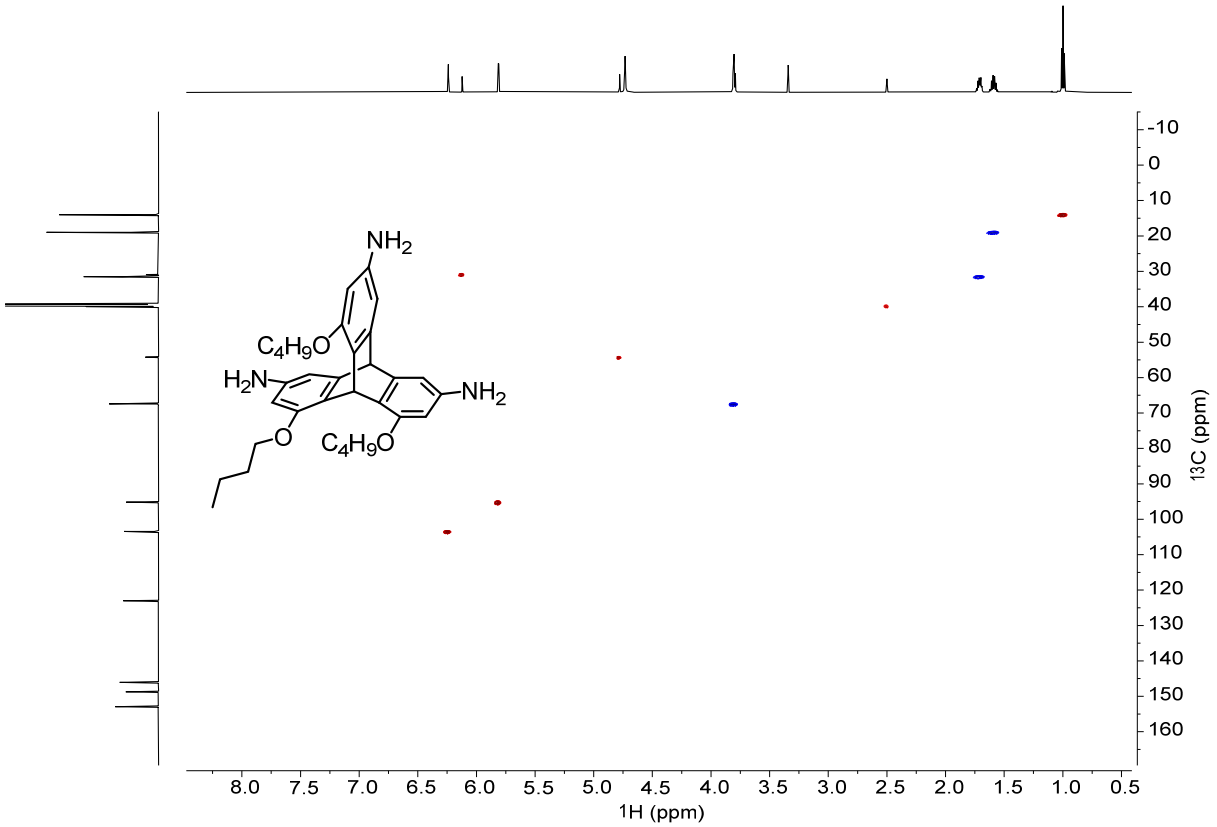

Figure 8.1.70: ^{1}H-^{13}C HSQC NMR spectrum (600/151 MHz, DMSO-d_6) of **112**.

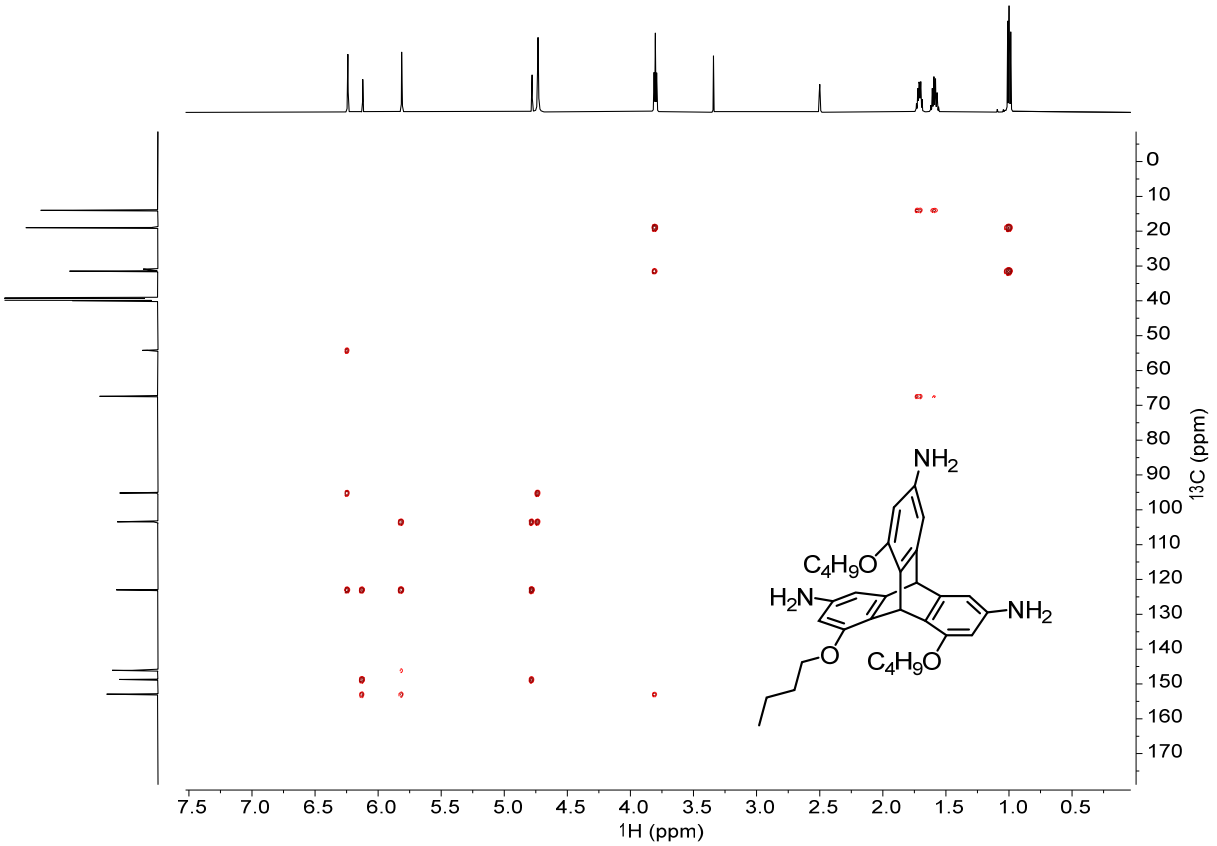

Figure 8.1.71: ^{1}H-^{13}C HMBC NMR spectrum (600/151 MHz, DMSO-d_6) of **112**.

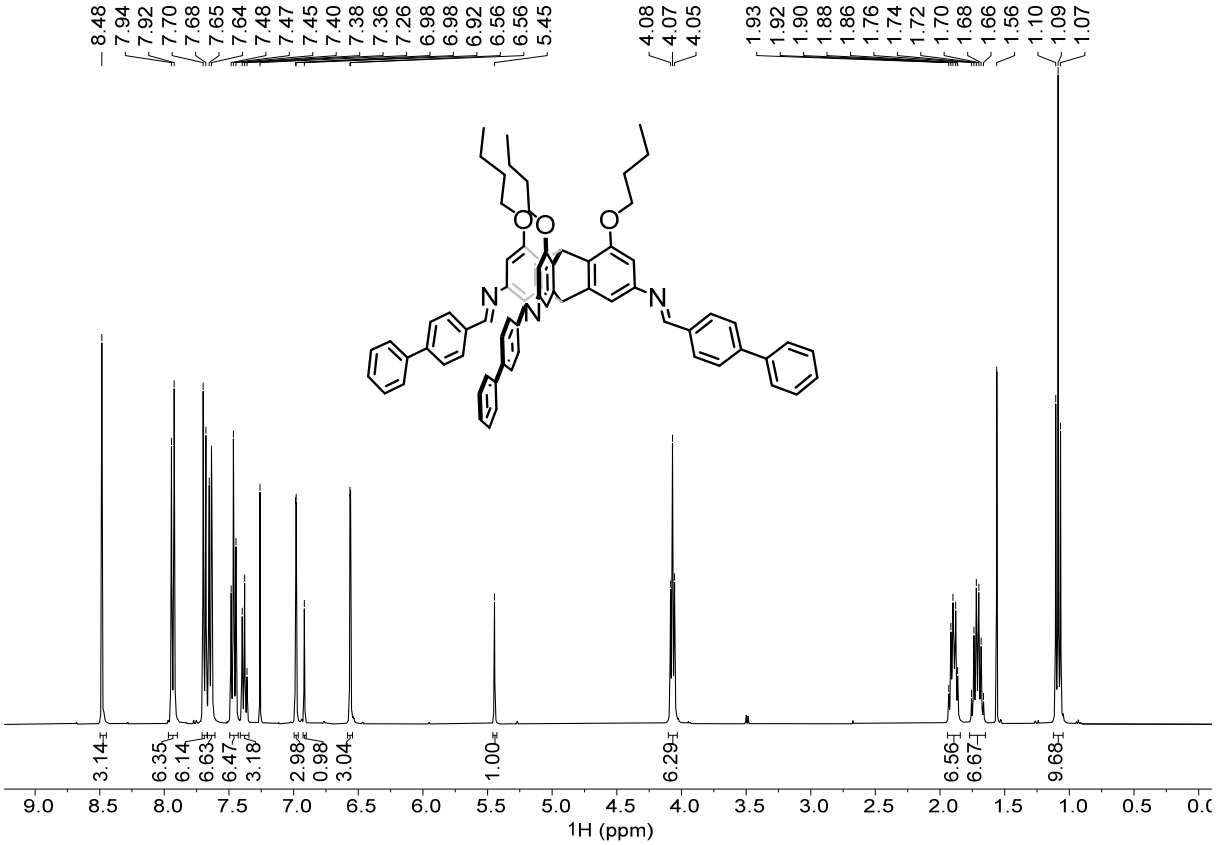

Figure 8.1.72: ^{1}H NMR spectrum (600 MHz, $CDCl_3$) of **115**.

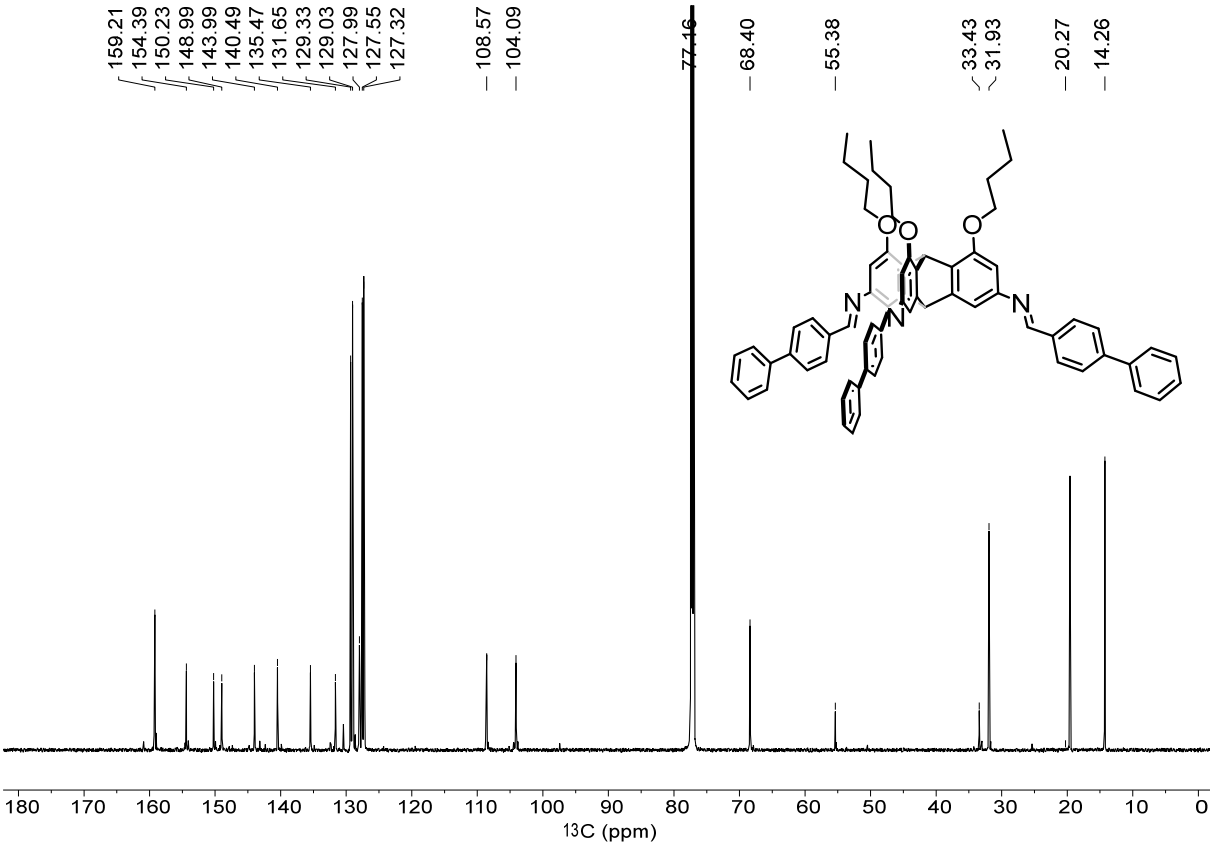

Figure 8.1.73: ^{13}C NMR spectrum (151 MHz, $CDCl_3$) of **115**.

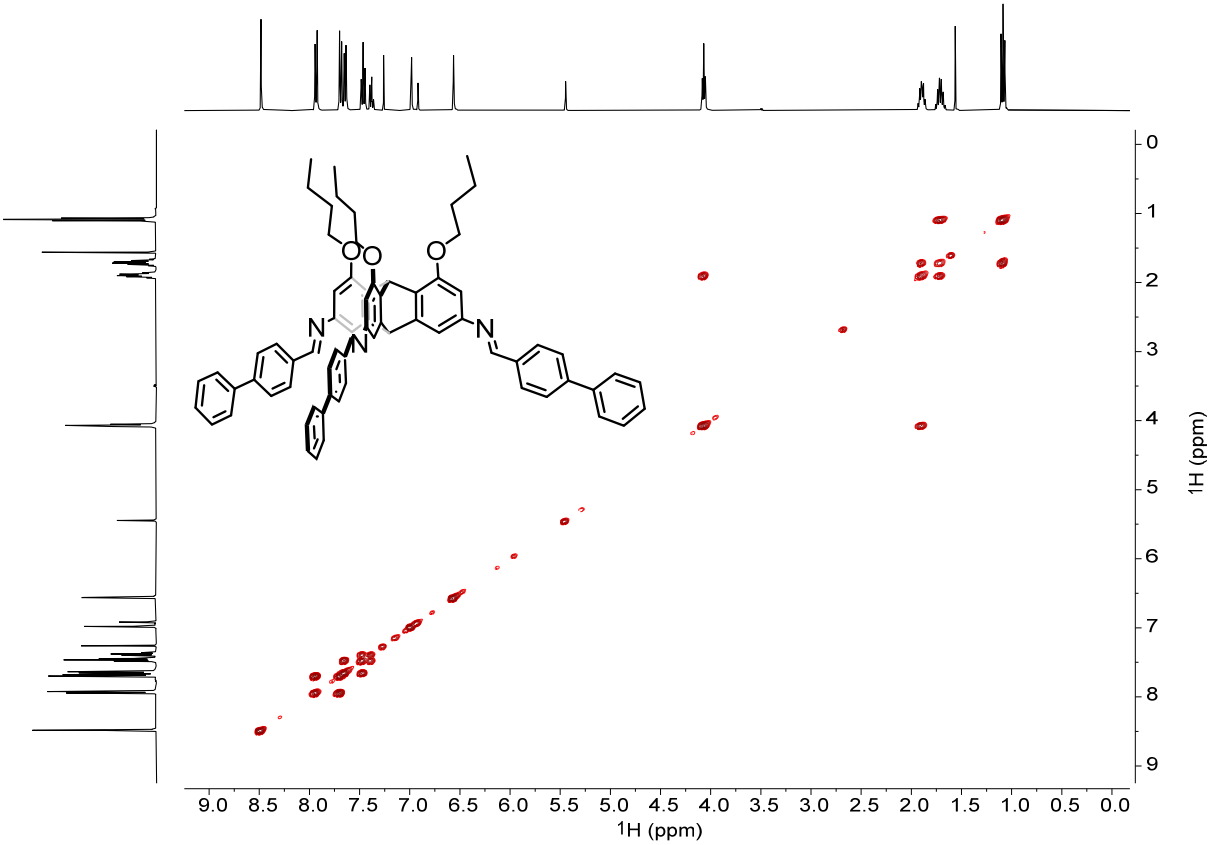

Figure 8.1.74: ^{1}H-^{1}H COSY NMR spectrum (600/600 MHz, $CDCl_3$) of **115**.

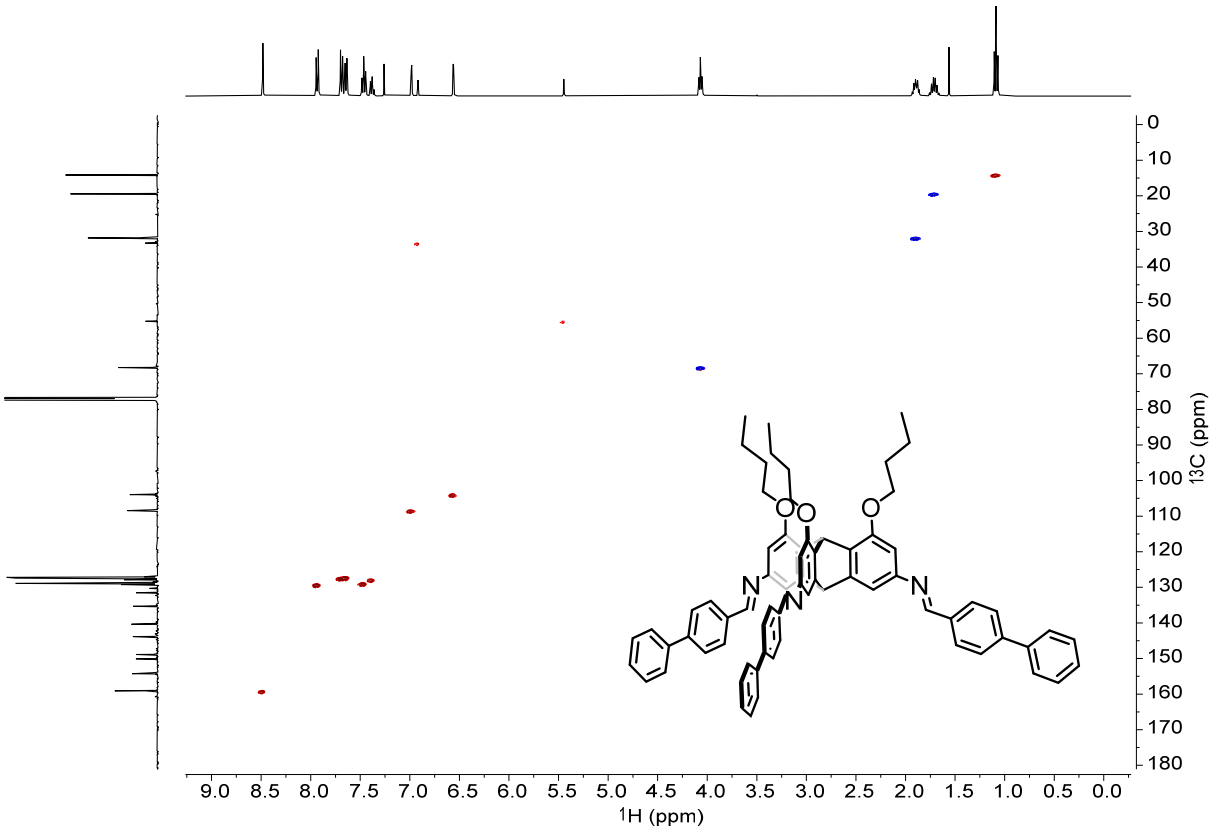

Figure 8.1.75: ^{1}H-^{13}C HSQC NMR spectrum (600/151 MHz, $CDCl_3$) of **115**.

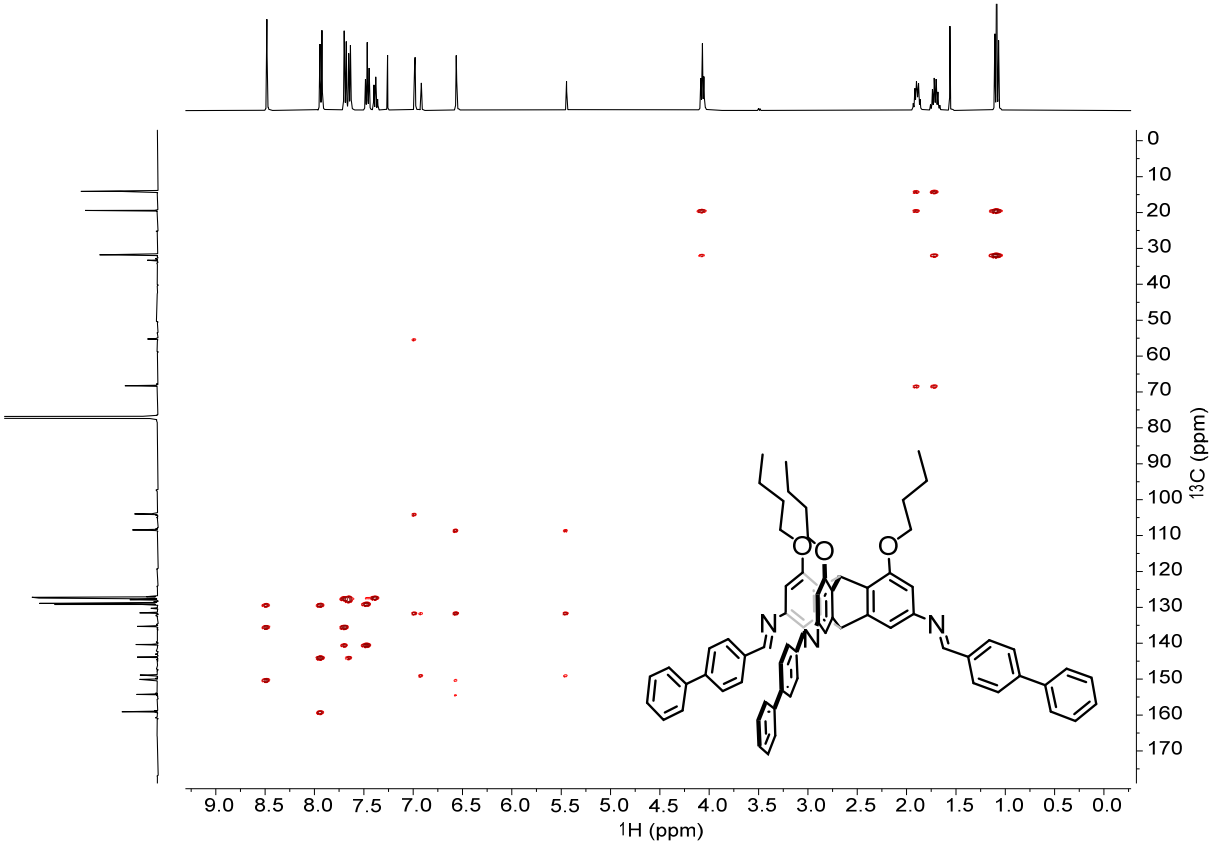

Figure 8.1.76: ^{1}H-^{13}C HMBC NMR spectrum (600/151 MHz, $CDCl_3$) of **115**.

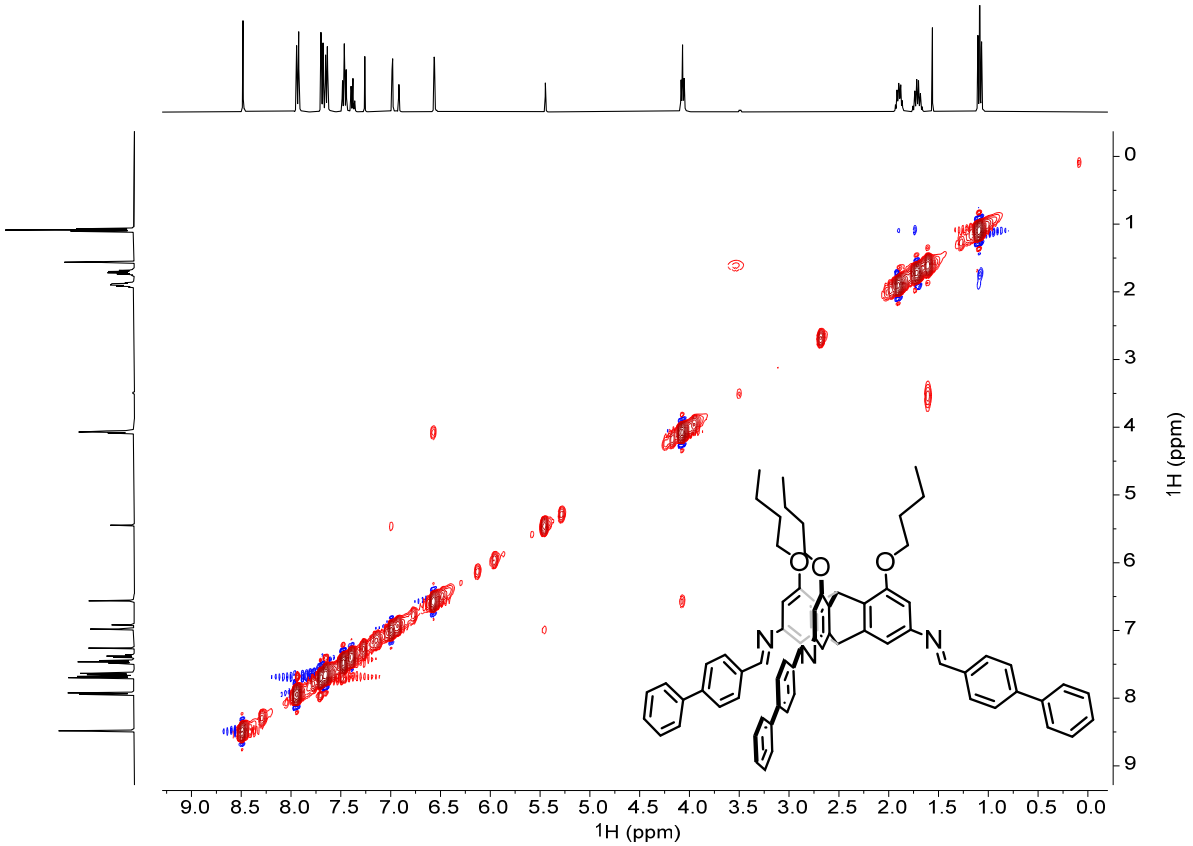

Figure 8.1.77: ^{1}H-^{1}H NOESY NMR spectrum (600/600 MHz, $CDCl_3$) of **115**.

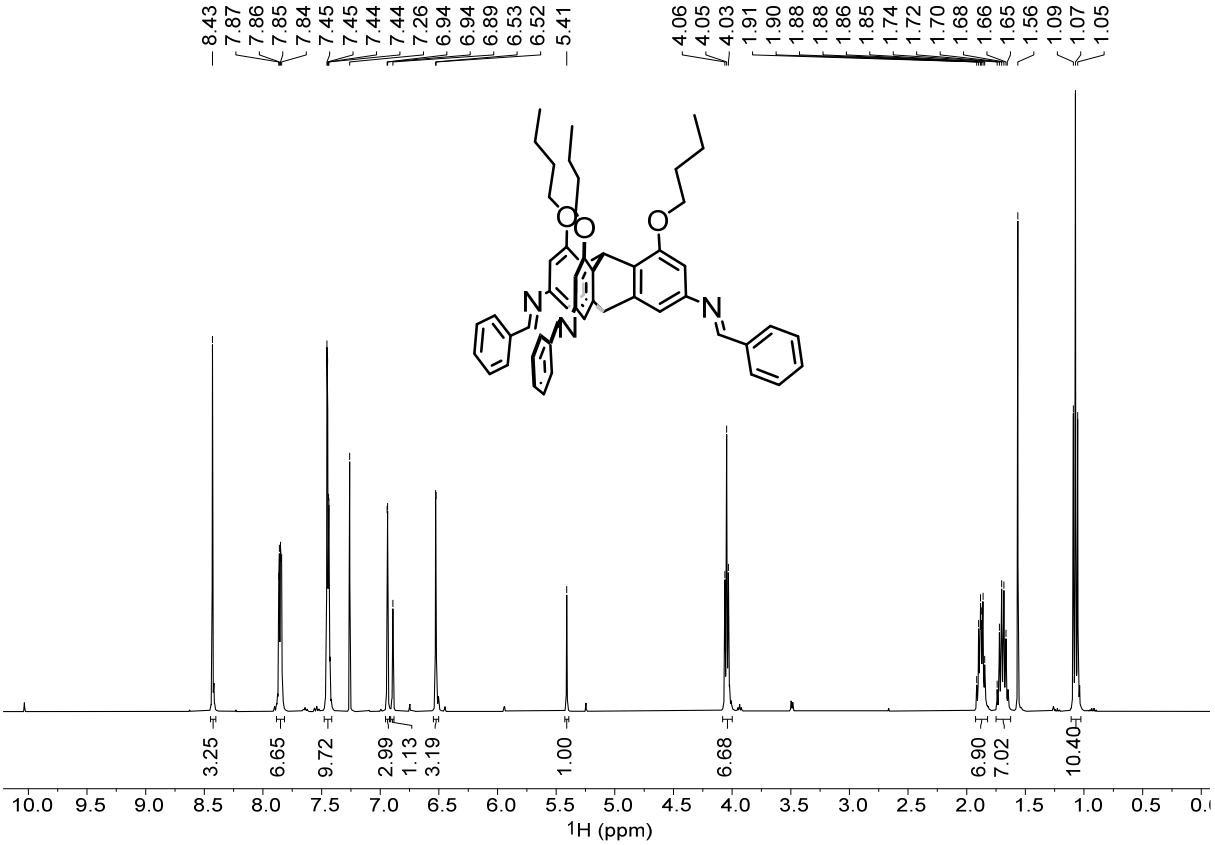

Figure 8.1.78: ^{1}H NMR spectrum (600 MHz, $CDCl_3$) of **116**.

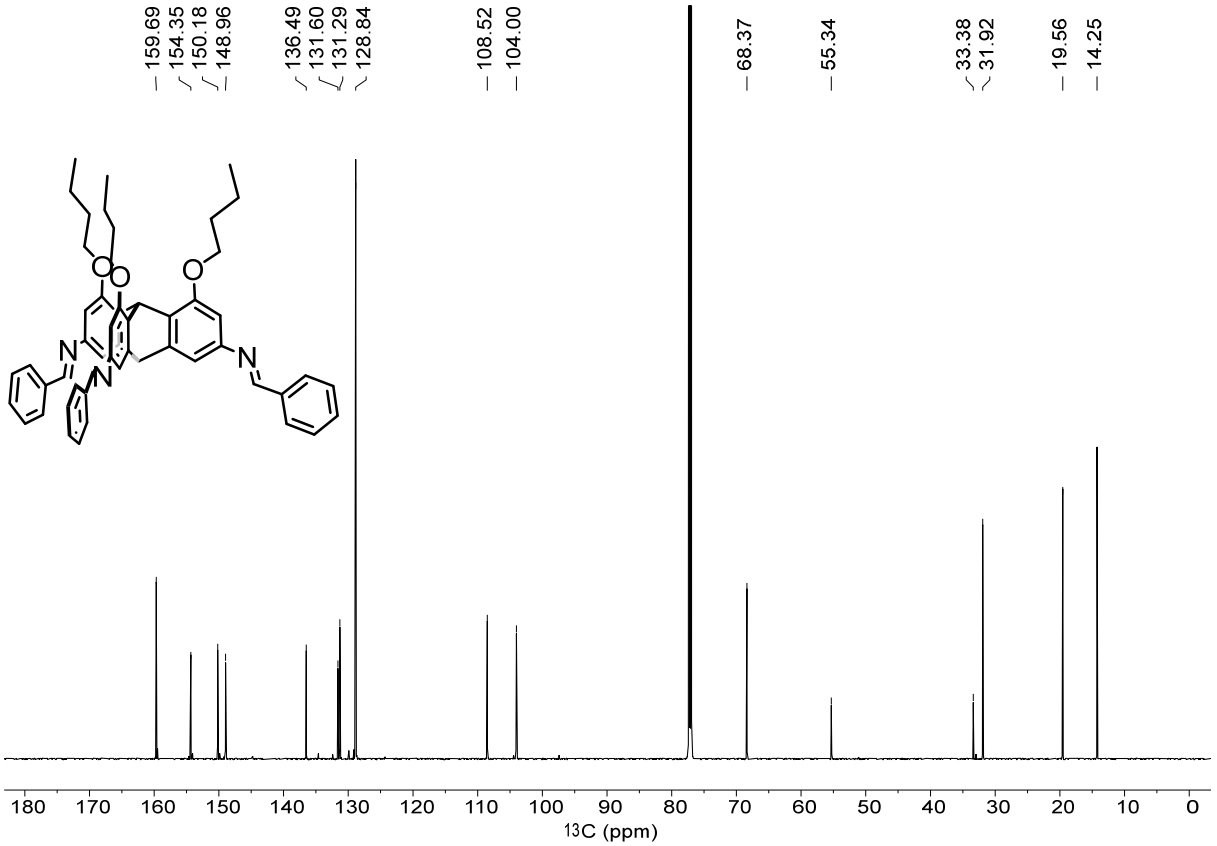

Figure 8.1.79: ^{13}C NMR spectrum (151 MHz, $CDCl_3$) of **116**.

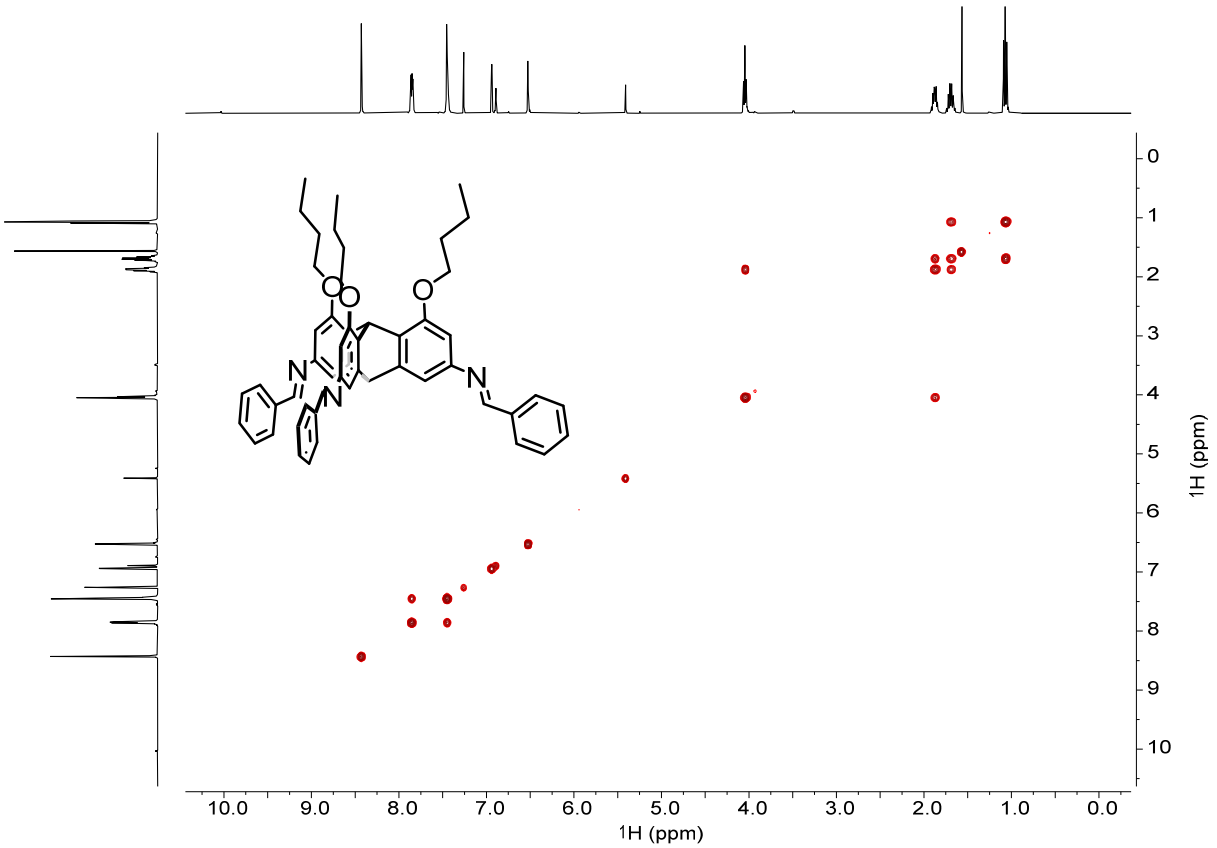

Figure 8.1.80: ^{1}H-^{1}H COSY NMR spectrum (600/600 MHz, $CDCl_3$) of **116**.

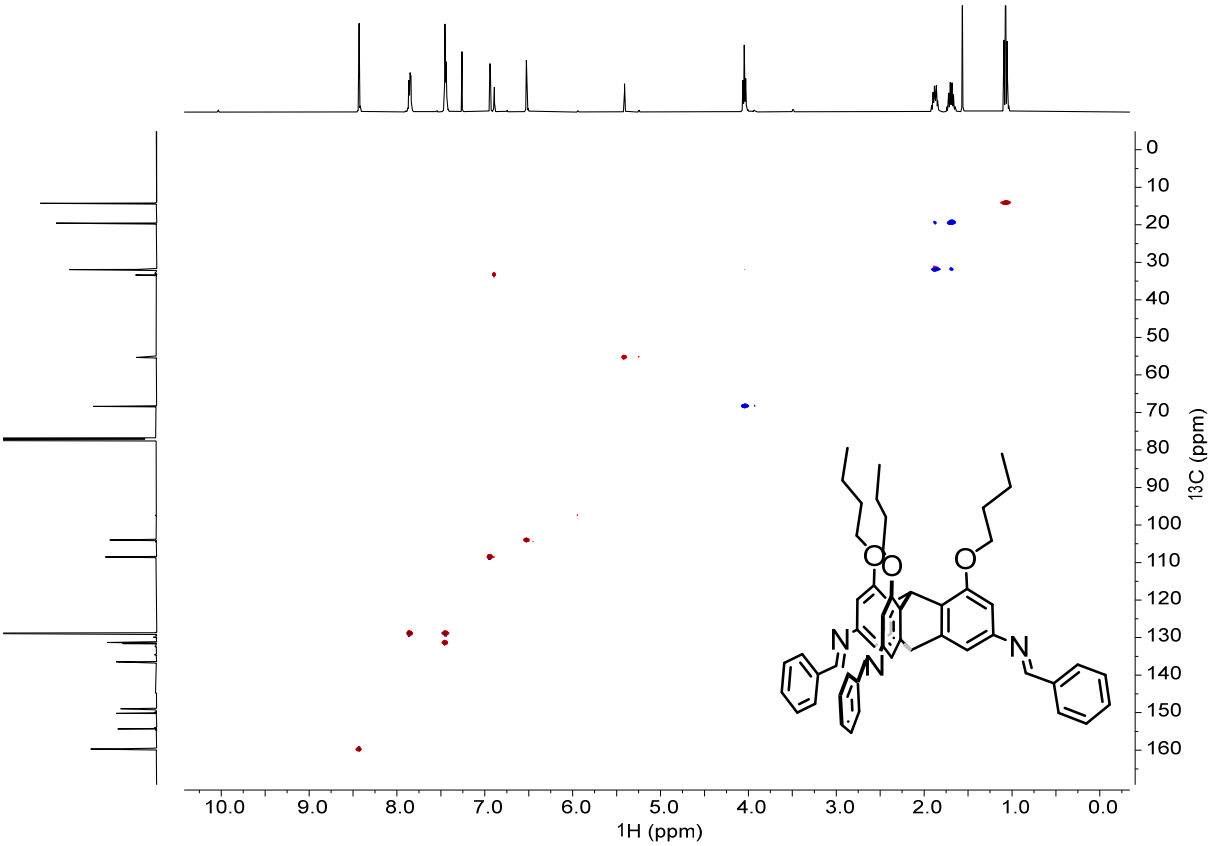

Figure 8.1.81: ^{1}H-^{13}C HSQC NMR spectrum (600/151 MHz, $CDCl_3$) of **116**.

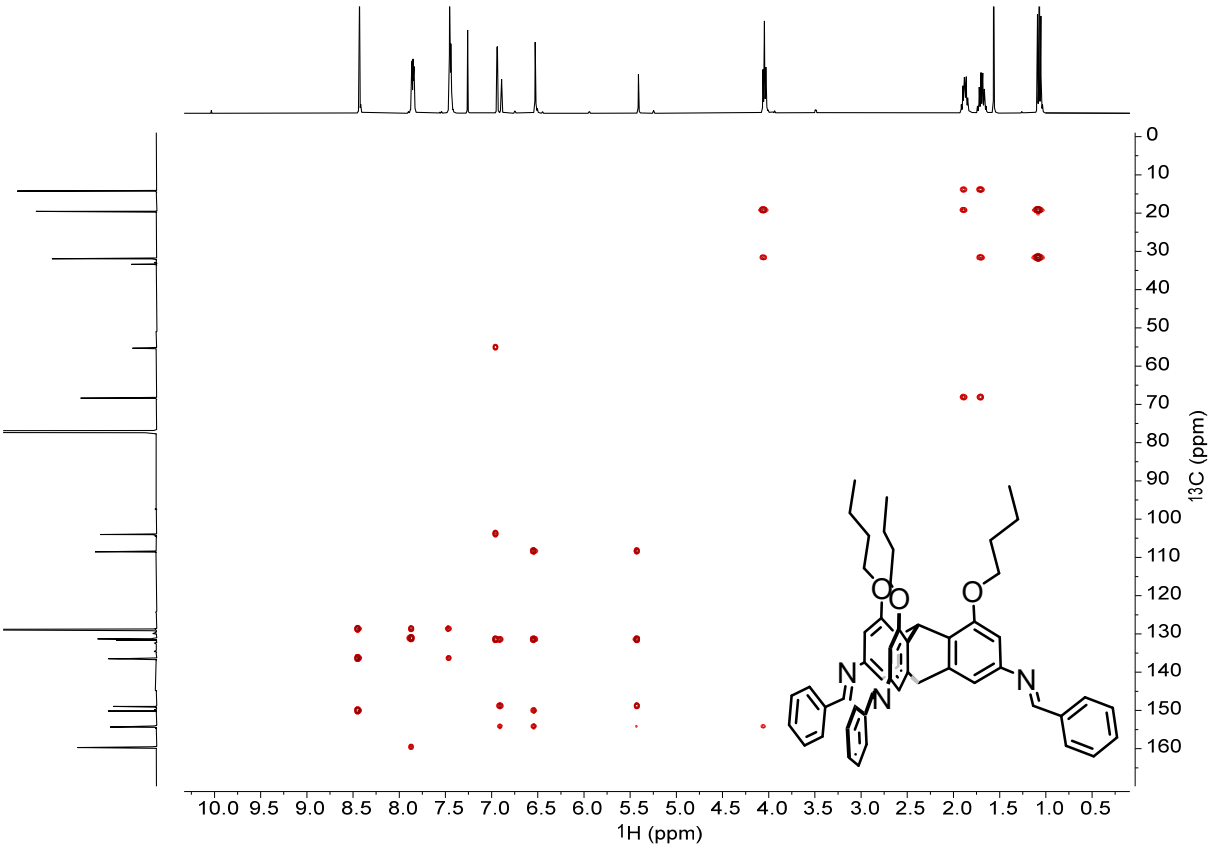

Figure 8.1.82: ^{1}H-^{13}C HMBC NMR spectrum (600/151 MHz, $CDCl_3$) of **116**.

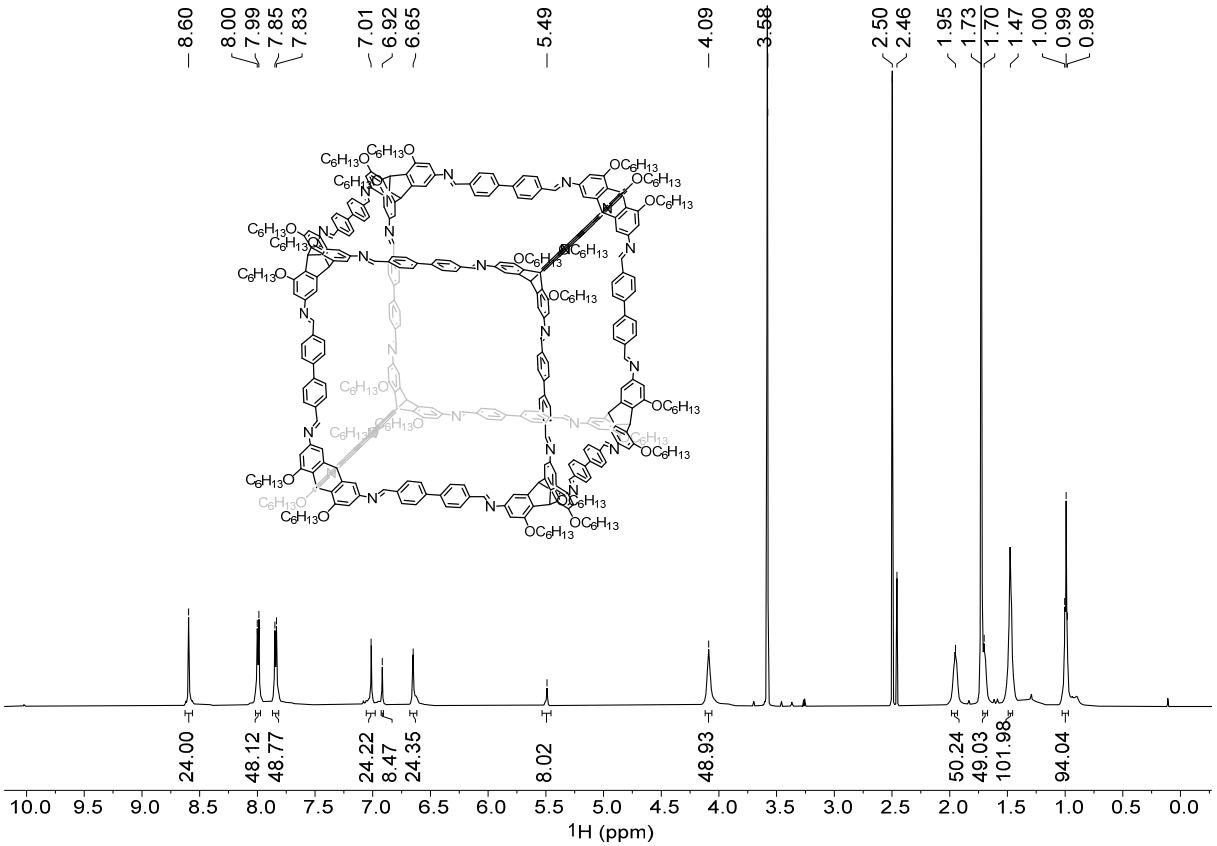

Figure 8.1.83: ^{1}H NMR spectrum (600 MHz, THF-d_8) of **HeiBi-Cage**.

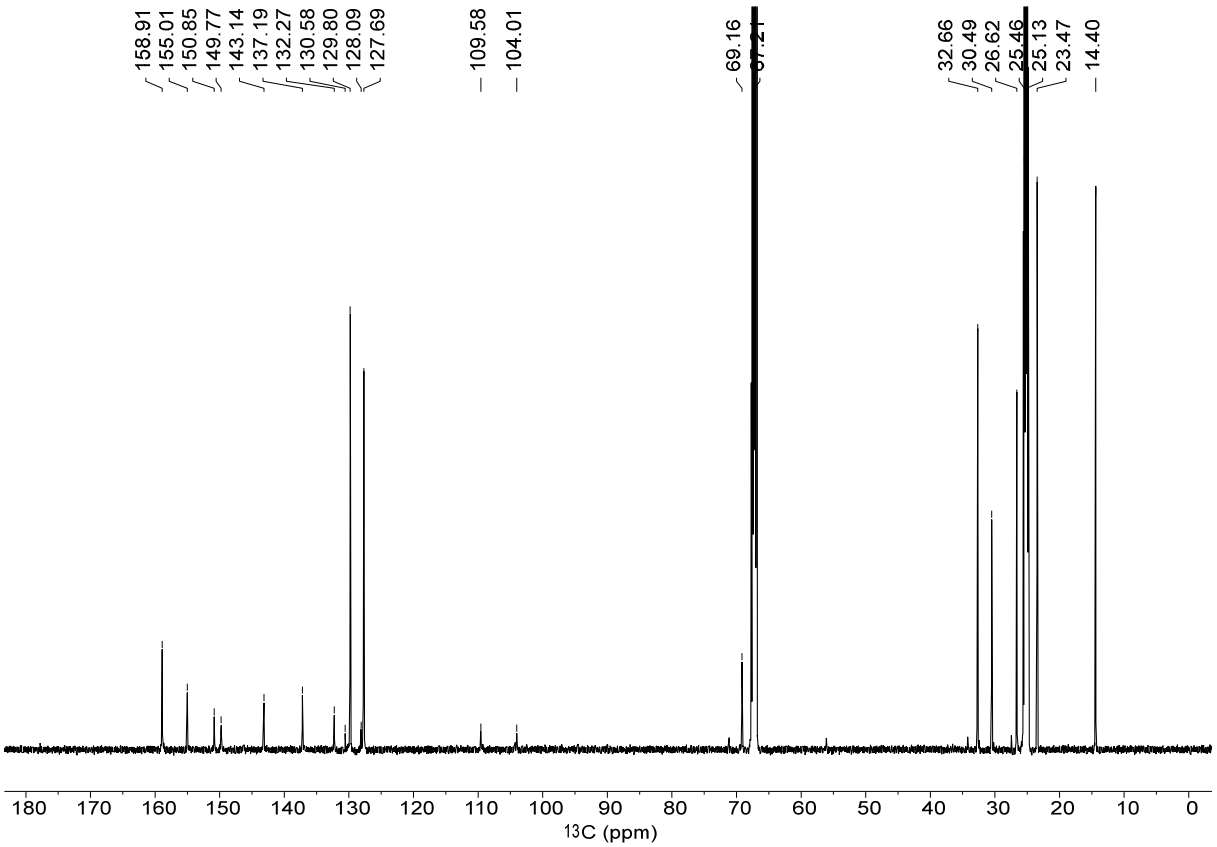

Figure 8.1.84: ^{13}C NMR spectrum (151 MHz, THF-d_8) of **HeiBi-Cage**.

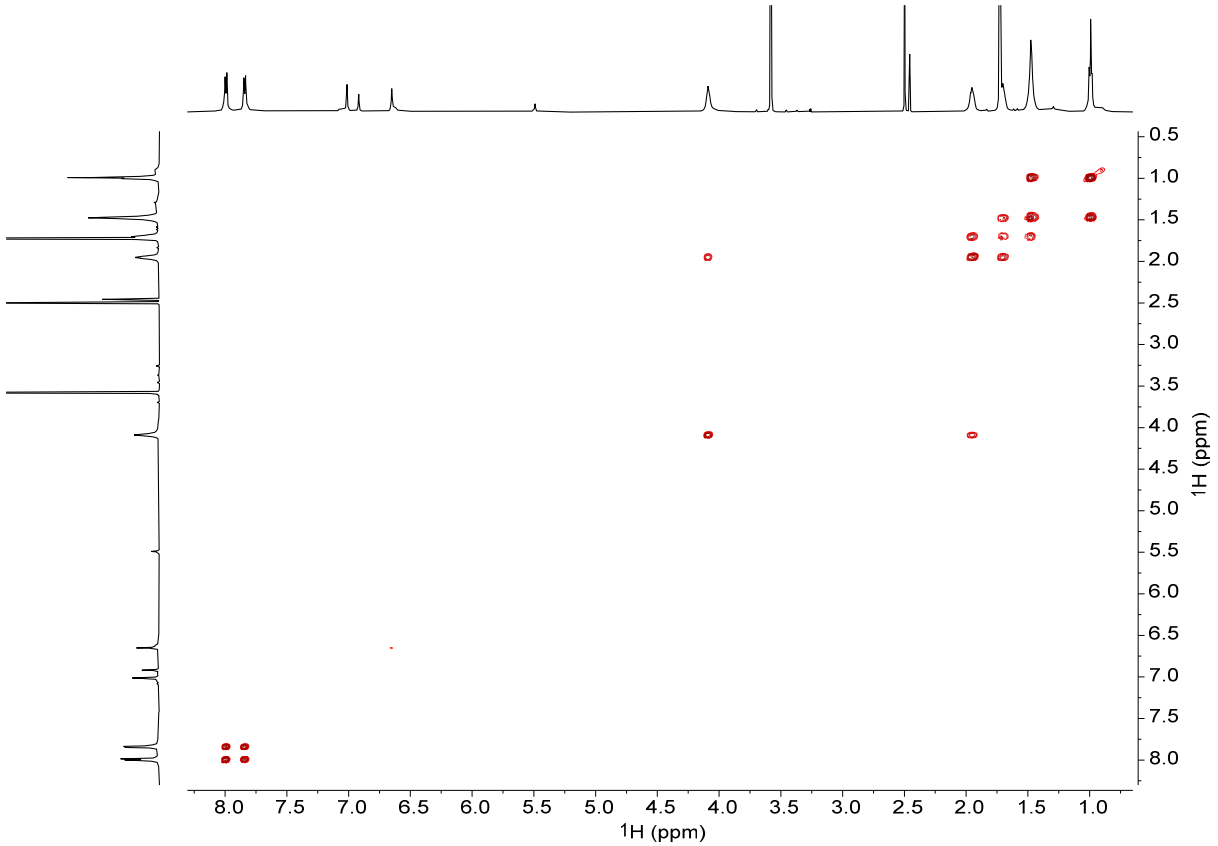

Figure 8.1.85: ^{1}H-^{1}H COSY NMR spectrum (600/600 MHz, THF-d_8) of **HeiBi-Cage**.

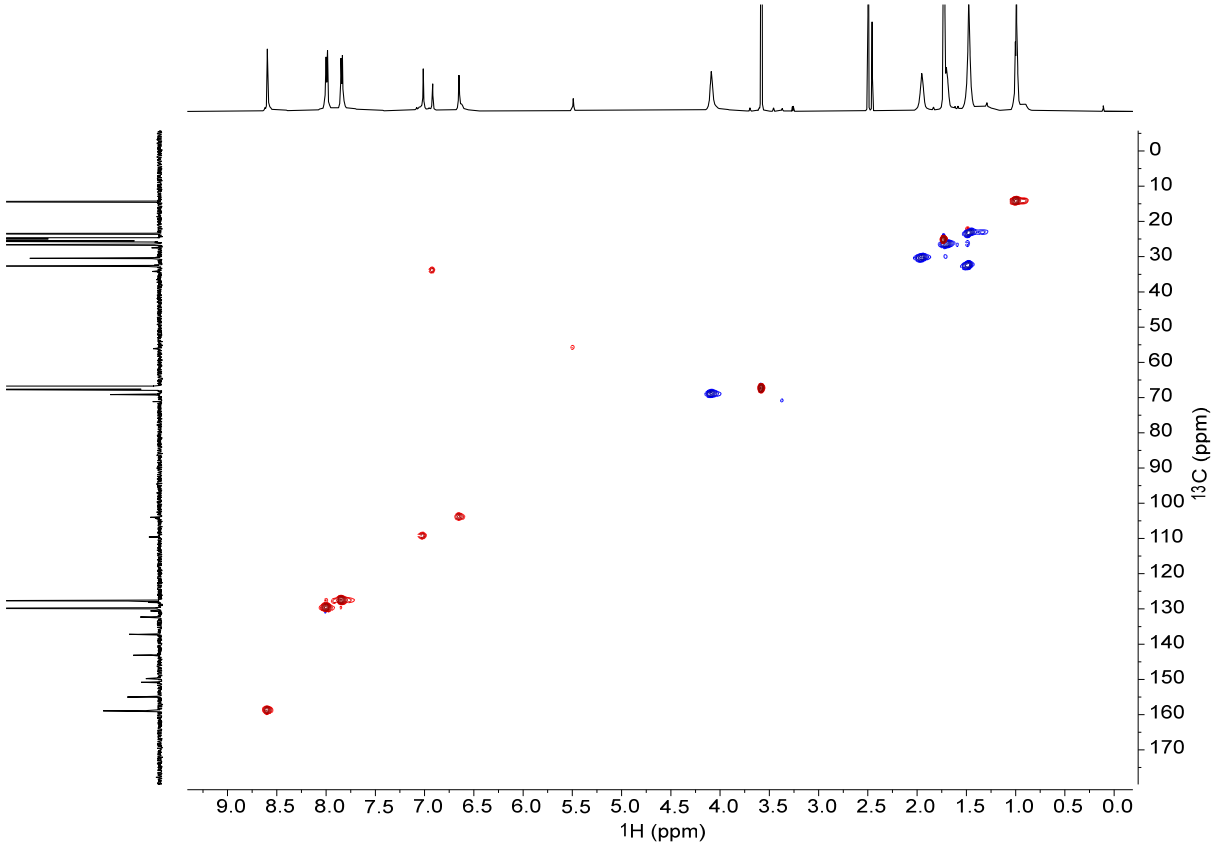

Figure 8.1.86: ^{1}H-^{13}C HSQC NMR spectrum (600/151 MHz, THF-d_8) of **HeiBi-Cage**.

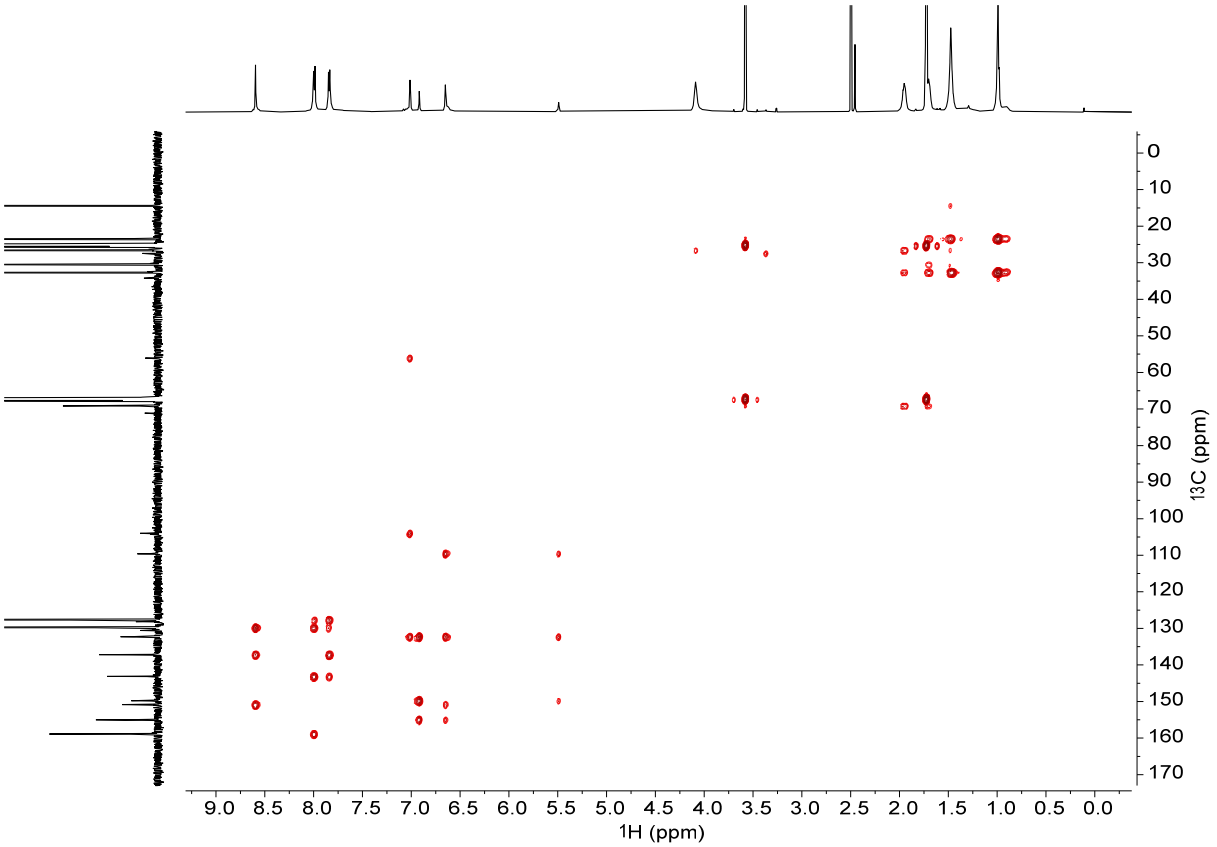

Figure 8.1.87: ^{1}H-^{13}C HMBC NMR spectrum (600/151 MHz, THF-d_8) of **HeiBi-Cage**.

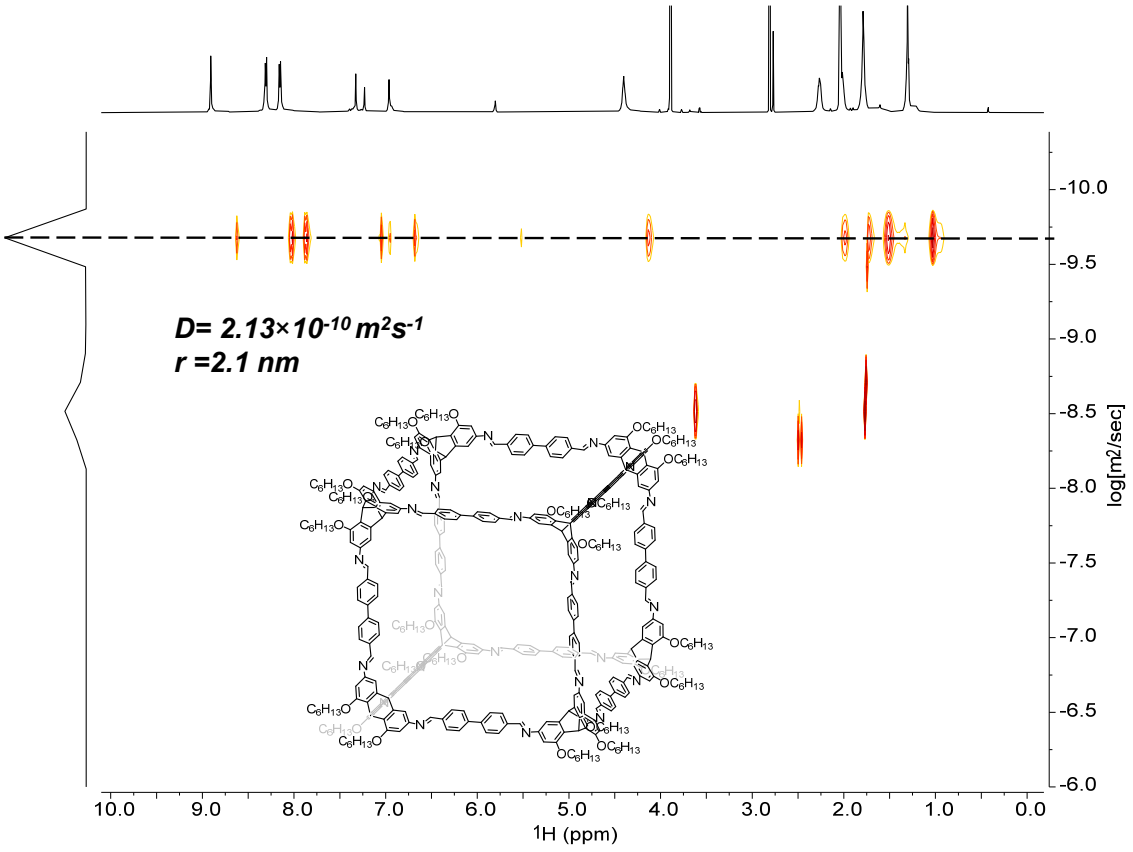

Figure 8.1.88: DOSY NMR spectrum (400 MHz, THF-d_8) of **HeiBi-Cage**.

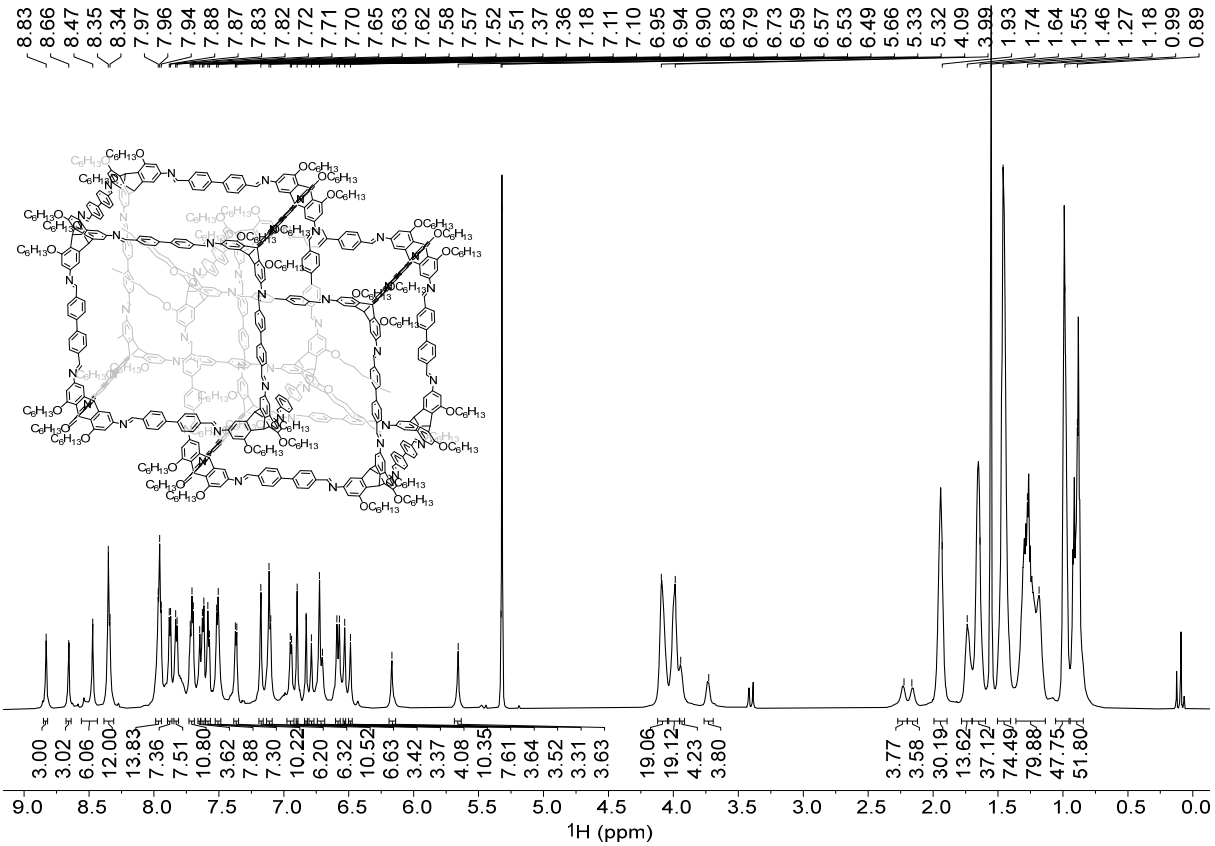

Figure 8.1.89: ^{1}H NMR spectrum (700 MHz, CD_2Cl_2) of **HeiBi-Catenane**.

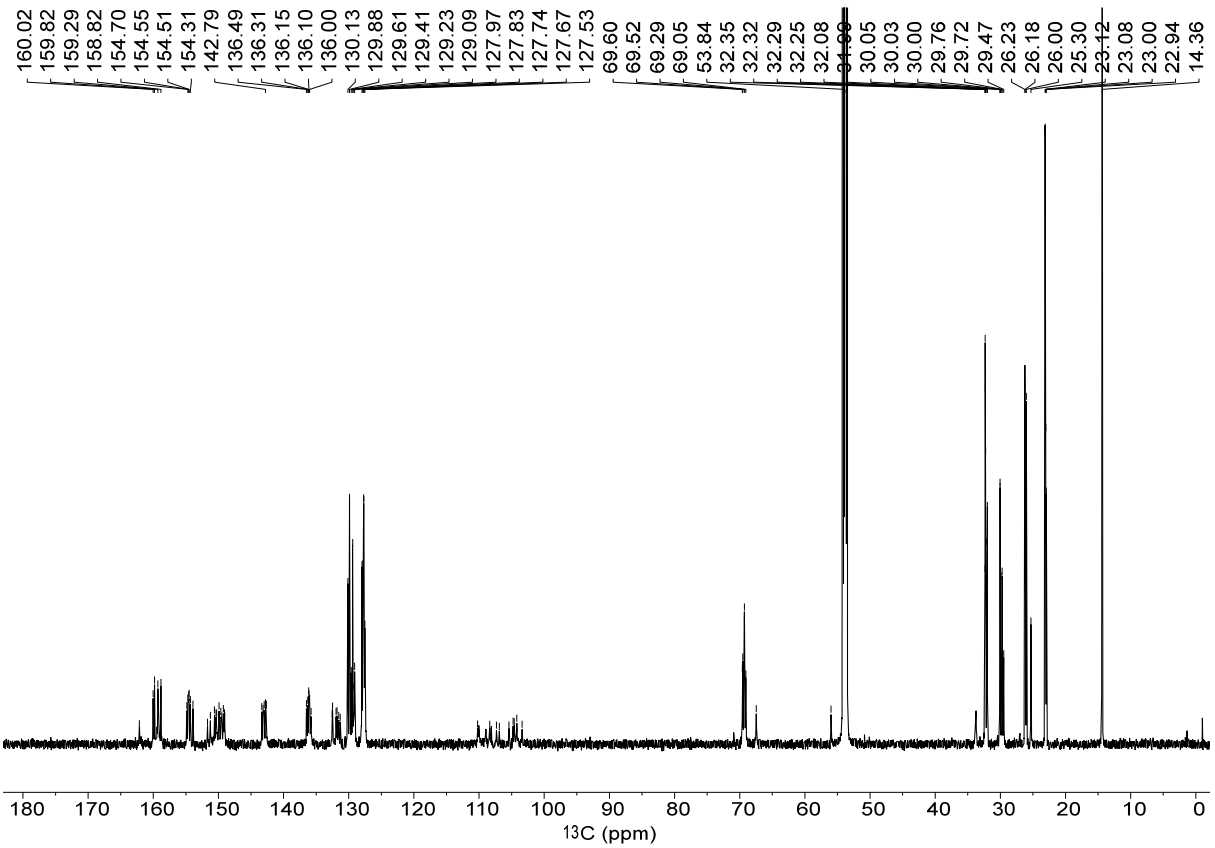

Figure 8.1.90: ^{13}C NMR spectrum (176 MHz, CD_2Cl_2) of **HeiBi-Catenane**.

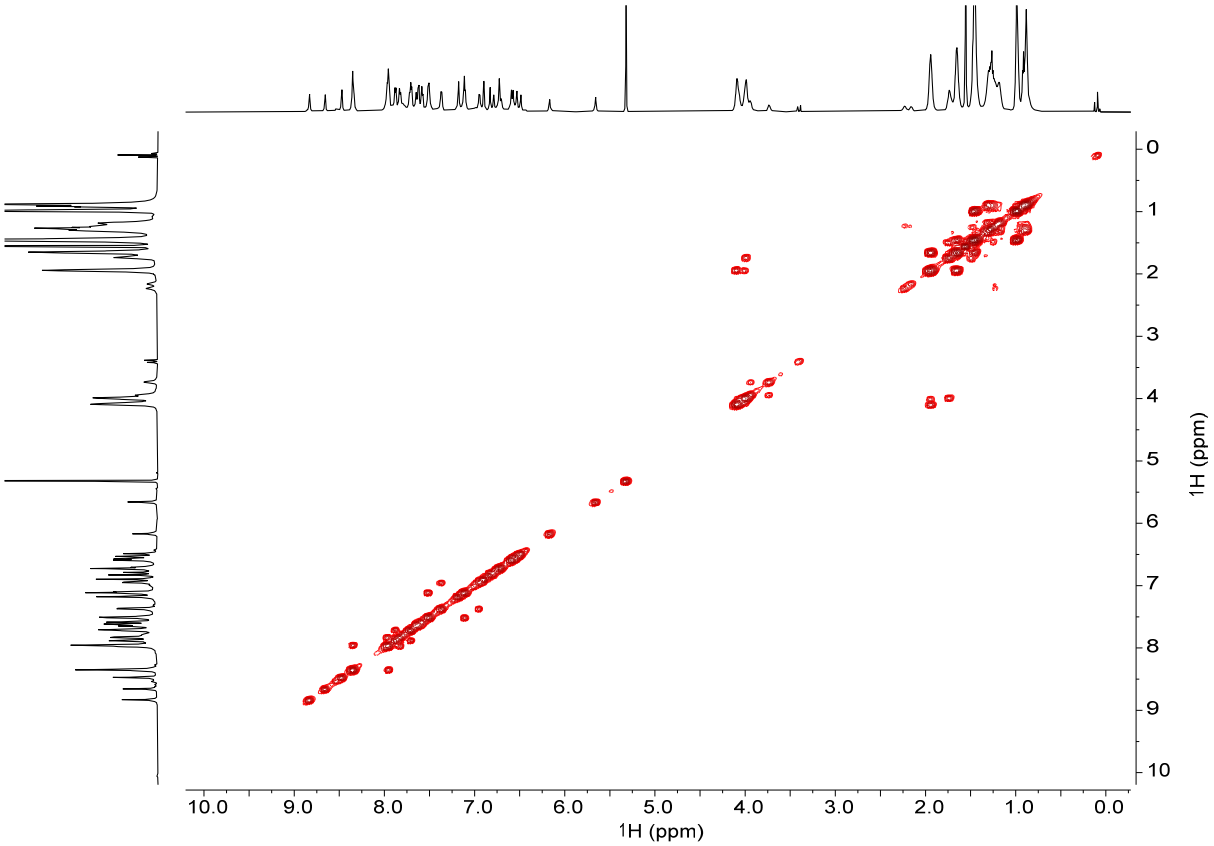

Figure 8.1.91: ^{1}H-^{1}H COSY NMR spectrum (700/700 MHz, CD_2Cl_2) of **HeiBi-Catenane**.

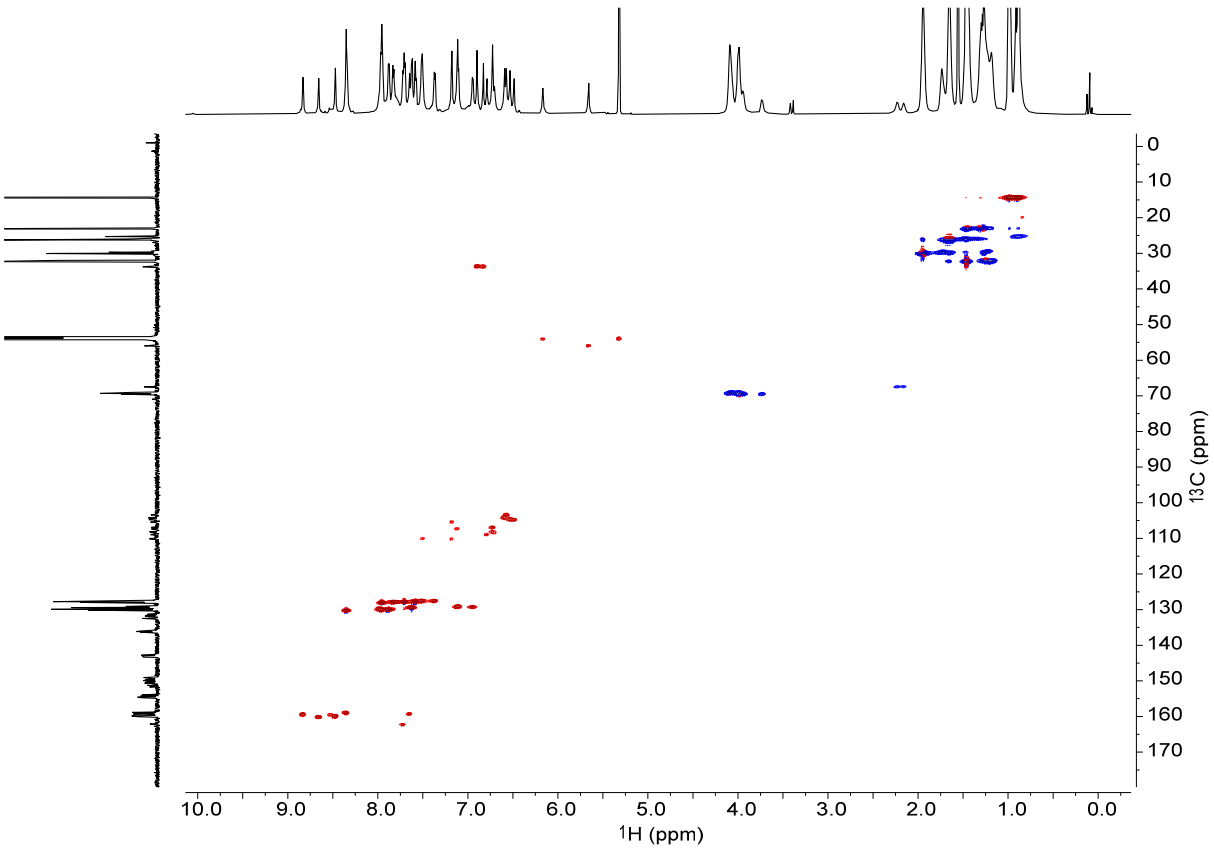

Figure 8.1.92: ^{1}H-^{13}C HSQC NMR spectrum (700/176 MHz, CD_2Cl_2) of **HeiBi-Catenane**.

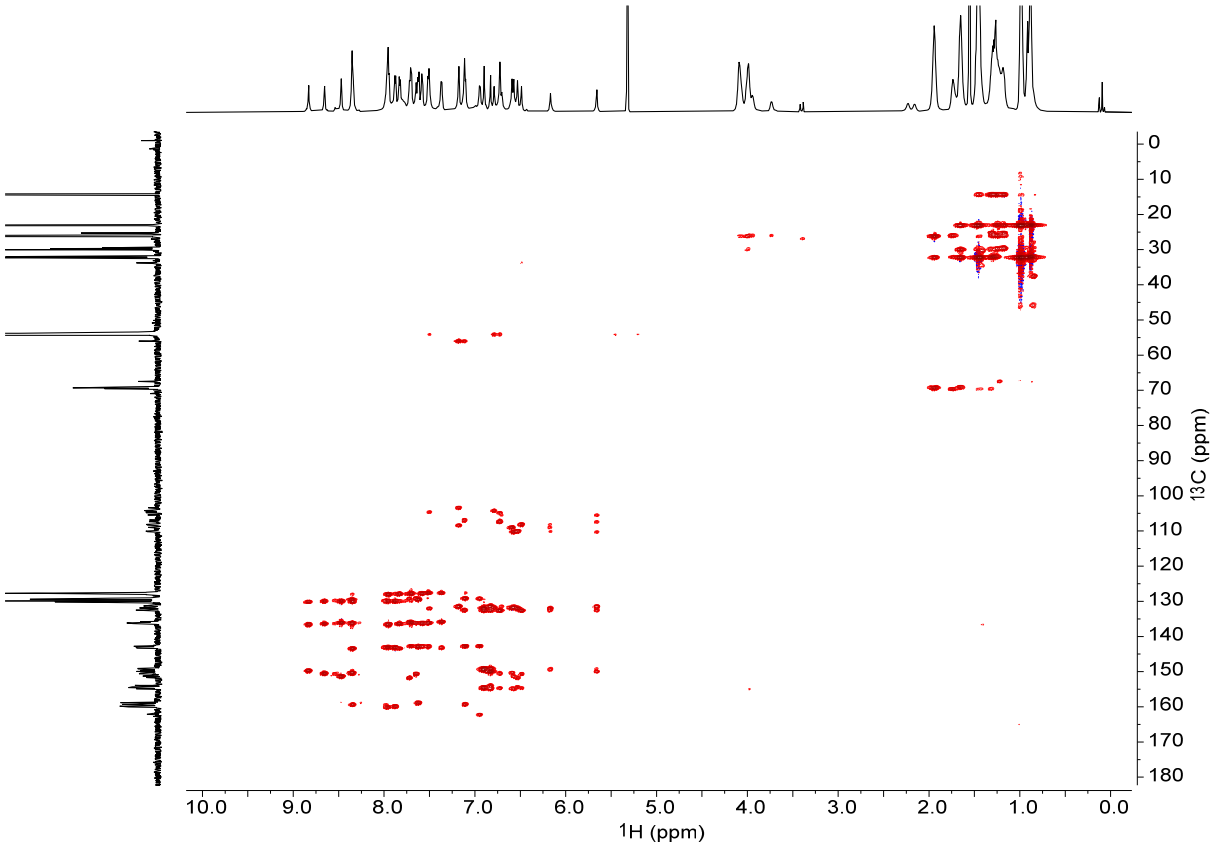

Figure 8.1.93: ^{1}H-^{13}C HMBC NMR spectrum (700/176 MHz, CD_2Cl_2) of **HeiBi-Catenane**.

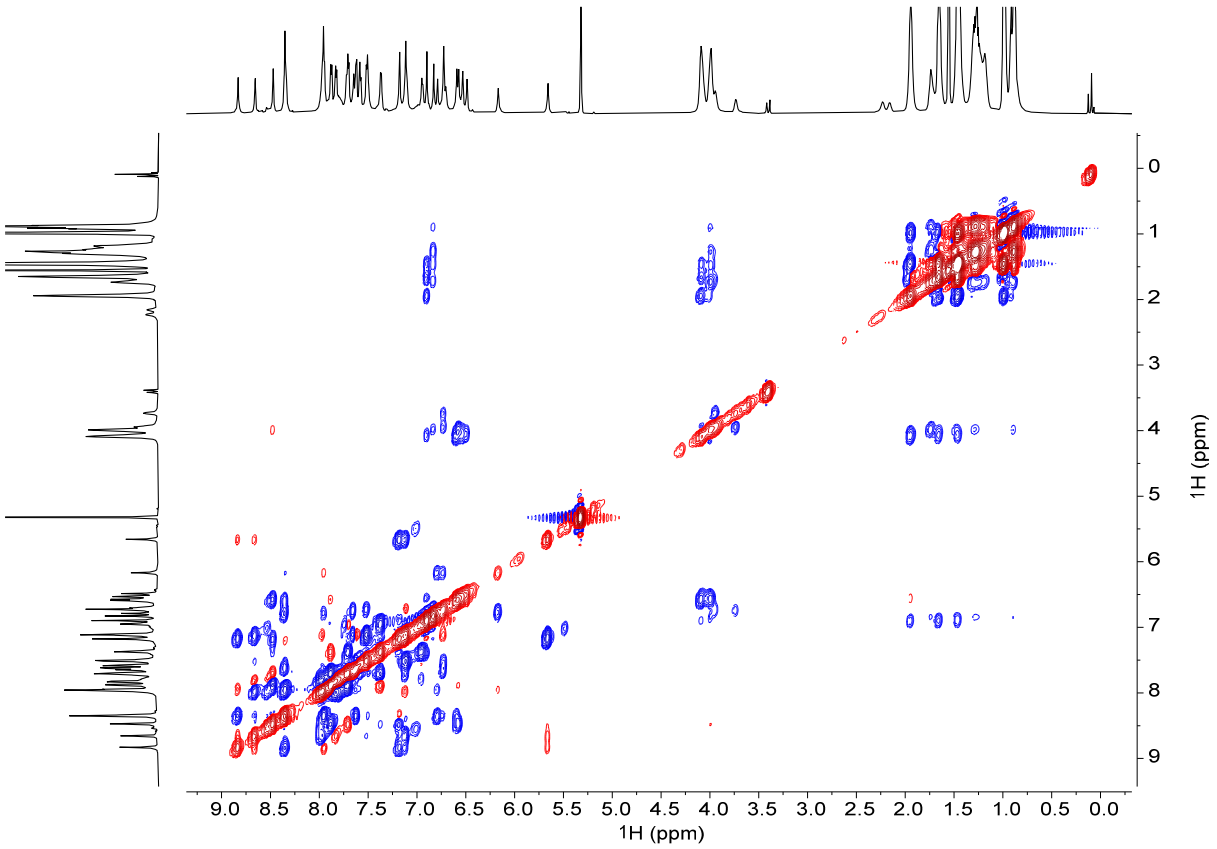

Figure 8.1.94: ^{1}H-^{1}H NOESY NMR spectrum (700/700 MHz, CD_2Cl_2) of **HeiBi-Catenane**.

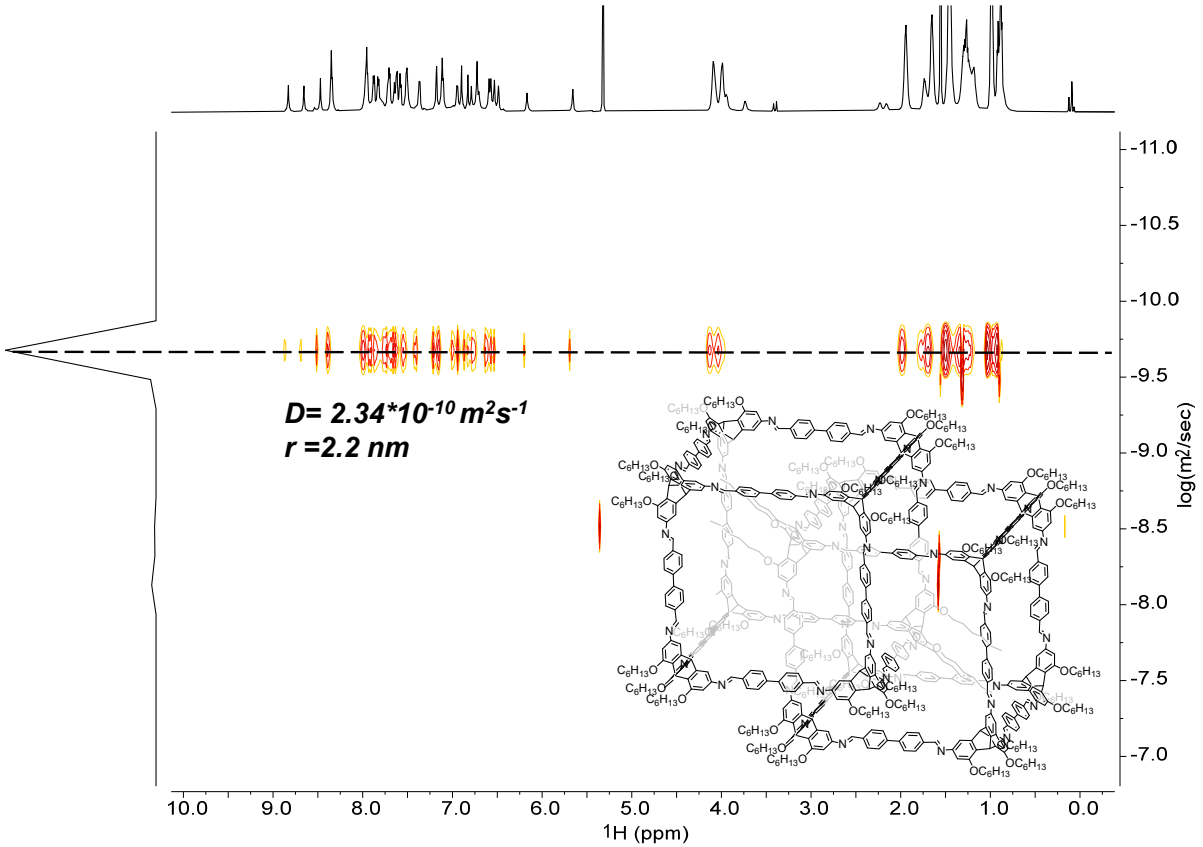

Figure 8.1.95: DOSY NMR spectrum (400 MHz, CD_2Cl_2) of **HeiBi-Catenane**.

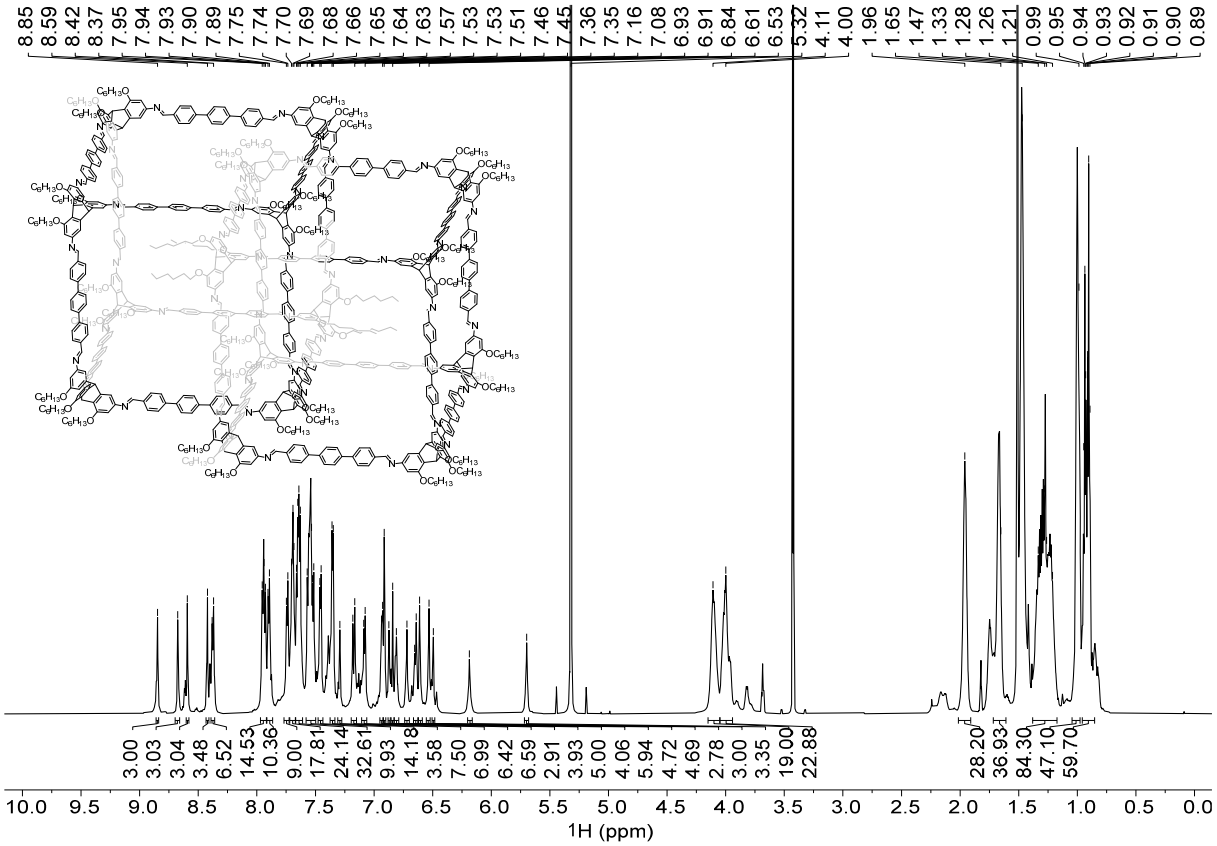

Figure 8.1.96: ^{1}H NMR spectrum (700 MHz, CD_2Cl_2) of **HeiTri-[2]Catenane**.

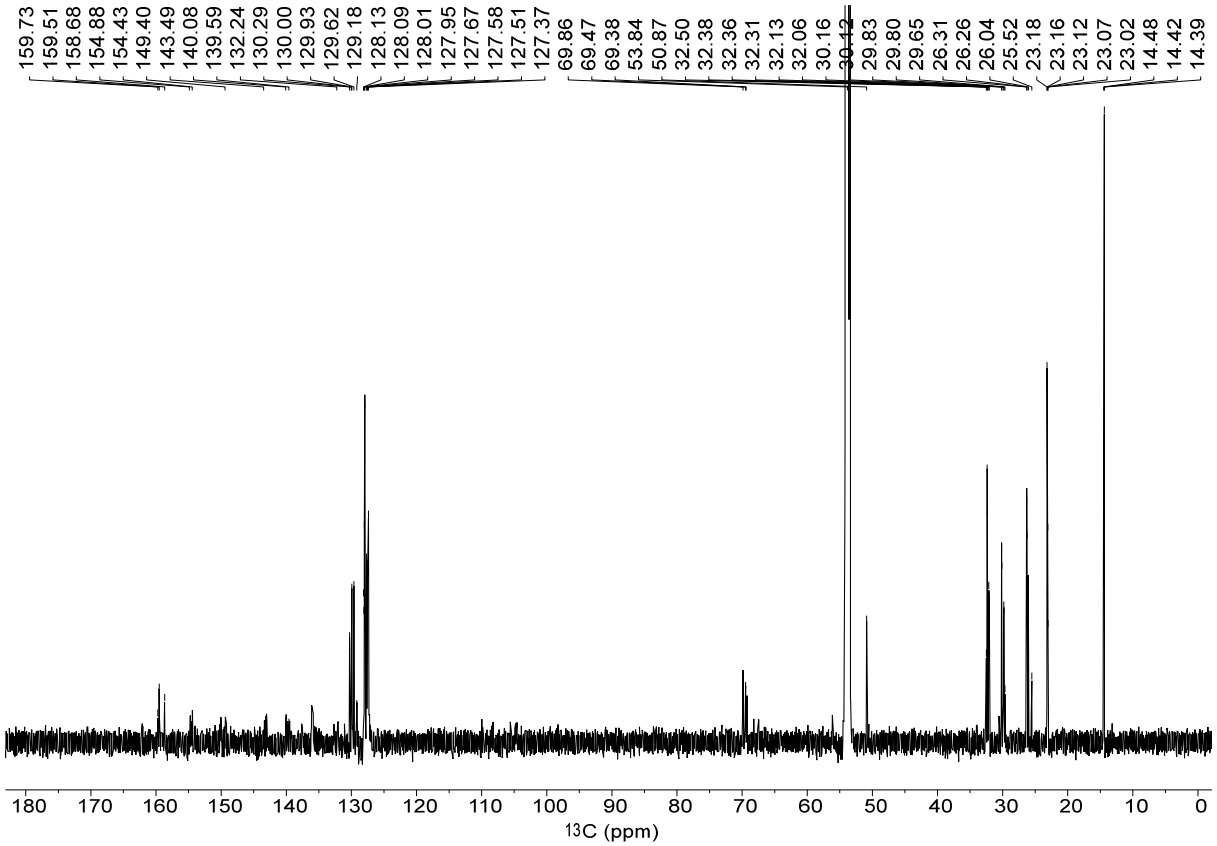

Figure 8.1.97: ^{13}C NMR spectrum (176 MHz, CD_2Cl_2) of **HeiTri-[2]Catenane**.

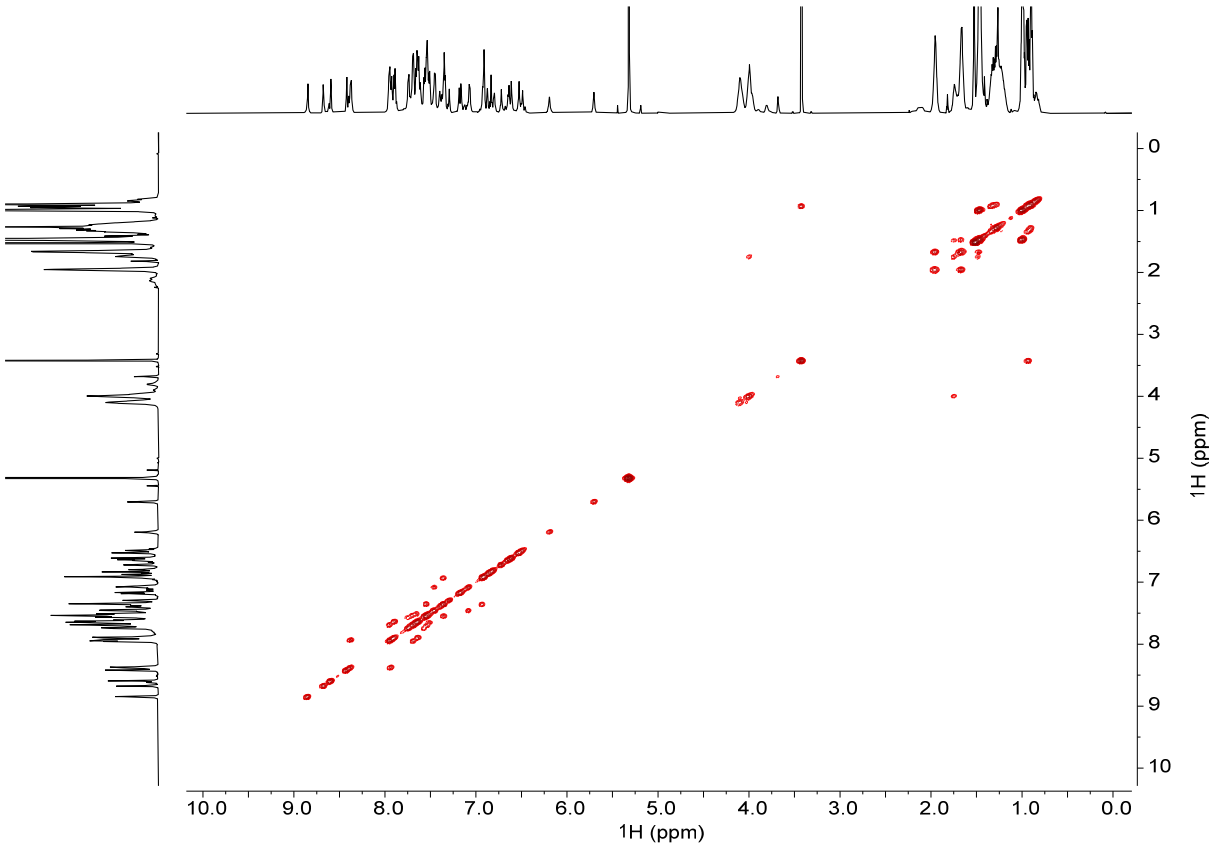

Figure 8.1.98: ^{1}H-^{1}H COSY NMR spectrum (700/700 MHz, CD_2Cl_2) of **HeiTri-[2]Catenane**.

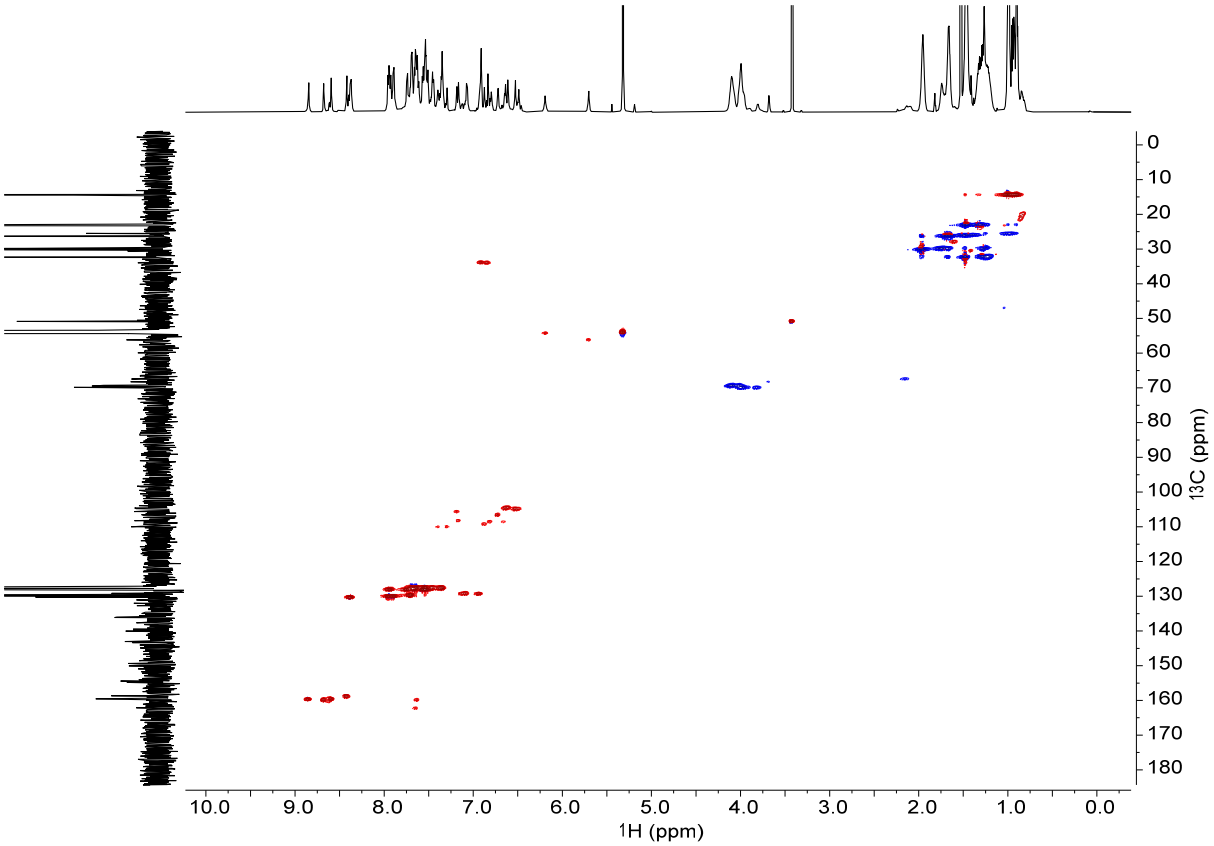

Figure 8.1.99: ^{1}H-^{13}C HSQC NMR spectrum (700/176 MHz, CD_2Cl_2) of **HeiTri-[2]Catenane**.

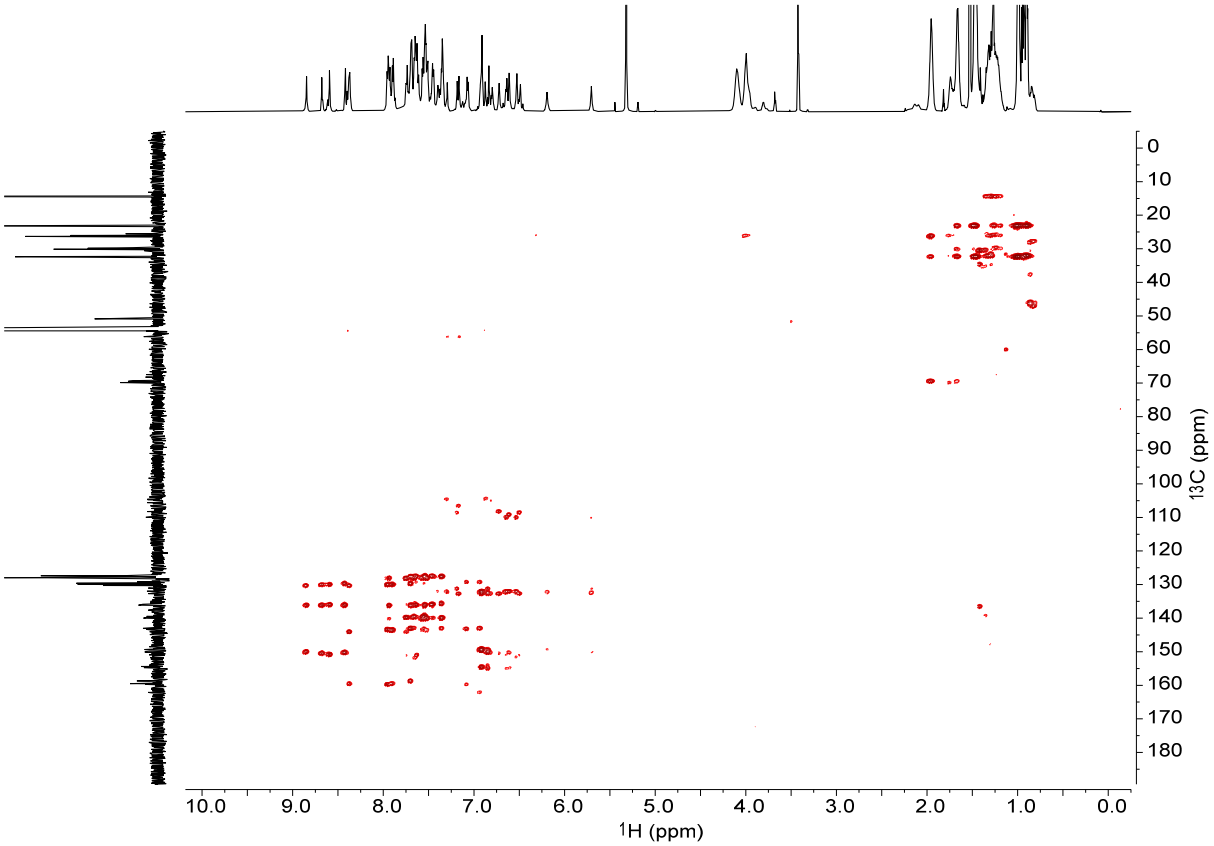

Figure 8.1.100: ^{1}H-^{13}C HMBC NMR spectrum (700/176 MHz, CD_2Cl_2) of **HeiTri-[2]Catenane**.

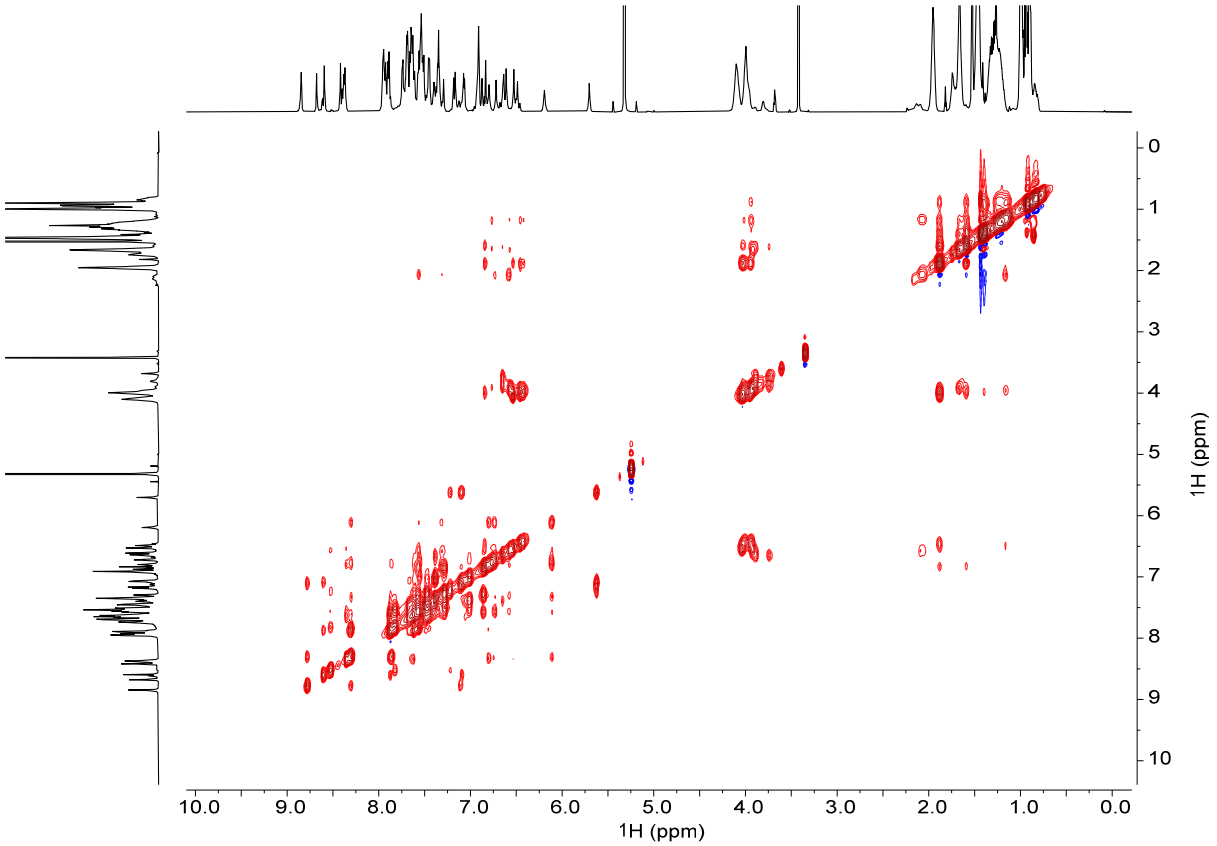

Figure 8.1.101: ^{1}H-^{1}H NOESY NMR spectrum (700/700 MHz, CD_2Cl_2) of **HeiTri-[2]Catenane**.

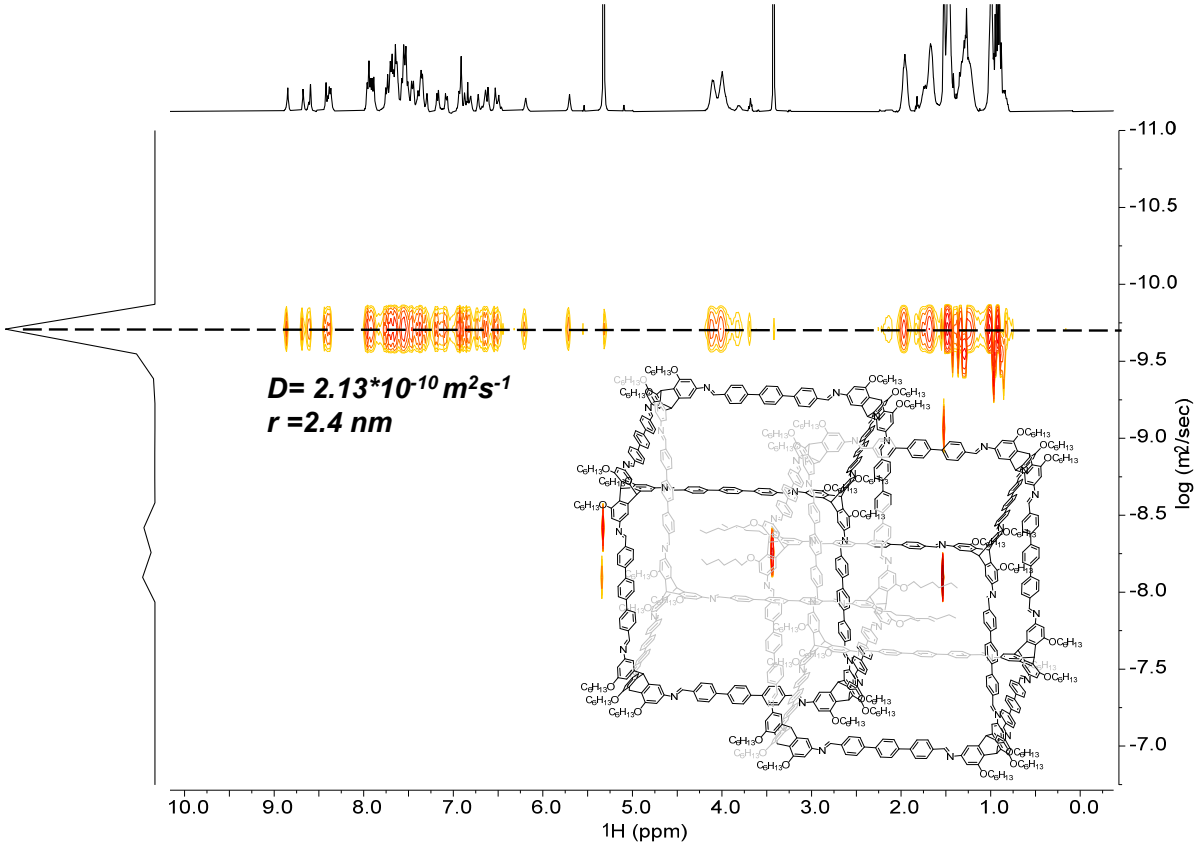

Figure 8.1.102: DOSY NMR spectrum (400 MHz, CD_2Cl_2) of **HeiTri-[2]Catenane**.

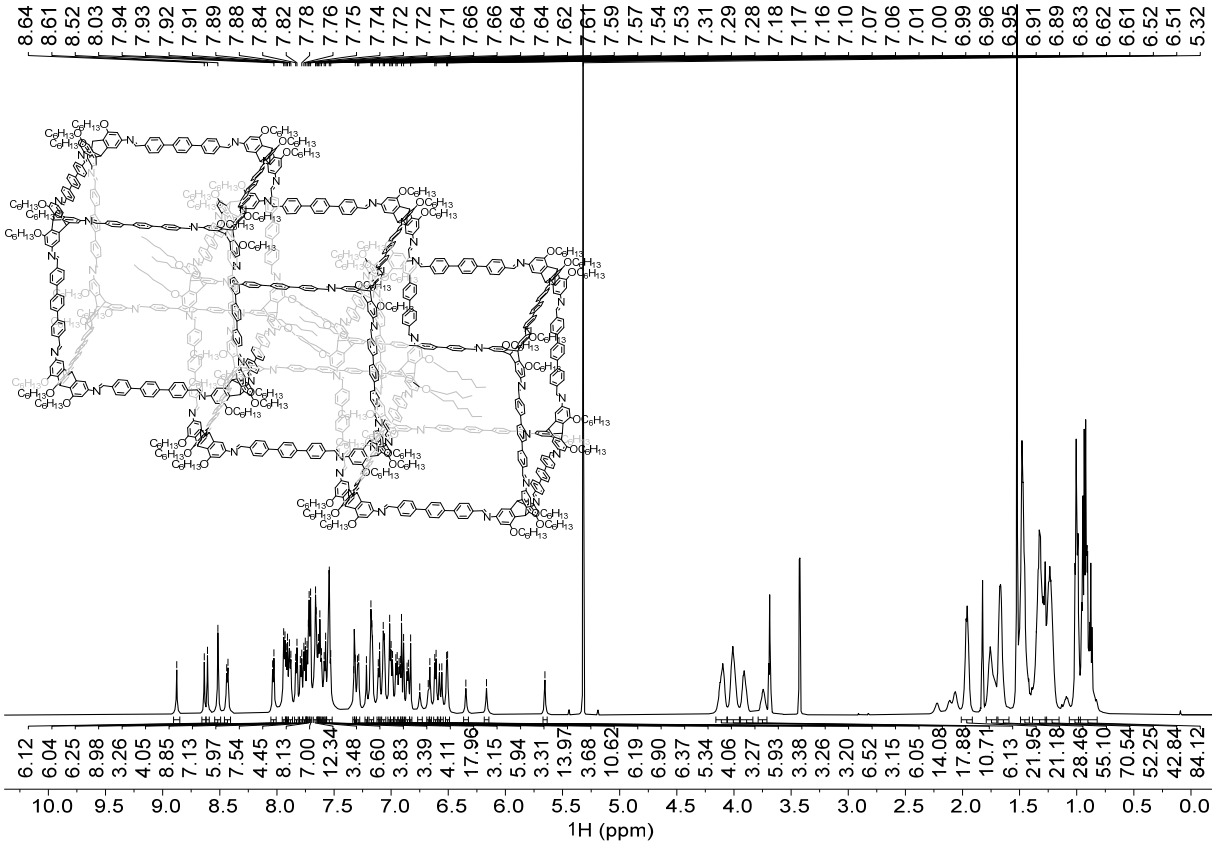

Figure 8.1.103: ^{1}H NMR spectrum (700 MHz, CD_2Cl_2) of **HeiTri-[3]Catenane**.

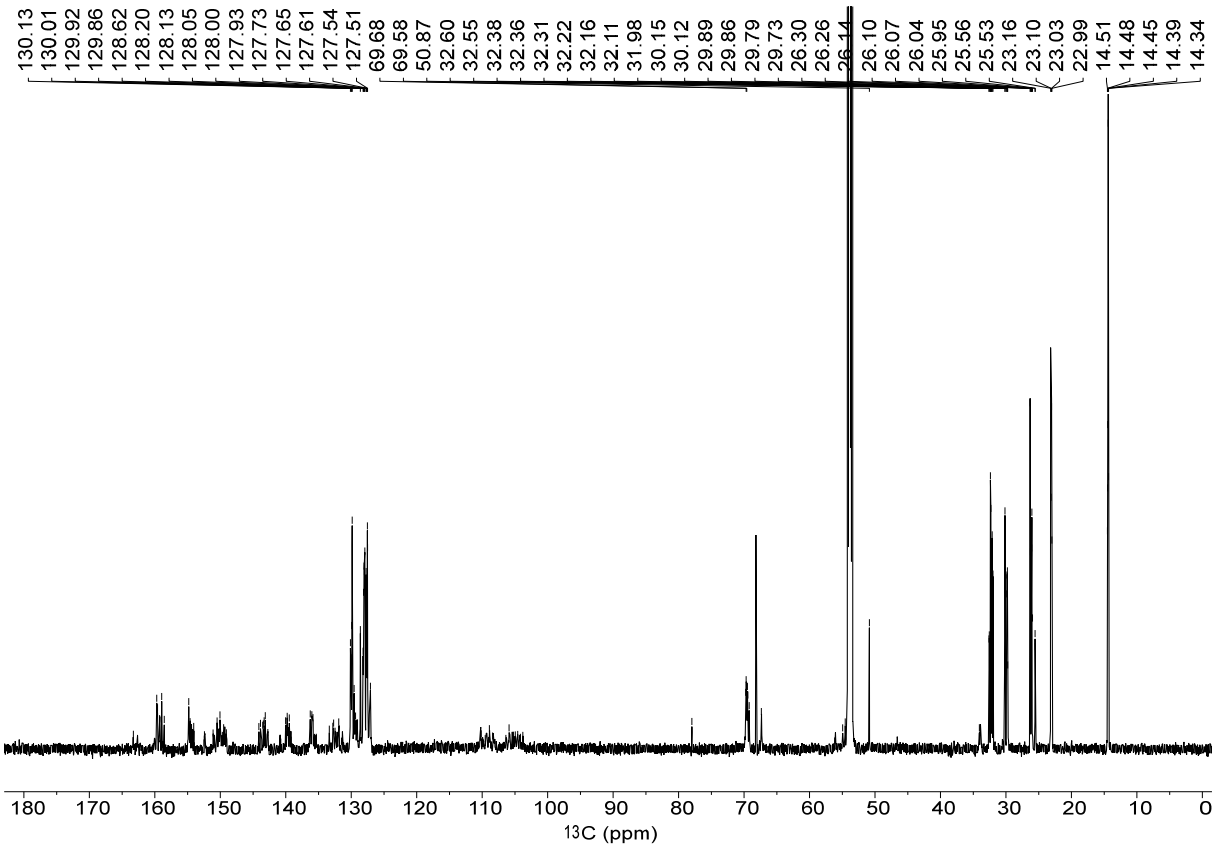

Figure 8.1.104: ^{13}C NMR spectrum (176 MHz, CD_2Cl_2) of **HeiTri-[3]Catenane**.

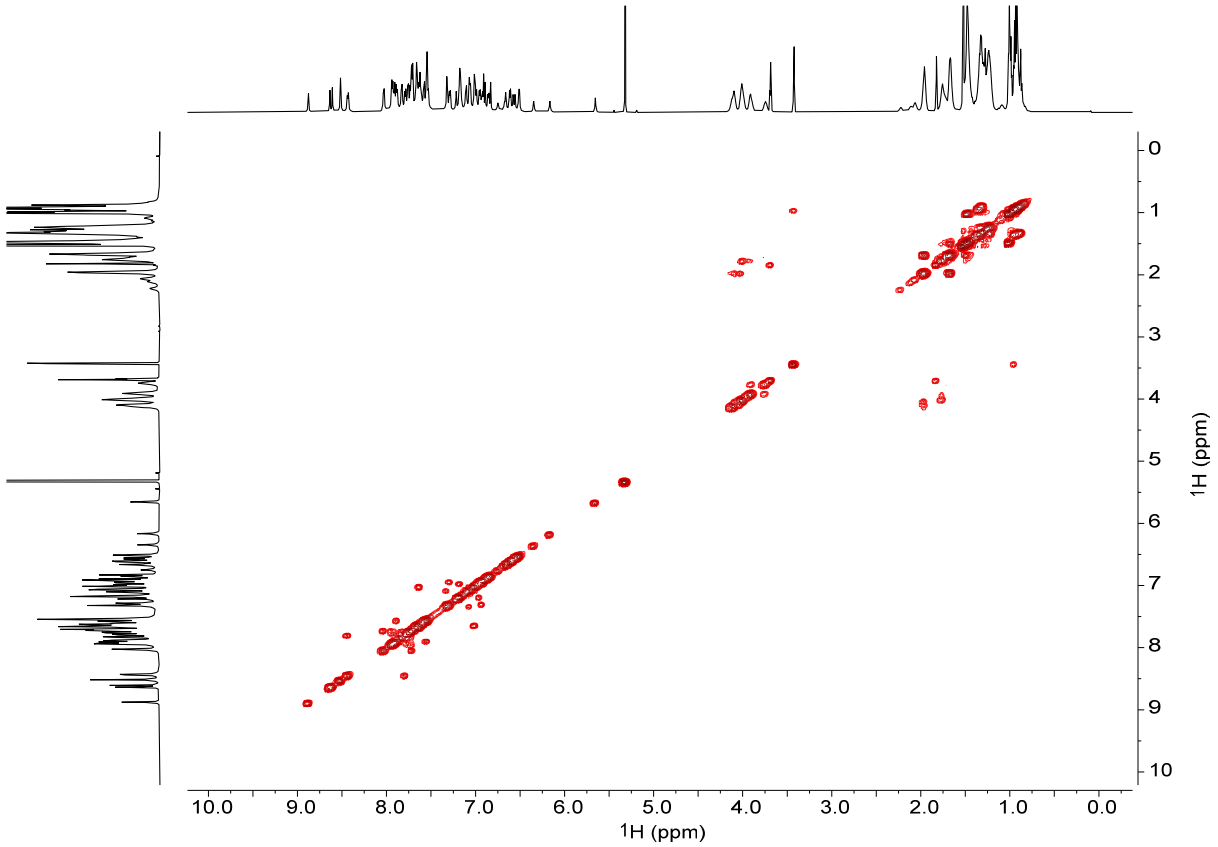

Figure 8.1.105: ^{1}H-^{1}H COSY NMR spectrum (700/700 MHz, CD_2Cl_2) of **HeiTri-[3]Catenane**.

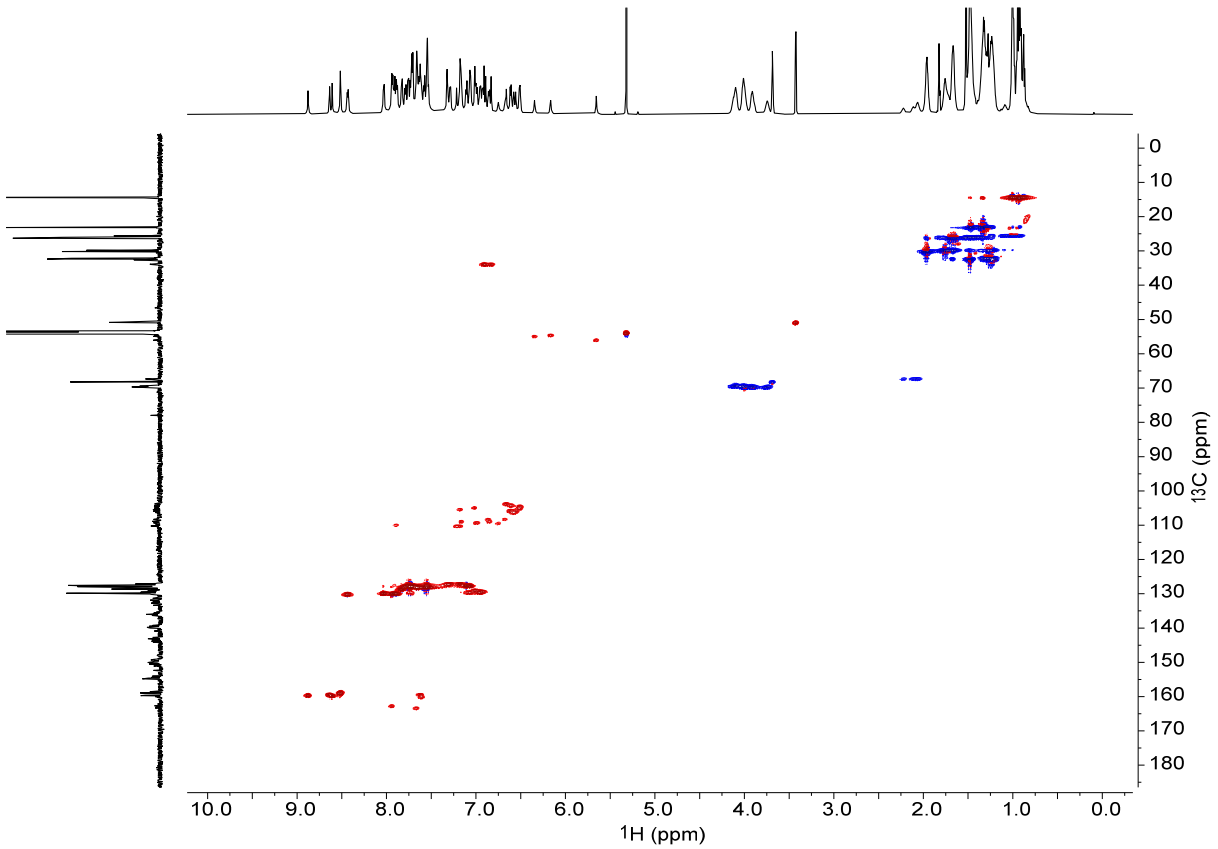

Figure 8.1.106: ^{1}H-^{13}C HSQC NMR spectrum (700/176 MHz, CD_2Cl_2) of **HeiTri-[3]Catenane**.

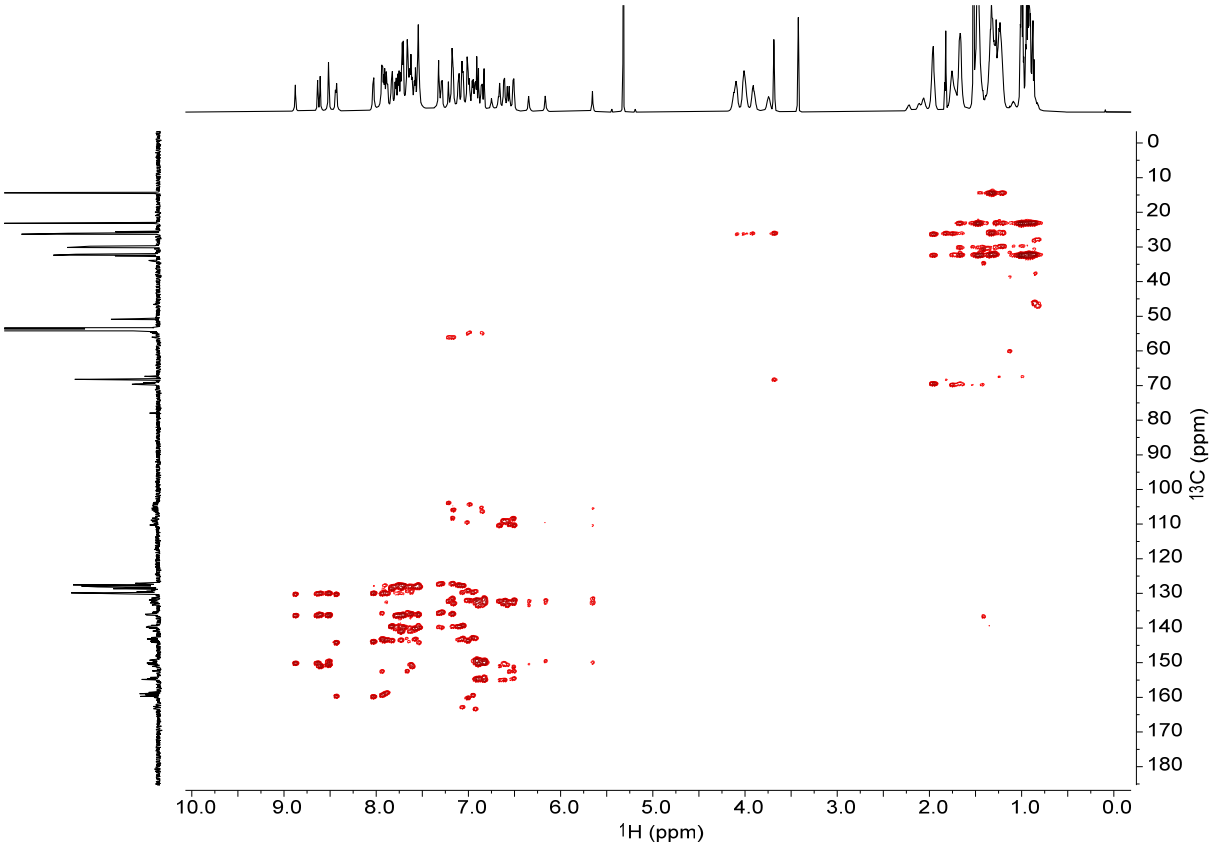

Figure 8.1.107: ^{1}H-^{13}C HMBC NMR spectrum (700/176 MHz, CD_2Cl_2) of **HeiTri-[3]Catenane**.

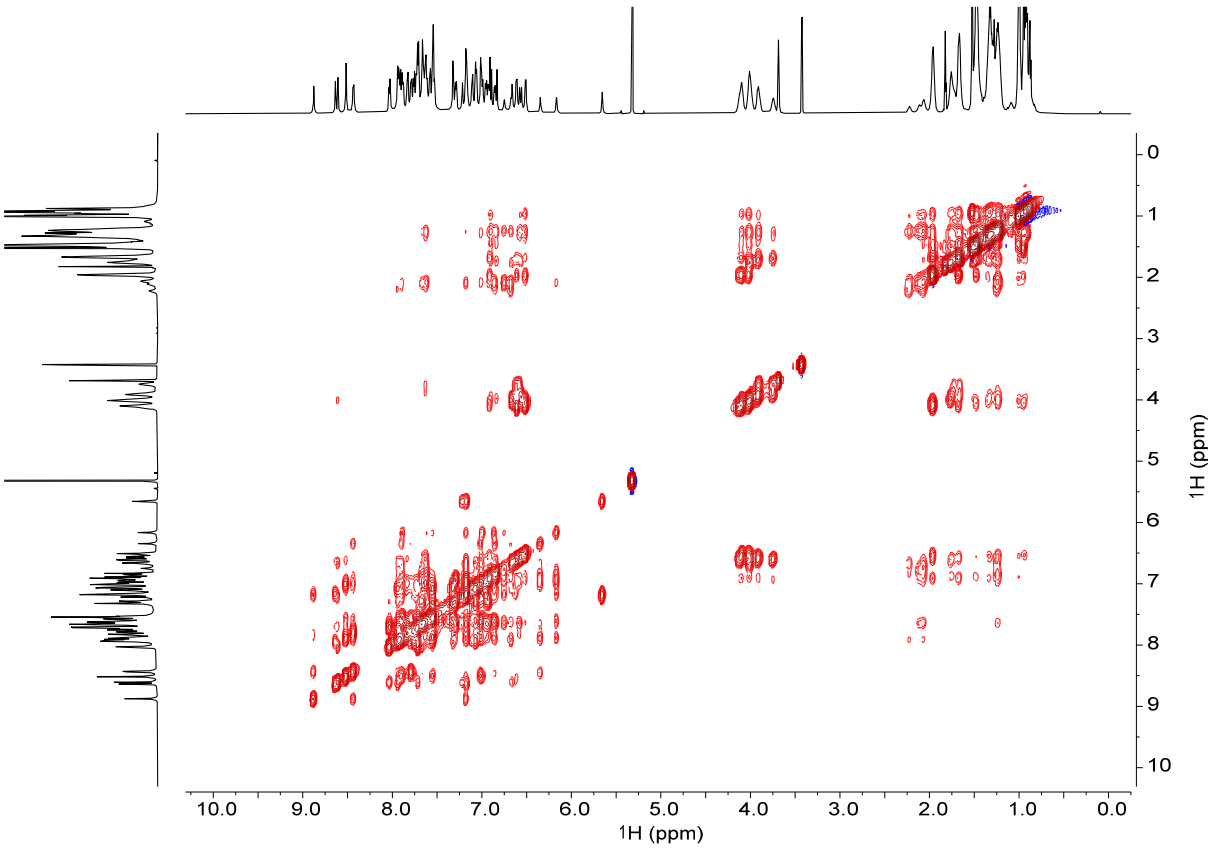

Figure 8.1.108: ^{1}H-^{1}H NOESY NMR spectrum (700/700 MHz, CD_2Cl_2) of **HeiTri-[3]Catenane**.

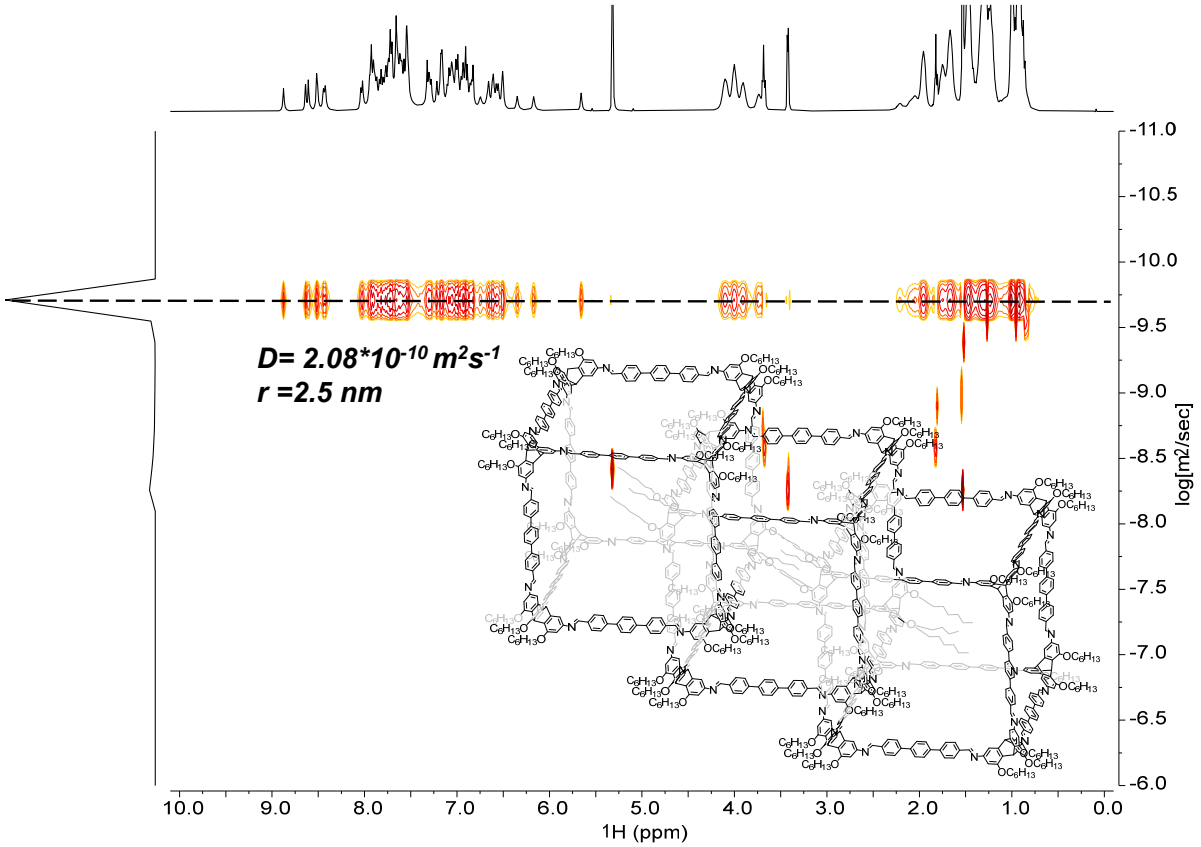

Figure 8.1.109: DOSY NMR spectrum (400 MHz, CD_2Cl_2) of **HeiTri-[3]Catenane**.

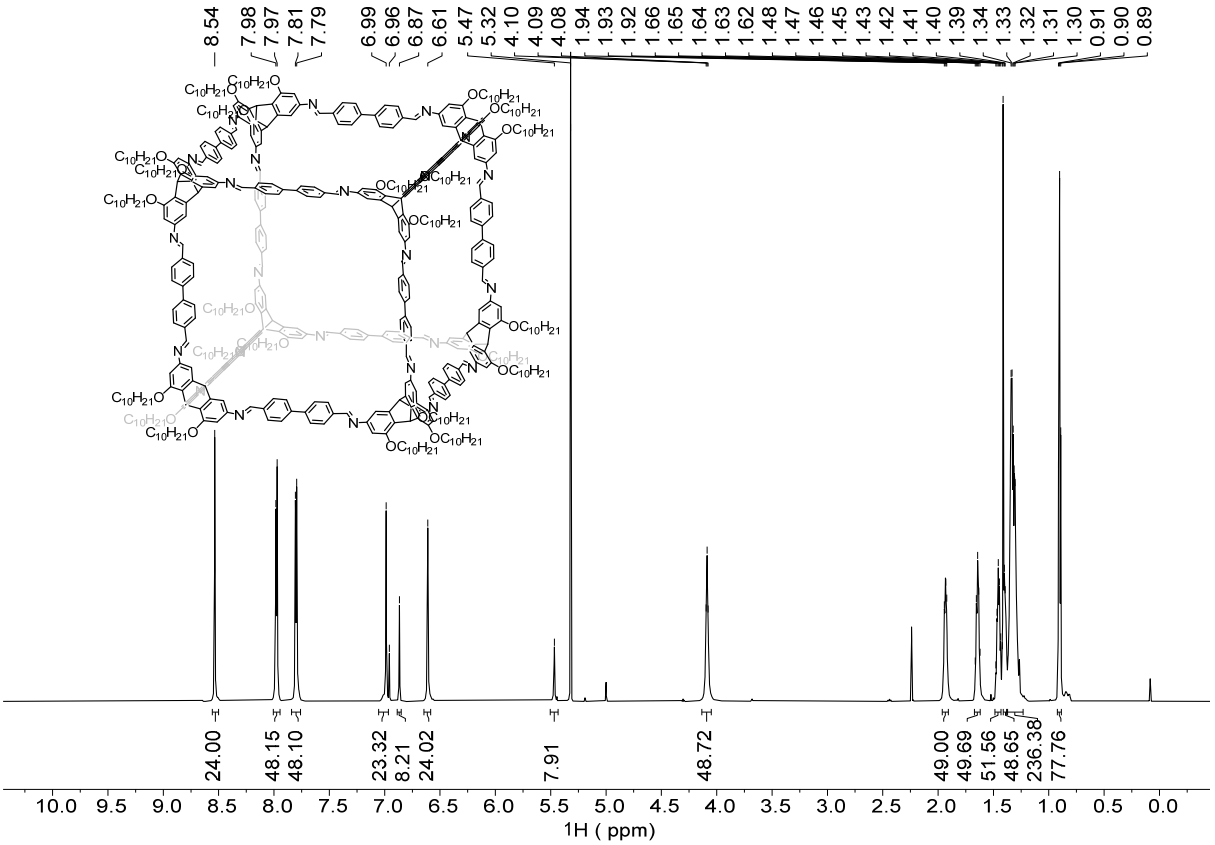

Figure 8.1.110: ^1H NMR spectrum (700 MHz, CD_2Cl_2) of **DecBi-Cage**.

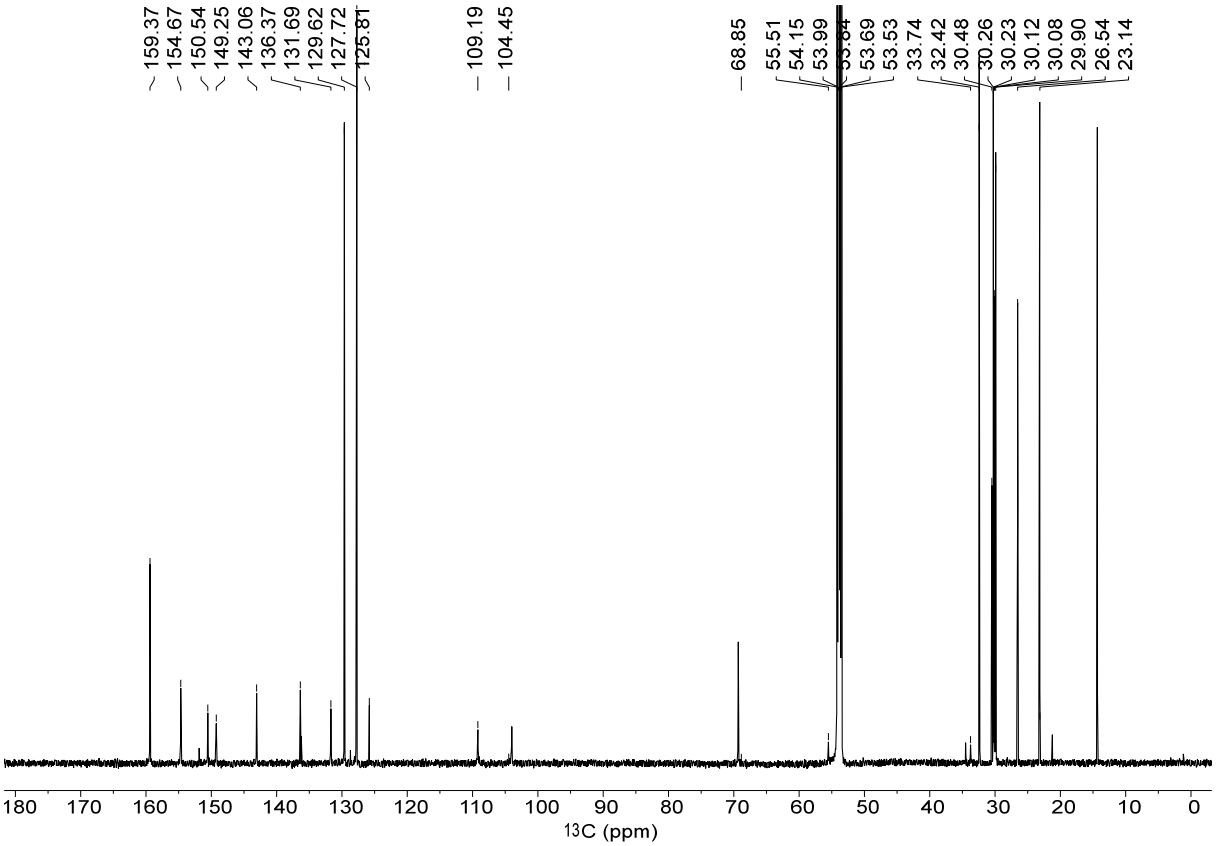

Figure 8.1.111: ^{13}C NMR spectrum (176 MHz, CD_2Cl_2) of **DecBi-Cage**.

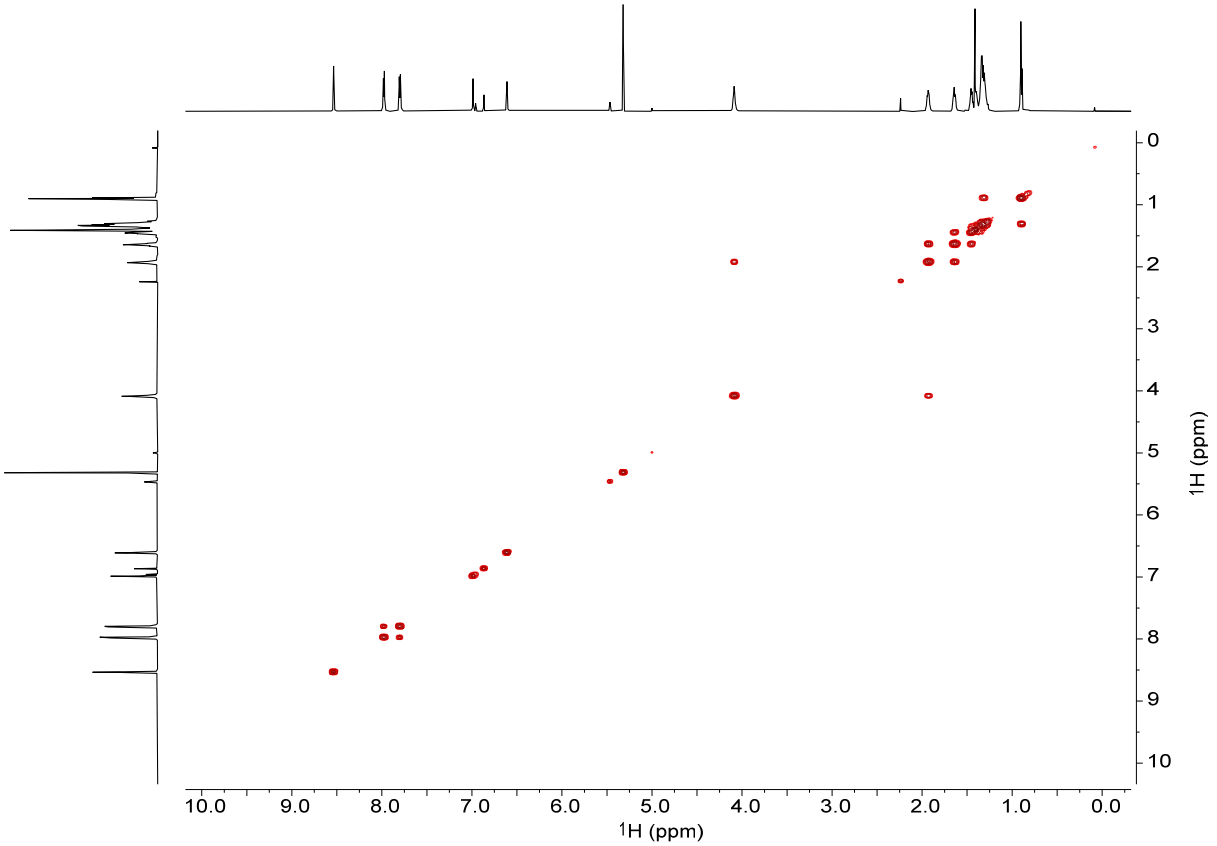

Figure 8.1.112: ^{1}H-^{1}H COSY NMR spectrum (700/700 MHz, CD_2Cl_2) of **DecBi-Cage**.

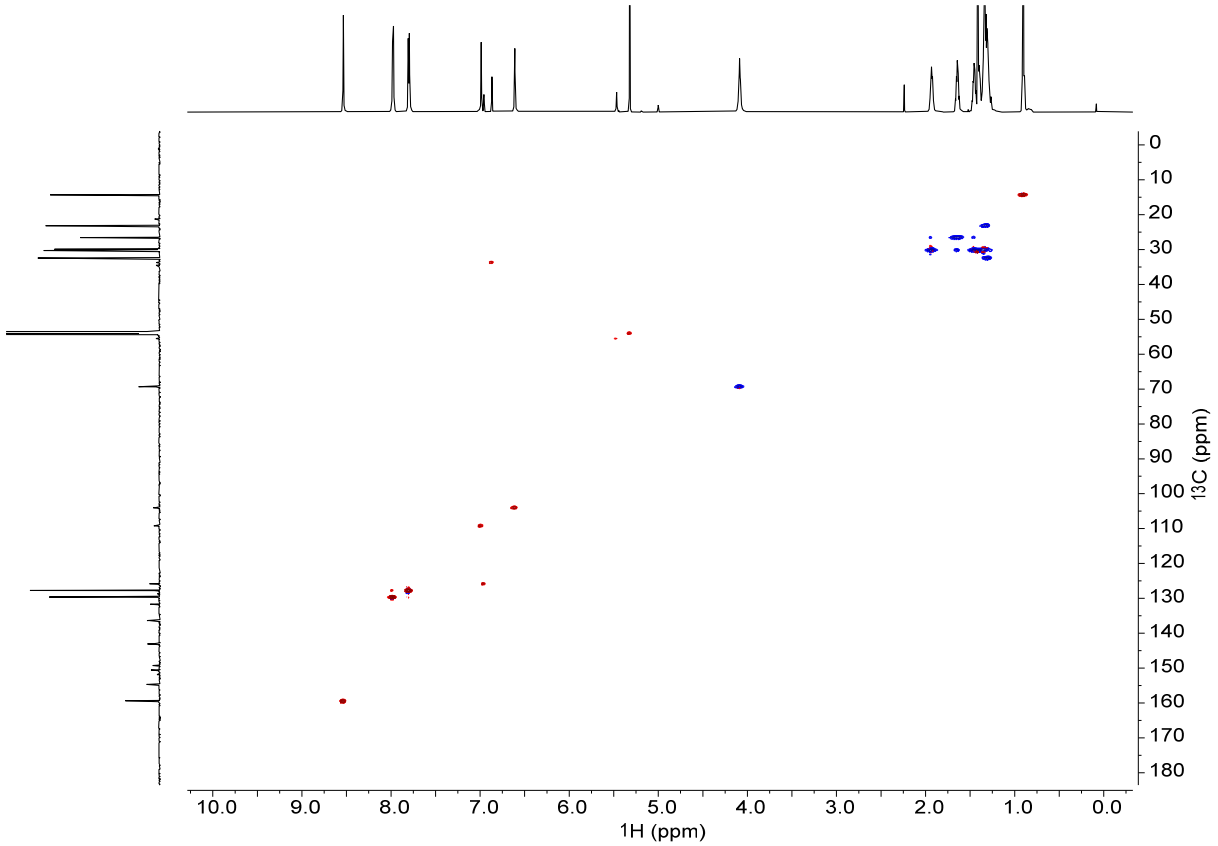

Figure 8.1.113: ^{1}H-^{13}C HSQC NMR spectrum (700/176 MHz, CD_2Cl_2) of **DecBi-Cage**.

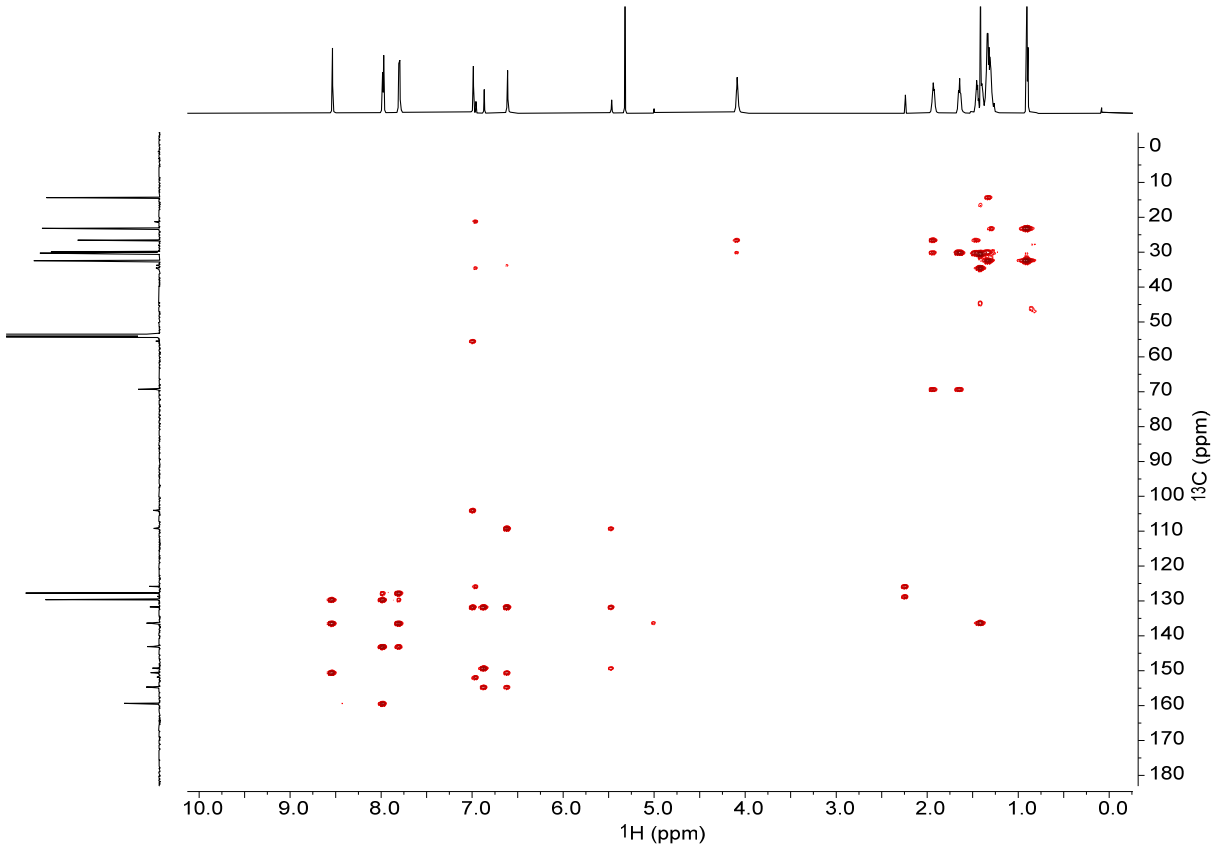

Figure 8.1.114: ^{1}H-^{13}C HMBC NMR spectrum (700/176 MHz, CD_2Cl_2) of **DecBi-Cage**.

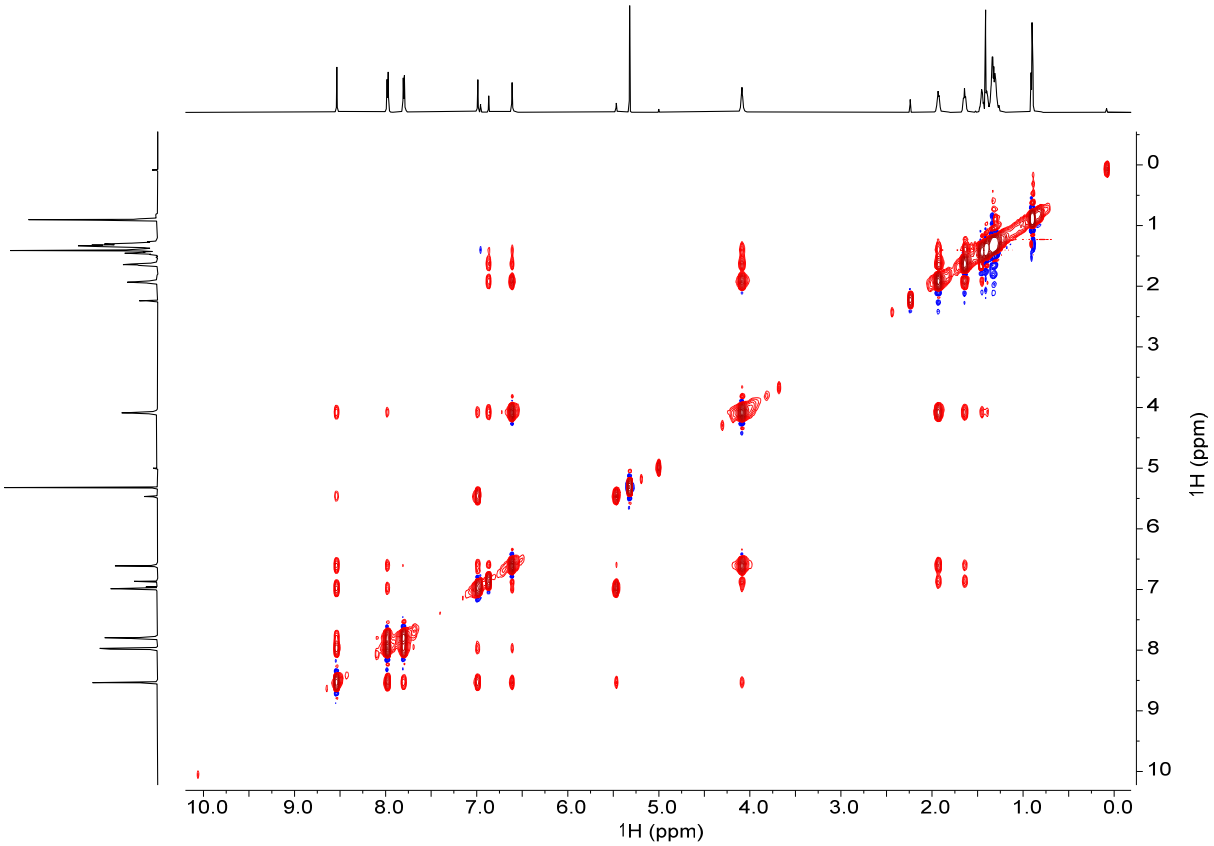

Figure 8.1.115: ^{1}H-^{1}H NOESY NMR spectrum (700/700 MHz, CD_2Cl_2) of **DecBi-Cage**.

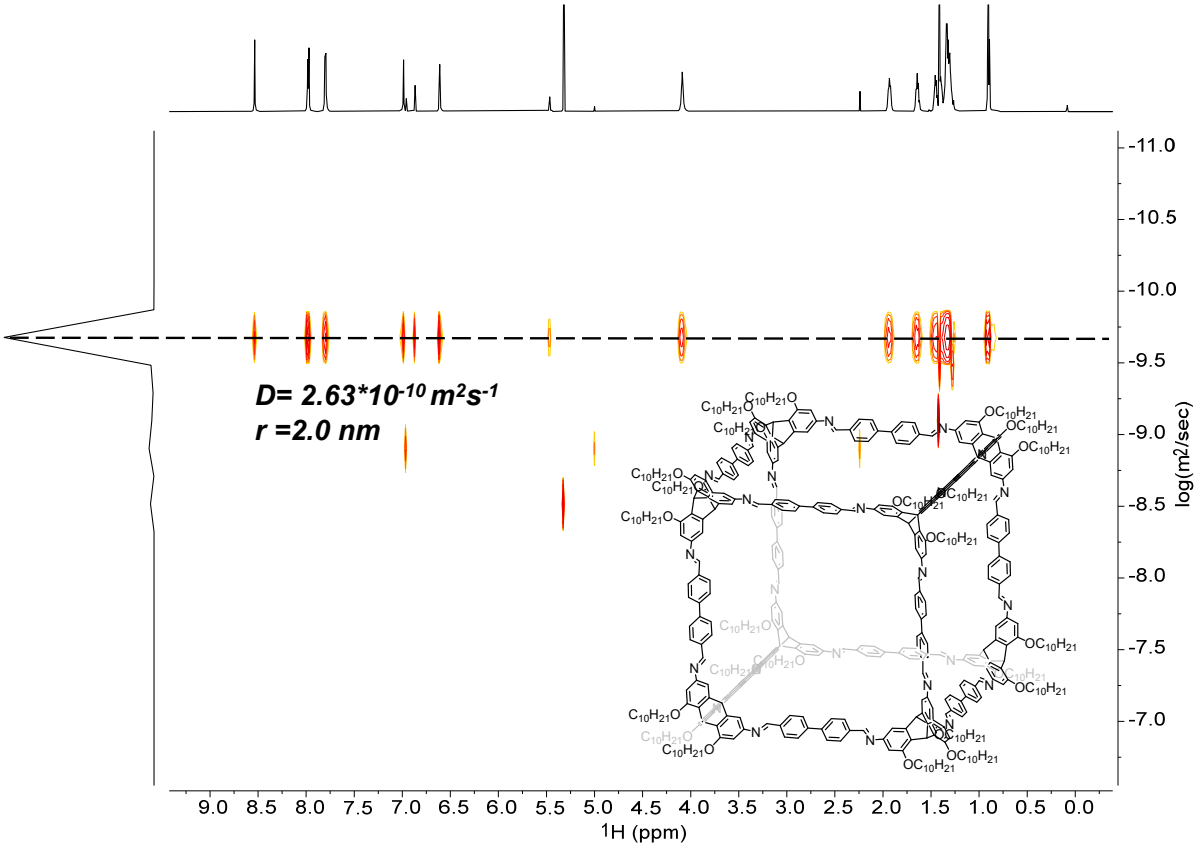

Figure 8.1.116: DOSY NMR spectrum (400 MHz, CD_2Cl_2) of **HeiBi-Cage**.

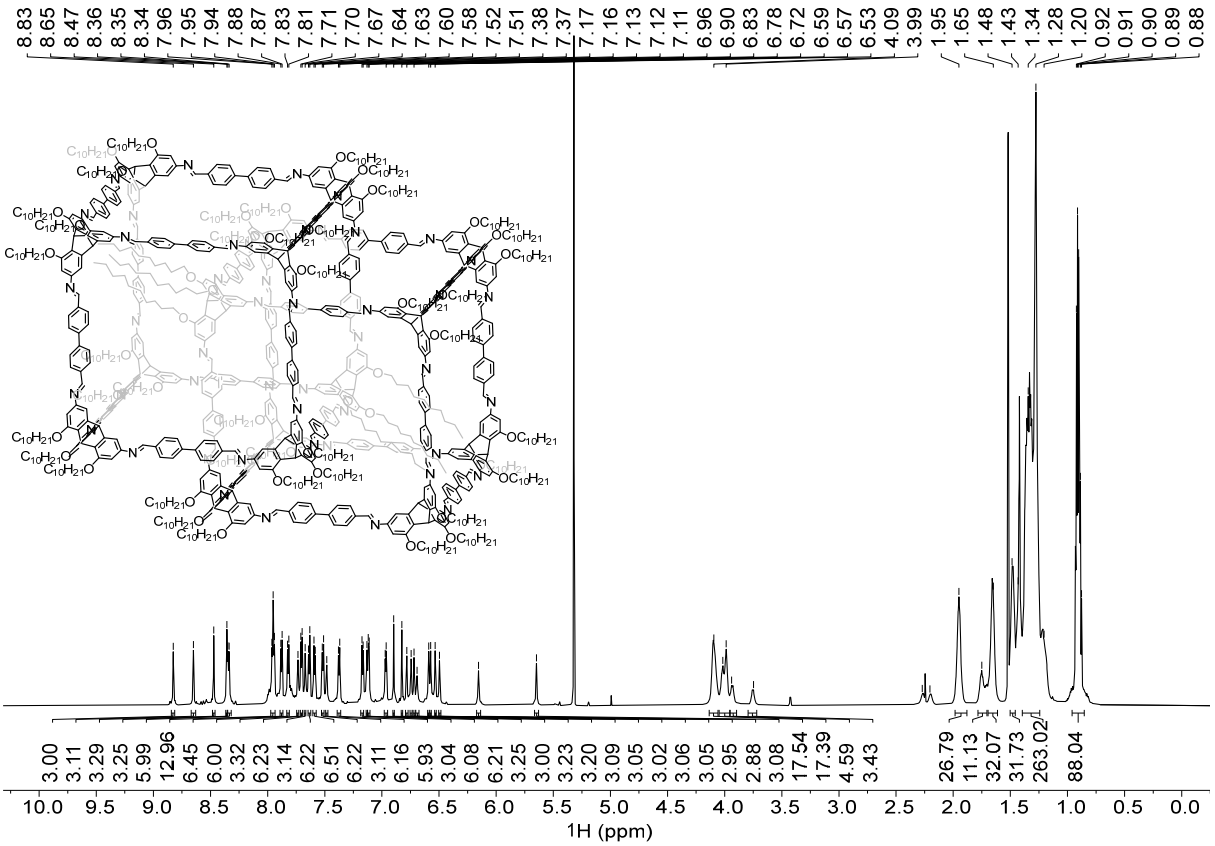

Figure 8.1.117: ^{1}H NMR spectrum (700 MHz, CD_2Cl_2) of **DecBi-Catenane**.

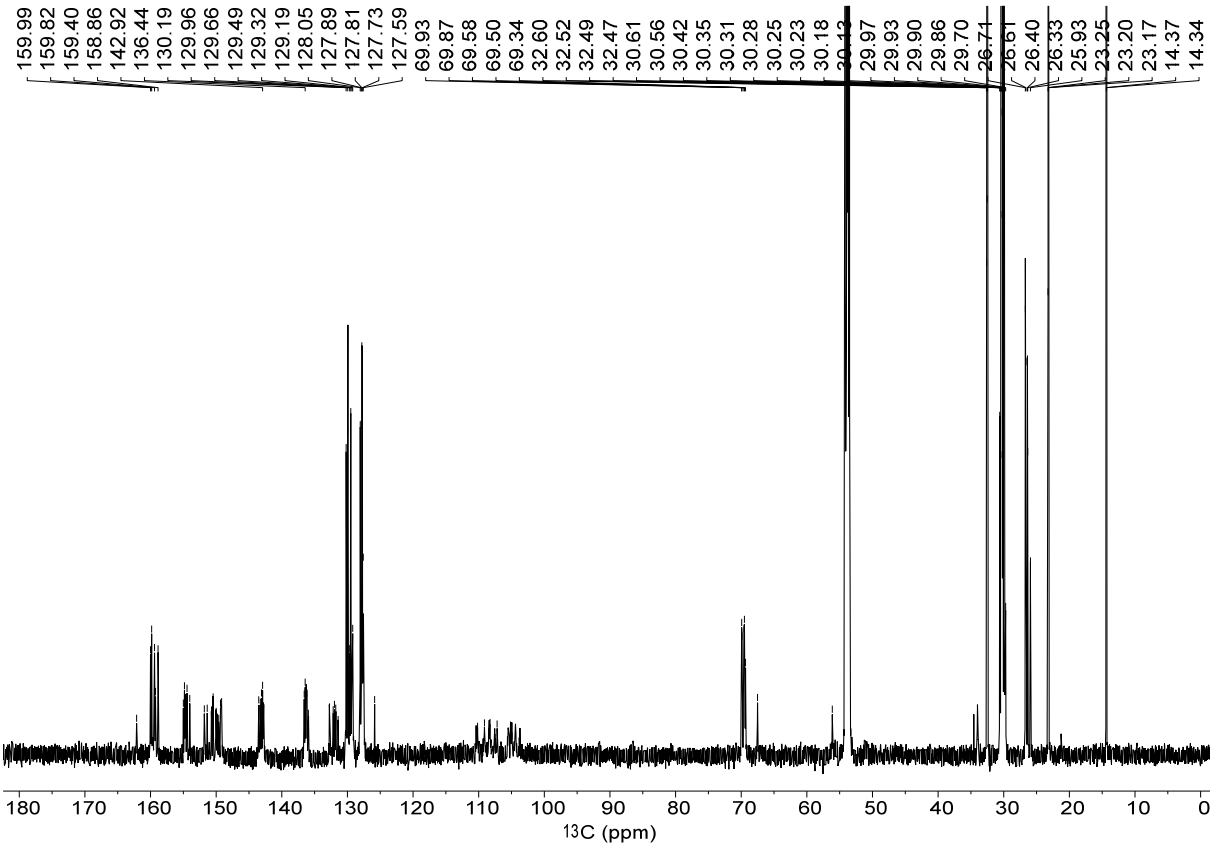

Figure 8.1.118: ^{13}C NMR spectrum (176 MHz, CD_2Cl_2) of **DecBi-Catenane**.

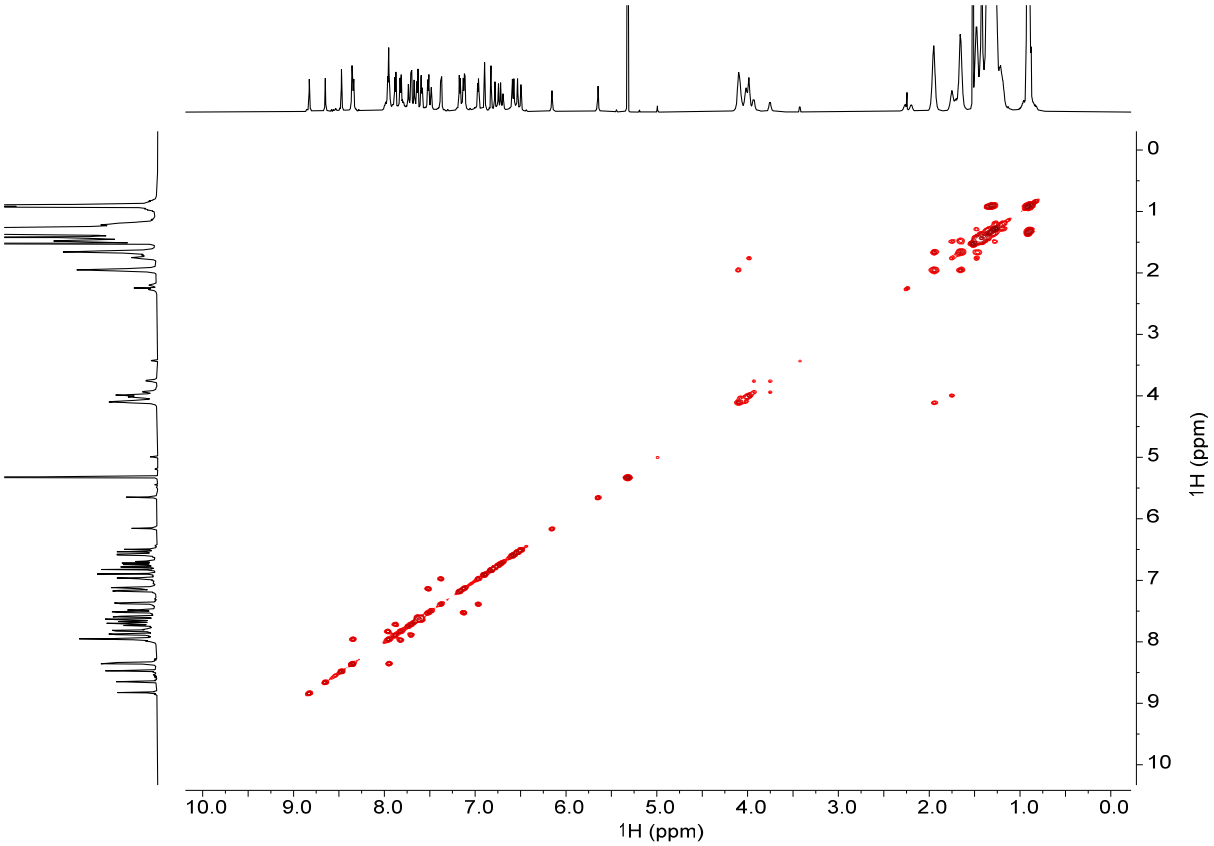

Figure 8.1.119: ^{1}H-^{1}H COSY NMR spectrum (700/700 MHz, CD_2Cl_2) of **DecBi-Catenane**.

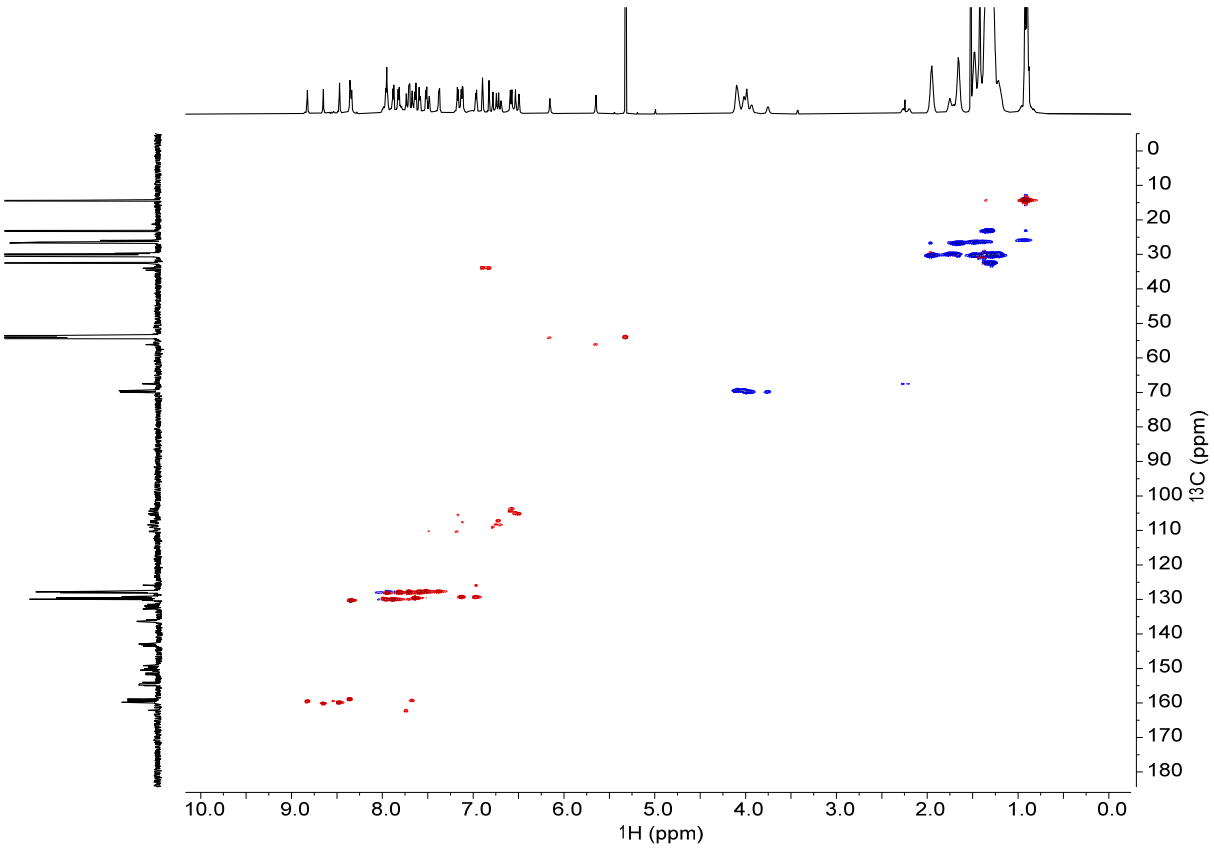

Figure 8.1.120: ^{1}H-^{13}C HSQC NMR spectrum (700/176 MHz, CD_2Cl_2) of **DecBi-Catenane**.

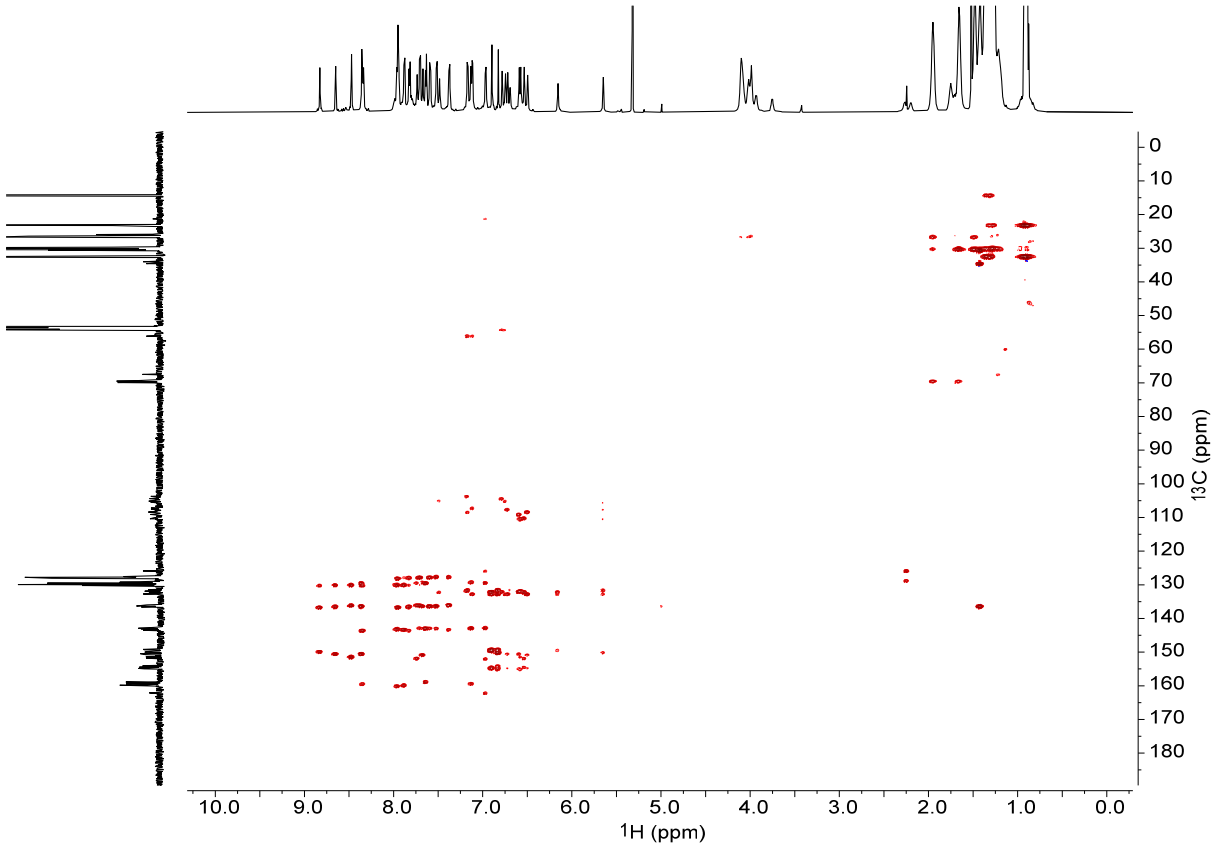

Figure 8.1.121: ^{1}H-^{13}C HMBC NMR spectrum (700/176 MHz, CD_2Cl_2) of **DecBi-Catenane**.

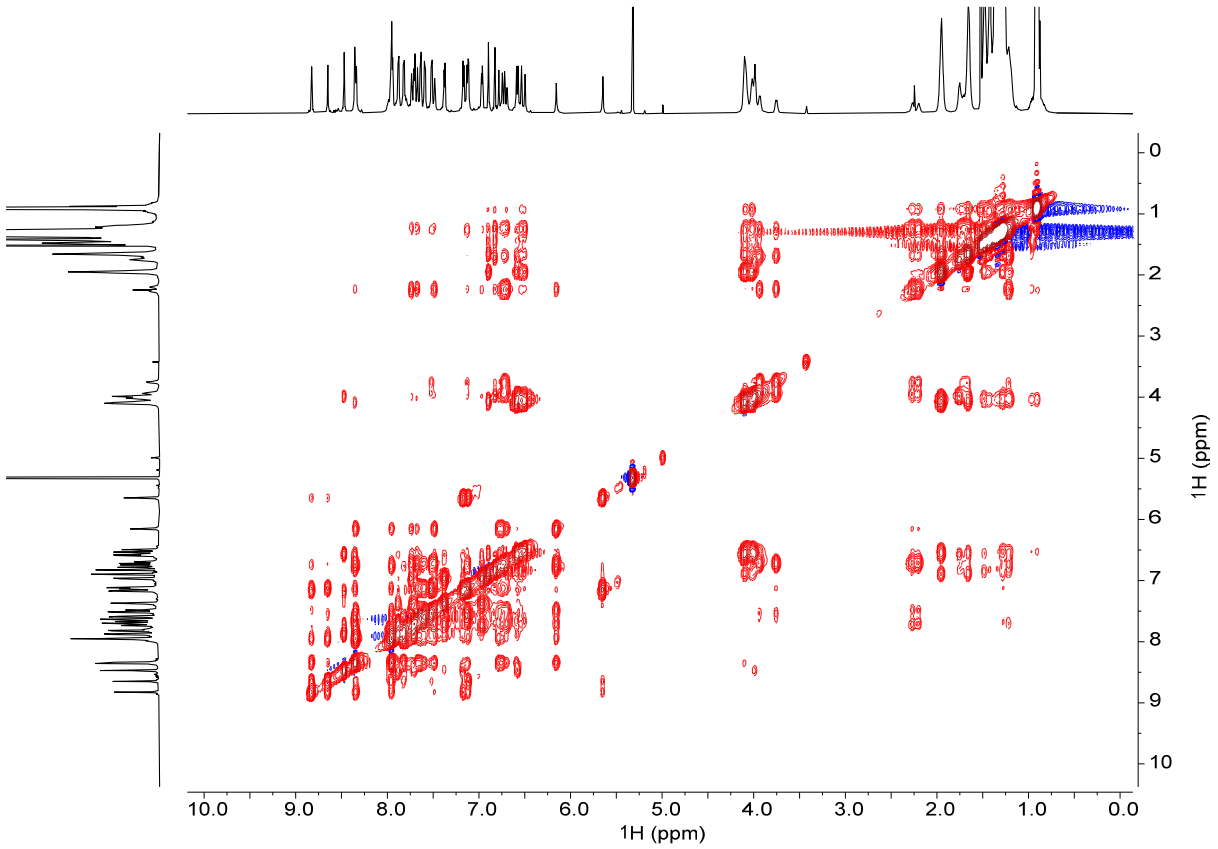

Figure 8.1.122: ^{1}H-^{1}H NOESY NMR spectrum (700/700 MHz, CD_2Cl_2) of **DecBi-Catenane**.

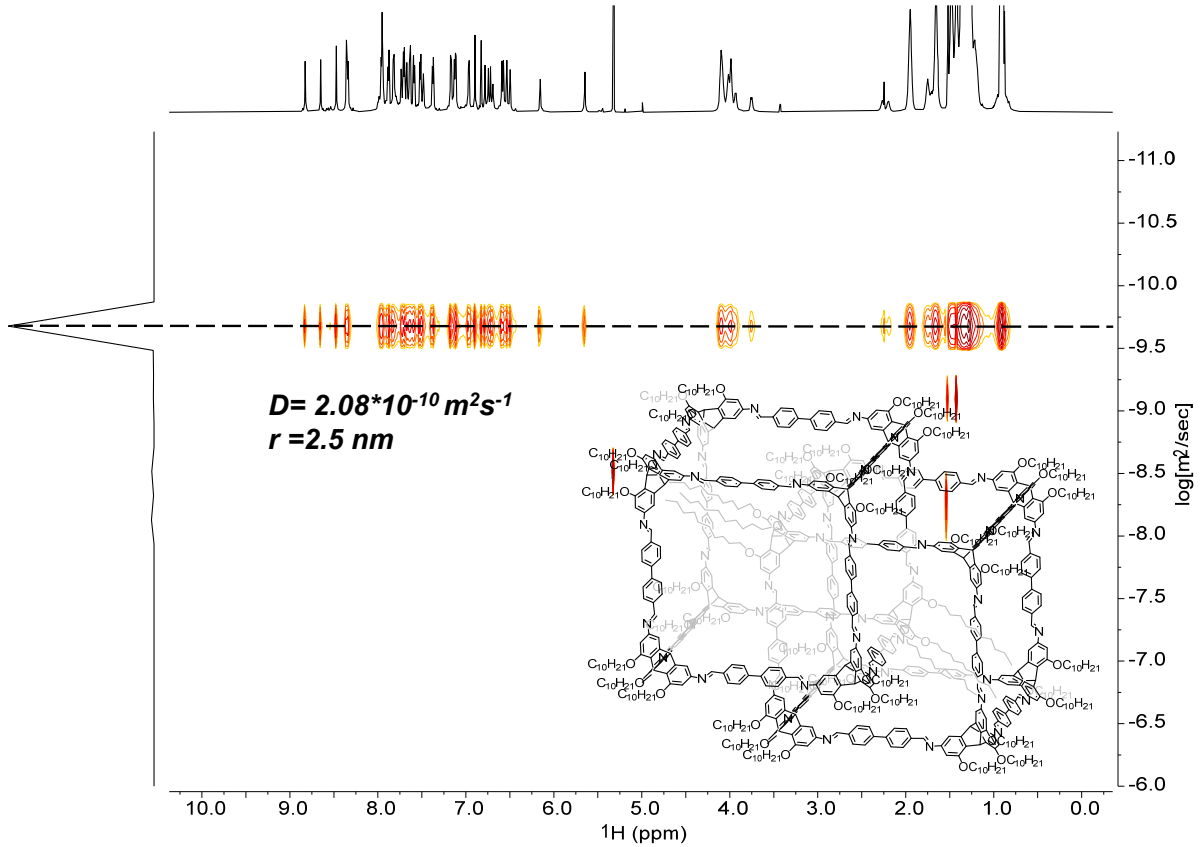

Figure 8.1.123: DOSY NMR spectrum (400 MHz, CD_2Cl_2) of **DecBi-Catenane**.

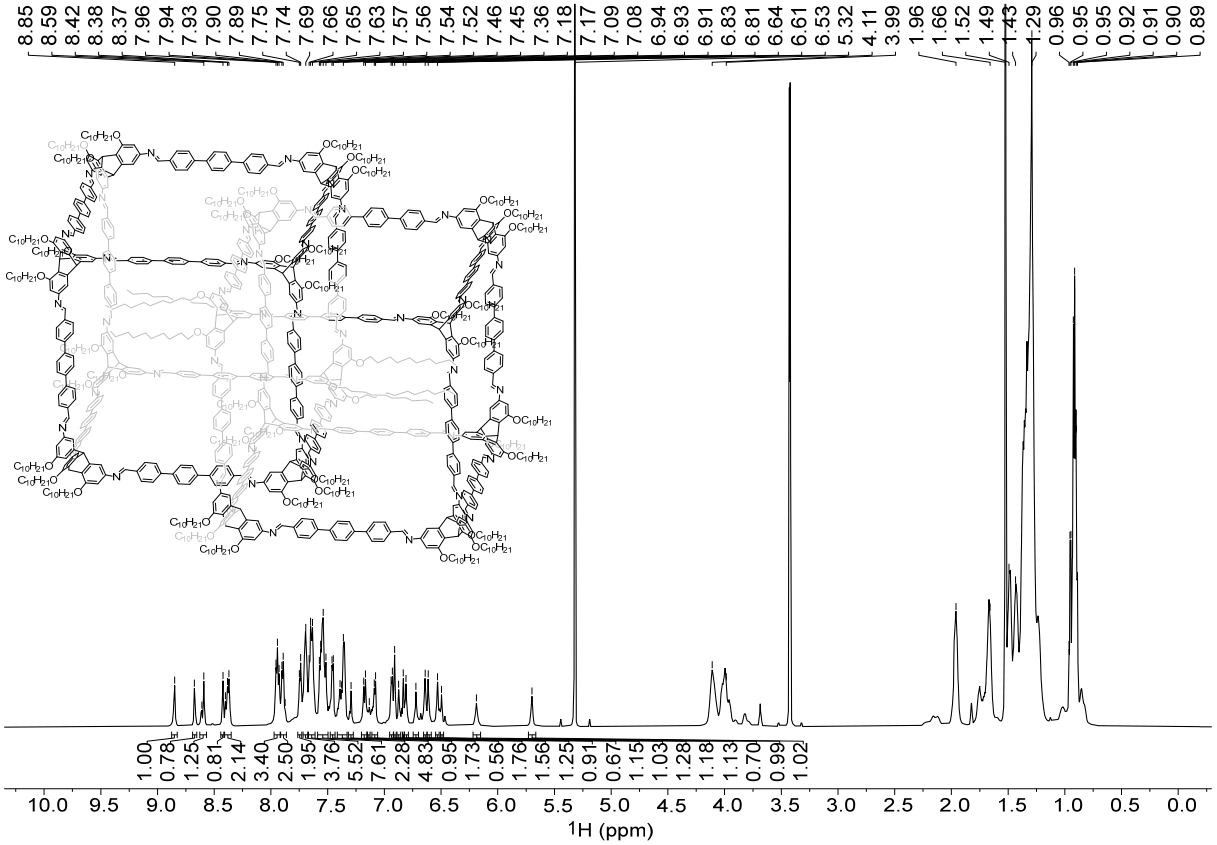

Figure 8.1.124: ^1H NMR spectrum (700 MHz, CD_2Cl_2) of **DecTri-Catenane**.

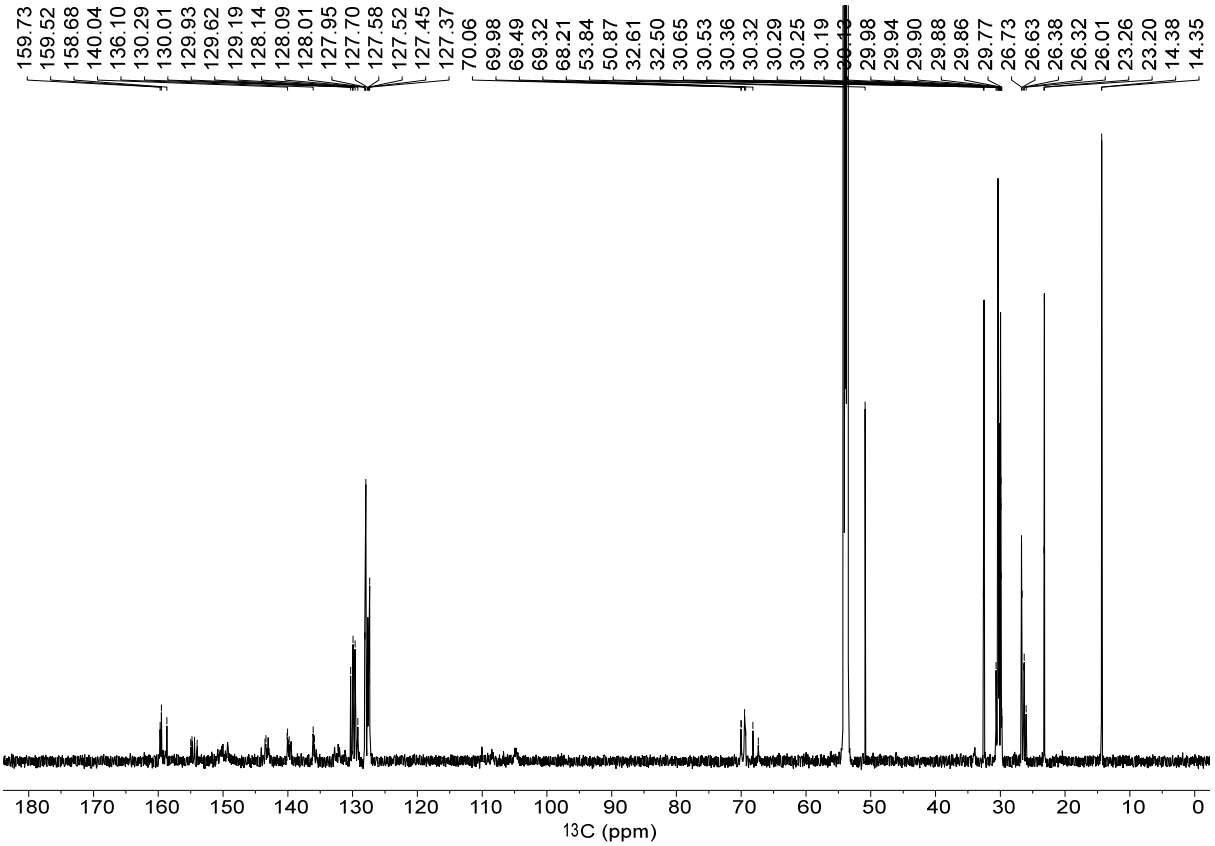

Figure 8.1.125: ^{13}C NMR spectrum (176 MHz, CD_2Cl_2) of **DecTri-Catenane**.

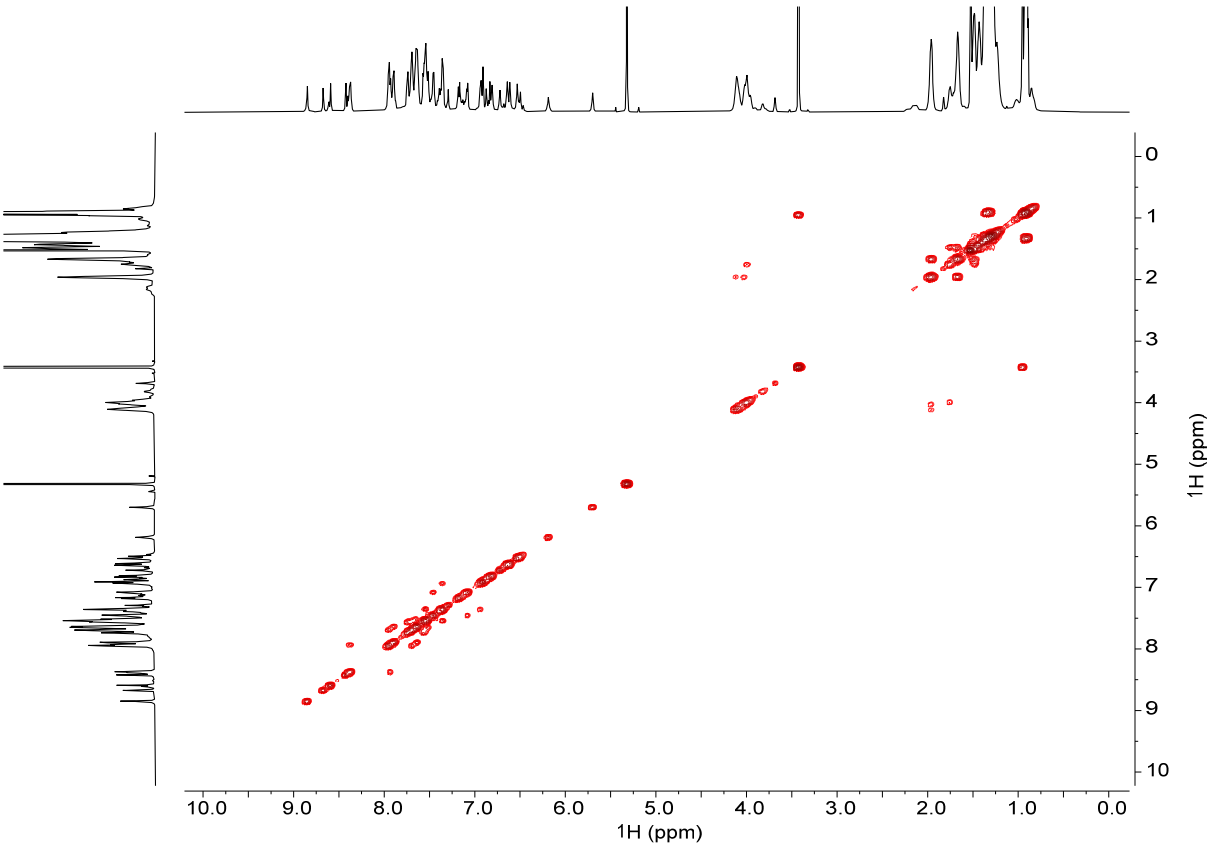

Figure 8.1.126: ^{1}H-^{1}H COSY NMR spectrum (700/700 MHz, CD_2Cl_2) of **DecTri-Catenane**.

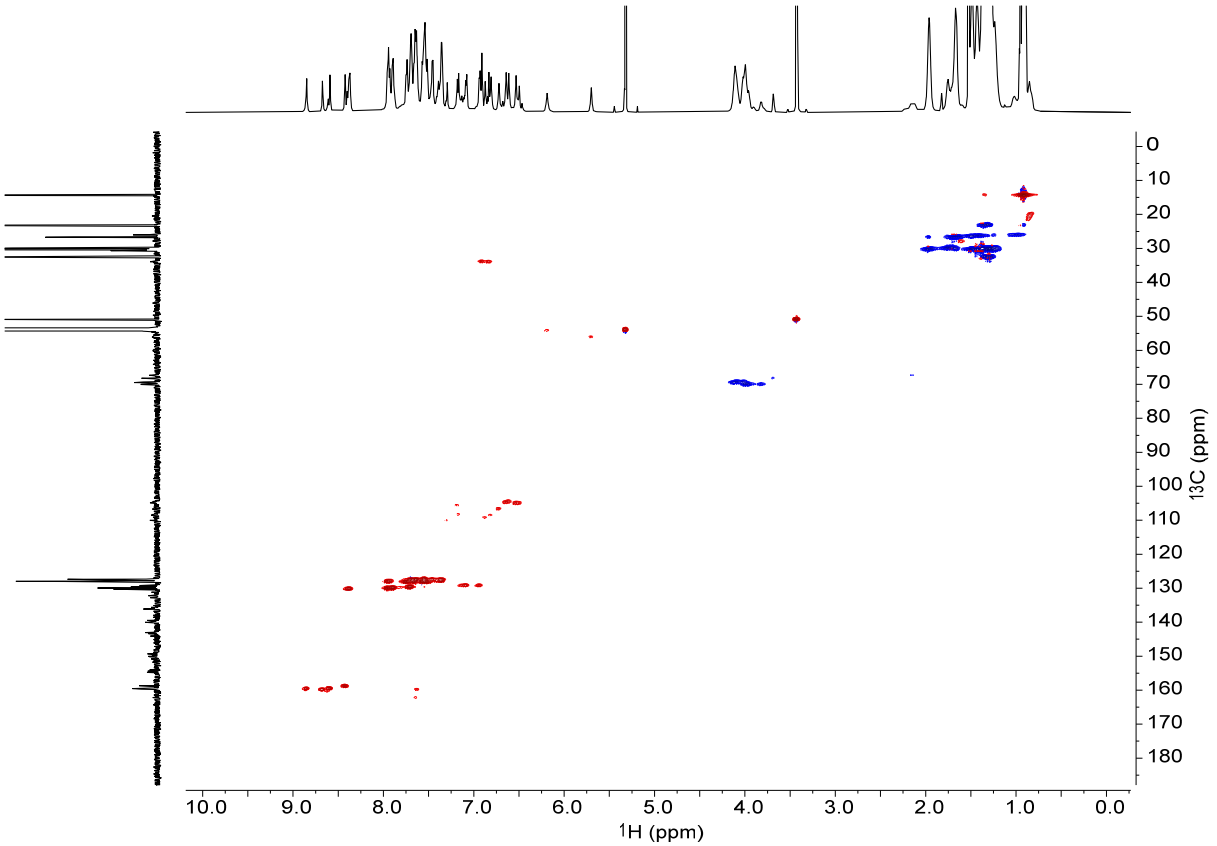

Figure 8.1.127: ^{1}H-^{13}C HSQC NMR spectrum (700/176 MHz, CD_2Cl_2) of **DecTri-Catenane**.

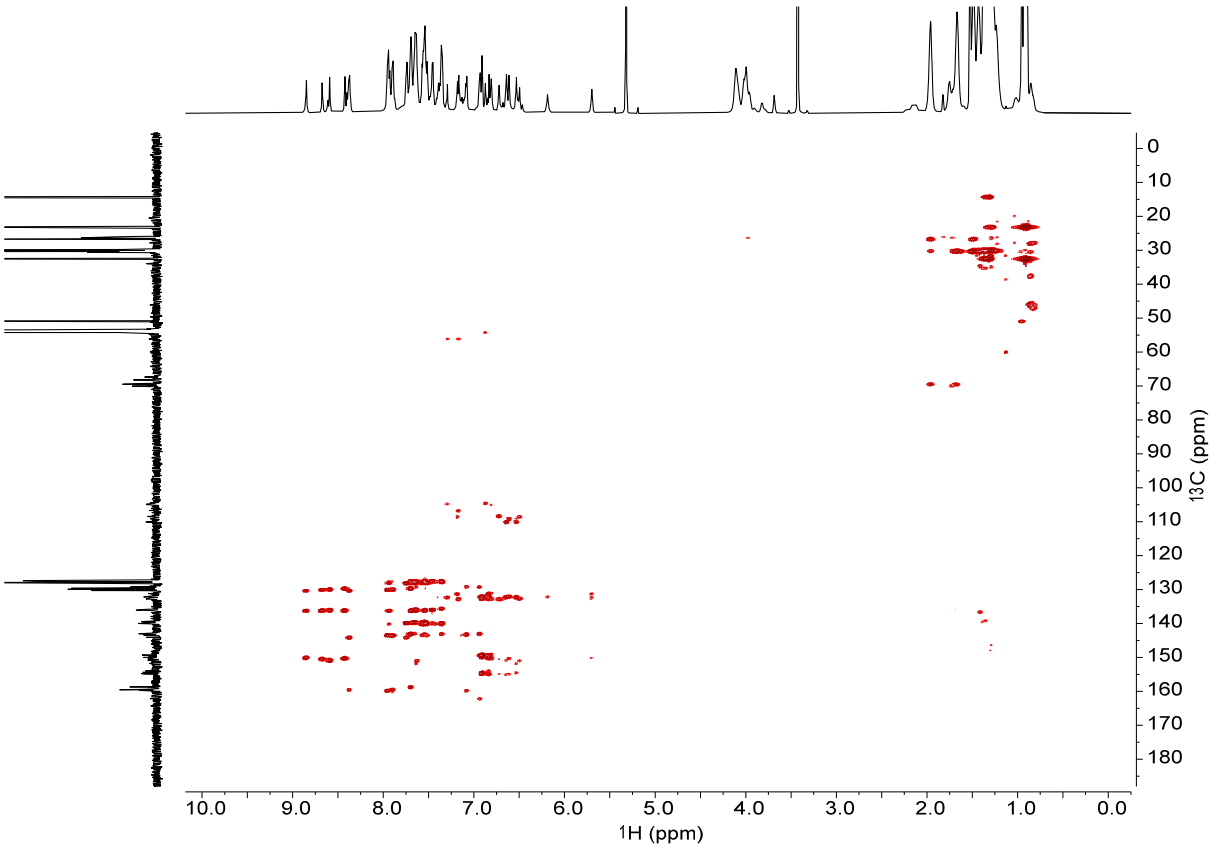

Figure 8.1.128: ^{1}H-^{13}C HMBC NMR spectrum (700/176 MHz, CD_2Cl_2) of **DecTri-Catenane**.

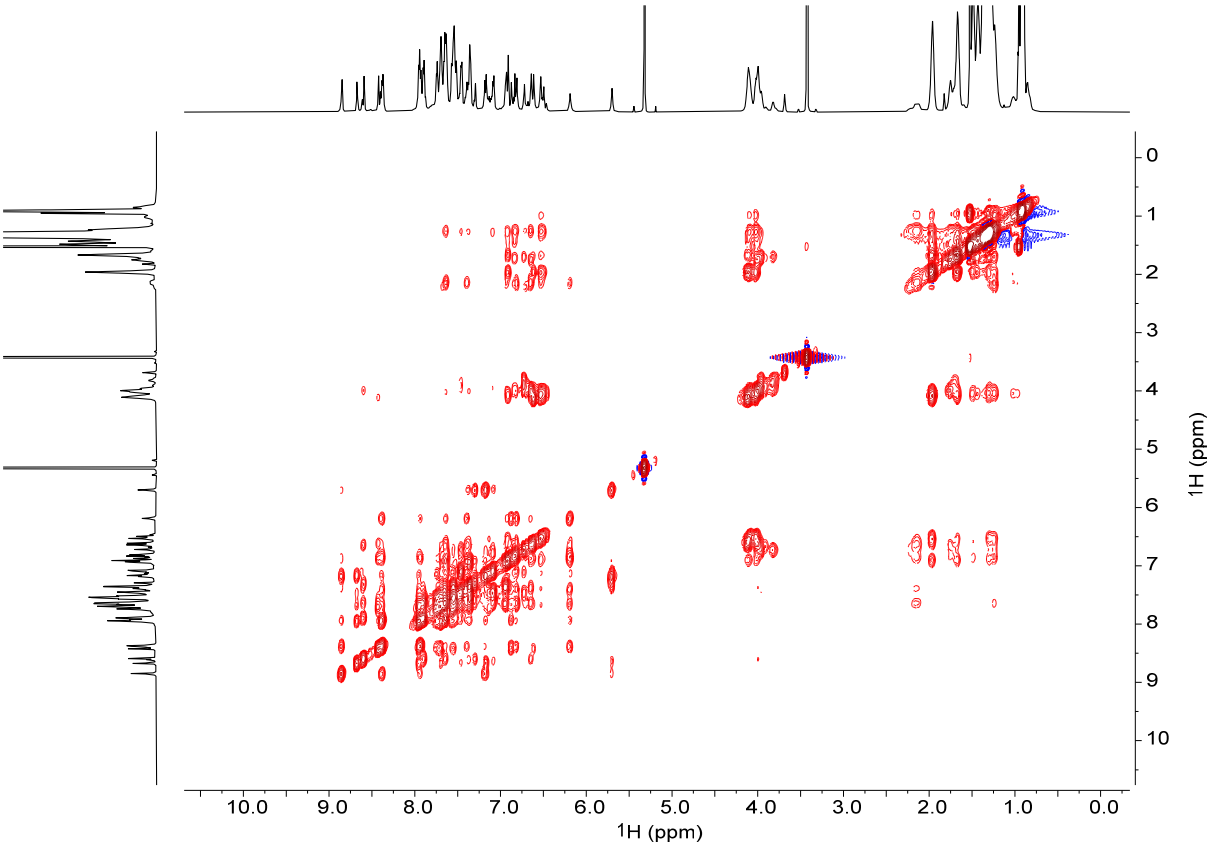

Figure 8.1.129: ^{1}H-^{1}H NOESY NMR spectrum (700/700 MHz, CD_2Cl_2) of **DecTri-Catenane**.

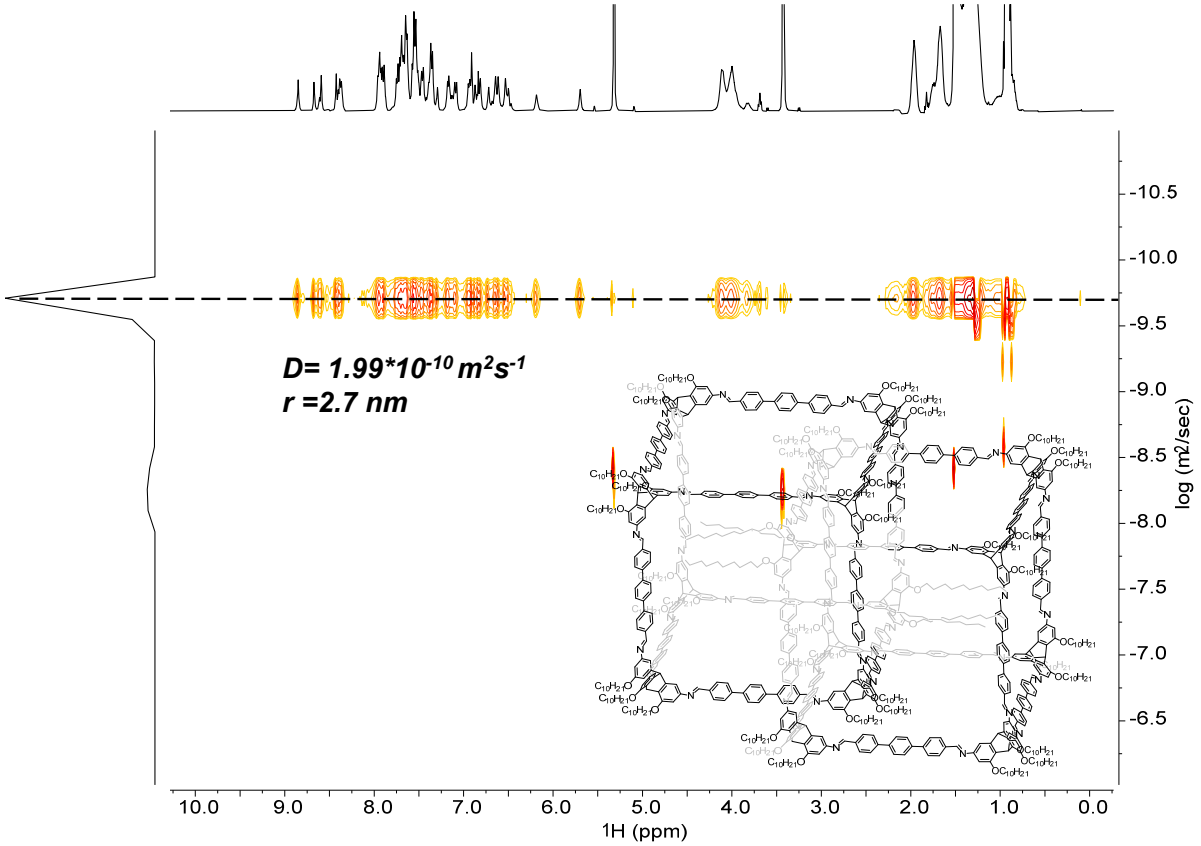

Figure 8.1.130: DOSY NMR spectrum (400 MHz, CD_2Cl_2) of **DecTri-Catenane**.

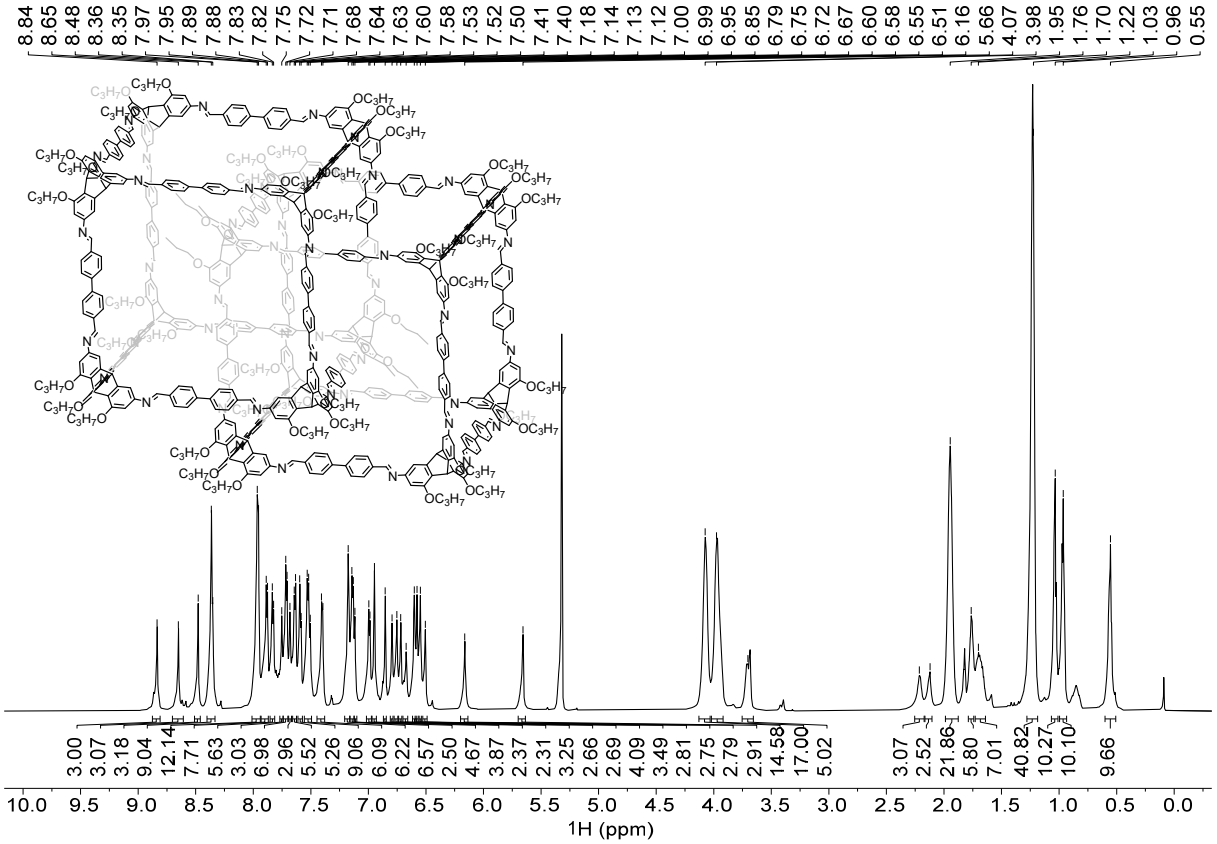

Figure 8.1.131: ^{1}H NMR spectrum (700 MHz, CD_2Cl_2) of **ProBi-Catenane**.

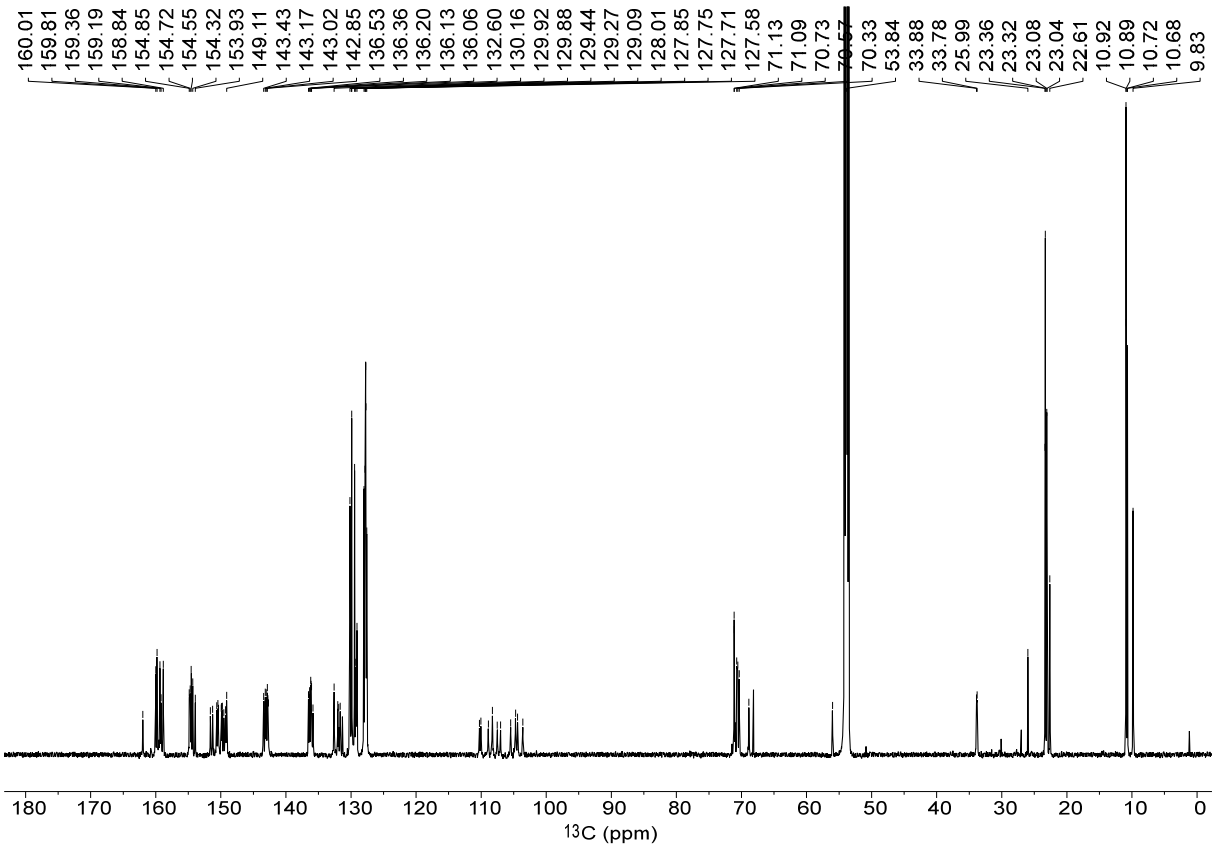

Figure 8.132: ^{13}C NMR spectrum (176 MHz, CD_2Cl_2) of **ProBi-Catenane**.

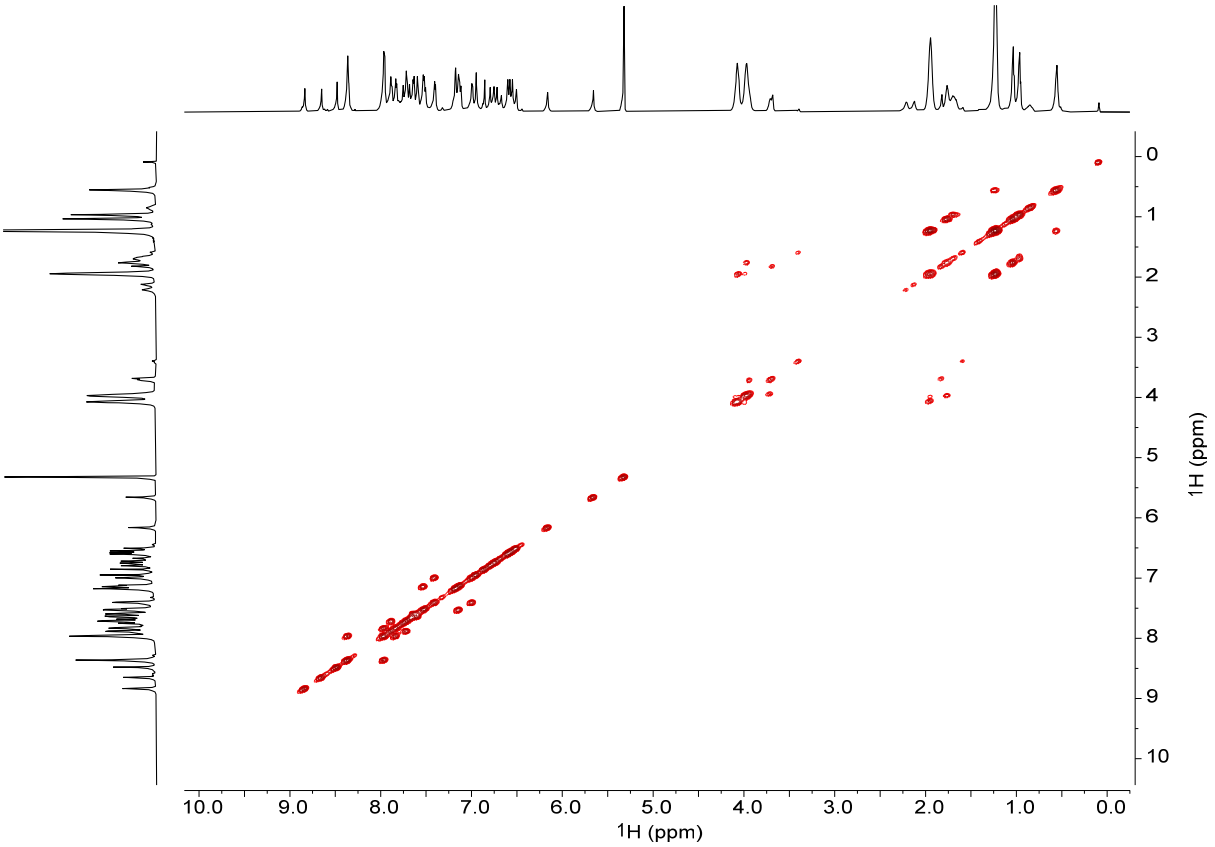

Figure 8.1.133: ^{1}H-^{1}H COSY NMR spectrum (700/700 MHz, CD_2Cl_2) of **ProBi-Catenane**.

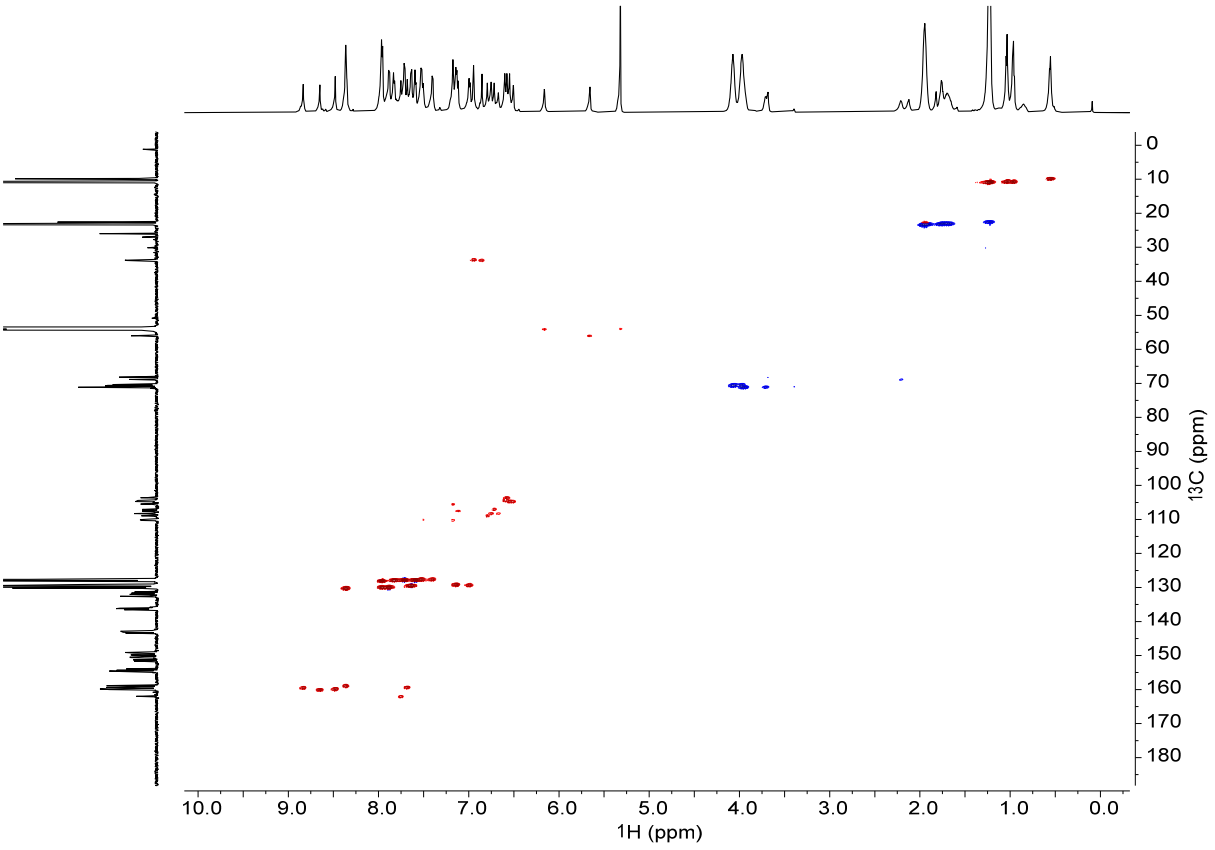

Figure 8.1.134: ^{1}H-^{13}C HSQC NMR spectrum (700/176 MHz, CD_2Cl_2) of **ProBi-Catenane**.

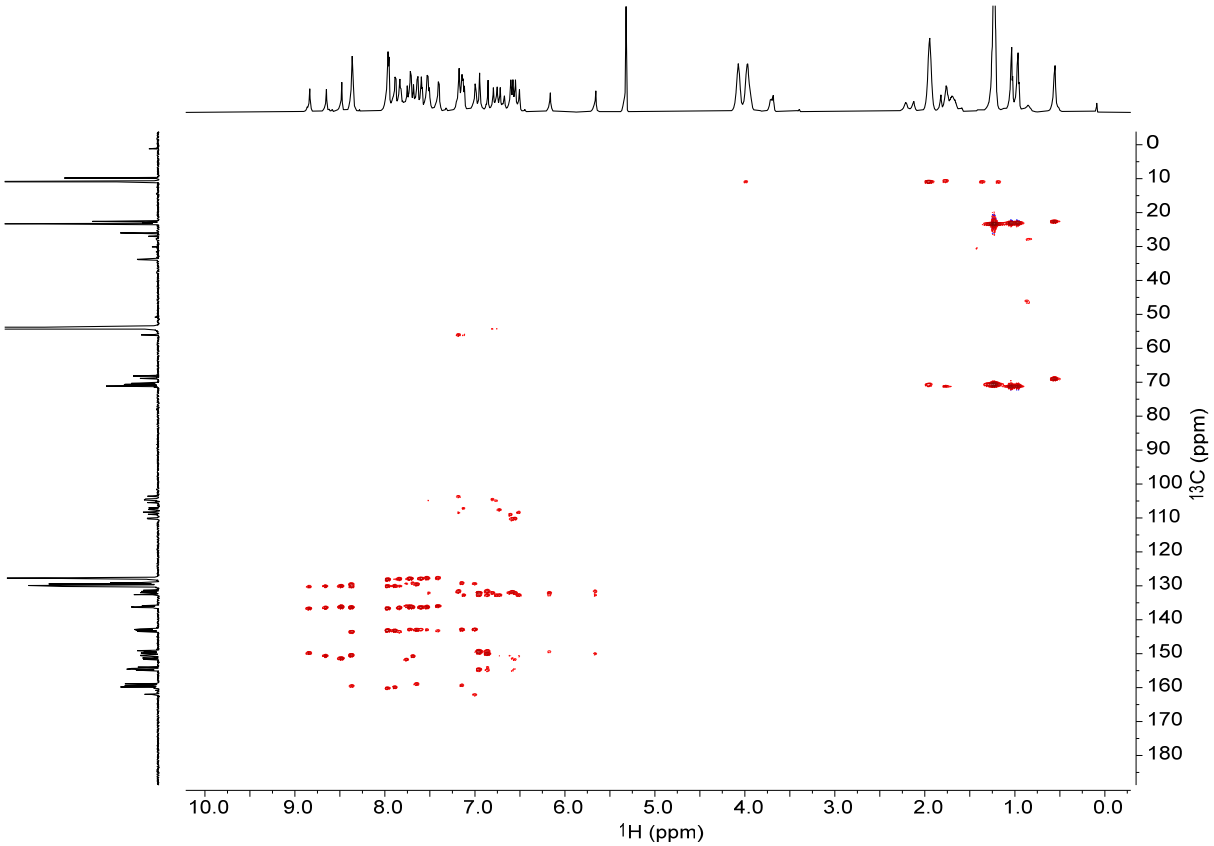

Figure 8.1.135: ^{1}H-^{13}C HMBC NMR spectrum (700/176 MHz, CD_2Cl_2) of **ProBi-Catenane**.

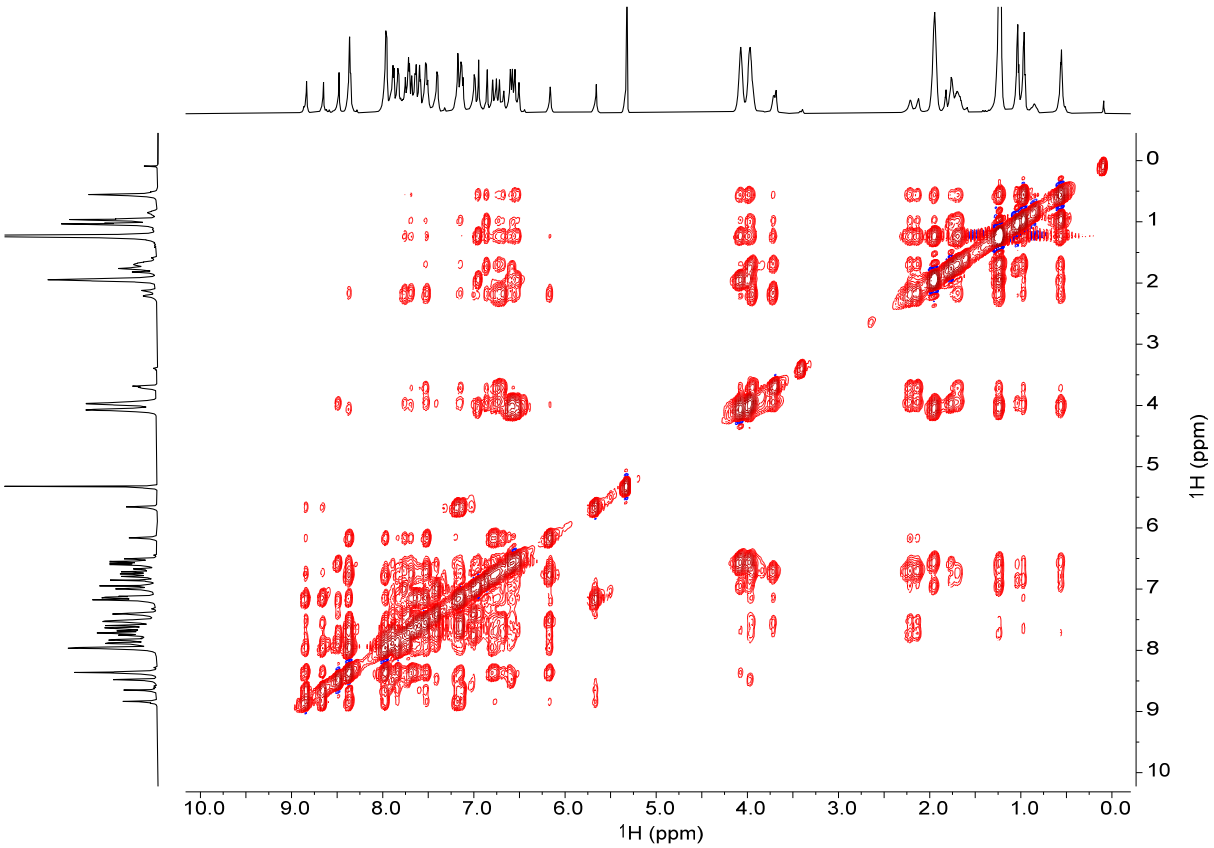

Figure 8.1.136: ^{1}H-^{1}H NOESY NMR spectrum (700/700 MHz, CD_2Cl_2) of **ProBi-Catenane**.

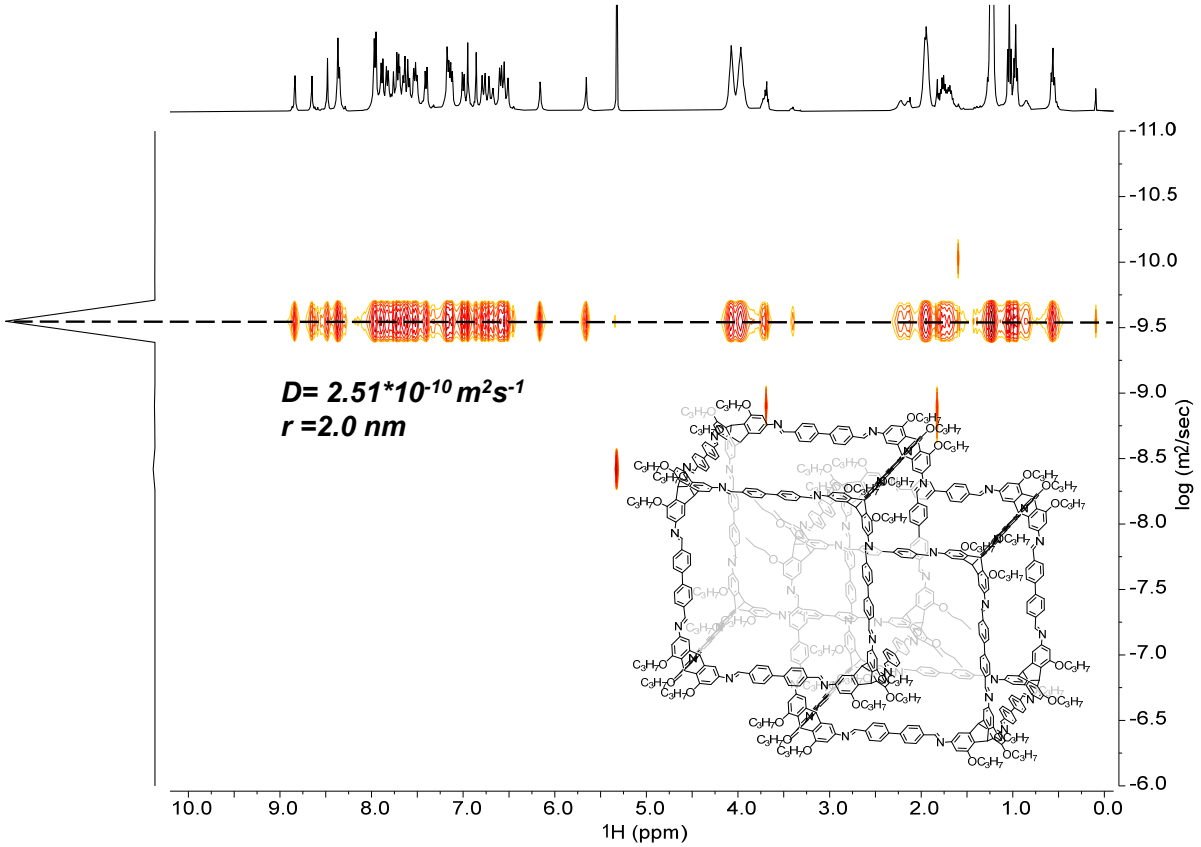

Figure 8.1.137: DOSY NMR spectrum (400 MHz, CD_2Cl_2) of **ProBi-Catenane**.

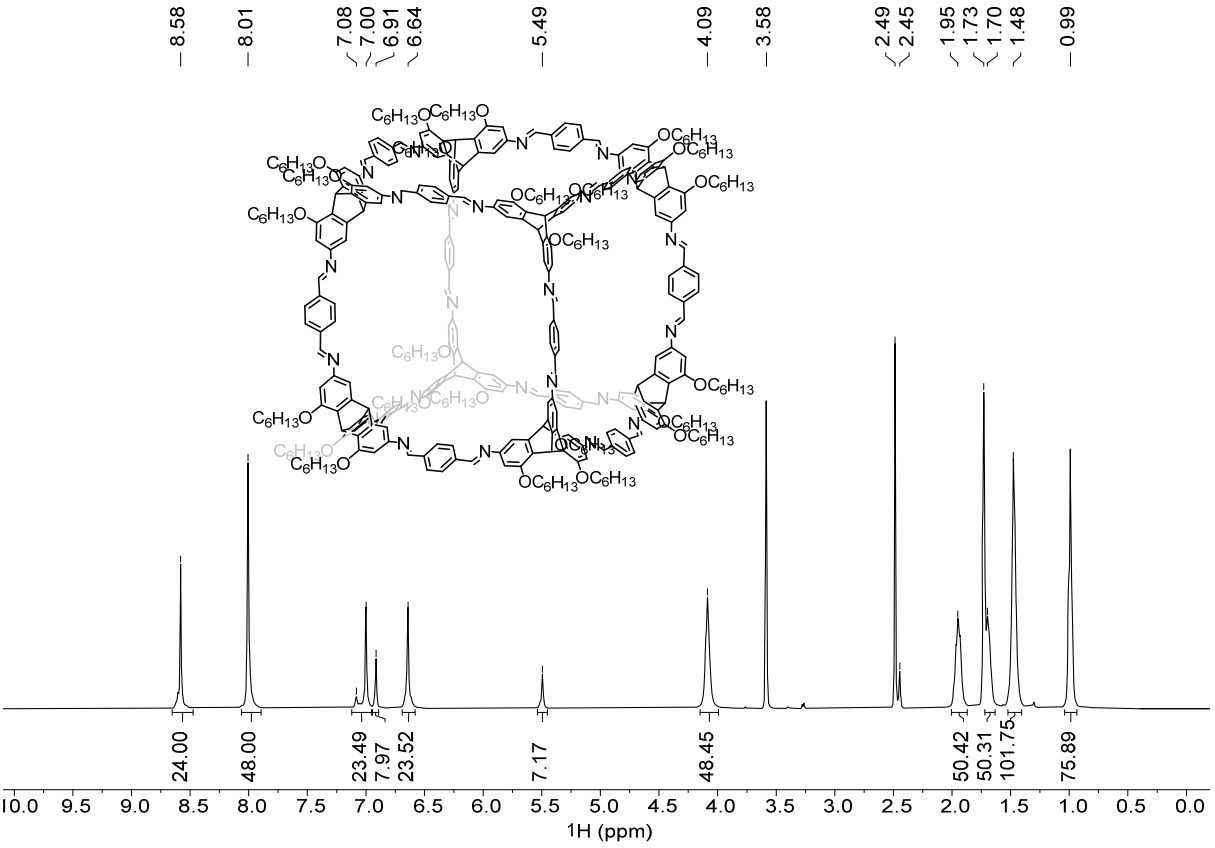

Figure 8.1.138: ^{1}H NMR spectrum (600 MHz, THF-d_8) of **HexTe-Cage**.

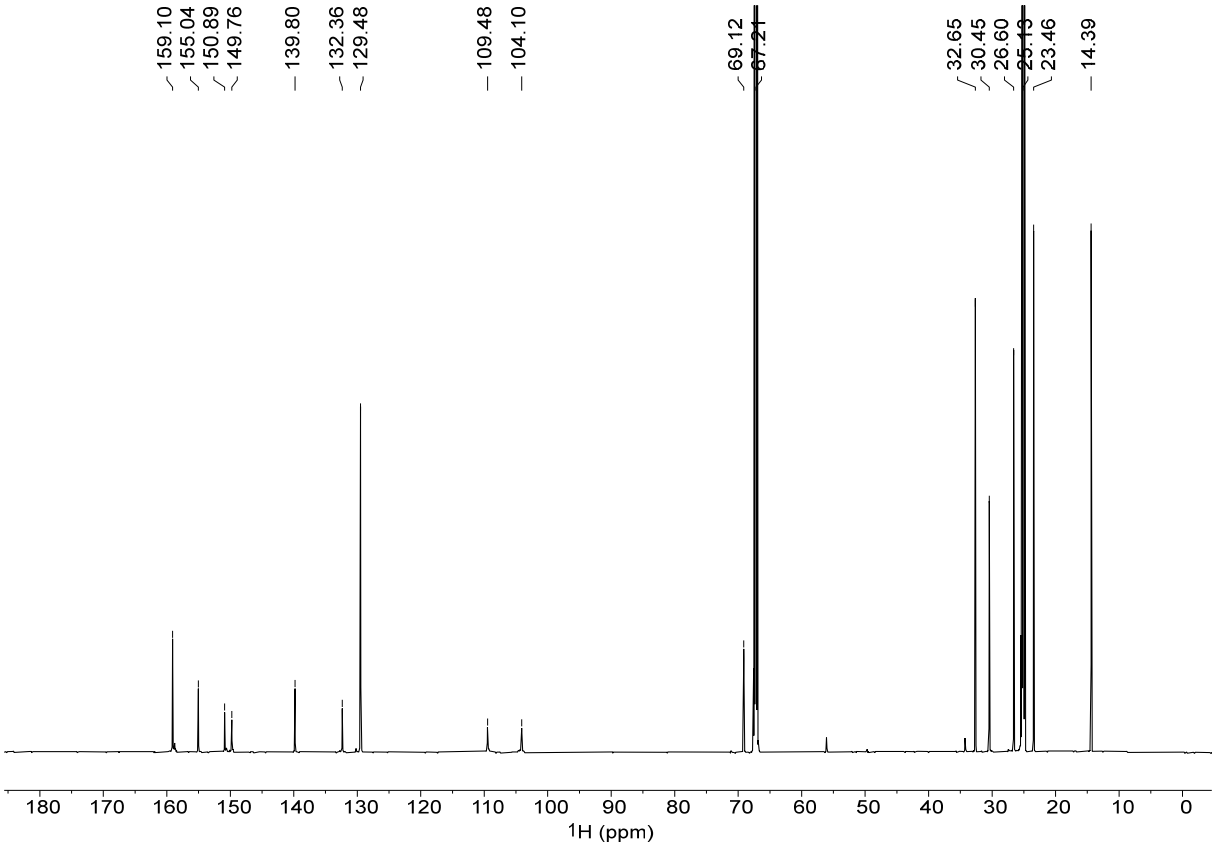

Figure 8.1.139: ^{13}C NMR spectrum (151 MHz, THF-d_8) of **HexTe-Cage**.

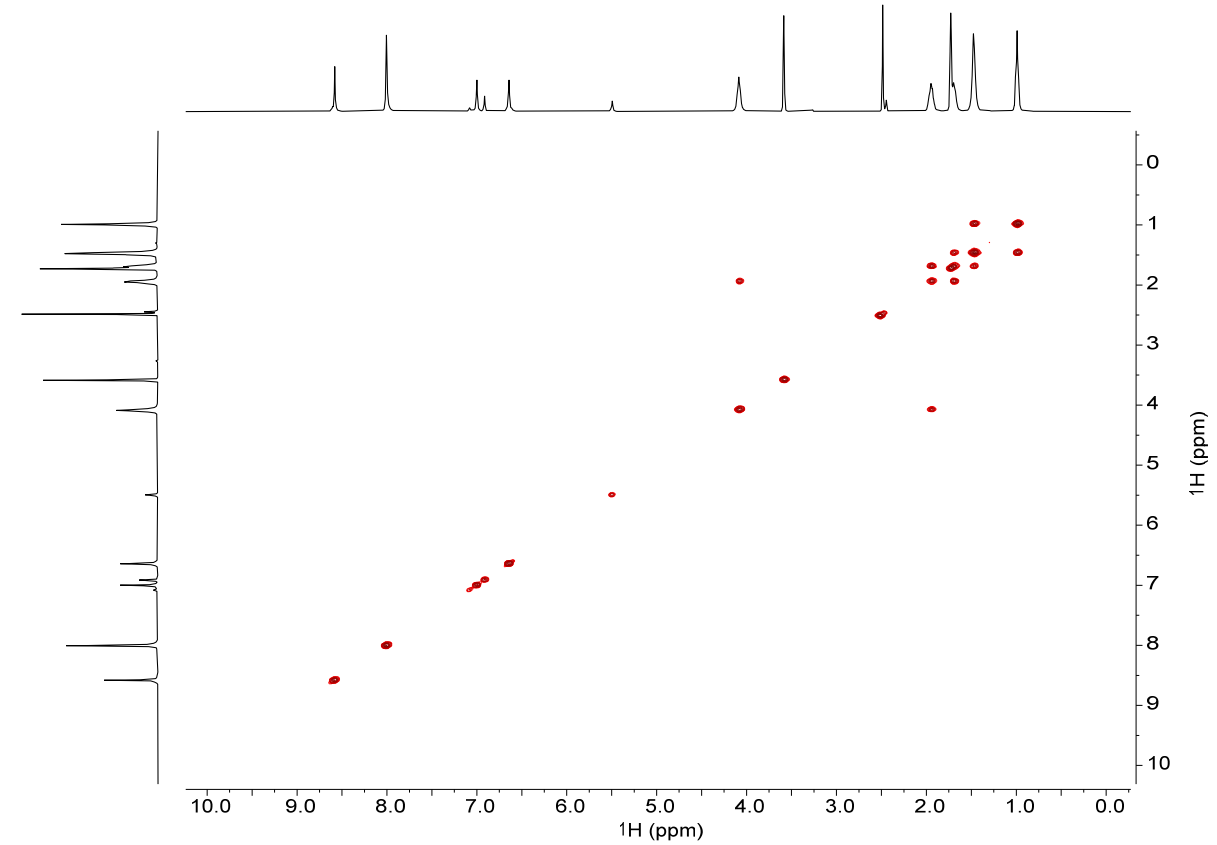

Figure 8.1.140: ^{1}H-^{1}H COSY NMR spectrum (600/600 MHz, THF-d_8) of **HexTe-Cage**.

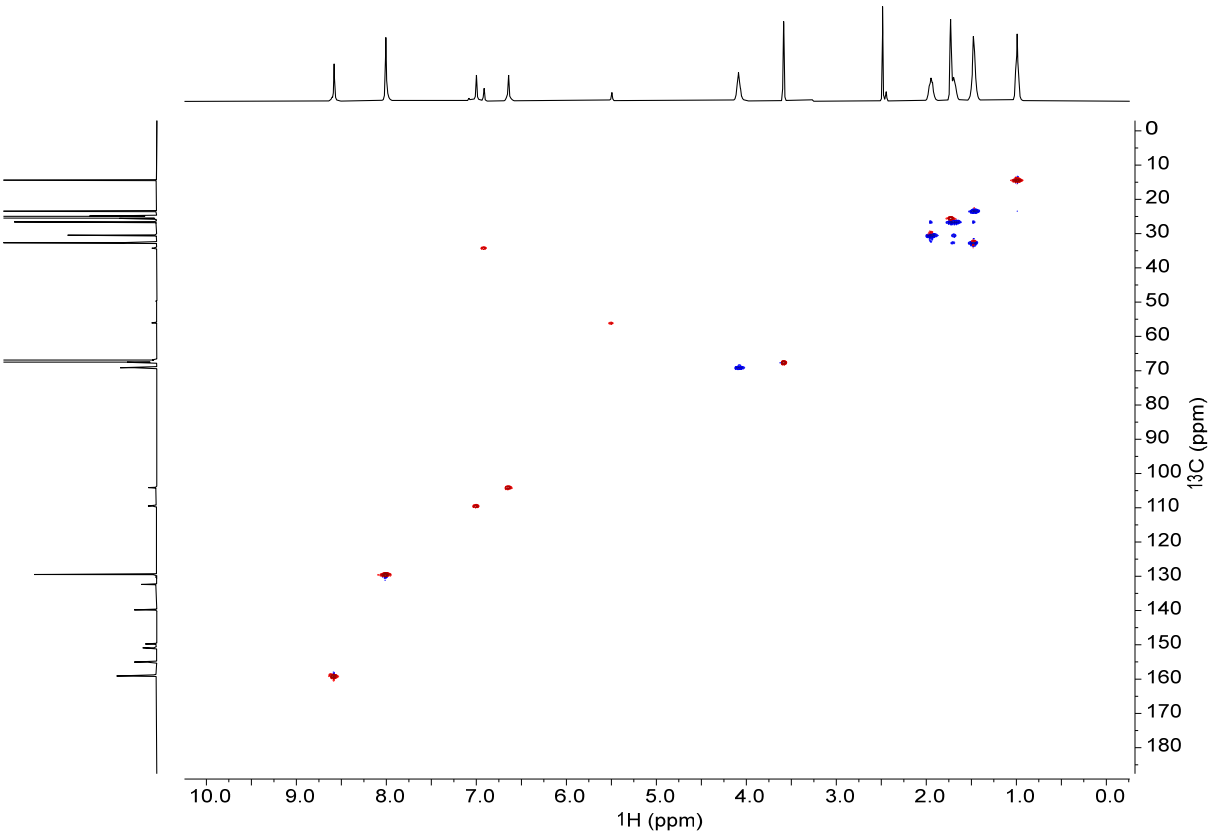

Figure 8.1.141: ^{1}H-^{13}C HSQC NMR spectrum (600/151 MHz, THF-d_8) of **HexTe-Cage**.

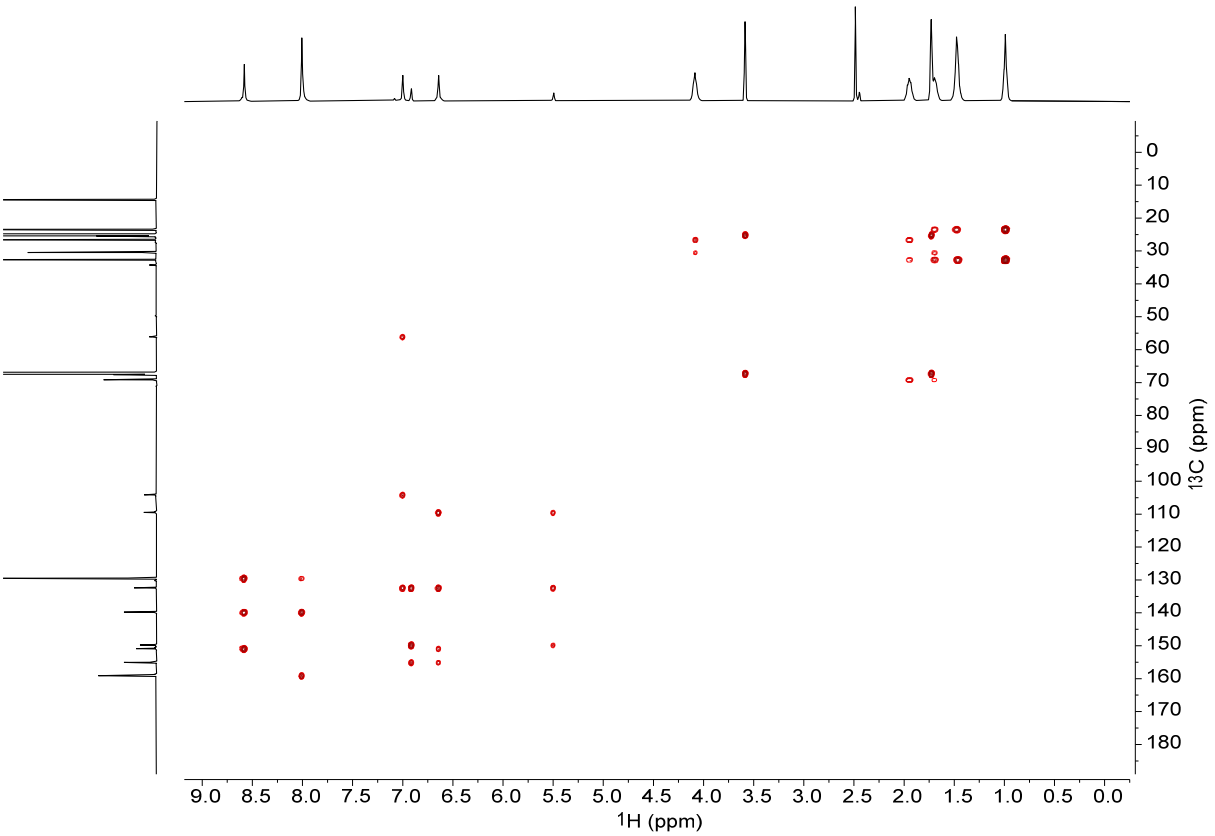

Figure 8.1.142: ^{1}H-^{13}C HMBC NMR spectrum (600/151 MHz, THF-d_8) of **HexTe-Cage**.

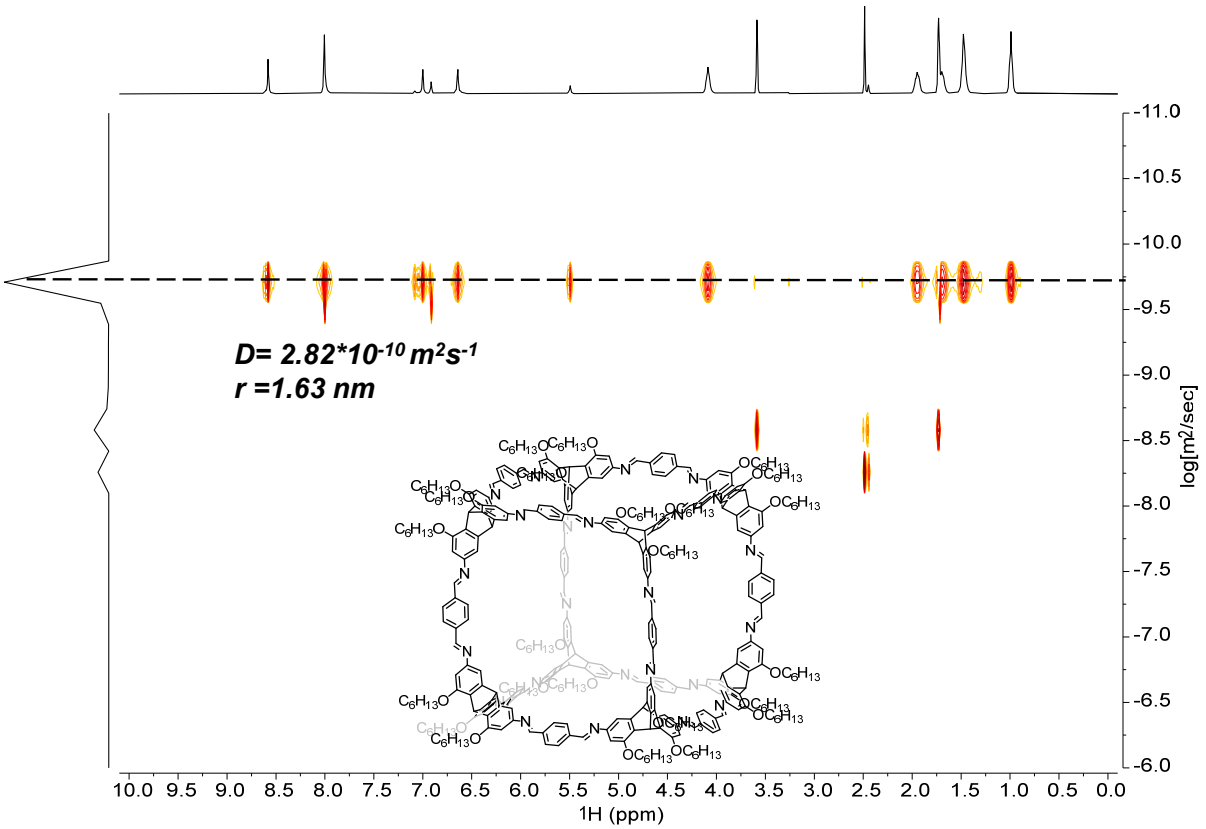

Figure 8.1.143: DOSY NMR spectrum (400 MHz, CD_2Cl_2) of **HeiTe-Cage**.

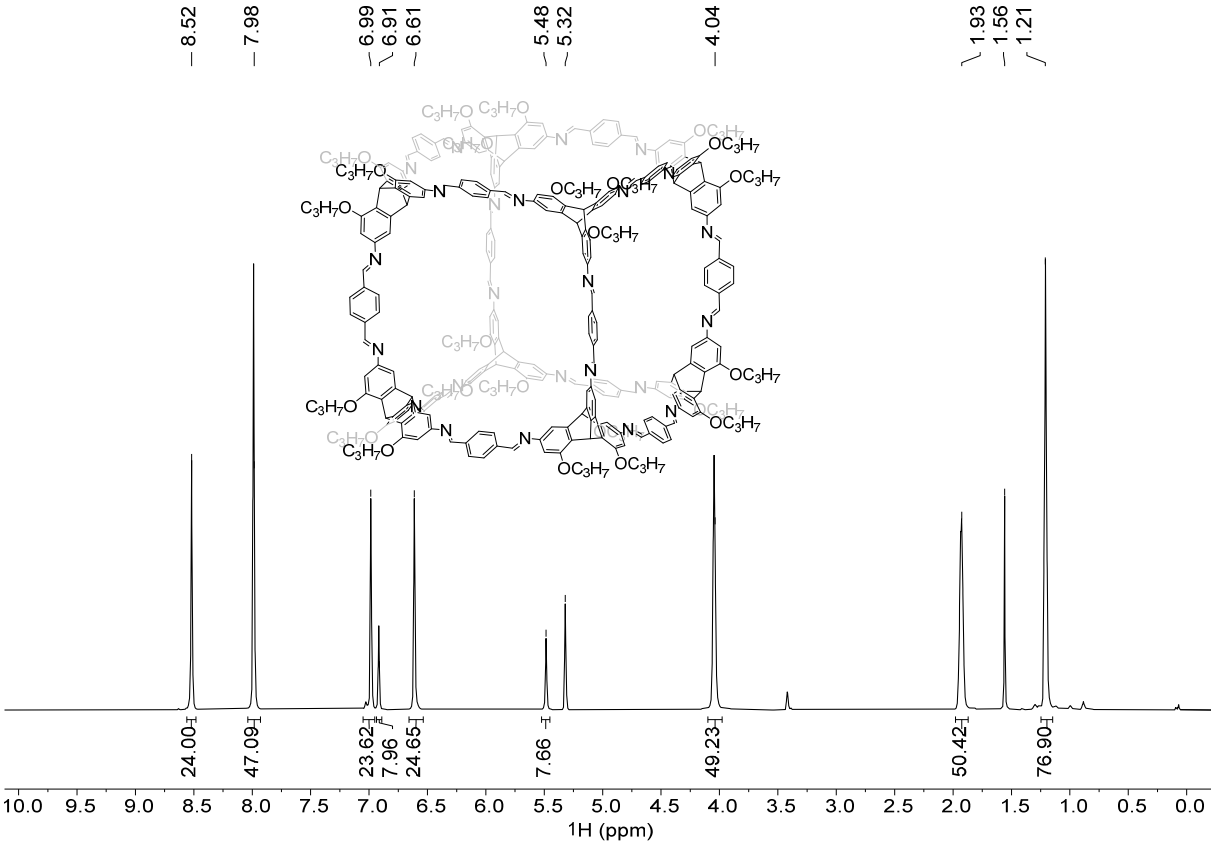

Figure 8.1.144: ^1H NMR spectrum (700 MHz, CD_2Cl_2) of **ProTe-Cage**.

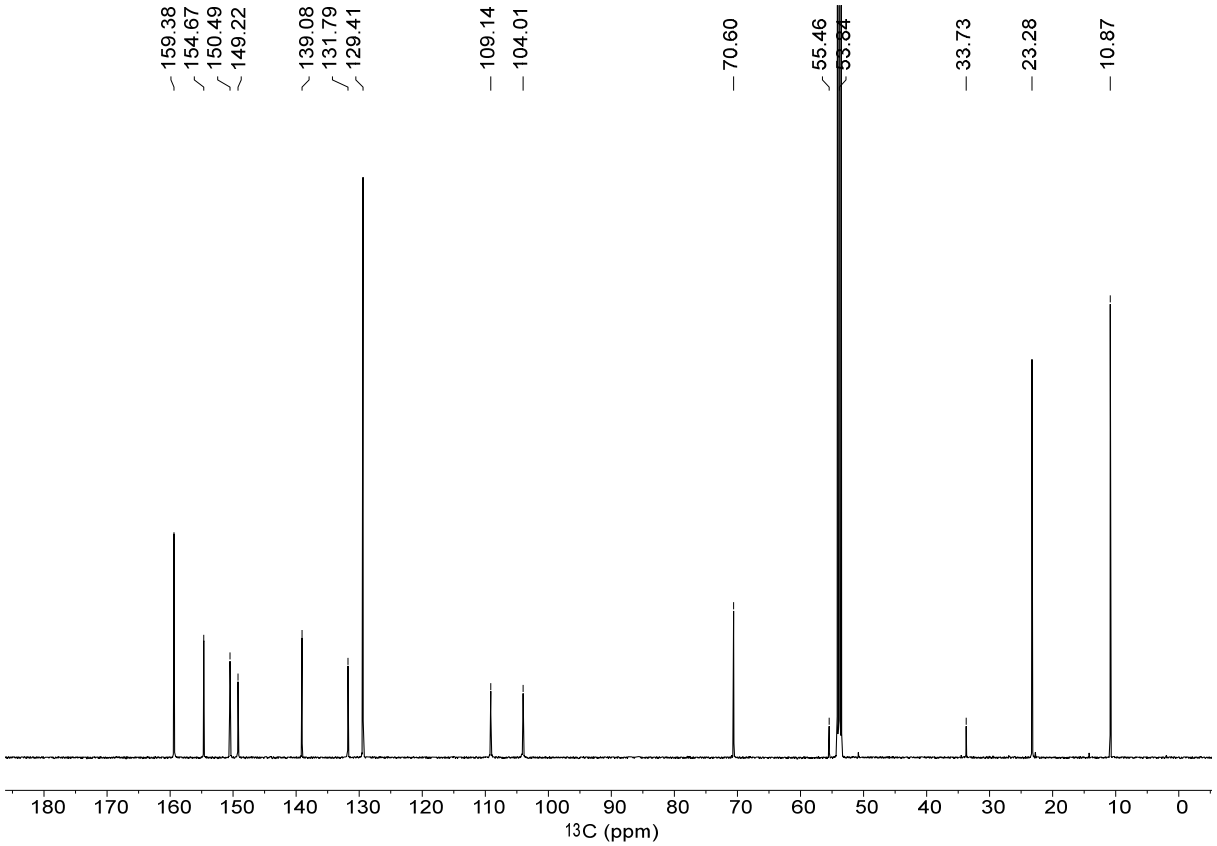

Figure 8.1.145: ^{13}C NMR spectrum (176 MHz, CD_2Cl_2) of **ProTe-Cage**.

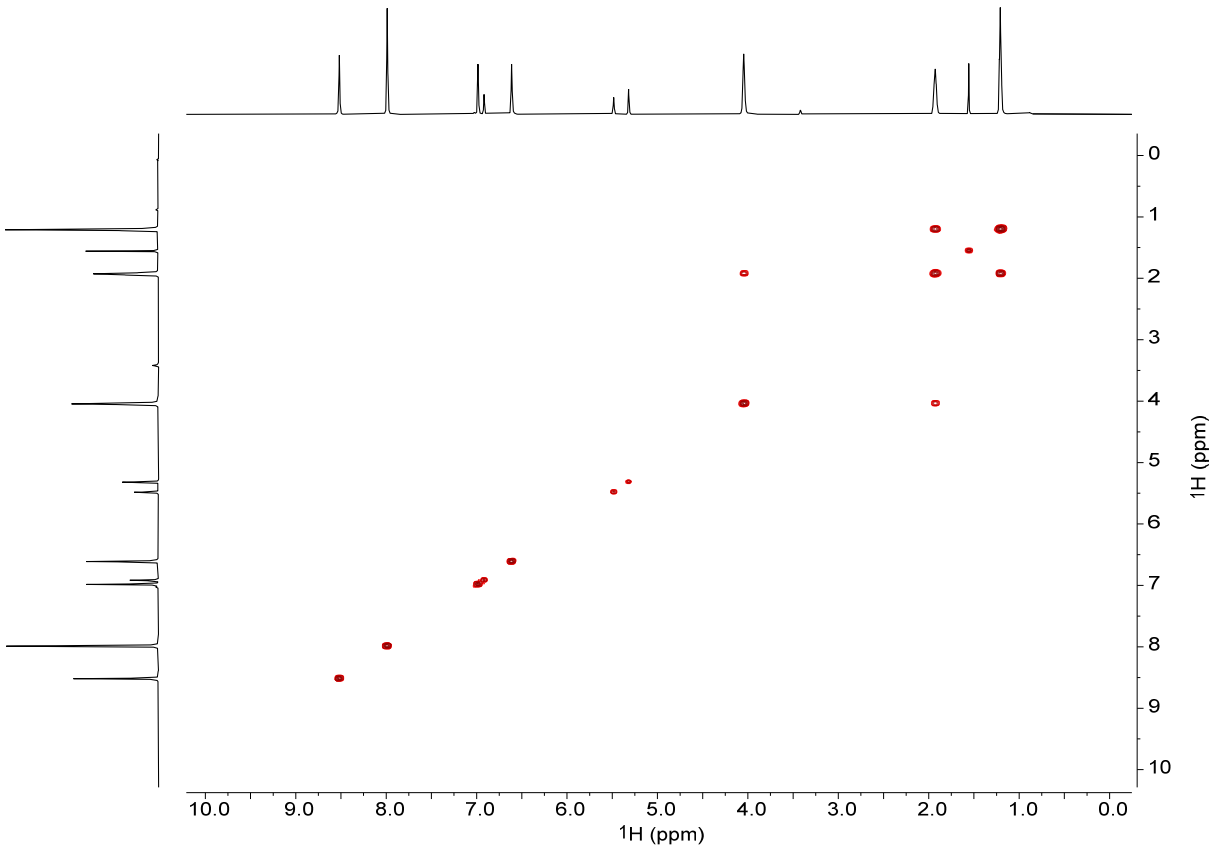

Figure 8.1.146: ^{1}H-^{1}H COSY NMR spectrum (700/700 MHz, CD_2Cl_2) of **ProTe-Cage**.

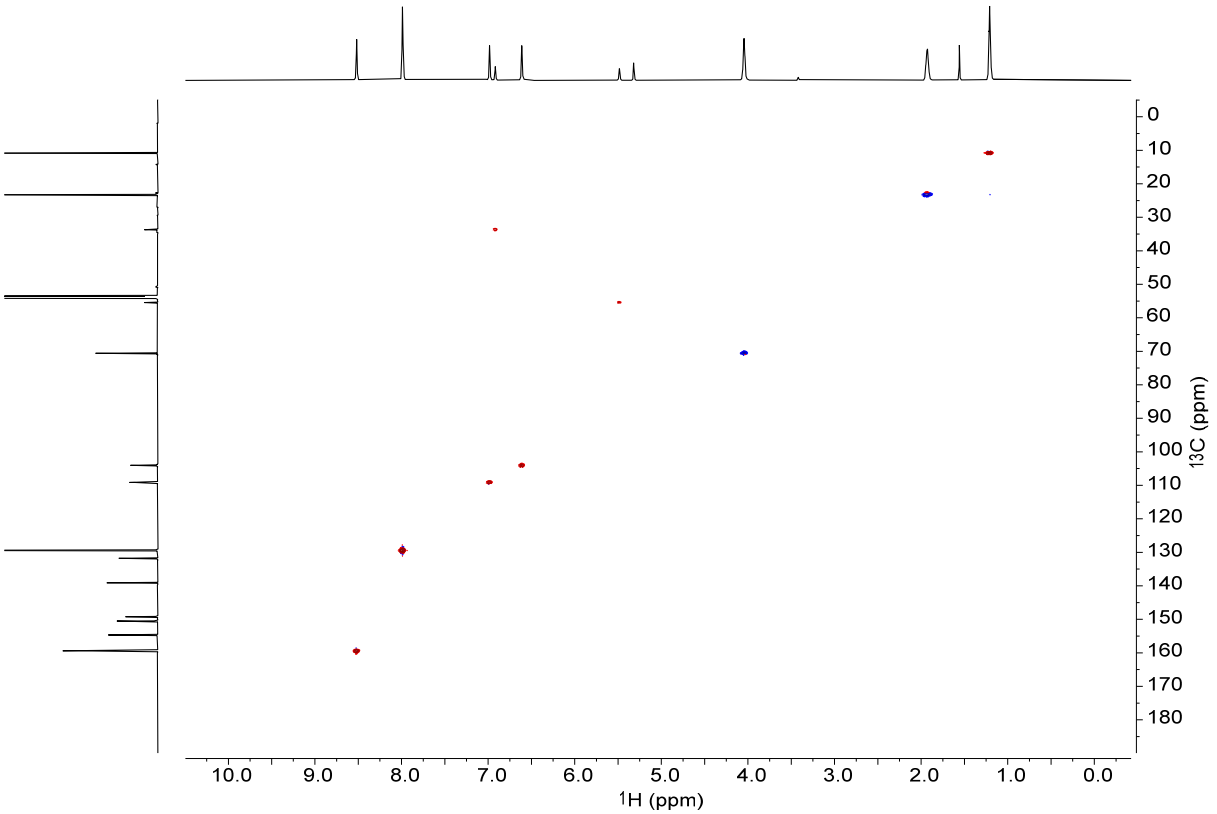

Figure 8.1.147: ^{1}H-^{13}C HSQC NMR spectrum (700/176 MHz, CD_2Cl_2) of **ProTe-Cage**.

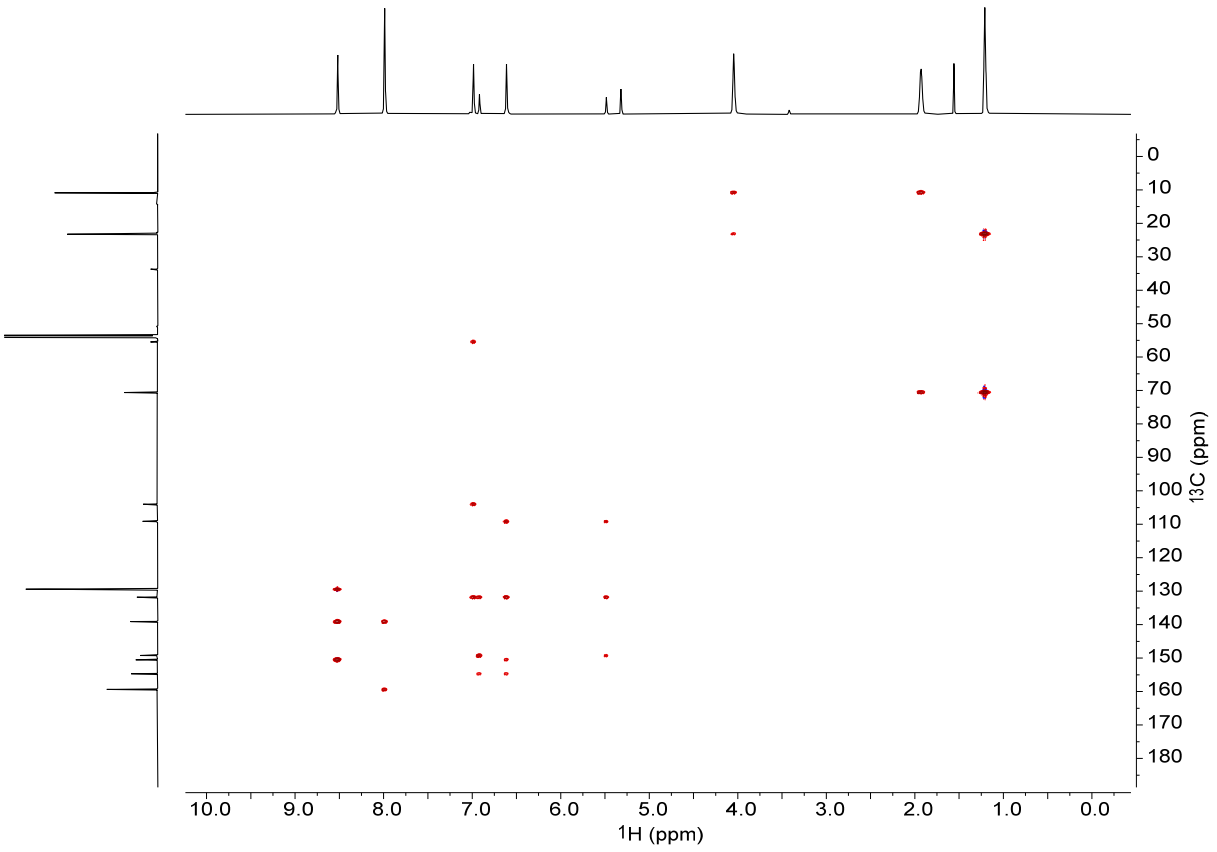

Figure 8.1.148: ^{1}H-^{13}C HMBC NMR spectrum (700/176 MHz, CD_2Cl_2) of **ProTe-Cage**.

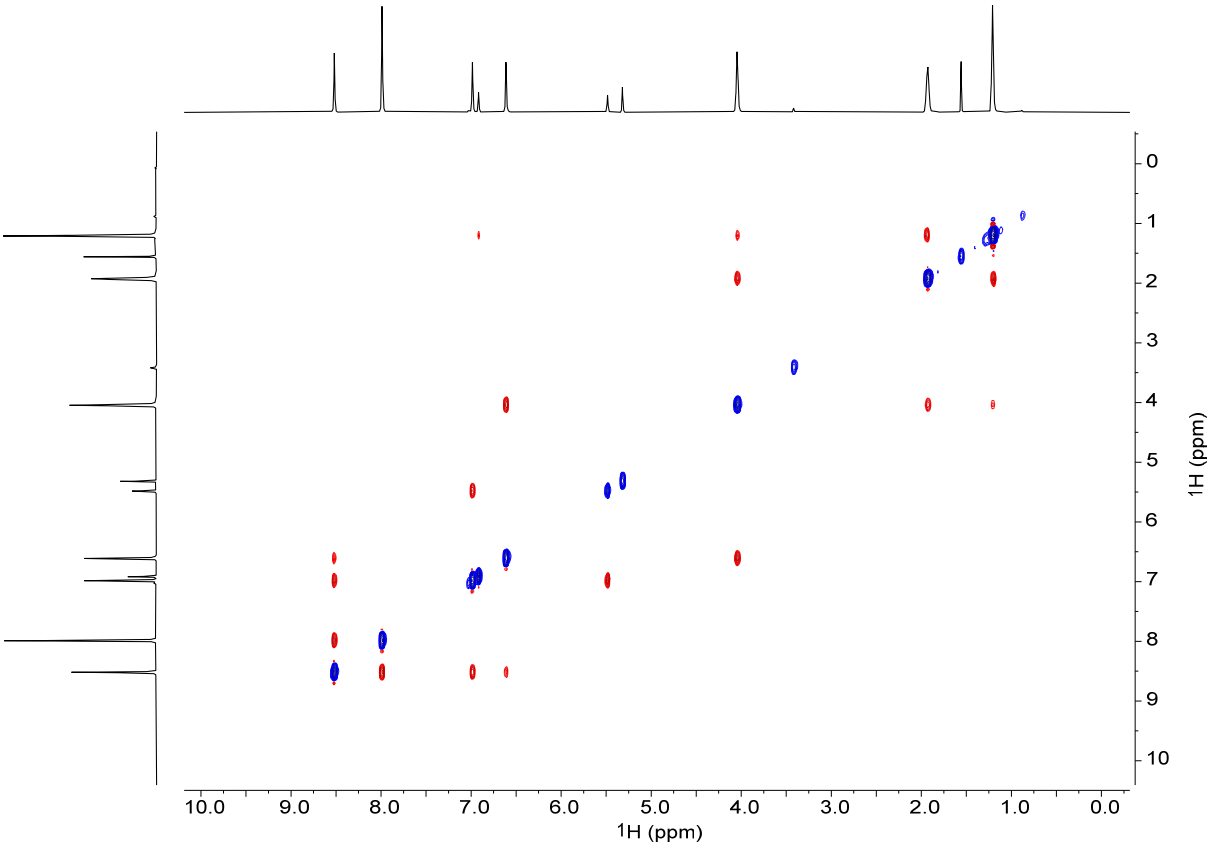

Figure 8.1.149: ^{1}H-^{1}H NOESY NMR spectrum (700/700 MHz, CD_2Cl_2) of **ProTe-Cage**.

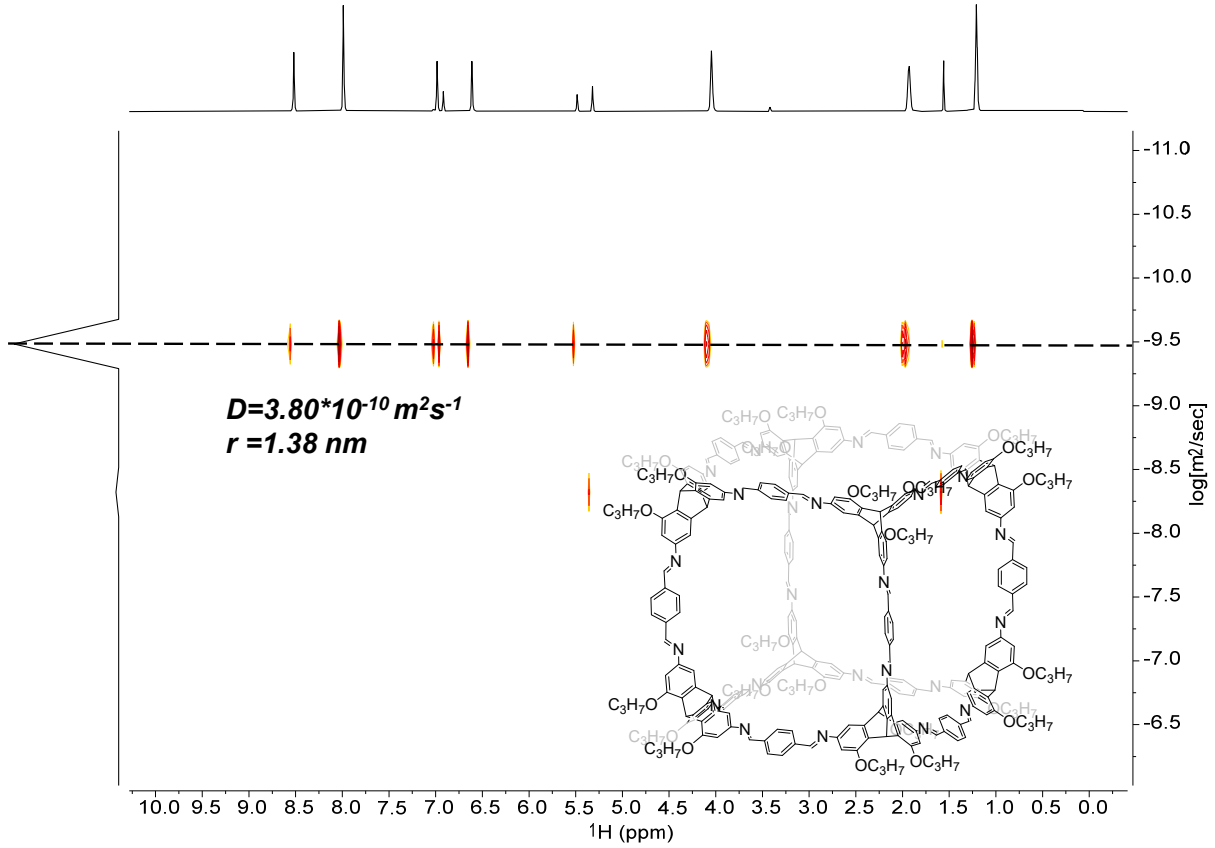

Figure 8.1.150: DOSY NMR spectrum (400 MHz, CD_2Cl_2) of **ProTe-Cage**.

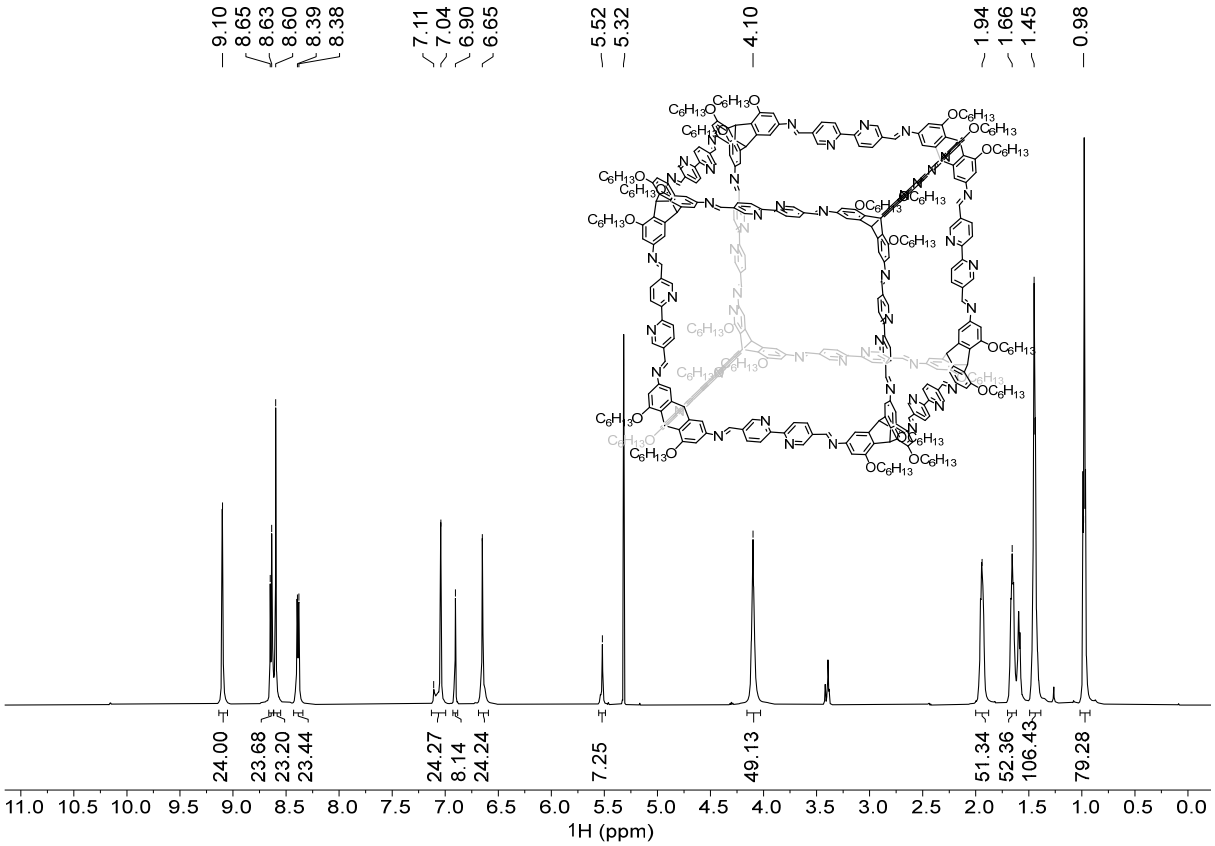

Figure 8.1.151: ^{1}H NMR spectrum (700 MHz, CD_2Cl_2) of **HexPy-Cage**.

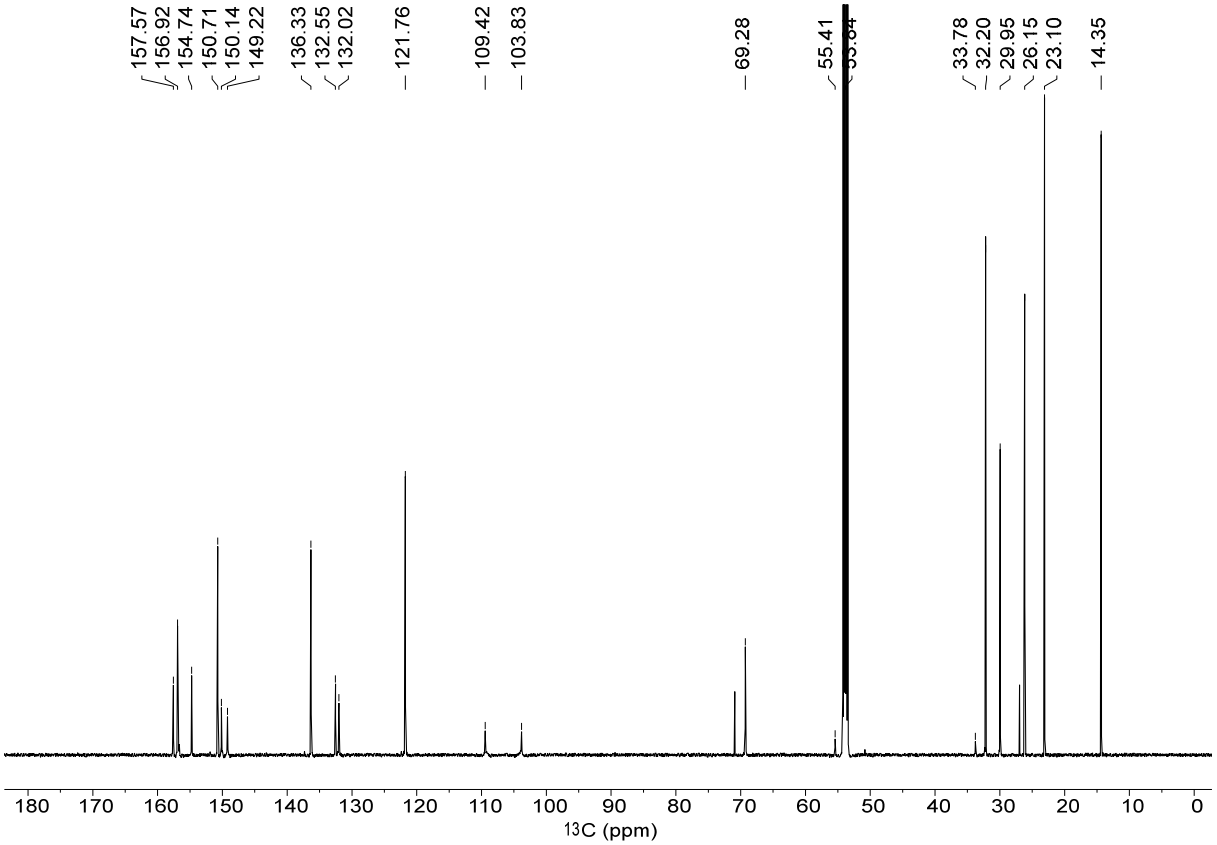

Figure 8.1.152: ^{13}C NMR spectrum (176 MHz, CD_2Cl_2) of **HexPy-Cage**.

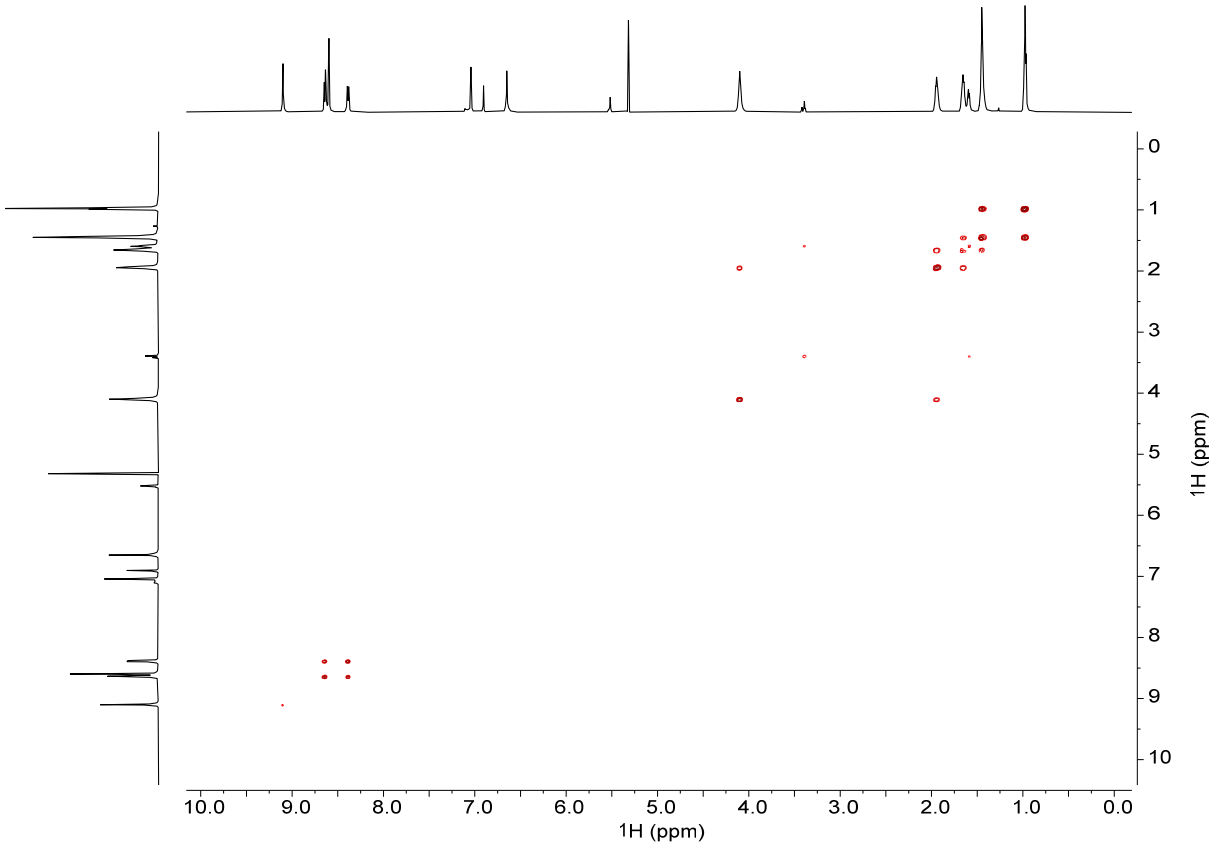

Figure 8.1.153: ^{1}H-^{1}H COSY NMR spectrum (700/700 MHz, CD_2Cl_2) of **HexPy-Cage**.

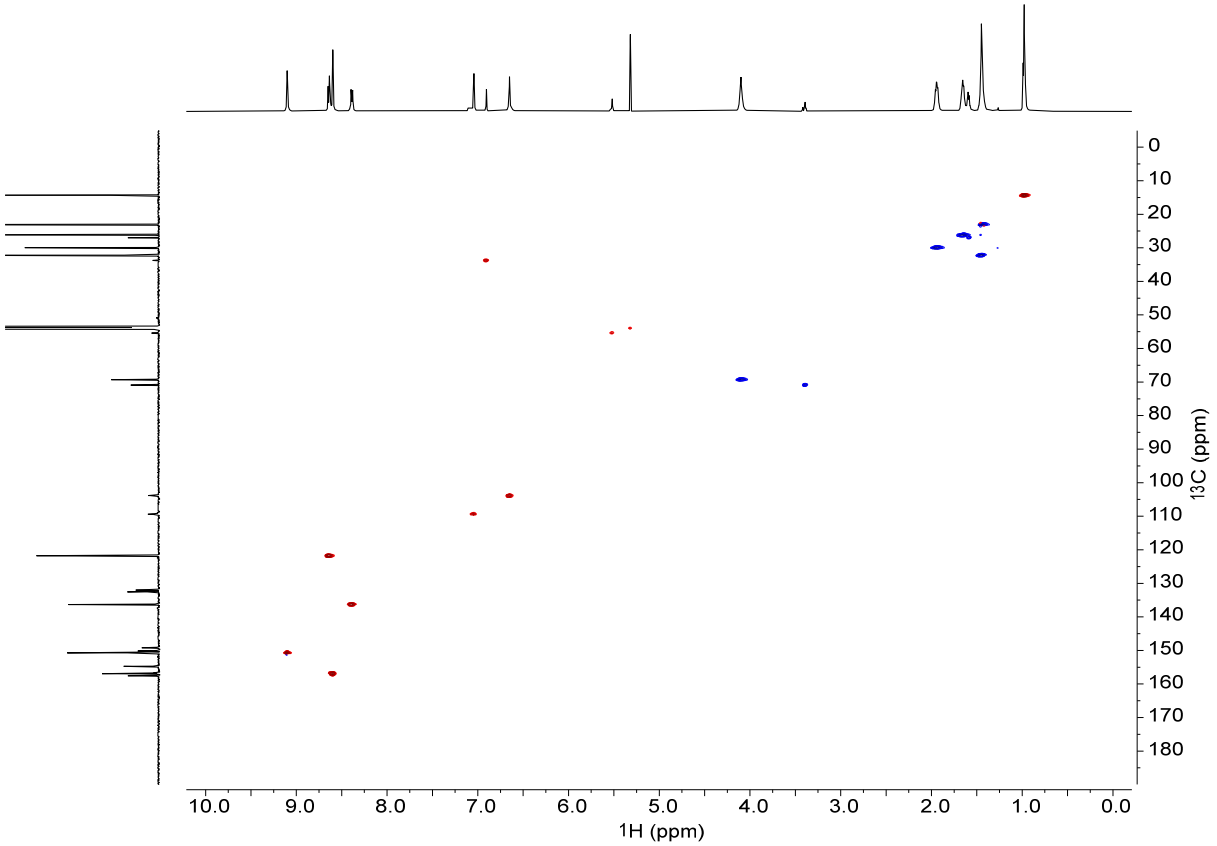

Figure 8.1.154: ^{1}H-^{13}C HSQC NMR spectrum (700/176 MHz, CD_2Cl_2) of **HexPy-Cage**.

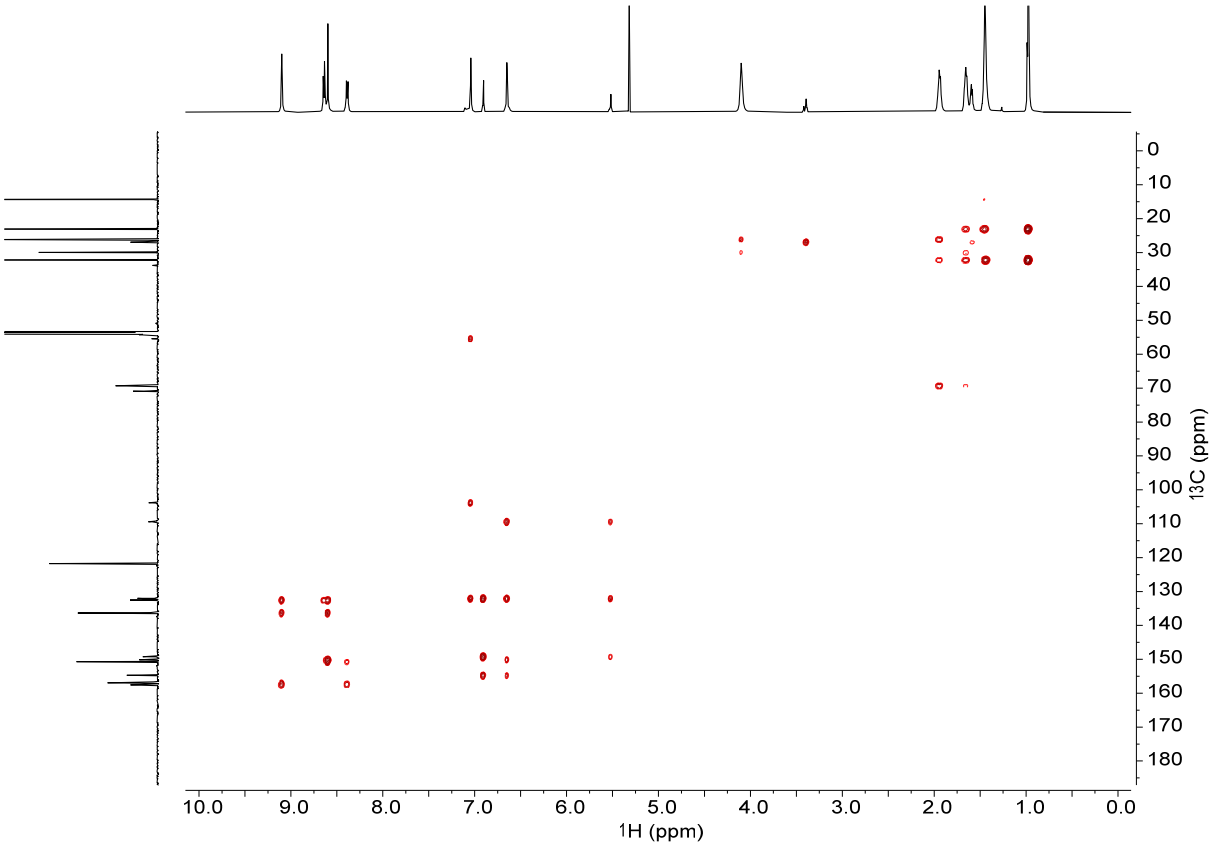

Figure 8.1.155: ^{1}H-^{13}C HMBC NMR spectrum (700/176 MHz, CD_2Cl_2) of **HexPy-Cage**.

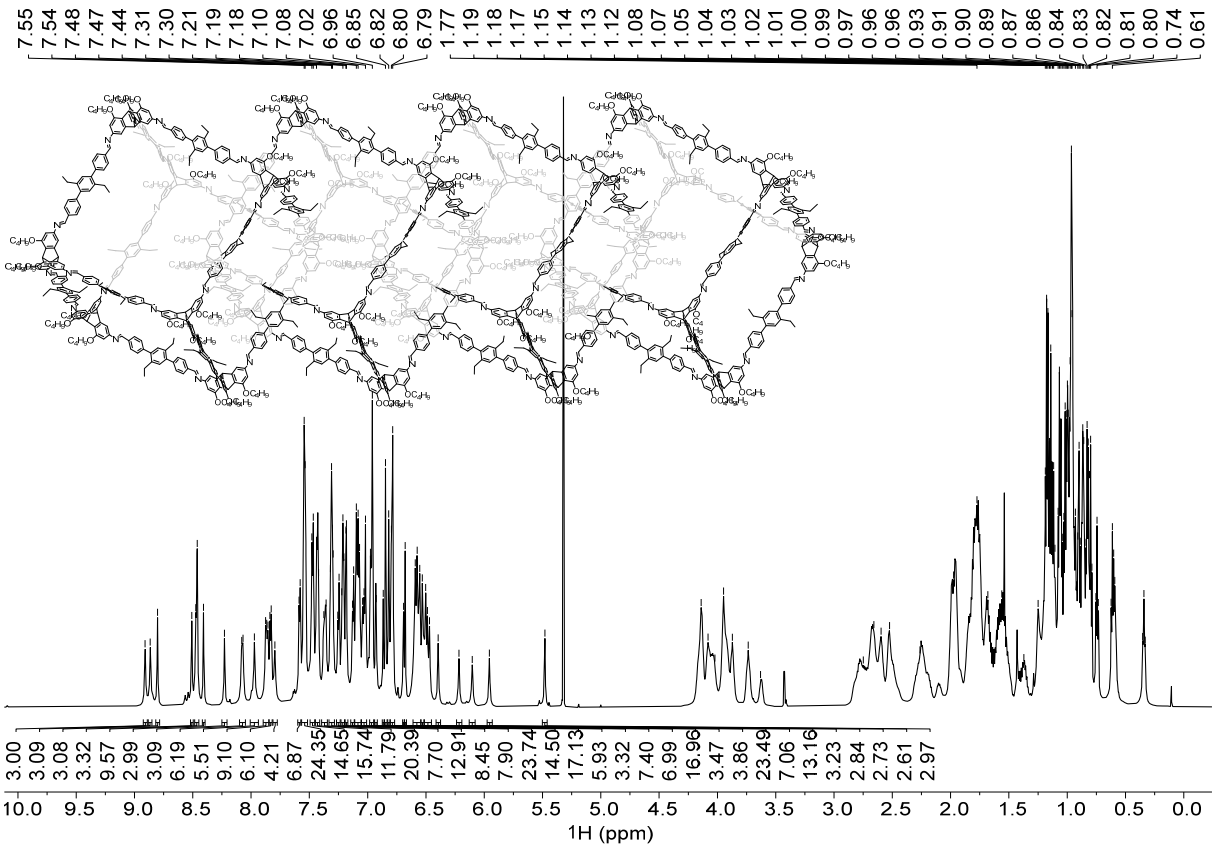

Figure 8.1.156: ^{1}H NMR spectrum (700 MHz, CD_2Cl_2) of **ButDie-[4]Catenane**.

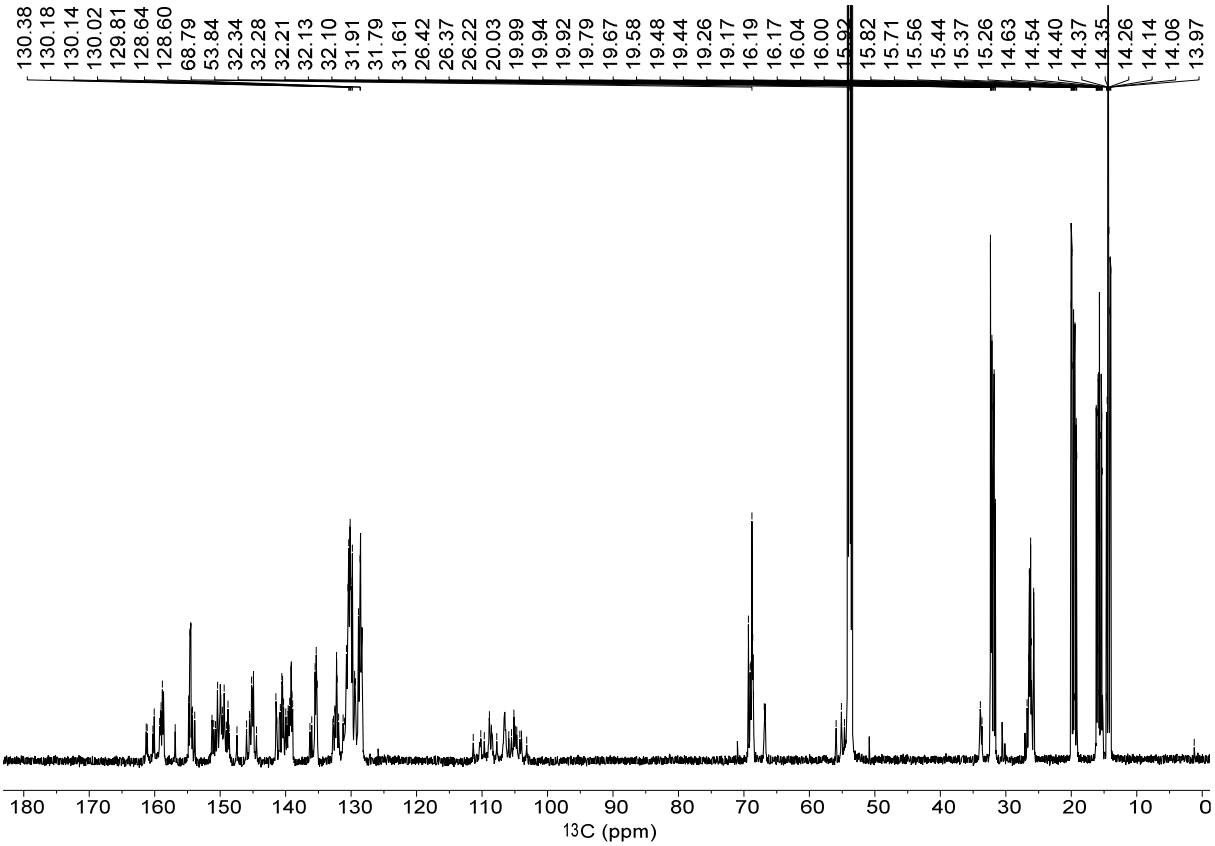

Figure 8.1.157: ^{13}C NMR spectrum (176 MHz, CD_2Cl_2) of **ButDie-[4]Catenane**.

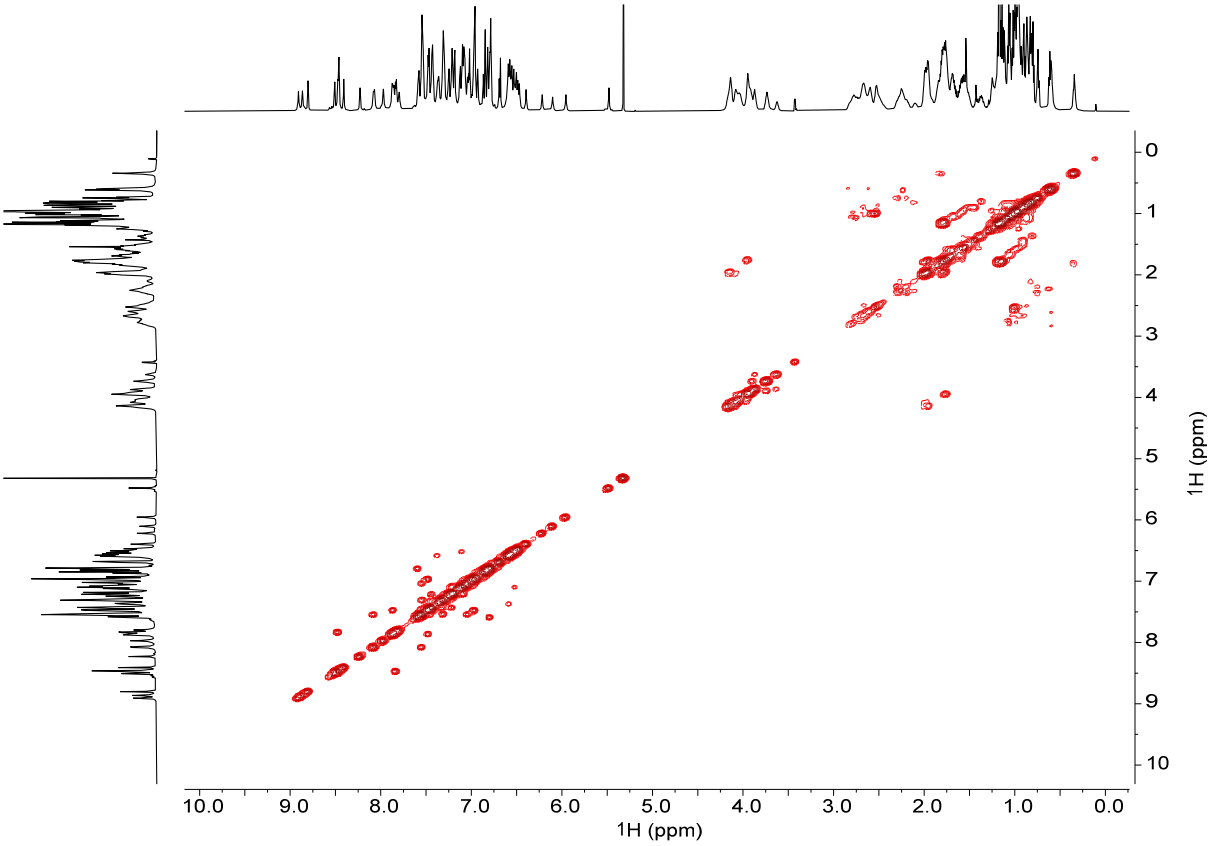

Figure 8.1.158: ^{1}H-^{1}H COSY NMR spectrum (700/700 MHz, CD_2Cl_2) of **ButDie-[4]Catenane**.

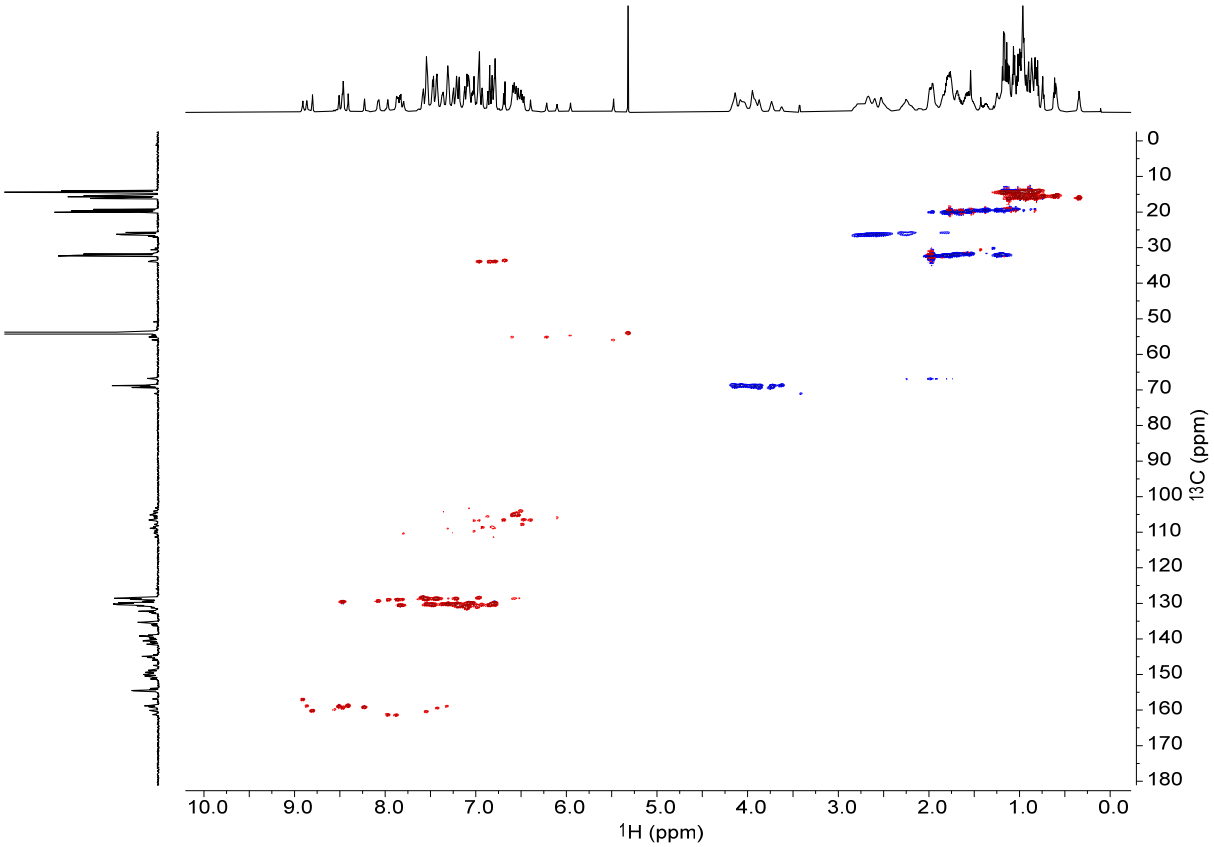

Figure 8.1.159: ^{1}H-^{13}C HSQC NMR spectrum (700/176 MHz, CD_2Cl_2) of **ButDie-[4]Catenane**.

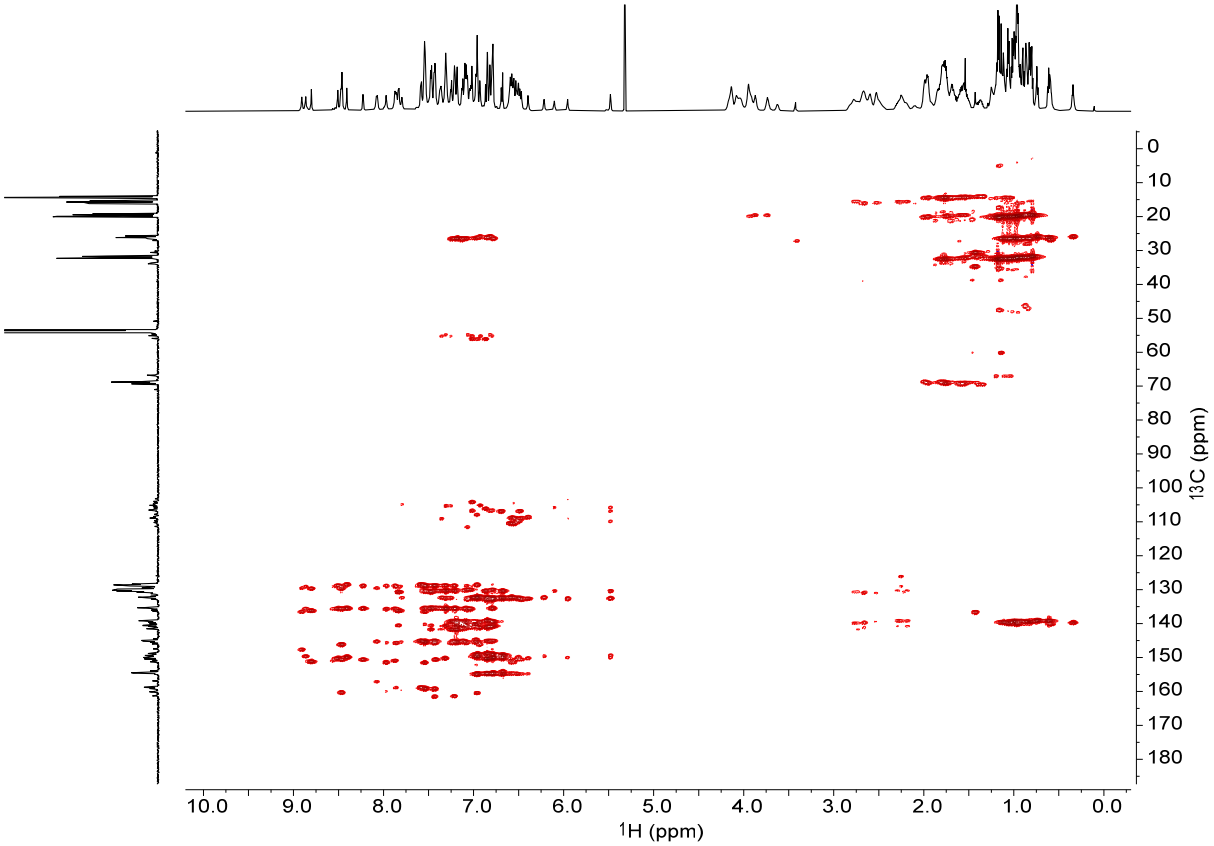

Figure 8.1.160: ^{1}H-^{13}C HMBC NMR spectrum (700/176 MHz, CD_2Cl_2) of **ButDie-[4]Catenane**.

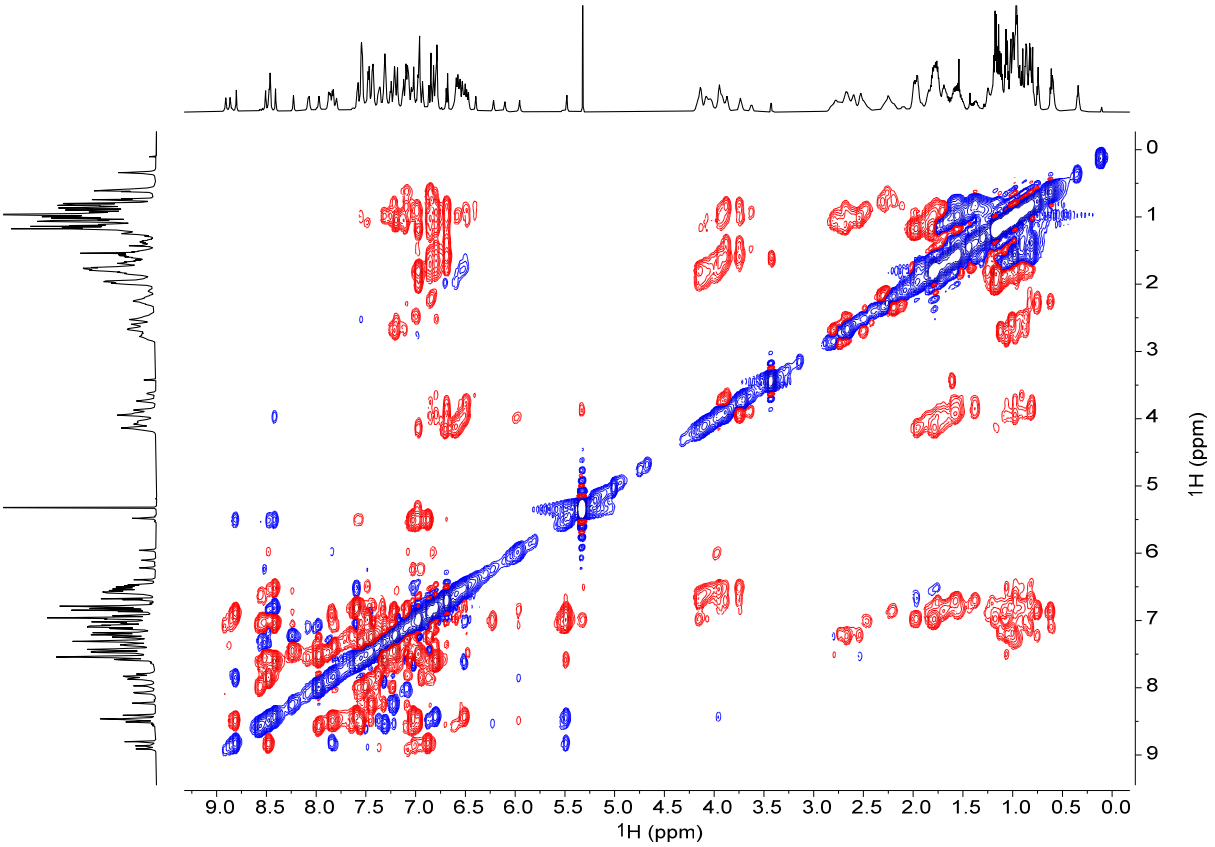

Figure 8.1.161: ^{1}H-^{1}H NOESY NMR spectrum (700/700 MHz, CD_2Cl_2) of **ButDie-[4]Catenane**.

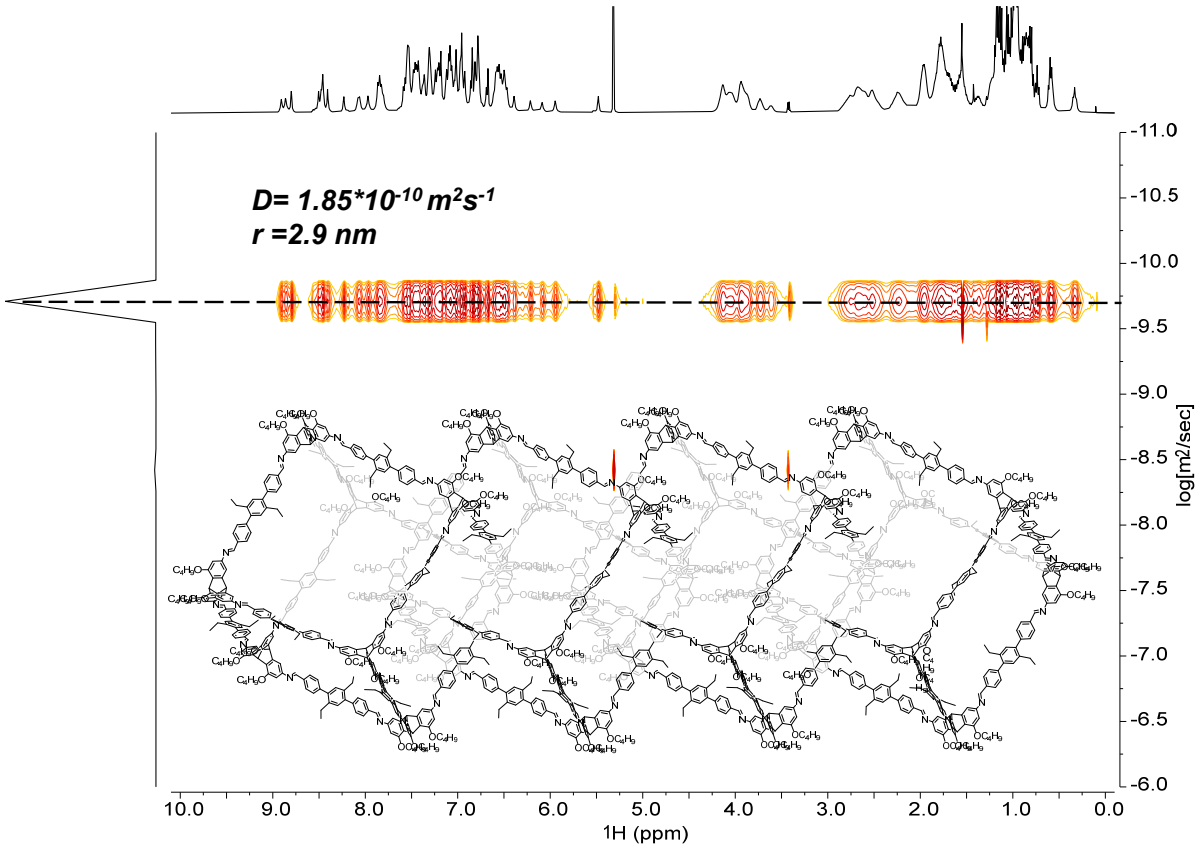

Figure 8.1.162: DOSY NMR spectrum (400 MHz, CD_2Cl_2) of **ButDie-[4]Catenane**.

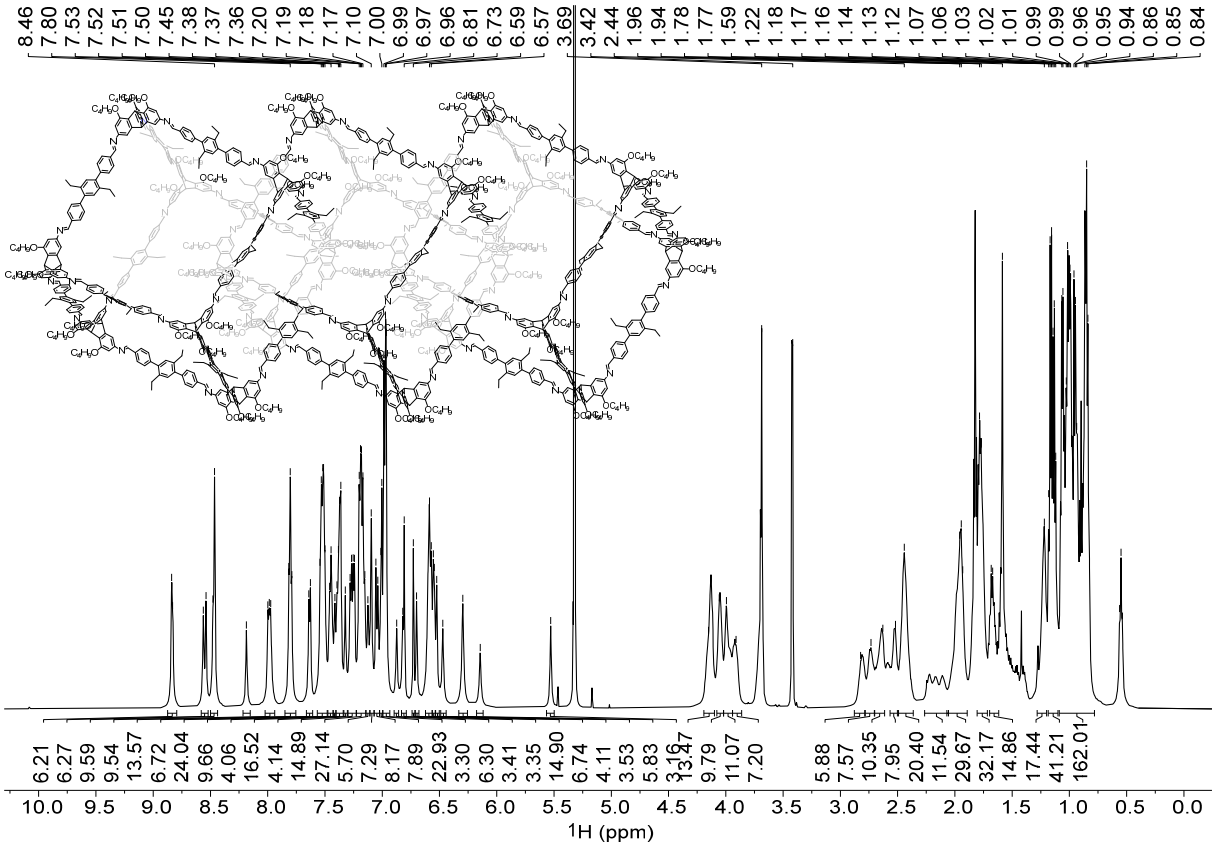

Figure 8.1.163: ^{1}H NMR spectrum (700 MHz, CD_2Cl_2) of **ButDie-[3]Catenane**.

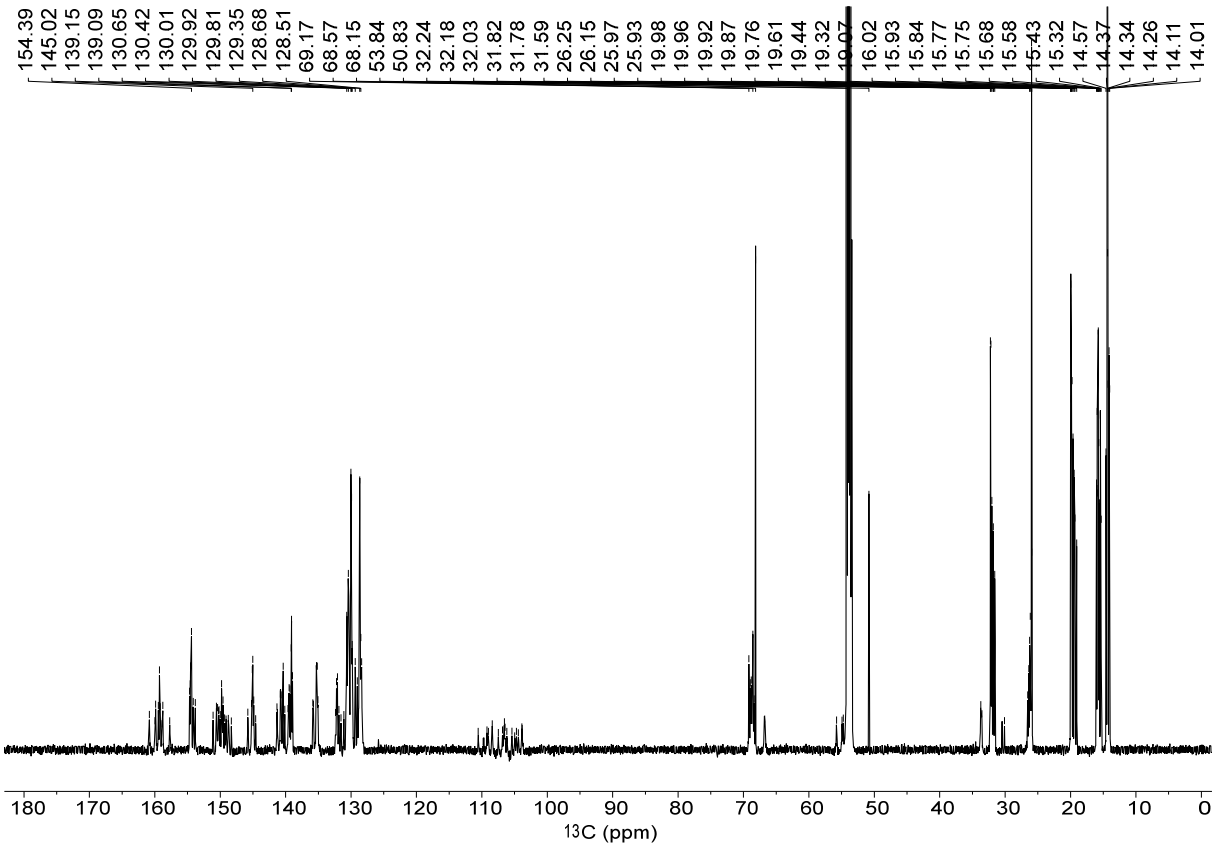

Figure 8.1.164: ^{13}C NMR spectrum (176 MHz, CD_2Cl_2) of **ButDie-[3]Catenane**.

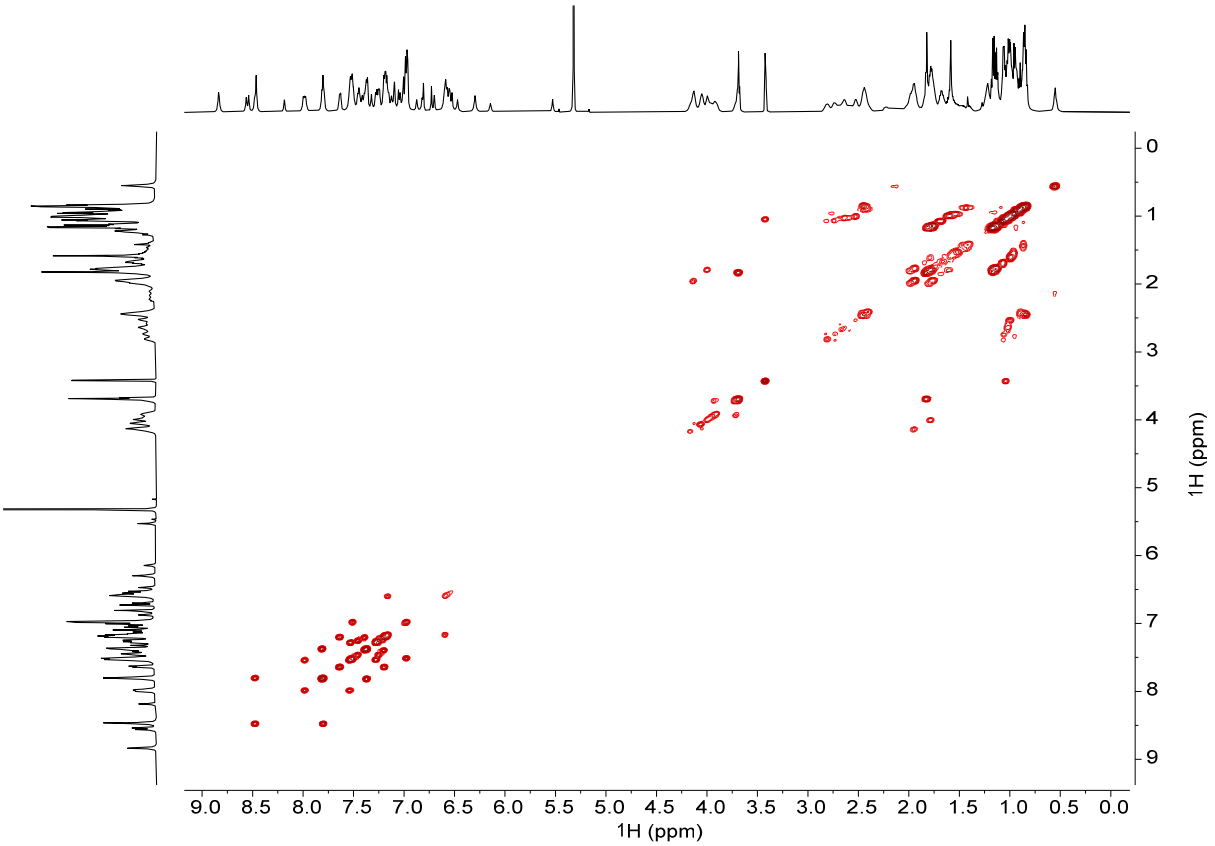

Figure 8.1.165: ^{1}H-^{1}H COSY NMR spectrum (700/700 MHz, CD_2Cl_2) of **ButDie-[3]Catenane**.

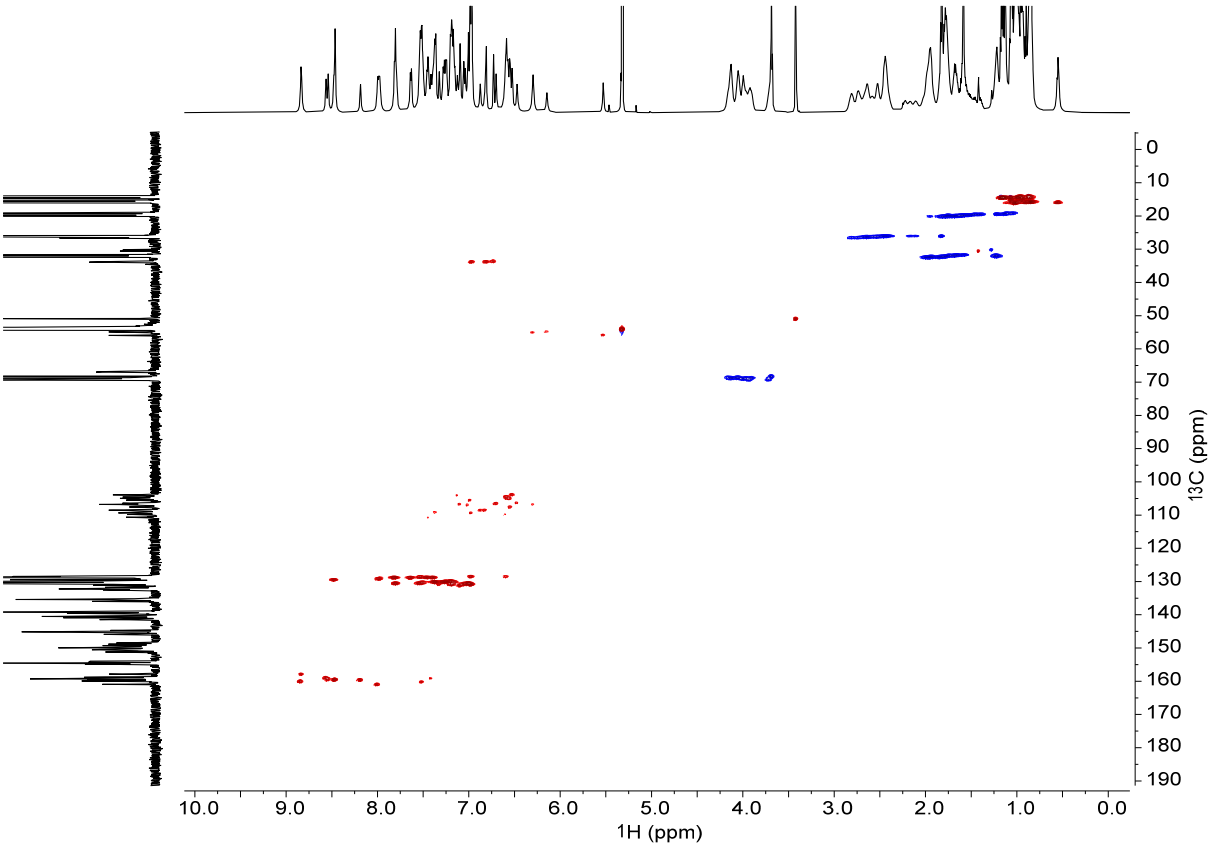

Figure 8.1.166: ^{1}H-^{13}C HSQC NMR spectrum (700/176 MHz, CD_2Cl_2) of **ButDie-[3]Catenane**.

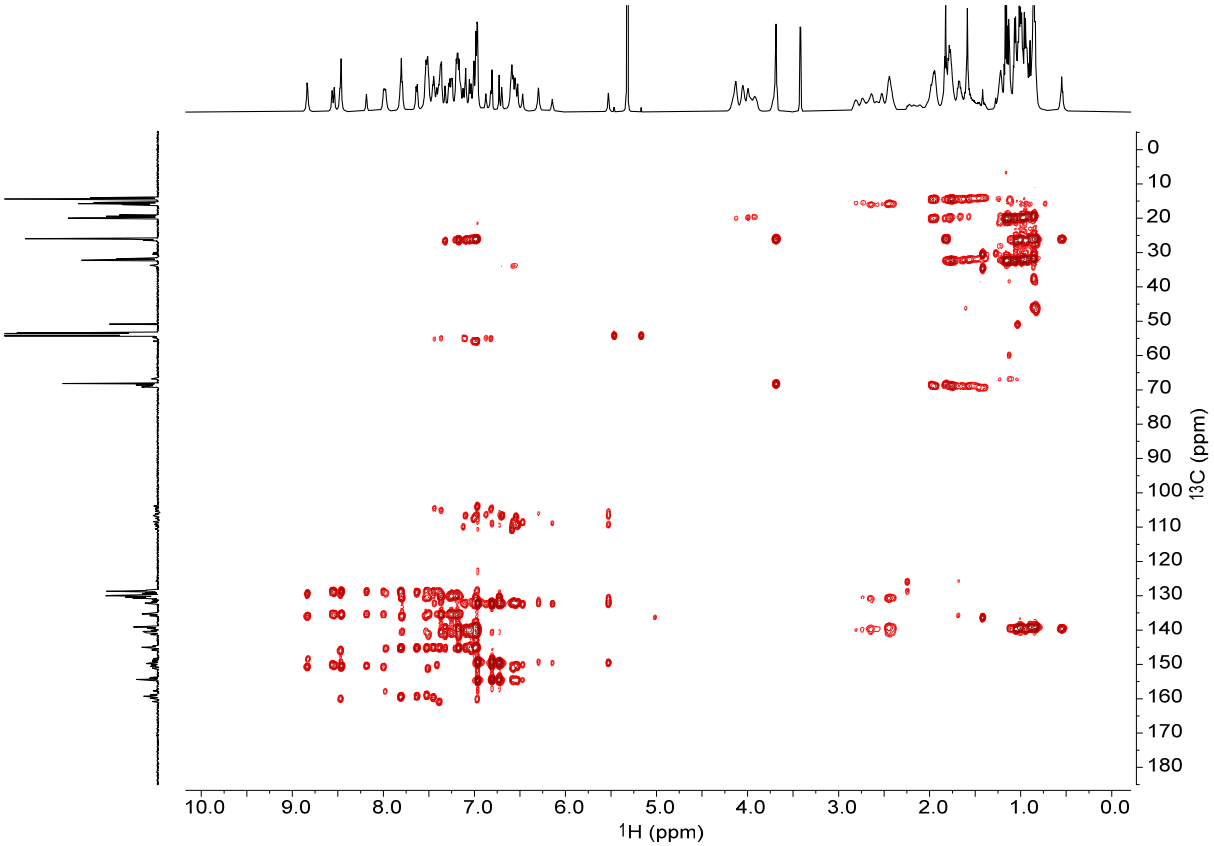

Figure 8.1.167: ^{1}H-^{13}C HMBC NMR spectrum (700/176 MHz, CD_2Cl_2) of **ButDie-[3]Catenane**.

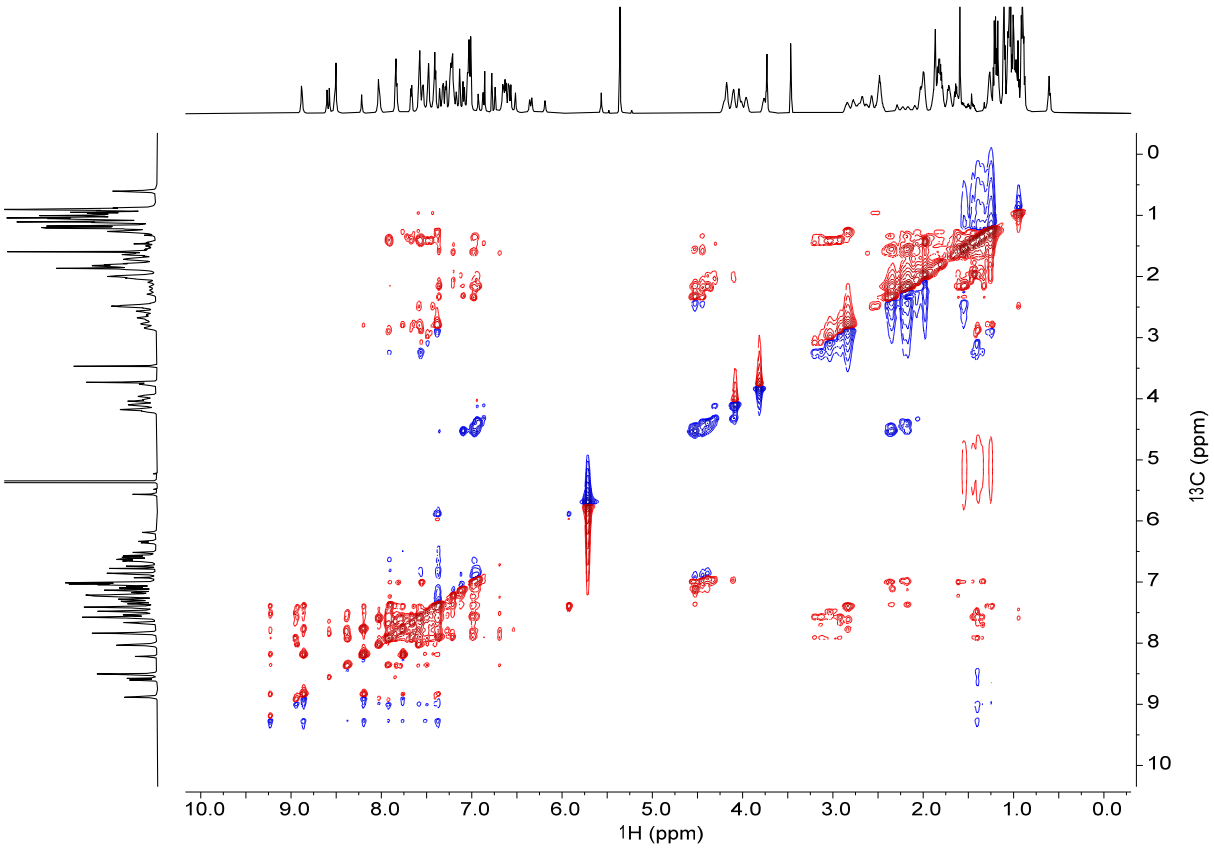

Figure 8.1.168: ^{1}H-^{1}H NOESY NMR spectrum (700/700 MHz, CD_2Cl_2) of **ButDie-[3]Catenane**.

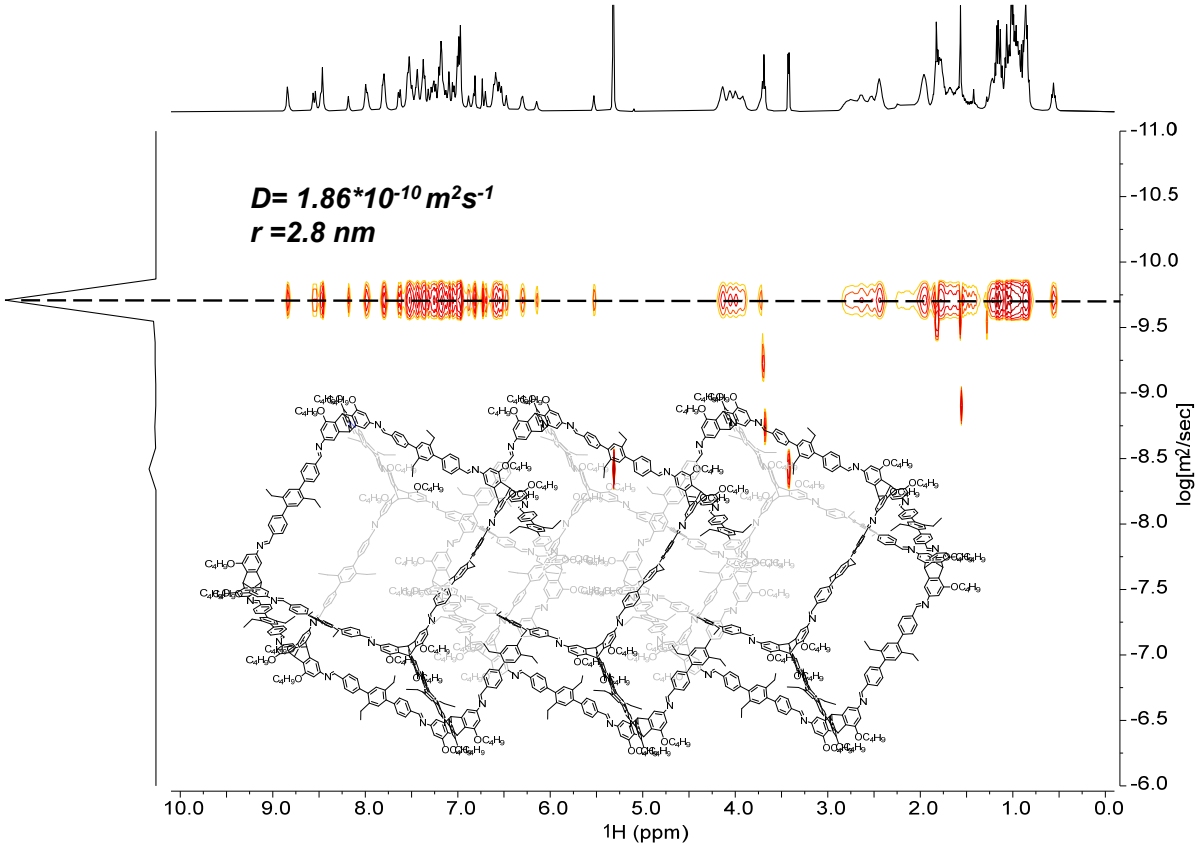

Figure 8.1.169: DOSY NMR spectrum (400 MHz, CD_2Cl_2) of **ButDie-[3]Catenane**.

8.2 Mass Spectra

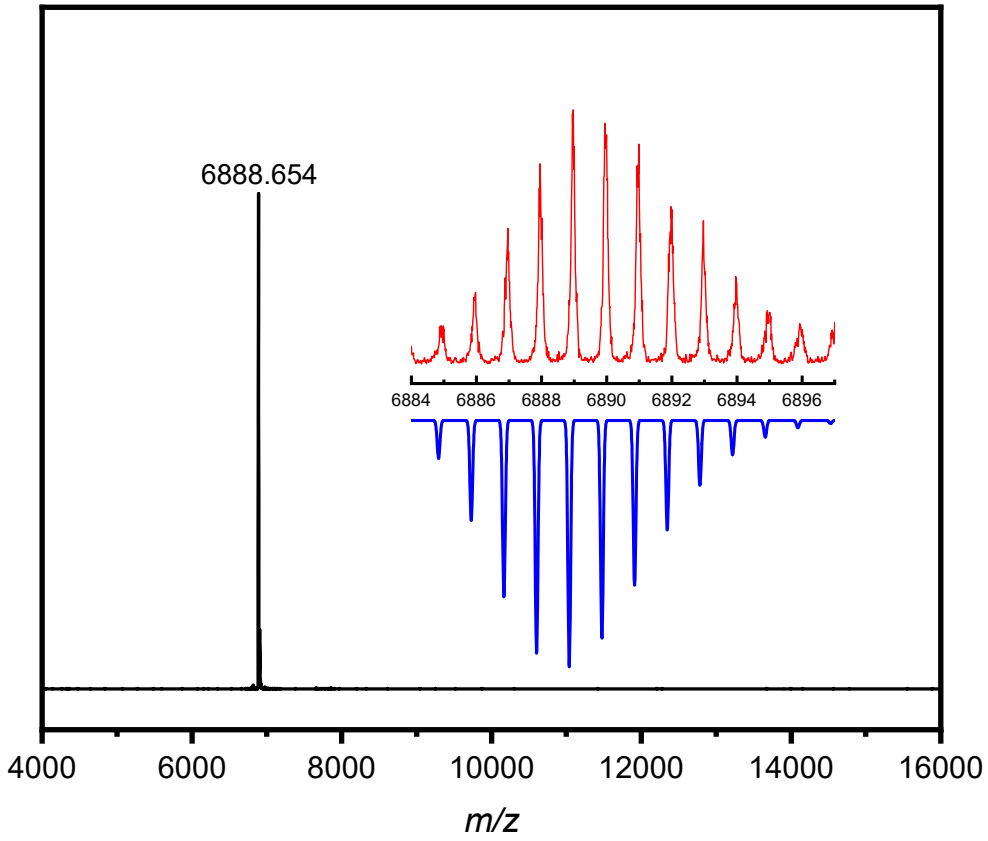

Figure 8.2.1: MALDI-TOF mass spectrum of **HexBi-Cage**.

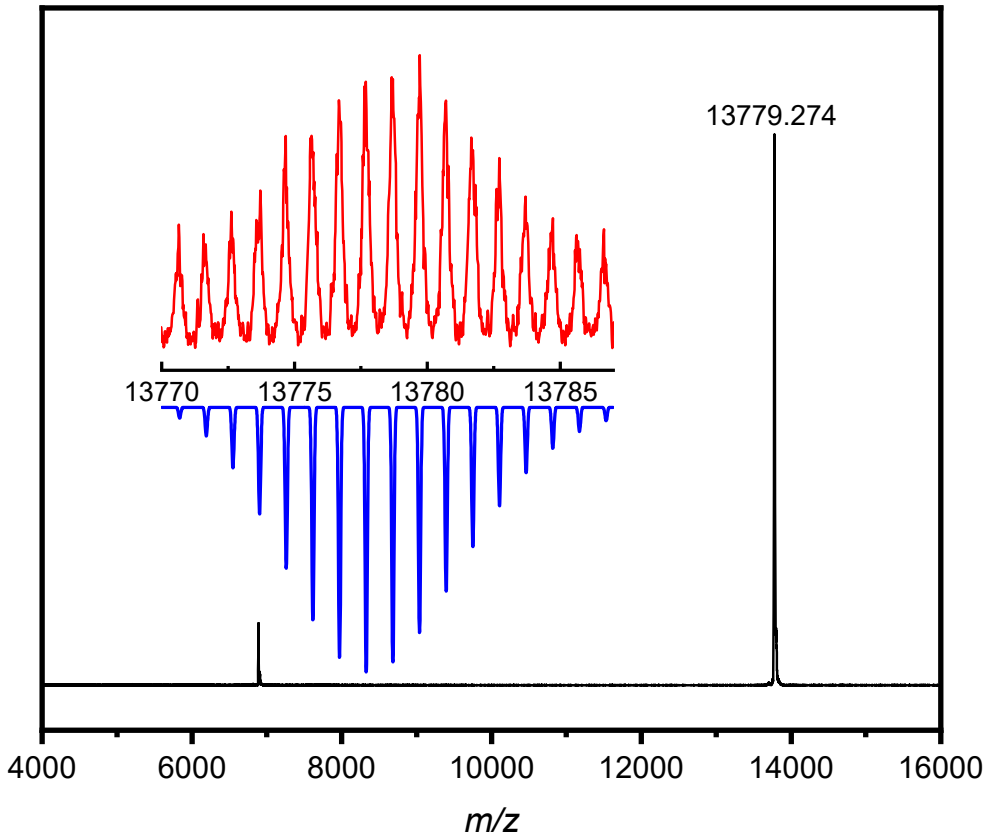

Figure 8.2.2: MALDI-TOF mass spectrum of **HexBi-Catenane**.

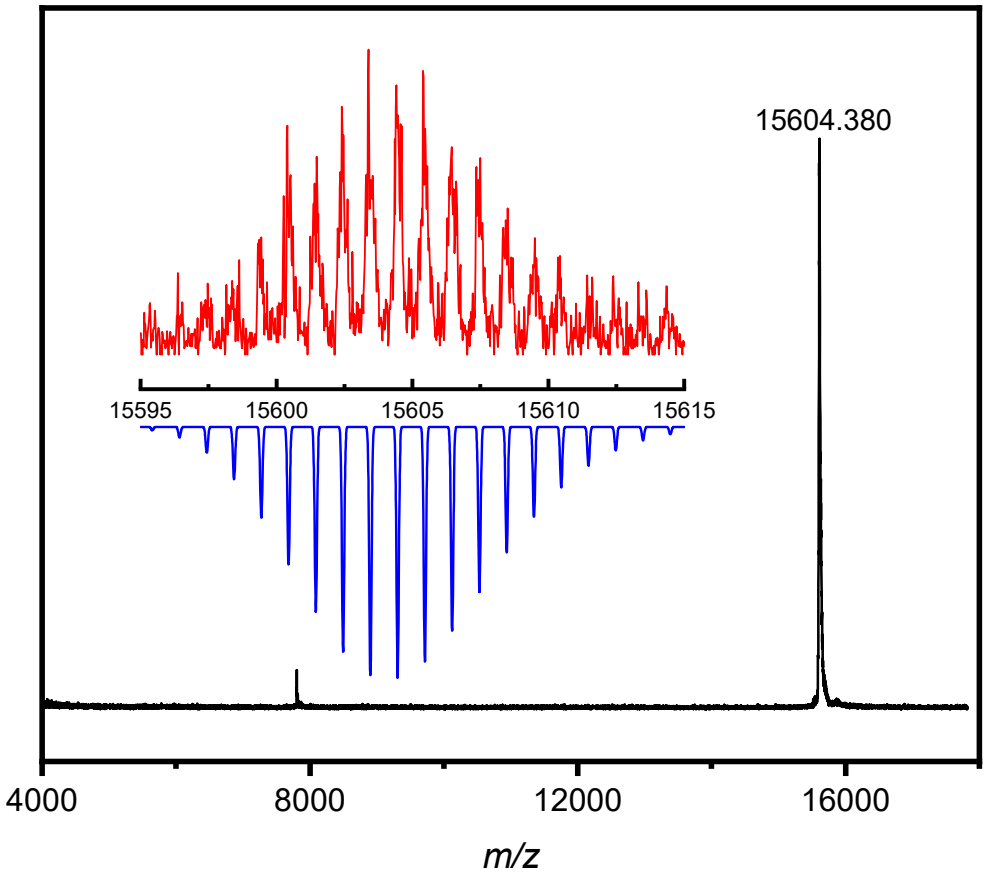

Figure 8.2.3: MALDI-TOF mass spectrum of **HexTri-Catenane**.

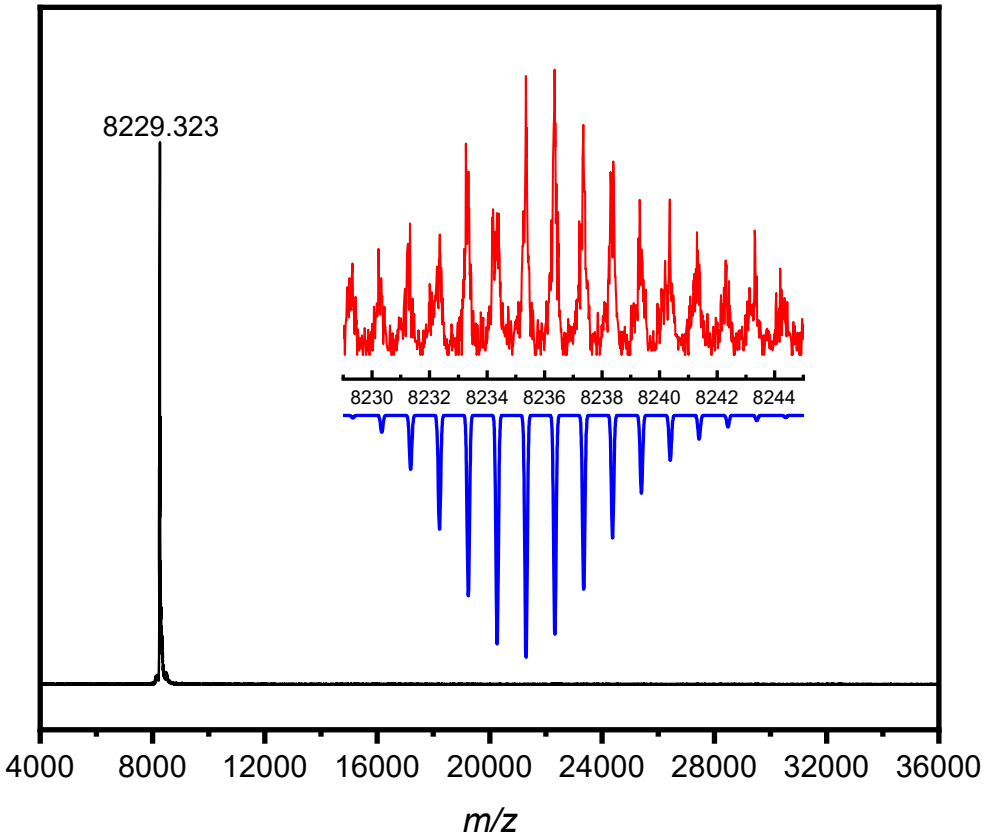

Figure 8.2.4: MALDI-TOF mass spectrum of **DecBi-Cage**.

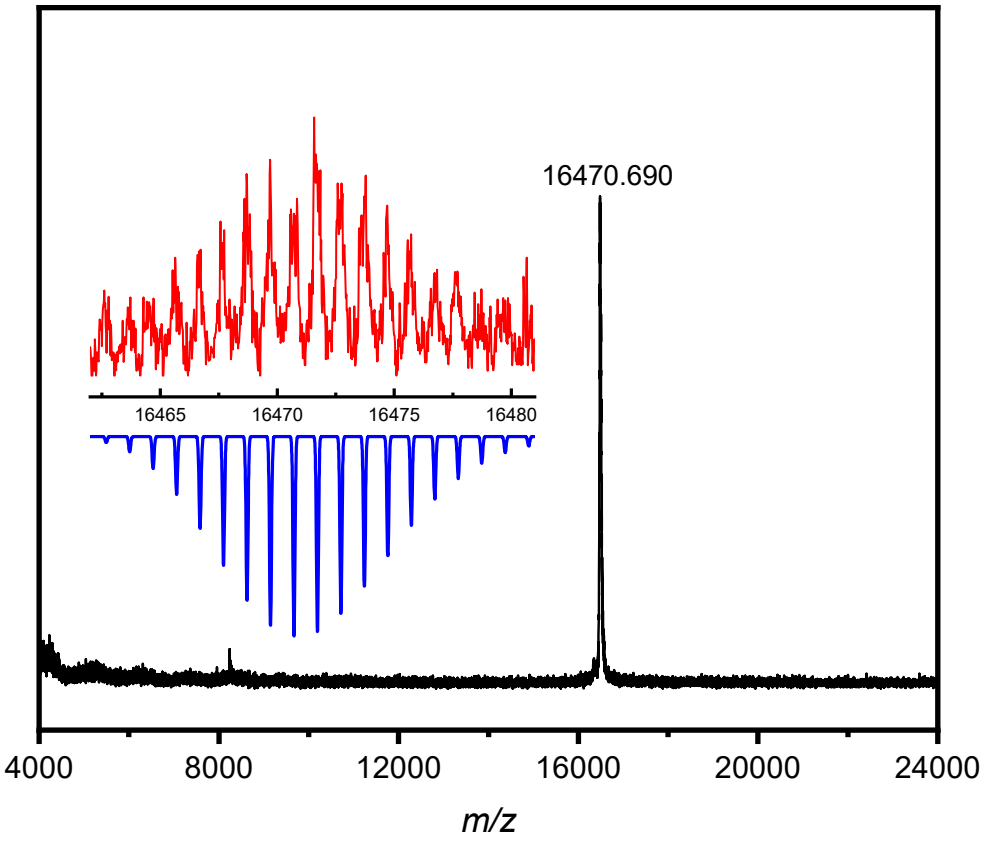

Figure 8.2.5: MALDI-TOF mass spectrum of **DecBi-Catenane**.

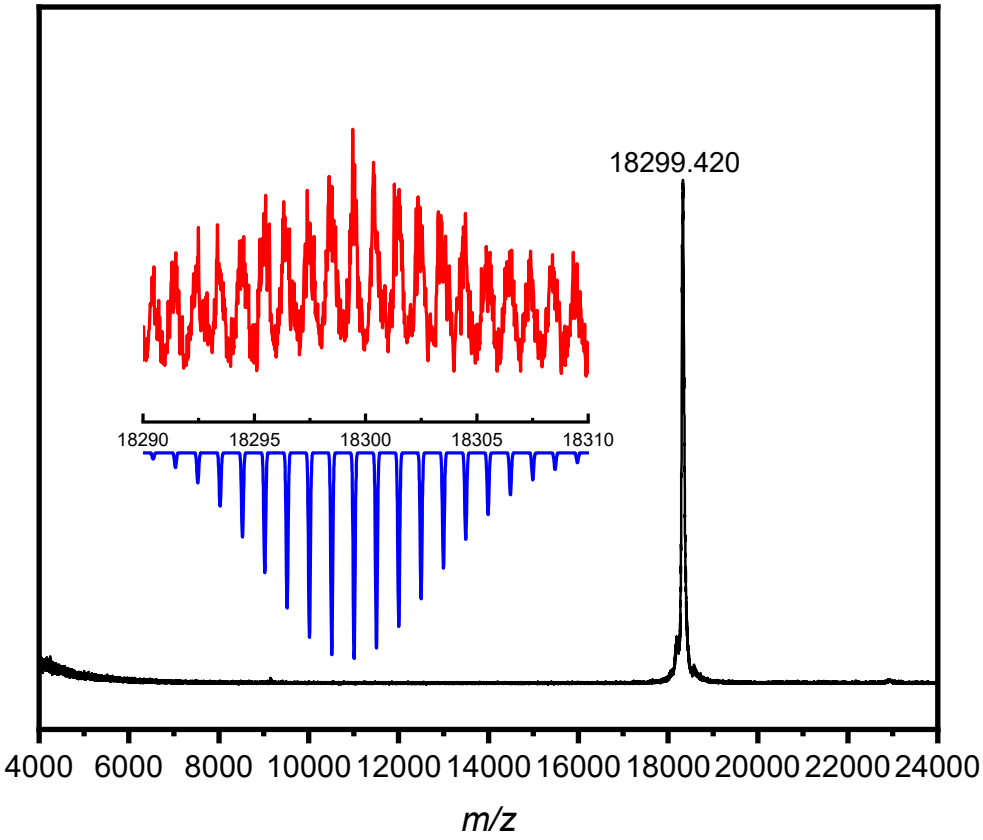

Figure 8.2.6: MALDI-TOF mass spectrum of **DecTri-Catenane**.

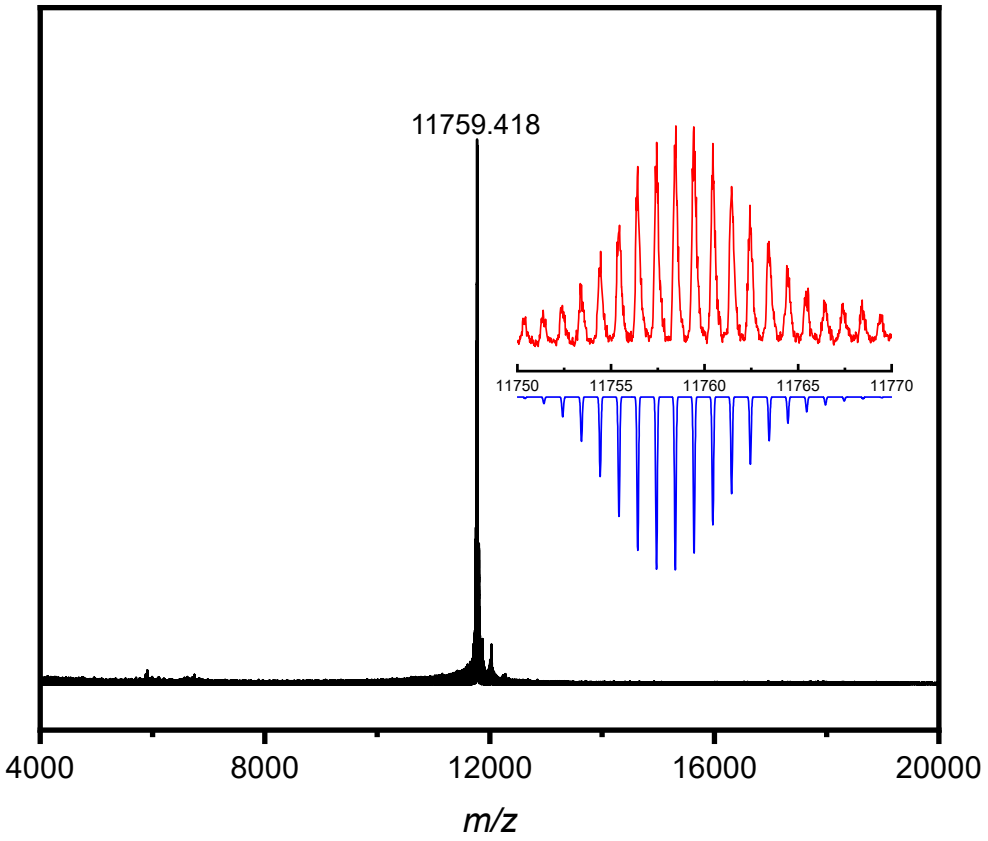

Figure 8.2.7: MALDI-TOF mass spectrum of **ProBi-Catenane**.

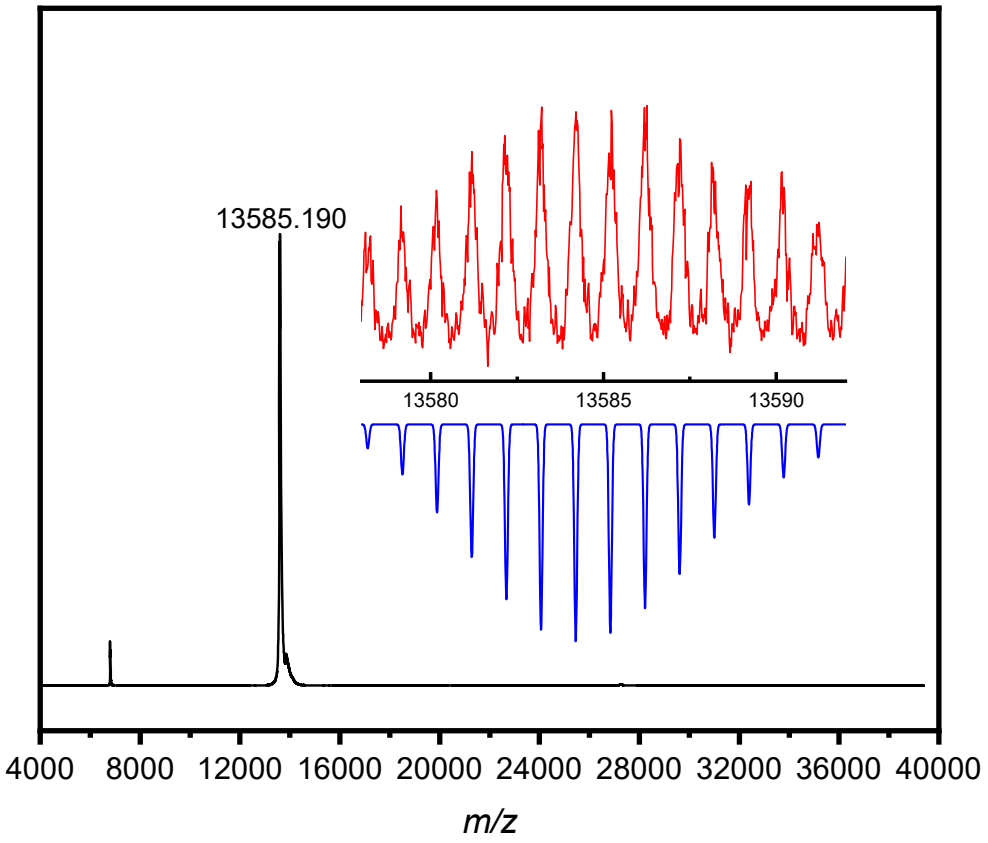

Figure 8.2.8: MALDI-TOF mass spectrum of **ProTri-Catenane**.

8.3 X-ray Crystallographic Structure Determination

Table 8.3.1 Crystal data and structure refinement for **116**.

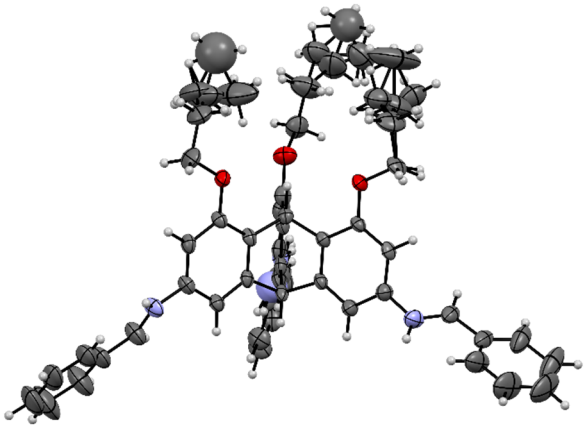

Empirical formula	C54H60N3O4
Formula weight	518.05
Temperature	200(2) K
Wavelength	0.71073 Å
Crystal system	Monoclinic
Space group	$P2_1/n$
Z	4
Unit cell dimensions	a = 8.6710(11) Å α = 90 deg. b = 18.916(2) Å β = 91.380(3) deg. c = 28.092(3) Å γ = 90 deg.
Volume	4606.3(10) $Å^3$
Density (calculated)	1.17 g/cm_3
Absorption coefficient	0.07 mm^{-1}
Crystal shape	plank
Crystal size	0.246 × 0.108 × 0.038 mm^3
Crystal color	brown
Theta range for data collection	1.3 to 23.8 deg.
Index ranges	-9≤ h ≤9, -21≤ k ≤21, -30≤ l ≤31
Reflections collected	38619
Independent reflections	7067 (R(int) = 0.1057)
Observed reflections	4297 (I > 2σ (I))
Absorption correction	Semi-empirical from equivalents
Max. and min. transmission	0.96 and 0.88
Refinement method	Full-matrix least-squares on F^2
Data/restraints/parameters	7067 / 1023 / 618
Goodness-of-fit on F^2	1.09
Final R indices (I>2sigma(I))	R1 = 0.095, wR2 = 0.215
Largest diff. peak and hole	0.30 and -0.37 $eÅ^{-3}$

Table 8.3.2 Crystal data and structure refinement for **115**.

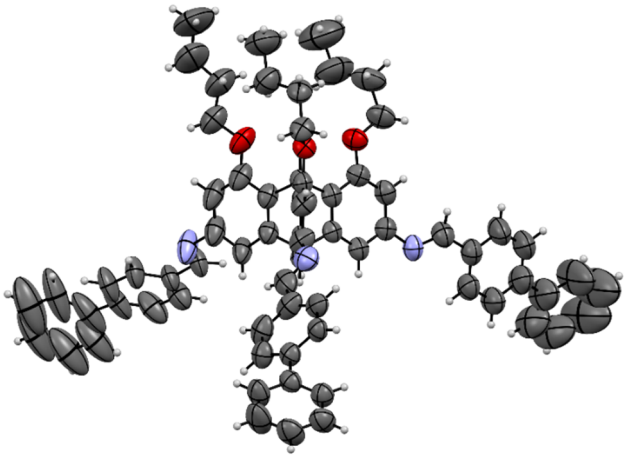

Empirical formula	$C_{71}H_{65}N_3O_3$
Formula weight	1008.26
Temperature	200(2) K
Wavelength	1.54178 Å
Crystal system	triclinic
Space group	$P\bar{1}$
Z	4
Unit cell dimensions	a =8.4592(2) Å α =78.062(2) deg. b =19.2151(5) Å β =84.054(2) deg. c =37.9238(10) Å γ =78.913(2) deg.
Volume	5905.3(3) $Å^3$
Density (calculated)	1.13 g/cm^3
Absorption coefficient	0.53 mm^{-1}
Crystal shape	plate
Crystal size	0.176×0.093×0.068 mm^3
Crystal color	yellow
Theta range for data collection	2.4 to 65.5 deg.
Index ranges	-8≤ h ≤9, -20≤ k ≤22, -44≤ l ≤37
Reflections collected	46792
Independent reflections	18590 (R(int) = 0.0445)
Observed reflections	12144 (I > 2σ (I))
Absorption correction	Semi-empirical from equivalents
Max. and min. transmission	0.97 and 0.53
Refinement method	Full-matrix least-squares on F^2
Data/restraints/parameters	18590 / 4531 / 1343
Goodness-of-fit on F^2	2.29
Final R indices (I>2sigma(I))	R1 = 0.118, wR2 = 0.331
Largest diff. peak and hole	0.69 and -0.62 $eÅ^{-3}$

9. Abbreviations

°C	degree centigrade
°	degree
1D	one-dimensional
2D	two-dimensional
3D	three-dimensional
Å	angstrom
ATR	attenuated total reflection
B_2pin_2	bis(pinacolato)diboron
B3LYP	Becke, 3-parameter, Lee-Yang-Parr
BHT	butylated hydroxytoluene
Bpin	boronic acid pinacol ester
bpy	2,2'-bipyridine
Bu	*n*-butyl
Calcd.	calculated
CCDC	Cambridge Crystallographic Data Centre
cm	centimeter
conc.	concentrated
COSY	correlation spectroscopy
DCM	dichloromethane
dec.	decomposition
DFT	density functional theory
DMF	*N*, *N*-dimethylformamide
dtbpy	4,4'-di-*tert*-butyl-2,2'-dipyridine
EA	elemental analysis
equiv.	equivalent
Et	ethyl
FT-IR	Fourier transform-infrared
g	gram
GP	general procedure
h	hour
HMBC	heteronuclear multiple-bond correlation spectroscopy
DOSY	diffusion-ordered spectroscopy
HPLC	high-performance liquid chromatography
HRMS	high-resolution mass spectrometry
HSQC	heteronuclear single-quantum correlation spectroscopy

i-Pr	*iso*-propyl
K	Kelvin
kcal	kilocalorie
kJ	kilojoule
M	mol per liter
MALDI	matrix-assisted laser desorption
max	maximal
Me	methyl
Mes	mesityl
MHz	megahertz
min	minute
mM	millimol per liter
MS	mass spectrometry
m.p.	melting point
NBS	*N*-bromosuccinimide
nm	nanometer
NMR	nuclear magnetic resonance
NOESY	nuclear Overhauser effect spectroscopy
o-	*ortho*-
o-DCB	*ortho*-dichlorobenzene
Ph	phenyl
r.t.	room temperature
RCM	ring-closing olefin metathesis
Ref.	reference
r-GPC	recycling gel permeation chromatography
ROESY	rotating frame nuclear overhauser effect spectroscopy
s	second
TFA	trifluoroacetic acid
THF	tetrahydrofuran
TLC	thin layer chromatography
TMS	trimethylsilyl
TOF	time of flight
XRD	X-ray diffraction
δ	chemical shift
µm	micrometer

10. Acknowledgments

Time flies and four years have passed in the blink of an eye. This thesis marks the end of a fantastic journey in Heidelberg that has witnessed the growth of both my spirit and mind. To be honest, pursuing the Ph.D. was challenging academically and personally, especially during the Covid-19 pandemic. It is impossible for me to make it without the help, support, and encouragement of the following people:

First and foremost, I am immensely grateful to Professor Micheal Mastalerz for being such a tremendous supervisor. His support, constant encouragement and guidance were significant for the progress of my scientific projects. His emphasis on experimental safety also ensures us a good research environment. His passion and critical mind for science are also inspiring me to be a better scientist.

Further thanks go to all the staff and technicians from the Organisch-Chemisches Institut: Dr. Jürgen Graf and his colleagues (NMR measurements), Dr. Jürgen Gross and his colleagues (MS measurements), Dr. Frank Rominger, and Margit Brückner (crystal structure analysis) for the technical and analytical support. Special thanks to Dr. Wen-Shan Zhang in the BioQuant for doing SEM experiments. Without her collaboration, I couldn't make any progress on my first project.

I would like to thank all the group members of Mastalerz's group, they have provided me with lots of support and help. Thanks to Dr. Sven Elbert, our scientific coordinator, who introduced me to the group and helped me a lot in my Ph.D. career. His enthusiasm for science and life also impressed me. I am also thankful to Jochen Lauer, my box mate. He is so friendly and supportive, and we had a lot of conversations, which help me acquire more scientific knowledge and also German culture. Special thanks to Dr. Bahiru Punja Benke, Alexander Galow né Ullrich, Tobias Kirschbaum, Mattes Holsten, and Dr. Sviatoslav Batsyts for the discussions of my projects and the kind revision of this thesis. I would thank Tobias Kirschbaum for teaching me to use the calculation software and also for helping me resolve lots of problems during writing the thesis. I also thank Ms. Ute Gärtner for her help in chemical supplies and equipment maintenance.

Especially, I am grateful that I have these Chinese friends at Heidelberg: Dr. Xubin Wang, Dr. Yangyang Yang, Dr. Xinyue Hu, Dr. Xuan Yang, Dr. Zishuo Zhou, Dr. Chunyu Han, Ke Tian, Hongwei Shi, Dan Wang, and Xuping Yan. They light up my life and make my time in Heidelberg more enjoyable. I want to thank Dr. Xubin Wang, Dr. Yangyang Yang, and Ke Tian for taking care of me when I was sick in the hospital.

I’m also thankful to the CSC (Chinese Scholarship Council) scholarship for their financial support of my Ph.D. research.

Last but not least, I would like to thank my family. No words could express my thanks to my parents for supporting me tirelessly throughout my life. Most of all I want to thank my wife, Qi Yu, the love of my life. She is always so supportive, loving, and understanding, and always being there for me and for supporting my goals and dreams.

This thesis is dedicated to my family.

Gangxiang Zhou, September 2022

Eidesstattliche Versicherung gemäß § 8 der Promotionsordnung für die Gesamtfakultät für Mathematik, Ingenieur- und Naturwissenschaften der Universität Heidelberg

1. Bei der eingereichten Dissertation zu dem Thema „**Synthesis of Interlocked [8+12] Organic Cages and Investigation of Catenation Mechanism**“ handelt es sich um meine eigenständig erbrachte Leistung.

2. Ich habe nur die angegebenen Quellen und Hilfsmittel benutzt und mich keiner unzulässigen Hilfe Dritter bedient. Insbesondere habe ich wörtlich oder sinngemäß aus anderen Werken übernommene Inhalte als solche kenntlich gemacht.

3. Die Arbeit oder Teile davon habe ich bislang nicht an einer Hochschule des In- oder Auslands als Bestandteil einer Prüfungs- oder Qualifikationsleistung vorgelegt.

4. Die Richtigkeit der vorstehenden Erklärungen bestätige ich.

5. Die Bedeutung der eidesstattlichen Versicherung und die strafrechtlichen Folgen einer unrichtigen oder unvollständigen eidesstattlichen Versicherung sind mir bekannt.

Ich versichere an Eides statt, dass ich nach bestem Wissen die reine Wahrheit erklärt und nichts verschwiegen habe.

Ort und Datum	Unterschrift